Physics of Atomic Nuclei, Vol. 65, No. 10, 2002, pp. 1749–1770. From Yadernaya Fizika, Vol. 65, No. 10, 2002, pp. 1795–1818.

REVIEWS

Overview of the CKM Physics Opportunities beyond $K^+ \to \pi^+ \nu\bar{\nu}$*[1)]

L. G. Landsberg

Institute for High Energy Physics, Protvino, Moscow oblast, 142284 Russia

Received December 6, 2001

Abstract—A new experiment CKM is accepted by Fermilab for a very sensitive study of rare kaon decay $K^+ \to \pi^+ \nu\bar{\nu}$ on an intense separated kaon beam. The high quality of the beam and CKM setup make it possible to perform an important set of other kaon-decay measurements in parallel with the main research program: (1) the search for new physics effects beyond the Standard Model (search for new P, S, T interactions and lepton flavor violation in kaon decays); (2) further search for direct CP violation in charged kaon decays; (3) study of low-energy hadron physics in pure conditions of decay processes ($K^+ \to \pi^+ l^+ l^-$; $\pi\pi l\nu_l$; $\pi^0\gamma\gamma$, etc.). The expected results of these studies are compared with other experimental programs.

1. INTRODUCTION

In 2001, a new experiment "Charged Kaon at Main Injector" [1] (CKM, or E921) was accepted by Fermilab and is now in the stage of technical design and preparation. The main aim of this experiment is to measure the branching ratio of the ultrarare charged kaon decay $K^+ \to \pi^+ \nu\bar{\nu}$ by observing approximately 10^2 events of this decay with small background.

The CKM experiment will open the possibility of determining the magnitude of the Cabibbo–Kobayashi–Maskawa matrix element $|V_{td}|$ with statistical uncertainty of about 5% and total precision around 10%. This decay mode is known to be theoretically clean with the only significant correction due to charm contribution (see details in [1] and in the references therein). It will play a crucial role in the testing of the Standard Model (SM) predictions for the mechanism of CP violation and for properties of FCNC (flavor-changing neutral current) processes.

Evidence for $K^+ \to \pi^+ \nu\bar{\nu}$ was obtained in the BNL E787 experiment with kaon decays at rest where two clear events of this decay was observed and the branching ratio $\mathrm{BR}(K^+ \to \pi^+ \nu\bar{\nu}) = (1.57^{+1.75}_{-0.82}) \times 10^{-10}$ was measured [2]. In the new version of this experiment with the upgraded setup (BNL E949), which is now beginning at BNL [3], it will be possible to obtain several events of $K^+ \to \pi^+ \nu\bar{\nu}$ in the kaon decays at rest. But a really large increase in statistics is expected in a new type of experiment—the CKM at Fermilab.

The experimental technique that will be used in this experiment is decay in flight in a ~22 GeV separated K^+ beam with kaon flux of 30 MHz and a purity of higher than 70%. K^+ are generated by about 5×10^{12} 120-GeV protons per spill from Main Injector. The CKM detector will have redundant measurements for both the primary K^+ and the secondary π^+ with high-rate magnetic spectrometers and RICH velocity spectrometers based on phototube ring imaging Cherenkov counters for each particle. A hermetic photon veto system capable of rejecting π^0 decays from background processes with inefficiency less than 1.6×10^{-7} and a muon range hodoscope veto system with inefficiency less than 1×10^{-5} are also required. The expected signal acceptance of the CKM setup for $K^+ \to \pi^+ \nu\bar{\nu}$ after all cuts will be ~2%. A date collection period of 2 years should yield a signal ~10^2 events over a background of less than 10 events (assuming theoretical branching ratio BR $(K^+ \to \pi^+ \nu\bar{\nu}) \simeq 1 \times 10^{-10}$).

The possible agreement between the results of independent measurements for kaon- and B-meson-decay processes would implement a very stringent test of the SM CP-violation mechanism associated with the complexness of the quark-mixing CKM matrix. But if there are some other CP-violation mechanisms beyond the SM, these new mechanisms quite probably would affect differently the properties of different processes and all sets of measurements will demonstrate these differences quite unambiguously.

But in any case, it is important to stress here that, quite recently in the BaBar and Belle experiments, the study of charge asymmetry in $B^0_d(\bar{B}^0_d) \to \psi K^0_S$ decay gave the value of $a_{\psi K_S} = \sin 2\beta = 0.79 \pm 0.10$ [4], which is in very good agreement with the SM prediction (here, β is an angle in a unitarity triangle—see

*This article was submitted by the author in English.

[1)]The extended version of the author's talk on the Meeting of the CKM Collaboration, University of Michigan, Ann Arbor, July 2001.

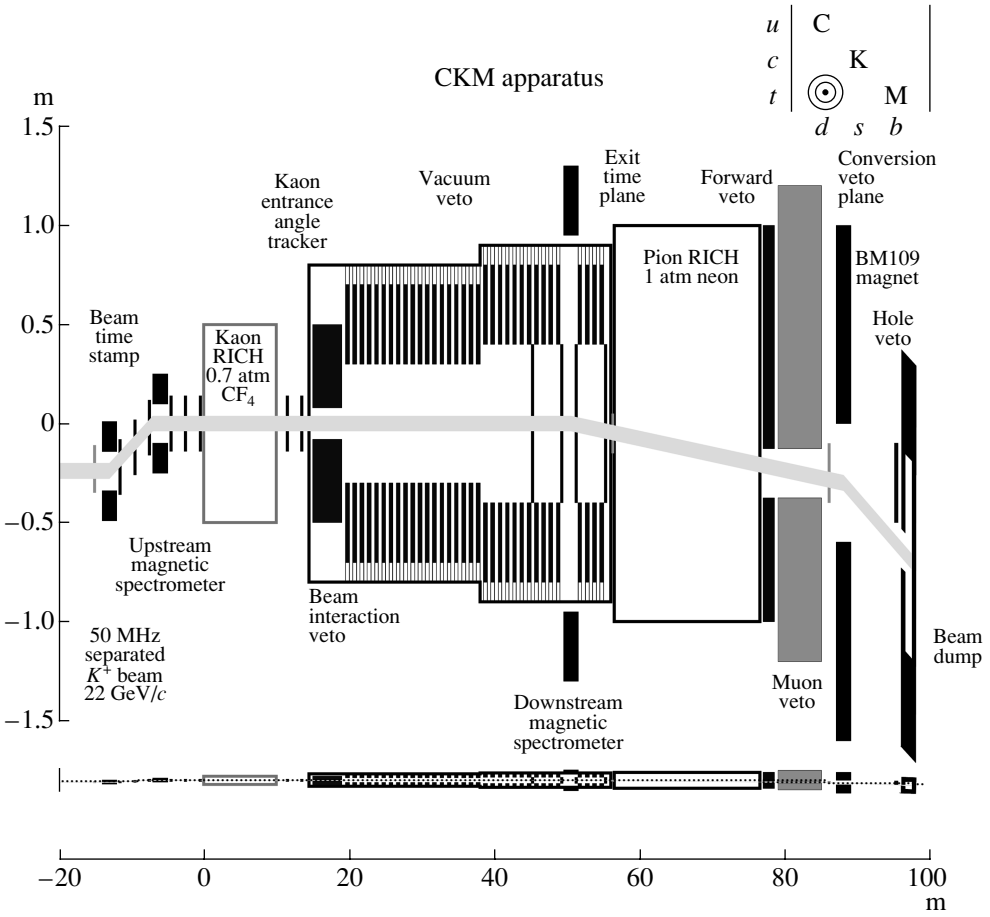

Fig. 1. The CKM Detector [1]. The lower section shows the true proportions of the apparatus. The main components of the setup are presented in this figure (see also text).

below in Fig. 3). As I understand, it is the first precision test of the CP violation in the SM and may be of considerable importance in the future understanding of leading mechanisms of the CP violation. It also increases the significance of $K^+ \to \pi^+\nu\bar{\nu}$ results of the CKM and BNL E949.

The study of $K^+ \to \pi^+\nu\bar{\nu}$ is the main aim of the CKM experiment. But the large intensity of the charged kaon beam and high quality and capability of the apparatus also open the possibility of performing in parallel or in special short dedicated runs other important measurements in kaon physics. These possibilities are considered in some detail below.

Table 1. Required inefficiency performance of the CKM photon veto systems

Energy range low–high, GeV	Inefficiency		
	VVS	FVS	PHVS
0.00–0.02	4×10^{-1}	1	1
0.02–0.04	3×10^{-2}	5×10^{-1}	1
0.04–0.06	3×10^{-3}	5×10^{-2}	1
0.06–0.10	7×10^{-4}	5×10^{-3}	1
0.10–0.20	4×10^{-4}	2×10^{-3}	2×10^{-2}
0.20–0.40	1×10^{-4}	5×10^{-4}	5×10^{-3}
0.40–1.00	1×10^{-4}	2×10^{-4}	2×10^{-3}
1.00–10.00	3×10^{-5}	1×10^{-4}	2×10^{-3}

2. APPARATUS

The general layout of the CKM setup is presented in Fig. 1. The CKM detector includes the following:

(1) Primary K^+-meson identification system and measuring double spectrometer with upstream magnetic spectrometer (UMS) with proportional chambers and scintillation kaon entrance angle tracker (KEAT) and Kaon RICH velocity spectrometer (double redundant measurement of primary kaon);

(2) High-vacuum 30-m-long decay region with quite effective photon vacuum veto system (VVS) and beam interaction veto system (BIVS);

(3) Downstream magnetic spectrometer (DMS) with straw tubes in vacuum and with two exit time planes (ETP) of scintillation hodoscopes and Pion

RICH velocity spectrometer (double redundant measurement of the secondary π^+);

(4) High efficiency photon forward veto system (FVS)—γ spectrometer with high resolution CsI scintillation counters;

(5) Muon veto system (MVS)—hodoscopical rang stack system for muon rejection with inefficiency $<10^{-5}$;

(6) Photon hole veto system (PHVS) after additional magnet at the end of the setup to increase the hermetism of photon veto system.

The CKM experiment will be performed on a new RF separated charged kaon beam with momentum of 22 GeV and full intensity of 50 MHz (30-MHz kaons, 7.5-MHz pions, 7.5-MHz muons).

The photon veto is characterized by high efficiency, which is presented in Table 1. These values are important for estimation of the background level for many processes.

The possibility of the CKM setup for background rejection for $K^+ \to \pi^+\nu\bar{\nu}$ is characterized in Table 2, in which the numbers of background events from different processes are presented. We see that this expected background is favorable for measuring of BR($K^+ \to \pi^+\nu\bar{\nu}$) on the statistics of $\sim 10^2$ events. The selection of $K^+ \to \pi^+\nu\bar{\nu}$ events and the suppression of the $K^+ \to \pi^+\pi^0$ background is illustrated in Fig. 2. The expected result of the CKM experiment for the determination of the SM unitary triangle parameters is presented in Fig. 3 together with the data of other kaon and B-meson experiments.

3. GENERAL DESCRIPTION OF OTHER KAON DECAYS

The CKM setup is characterized by excellent spatial and time resolution and includes two magnetic spectrometers and two RICH velocity spectrometers that will provide particle identification through precise velocity measurements. The CKM setup also includes a quite efficient photon veto system, photon spectrometers, a muon veto system, and muon identification, as well as a quite complicated and reliable trigger and data acquisition system (DAQ) of the pipeline type. The setup will provide the redundant measurement capabilities necessary for contemporary rare kaon decay studies with sensitivity up to 10^{-12}.

While the CKM experiment will accept no compromises in either the sensitivity or background rejection required for the main $K^+ \to \pi^+\nu\bar{\nu}$ measurement, several other interesting physics measurements should be possible with this apparatus.

The main directions of these additional measurements are the following:

(1) The search for new physical effects beyond the SM (lepton-flavor-violation processes; search for new scalar (S), pseudoscalar (P), and tensor (T) weak interactions in $K^+ \to e^+\nu, \pi^0 e^+\nu_e$ decays; etc.).

Table 2. Background estimates in terms of effective branching ratio

Background source	Effective BR, 10^{-12}
$K^+ \to \mu^+\nu_\mu$	< 0.04
$K^+ \to \pi^+\pi^0$	3.7
$K^+ \to \mu^+\nu_\mu\gamma$	< 0.09
$K^+A \to K_L X$ followed by $K_L \to \pi^+ e^-\nu$	< 0.14
$K^+A \to \pi^+ X$ in trackers	< 4.0
$K^+A \to \pi^+ X$ in residual gas (10^{-6}torr)	< 2.1
Accidentals (2 K^+ decays)	0.51
Total	< 10.6

(2) Further search for direct CP violation in K^+ decays (charge asymmetry in $K^\pm \to \pi^\pm\pi\pi; \pi^\pm\pi^0\gamma$; T-odd correlations in $K^+ \to \pi^0 l^+\nu_l\gamma$ decays). The observable effects in these searches are possible only beyond the SM.

(3) Low-energy hadron physics studies in the pure conditions of kaon decays ($K^+ \to \pi^+ l^+ l^-; \pi^+\pi^0\gamma$; $\pi\pi l^+\nu_l; l^+\nu_l\gamma$, $\pi^0\gamma\gamma$, etc.). The importance of these investigations is connected with fundamental quark confinement problem and with further development of lattice QCD, CHPT (chiral perturbation theory), and other hadron theories.

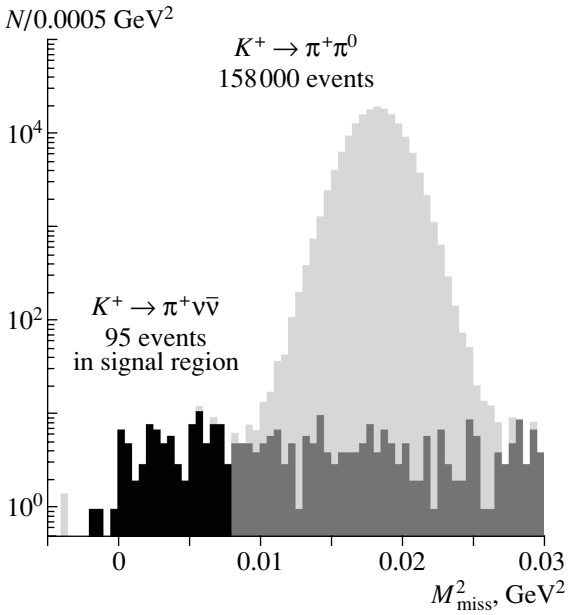

Fig. 2. The combined measured missing mass squared $M^2_{\rm miss}$ of the two spectrometers reconstructed in CKM GEANT ($M^2_{\rm miss} = M^2_{\nu\bar{\nu}}$ for $K^+ \to \pi^+\nu\bar{\nu}$). The signal region is shaded [1].

A general description of the CKM experimental possibilities for studying several kaon decays is illustrated in Table 3, which presents the efficiency calculations and expected statistical evaluation of these processes. For the efficiency estimates in Table 3, it was assumed that all decay photons are detected and measured in FVS and all charged decay products are detected in the DMS and can be identified (if it is necessary) in the Pion RICH and muon system.

To increase the efficiency for photon detection in multiphoton events, it was assumed that in some cases the VVS can be used as a photon spectrometer with reduced precision for coordinate and energy measurements (see Section 5). The main problem here is a possible energy leakage for photons with small input angles to the forward surface of the VVS. This question needs further GEANT simulation studies and experimental investigation for final justification.

At this stage, we will not consider the trigger signals for the registration of several rare kaon decays in parallel with the main $K^+ \to \pi^+\nu\bar{\nu}$ measurements. As was clear from some preliminary discussions, the future development of the CKM DAQ system will allow us to use a very intensive data flux and will provide many possibilities of developing the higher trigger levels to select the desired processes.

It is instructive to compare the data of Table 3 with the possibilities of the OKA experiment on the separated charged kaon beam with momentum of 12.5 GeV, which is now in preparation at the IHEP accelerator (Protvino, Russia) [5]. The corresponding sensitivity estimates for the OKA measurements are presented in Table 4 (see [5]).

As is seen from these Tables 3 and 4, the expected decay rate at the Fermilab kaon beam (3.6×10^{11} K^+ decay/week) exceeds the same value for IHEP beam (1.6×10^{10} K^+ decay/week) by a factor of $\sim$20.

An additional factor of $\sim$2.5 can be expected from longer duration of the CKM runs. But the acceptances of the CKM for most of the additional measurements are smaller than in the OKA by a factor of 1/4–1/10 (especially for multiphoton events).

Thus, the expected ratio of integral detected decay numbers for these two experiments is $N(\mathrm{CKM})/N(\mathrm{OKA}) \sim 10$–$15$ in favor of the CKM. But wider acceptance of the OKA setup gives some advantages in studying of the characteristics for some decay channels in this experiment.

The comparison of the future possibilities of the CKM and OKA allows one to make several conclusions:

1. The CKM experiment has a definite advantage in the searches for new processes like lepton flavor nonconservation and new mechanisms of CP violation in charged kaon decays.

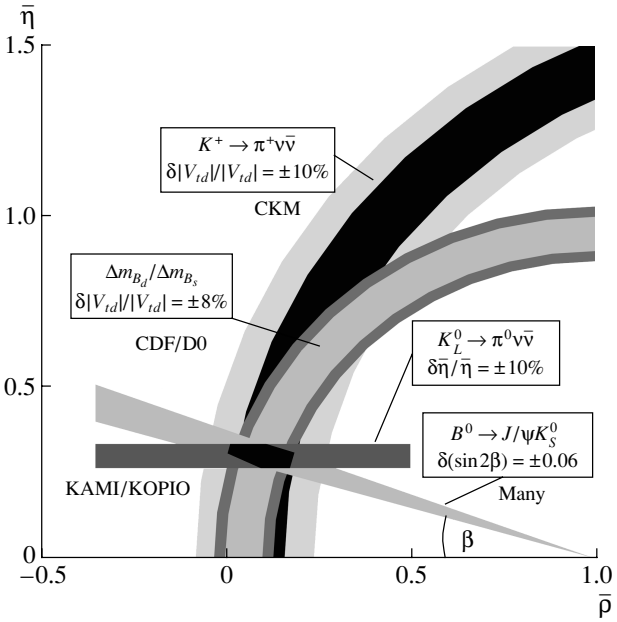

Fig. 3. A possible outcome for parameters of unitary triangle $\bar{\eta}$, $\bar{\rho}$, and β obtained from future K-meson experiments [$K^+ \to \pi^+\nu\bar{\nu}$ (CKM); $K_L^0 \to \pi^0\nu\bar{\nu}$ (KAMI/KOPIO)] and B-meson experiments [$\Delta m_{B_d}/\Delta m_{B_s}$; $B^0(\bar{B}^0) \to J/\psi K_S^0$]. The light region includes possible theoretical uncertainties in $\mathrm{BR}(K^+ \to \pi^+\nu\bar{\nu})$ connected with the influence of c quarks [1].

2. The advantage in the acceptance of the OKA setup makes it possible to do more careful studies of the Dalitz plot distributions, form factors, and other properties for decays with intermediate branching ratios (like $K^+ \to \pi\pi l^+\nu_l$; $\pi^+\pi^0\gamma$, search for scalar and tensor interactions in $K^+ \to \pi^0 l^+\nu_l$, etc.).

3. Thus both experiments are complimentary to each other and together will give the opportunity for careful studies of many decays. In addition, it is useful to bear in mind that the OKA experiment will begin several years earlier that the CKM. A large group of physicists are participating in both experiments, and that gives us a suitable opportunity to obtain in the OKA measurements the first physical results for several decay channels, important information about the separation criteria, and the background situation and systematics for some processes under investigation and to continue these studies on a new level in the CKM experiment.

Now, we will discuss several kaon-decay processes in more detail (see also [1, 6, 7]).

4. LEPTON-FLAVOR-VIOLATING PROCESSES IN K^+ DECAYS IN CKM

The main kaon-decay processes with lepton flavor violation (LFV) are summarized in Table 5, where upper limits for these decays obtained mainly in the

Table 3. The efficiency for the detection and sample size of several kaon decay modes in the CKM detector

Decay	BR	Efficiency	Events/week
$K^+ \to \pi^0\mu^+\nu_\mu\gamma$	$\sim 2 \times 10^{-5}$	0.0080	5.8×10^4
$K^+ \to \pi^0 e^+\nu_e\gamma$	$(2.62 \pm 0.20) \times 10^{-4}$	0.0022	2.1×10^5
$K^+ \to \pi^+\pi^+\pi^-$	$(5.59 \pm 0.05) \times 10^{-2}$	0.20	4.0×10^9
$K^+ \to \pi^+\pi^0\pi^0$	$(1.73 \pm 0.04) \times 10^{-2}$	0.0040	2.5×10^7
$K^+ \to \pi^+\pi^0\gamma$	$(2.75 \pm 0.15) \times 10^{-4}$	0.011	1.1×10^6
$K^+ \to \pi^+ e^+ e^-$	$(2.88 \pm 0.13) \times 10^{-7}$	0.012	1.2×10^3
$K^+ \to \pi^+\mu^+\mu^-$	$(7.6 \pm 2.1) \times 10^{-8}$	0.086	2.3×10^3
$K^+ \to \mu^+\nu_\mu\gamma$	$(5.50 \pm 0.28) \times 10^{-3}$	0.050	1.0×10^8
$K^+ \to \pi^+\pi^- e^+\nu_e$	$(3.91 \pm 0.17) \times 10^{-5}$	0.066	9.3×10^5
$K^+ \to \pi^0\pi^0 e^+\nu_e$	$(2.1 \pm 0.4) \times 10^{-5}$	0.0093	7.0×10^4
$K^+ \to \pi^+\pi^-\mu^+\nu_\mu$	$(1.4 \pm 0.9) \times 10^{-5}$	0.28	1.4×10^6
$K^+ \to \pi^0\pi^0\mu^+\nu_\mu$	$\sim 0.7 \times 10^{-5}$	0.0024	6.1×10^3

Notes: 1. For expected statistics evaluation, we used MC values for efficiencies of different decays, the K^+ flux of 3×10^7 K^+/spill, decay region of 30 m (17% K^+ decays), and effective number of spill/week of 1.4×10^5 (70% effective time). These numbers correspond to 7.1×10^{11} K^+ decay/week. To take into consideration dead-time effects (30%) and possible additional cuts to suppress background, we use in these estimations the reduced effective number of 3.6×10^{11} K^+ decay/week.

2. In the efficiency calculations, it was assumed that all photons are measured in the FVS. If some of the photons in $\pi^0\pi^0$ decays are measured in VVS, the efficiency of corresponding process will increase by 2–3 times.

E865 BNL experiment [8, 9] are presented. For completeness, we also included in this table the last LFV results from K_L^0 decays [10–12].

From the statistical consideration, there is a clear opportunity for the CKM experiment to perform (in parallel with the main $K^+ \to \pi^+\nu\bar{\nu}$ study) much more sensitive searches for all those K^+ LFV decays up to the level BR $\sim 10^{-12}$. These limits correspond to effective number of K^+ decays in two years of measurement $N(K^+ \text{ decays}) = (3.6 \times 10^{11}$ decays/week$) \times (78$ weeks$) = 2.81 \times 10^{13}(K^+$ decays). The details are presented in Table 3. These numbers include a safety factor of 0.5 to take into account dead-time effects and additional cuts. Certainly, very careful investigations of possible background limitations for LFV kaon decays must be done. Some of these works have already begun.

Even a sensitivity of 10^{-12} for kaon LFV processes looks now modest in comparison with ambitious new proposals for the search for $\mu \to e\gamma$ and $\mu^- + (A, Z) \to e^- + (A, Z)$ LFV processes on the level BR $< 10^{-14}$–10^{-16} [13]. The difference in the sensitivities of future muon and kaon LFV experiments would be even larger due to additional factor $\tau_\mu/\tau_K \sim 10^2$ included in the limitations for the corresponding partial decay widths: $\Gamma(\text{kaon LFV})/\Gamma(\text{muon LFV}) = [\text{BR(kaon LFV)}/\text{BR(muon LFV)}](\tau_\mu/\tau_K) \simeq (10^2$–$10^4) \times 10^2 \simeq 10^4$–$10^6$ (τ_μ and τ_K are the lifetimes for muons and kaons).

But it is very important to stress that the searches for LFV in kaon decays are complimentary to the $\mu \to e\gamma$ type of experiments. Kaon decays are the only processes that are sensitive to $s \to d\mu\bar{e}$ interactions which may possess very exceptional properties. These processes open a unique possibility of studying LFV decays with fundamental generation number conservation and of investigating the hypothetical selection rule for this number. In other words, for these decays, a change of generation in the leptonic sector can be compensated by a change of generation in the quark sector ([14]; see also [15]). Let us introduce the generation number $G_1 = 1$ for the first fundamental fermion generation and $G_2 = 2$ for the second one (for antifermions $G_1 = -1, G_2 = -2$). Then, as is seen from the diagrams in Fig. 4, it is possible to classify different processes according to changing ΔG, as follows from Table 6. The strength of the hypothetical ΔG selection rule is unclear now. Certainly, the new possibilities for the search for LFV processes in kaon decays will occur only if this strength is important and every next order on ΔG will lead to significant suppression of the corresponding process to compare with lower order. We must bear in mind an unexpected difference between $K^+ \to \pi^+\mu^+e^-$ and $K^+ \to \pi^+\mu^-e^+$ in the model with conserved generation number according to the ΔG selection rule.

In the diagrams in Fig. 4, the decay processes are governed by exchange of "horizontal" intermediate boson H^0. But it is also possible to consider

Table 4. The efficiency for the detection and sample size of several kaon decay channels for the OKA experiment on the separated K^+ beam of IHEP accelerator [5]

Decay	BR	New magnet		Old SPHINX magnet		New magnet
		ϵ_1	$(\text{events/week})_1$	ϵ_2	$(\text{events/week})_2$	events/5.76×10^{11} K^+ decays (36 weeks of measurements)
$K^+\to\pi^+\pi^+\pi^-$	$(5.59\pm0.05)\times10^{-2}$	0.76	6.8×10^8	0.64	5.7×10^8	2.4×10^{10}
$K^+\to\pi^+\pi^0\pi^0$	$(1.73\pm0.04)\times10^{-2}$	0.47	1.3×10^8	0.32	8.9×10^7	4.7×10^9
$K^+\to\mu^+\nu_\mu\gamma$	$(5.50\pm0.28)\times10^{-3}$	0.54	4.8×10^7	0.43	3.8×10^7	1.7×10^9
$K^+\to\pi^0\mu^+\nu_\mu\gamma$	$\sim2\times10^{-5}$	0.44	1.4×10^5	0.30	9.6×10^4	5.1×10^6
$K^+\to\pi^0e^+\nu_e\gamma$	$(2.62\pm0.20)\times10^{-4}$	0.24	1.0×10^6	0.16	6.7×10^5	3.6×10^7
$K^+\to\pi^+\pi^0\gamma$	$(2.75\pm0.15)\times10^{-4}$	0.47	2.1×10^6	0.32	1.4×10^6	7.4×10^7
$K^+\to\pi^+\pi^-e^+\nu_e$	$(3.91\pm0.17)\times10^{-5}$	0.27	1.7×10^5	0.21	1.3×10^5	6.1×10^6
$K^+\to\pi^0\pi^0e^+\nu_e$	$(2.1\pm0.4)\times10^{-5}$	0.18	6.0×10^4	0.12	4.0×10^4	2.2×10^6
$K^+\to\pi^+\pi^-\mu^+\nu_\mu$	$(1.4\pm0.9)\times10^{-5}$	0.73	1.6×10^5	0.61	1.4×10^5	5.9×10^6
$K^+\to\pi^0\pi^0\mu^+\nu_\mu$	$\sim0.7\times10^{-5}$	0.44	4.9×10^4	0.30	3.4×10^4	1.8×10^6
$K^+\to e^+\nu_e$	$(1.55\pm0.07)\times10^{-5}$	0.53	1.3×10^5	0.44	1.1×10^5	4.7×10^6
$K^+\to\pi^0e^+\nu_e$	$(4.82\pm0.06)\times10^{-2}$	0.32	2.5×10^8	0.23	1.8×10^8	8.9×10^9
$K^+\to\pi^0\mu^+\nu_\mu$	$(3.18\pm0.08)\times10^{-2}$	0.48	2.4×10^8	0.34	1.7×10^8	8.8×10^9
$K^+\to\pi^+e^+e^-$	$(2.88\pm0.13)\times10^{-7}$	0.12	5.5×10^2	0.07	3.2×10^2	2.0×10^4
$K^+\to\pi^+\mu^+\mu^-$	$(7.6\pm2.1)\times10^{-8}$	0.43	5.2×10^2	0.29	3.5×10^2	1.9×10^4

Notes: 1. For expected statistics evaluation, we used MC estimations for the efficiencies of different decay modes, K^+ flux of 5×10^6 K^+/spill, decay region of 12 m (12% K^+-decay probability), and effective number of spill/week of 5.2×10^4 (70% effective time). These numbers correspond to 3.2×10^{10} K^+ decay/week. To take into consideration effects of dead-time losses and additional cuts to suppress background, we will use in the effective number calculations the effective flux of 1.6×10^{10} K^+ decay/week (reduced by an additional factor of two).

2. To estimate the decay rates in the OKA setup, we used geometry with old SPHINX magnet $(\text{events/week})_2$ and with possible new magnet $(\text{events/week})_1$.

3. With a new magnet, it will be possible to realize a more effective setup arrangement and to obtain additional gains in the decay rates which were not considered in this table.

4. In the efficiency calculations, it was assumed that all photons for secondary-particle identification would be measured in two lead-glass γ spectrometers of the OKA setup. The effective photon veto system would not be used for photon spectroscopy aims.

Table 5. Lepton flavor violation in kaon decays

Mode	BR limit	Expected CKM BR limits
$K^+\to\pi^+\mu^+e^-$	2.8×10^{-11} [8]	2.2×10^{-12}
$K^+\to\pi^+\mu^-e^+$	5.2×10^{-10} [9]	2.2×10^{-12}
$K^+\to\pi^-\mu^+e^+$	5.0×10^{-10} [9]	2.2×10^{-12}
$K^+\to\pi^-\mu^+\mu^+$	3.0×10^{-9} [9]	7.2×10^{-13}
$K^+\to\pi^-e^+e^+$	6.4×10^{-10} [9]	5.6×10^{-12}
$K_L^0\to\mu e$	4.7×10^{-12} [10]	
$K_L^0\to\pi^0\mu e$	4.4×10^{-10} [11]	
$K_L^0\to e^\pm e^\pm\mu^\mp\mu^\mp$	1.36×10^{-10} [12]	

kaon-decay LFV processes which are governed by exchange of leptoquarks Y^* (see Fig. 5).

Amplitudes for the $s\to d\mu\bar e$ process of pseudoscalar and axial-vector type (for $K_L^0\to\mu\bar e$ decay) or with vector, scalar, and tensor structure (for $K\to\pi\mu\bar e$ decay) with the "horizontal" H^0 boson exchange can be presented with the help of general generation-number-conserving operators [16]:

$$\left.\begin{aligned} Q_{V,A} &= \frac{g_H^2}{2M_H^2}\bar d\gamma_\mu[C_{Lq}P_L + C_{Rq}P_R]s\cdot\bar\mu\gamma^\mu[C_{Ll}P_L + C_{Rl}P_R]e + \text{h.c.}\\ Q_{S,P} &= \frac{g_H^2}{2M_H^2}\bar d[C'_{Lq}P_L + C'_{Rq}P_R]s\cdot\bar\mu[C'_{Ll}P_L + C'_{Rl}P_R]e + \text{h.c.}\end{aligned}\right\}. \quad (1)$$

Table 6. Classification of LFV processes by change of generation quantum number ΔG in the model [14]

Order	$\lvert\Delta G\rvert$	Process
First	0	$K^+ \to \pi^+\mu^+e^-$; $K_L^0 \to \mu^\mp e^\pm$; $K_L^0 \to \pi^0\mu^\mp e^\pm$
Second	1	$\mu \to 3e$; $\mu \to e\gamma$; $\mu^- N \to e^- N$
Third	2	$K^0 \to \bar{K^0}$ ($\Delta m = m_{K_1} - m_{K_2}$); $\mu^- e^+ \to \mu^+ e^-$; $K^+ \to \pi^+\mu^- e^+$

Here, $P_L = (1+\gamma_5)/2; P_R = (1-\gamma_5)/2$; C and C' are constants.

The results of calculation of branching ratios $K \to \mu e$ and $K \to \pi\mu e$ decays for interactions (1) are presented for illustration in Fig. 6 as a function of the scale parameter M_H (for $g_H = g$—a weak constant corresponding to $C, C' = 1$).

There are other interesting models for $s \to d\mu\bar{e}$ processes in the supersymmetry theories with R-parity nonconservation [17, 18], in left–right models with heavy Majorana neutrino [19], and in the leptoquark-exchange model [20].

LFV processes are known to take place both in the Minimal Supersymmetric Model (MSSM) and in its modifications that include violation of R parity. As for the context of the MSSM, rare kaon decays allow one to correlate squark and slepton mixing, while in R-violating supersymmetry one can probe nontrivial products of Yukawa couplings.

Within framework of the MSSM, the magnitudes of the predicted rates depend on the details of the masses and mixings of sparticles including the sneutrinos. Maximal contributions for kaon LFV decays are expected from the box diagrams involving chargino and neutralino exchange.

However, the universal GUT-scale parameters for sfermions and gauginos, are bounded by the limits for pure leptonic LFV decays $\mu \to e\gamma$ and $\mu \to e^+e^+e^-$ and lead to a hopelessly low kaon LFV decay branchings on the order of 10^{-16}–10^{-18}. Only fine tuning of GUT parameters makes it of interest to search for lepton-flavor-violating K decays.

But the situation can be much different in R-parity-violating supersymmetry models as pointed out in [17, 18]. In this case, the gauge symmetry of the SUSY model allows additional Yukawa coupling terms in the superpotential of the form $\lambda L_i L_j \bar{E}_k$, $\lambda' L_i Q_j \bar{D}_k$, $\lambda'' \bar{U}_i \bar{D}_j \bar{D}_k$.

Here, the $L(Q)$ are the left-handed lepton (quark) superfields and the $\bar{E}(\bar{D}, \bar{U})$ are corresponding right-handed fields; $\lambda, \lambda', \lambda'', \lambda_{ijk}$ are coupling constants. Each of these terms gives three Yukawa couplings. For example, the first term is

$$\lambda_{ijk}(L_i L_j \bar{E}_k + L_i \tilde{L}_j \bar{E}_k + \tilde{L}_i L_j \bar{E}_k).$$

It may be seen that these terms involve a single SUSY state and are breaking the R parity of MSSM.

For electroweak $SU(2)$ and color $SU(3)$ symmetry, it was shown that there are 45 R-violating couplings. Certainly, there are many experimental constraints on this set of constants (nonobservation of proton decay and some exotic processes, lepton universality, nonobservation of possible modification of different SM processes). In spite of these limitations, it was stated in [17] that it is still possible that several R-violating operators may be large enough and useful limitations for some of them can be obtained from existing upper limits for LFV kaon decays and from their future searches. In this class of models, while $\mu \to e\gamma$ occurs at the one-loop level, $\mu \to 3e, \mu \to e$ conversion and $K_L^0 \to \mu^\pm e^\mp$ and $K \to \pi\mu^\pm e^\mp$ decays may occur at the tree level via different combinations of couplings. Thus, LFV kaon decays have the possibility of providing important complementary information for these R-parity-violating processes.

For illustration, it is possible to consider $d\bar{s} \to l_j^- l_k^+$ interaction with an effective Lagrangian written in terms of quark and lepton fields [17]:

$$\begin{aligned} L_{d\bar{s}\to l_j^- l_k^+} = \frac{1}{m^2_{\tilde{\nu}_i}}[&\lambda^*_{ijk}\lambda'_{i12}(\bar{s}_R d_L)(\bar{l}_{jL} l_{kR}) \\ &+ \lambda_{ikj}\lambda'^*_{i12}(\bar{s}_L d_R)(\bar{l}_{jR} l_{kR})] \\ &- \frac{\lambda'^*_{ji1}\lambda'_{ki2}}{2m^2_{\tilde{u}_i}}(\bar{s}_R\gamma_\mu d_R)(\bar{l}_{jL}\gamma^\mu l_{kL}). \end{aligned} \quad (2)$$

The tree diagrams for $K^0 \to l_j^- l_k^+$ and $K \to \pi l_j^- l_k^+$ decays are presented in Fig. 7.

The calculations with (2) and upper limits for $K_L^0 \to \mu^\pm e^\mp$ decays (Table 5) give limitations for the values of $\lambda\lambda'/m_{\tilde{\nu}}$ and $\lambda\lambda'/m_{\tilde{u}}$ with sneutrino ($\tilde{\nu}$) and up-squark ($\tilde{u}$) contributions:

$$\left.\begin{aligned} \lambda_{i21}\lambda'_{i12}\left(\frac{100\ \text{GeV}}{m_{\tilde{\nu}}}\right) &\le 6.2\times 10^{-9} \\ \lambda_{i21}\lambda'_{i12}\left(\frac{100\ \text{GeV}}{m_{\tilde{u}}}\right) &\le 1.9\times 10^{-7} \end{aligned}\right\}. \quad (3)$$

From $K \to \pi l_j^- l_k^+$ decays, the upper limits for $\lambda\lambda'/m_{\tilde{\nu}}$ and $\lambda\lambda'/m_{\tilde{u}}$ are 1–2 orders of magnitude larger than in (3).

It is also important to mention the unique properties of the double-muon-decay process $K^+ \to \pi^-\mu^+\mu^+$, which were discussed [18, 21–23] in the

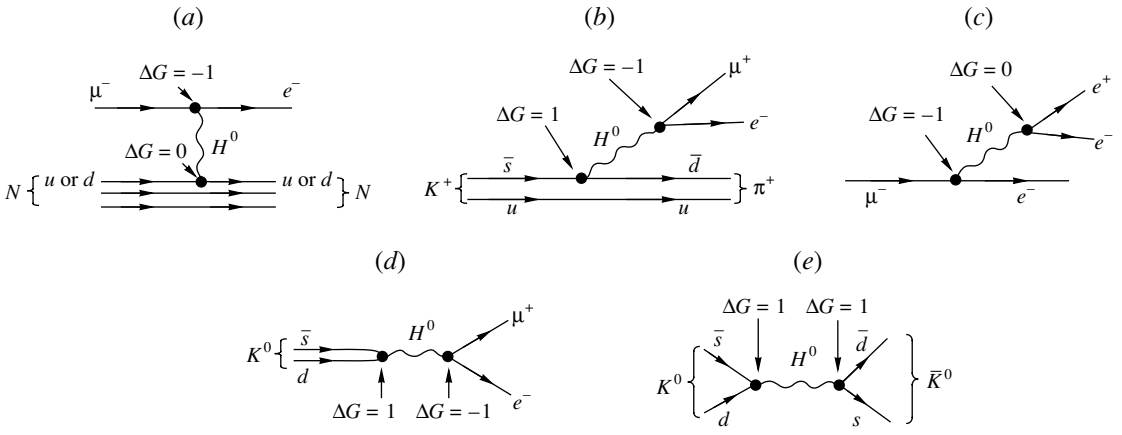

Fig. 4. Diagrams for lepton-flavor-violation processes in the model [14] with generation number selection rule (see text and Table 6).

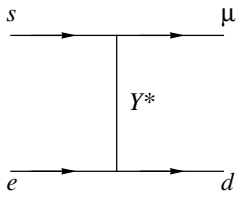

Fig. 5. Diagram for lepton flavor violation in K decay with the mechanism involving the exchange of a Y^* leptoquark.

model of cascade kaon decays with rather heavy Majorana neutrino (with mass of ~300 MeV) $K^+ \to \nu_h \mu^+; \nu_h \to \pi^- \mu^+$ and with a small admixture of ν_h to the muon neutrino ν_μ (this small admixture based on the well-known seesaw mechanism). Another possibility is to use $K^+ \to \pi^- e^+ e^+$ decay for the search for the same type of Majorana neutrino in the processes $K^+ \to \nu_h e^+; \nu_h \to \pi^- e^+$ (due to small admixture of ν_h in ν_e based also on the seesaw mechanism—see [22]).

Other possibilities for double-muon decay of kaons (with double-charge Higgs boson exchange [24] and with the heavy Majorana neutrino mechanism [23]) were also considered.

Thus, further searches for LFV kaon decays are very important since they can offer complementary information for possible theories with lepton flavor nonconservation that will not be covered even with very sensitive new projects on LFV searches in muon processes.

It is my opinion that, because of the unique character of the LFV kaon-decay process, it is very important to consider a new generation of such studies on new high-current accelerators with energy of ~20–70 GeV and with very high acceptance and precision setups with maximal redundancy measurements for background subtraction to increase the existing

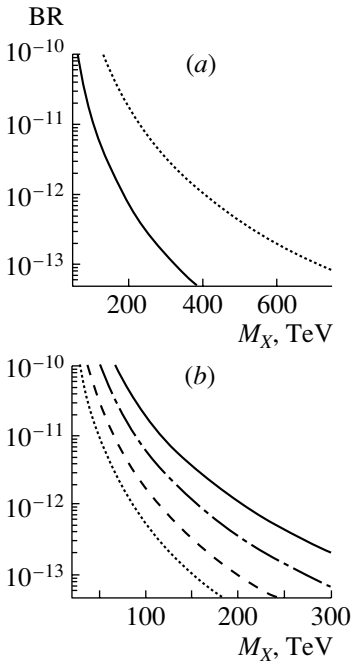

Fig. 6. Branching fractions for $K_L \to e\mu$ (a) and $K \to \pi e\mu$ (b) as a function of the scale parameter $M_X = M_H$ in (1) (assuming $g_H = g$ is a weak constant). In (a), the solid (dotted) curve corresponds to $A(P)$ exchange. In (b), the K_L^0 mode represented by the solid (S) and dashed (V) curves, while the K^+ mode is represented by the dash-dotted (S) and dotted (V) curves (see [16]). Here V, A, S, and P are vector, axial-vector, scalar, and pseudoscalar interactions.

sensitivity in Table 5 by 2–3 orders of magnitude for the future possibilities. These very difficult experiments must be considered as an important part of further efforts to study lepton nonconservation and kaon physics.

But at the end of this section, we will try to achieve

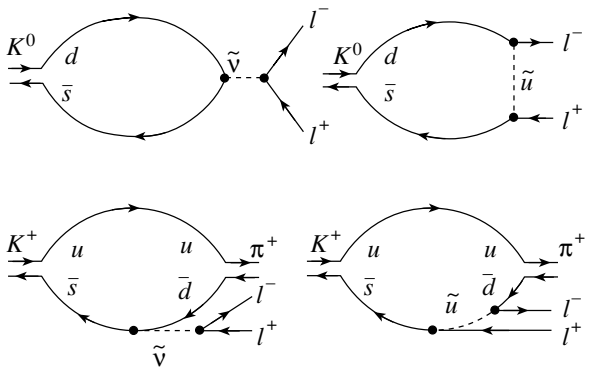

Fig. 7. Diagrams for $K \to \mu e$ and $K \to \pi \mu e$ in SUSY model with R-parity nonconservation [17].

more modest aims and to study several possibilities of the search for kaon decays with LFV in the framework of the CKM experiment. As was shown in Table 5, the expected statistical sensitivity of the CKM for the search for LFV kaon decays is on the level of BR $\sim 10^{-12}$. But the real sensitivity for these searches can be reduced due to background. Here, we consider only one example—the decay $K^+ \to \pi^-\mu^+\mu^+$, in which the sensitivity of E865 was the worst because of the background from $K^+ \to \pi^-\pi^+\pi^+$ with two pion decays in flight ($\pi^+ \to \mu^+\nu$). The sensitivity of E865 is limited by this background—see Fig. 8. We studied this background for the CKM setup with CKM GEANT MC simulation on the statistics of 10^7 $K^+ \to \pi^-\pi^+\pi^+$ events with forced $\pi^+ \to \mu^+\nu$ decays for both π^+ and with corresponding weights ($\sim 10^{-2}$) for proper normalization. We also performed MC simulation of the main LFV decay under study $K^+ \to \pi^-\mu^+\mu^+$.

As a first step we used "standard cuts" (some reasonable cuts on χ^2 values) for the quality of the reconstructed tracks and decay vertices, cuts for the secondary-particle energies in the magnetic spectrometer and calorimeters, and a cut on total transverse momentum $P_T^2 < 1.8 \times 10^{-4}$ GeV^2 (P_T is the sum of transverse momenta of secondaries compared to incident K^+ meson). These results are presented on Fig. 9*a*. They correspond to the expected sensitivity (controlled by background level) BR($K^+ \to \pi^-\mu^+\mu^+$) $< 2.5 \times 10^{-9}$ (90% C.L.), that is, on the same level as in E865 [9].

For further suppression of this background, we used two additional cuts:

(a) Under the assumption that all three charged secondary particles are pions, we calculate the effective mass $M_{3\pi}$ and reject the events with $M_{3\pi} < 0.52$ GeV (for the signal reaction assigning a pion mass to muon tracks produces a mass spectrum lying above this threshold). This cut reduces the secondary pion decays after the DMS spectrometer. The results with this cut in addition are presented in Fig. 9*b*. The background is reduced significantly, but in the dangerous region of $M_{\pi^-\mu^+\mu^+}$, it hardly changes.

(b) We performed a double measurement of the momentum of a fast muon (with $p_\mu \gtrsim 10$ GeV, which is over the threshold for the Pion RICH counter) in the DMS and in the velocity RICH spectrometer, and we selected events with

$$1.27 < R = \frac{p_\mu(DMS)}{p_\mu(RICH)} < 1.35$$

(in the existing program for Pion RICH, $R = 1$ corresponds to a pion and $R = 1.33$ corresponds to a muon).

The background simulation results after the cut (b) are presented in Fig. 9*c*, and the results with both cuts (a) and (b) are presented in Fig. 9*d*. As is seen in these pictures, the RICH cut reduced the background level drastically, although it also reduced the efficiency of $K^+ \to \pi^-\mu^+\mu^+$ registration because of the implic-

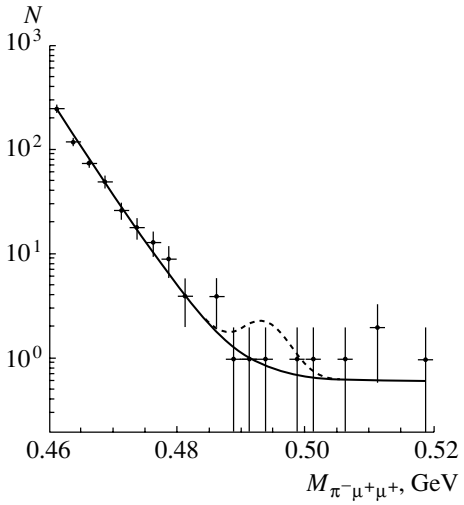

Fig. 8. E865 data for $K^+ \to \pi^-\mu^+\mu^+$. The dashed curve corresponds to BR($K^+ \to \pi^-\mu^+\mu^+$) $\simeq 3.0 \times 10^{-9}$.

itly applied momentum threshold $p_\mu \gtrsim 10$ GeV for a fast muon (from $\epsilon = 0.086$ to $\epsilon = 0.03$). Thus the possibility of using the RICH velocity spectrometer is very important for the search for LFV processes in the CKM experiment.

We do not have enough MC statistics for the simulation of background level for the measurements with the RICH selection cut. From comparison of Fig. 8 (E865) and Figs. 9*c* and 9*d* in the region where we see some background (near the mass $M_{\pi^-\mu^+\mu^+} = 0.46$ GeV), it is possible to conclude that the expected background level of the CKM experiment would be $\gtrsim$2 orders of magnitude smaller than in E865 (that is around $\sim 10^{-11}$).

Studies of background limitations for other LFV kaon decays in the CKM experiment are now in operation.

5. STUDY OF $K^+ \to \pi^0 l^+ \nu_l \gamma$ DECAYS IN THE CKM EXPERIMENT AND THE SEARCH FOR $T_{\rm odd}$ CORRELATIONS

The T invariance is one of the fundamental symmetries in physics (see, for example, [25–27]). It is still an open problem to be tested experimentally with high precision. If CPT invariance takes place, as is usually assumed, the CP violation is directly connected with T violation to conserve CPT. T invariance has been studied in many experiments. A typical example is the search for the electric dipole moments of elementary particles. Another possibility is to look for the T-odd correlations in particle decays, such as triple correlations including spin in the neutron decay. A well-known example of the T-odd correlation in kaon decays is the polarization of the muon normal to the decay plane in $K^+ \to \pi^0 \mu^+ \nu(K_{\mu 3})$:

$$\sigma_\perp^\mu = \frac{\boldsymbol{\sigma}_\mu \cdot (\mathbf{p}_\pi \times \mathbf{p}_\mu)}{|\mathbf{p}_\pi \times \mathbf{p}_\mu|}. \qquad (4)$$

It was first suggested by Sakurai [28] to look for T violation by $\sigma_\perp^\mu$ measurement. The unique feature of this process is that the "fake" T-odd correlation due to the final state interaction (FSI) is very small: $\sigma_\perp^{\mu\rm FSI} = 5 \times 10^{-6}$ [29]. Although the SM predicts zero effect, in some models (like Three Higgs Doublet Model (3HDM) of Weinberg type), values higher than (several units) $\times 10^{-3}$ or even up to 10^{-2} were predicted [30, 31]. The best measurement of the $\sigma_\perp^\mu$, performed about 20 years ago at the AGS BNL [32], gives $\sigma_\perp^\mu = 0.0031 \pm 0.0053$. The current result from KEK E246 [33] is $\sigma_\perp^\mu < 10^{-2}$ (90% C.L.), and they hope to reach the sensitivity $\sigma_\perp^\mu < 1.3 \times 10^{-3}$ at the end of the experiment. Even more sensitive projects to measure $\sigma_\perp^\mu$ were considered [34].

To measure effectively $\sigma_\perp^\mu$ polarization, one needs to stop muons from $K^+ \to \pi^0 \mu^+ \nu_\mu$ in thin layers of matter and to measure the electron asymmetry in their $\mu \to e$ decays. We do not plan at present to measure $\sigma_\perp^\mu$ in the CKM experiment: the kaon energy of 22 GeV and the energies of secondary muons look too high for that. On the contrary, we are seriously considering the possibility of measuring another triple T-odd correlation,

$$T_{\pi\mu\gamma} = \frac{\mathbf{p}_\gamma \cdot (\mathbf{p}_\pi \times \mathbf{p}_\mu)}{|\mathbf{p}_\gamma| \cdot |\mathbf{p}_\pi \times \mathbf{p}_\mu|}, \qquad (5)$$

in the decay $K \to \pi^0 \mu \nu_\mu \gamma$. Such a measurement was proposed for the first time by Gevais, Iliopoulous, and Kaplan in 1966 [35]. There are no theoretical predictions for this effect at present. The "fake" FSI correlation must not be strong: naively it must be similar to $\sigma_\perp^{\mu\rm FSI}$ in $K \to \mu\nu\gamma$, which is $\sim 10^{-4}$. The $K^\pm$ beam gives, in principle, the possibility of subtracting the FSI: the FSI correlation has the same sign in $K^\pm$, while the true effect changes sign.

The other way to check the existence of a direct effect of T violation and to have an estimation for possible "fake" asymmetry is to compare the triple correlations (5) $T_{\pi\mu\gamma}$ and $T_{\pi e\gamma}$ for $K^+ \to \pi^0 \mu^+ \nu_\mu \gamma$ and $K^+ \to \pi^0 e^+ \nu_e \gamma$ decays. In multi-Higgs doublet models the real measurable T-violation effect is expected only through the interactions of Higgs bosons with muons in $K^+ \to \pi^0 \mu^+ \nu_\mu \gamma$ decays. For $K^+ \to \pi^0 e^+ \nu_e \gamma$ in this model, $T_{\pi e\gamma}$ asymmetry is practically caused by FSI effects. Thus, the comparison of $T_{\pi\mu\gamma}$ and $T_{\pi e\gamma}$ correlations will provide us with a good criterion for observation of the real T-violation effect and for evaluation of "fake" asymmetry. As was calculated in [36], the "fake" asymmetries must be $T_{\pi e\gamma}^{\rm FSI} = -0.59 \times 10^{-4}$ and $T_{\pi\mu\gamma}^{\rm FSI} = 1.14 \times 10^{-4}$.

It also seems that kinematic cuts for photons in $K \to \pi^0 \mu \nu_\mu \gamma$ to separate direct emission radiative process and to suppress internal bremsstrahlung (IB) decay events will be important: we expect possible real T-violation effects in direct photon emission and can use IB events for the fake asymmetry tests.

The decay $K \to \pi^0 \mu \nu_\mu \gamma$ has not yet been observed; the prediction of the SM is [37] BR($K \to \pi^0 \mu \nu_\mu \gamma$) $\simeq 2 \times 10^{-5}$ (with the cuts on photon energy and emission angle $E_\gamma^{\rm c.m} > 30$ MeV and $\vartheta_{\mu\gamma} > 20^\circ$ in the kaon rest frame, which are used to suppress IB events). The only experimental measurement of the T-odd correlation in the decay $K \to \pi^0 e \nu_e \gamma$ is from ISTRA setup at the IHEP 70-GeV accelerator [38]: $\frac{\mathbf{p}_\gamma \cdot (\mathbf{p}_\pi \times \mathbf{p}_e)}{|\mathbf{p}_\gamma| \cdot |\mathbf{p}_\pi \times \mathbf{p}_e|} = 0.03 \pm 0.08$; it is based on 192 reconstructed events, which correspond to the BR = $(2.7 \pm 0.2) \times 10^{-4}$ (in the kaon rest frame, $E_\gamma^{\rm c.m} >$

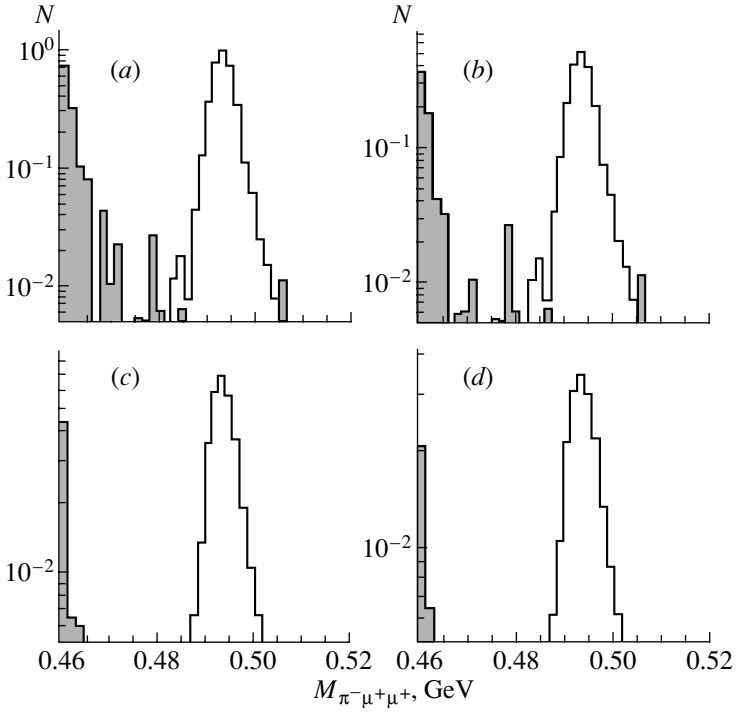

Fig. 9. $K^+ \to \pi^-\pi^+\pi^+$ background (filled histogram) after (*a*) "standard cuts," (*b*) $M_{3\pi}$ cut, (*c*) RICH cut, and (*d*) both (*b*) and (*c*) (N is number of events in relative units). Peaks in the middle correspond to the signal, but the vertical scale is different.

10 MeV; $0.6 < \cos\vartheta_{e\gamma} < 0.9$). Now, it is planned to measure the $T_{\pi\mu\gamma}$ correlation in the next IHEP kaon experiment OKA with the expected statistics of $\sim 10^6$ $K \to \pi^0\mu\nu_\mu\gamma$ decays [5]. The next step with increased statistics can be done in the CKM experiment [1, 7].

The IHEP theorists are now performing detailed calculations of the correlation (5) in SM and in the Weinberg 3HDM. This model is known to be a benchmark for the CP-violation searches beyond the SM. There are several parameters in the model relevant for our case: M_{H^+} is the mass of the lightest charged Higgs; v_1, v_2, v_3 are the vacuum expectation values of the three Higgs fields: $v_1^2 + v_2^2 + v_3^2 = 2\sqrt{2}G_\mathrm{F}$; $\alpha_i, \beta_i, \gamma_i (i = 1, 2)$ are six complex Yukawa coupling constants which are related to each other by the conditions [39]

$$\left.\begin{aligned} \frac{\mathrm{Im}(\alpha_2\beta_2^*)}{\mathrm{Im}(\alpha_1\beta_1^*)} = \frac{\mathrm{Im}(\beta_2\gamma_2^*)}{\mathrm{Im}(\beta_1\gamma_1^*)} = \frac{\mathrm{Im}(\alpha_2\gamma_2^*)}{\mathrm{Im}(\alpha_1\gamma_1^*)} = -1 \\ \frac{\mathrm{Im}(\alpha_1\gamma_1^*)}{v_2^2} = -\frac{\mathrm{Im}(\beta_1\gamma_1^*)}{v_1^2} = -\frac{\mathrm{Im}(\alpha_1\beta_1^*)}{v_3^2} \end{aligned}\right\}. \quad (6)$$

Further constraints on the model parameters can be extracted from the experimental data on d_n, the neutron electrical dipole moment; kaon CP-violation parameters ε and ε'; the mass difference for D^0 mesons Δm_D; etc. (see review [31]). Given all the constraints, one still can expect a large value for $T_{\pi\mu\gamma}$, which will soon be estimated. Let us recall that these models predict a significant value for $\sigma_\perp^\mu$ in $K \to \pi^0\mu\nu_\mu$ decays [30, 31].

To illustrate the possibilities for CKM experiments, we estimated the expected efficiency for registration of $K^+ \to \pi^0\mu^+\nu_\mu\gamma$ and $K^+ \to \pi^0 e^+\nu_e\gamma$ and the expected statistical precision for measurements of $T_{\pi\mu\gamma}$ and $T_{\pi e\gamma}$ asymmetry parameters. It is more convenient to use another normalization for this correlation

$$T'_{\pi\mu\gamma} = \frac{\mathbf{p}_\gamma \cdot (\mathbf{p}_\pi \times \mathbf{p}_\mu)}{m_K^3},$$

which takes into account the information on momentum distribution of the particles in the final states. We performed the calculations for $K^+ \to \pi^0\mu^+\nu_\mu\gamma$ decays with cuts (in the kaon rest frame) $E_\gamma > 30$ MeV and $\vartheta_{l\gamma} > 20^\circ$ to separate the direct photon emission process and to suppress IB radiation.[2)]

As will be shown below, we expect to obtain 1.1×10^7 $K^+ \to \pi^0\mu^+\nu_\mu\gamma$ events and $>10^8$ $K^+ \to \pi^0 e^+\nu_e\gamma$ events in the CKM experiment in parallel with the main $K^+ \to \pi^+\nu\bar{\nu}$ studies. For estimation of the statistical sensitivity for the average asymmetry of the $T'_{\pi\mu\gamma}$ distribution in $K^+ \to \pi^0\mu^+\nu_\mu\gamma$ decay, we performed a MC simulation for this distribution in

[2)] Maybe, we will need even more stringent cuts for this purpose.

the SM and obtained the sensitivity $T'_{\pi\mu\gamma} = \pm 2.5 \times 10^{-5}$ (for more common normalization $T_{\pi\mu\gamma} = \pm 3 \times 10^{-4}$). For $K^+ \to \pi^0 e^+ \nu_e \gamma$, the corresponding sensitivity is $T'_{\pi e\gamma} = \pm 7 \times 10^{-6} (T_{\pi e\gamma} = \pm 1 \times 10^{-4})$ [7].

The main problems for T-asymmetry measurements in $K^+ \to \pi^0 \mu^+ \nu_\mu \gamma$ are background processes and systematic uncertainties. It seems that the main background processes are $K^+ \to \pi^0 \pi^0 \mu^+ \nu_\mu$ with one lost photon, $K^+ \to \pi^+ \pi^0 \gamma$ with $\pi^+ \to \mu^+ \nu_\mu$ decay in flight, $K^+ \to \pi^+ \pi^0 \pi^0$ with one lost photon and with $\pi^+ \to \mu^+ \nu_\mu$ decay in flight, and $K^+ \to \pi^0 \mu^+ \nu_\mu$ with a random "photon." We considered here the first three background processes.

In our first approach, we consider only $K^+ \to \pi^0 \mu^+ \nu_\mu \gamma$ decays with all three photons detected in the FVS of the CKM setup (see Fig. 1), for which we will have the best energy and coordinate resolutions for photon detection (see estimates in Table 3). But we met with serious problems in this approach:

(1) The efficiency for $K^+ \to \pi^0 \mu^+ \nu_\mu \gamma$ registration was small enough ($\epsilon = 0.008$) even without additional cuts to suppress the main background processes.

(2) The muon spectrum for these $K^+ \to \pi^0 \mu^+ \nu_\mu \gamma$ events is very soft—practically all muons have momenta $p_\mu < 10$ GeV. They are below the threshold for Pion RICH of CKM. Pion RICH cannot be used to reduce the background from $\pi \to \mu\nu$ decays in flight by double-muon momentum measurement, and the background from $K^+ \to \pi^+ \pi^0 \pi^0$ (with $\pi^+ \to \mu^+ \nu$; one $\pi^0 \to \gamma(\gamma)$) and from $K^+ \to \pi^+ \pi^0 \gamma$ (with $\pi^+ \to \mu^+ \nu$) was too big.

Thus, we used another approach that opened more opportunities for background suppression with the help of additional cuts. In our GEANT simulation [7], we selected the events with three photons from $K^+ \to \pi^0 \mu^+ \nu_\mu \gamma$ decays detected in FVS and VVS[3)] and with a charged particle that was registered in the DMS spectrometer and passed through Pion RICH and MVS of the CKM setup.

We used the requirements for signal photon registration in FVS $E_\gamma > 150$ MeV and in VVS $E_\gamma > 100$ MeV and included the energy and coordinate resolutions in our simulation. For both systems, the energy resolution was assumed to be $\delta E_\gamma / E_\gamma = 0.10/\sqrt{E_\gamma[\mathrm{GeV}]} + 0.01$.[4)] The coordinate resolution for VVS was $\delta\phi = \pm\pi/16$ and $\delta z = \pm 12.5$ cm (this resolution is due to the mechanical structure of VVS; see [1]), and for FVS, it was δx, $\delta y = \pm 5\ \mathrm{mm}/\sqrt{E_\gamma[\mathrm{GeV}]} + 1$ mm. For two signal photons, the constraint for the table value of π^0 mass was imposed. The photon veto requirements for additional photons were used in accordance with Table 1. For a charged particle, we imposed the momentum cut $p > 10$ GeV.

After thorough study of different cuts to optimize the registration of the $K^+ \to \pi^0 \mu^+ \nu_\mu \gamma$ decay and the background rejection, we chose the following additional cuts for the above decay and for background processes $K^+ \to \pi^+ \pi^0 \pi^0$ ($\pi^+ \to \mu^+ \nu$; one $\pi^0 \to \gamma(\gamma)$), $K^+ \to \pi^+ \pi^0 \gamma$ ($\pi^+ \to \mu^+ \nu$), and $K^+ \to \pi^0 \pi^0 \mu^+ \nu_\mu$ (one $\pi^0 \to \gamma(\gamma)$):

1. For all the decays, we defined three systems of particles in final states X_1, X_2, X_3 with a different assumption for charged particle (π^+ or μ^+) and we found the missing masses relative to these systems M_1, M_2, and M_3 in $K^+ \to X_i + M_i$ decays:

(a) $X_1 = \mu^+ \pi^0 \gamma$ (charged particle was assumed to be μ^+) and M_1 for $K^+ \to \pi^0 \mu^+ \nu_\mu \gamma$ is the mass of neutrino; we selected events with $-0.01 < M_1^2 < 0.01$ GeV^2.

(b) $X_2 = \pi^+ \pi^0$ (charged particle was assumed to be π^+); for $K^+ \to \pi^+ \pi^0 \pi^0$ decay, $M_2^2 = m_{\pi^0}^2$ and we used the cut $M_2^2 > 0.025$ GeV^2 or $-0.01 < M_2^2 < 0.01$ GeV^2; i.e., we rejected the events with $0.01 < M_2^2 < 0.025$ GeV^2. This cut significantly reduced the background from $K^+ \to \pi^+ \pi^0 \pi^0$.

(c) $X_3 = \pi^0 \gamma$ and we used the cut $M_3^2 > 0.04$ GeV^2 to reduce the background from $K^+ \to \pi^+ \pi^0 \gamma$.

2. To reduce the background from $\pi \to \mu\nu$ decays in flight, we used double measurement of muon momenta in the DMS and in the Pion RICH velocity spectrometer

$$1.285 < R = \frac{p_{\text{charge part}}(\mathrm{RICH})}{p_{\text{charge part}}(\mathrm{DMS})} < 1.355$$

(in the existing program for Pion RICH, $R = 1$ corresponds to a pion and $R = 1.33$ corresponds to a muon).

3. To increase the efficiency of the photon veto system, we used the cut for the coordinate of the kaon-decay vertex in the beam $20 < z < 44$ m (this cut is different from the standard CKM cut $14 < z < 44$ m because BIVS was not included in the simulation procedure). In the future, this temporary limitation can be omitted.

In the GEANT simulation procedure to increase statistics for background estimates, we forced $\pi^+ \to \mu^+ \nu_\mu$ decay and then used corresponding weights ($\sim$0.1 on average) for proper background evaluation.

[3)] As was stated above, this possibility must be further studied by GEANT simulation and a special experimental investigation to understand the influence of the photon impact angles for VVS.

[4)] For FVS, it is a very crude approximation because in this CsI spectrometer $\delta E_\gamma / E_\gamma = 0.02/\sqrt{E_\gamma[\mathrm{GeV}]} + 0.01$.

Table 7. The results of GEANT simulation of $K^+ \to \pi^0\mu^+\nu_\mu\gamma$ decay and background processes for the CKM setup

Decay	BR	MC statistics	The number of accepted events	Efficiency ϵ	Backgr./signal
$K^+ \to \pi^0\mu^+\nu_\mu\gamma$	$\sim 2 \times 10^{-5}$	80 000	1320	1.4%	
$K^+ \to \pi^+\pi^0\pi^0$ $\hookrightarrow \gamma(\gamma)$ $\hookrightarrow \mu^+\nu$	1.73×10^{-2}	300 000	0	$< 1 \times 10^{-6}$ (90% C.L.)	$< 6 \times 10^{-2}$ (90% C.L.)
$K^+ \to \pi^+\pi^0\gamma$ $\hookrightarrow \mu^+\nu$	2.75×10^{-4}	80 000	452	5.5×10^{-5}	5.4×10^{-2}
$K^+ \to \pi^0\pi^0\mu^+\nu_\mu$ $\hookrightarrow \gamma(\gamma)$	$\sim 0.7 \times 10^{-5}$	80 000	1	1.25×10^{-5}	$< 1.1 \times 10^{-3}$ (90% C.L.)

The results of the GEANT simulation are presented in Table 7, from which we conclude that backgrounds are at acceptable level.

It is also instructive to see how general additional cuts reduce the efficiency of $K^+ \to \pi^0\mu^+\nu_\mu\gamma$ detection (Table 8). We see that, by reducing the $\epsilon(K^+ \to \pi^0\mu^+\nu_\mu\gamma)$ by a factor of three, we can reduce the background by more than an order of magnitude. Certainly, it is possible to have some intermediate cuts to optimize the measurements.

Under the condition of the CKM experiment, it is possible to obtain 4.0×10^{13} K^+ decays for two years of measurements (0.51×10^7 K^+ decay/spill; 1.4×10^5 spill/week; 0.50×10^{12} decay/week with dead-time losses of 30%; 78 weeks of measurements per 2 years) [1]. This value corresponds to 1.1×10^7 $K^+ \to \pi^0\mu^+\nu_\mu\gamma$ decays, which we discussed before. For more details of studying T-odd effects in $K^+ \to \pi^0 l^+\nu_l\gamma$ in the CKM experiment, see [7].

6. SEARCHES FOR NEW TYPES OF INTERACTIONS IN K DECAYS

Searches for new types of weak interactions that are associated with exchange of new intermediate bosons [scalar (S), pseudoscalar (P), tensor (T), and right-handed vector bosons W_R], with leptoquark processes, or with other possible mechanisms are of great interest in the quest for new physics beyond the SM. One preliminary comment concerning the sensitivity of experiments devoted to searches for new interactions that could be manifested, for example, in $K^+ \to l^+\nu_l$, $K^+ \to \pi^0 l^+\nu_l$, and $K^+ \to l^+\nu_l\gamma$ decays is in order here. The amplitude of each of these processes can be represented in the form

$$A = A_{\rm SM} + A_{\rm NI} = |A_{\rm SM}| + |A_{\rm NI}|e^{i\varphi}, \qquad (7)$$

where $A_{\rm SM}$ is the SM amplitude of the processes, $A_{\rm NI}$ is the amplitude associated with new interactions, and φ is their relative phase. Therefore, we have

$$|A|^2 = |A_{\rm SM}|^2 + |A_{\rm NI}|^2 + 2{\rm Re}(A_{\rm SM}A^*_{\rm NI}) \qquad (8)$$
$$= |A_{\rm SM}|^2 + |A_{\rm NI}|^2 + 2\cos\varphi|A_{\rm SM}||A^*_{\rm NI}|$$
$$\simeq |A_{\rm SM}|^2[1 \pm \underbrace{|A_{\rm NI}/A_{\rm SM}|}_{\rm IT}]$$

(the estimate was obtained under the assumption that the average value of the interference phase is $2\cos\varphi = \pm 1$). Thus, corrections due to new interactions are determined by the interference term IT, which is in inverse proportion to the square of the mass of the corresponding intermediate boson (IT $\sim M^{-2}_{\rm boson}$). Experiments of the type being discussed appear to be more sensitive to new interactions than, for example, processes with nonconserving lepton flavor ($\mu^- + (A,Z) \to e^- + (A,Z)$, $K^0 \to \mu e$, etc.), which are characterized by probabilities proportional to $|A|^2 \simeq |A_{\rm NI}|^2 \sim M^{-4}_{\rm boson}$ (see also [40]).

6.1. $K^+ \to e\nu_e$ Decay and the Search for Pseudoscalar Interactions

We will consider here only one possible measurement in the CKM for the quest for a new type of interactions—search for pseudoscalar coupling in precise study of $K^+ \to e\nu_e$ decay.

The lepton decays of K mesons are especially sensitive to possible admixtures of this new interaction of the pseudoscalar type. Within the SM involving $V-A$ weak interactions, $K^+ \to l^+\nu_l$ decays are suppressed by helicity conservation (see Fig. 10*a*).

Table 8. The influence of additional cuts on the efficiency of $K^+ \to \pi^0\mu^+\nu_\mu\gamma$ detection

Cut	$\epsilon(K^+ \to \pi^0\mu^+\nu_\mu\gamma)$, %
Preliminary	4.7
$-0.01 < M_1^2 < 0.01$ GeV^2	4.4
$1.285 < R < 1.355$	4.0
$M_2^2 > 0.025$ GeV^2 or $-0.01 < M_2^2 < 0.01$ GeV^2	2.8
$M_3^2 > 0.04$ GeV^2	1.4

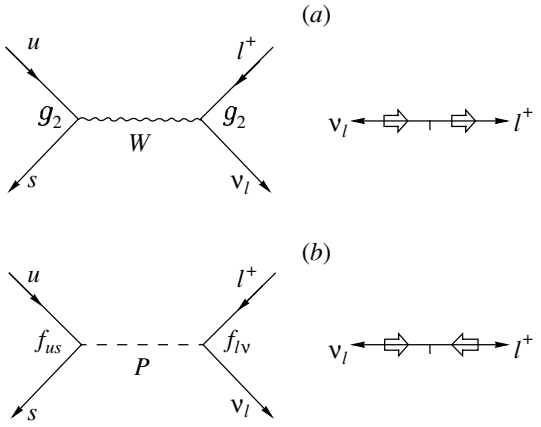

Fig. 10. (a) Diagram for decay $K^+ \to l^+\nu_l$ within the SM ($V-A$ interaction) for the case where the decay process proceeds through the exchange of a vector W boson. The Fermi coupling constant is $G_{\rm F} = g_2^2/4\sqrt{2}M_W^2$. In this model the helicities of leptons and antileptons are, respectively, left- and right-handed. The decay $K^+ \to l^+\nu_l$ is suppressed by helicity conservation (the K^+-meson spin is zero); the helicity-flip amplitude is proportional to the mass m_l. (b) Diagram for the decay $K^+ \to l^+\nu_l$ within the model involving anomalous pseudoscalar weak interaction whose coupling constant is $(G_{US}^{l\nu})_{\rm PS} = f_{l\nu}f_{US}/4\sqrt{2}M_P^2$. In the case of P interaction, the decay is no longer suppressed by helicity conservation.

The corresponding matrix element for $K^+(P_K) \to l^+(p_l) + \nu_l(p_\nu)$ decays has the form

$$A(K^+ \to l^+\nu_l)_{\rm SM} = \frac{G_{\rm F}}{\sqrt{2}} V_{us} f_K P_K^\alpha \bar{u}_\nu \gamma_\alpha (1+\gamma_5) u_l, \quad (9)$$

where $f_K = 159.8 \pm 1.5$ MeV is the K-decay constant. The probability of $K^+ \to l^+\nu_l$ decays has the form

$$\Gamma(K^+ \to l^+\nu_l)_{\rm SM} = \frac{G_{\rm F}^2}{8\pi} f_K^2 |V_{us}|^2 m_K m_l^2 \left(1 - \frac{m_l^2}{m_K^2}\right)^2. \quad (10)$$

Because of helicity conservation, this decay probability is proportional to the lepton mass squared m_l^2.

One can find the ratio of the relevant branching fractions

$$R(K^+ \to l^+\nu_l)_{\rm SM} = \left.\frac{{\rm BR}(K^+ \to e^+\nu_e)}{{\rm BR}(K^+ \to \mu^+\nu_\mu)}\right|_{\rm SM} \quad (11)$$
$$= \frac{m_e^2}{m_\mu^2}\frac{(m_K^2 - m_e^2)^2}{(m_K^2 - m_\mu^2)^2}(1+\delta_r)$$
$$= 2.569 \times 10^{-5}(1 - 0.0378 \pm 0.0004)$$
$$= (2.4719 \pm 0.0010) \times 10^{-5},$$

where δ_r is the radiative correction calculated with a high accuracy [41]. By using data on τ_{K^+}, ${\rm BR}(K^+ \to \mu^+\nu_\mu)$, and the value of $R(K^+ \to \mu^+\nu_\mu)_{\rm SM}$ in (11), we derive the SM predictions for the width with respect to the rare decay $K^+ \to e^+\nu_e$ and its relative probability:

$$\Gamma(K^+ \to e^+\nu_e)_{\rm SM} = (0.834 \pm 0.003) \times 10^{-18}\,{\rm MeV}, \quad (12)$$
$${\rm BR}(K^+ \to e^+\nu_e)_{\rm SM} = (1.570 \pm 0.005) \times 10^{-5}.$$

For the case of pseudoscalar interaction, the decay $K^+ \to l^+\nu_l$ would not be suppressed by helicity conservation (see Fig. 10b), and its probability would be given by

$$\Gamma(K^+ \to l^+\nu_l)_{\rm PS} = \frac{G_{\rm PS}^2}{8\pi} f_K^2 m_K M^2 \left(1 - \frac{m_l^2}{m_K^2}\right)^2, \quad (13)$$

where M is some constant having the dimension of mass. Here, the pseudoscalar coupling constant $G_{\rm PS}$ is defined by analogy with $G_{\rm F} = g_2^2/4\sqrt{2}M_W^2$ and has the same dimensionality in (13). The pseudoscalar interactions between the quark and lepton currents were considered in more detail in [42], where the corresponding constant was defined as $(G_{UD}^{l\nu})_{\rm PS} = f_{l\nu}f_{UD}/4\sqrt{2}M_P^2$, where $f_{l\nu}$ and f_{UD} are the constants of lepton and quark coupling to the intermediate pseudoscalar bosons of the mass M_P ($U = u, c, t$ stand for the up-quarks, while $D = d, s, b$ stand for the down-quarks). In [42], the mass factor M has the form $M = m_K^2/(m_u + m_s)$, where $m_u = 5$ MeV and $m_s = 150$ MeV are the current masses of the quarks entering into the composition of the K^+ meson.

In the case of pseudoscalar interaction, the probabilities of the decays $K^+ \to e^+\nu_e$ and $K^+ \to \mu^+\nu_\mu$ were close:

$$R(K^+ \to l^+\nu_l)_{\rm PS} \simeq (1 - m_e^2/m_K^2)^2/(1 - m_\mu^2/m_K^2)^2 \simeq 1.1. \quad (14)$$

A modest difference between them is explained by the smaller phase space for the decay $K^+ \to \mu^+\nu_\mu$.

Because the decay $K^+ \to e^+\nu_e$ is strongly suppressed within the SM by helicity conservation, it proves to be especially sensitive to even a moderate admixture of pseudoscalar interaction, as was mentioned above. We assume that the amplitude of $K^+ \to l^+\nu_l$ decay is determined by the contributions of $V-A$ (SM) and anomalous PS interaction: $A(K^+ \to l^+\nu_l) = A(K^+ \to l^+\nu_l)_{\rm SM} + A(K^+ \to l^+\nu_l)_{\rm PS}$; as was discussed above, $A(K^+ \to \mu^+\nu_\mu)_{\rm SM} \gg$

$A(K^+ \to e^+\nu_e)_{\rm SM}$, while $A(K^+ \to \mu^+\nu_\mu)_{\rm PS} \simeq A(K^+ \to e^+\nu_e)_{\rm PS}$. Thus,

$$R(K^+ \to l^+\nu_l) = \frac{{\rm BR}(K^+ \to e^+\nu_e)}{{\rm BR}(K^+ \to \mu^+\nu_\mu)} \simeq R(K^+ \to l^+\nu_l)_{\rm SM}[1 \pm |A_{\rm PS}/A_{\rm SM}|]. \quad (15)$$

The available experimental data [43] yield

$$R(K^+ \to l^+\nu_l)_{\rm exp} = \frac{(1.55 \pm 0.07) \times 10^{-5}}{0.6351 \pm 0.0018} = (2.441 \pm 0.110) \times 10^{-5} = R(K^+ \to l^+\nu_l)_{\rm SM} \cdot (0.987 \pm 0.045), \quad (16)$$

which corresponds to $\Gamma(K^+ \to e^+\nu_e)_{\rm exp} = (0.824 \pm 0.037) \times 10^{-18}$ MeV. From (15) and (16), it follows that the experimental limits on the pseudoscalar-interaction contribution to the decay $K^+ \to e^+\nu_e$ are

$$|A(K^+ \to e^+\nu_e)_{\rm PS}| < 5.8 \times 10^{-2}|A(K^+ \to e^+\nu_e)_{\rm SM}|, \quad (17)$$

$$\Gamma(K^+ \to e^+\nu_e)_{\rm PS} < 3.4 \times 10^{-3}\Gamma(K^+ \to e^+\nu_e)_{\rm SM} \simeq 3 \times 10^{-21}\ {\rm MeV}.$$

It was shown in [42] that

$$R(K^+ \to l^+\nu_l) = R(K^+ \to l^+\nu_l)_{\rm SM} \times \left[1 \pm \frac{|G_{us}^{e\nu}|_{\rm PS}}{G_{\rm F}V_{us}} \frac{m_K^2}{(m_s + m_u)m_e}\right], \quad (18)$$

where $|G_{us}^{e\nu}|_{\rm PS}$ is the pseudoscalar-interaction constant coupling the us and $e\nu$ states (for the decay $\pi^+ \to e^+\nu_e$, pseudoscalar-interaction contribution is determined by another constant, $|G_{ud}^{e\nu}|_{\rm PS}$).

From (17) and (18), one can find an experimental constraint on the pseudoscalar coupling constant: $|G_{us}^{e\nu}|_{\rm PS} < 3.6 \times 10^{-11}\ {\rm GeV}^{-2}$. In the future kaon experiment OKA in IHEP, the sensitivity of the measurement of $R(K^+ \to l^+\nu_l)$ is expected to be $(1-3) \times 10^{-3}$, which corresponds to the search for pseudoscalar interaction on the level

$$|A(K^+ \to l^+\nu_l)_{\rm PS}|^2 < (10^{-6}-10^{-5})|A(K^+ \to l^+\nu_l)_{\rm SM}|^2 \simeq 10^{-24}-10^{-23}\ {\rm MeV}. \quad (19)$$

It should be pointed out that, to reduce the systematic uncertainties in $R(K^+ \to l^+\nu_l)$ measurements, it is very important to have a clear electron identification and precise determination of the detection efficiency, as well as a very effective photon veto system to reduce the background from $K^+ \to \pi^0 e^+\nu_e$ and $K^+ \to e^+\nu_e\gamma$ decays. The CKM setup would have strong tools for these measurements (very effective photon veto system, good electron detection in pion RICH). Thus, it will be reasonable to perform further studies of $K^+ \to e^+\nu_e$ decay in the CKM experiment to increase the sensitivity in the search for pseudoscalar interactions which is expected in the OKA experiment.

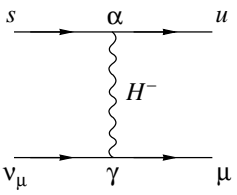

Fig. 11. Diagram for $\mathrm{Im}\, g_S$ from H^--Higgs-boson exchange; α and γ are Higgs interaction constants; m_{K^-} and M_{H^-} are the masses of kaon and Higgs boson. $\mathrm{Im}\, g_S = \mathrm{Im}\, \alpha^*\gamma(m_{K^-}/M_{H^-})^2$.

It must be noted that the value $R(K^+ \to l^+\nu_l)_{\rm SM}$ in (11) is really the ratio ${\rm BR}[K^+ \to e^+\nu_e(\gamma)]/{\rm BR}[K^+ \to \mu^+\nu_\mu(\gamma)]$ and includes the soft IB photons which are not observed in the experiments [41]. The value $R[K^+ \to l^+\nu_l(\gamma)]_{\rm SM}$ is the ratio that will be measured in the same conditions for $K^+ \to e^+\nu_e(\gamma)$ and $K^+ \to \mu^+\nu_\mu(\gamma)$. Thus, soft IB photons have no influence on the precision of the search for deviation from SM predictions and for possible contribution of a new pseudoscalar interaction which was estimated in (19).

The study of $K^+ \to e^+\nu_e$ is the most effective way for the search for this pseudoscalar coupling. As was shown in [5], this decay is much more sensitive for pseudoscalar searches in comparison, for example, with $K_L^0 \to e^+e^-$ (both these decays are helicity-suppressed in the SM and thus are very sensitive to new anomalous interactions).

7. THE COMPARISON OF $K^+ \to \pi^0\mu^+\nu_\mu$ AND $K^+ \to \pi^0 e^+\nu_e$ DECAYS AND SOME NEW TYPES OF WEAK INTERACTIONS

Let us also consider the study of $K^+ \to \pi^0\mu^+\nu_\mu$ decay and the possibility of searching for some influence of the scalar interactions (Higgs boson effects?) in the comparison of $K_{\mu 3}^+$ and K_{e3}^+ decays.

As is well known (see [43]), in the SM, the $V-A$ matrix element of $K^+ \to \pi^0\mu^+\nu_\mu$ decay can be influenced by two form factors $f_+(q)$ and $f_-(q)$ and can be presented in the form

$$A = \left(G_{\rm F}/\sqrt{2}\right)\lambda f_+(q^2) \times \left[(P_K + p_\pi)_\rho \bar{\mu}\gamma^\rho(1+\gamma_5)\nu_\mu + \frac{f_-(q^2)}{f_+(q^2)} m_\mu \bar{\mu}(1+\gamma_5)\nu_\mu\right]. \quad (20)$$

Table 9. Sensitivity of performed and proposed experiments for CP-violation decay asymmetry in $K^\pm \to 3\pi$ decays

Experiment	Decay	Existing (*) or expected (**) statistics for $K^\pm \to 3\pi$	Existing (*) or expected (**) statistical precision in asymmetry (δg)
PDG [43]	$K^\pm \to \pi^\pm\pi^+\pi^-$	$3.2 \times 10^6 (K^+ + K^-)$ (*)	$(-0.70 \pm 0.53) \times 10^{-2}$ (*)
HyperCP, Fermilab [48]	$K^\pm \to \pi^\pm\pi^+\pi^-$	$3.2 \times 10^8 (K^+) + 1.3 \times 10^8 (K^-)$(*)	$\sim 6 \times 10^{-4}$ (**)
TNF, IHEP [47]	$K^\pm \to \pi^\pm\pi^0\pi^0$	$10^6 (K^+) + 10^6 (K^-)$ (*)	$\sim 2 \times 10^{-3}$ (**)
NA48, CERN [49]	$K^\pm \to \pi^\pm\pi^+\pi^-$	$1.3 \times 10^9 (K^+) + 0.75 \times 10^9 (K^-)$(**)	$\sim 1.7 \times 10^{-4}$ (**)
	$K^\pm \to \pi^\pm\pi^0\pi^0$	$0.82 \times 10^8 (K^+) + 0.47 \times 10^8 (K^-)$(**)	$\sim 3 \times 10^{-4}$ (**)
OKA, IHEP [5]	$K^\pm \to \pi^\pm\pi^+\pi^-$	$3.8 \times 10^9 (K^+) + 2.1 \times 10^9 (K^-)$(**)	$\sim 1.0 \times 10^{-4}$ (**)
	$K^\pm \to \pi^\pm\pi^0\pi^0$	$3.3 \times 10^8 (K^+) + 1.9 \times 10^8 (K^-)$(**)	$\sim 1.3 \times 10^{-4}$ (**)

Table 10. Possible search for CP-violation asymmetry in $K^\pm \to 3\pi$ and $K^\pm \to \pi^\pm\pi^0\gamma_{\rm direct}$ in CKM

Decay	BR	Events/week	Number of decays $n(K^+)$ and $n(K^-)$	$(\delta\Gamma)$	$(\delta g) = R \times (\delta\Gamma)$
$K^\pm \to \pi^\pm\pi^+\pi^-$	$(5.59 \pm 0.05) \times 10^{-2}$	$4.0 \times 10^9 (K^+)$ $2.0 \times 10^9 (K^-)$	$2.6 \times 10^{10} (K^+)$ $1.9 \times 10^{10} (K^-)$	4.8×10^{-6}	3.6×10^{-5}
$K^\pm \to \pi^\pm\pi^0\pi^0$	$(1.73 \pm 0.04) \times 10^{-2}$	$2.5 \times 10^7 (K^+)$ $1.25 \times 10^7 (K^-)$	$1.6 \times 10^8 (K^+)$ $1.2 \times 10^8 (K^-)$	6.6×10^{-5}	2.0×10^{-4}
$K^\pm \to \pi^\pm\pi^0\gamma_{\rm direct}$	$(1.00 \pm 0.16) \times 10^{-5}$	$4.0 \times 10^4 (K^+)$ $2.0 \times 10^4 (K^-)$	$2.6 \times 10^5 (K^+)$ $1.9 \times 10^5 (K^-)$	1.5×10^{-3}	

Notes: 1. Measurements for 16 weeks (dedicated run).

2. Optimal time sharing between K^+ and K^- beams with $r = I(K^-)/I(K^+) = 1/2$ (the same intensity of protons), $t(K^+) = T\frac{\sqrt{r}}{1+\sqrt{r}} = 0.41T \simeq 6.5$ weeks (3.6×10^{11} K^+ decay/week—see Table 3), $t(K^-) = T\frac{1}{1+\sqrt{r}} = 0.59T \simeq 9.5$ weeks (1.8×10^{11} K^- decay/week—see Table 3 and r).

3. $(\delta\Gamma) = \frac{\sqrt{n(K^+)+n(K^-)}}{2\sqrt{n(K^+)n(K^-)}}$.

4. For $K^\pm \to \pi^\pm\pi^+\pi^-$, $R = 7.56$; for $K^\pm \to \pi^\pm\pi^0\pi^0$, $R = 3.0$.

As was shown in the paper of Peccei [30], the influence of the H^--Higgs-boson-exchange diagram in Fig. 11 will modify expression (20) as

$$A = \left(G_{\rm F}/\sqrt{2}\right)\lambda f_+(q^2) \times \left[(P_K + p_\pi)_\rho \bar{\mu}\gamma^\rho(1+\gamma_5)\nu_\mu + \frac{f_-(q^2)}{f_+(q^2)} m_\mu \bar{\mu}(1+\gamma_5)\nu_\mu + g_S(q^2) m_\mu \bar{\mu}(1+\gamma_5)\nu_\mu\right]. \quad (21)$$

Here, g_S is the scalar interaction form factor. From the diagram in Fig. 11 with the Higgs boson exchange, $\mathrm{Im}\, g_S = \mathrm{Im}\,\alpha^*\gamma(m_{K^-}/M_{H^-})^2$. There is some relation between normal T-odd muon polarization in $K^+ \to \pi^0\mu^+\nu_\mu$, $\mathrm{Im}\, g_S$, and kinematic factor 0.2:

$$\langle p_T^\mu \rangle \simeq 0.2 \mathrm{Im}\, g_S. \quad (22)$$

This condition is a basis for the search for normal muon polarization in kaon decay in multi-Higgs models of the Weinberg type.

But there is another question for which I do not know the precise answer now: Is it possible to search for the influence of scalar interaction $g_S(q^2)$ by studying the anomalous value of the coefficient $\left[f_-(q^2)/f_+(q^2) + g_S(q^2)\right]$ in the second part of Eq. (21). [5] In any case, it seems to me that, to search very carefully for new types of weak interactions, we need a precise comparison of different kaon-decay modes with muons and electrons.

8. NONLEPTONIC CHARGED-KAON DECAYS AND THE SEARCH FOR DIRECT CP VIOLATION IN $K^\pm$ DECAYS

Studies of the nonleptonic charged-kaon decays, $K^\pm \to \pi^\pm\pi^+\pi^-$; $\pi^\pm\pi^0\pi^0$; $\pi^\pm\pi^0\gamma$; $\pi^\pm\gamma\gamma$, are important for the understanding of the mechanisms of strangeness-changing hadronic weak decays with $\Delta S = 1$ and of the main properties of CHPT for these processes. In addition to precision CHPT tests, new measurements in this field with greatly enlarged statistics can in general enable the search for direct CP-violation effects through measurement of rate

[5] See, for example, V.V. Kiselev *et al.*, hep-ph/0204066.

asymmetries in $(K^+ \to f)/K^- \to \bar{f})$ or Dalitz plot asymmetries.

In principle, it is straightforward to operate the charged-kaon beam line at both polarities, allowing K^+ and K^- data sets to be collected at different times. But in practice, the precision measurements described below will be vulnerable to the different beam background environments of K^+ and K^- running. In addition, detector efficiencies between different K^+ and K^- running periods would have to be controlled to a very high level. Nevertheless, there is some value in listing the potential measurements with the understanding that a serious attack on these physics topics requires detailed study for which we did only the first small steps.

The direct CP violation would manifest itself by the difference between the K^+- and K^--decay matrix elements if (see, for example, [31, 44]) there are at least two amplitudes with different "weak" phases and different "strong" final state interaction phases.

In more detail, let us assume that the amplitudes for charge conjugated decays

$$A_f = \langle f|H|K^+\rangle, \quad A_{\bar{f}} = \langle \bar{f}|H|K^-\rangle \tag{23}$$

are the sum of the independent components:

$$\begin{aligned} A_f &= ae^{i\delta_a} + be^{i\delta_b} \\ &= |a|\exp(i\delta_a + i\varphi) + |b|\exp(i\delta_b), \\ A_{\bar{f}} &= a^* e^{i\delta_a} + b^* e^{i\delta_b} \\ &= |a|\exp(i\delta_a - i\varphi) + |b|\exp(i\delta_b). \end{aligned} \tag{24}$$

Here, δ_a and δ_b are the scattering phases in the final-state interactions, and $\varphi = \varphi_a - \varphi_b$ is the phase difference for two weak decay amplitudes $a = |a|e^{i\varphi_a}$ and $b = |b|e^{i\varphi_b}$. The squares of the amplitudes are

$$\left.\begin{aligned} |A_f|^2 &= \{|a|\exp[i(\delta_a + \varphi)] + |b|\exp(i\delta_b)\} \\ &\times \{|a|\exp[-i(\delta_a + \varphi)] + |b|\exp(-i\delta_b)\} \\ &= |a|^2 + |b|^2 + |a||b|\{\exp[i(\delta_a - \delta_b + \varphi)] \\ &+ \exp[-i(\delta_a - \delta_b + \varphi)]\} \\ &= |a|^2 + |b|^2 + 2|a||b|\cos[(\delta_a - \delta_b) + \varphi] \\ |A_{\bar{f}}|^2 &= |a|^2 + |b|^2 + 2|a||b|\cos[(\delta_a - \delta_b) - \varphi] \end{aligned}\right\}. \tag{25}$$

The charge asymmetry of these decays is

$$\begin{aligned} \tilde{\Delta} = \frac{|A_f|^2 - |A_{\bar{f}}|^2}{|A_f|^2 + |A_{\bar{f}}|^2} &= \frac{2|a||b|\{\cos[(\delta_a + \delta_b) + \varphi] - \cos[(\delta_a - \delta_b) - \varphi]\}}{2|a|^2 + 2|b|^2 + 2|a||b|\{\cos[(\delta_a - \delta_b) + \varphi] + \cos[(\delta_a - \delta_b) - \varphi]\}} \\ &= \frac{-2|a||b|\sin(\delta_a - \delta_b)\sin\varphi}{|a|^2 + |b|^2 + 2|a||b|\cos(\delta_a - \delta_b)\cos\varphi}. \end{aligned} \tag{26}$$

Thus, it is clear from (26) that the charge asymmetry in $K^+ \to f$ and $K^- \to \bar{f}$ decays, which is determined by direct CP violation, will manifest itself only if, in the final state, there are at least two different dynamical amplitudes a and b with different phases φ_a and φ_b (relative phase $\varphi_a - \varphi_b = \varphi \neq 0$) and with different phase shifts δ_a and δ_b for the final state scattering $(\delta_a - \delta_b \neq 0)$.

We will consider below the decays $K^\pm(P_K) \to \pi^\pm(p_1)\pi^\pm(p_2)\pi^\mp(p_3)$ (τ decays) and $K^\pm(P_K) \to \pi^0(p_1)\pi^0(p_2)\pi^\pm(p_3)$ (τ' decays), which satisfy these requirements (see, for example, [31, 43–45]).

The distribution of $K \to 3\pi$ events in the Dalitz plot is described by the expression

$$\begin{aligned} &|A(K \to 3\pi)|^2 \\ &= \text{const} \times [1 + gX + hX^2 + jY + kY^2] \sim 1 + gX. \end{aligned} \tag{27}$$

Here, $X = s_3 - s_0/m_\pi^2$; $Y = s_2 - s_0/m_\pi^2$; $s_i = (P_K - p_i)^2 = (m_K - m_{\pi i})^2 - 2m_K T_i$; $s_0 = (s_1 + s_2 + s_3)/3 = (m_K^2 + m_\pi^2)/3$ ($i = 1, 2, 3$, where $i = 3$ for nonsymmetric pion); P_K, p_i and $m_K, m_{\pi i}$ are the 4-momenta and masses of kaon and pions; T_i is the kinetic energy of pions. The measured values of the slopes in the variable s_3 of the Dalitz plot distributions are $g_\tau = -0.2154 \pm 0.0035$ and $g_{\tau'} = 0.652 \pm 0.031$ [43].

The amplitudes of $K \to 3\pi$ decays can be presented in accordance with (24) in the form

$$\begin{aligned} A(K^+) &= |a(s_1; s_2; s_3)|\exp[i(\delta_a + \varphi)] \\ &+ |b(s_1; s_2; s_3)|\exp(i\delta_b), \\ A(K^-) &= |a(s_1; s_2; s_3)|\exp[i(\delta_a - \varphi)] \\ &+ |b(s_1; s_2; s_3)|\exp(i\delta_b). \end{aligned} \tag{28}$$

In the main approximation of the momentum expansion, amplitudes a and b are determined by the $\Delta T = 1/2$ and $\Delta T = 3/2$ transition and the phase φ is related to the phase of CKM matrix.

The direct CP violation in $K^\pm \to 3\pi$ decays can be measured in studies of the asymmetry of the type

of (26) in partial decay rates

$$\frac{\Gamma(K^+ \to \pi^+\pi^+\pi^-) - \Gamma(K^- \to \pi^-\pi^-\pi^+)}{\Gamma(K^+ \to \pi^+\pi^+\pi^-) + \Gamma(K^- \to \pi^-\pi^-\pi^+)} \equiv (\delta\Gamma)_\tau = \frac{\Delta\Gamma_\tau}{2\Gamma_\tau} \quad (29)$$

or in slopes of the Dalitz-plot distributions

$$\frac{g(K^+ \to \pi^+\pi^+\pi^-) - g(K^- \to \pi^-\pi^-\pi^+)}{g(K^+ \to \pi^+\pi^+\pi^-) + g(K^- \to \pi^-\pi^-\pi^+)} \equiv (\delta g)_\tau = \frac{\Delta g_\tau}{2g_\tau} \quad (30)$$

(for τ decays). The corresponding values $(\delta\Gamma)_{\tau'}$ and $(\delta g)_{\tau'}$ are for τ' decay. The accuracy in measuring the slope g of the distribution is related to the accuracy in determining the total width with respect to $K^\pm \to 3\pi$ decays, $\Gamma(K^\pm \to 3\pi)$, by the equation

$$(\delta g) = R \cdot (\delta\Gamma) = R\frac{\sqrt{n(K^+) + n(K^-)}}{2\sqrt{n(K^+) \cdot n(K^-)}} = R\frac{\sqrt{1 + (1/r)}}{2\sqrt{n(K^+)}}. \quad (31)$$

Here, $n(K^+)$ $[n(K^-)]$ is the number of decays $K^+ \to 3\pi[K^- \to 3\pi]$ in the $K^+(K^-)$ beam and $r = n(K^-)/n(K^+)$. The factor R depends on the slope g; $R_\tau = 7.56$ [46] and $R_{\tau'} = 3.0$ [47].

Despite the introduction of the large factor R, the sensitivity for the charge asymmetry of the slope (δg) is better than for the charge asymmetry of the rate $(\delta\Gamma)$, where the asymmetry effect is reduced by integration over the entire Dalitz plot. Thus, for example, the measurements with τ' decays are a factor $(R_\tau/R_{\tau'})^2 \simeq 6$ more "effective" for the search for CP violation than with τ decays.

In Table 9, the sensitivity of the performed and proposed experiments for CP-violation asymmetry measurements in $K^\pm \to 3\pi$ decays is presented [5, 47–49].

Table 10 displays the expected statistics and planned accuracy of the measurement of CP asymmetry in the decays $K^\pm \to \pi^\pm\pi^\pm\pi^\mp$, $K^\pm \to \pi^0\pi^0\pi^\pm$, and $K^\pm \to \pi^\pm\pi^0\gamma_{\text{direct}}$ (direct photon emission) in the CKM experiment. This table corresponds to a dedicated run with periodically changed kaon polarity with a total duration of 16 weeks for a standard K^+ beam with intensity of 3×10^7 K^+/spill and K^- beam with intensity of 1.5×10^7 K^-/spill (with the same intensity of the primary proton beam). Statistically optimal sharing of time is in total 6.5 weeks with the K^+ beam and 9.5 weeks with the K^- beam. The expected statistical sensitivity of this measurement is $(\delta g)_\tau \leq 3.6 \times 10^{-5}$ and $(\delta g)_{\tau'} \leq 2.0 \times 10^{-4}$.

The main difficulty of the proposed experiments is to demonstrate that, indeed, there is no "dangerous" systematics at the level of $<10^{-4}$. A possible strategy of the measurements is the change of the polarities of all the beam elements, say, every 6 hours. It is important then to change the polarity of the main spectrometer magnets at the same time. The possible sources of the systematics are the following:

1. Difference in the hadronic interactions between π^+ and π^-.
2. Different parameters of the positive and negative beams. In particular, the tilt of the beams with respect to each other is potentially dangerous.
3. Effects of the mass resolution and background under the mass peaks.
4. Variation of the setup and the beam parameters with time, etc.

The first attempts to investigate possible systematic uncertainties, which were presented in [5], demonstrate that these uncertainties are smaller than 10^{-3}. It is clear that this is only the first step and a much more serious investigation of systematics must be performed in the future.

What is interesting to mention is that there are several decays where the $K^\pm$ asymmetry must be negligible. For example, in the decay $K \to \pi^0 e(\mu)\nu$, the asymmetry must be very small because there is practically no final-state interactions. The intense decay $K^+ \to \pi^+\pi^0$ is another example; here, the expected effect is very small $[(\delta\Gamma) < 10^{-9}$ [50]], because the decay mainly goes through one amplitude (S wave, $\Delta T = 3/2$). These decays can be used to control the systematics.

Clearly, a large amount of work is still required to determine if the CKM apparatus is capable of this measurement, but it is at least encouraging that a reasonably robust experimental checking of the apparatus can be performed.

Let us briefly discuss the theoretical predictions for effects of direct CP violation in $K^\pm \to 3\pi$ decays. As a rule, in the SM, these effects are very small and are beyond the possibilities of existing experimental technique. Some theoretical predictions for asymmetries $(\delta\Gamma)$ and (δg) in $K^\pm \to 3\pi$ and in some other decays are presented in Table 11.

In Table 11a, there are the results of SM calculations [45] based on the lowest order of CHPT approximation $O(p^2)$.

But in [51, 52], it was stated that asymmetry effects can be very strongly enhanced by the higher order contributions of CHPT (with enhancement factor $F \gtrsim 10^2$—see Table 11b), which leads to a large enough and possibly measurable asymmetry $(\delta g) \sim$ (several units) $\times 10^{-4}$. Unfortunately, this result is in contradiction with other works [45, 53], in which it

Table 11. Theoretical predictions for CP-violation asymmetries in $K^\pm \to 3\pi$, $K^\pm \to \pi^+\pi^0\gamma$, $K^\pm \to \pi^\pm\gamma\gamma$

		The decays $K^\pm \to 3\pi$	
a	[45]	$(\delta g)_\tau = -(2.3 \pm 0.6) \times 10^{-6}$; $(\delta\Gamma)_\tau = -(6.0 \pm 2.0) \times 10^{-8}$ $(\delta g)_{\tau'} = (1.3 \pm 0.4) \times 10^{-6}$; $(\delta\Gamma)_{\tau'} = (2.4 \pm 0.8) \times 10^{-7}$	SM Lower order in CHPT ($O(p^2)$)
b	[52]	$(\delta g)_\tau \simeq (2.5\text{–}6.0) \times 10^{-4}$ $(\delta g)_{\tau'} \simeq (1.5\text{–}3.4) \times 10^{-4}$	SM Large enhancement of asymmetry $(\delta g)_{\tau,\tau'}$ in higher orders of CHPT ($O(p^6)$) (the enhancement factor $F \gtrsim 10^2$)
c	[31, 53]	$(\delta g)_\tau \lesssim 3 \times 10^{-5} \sin\delta$; $(\delta\Gamma)_\tau \lesssim 2.5 \times 10^{-6} \sin\delta$ $(\sin\delta \lesssim 1)$	SM Calculation in $O(p^4)$ approximation of CHPT (the enhancement factor is rather limited $F \sim 10$)
d	[54]	$(\delta g)_\tau\vert_{\mathrm{SM}+W} \lesssim 10^{-4}$	Model with CP violation in multi-Higgs mechanism of Weinberg type
e	[55]	$(\delta g)_\tau \sim 10^{-5}$ (in some assumptions up to $\sim 10^{-4}$)	Supersymmetry extension of SM induced by SUSY chomomagnetic penguins
		The decays $K^\pm \to \pi^\pm\pi^0\gamma$	
f	[44]	$[\delta\Gamma(\pi^\pm\pi^0\gamma)] \lesssim 10^{-5}$; for direct emission radiation $[\delta\Gamma(\pi^\pm\pi^0\gamma)]_{\mathrm{DE}} \lesssim 10^{-4}$	SM
g	[56]	$[\delta\Gamma(\pi^\pm\pi^0\gamma)] \lesssim 10^{-5}$; but for some special region of the Dalitz plot $[\delta\Gamma(\pi^\pm\pi^0\gamma)] \lesssim 10^{-4}$	Supersymmetry extension of SM
		The decays $K^\pm \to \pi^\pm\gamma\gamma$	
h	[44]	$[\delta\Gamma(\pi^\pm\gamma\gamma)] \lesssim 10^{-4}$	SM

was shown that, although the asymmetry can be enhanced in higher orders of CHPT, this enhancement factor is moderate ($F < 10$–20). Thus, in Table 11c, the results of [53] are presented in which $O(p^4)$ calculations were performed, and it seems that, in the framework of SM, it is difficult to expect the value of $(\delta g)_{\tau,\tau'} > (2\text{–}3) \times 10^{-5}$, which is still beyond the possibilities of current experiment (see also [31]).

Upon the discovery of large value of $\mathrm{Re}(\varepsilon'/\varepsilon)$, special attention was given to mechanisms of direct CP violation beyond the SM. Effects of charge asymmetry in $K^\pm \to 3\pi$ decays were analyzed under conditions of spontaneous breakdown of CP invariance within the model involving a few Higgs doublets [54]. This analysis revealed that the possible value of charge asymmetry in the slopes g can significantly exceed the SM prediction, reaching a level of $\sim 10^{-4}$ (Table 11d). The value of $(\delta g)_\tau \sim 10^{-5}$ and even more under some special assumptions about the parameters of the model was obtained in the supersymmetry extension of SM [55]—see Table 11e.

Some predictions for CP-violating asymmetries in $K^\pm \to \pi^\pm\pi^0\gamma$ and $K^\pm \to \pi^\pm\gamma\gamma$ decays were presented in [44, 56]—see Tables 11f–11h. All these effects seem to be unmeasurably small.

In connection with the currently prevalent situation, it seems that, despite the pessimistic predictions of the SM, we need thorough measurements of charge asymmetry in $K^\pm \to 3\pi$ decays with the highest possible experimental precision (about 10^{-4}). This is motivated by the possible manifestations of new CP-violation mechanisms and by difficulties in performing CHPT calculations, especially in higher orders.

Certainly, we should consider pioneering some of these measurements at levels of sensitivity above the current predications in order to learn to what extent measurements are possible in the future with more dedicated efforts. We are also well positioned to explore large charge asymmetries, as might be discovered in the present HyperCP experiment [48] and in other experiments [5, 49] which are in preparation now. Thus, it would be clearer at the beginning of CKM measurements if it were reasonable to do a next and more precise step in further extension of these very difficult experiments on charge asymmetry in K^+ and K^- decays.

9. $K^+ \to \pi^+e^+e^-, K^+ \to \pi^+\mu^+\mu^-$ FORM FACTOR AND BRANCHING-RATIO MEASUREMENTS

The precise study of the decays $K^+ \to \pi^+e^+e^-$ and $K^+ \to \pi^+\mu^+\mu^-$ opens new possibilities for the

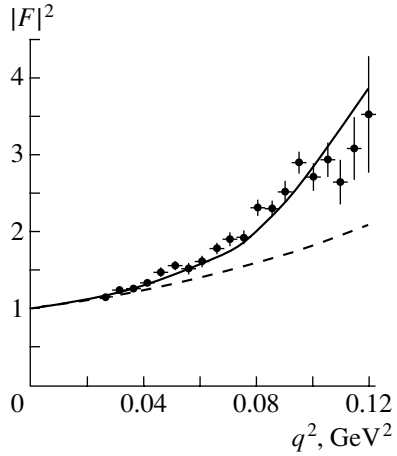

Fig. 12. Form factor squared $|F(q^2)|^2$ for $K^+ \to \pi^+e^+e^-$ as a function of $q^2 = m^2_{e^+e^-}$ from [60]. $F(q^2)$ is the same form factor as $f_v(z)$, but instead of dimensionless variable $z = q^2/m_K^2$, here the form factor is presented as a function of q^2. The dashed curve shows the approximation without the charge pion loop term. The solid curve includes the loop term. The theoretical curves are normalized to 1 at $q^2 = 0$ [62].

investigation of CHPT in the $\triangle S = 1$ weak interactions and the search for anomalous couplings. Careful measurements of the corresponding branching ratios and Dalitz plot analyses to measure the form factors in these decay modes are tests of CHPT predictions.

The integral ratio of these two modes $R(\mu^+\mu^-/e^+e^-) = \mathrm{BR}[K^+ \to \pi^+\mu^+\mu^-)]/\mathrm{BR}[K^+ \to \pi^+e^+e^-]$ and the differential ratios as functions of kinematic variables $\rho(\mu^+\mu^-/e^+e^-)$ cancel many of the theoretical uncertainties and provide a focused comparison of CHPT predictions for these weak semileptonic interactions [57, 58]. In different models, the predicted values of $R(\mu^+\mu^-/e^+e^-)$ vary in the range 0.2–0.3. Measurements with experimental accuracy of $\delta R = 2$–3% should give clean tests of the CHPT predictions to the 10% level. One early paper [59] suggested that the differential ratio $\rho(\mu^+\mu^-/e^+e^-)$ in the region of small π^+ energies is sensitive to the contribution of second-order weak diagrams.

The existing data for these two decay modes are dominated by results from recent BNL K^+ experiments and first of all by detailed study of $K^+ \to \pi^+e^+e^-$ decay in E865 [60]. The large statistics obtained for this decay mode (10 300 events) give the possibility of making the following conclusions:

(1) Experimental data are consistent with the vector model for the decay process (which proceeds through one-photon exchange) with amplitude $\frac{\alpha G_\mathrm{F}}{4\pi} f_v(z) p^\mu \bar{u}_e \gamma_\mu u_e$ (here, $p^\mu = P_K^\mu + p_\pi^\mu$, $q^\nu = P_K^\nu - p_\pi^\nu$, and $z = q^2/m_K^2 = m^2_{e^+e^-}/m_K^2$). For 90% C.L., at most 2% of the decay width $\Gamma(K^+ \to \pi^+e^+e^-)$ could result for either scalar or tensor interactions (with amplitudes $G_\mathrm{F} m_K f_S(z) \bar{u}_e u_e$ and $G_\mathrm{F} f_T(z) \times \frac{p^\mu q^\nu}{m_K} \bar{u}_e \sigma_{\mu\nu} u_e$). This corresponds to upper limits $|f_S| < 6.6 \times 10^{-5}$ and $|f_T| < 3.7 \times 10^{-4}$.

(2) Form factor $f_v(z)$ can be parametrized in the CHPT model [61] by expression $f_v(z) = a_+ + b_+ z + W^{\pi\pi}(z)$, where a_+ and b_+ are parameters of the model and $W^{\pi\pi}(z)$ is contribution from a charged-pion loop coupled through a virtual photon to e^+e^- current. This form factor was measured in [60] by studying the $d\Gamma/dz$ spectrum of e^+e^- pairs. The slope of the form factor is significantly larger than that which was predicted in CHPT calculations in $O(p^4)$ order (in this order, $b_+ \simeq 0$, and from the experiment, $a_+ = -0.587 \pm 0.010$ and $b_+ = -0.655 \pm 0.044$). Although linear approximation for the form factor is reasonable for $z \lesssim 0.3$, the experimental data clearly indicated the nonlinearity for larger values of $z(q^2)$, which is well fitted by the CHPT loop term (see Fig. 12). In [62], it was shown that the observed $f_v(z)$ is also well explained by the combined effect of the pion and kaon form factors in the vector-meson-dominance model and pion-loop graph. After including form-factor corrections, the branching ratio $\mathrm{BR}(K^+ \to \pi^+e^+e^-) = [2.94 \pm 0.05(\mathrm{stat.}) \pm 0.13(\mathrm{syst.}) \pm 0.05(\mathrm{model})] \times 10^{-7}$ was obtained.

All the main $K^+ \to \pi^+l^+l^-$ data [60, 63–66] are presented in Table 12. From this table, it is clear that for $K^+ \to \pi^+e^+e^-$ decay there is a reasonable agreement between the experiments [60] and [64]. But the data for $K^+ \to \pi^+\mu^+\mu^-$ decay from E787 [66] and E865 [65] are in disagreement[6)] by more than 3.6σ for reasons that are not yet understood. From the E865 data, the ratio $R(\mu^+\mu^-/e^+e^-)_\mathrm{exp} = \mathrm{BR}(K^+ \to \pi^+\mu^+\mu^-)/\mathrm{BR}(K^+ \to \pi^+e^+e^-) = 0.314 \pm 0.031$, which can be compared with $R(\mu^+\mu^-/e^+e^-)_\mathrm{CHPT} \gtrsim 0.23$ [61].

In the CKM, we estimate the sensitivity to these two decay modes to be $\sim 10^3$ and $\sim 2 \times 10^3$ events per week for $K^+ \to \pi^+e^+e^-$ and $K^+ \to \pi^+\mu^+\mu^-$, respectively (in parallel with the main $K^+ \to \pi^+\nu\bar{\nu}$ measurements). Thus, it would be possible to obtain tremendous statistics that can be used for very careful form-factor measurements and their comparison with

[6)] The new result of the HyperCP experiment at Fermilab was presented by C. Dukes at the XXXVII Rencontreas de Moriond (Les Ares, France, March 9–16, 2002); see also hep-ex/0205063. In this measurement, it was found that BR $(K^\pm \to \pi^\pm\mu^+\mu^-) = (9.8 \pm 1.0 \pm 0.5) \times 10^{-8} = (9.8 \pm 1.1) \times 10^{-8}$, in good agreement with the result of E865 BNL [65]. The new result is consistent with the CHPT prediction.

Table 12. The results from BNL experiments for studying $K^+ \to \pi^+ l^+ l^-$ decays and expected CKM statistics

Experiment	N events {BR}		$R(\mu^+\mu^-/e^+e^-)$	λ (for form factor parametrization $F(z) = 1 + \lambda z$)
	$K^+ \to \pi^+ e^+ e^-$	$K^+ \to \pi^+ \mu^+ \mu^-$		
E777 BNL [64]	~ 500 $\{(2.75 \pm 0.26) \times 10^{-7}\}$	–	–	1.31 ± 0.48
E851 BNL [63]	~ 800 $\{(2.81 \pm 0.20) \times 10^{-7}\}$	–	–	–
E787 BNL [66]	–	196 ± 17 $\{(5.0 \pm 1.0) \times 10^{-8}\}$	–	–
E865 BNL [60, 65]	$\sim 10\,300$ [60] $\{(2.94 \pm 0.15) \times 10^{-7}\}$ [60]	~ 430 [65] $\{(9.22 \pm 0.77) \times 10^{-8}\}$ [65]	0.314 ± 0.031	2.14 ± 0.20 $(K^+ \to \pi^+ e^+ e^-)$ [60] $2.45^{+1.30}_{-0.95}$ $(K^+ \to \pi^+ \mu^+ \mu^-)$ [65]
Expected CKM statistics	1.2×10^5	2.2×10^5		

very complicated future $O(p^6)$ predictions for CHPT, for a real significant test of the chiral approach, and for a further search for new types of interactions (scalar and tensor).

In the CKM, it is possible to use additional identification of one of the muons in $K^+ \to \pi^+ \mu^+ \mu^-$ in Pion RICH (by reducing the efficiency for this process by factor of 2) to suppress the background for this reaction from $K^+ \to \pi^+ \pi^+ \pi^-$ with two pion decays in flight. We also have very good identification of electrons in $K^+ \to \pi^+ e^+ e^-$.

10. CONCLUSION

We considered in this paper only several rare kaon decays to illustrate the possibility of the CKM experiment and to compare them with other measurements. Certainly, the number of interesting processes can be significantly increased, as is seen from Table 3.

It is clear from this paper that the CKM experiment will open many exciting possibilities for the search for new effects and for careful study of low-energy hadron physics in favorable conditions of kaon-decay processes. The sensitivity of the CKM experiment for the rare processes is on the level of 10^{-12} and exceeds all other experiments by one or two orders of magnitude. New advances in the searches for LFV in kaon decays, for direct CP-violation effects, for new types of interactions, and for hadronic dynamics studies are the highlights of the CKM, which can be comparable for their importance with the main experimental program of studying FCNC effects and properties of the CKM matrix in $K^+ \to \pi^+ \nu\bar{\nu}$ decays.

For further development of this experimental program, we continue now a careful study of possibilities of the setup, its trigger and DAQ requirements, background, and systematics for processes under study. Further extending the CKM physical program is also under consideration.

ACKNOWLEDGMENTS

I am greatly obliged to the members of the CKM collaboration for stimulating discussions and their help. My special gratitude goes to V.F. Obraztsov for some discussion of T-odd correlation in K decays and the search for different types of interactions and to D.V. Vavilov for the help with many calculations and with pictures.

REFERENCES

1. J. Frank *et al.* (Fermilab E921-CKM), *A Proposal for a Precision Measurement of the Decay $K^+ \to \pi^+ \nu\bar{\nu}$ and Other Rare K^+ Processes at Fermilab Using the Main Injector* (Fermilab, 2001).
2. S. Adler *et al.* (BNL E787), Phys. Rev. Lett. **79**, 2204 (1997); **84**, 3768 (2000); hep-ex/0111091.
3. B. Bassalleck *et al.* (BNL E949), *An Experiment to Measure $B(K^+ \to \pi^+ \nu\bar{\nu})$ at BNL*, BNL-67247 (1999).
4. B. Aubert *et al.* (BaBar Collab.), hep-ex/0107013; Phys. Rev. Lett. **87**, 091801 (2001); K. Abe *et al.* (Belle Collab.), hep-ex/0107061; Phys. Rev. Lett. **87**, 091802 (2001).
5. L. G. Landsberg and V. F. Obraztsov, in *Proceedings of the Workshop on K Physics (KAON-99), Chicago, 1999* (Univ. of Chicago Press, Chicago, 2000), p. 589; V. F. Obraztsov and L. G. Landsberg, hep-ex/0011033; in *Proceedings of the International Conference on CP Violation Physics, Ferrara, 2000*; L. G. Landsberg, Yad. Fiz. **64**, 1811 (2001) [Phys. At. Nucl. **64**, 1729 (2001)].
6. L. G. Landsberg and D. V. Vavilov, CKM Note 48 (2001).
7. L. G. Landsberg *et al.*, CKM Note 47 (2001).
8. R. Appel *et al.* (BNL E865), Phys. Rev. Lett. **85**, 2450 (2000).
9. R. Appel *et al.* (BNL E865), Phys. Rev. Lett. **85**, 2877 (2000).
10. D. Ambrose *et al.* (BNL E871), Phys. Rev. Lett. **81**, 5734 (1998).

11. KTeV Preliminary Results, *Conference APS Division of Particles and Fields, Columbus, Ohio, 2000;* A. Ledovskoy, in *Proceedings of the Workshop on K Physics (KAON-2001)*.
12. A. Alavi-Harati *et al.* (KTeV), hep-ex/0108037; Phys. Rev. Lett. **87**, 111802 (2001).
13. L. M. Barkov *et al.*, Research Proposal to PSI (1999); http://www.icepp.s.utokyo.ac.jpmeg; M. Bachman *et al.*, MECO Proposal to BNL (1997); http://meco.ps.uci.edu.
14. R. N. Cahn and H. Harari, Nucl. Phys. B **176**, 135 (1980).
15. J. Ritchie and S. Wojcicki, Rev. Mod. Phys. **65**, 1149 (1993); T. S. Kosmas *et al.*, Preprint IOA: 300/93 (Univ. of Ioannina, Ioannina, 1993); J. Bordes *et al.*, Phys. Rev. D **60**, 013005 (1999).
16. T. G. Rizzo, hep-ph/9809526; in *Proceedings of the Workshop on CP Violation, University of Adelaide, Adelaide, Australia, 1998*.
17. A. Belyaev *et al.*, hep-ph/0008276; hep-ph/0107046.
18. L. Littenberg and R. Shrok, Phys. Rev. Lett. **68**, 443 (1992); hep-ph/0005285.
19. Z. Gagyi-Palffy *et al.*, Nucl. Phys. B **513**, 517 (1998); Preprint RAL-090 (Chilton, 1994).
20. S. Davidson *et al.*, Z. Phys. C **61**, 613 (1994).
21. C. Dib *et al.*, Phys. Lett. B **493**, 82 (2000); hep-ph/0006277.
22. M. Schepkin, private communication, CKM Note 43 (2001).
23. K. Zuber, Phys. Lett. B **479**, 33 (2000); hep-ph/0003160.
24. C. Picciotto, Phys. Rev. D **56**, 1612 (1997).
25. R. G. Sachs, *The Physics of Time Reversal* (Univ. of Chicago Press, Chicago, 1987).
26. G. C. Branko, L. Lavora, and J. P. Silva, *CP Violation* (Clarendon, Oxford, 1999).
27. I. J. Bigi and A. I. Sanda, *CP Violation* (Cambridge Univ. Press, Cambridge, 1999).
28. J. J. Sakurai, Phys. Rev. **109**, 980 (1958).
29. A. R. Zhitnitskii, Yad. Fiz. **31**, 1024 (1980) [Sov. J. Nucl. Phys. **31**, 529 (1980)]; V. P. Efrosinin *et al.*, hep-ph/0008199.
30. Y. Grossman, Nucl. Phys. B **426**, 355 (1994); G. Belanger and C. Geng, Phys. Rev. D **44**, 2789 (1991); R. D. Peccei, hep-ph/9909236; in *Proceedings of the Workshop on K Physics (KAON-99), Chicago, 1999* (Univ. of Chicago Press, Chicago, 2000), p. 23.
31. E. P. Shabalin, Usp. Fiz. Nauk **171**, 951 (2001).
32. S. Blatt *et al.*, Phys. Rev. D **27**, 1056 (1983).
33. M. Abe *et al.* (KEK E246), Phys. Rev. Lett. **83**, 4253 (1999).
34. L. Littenberg, in *Proceedings of International KEK Workshop "Kaons, Muons, Neutrino Physics and Future," KEK, 1997,* Ed. by Y. Kuno and T. Shinkava, KEK Proc. 97-24, p. 27.
35. J. Gevais, J. Iliopoulos, and J. Kaplan, Phys. Lett. **20**, 432 (1966).
36. V. Braguta *et al.*, hep-ph/0106147.
37. J. Bijnens *et al., The Second DAΦNE Physics Handbook,* Ed. by L. Maiani *et al.* (LNF, Frascati, 1995), Vol. 1, p. 315.
38. V. N. Bolotov *et al.*, Yad. Fiz. **44**, 108 (1986) [Sov. J. Nucl. Phys. **44**, 68 (1986)].
39. H. Y. Cheng, Phys. Rev. D **26**, 143 (1982).
40. O. Shanker, Nucl. Phys. B **204**, 375 (1982); **206**, 253 (1982).
41. M. Finkemeier, *The Second DAΦNE Physics Handbook,* Ed. by L. Maiani *et al.* (LNF, Frascati, 1995), Vol. 1, p. 389.
42. S. S. Bulanov, Master Thesis (Mosk. Fiz.-Tekh. Inst., Moscow, 1999).
43. Particle Data Group (D. E. Groum *et al.*), Eur. Phys. J. C **15**, 1 (2000).
44. G. D'Ambrosio and G. Isidori, Int. J. Mod. Phys. A **13**, 1 (1998).
45. L. Maiani and P. Paver, *The Second DAΦNE Physics Handbook,* Ed. by L. Maiani *et al.* (LNF, Frascati, 1995), Vol. 1, p. 51.
46. P. Franzini, *The DAΦNE Physics Handbook,* Ed. by L. Maiani *et al.* (LNF, Frascati, 1992), Vol. 1, p. 15.
47. V. V. Ammosov *et al.*, Preprint No. 98-2 (IHEP, Protvino, 1998).
48. N. Leros, Nucl. Phys. B (Proc. Suppl.) **99**, 211 (2001).
49. R. Batley *et al.*, Proposal P253/CERN (SPSC); CERN/SPSC 2000-003.
50. C. O. Dib and R. D. Peccei, Phys. Lett. B **249**, 325 (1990).
51. A. A. Bel'kov *et al.*, Phys. Lett. B **232**, 118 (1989); **300**, 283 (1993).
52. A. A. Bel'kov *et al.*, hep-ph/0010142.
53. E. P. Shabalin, Nucl. Phys. B **409**, 87 (1993).
54. E. P. Shabalin, Yad. Fiz. **62**, 1657 (1999) [Phys. At. Nucl. **62**, 1552 (1999)].
55. G. D'Ambrosio, hep-ph/9911522.
56. G. Colangelo *et al.*, hep-ph/9908415.
57. G. Ecker *et al.*, Nucl. Phys. B **291**, 692 (1987).
58. L. Bergstrom and P. Singer, Phys. Rev. Lett. **55**, 2633 (1985); Phys. Rev. D **43**, 1568 (1991).
59. E. P. Shabalin, Pis'ma Zh. Éksp. Teor. Fiz. **22**, 117 (1975) [JETP Lett. **22**, 53 (1975)].
60. R. Appel *et al.*, Phys. Rev. Lett. **83**, 4482 (1999).
61. G. D'Ambrosio *et al.*, JHEP **08**, 004 (1998).
62. H. Burkhardt *et al.*, hep-ph/0011345.
63. A. L. Despande, Ph.D. Thesis (Yale University, 1995).
64. C. Alliegro *et al.* (BNL E777), Phys. Rev. Lett. **68**, 278 (1992).
65. H. Ma *et al.* (BNL E865), Phys. Rev. Lett. **84**, 2580 (2000).
66. S. Adler *et al.* (BNL E787), Phys. Rev. Lett. **79**, 4756 (1997).

Physics of Atomic Nuclei, Vol. 65, No. 10, 2002, pp. 1771–1777. Translated from Yadernaya Fizika, Vol. 65, No. 10, 2002, pp. 1819–1825.

NUCLEI
Experiment

Experimental Investigation of Highly Excited States of the ^{5,6}He and ^{5,6}Li Nuclei in the (^{6}Li, ^{7}Be) and (^{6}Li, ^{7}Li) One-Nucleon Pickup Reactions

S. B. Sakuta, B. G. Novatsky, D. N. Stepanov, D. V. Aleksandrov, Yu. A. Glukhov, and E. Yu. Nikol'sky

Russian Research Centre Kurchatov Institute, pl. Kurchatova 1, Moscow, 123182 Russia

Received August 28, 2001; in final form, November 5, 2001

Abstract—The (^{6}Li, ^{7}Be) and (^{6}Li, ^{7}Li) reactions on ^{6}Li and ^{7}Li nuclei were investigated in the angular interval 0°–20° in the laboratory system at a ^{6}Li energy of 93 MeV. In addition to low-lying states of the ^{5,6}He and ^{5,6}Li nuclei, broad structures were observed near the $t(^3\mathrm{He}) + d$ and $t(^3\mathrm{He}) + t$ thresholds at the excitation energies of 16.75 ($3/2^+$) and ~20 MeV (for ^{5}He), 16.66 ($3/2^+$) and ~20 MeV (^{5}Li), 14.0 and 25 MeV (^{6}He), and ~20 MeV (^{6}Li). The angular distributions measured in the ^{7}Li(^{6}Li, ^{7}Be)^{6}He reaction for transitions to the ground state (0^+) and excited states at $E_x = 1.8$ MeV (2^+) and 14.0 MeV of the ^{6}He nucleus were analyzed by the finite-range distorted-wave method assuming the $1p$- and $1s$-proton pickup mechanism. The (^{6}Li, ^{7}Be) and (^{6}Li, ^{7}Li) reactions were shown to proceed predominantly through the one-step pickup mechanism, and the broad structures observed at high excitation energies are considered as quasimolecular states of the $t(^3\mathrm{He}) + d$ and $t(^3\mathrm{He}) + t$ types. © *2002 MAIK "Nauka/Interperiodica".*

1. INTRODUCTION

It is well known that, owing to low thresholds of α-particle emission, the ground and low-lying states of nuclei with $A = 5$–9 possess a pronounced quasimolecular structure, whose components are an α particle and a residual $A - 4$ nucleus (n, p, d, t, ^{3}He, and α). An increase in the excitation energy up to a value sufficient for disintegration of the α-particle cluster leads to a kind of phase transition from the α-particle structure to structures involving lighter fragments. Despite a high excitation energy, fairly narrow resonances can exist in this case because their decay via the α-particle channel turns out to be inhibited. In particular, quasimolecular states of the $t(^3\mathrm{He}) + d$ and $t(^3\mathrm{He}) + t$ types with the $(1s_{1/2})^3(1p)^2$ and $(1s_{1/2})^3(1p)^3$ shell configurations must be observed in the nuclei with $A = 5$ and 6 at excitation energies close to the corresponding breakup thresholds. Nowadays, only two reliable examples of this kind are known; these are the states at 16.75 MeV ($3/2^+$) in the ^{5}He nucleus and 16.66 MeV ($3/2^+$) in the ^{5}Li nucleus [1], which are of great importance for the physics of thermonuclear reactions. No convincing evidence for the existence of other states of this kind has been obtained up to now in spite of the more than 30-year history of investigating the ^{5,6}He and ^{5,6}Li nuclear systems.

The most direct method for synthesizing quasimolecules of the $t(^3\mathrm{He}) + d(t)$ type is to transfer deuteron and triton clusters to tritium and ^{3}He nuclei in the (^{6}Li, α) and (^{7}Li, α) reactions. However, our previous investigations [2] showed that the states corresponding to these quasimolecules, if they do exist, must fall within a very intense breakup spectrum of α particles, which hampers obtaining reliable characteristics of desired resonance structures in the region of high excitation energies. Other methods of investigation are resonance scattering [3, 4]; the quasielastic proton knockout (p, $2p$) [5, 6] or (e, $e'p$) [7]; and also the one-nucleon pickup reactions (^{3}He, α) [8], (n, d) [9], and (p, d) [10]. In the indicated reactions, highly excited nuclei with the shell configurations $(1s_{1/2})^3(1p)^2$ and $(1s_{1/2})^3(1p)^3$ can be rather easily formed through breaking away a nucleon from the α-particle core of the ^{6}Li and ^{7}Li nuclei, whose ground states already contain deuteron and triton clusters.

Information available today about the ^{5}He, ^{5}Li, ^{6}He, and ^{6}Li nuclei at energies above the breakup thresholds for the $t(^3\mathrm{He}) + d$ and $t(^3\mathrm{He}) + t$ states is rather contradictory. For example, the ^{5}He states were observed at the excitation energies of $E_x =$ 20.2 MeV ($\Gamma = 2$ MeV) and 23.8 MeV ($\Gamma = 1$ MeV) in the ^{7}Li(d, α) and ^{6}Li(^{3}He, α) reactions; the ^{5}Li states were found in these reactions at $E_x =$ 19.8 MeV ($\Gamma = 2$ MeV) and 22.7 MeV ($\Gamma = 1$ MeV) [8]. The ^{5}He states were also observed at $E_x = 18.5$ and 20.5 MeV ($\Gamma = 2$ MeV) in the ^{6}Li(n, d)^{5}He reaction [9]. On the contrary, only one broad peak was

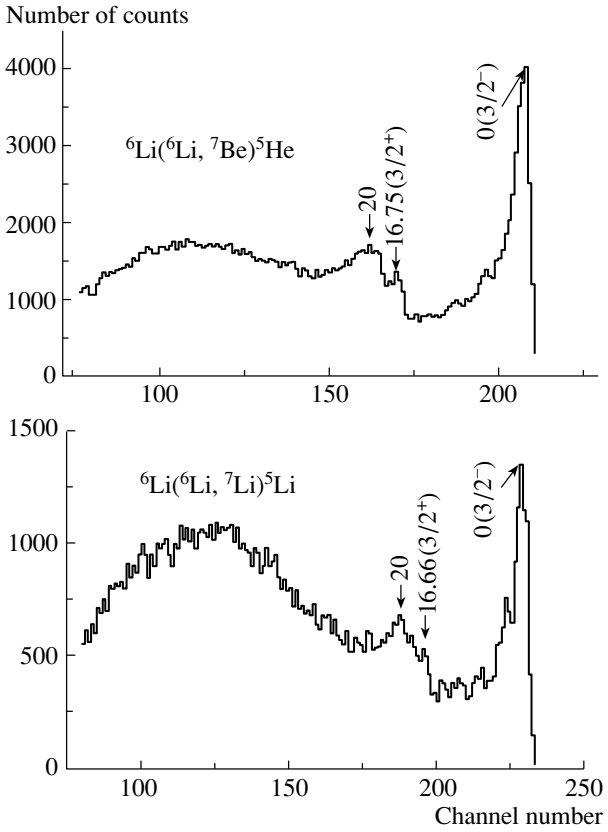

Fig. 1. Energy spectra of the ^{7}Be and ^{7}Li nuclei from the (^{6}Li, ^{7}Be) and (^{6}Li, ^{7}Li) reactions on the ^{6}Li nuclei at an angle of $\theta_{\text{lab}} = 14°$ for a beam energy of 93 MeV.

found in the $(p, 2p)$ reaction at an excitation energy of $\sim$20 MeV ($\Gamma \sim 4$ MeV) [5]. A broader distribution in this energy region ($\Gamma = 8$–10 MeV) was observed in the (p, d) reaction [10].

In the ^{7}Li$(n, d)^6$He reaction above the $t + t$ threshold ($\varepsilon = 12.305$ MeV) [9], the groups of deuterons corresponding to excitation energies of 13.6, 17.7, and 23.7 MeV were found, whereas only one peak with the center at $E_x \cong 14$ MeV and a width of about 4 MeV was observed in $(p, 2p)$ [6].

The cause of these contradictions is probably not only a poor energy resolution and insufficient statistical accuracy in certain experiments but also a high level of continuous background from the decay of both the states under consideration and the states of intermediate nuclei through the channel of the reaction under investigation, these intermediate nuclei being formed via two step-processes. The cross section of the two-step processes can be expected to decrease with increasing mass of the emitted particle.

In this study, we investigate the (^{6}Li, ^{7}Be) and (^{6}Li, ^{7}Li) one-nucleon pickup reactions on ^{6}Li and ^{7}Li nuclei at a ^{6}Li beam energy of 93 MeV. The main purpose was to derive information about nuclear quasimolecular states of the $t + d$, ^{3}He $+ d$, $t + t$, and ^{3}He $+ t$ types.

2. EXPERIMENTAL PROCEDURE AND RESULTS

The measurements were carried out at the Kurchatov Institute by using a beam of triply charged ^{6}Li ions accelerated by an isochronous cyclotron up to an energy of 93 MeV. Lithium targets were prepared by sputter deposition of enriched ^{6}Li and ^{7}Li isotopes in a vacuum onto a thin (0.2 μm) organic film. The samples were enriched to 90.9 and 99.9% in ^{6}Li and ^{7}Li, respectively. The experiments were performed with targets of thickness in the range 0.5–0.7 mg/cm^2, which were transported from the sputtering setup into the scattering chamber without vacuum deterioration in a special container with a vacuum lock.

The energy spectra of the ^{6}Li(^{6}Li, ^{7}Be), ^{6}Li(^{6}Li, ^{7}Li), ^{7}Li(^{6}Li, ^{7}Be), and ^{7}Li(^{6}Li, ^{7}Li) reactions were measured in the interval of angles from 10° to 20° in the laboratory system. The ^{7}Be and ^{7}Li nuclei were simultaneously detected by using a telescope that consisted of two silicon counters of thickness 50 μm and 1 mm, respectively. The charged products were identified by a conventional procedure of two-dimensional ΔE–E analysis. The energy resolution depended primarily on the beam-energy spread and was not worse than 500–600 keV. In the case of the ^{7}Li(^{6}Li, ^{7}Be)^{6}He reaction, additional measurements were carried out near 0° with a magnetic separator (MASE) [11] and a single 1-mm-thick silicon counter connected according to the scheme of energy–time-of-flight two-dimensional analysis. The flight-base length amounted to 4 m. The overall energy resolution in the MASE measurements was not poorer than 400 keV. Since the MASE system can transmit particles with an efficiency of 100% only in the range 10–15% from a detected-particle mean energy for a given magnetic rigidity of the system, the total spectrum was obtained by matching partial spectra (obtained for different tunings of the MASE) in overlapping regions. This was achieved by using a computer. The transmission efficiency as a function of the magnetic rigidity was experimentally determined from the ratio of the number of counts for the ^{7}Be nuclei from the ^{12}C(^{6}Li, ^{7}Be)^{11}B$_{\text{ground}}$ reaction to the number of counts in the monitor detector. The measurements showed the presence of a plateau with a width of not less than 10% of the average energy corresponding to a 100% transmission.

Figure 1 shows the energy spectra of the ^{7}Be and ^{7}Li nuclei in the (^{6}Li, ^{7}Be) and (^{6}Li, ^{7}Li) reactions on ^{6}Li nuclei at an angle of 14° in laboratory system.

The hard region of these spectra displays asymmetric peaks corresponding to excitation of the ground states of the ^{5}He and ^{5}Li ($J^\pi = 3/2^-$) nuclei in the reaction of the proton and neutron pickup from the p shell. Because the ground states of ^{5}He and ^{5}Li are unstable, the observed asymmetry is associated primarily with effects of the $^4\mathrm{He} + n(p)$ final-state interaction. In addition, it is possible that the presence of broad $p_{1/2}$ states ($J^\pi = 1/2^-$) [1] also affects the character of these spectra at excitation energies of up to 10–12 MeV. Small narrow peaks distinguishable in the range 2–10 MeV are associated with carbon and oxygen impurities in the target. The soft region of spectra near the thresholds for the breakup processes $^5\mathrm{He} \to t + d$ ($\varepsilon = 16.7$ MeV) and $^5\mathrm{Li} \to {}^3\mathrm{He} + d$ ($\varepsilon = 16.39$ MeV) shows structures composed of narrow peaks at $E_x = 16.75$ MeV ($3/2^+$) (^{5}He) and 16.66 MeV ($3/2^+$) (^{5}Li) and a broad distribution with a maximum at $E_x \approx 20$ MeV ($\Gamma \approx 5$ MeV). No other maxima beyond the statistical error were found. The $J^\pi = 3/2^+$ state is the well-known level with a pronounced quasimolecular $t(^3\mathrm{He}) + d$ structure, which corresponds to the $(1s_{1/2})^3(1p)^2$ shell configuration; it can be excited by the mechanism of the $1s$ nucleon pickup from the α-particle core.

Examples of spectra measured in the (^{6}Li, ^{7}Be) and (^{6}Li, ^{7}Li) reactions on ^{7}Li nuclei at an angle of 10° in the laboratory system are shown in Fig. 2. Transitions to the ground and low-lying states with 1.8 MeV(2^+) of the ^{6}He nucleus and with 2.186 MeV (3^+) and 3.562 MeV (0^+, $T = 1$) of the ^{6}Li nucleus are induced by the p nucleon pickup from ^{7}Li. In addition to these transitions, we observe a broad distribution, centered at $E_x = 14.0$ MeV ($\Gamma \approx 5$ MeV) for the ^{6}He nucleus and $E_x \approx 20$ MeV ($\Gamma \approx 10$ MeV) for the ^{6}Li nucleus, in the region of excitation energies above the triton-emission thresholds $\varepsilon = 12.305$ MeV (for ^{6}He) and $\varepsilon = 15.794$ MeV (for ^{6}Li). This region of excitation corresponds to hole states of the $1s$ shell. No other structure was found. A broader distribution for ^{6}Li can be explained by the excitation of states with isospin values of $T = 0$ and 1.

Figure 3 shows the energy spectrum of the ^{7}Li(^{6}Li, ^{7}Be)^{6}He reaction measured at an angle of 0° with the MASE. As can be seen from this figure, a nonresonance background in this spectrum is substantially lower than in the spectra measured at angles larger than 10° in the laboratory system. The spectrum measured at 0° is characterized by a good statistical accuracy and an overall energy resolution better than 400 keV. This energy spectrum shows a peak at $E_x = 14.0$ MeV ($\Gamma = 5$ MeV) without a fine structure. In addition to this peak, a distribution centered at $E_x \approx 25.0$ MeV ($\Gamma \approx 10$ MeV) can be clearly observed.

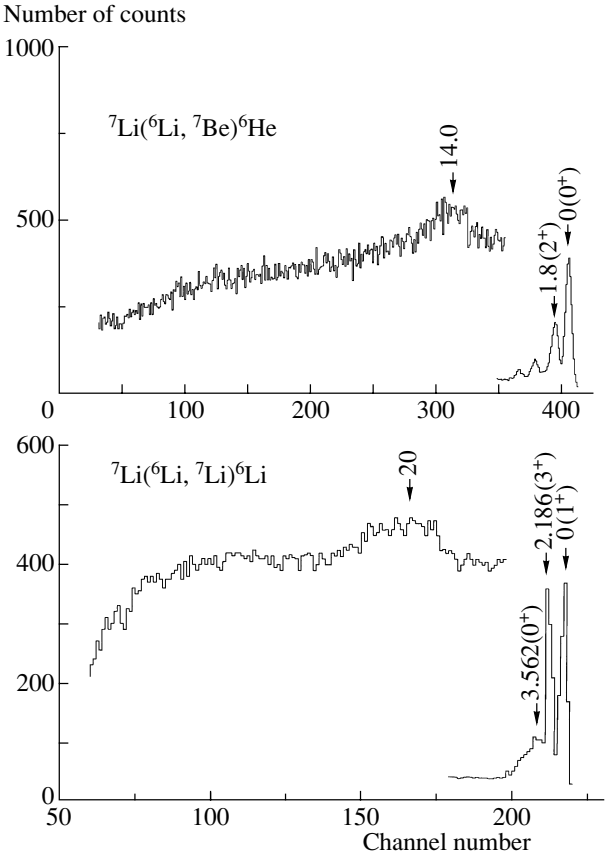

Fig. 2. Energy spectra of the ^{7}Be and ^{7}Li nuclei from the (^{6}Li, ^{7}Be) and (^{6}Li, ^{7}Li) reactions on the ^{7}Li nuclei at an angle of $\theta_{\mathrm{lab}} = 10°$ for a beam energy of 93 MeV.

The angular distributions measured for the transitions into the ground and excited states of the ^{6}He nucleus at $E_x = 1.8$ and 14.0 MeV are shown in Fig. 4.

3. ANALYSIS AND DISCUSSION OF RESULTS

3.1. Energy Spectra

The ^{6}Li nucleus represents an $\alpha + d$ quasimolecule, the deuteron being in the S state relative to the α-particle core [12] and having the total spin of $J = 1$. In this case, the one-step mechanism of the $1s$ nucleon pickup must populate only two positive-parity states $J^\pi = 1/2^+$ and $3/2^+$ in the ^{5}He and ^{5}Li nuclei. Other states can be excited only due to the mixing of the $(1s_{1/2})^3(1p)^2$ and $(1s_{1/2})^4(2s1d)$ configurations. As can be seen from Fig. 1, a distribution at $E_x \approx 20$ MeV with a width of about 5 MeV is observed in the spectra of the (^{6}Li, ^{7}Be) and (^{6}Li, ^{7}Li) reactions in addition to the well-known levels $J^\pi = 3/2^+$ at $E_x = 16.75$ MeV (^{5}He) and

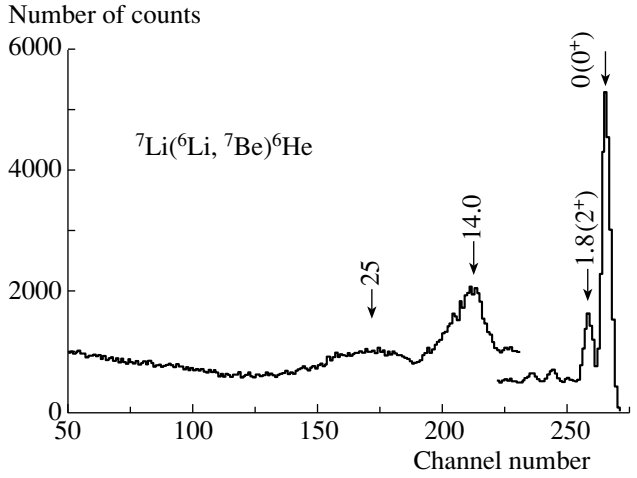

Fig. 3. Energy spectrum of the ^{7}Be nuclei from the (^{6}Li, ^{7}Be) reaction at an angle of $\theta_{lab} = 0°$ for a beam energy of 93 MeV.

16.66 MeV (^{5}Li). No other structure was found to within the statistical accuracy of the measurements. This result agrees with the data on the $(p, 2p)$ reaction [5] and contradicts the pieces of evidence that were obtained in investigating the (d, α), (^{3}He, α) [8], and (n, d) [9] reactions and which are indicative of the possible existence of relatively narrow resonances in the excitation-energy range 18–25 MeV. Shell-model calculations [13, 14] predict several levels of positive parity in the ^{5}He and ^{5}Li nuclei at energies above the $t(^3\mathrm{He}) + d$ threshold. According to these calculations, the $1/2^+$ level must occur above the $3/2^+$ level and fall in the region of excitation energies near 20 MeV. According to calculations using the resonating-group method for the $t + d$ and $^3\mathrm{He} + d$ systems, the $1/2^+$ level is expected to be at 19.1 and 19.3 MeV, respectively [15]. In view of the above facts, the structure observed in the (^{6}Li, ^{7}Be) and (^{6}Li, ^{7}Li) reactions at $E_x \approx 20$ MeV can correspond to the $J^\pi = 1/2^+$ state.

The supermultiplet potential model used to describe the interaction between the lightest clusters [16] makes it possible to understand qualitatively why the $1/2^+$ state is broader than the $3/2^+$ state. The reason is that the last case (the spin of the channel is $S = 3/2$) corresponds to only one type of symmetry, which is characterized by the Young diagram $\{f\} = \{32\}$, whereas both $\{41\}$ and $\{32\}$ are admissible for $J^\pi = 1/2^+$ ($S = 1/2$, $L = 0$), which leads to stronger coupling with the ^{5}He and ^{5}Li ground states $\{41\}$, increasing the probability of the $t(^3\mathrm{He}) + d \to \alpha + N$ decay.

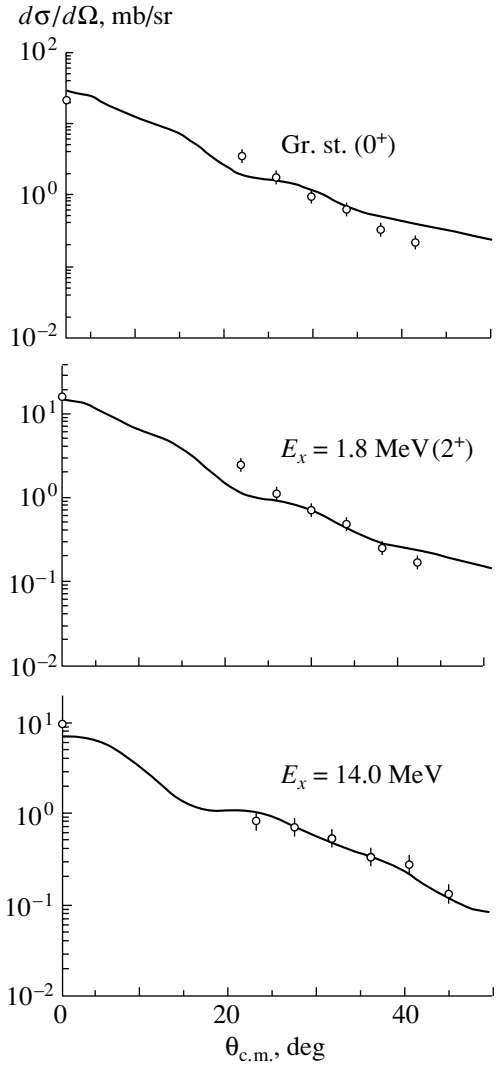

Fig. 4. Angular distributions for transitions to the ground state (0^+) and the excited states ($E_x = 1.8$ MeV (2^+) and 14.0 MeV) of the ^{6}He nucleus from the ^{7}Li (^{6}Li, ^{7}Be)^{6}He reaction at a beam energy of 93 MeV. The curves are calculated by the distorted-wave method with the potential parameters from Table 1 and the spectroscopic factors from Table 2. The open circles represent the experimental cross sections measured in this study.

In contrast to the case of $t(^3\mathrm{He}) + d$, the $t(^3\mathrm{He}) + t$, quasimolecular systems occur in the P state rather than in the S state [16] and, as expected, are less bound and, hence, broader. Since a triton in the ^{7}Li nucleus has the total angular momentum of $J = 3/2$, two states $J^\pi = 1^-$ and 2^- can be excited in the ^{6}He and ^{6}Li nuclei through the one-step mechanism of the $1s$ nucleon pickup. The positions of highly excited P levels in the ^{6}He and ^{6}Li nuclei formed by the ^{3}He and t clusters were calculated by the resonating-group method in [17]. According to these calculations, the ^3P levels (the channel spin is $S = 1$) must occur at

Table 1. Parameters of the optical potential used for calculating the ^{7}Li(^{6}Li, ^{7}Be)^{6}He reaction by the distorted-wave method

$-V$, MeV	r_V, fm	a_V, fm	$-W$, MeV	r_W, fm	a_W, fm	r_C, fm
122.5	0.577	0.905	51.71	0.54	1.178	0.588

Note: $R = r_i(A_p^{1/3} + A_t^{1/3})$; $i = V, W$.

the ^{6}He nucleus excitation energy of 18.1 MeV, while the $^1P(T = 0)$ and $^3P(T = 1)$ levels of the ^{6}Li nuclei are at $E_x = 21.3$ and 22.3 MeV, respectively. In [3], a partial-wave analysis of the angular distributions and the excitation and polarization functions for the elastic scattering of ^{3}He by ^{3}H in the energy range 20–33 MeV revealed a 2^- excitation in the ^{6}Li nucleus in the energy region $E_x \approx 21$ MeV. As for the 1^- excitation, there is only a small rise in the $^3P_1$ phase at a higher excitation energy.

In the spectra of the (^{6}Li, ^{7}Be) and (^{6}Li, ^{7}Li) reactions on ^{7}Li nuclei, we observed (Fig. 2) broad distributions centered at $E_x = 14$ MeV ($\Gamma = 5$ MeV) for the ^{6}He nucleus and at $E_x \approx 20$ MeV for the ^{6}Li nucleus. Assuming the pickup mechanism for these reactions and taking into account theoretical predictions, one can suggest that the peak at 14 MeV for the ^{6}He nucleus involves two states of the $t + t$ system with $J^\pi = 1^-$ and 2^-. The same states, together with the 1^- ($T = 0$) state, form a broad peak at $E_x \approx 20$ MeV ($\Gamma = 10$ MeV) in the ^{6}Li nucleus.

Now we consider the problem of the possible nature of the broad distribution observed in the ^{6}He nucleus at an excitation energy of 25 MeV. This distribution is clearly defined in the spectrum measured at 0° (Fig. 3). In the pickup and knockout reactions, this structure was not observed previously. According to the calculations by the translation-invariant shell model [18, 19], this region must involve a group of negative-parity levels ($J^\pi = 0^-, 1^-$, and 2^-) whose wave functions are dominated by a component characterized by the Young diagram {321}. These states must be effectively excited through the pickup mechanism due to a rather significant admixture of the {421} component in the wave function of the ^{7}Li nucleus [12]. The indicated compact group is well isolated because there is a wide energy gap between the states with different Young diagrams.

3.2. Angular Distributions

The above analysis of the energy spectra already gives a clear qualitative picture of the pickup nature of the mechanism of the (^{6}Li, ^{7}Be) and (^{6}Li, ^{7}Li) reactions, which is corroborated by the selective behavior of the reactions with respect to the states with a simple hole structure. Quantitative information about the mechanism is provided by an analysis of the differential cross sections. Considering the (^{6}Li, ^{7}Be) reaction as a simple proton pickup from the $1p$ and $1s$ shells, we analyzed the angular distributions for transitions into the states at $E_x = 0(0^+)$, 1.8 (2^+), and 14 MeV of the ^{6}He nucleus within the finite-range distorted-wave method using the DWUCK5 program [20]. In calculating the differential cross sections of the (^{6}Li, ^{7}Be) reaction, we took into account both bound states in ^{7}Be (the $3/2^-$ ground state and the $E_x = 0.43$ MeV, $1/2^-$ excited state), which were not separated in our measurements.

According to the shell model, the ground state of the ^{7}Li nucleus has a complicated configuration involving both $1p_{3/2}$ and $1p_{1/2}$ orbits. However, the selection rules are such that the transition into the ground state of the ^{6}He nucleus in the ^{7}Li(^{6}Li, ^{7}Be) $(3/2^-, 1/2) \to (0^+, 1)$ reaction can be realized only by the pickup of the $1p_{3/2}$ proton, whose binding energy in the ^{7}Li nucleus is equal to 9.988 MeV. In the transition into an excited state ($E_x = 1.8$ MeV, 2^+), the pickup of the $1p_{1/2}$ proton with a binding energy of 7.378 MeV (for the spin–orbit splitting of 2.6 MeV) is possible. Since the j dependence of differential cross sections calculated by the distorted-wave method is very weak [9], the particular calculations were carried out in this case under the assumption of only the $1p_{3/2}$-nucleon pickup. The state at $E_x = 14$ MeV was assumed to be excited by the $1s$-proton pickup.

For taking into account distortions in the input and output channels, we used the Woods–Saxon potential found from an analysis of the elastic scattering of ^{7}Li by ^{6}Li at an energy of 78 MeV [21]. The potential parameters are listed in Table 1. The wave functions of the bound states in ^{7}Li and ^{7}Be were calculated in the conventional way with a reduced radius of $r_0 = 1.2$ fm and a diffuseness parameter of $a = 0.65$ fm. The depth of the potential was chosen such a way as to reproduce the proton binding energy in the ^{7}Li and ^{7}Be nuclei. The spectroscopic factors

Table 2. Comparison of experimental and theoretical values of C^2S ($^7\mathrm{Li} \rightarrow {}^6\mathrm{He} + p$)

$E_x(^6\mathrm{He})$, MeV	J^π	C^2S				
		this study		[9]	theory	
		$1p_{3/2}$	$1s_{1/2}$		[12]	[22]
0	0^+	0.6		0.62	0.570	0.590
1.8	2^+	0.4		0.37	0.416	0.406
14.0	$(1^-, 2^-)$		2.2			
15.6	$(1^-, 2^-)$			1.53		

$S(^7\mathrm{Li} \rightarrow {}^6\mathrm{He} + p)$ were determined from the relationship

$$(d\sigma/d\Omega)_{\mathrm{exp}} = C^2S[S_0(d\sigma/d\Omega)_{0,\mathrm{DW}} + S_1(d\sigma/d\Omega)_{1,\mathrm{DW}}],$$

where $(d\sigma/d\Omega)_{\mathrm{DW}}$ are the cross sections calculated using the DWUCK5 program with the coherent summation over the angular-momentum transfers satisfying the selection rules; S_0 and S_1 are the spectroscopic factors of the $^7\mathrm{Be}_0 \rightarrow {}^6\mathrm{Li} + p$ and $^7\mathrm{Be}_{0.43} \rightarrow {}^6\mathrm{Li} + p$ systems, respectively; and C^2 is the square of the Clebsch–Gordan isospin coefficient $\langle T_f N_f, 1/2{-}1/2 | T_i N_i \rangle^2$, T_f, N_f, T_i, and N_i being the isotopic spins and their projections for the target and the residual nucleus. The values of S_0 and S_1 taken from [22] amounted to 0.721 and 0.893, respectively.

Figure 4 illustrates a comparison of the calculated and experimental angular distributions. The spectroscopic factors derived as a result of analysis and multiplied by C^2 are listed in Table 2 together with the theoretical values calculated using the shell model [12, 22] and with the results of analysis of the $^7\mathrm{Li}(n, p)^6\mathrm{He}$ reaction investigated in [9] at a neutron energy of 56.3 MeV. It can be seen that the proton-pickup mechanism in the (^{6}Li, ^{7}Be) reaction describes well the measured angular distributions for the spectroscopic factors close to those from the theoretical predictions and to the experimental values from [9]. Although the previous investigation [23] of angular distributions for the transitions to the ground states of the ^{5}He and ^{5}Li nuclei in the $^6\mathrm{Li}(^6\mathrm{Li}, ^7\mathrm{Be})$ and $^6\mathrm{Li}(^6\mathrm{Li}, ^7\mathrm{Li})$ reactions at a ^{6}Li energy of 156 MeV showed that the theoretical description of differential cross sections within the one-step pickup mechanism is not perfect, the general character of experimental distributions is reproduced fairly well.

Thus, information available now indicates that the (^{6}Li, ^{7}Be) and (^{6}Li, ^{7}Li) reactions at energies of approximately 100 MeV do indeed proceed through the one-step nucleon-pickup mechanism. This means that the observed highly excited states of the ^{5}He, ^{5}Li, ^{6}He, and ^{6}Li nuclei are quasimolecular states of the $t(^3\mathrm{He}) + d$ ($J^\pi = 3/2^+$ and $1/2^+$) and $t(^3\mathrm{He}) + t$ ($J^\pi = 2^-$ and 1^-) types.

4. CONCLUSION

In a single experiment, we have investigated the (^{6}Li, ^{7}Be) and (^{6}Li, ^{7}Li) reactions on ^{6}Li and ^{7}Li nuclei at a ^{6}Li beam energy of 93 MeV. In all the measured spectra, we have observed two groups of states separated by a wide energy gap (more than 10 MeV). The first group of states is assumed to be induced by the nucleon pickup by an incident ^{6}Li particle from the p shell of the target nucleus, whereas the second group of states near the thresholds of the $t(^3\mathrm{He}) + d$ break-up of the ^{5}He (^{5}Li) nuclei and the $t(^3\mathrm{He}) + t$ breakup of the ^{6}He (^{6}Li) nuclei is due to the pickup from the $1s$ shell.

For a more detailed investigation of the mechanism of the (^{6}Li, ^{7}Be) and (^{6}Li, ^{7}Li) reactions, we have measured the angular distributions of the $^7\mathrm{Li}(^6\mathrm{Li}, ^7\mathrm{Be})^6\mathrm{He}$ reaction for transitions into the ground and excited states of the ^{6}He nucleus. The experimental differential cross sections have been analyzed by the finite-range distorted-wave method under the assumption of the pickup mechanism. The calculated cross sections reproduce well the experimental ones for the spectroscopic factors close to those predicted in the shell model. This fact totally corroborates the assumption that the one-step pickup mechanism dominates in the (^{6}Li, ^{7}Be) reaction and, hence, in the (^{6}Li, ^{7}Li) reaction (by virtue of the mirror structure of the ^{7}Li and ^{7}Be nuclei) at an energy near 90 MeV.

Because of the pickup character of the (^{6}Li, ^{7}Be) and (^{6}Li, ^{7}Li) reactions, only two positive-parity states ($3/2^+$, $1/2^+$) in the ^{5}He and ^{5}Li nuclei and two negative-parity states (2^-, 1^-) in the ^{6}He and ^{6}Li nuclei can be populated in these reactions (of course, if mixing of the configurations is not significant). According to the available predictions of the shell model and the resonating-group method, it is possible to assign a spin value $J^\pi = 1/2^+$ to the broad states

appearing in the ^{5}He and ^{5}Li nuclei at $E_x \approx 20$ MeV, while the structures observed in the ^{6}He nucleus at $E_x = 14$ MeV and in the ^{6}Li nucleus at $E_x \approx 20$ MeV are formed by the states with $J^\pi = 2^-$ and 1^-.

A broad distribution clearly manifested at the excitation energy of about 25 MeV for the ^{6}He nucleus at 0° is also associated with the excitation of the 1^- and 2^- states, but of a different symmetry type characterized by the Young diagram {321}. This compact group of states was predicted long ago in theoretical calculations based on the translation-invariant shell model.

The broad structures observed in the ^{5}He, ^{5}Li, ^{6}He, and ^{6}Li nuclei at high excitation energies correspond to two-cluster quasimolecular states of the $t(^3\mathrm{He}) + d$ and $t(^3\mathrm{He}) + t$ types populated by breaking away one nucleon from the α-particle core of the ^{6}Li and ^{7}Li nuclei, whose ground states already have deuteron and triton clusters.

ACKNOWLEDGMENTS

This work was supported by the Russian Foundation for Basic Research, project no. 00-02-16626.

REFERENCES

1. F. Ajzenberg-Selove, Nucl. Phys. A **490**, 1 (1988).
2. D. V. Aleksandrov, Yu. A. Glukhov, E. Yu. Nikol'skiĭ, *et al.*, Yad. Fiz. **46**, 385 (1987) [Sov. J. Nucl. Phys. **46**, 197 (1987)].
3. R. Vlastou, J. B. A. England, O. Karban, and S. Baird, Nucl. Phys. A **292**, 29 (1977).
4. R. J. Batten, D. L. Clough, J. B. A. England, *et al.*, Nucl. Phys. A **151**, 56 (1970).
5. R. K. Bhowmik, C. C. Chang, P. G. Roos, and H. D. Holmgren, Nucl. Phys. A **226**, 365 (1974).
6. R. K. Bhowmik, C. C. Chang, J.-P. Didelez, and H. D. Holmgren, Phys. Rev. C **13**, 2105 (1976).
7. T. Hotta, T. Tamae, T. Miura, *et al.*, Nucl. Phys. A **645**, 492 (1999).
8. M. P. Baker, J. M. Cameron, N. S. Chant, and N. F. Mangelson, Nucl. Phys. A **184**, 97 (1972).
9. F. P. Brady, N. S. King, B. E. Bonner, *et al.*, Phys. Rev. C **16**, 31 (1977).
10. B. Fagerström, J. Källne, O. Sundberg, and G. Tibell, Phys. Scr. **13**, 101 (1976).
11. V. V. Buranov, N. I. Venikov, A. M. Dobychin, *et al.*, Preprint No. 4816/2, IAÉ (Inst. of Atomic Energy, Moscow, 1989).
12. A. N. Boyarkina, *Structure of the p-Shell Nuclei* (Mosk. Gos. Univ., Moscow, 1973).
13. K. Ramavataram and S. Ramavataram, Nucl. Phys. A **147**, 293 (1970).
14. R. F. Wagner and C. Werntz, Phys. Rev. C **4**, 1 (1971).
15. F. S. Chwieroth, R. E. Brown, Y. C. Tang, and D. R. Thompson, Phys. Rev. C **8**, 938 (1973).
16. V. M. Lebedev, V. G. Neudatchin, and A. A. Sakharuk, Yad. Fiz. **63**, 248 (2000) [Phys. At. Nucl. **63**, 195 (2000)].
17. D. R. Thompson and Y. C. Tang, Nucl. Phys. A **106**, 591 (1968).
18. I. V. Kurdyumov, Yu. F. Smirnov, K. V. Shitikova, and S. Kh. El Samarai, Phys. Lett. B **31B**, 163 (1970).
19. B. S. Ishkhanov, I. M. Kapitonov, V. G. Neudatchin, and R. A. Éramzhyan, Fiz. Élem. Chastits At. Yadra **12**, 905 (1981) [Sov. J. Part. Nucl. **12**, 362 (1981)].
20. P. D. Kunz, Computer Program DWUCK5.
21. Yu. A. Glukhov, O. Yu. Goryunov, E. I. Koshchiĭ, *et al.*, Yad. Fiz. **49**, 1243 (1989) [Sov. J. Nucl. Phys. **49**, 774 (1989)].
22. S. Cohen and D. Kurath, Nucl. Phys. A **101**, 1 (1967).
23. S. Micek, H. Rebel, H. J. Gils, *et al.*, Z. Phys. A **328**, 467 (1987).

Translated by V. Bukhanov

Physics of Atomic Nuclei, Vol. 65, No. 10, 2002, pp. 1778–1784. From Yadernaya Fizika, Vol. 65, No. 10, 2002, pp. 1826–1832.

NUCLEI
Experiment

Search for the Radiative Capture Reaction $d + d \rightarrow {}^4\mathrm{He} + \gamma$ from the $dd\mu$ Muonic Molecule State*

L. N. Bogdanova[1], V. R. Bom[2], D. L. Demin[3], C. W. E. van Eijk[2], V. V. Filchenkov[3], N. N. Grafov[3], V. G. Grebinnik[3], K. I. Gritsaj[3], A. D. Konin[3], A. V. Kuryakin[4], V. A. Nazarov[4], V. V. Perevozchikov[4], A. I. Rudenko[3], S. M. Sadetsky[5], Yu. I. Vinogradov[4], A. A. Yukhimchuk[4], S. A. Yukhimchuk[3], V. G. Zinov[3], and S. V. Zlatoustovskii[4]

Received January 15, 2002; in final form, April 25, 2002

Abstract—A search for the muon-catalyzed fusion (MCF) reaction $d + d \rightarrow {}^4\mathrm{He} + \gamma$ in the $dd\mu$ muonic molecule was performed using the experimental MCF installation TRITON and NaI(Tl) detectors for γ quanta. A high-pressure target filled with deuterium was exposed to the negative muon beam of the JINR phasotron to detect γ quanta with an energy of 23.8 MeV. The first experimental estimation for the yield of radiative deuteron capture from the $dd\mu$ state $J = 1$ was obtained at a level of $\eta_\gamma \leq 2 \times 10^{-5}$ per one fusion.

1. INTRODUCTION

It is understood that investigations of fusion reactions between hydrogen isotope nuclei at low energies are of great importance for determining properties of the lightest nuclei and for astrophysics. In particular, there is a need for new or improved measurements of many radiation capture reactions included in various astrophysical scenarios. Due to the Coulomb repulsion fusion, cross sections $\sigma(E)$ drop rapidly at low ($E \leq 100$ keV) collision energies (in an exponential scale for "bare" nuclei).

The reaction

$$d + d \longrightarrow {}^4\mathrm{He} + \gamma + 23.8\ \mathrm{MeV} \qquad (1)$$

is involved in both primordial and stellar nucleosynthesis. Its cross section is rather small (about 1 pb at 50 keV, compared to 1 mb for the main fusion channels $d(d,n)^3\mathrm{He}$ and $d(d,p)^3\mathrm{H}$), and its experimental investigations in dd collisions are rather difficult.

At energies $E > 400$ keV, reaction (1) proceeds mainly by a d-wave $E2$ transition to the ${}^1S_0$ state of ^{4}He [1]. The reason is the identical boson character of the entrance channel requiring $L + S$ to be even (L and S are the orbital angular momentum and the total spin of the dd system). At lower energies, the centrifugal barrier suppresses the d-wave $E2$ capture, allowing an s-wave $E2$ transition to the D-state admixture of ^{4}He. Measurements extended to energies below 100 keV [2] have confirmed this picture. However, the existence of multipoles other than $E2$ in reaction (1) was not excluded experimentally despite the belief that dipole transitions $E1$ and $M1$ with $\Delta S = 0$ should be suppressed due to the standard isospin selection rule $\Delta T = 0$.

Measurements of cross section angular distributions $\sigma(\theta)$ of vector A_y and tensor A_{yy} analyzing powers performed with a polarized deuteron beam with an energy of $E_d^{\mathrm{lab}} = 80$ keV stopping in the target have yielded an unexpected observation of the p wave strength in $^2\mathrm{H}(\vec{d},\gamma)^4\mathrm{He}$ reaction [3]. It was found that over 50% of the cross section strength at these low energies were due to $E1$ and $M2$ p wave capture. This finding might be considered as a violation of the isospin selection rule and affect the low-energy behavior of the total cross section and its extrapolation to substantially sub-Coulomb energies (as required, e.g., by stellar calculations). Other evidence for non-$E2$ radiation can be found in [3]. It would be extremely interesting to observe any direct manifestation of the p wave in an independent measurement.

During recent decades, experiments in which various fusion reactions between hydrogen isotopes are

*This article was submitted by the authors in English.

[1]Institute of Theoretical and Experimental Physics, Moscow, 117259 Russia.
[2]Delft University of Technology, the Netherlands.
[3]Joint Institute for Nuclear Research, Dzhelepov Laboratory of Nuclear Problems, Dubna, 141980 Russia.
[4]Russian Federal Nuclear Center, All-Russian Research Institute of Experimental Physics, Sarov, Russia.
[5]Petersburg Nuclear Physics Institute, Russian Academy of Sciences, Gatchina, 188350 Russia.

catalyzed by muons have provided supplementary information about these reactions at energies well below the lowest energies accessible by conventional beam–target experiments [4]. In the muon-catalyzed (MC) process, fusion takes place from the bound states of muonic molecules. Nuclei inside muonic molecules are practically at rest, being separated by average distances $a_\mu \sim \hbar^2/e^2 m_\mu^2 = 2.5 \times 10^{-11}$ cm (m_μ is the muon mass).

Muonic molecules can be formed in states with total angular momenta $J = 0$ and $J = 1$ that correspond to the relative orbital angular momenta of nuclei $L = 0$ and $L = 1$. Depending on the hydrogen-isotope-mixture parameters, various states of muonic molecules can be populated. This makes it possible to study fusion reactions at superlow energies from prepared s- and p-nuclear states with definite spins.

Study of the MC fusion process in a $dd\mu$ muonic molecule resulted in complementary and detailed information about charge-symmetric reactions $d(d,n)^3\mathrm{He}$ and $d(d,p)^3\mathrm{H}$. A significant difference in the p wave parts of the $d(d,p)^3\mathrm{H}$ and $d(d,n)^3\mathrm{He}$ reaction yields was observed in the experiments with low-energy polarized deuteron beams [5]. Comparison of two reaction branches showed some s-wave enhancement together with substantial p wave suppression of the proton branch. (This result was then interpreted by some as evidence for charge symmetry breaking forces.)

Direct measurement of the yield ratio $R_p(n/p)$ for the reactions

$$dd\mu \longrightarrow {}^3\mathrm{He} + n + \mu, {}^3\mathrm{He}\mu + n, \qquad (2)$$

$$dd\mu \longrightarrow t + p + \mu \qquad (3)$$

proceeding from the $J = 1$ state of $dd\mu$ molecules (p-wave dd fusion) [6, 7] gave the value $R_p(n/p) = 1.42 \pm 0.03$. It agreed with the ratio from [5] determined from an elaborate (and model-dependent) analysis of the in-flight data. Rates of $dd\mu$ fusion reactions (2) and (3) from the p wave were experimentally determined from the MC data [8], and the corresponding nuclear reaction constants were extracted [9].

The deuteron radiative capture reaction in the $dd\mu$ molecule

$$dd\mu \longrightarrow {}^4\mathrm{He}\mu + \gamma + 23.8\ \mathrm{MeV} \qquad (4)$$

was not previously investigated because of the extreme smallness of its expected yield. In the systematic study of the MC process in deuterium, we have recently performed [10] measurements in the temperature range $T = 85$–790 K. As in our earlier experiments [11], neutrons from reaction (2) were detected. At temperatures $T > 150$ K, $dd\mu$ molecules

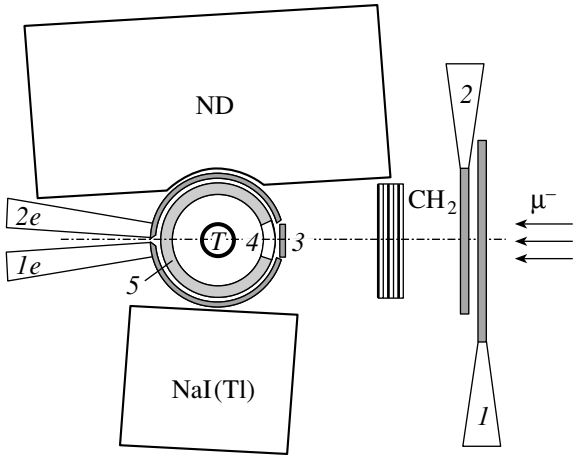

Fig. 1. Experimental layout.

are mainly formed in the $J = 1$ state and fusion reactions proceed from the p wave of relative nuclear motion. Hence, if detected, 23.8-MeV γ quanta would unambiguously indicate a finite p wave contribution to the rate of process (4).

In view of this, we investigated the possibility of process (4) being detected in our last measurements of the $dd\mu$-molecule formation rate [10]. For this aim, one of two usually used neutron detectors [11] was removed and a gamma detector was installed instead. The level of the radiation background in our installation was measured. We present the first experimental estimation for the yield of the p wave radiative dd capture from the $dd\mu$ molecule.

2. EXPERIMENTAL METHOD

The experimental setup (its layout is shown in Fig. 1) is described in detail in [12]. A high-pressure deuterium target (HPDT) [13] was exposed to the muon beam of the JINR phasotron. Scintillation counters *1*–*3* in front of the HPDT detected the incoming muons. Cylinder-shaped multiwire proportional chambers *4* and *5* served to identify the muon stop in the target and to detect electrons from muon decay. A coincidence between signals of counters *5* and *1e*, *2e* served as the electron signal.

A full absorption neutron detector (ND) (volume of NE-213, $v = 12.5$ l) [12, 14] was aimed to detect neutrons from reaction (2). To reduce the background, n–γ separation was realized by comparing the signals for the total charge and the fast component charge of the ND pulse. The efficiency of the γ-quantum discrimination was better than 10^{-3} for energies $E_{\gamma,e} > 100$ keV.

The γ quanta were detected with a NaI(Tl) crystal of 150-mm diameter and 100-mm height. It was calibrated with γ sources of ^{60}Co (total energy of two γ's

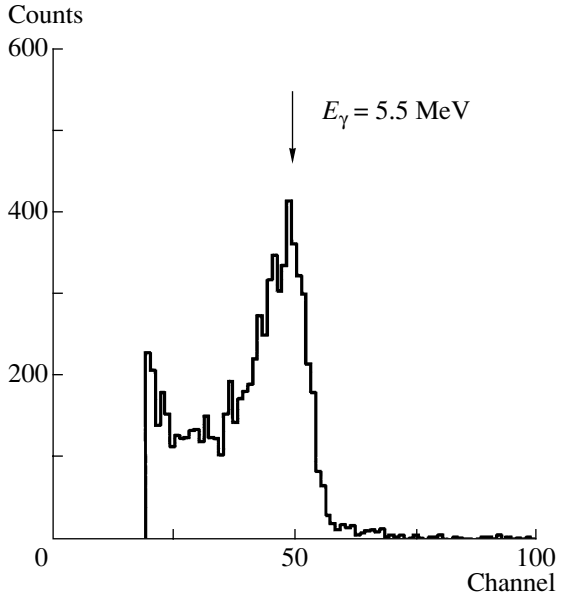

Fig. 2. Amplitude distribution of the events detected by the NaI(Tl) detector in the exposures with the H/D mixture.

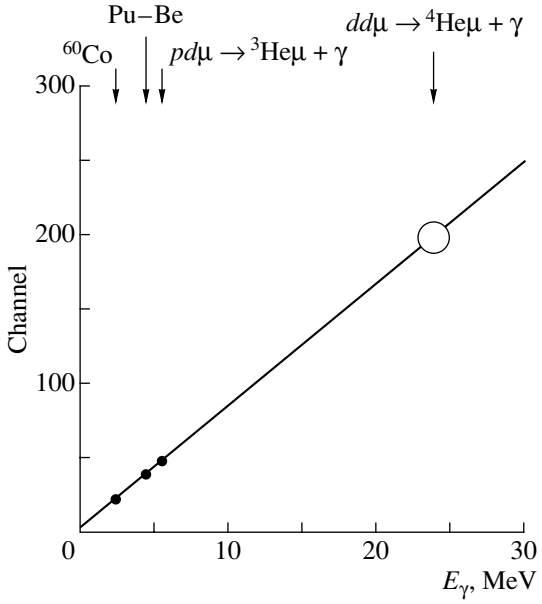

Fig. 3. Calibrating line of the γ spectrometer. Points correspond to the calibration with the ^{60}Co and Pu–Be γ sources and with γ's from reaction (6).

$E_{2\gamma} = 2.5$ MeV), Pu–Be ($E_\gamma = 4.43$ MeV), and with 5.5-MeV γ's from the reaction

$$pd\mu \to {}^3\mathrm{He}\mu + \gamma. \qquad (5)$$

Reaction (5) was observed in the test exposures when the target was filled with a hydrogen–deuterium (H/D) mixture containing about 20% protium. The amplitude distribution for 5.5-MeV γ's is shown in Fig. 2. The obtained energy resolution of the detector is 15% FWHM.

The calibrating line for the γ detector is presented in Fig. 3. Linearity of the energy scale was checked under different voltages supplied to the detector in measurements with the available ^{60}Co and Pu–Be γ sources. In the amplitude region used, it proved to be linear at a level of 2–3%. The expected position for γ's from (4) is then approximately the 200th channel. Stability of the spectrometric system was controlled with γ sources during the run.

The detection efficiency for γ quanta was estimated from their cross sections in NaI and the known solid angle of the detector. Taking into account the efficiency losses (30–40%) due to the bremsstrahlung in the target walls, we found the detection efficiency for 24-MeV γ quanta:

$$\epsilon_\gamma = (5 \pm 1)\%. \qquad (6)$$

Primary selection of the events detected by the neutron and γ detectors was realized by the trigger. It allowed only those events for further time and amplitude analysis which were connected with electron registration; that is, delayed $\mu - n, \gamma - e$ coincidences were used. Under this condition, the timing sequence of the NaI and ND signals was registered by flash ADC and recorded on the PC. An example of the "oscillogram" of events thus stored is shown in Fig. 4.

3. MEASUREMENTS AND ANALYSIS OF ND DATA

During the run, eight exposures were performed at different deuterium temperatures and densities. Experimental conditions for them are presented in the table. Deuterium density is given in relative units: $\phi = n/n_0$, where $n_0 = 4.25 \times 10^{22}$ nucl./cm^3 is the liquid hydrogen density (LHD). For all exposures, the intensity of muons detected by counters *1–4* was 2.5×10^3 s^{-1}. The electron counting rate was 15–30 s^{-1} depending on the deuterium density.

The number of detected electrons from muon decay N_e was determined from the fit of the electron time spectra taking into account the background from muon stops in the target walls. The latter was found in the exposure with the empty target. The number of electrons detected for 10 h of phasotron operation (one exposure) was $\simeq (0.5-1.0) \times 10^6$ depending of a gas density. Details of the analysis can be found in [11].

The number of neutrons from reaction (2) N_n was obtained from the analysis of the time spectra of the events detected by ND and belonging to the neutron region in the $n - \gamma$ plot [14]. The neutron background

Experimental conditions

Exposure	T, K	Content, %		ϕ, LHD	N_e	N_n	$N_{dd\mu} \times 10^{-5}$
		H	D				
1	85 (5)	20.7 (0.5)	79.3 (0.5)	0.84 (0.03)	712 300	4000	1.2
2	110 (5)	20.7 (0.5)	79.3 (0.5)	0.84 (0.03)	474 600	4700	1.2
3	230 (5)	20.7 (0.5)	79.3 (0.5)	0.83 (0.03)	433 200	15 000	4.5
4	301 (4)	20.7 (0.5)	79.3 (0.5)	0.83 (0.03)	443 700	20 200	6.1
5	299 (4)	20.7 (0.5)	79.3 (0.5)	0.47 (0.02)	388 900	13 900	4.2
6	298 (4)	0.1 (0.1)	99.9 (0.1)	0.50 (0.02)	232 500	18 100	5.7
7	548 (10)	0.1 (0.1)	99.9 (0.1)	0.50 (0.02)	240 000	19 500	5.1
8	791 (15)	0.1 (0.1)	99.9 (0.1)	0.49 (0.02)	315 000	20 500	6.1

was measured in a special exposure with the empty target. The N_e and N_n numbers determined are presented in the table.

As is seen from the table, part of the exposures were made with an H/D mixture. It allows detection of reaction (5), which was used for energy calibration and for checking the γ-quanta-detection efficiency.

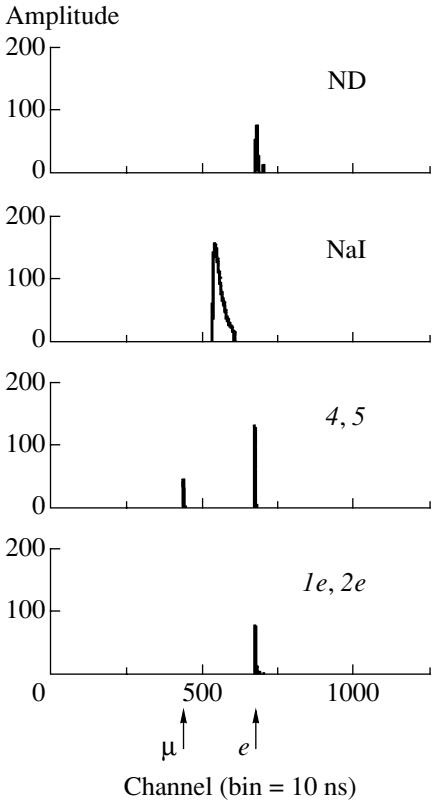

Fig. 4. Signals on flash ADC. The muon is detected by counter *4* (see Fig. 1). The electron from μ decay is detected by counters *5*, *1e* or *2e*. For the presented event the electron is detected by counters *5*, *2e* and by ND too.

The kinetics scheme of the main processes occurring after the muon stop in the H/D mixture is shown in Fig. 5 [15]. As expected, exposures 1 and 2 are characterized by a low neutron–electron ratio. In other words, only a small fraction of the muon stops in the target lead to formation of $dd\mu$ molecules and subsequent reaction (2), detected in our experiment. It is due to the fact [6–8, 11] that at low temperatures $T < 150$ K, the $dd\mu$-formation rate $\lambda_{dd\mu}\phi < 0.1 \times 10^6$ s^{-1} is small compared to the $d\mu$-atom disappearance rate $\lambda_{d\mu} = \lambda_0 + \lambda_{dd\mu}\phi(1 - C_p) + \lambda_{pd\mu}\phi C_p$, where $\lambda_0 = 4.55 \times 10^5$ s^{-1} is the free-muon disappearance rate and $\lambda_{pd\mu} = (5.53 \pm 0.16) \times 10^6$ s^{-1} [17] is the $pd\mu$-formation rate. This allowed the use of these exposures for estimating the accidental background. Exposures 3–8 were accepted for the search of γ's from reaction (4) and the estimation of its relative yield.

From the measured numbers of neutrons N_n, known neutron detection efficiency $\epsilon_n = 13\%$ [18], and the partial probability of reaction (2) $\beta \cong 0.58$ [7], the $dd\mu$-formation rates $\lambda_{dd\mu}$ were obtained for each exposure.

With values $\lambda_{dd\mu}$ thus obtained and data from the table, we calculated the average number of catalysis cycles n_c per muon using a simplified formula describing MC fusion kinetics in the H/D mixture corresponding to the scheme in Fig. 5:

$$n_c = \lambda_{dd\mu}\phi(1 - C_p)/[\lambda_0 + \lambda_{dd\mu}\phi(1 - C_p)\varpi_{dd} + \lambda_{pd\mu}\phi C_p\varpi_{pd}]. \quad (7)$$

Here, $\varpi_{dd} = \beta\omega_{dd} = 0.07$ [6, 7] and $\varpi_{pd} = 0.85$ [15, 19] are branching ratios of fusion reactions with muon sticking to helium with respect to all

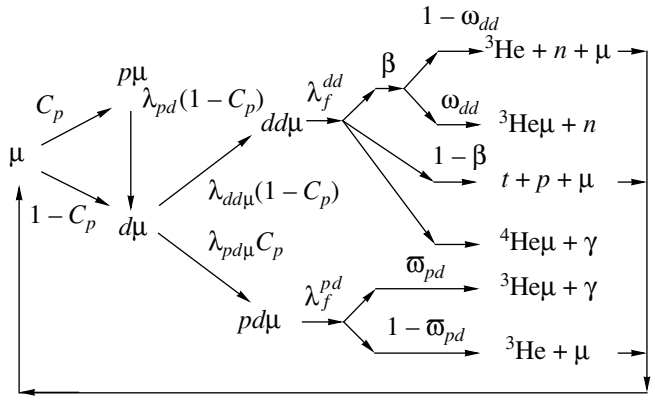

Fig. 5. A simplified scheme of the MC fusion cycle in the H/D mixture. Channel $pd\mu \rightarrow {}^3\mathrm{He} + \mu + \gamma$ is not shown in the scheme, since the probability for the radiative pd capture with subsequent muon sticking to helium ϖ_{pd} is about 99% [16].

fusion channels in muonic molecules $dd\mu$ and $pd\mu$, respectively. These reactions lead to muon loss from the catalysis cycle. Using n_c thus determined and measured numbers of electrons N_e, we could calculate numbers of $dd\mu$ molecules $N_{dd\mu}$ formed in each exposure as $N_{dd\mu} = N_e n_c$. The results are presented in the table and the total number of $dd\mu$ molecules for exposures 3–8 was used for the estimation of reaction (4) yield.

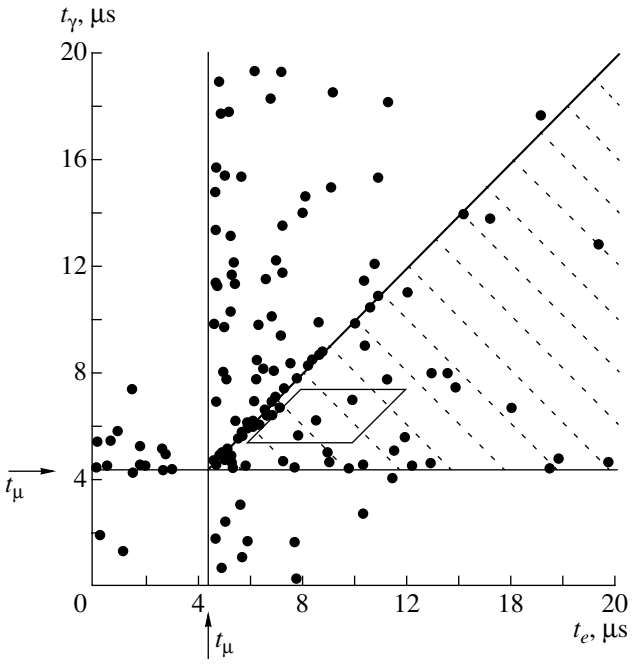

Fig. 6. Two-dimensional $t_e - t_\gamma$ plot for the events with $E_\gamma > 17$ MeV detected by the NaI detector in exposures 3–8.

4. ANALYSIS OF γ-EVENTS

Of all events detected by the γ detector, those with the γ energy

$$E_\gamma > 17 \text{ MeV} \qquad (8)$$

were selected for further analysis. Those events accumulated in exposures 3–8 were displayed in a two-dimensional electron time (t_e)–γ-time (t_γ) plot, shown in Fig. 6.

Fusion events from reaction (4) should arrive after the muon entrance (t_μ) and before the muon decay (t_e), so for the primary selection the required time sequence is $t_e > t_\gamma > t_\mu$ (dashed area in Fig. 6).

It is seen that a noticeable fraction of events in this plot is concentrated at small $t_e - t_\mu$, $t_\gamma - t_\mu$. These events might be a manifestation of the muon stops in the target walls. In the wall material (Ni, Fe), the muon disappears after the average time $\tau_\mu = 0.2$ μs,

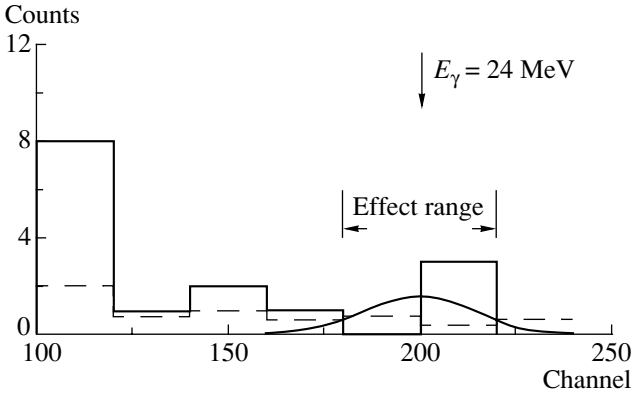

Fig. 7. Amplitude γ-quantum spectra for the events selected with criteria (9) for exposures 3–8 (solid line) and the normalized "background" spectra (dashed line). The response function of the NaI detector is represented by the Gaussian.

either due to its decay, starting the false trigger, or due to the nuclear capture with emission of capture products. To reduce the background originating from such processes, events corresponding to fast γ and electron emission should be excluded from consideration by introducing a time delay with respect to t_μ.

On the other hand, the time distribution of events resulting from the $dd\mu$-molecule fusion (4) should obey the exponential law

$$f_\gamma(t) = \text{const} \cdot \exp[-(\lambda_0 + \phi\lambda_{dd\mu}\omega_{dd})t],$$

thus allowing a large time delay that would lead to the loss of the efficiency.

To suppress the accidental background and simultaneously avoid efficiency losses, the following time intervals were chosen:

$$1 < t_\gamma - t_\mu < 3\ \mu\text{s}; \quad 0.5 < t_e - t_\gamma < 4.5\ \mu\text{s}. \quad (9)$$

The corresponding region is indicated by the box in Fig. 6 with three N_γ^t events within it.

To estimate the background, we selected the area $t_\gamma > 1\ \mu$s, $0.5 < t_e < 4.5\ \mu$s and found seven events there. This corresponds to the number of background events in region (9), $N_\gamma^{b1} = 2 \pm 1$.

In addition, for independent estimation of the accidental background, events from exposures 1 and 2 satisfying (8) and (9) were selected. The number of such events normalized to the number of electrons in exposures 3–8 was found to be $N_\gamma^{b2} = 2$. It proved to be at the level of the previous estimate obtained from exposures 3–8.

The background level is found to exceed the measured intrinsic background of the installation, corresponding to the cosmic ray intensity [0.05/(MeV s)] by a factor of 2. We conclude that additional background is correlated with the phasotron operation.

The energy distribution of the events detected by the NaI detector and selected with criteria (9) for exposures 3–8 (solid line) is shown in Fig. 7. The dashed line is the spectrum for the normalized background.

It is seen from the figure that these spectra practically coincide for energies $E_\gamma > 17$ MeV. Some excess of events for lower energies can be ascribed to the background induced by neutrons from reaction (2).

From the above considerations, the number of candidate events can be obtained:

$$N_\gamma = N_\gamma^t - N_\gamma^b = 1 \pm 2. \quad (10)$$

The measured yield of reaction (4) per $dd\mu$ molecule is evaluated as

$$\eta_\gamma = \frac{N_\gamma}{\epsilon_\gamma N_{dd\mu}^{\text{tot}}}, \quad (11)$$

where $N_{dd\mu}^{\text{tot}}$ is the total number of $N_{dd\mu}$ molecules accumulated in exposures 3–8:

$$N_{dd\mu}^{\text{tot}} = 3.4 \times 10^6. \quad (12)$$

Using estimate (6) for the efficiency of γ-quantum registration and taking into account the selection efficiency due to the accepted criteria (9), one obtains the detection efficiency of γ's from reaction (4):

$$\epsilon_\gamma = (3 \pm 0.5)\%. \quad (13)$$

Substituting (10), (12), and (13) into Eq. (11) we obtain

$$\eta_\gamma^1 = (1 \pm 2) \times 10^{-5} \quad (14)$$

for the absolute γ yield per $dd\mu$ molecule.

After the article was prepared, additional measurements with a deuterium target and a NaI(Tl) detector of larger size have been conducted and a similar analysis has been performed. The result is

$$\eta_\gamma^2 = (0.8 \pm 1.5) \times 10^{-5}. \quad (15)$$

Combining (14) and (15) we obtain

$$\eta_\gamma < 2 \times 10^{-5} \quad (16)$$

at 90% C.L.

From here, an upper limit for the radiative fusion rate λ_γ^1 from the $J = 1$ state of the $dd\mu$ molecule can be deduced using the experimental value of the total fusion rate $\lambda_f^1 = 4 \times 10^8\ \text{s}^{-1}$ [8]:

$$\lambda_\gamma^1 < 8 \times 10^3\ \text{s}^{-1}.$$

5. CONCLUSION

The first attempt has been made to estimate the yield of radiative capture reaction (4) from the $J = 1$ state of the $dd\mu$ muonic molecule. The background conditions were evaluated, and the appropriate methods of data analysis were elaborated. The sensitivity of the present experiment is not enough to make a decisive conclusion about the p wave contribution to the process of radiative dd capture. (The expected level estimated from the data [3] is $\eta_\gamma \sim 10^{-6}$.) The improvement of our result by one or two orders of magnitude will be possible with a new γ detector of larger efficiency and more intense muon beams. Of crucial importance is the understanding of the background structure and elaboration of background suppression methods.

ACKNOWLEDGMENTS

The authors thank L.I. Ponomarev for his support and V.B. Belyaev, V.E. Markushin, and L.N. Strunov for stimulating discussions.

This work was supported by the Department of Atomic Science and Technology of the Ministry of Atomic Energy of the Russian Federation under contract 6.25.19.19.00.969.

REFERENCES

1. F. J. Wilkinson and F. E. Cecil, Phys. Rev. C **31**, 2036 (1985).
2. C. A. Barnes *et al.*, Phys. Lett. B **197**, 315 (1987).
3. L. H. Kramer *et al.*, Phys. Lett. B **304**, 208 (1993).
4. L. N. Bogdanova, Surv. High Energy Phys. **6**, 177 (1992).
5. B. P. Ad'yasevich, V. G. Antonenko, and V. E. Bragin, Yad. Fiz. **33**, 1167 (1981) [Sov. J. Nucl. Phys. **33**, 619 (1981)].
6. D. V. Balin *et al.*, Phys. Lett. B **141B**, 173 (1984); Pis'ma Zh. Éksp. Teor. Fiz. **40**, 318 (1984) [JETP Lett. **40**, 1112 (1984)].
7. D. V. Balin *et al.*, Muon Catal. Fusion **1**, 127 (1987).
8. D. V. Balin *et al.*, Muon Catal. Fusion **5/6**, 163 (1990/1991).
9. G. M. Hale, Muon Catal. Fusion **5/6**, 227 (1990/1991).
10. V. R. Bom *et al.*, in *Proceedings of International RIKEN Conference μCF-01 "Muon Catalyzed Fusion and Related Exotic Atoms," Shimoda, Japan, 2001*.
11. V. P. Dzhelepov *et al.*, Zh. Éksp. Teor. Fiz. **101**, 1105 (1992) [Sov. Phys. JETP **74**, 589 (1992)].
12. Yu. P. Averin *et al.*, Hyperfine Interact. **118**, 111 (1999).
13. V. V. Perevozchikov *et al.*, in *Proceedings of International RIKEN Conference μCF-01 "Muon Catalyzed Fusion and Related Exotic Atoms," Shimoda, Japan, 2001*.
14. V. P. Dzhelepov *et al.*, Nucl. Instrum. Methods Phys. Res. A **269**, 634 (1988).
15. L. N. Bogdanova and V. E. Markushin, Muon Catal. Fusion **5/6**, 189 (1990/1991).
16. V. E. Markushin, Muon Catal. Fusion **3**, 395 (1988).
17. V. M. Bystritsky *et al.*, Zh. Éksp. Teor. Fiz. **70**, 1167 (1976) [Sov. Phys. JETP **43**, 606 (1976)].
18. V. R. Bom and V. V. Filchenkov, Hyperfine Interact. **119**, 365 (1999); V. V. Filchenkov and L. Marczis, Preprint No. E13-88-566, OIYaI (Joint Institute for Nuclear Research, Dubna, 1988).
19. C. Petitjean, K. Lou, P. Ackerbauer, *et al.*, Muon Catal. Fusion **5/6**, 199 (1990/1991).

Physics of Atomic Nuclei, Vol. 65, No. 10, 2002, pp. 1785–1794. Translated from Yadernaya Fizika, Vol. 65, No. 10, 2002, pp. 1833–1842.

NUCLEI
Theory

Ternary Fission of Nuclei in the Adiabatic Approximation

S. G. Kadmensky

Voronezh State University, Universitetskaya pl. 1, Voronezh, 394693 Russia

Received August 8, 2001; in final form, January 17, 2002

Abstract—On the basis of a generalization of integral formulas for nuclear-decay widths to the three-body case, the spontaneous and the low-energy induced ternary fission of nuclei are investigated by using the adiabatic approximation. The properties of energy distributions, of partial fission widths, and of the angular distributions of fission fragments are analyzed for the case of ternary fission. Conditions are found under which the angular distributions of two heavy fragments originating from ternary fission are similar to the analogous distributions of fragments originating from binary fission. The features of angular distributions are investigated, along with the parities and angular momenta of the third (light) ternary-fission fragment.

1. INTRODUCTION

The adiabatic approximation, which is based on the fact that the characteristic times of nucleon motion in nuclei are much shorter than the characteristic times associated with collective modes [1], is often invoked in describing the collective features of spherical and deformed nuclei. This approximation is used to implement the strong-coupling model for nonspherical nuclei and to construct nuclear-deformation potentials. The model in question underlies the treatment of the spontaneous and of the low-energy induced fission of nuclei at the stage of fissile-nucleus evolution from the initial configuration to the configuration at the outer saddle point of the deformation potential, the latter determining the structure of transition fission states [1].

The possibility of describing various forms of nuclear decays within the adiabatic approximation was analyzed in [2, 3]. It appeared that, because of a strong subbarrier character of protonic, alpha, and cluster decays, the adiabatic approximation cannot be used to describe either partial widths with respect to these decay modes or the angular distributions of fragments originating from them. At the same time, the conditions ensuring the applicability of the adiabatic approximation are reliably satisfied for the spontaneous and for the low-energy induced binary fission of nuclei, and the relevant partial fission widths for oriented nuclei were calculated on the basis of this approximation, along with the angular distributions of corresponding fission fragments. These computations required employing a quantum-mechanical approach to the nuclear-fission process and the results of the multiparticle theory of nuclear reactions and decays, which is based on applying the method of projection operators [4] and the theory of open Fermi systems [5].

The situation that emerged from the analysis of the angular distributions of fragments originating from the fission of oriented and polarized nuclei is of particular interest. In order to describe these distributions, use is usually made of the A. Bohr formula [6, 1], which is based on the qualitative physical assumption that the fragments produced in the fission of an axisymmetric deformed parent nucleus travel only along or against the direction of the symmetry axis of this nucleus. Because of the quantum-mechanical uncertainty relation between the orbital angular momentum l of a particle and its emission angle, this assumption is, however, valid only in the case where l values are absolutely uncertain ($0 \leq l \leq \infty$). It was shown in [3] that the Bohr formula is approximately valid only within the adiabatic pattern of fission, with the evolution of fission fragments upon their escape from the parent nucleus being included in it, and deviations from this formula were derived. Concurrently, the dependences of partial fission widths and of potential phase shifts on the relative orbital angular momenta and spins of fission fragments were obtained. These dependences have a dynamical character and differ considerably from their counterparts obtained by using various statistical assumptions [7].

The objective of the present study is to extend the methods proposed in [2, 5] in order to render them applicable to describing the ternary fission of nuclei on the basis of the adiabatic approximation and the quantum-mechanical pattern of this process.

1063-7788/02/6510-1785$22.00

2. DYNAMICS OF THE TERNARY FISSION OF NUCLEI

The ensuing analysis is performed by considering the example of a parent nucleus having an atomic weight A and a charge Z and undergoing ternary fission into two rather heavy fragments of atomic weight A_1 and A_2 and charge Z_1 and Z_2 ($A_1 \geq A_2$) and a light fragment whose atomic weight and charge are, respectively, A_3 and Z_3, fulfillment of the condition $A_3 \ll A_2$ being implied. The wave function ψ_σ^{JM} describing an isolated quasistationary parent-nucleus state characterized by the spin J, its projection M onto the z axis in the laboratory frame, and other quantum numbers σ (which include the parity π) satisfies the Schrödinger equation

$$H_A \psi_\sigma^{JM} = \bar{E}_\sigma^J \psi_\sigma^{JM}, \tag{1}$$

where H_A is the Hamiltonian of the nucleus A in the c.m. frame and $\bar{E}_\sigma^J = (E_\sigma^J - i\Gamma_\sigma^J/2)$ is a complex energy whose real part E_σ^J is coincident with the sign-reversed binding energy of the nucleus A and whose imaginary part is related to the total width Γ_σ^J of the nuclear state in question with respect to its decay through all open decay channels.

We restrict ourselves to considering the first stage of the fission of the parent nucleus into three primary fragments. At this stage, the primary fission fragments A_1 and A_2 arise in rather cold states that are nonequilibrium with respect to their deformation-parameter values, while the comparatively light fragment A_3 appears to be in the ground state and has a spherical shape, the intrinsic wave function $\psi^{J_3 M_3}$, and the energy E^{J_3}. Because of nonsphericity of the nuclear and Coulomb potentials V_{12}, V_{13}, and V_{23} describing the interaction of the primary fission fragments A_1, A_2, and A_3, the relative orbital angular momenta L and l of the fragments A_1, A_2, and A_3 increase and so do the spins of the fragments A_1 and A_2, which go over to the states characterized by the intrinsic wave functions $\psi_{\sigma_1}^{J_1 M_1}$ and $\psi_{\sigma_2}^{J_2 M_2}$ and the internal energies $E_{\sigma_1}^{J_1}$ and $E_{\sigma_2}^{J_2}$. In the fission process, these states appear as the initial states for the second stage, within which the primary fragments A_1 and A_2 go over, via neutron and photon emission, to states that are more equilibrium with respect to their deformation-parameter values, forming, at the final stage, long-lived states of fission fragments that are actually observed.

Following the ideas of the theory of nuclear reactions [8, 9], we introduce a configuration space that is specified by the set of coordinates of all nucleons of the parent nucleus, with the exception of its center-of-mass coordinate. In this space, we single out the region where the ternary-fission fragments A_1, A_2, and A_3 corresponding to the end of the first stage of the fission process have already been formed. In order to describe the relative motion of these fragments, we introduce the variables $\mathbf{R} = \mathbf{R}_1 - \mathbf{R}_2$ and $\mathbf{r} = \mathbf{R}_3 - (A_1\mathbf{R}_1 + A_2\mathbf{R}_2)/(A_1 + A_2)$, where $\mathbf{R}_1$, $\mathbf{R}_2$, and $\mathbf{R}_3$ are the center-of-mass coordinates of the corresponding fragments, and the solid angles $\Omega_\mathbf{R}$ and $\Omega_\mathbf{r}$ determining the directions of the radius vectors $\mathbf{R}$ and $\mathbf{r}$ in the laboratory frame. The channel function $U_{c\beta Ll}^{JM}$, where $c \equiv \sigma_1 J_1 \sigma_2 J_2 J_3$ and $\beta = J_0 j j_3$, that possesses the correct transformation properties under time inversion can be chosen in the form [1]

$$U_{c\beta Ll}^{JM} = \left\{ \left\{ \psi_{\sigma_1}^{J_1 M_1} \left\{ \psi_{\sigma_2}^{J_2 M_2} i^L Y_{LM_L}(\Omega_\mathbf{R}) \right\}_{jm_j} \right\}_{J_0 M_0} \right. \tag{2}$$
$$\left. \times \left\{ \psi^{J_3 M_3} i^l Y_{lm_l}(\Omega_\mathbf{r}) \right\}_{j_3 m_3} \right\}_{JM},$$

where braces denote the vector coupling of angular momenta; j, J_0, and j_3 are intermediate spins; and the spherical harmonics $Y_{LM_L}(\Omega_\mathbf{R})$ and $Y_{lm_l}(\Omega_\mathbf{r})$ describe the relative orbital motion of fission fragments that have the orbital angular momenta L and l, respectively. The energy Q_c of the relative motion of the fragments in the channel c is given by

$$Q_c = E_\sigma^J - E_{\sigma_1}^{J_1} - E_{\sigma_2}^{J_2} - E^{J_3}. \tag{3}$$

Let us first consider the situation where all ternary-fission fragments are formed simultaneously upon the rupture of the neck of the parent nucleus, the third fission fragment A_3 being composed of the nucleons of the neck. As in the case of binary fission, we make use of the A. Bohr concept of transition fission states [6, 1] and describe these states in terms of the wave functions ψ_t^{JM}. These functions are involved, with amplitudes $b_{\sigma t} = \langle \psi_t^{JM} | \psi_\sigma^{JM} \rangle$, in the states of the parent nucleus, so that the partial width $\Gamma_{\sigma c\beta Ll}^J$ with respect to the ternary fission of the parent nucleus can be represented as

$$\Gamma_{\sigma c\beta Ll}^J = \sum_t |b_{\sigma t}|^2 \Gamma_{tc\beta Ll}^J, \tag{4}$$

where $\Gamma_{tc\beta Ll}^J$ is the partial width with respect to ternary fission for the transition state t.

Using the concepts of the interpolation model developed in [4, 10, 5] for two-body nuclear reactions and decays and in [11] for three-body nuclear reactions, we can represent the wave functions ψ_t^{JM} for the transition states in the form

$$\psi_t^{JM} = (\psi_t^{JM})_{\mathrm{sh}} + (\psi_t^{JM})_{\mathrm{cl}}, \tag{5}$$

where the function $(\psi_t^{JM})_{\rm sh}$ does not vanish in the internal configuration-space region corresponding to the compact state of the parent nucleus—that is, in the region of applicability of the multiparticle shell model constructed with allowance for not only normal and superfluid nucleon–nucleon correlations but also collective modes associated with the motion of the A nucleus. The function $(\psi_t^{JM})_{\rm sh}$ includes, in addition to the wave function $(\psi_t^{JM})_{\rm sh}^0$ determined by symmetry and by the deformation-parameter values at the outer saddle point of the deformation potential of the A nucleus, the shell functions at other deformation-parameter values that determine the evolution of the nucleus from the saddle point to the point where this nucleus undergoes scission into three fragments. In formula (5), the cluster component $(\psi_t^{JM})_{\rm cl}$ of the wave function is associated with the configuration-space region where fragments arising at the first stage of the ternary-fission process have already been formed and can be expressed in terms of the channel function (2) as [5]

$$(\psi_t^{JM})_{\rm cl} = \sum_{c\beta Ll} \widehat{A}\left\{F_{tc\beta Ll}(R,r)U_{c\beta Ll}^{JM}\right\}, \qquad (6)$$

where $\widehat{A}$ is the operator of antisymmetrization with respect to the A_1, A_2, and A_3 fragments and where the form factor $F_{tc\beta Ll}$ is related to the regular and irregular radial wave functions [$f_{c\beta Ll}(R,r)$ and $g_{c\beta Ll}(R,r)$, respectively]. From Eq. (1) used with the Hamiltonian H_A in the form

$$H_A = -\frac{\hbar^2}{2M_a}\Delta_{\mathbf{R}} - \frac{\hbar^2}{2M_b}\Delta_{\mathbf{r}} + H_{A_1} + H_{A_2} + H_{A_3} + V_{123} \qquad (7)$$

where H_{A_1}, H_{A_2}, and H_{A_3} are the intrinsic Hamiltonians of the fission fragments A_1, A_2 and A_3, respectively; $V_{123} = (V_{12} + V_{13} + V_{23})$ is the sum of the fragment-interaction potentials; $M_a = mA_1A_2/(A_1 + A_2)$; and $M_b = mA_3(A_1 + A_2)/(A_1 + A_2 + A_3)$ (m is the nucleon mass), we find that the regular radial wave function $f_{c\beta Ll}(R,r)$ satisfies the set of the coupled equations

$$\left\{-\frac{\hbar^2}{2M_a}\frac{1}{R^2}\frac{\partial}{\partial R}\left(R^2\frac{\partial}{\partial R}\right) - \frac{\hbar^2}{2M_b}\frac{1}{r^2}\frac{\partial}{\partial r}\left(r^2\frac{\partial}{\partial r}\right) + \frac{\hbar^2 L(L+1)}{2M_aR^2} + \frac{\hbar^2 l(l+1)}{2M_br^2} - Q_c\right\} f_{c\beta Ll}(R,r) + \sum_{c'\beta' L'l'} \left\langle U_{c\beta Ll}^{JM}|V_{123}|U_{c'\beta' L'l'}^{JM}\right\rangle f_{c'\beta' L'l'}(R,r) = 0. \qquad (8)$$

The irregular radial wave function $g_{c\beta Ll}(R,r)$ is found in a similar way. The function $(\psi_t^{JM})_{\rm cl}$ (6) is required [5] to be orthogonal to the set of basis shell functions used to determine the functions $(\psi_t^{JM})_{\rm sh}$.

In the asymptotic region, where the potential V_{123} describing the interaction between ternary-fission fragments is negligible, the function $f_{c\beta Ll}(R,r)$ reduces to the function $f^0_{cL l\lambda}(R,r)$ satisfying Eq. (8) without the last term on its left-hand side. Following [12, 9], we introduce, instead of R and r, the variables ρ and α as

$$R = \left(\frac{M_b}{M_a}\right)^{1/4}\rho\sin\alpha, \quad r = \left(\frac{M_a}{M_b}\right)^{1/4}\rho\cos\alpha, \qquad 0 \le \alpha \le \pi/2, \qquad (9)$$

where $\rho^2 = \sqrt{M_a/M_b}R^2 + \sqrt{M_b/M_a}r^2$, the phase-space element being transformed as

$$R^2dRr^2dr = \rho^5 d\rho \sin^2\alpha\cos^2\alpha d\alpha. \qquad (10)$$

The variable α determines the distribution of energy among three fission fragments in the asymptotic region. Indeed, the transformation specified by Eqs. (9) yields the relation

$$\tan\alpha = \sqrt{\frac{M_a}{M_b}}\frac{R}{r}.$$

Since, beyond the region where the forces between fission fragments are operative, these fragments move at fixed relative velocities and momenta, we have $R/r = v_a/v_b$ and

$$\tan\alpha = \sqrt{\frac{M_a}{M_b}}\frac{v_a}{v_b}, \qquad (11)$$

where v_a is the relative velocity of the A_1 and A_2 fragments and v_b is the velocity of the A_3 fragment with respect to the center of mass of the A_1 and A_2 fragments. We also have

$$\frac{M_av_a^2}{2} + \frac{M_bv_b^2}{2} = Q_c.$$

In the asymptotic region, the function $f^0_{cLl\lambda}(R,r)$ can be represented in the factorized form [12]

$$f^0_{cLl\lambda}(R,r) = \frac{Y_c(L,l,\lambda,\alpha)R_{cL_0}(\rho)}{\rho^{5/2}\sin\alpha\cos\alpha}, \qquad (12)$$

where the quantity λ takes the values of $\lambda = 0, 1, 2, \ldots$ and the function $Y_c(L,l,\lambda,\alpha)$ is given by

$$Y_c(L,l,\lambda,\alpha) = N(\sin\alpha)^{L+1}(\cos\alpha)^{l+1} \times F(-\lambda; L+l+\lambda+2; L+3/2; \sin^2\alpha), \qquad (13)$$

Here, $F(a;b;c;z)$ is a hypergeometric function; at negative integral values of $a = -\lambda$, it reduces to a Jacobi polynomial. Using the relation between the asymptotic momenta of fission fragments and their

relative momenta, one can find that, in the asymptotic region, the kinetic energies E_1, E_2, and E_3 of the fragments are [12]

$$\frac{E_1}{Q_c} = \frac{A_2}{A_1+A_2}\sin^2\alpha + \frac{A_1A_3\cos^2\alpha}{(A_1+A_2)(A_1+A_2+A_3)} - \frac{\sqrt{A_1A_2A_3}\cos\alpha\sin\alpha\cos\theta}{(A_1+A_2)\sqrt{A_1+A_2+A_3}},$$

$$\frac{E_2}{Q_c} = \frac{A_2}{A_1+A_2}\sin^2\alpha + \frac{A_2A_3\cos^2\alpha}{(A_1+A_2)(A_1+A_2+A_3)} + \frac{\sqrt{A_1A_2A_3}\cos\alpha\sin\alpha\cos\theta}{(A_1+A_2)\sqrt{A_1+A_2+A_3}},$$

$$\frac{E_3}{Q_c} = \frac{A_1+A_2}{A_1+A_2+A_3}\cos^2\alpha, \qquad (14)$$

where θ is the angle between the vectors $\mathbf{R}$ and $\mathbf{r}$. From the last formula in (14), it follows that the maximum kinetic energy E_3^m of the third fission fragment A_3 is $E_3^m = (A_1+A_2)/(A_1+A_2+A_3)Q_c$. Using relations (10), (11), and (14), we can determine the probability that the third particle has an energy E_3 in the interval (E_3, E_3+dE_3) [12]. The result is

$$\frac{|Y_c(L,l,\lambda,\arccos x)|^2\,dE_3}{\sqrt{x(1-x)}}, \qquad (15)$$

where $x = E_3/E_3^m$.

In turn, the function $R_{cL_0}(\rho)$ appearing in (12) satisfies the Schrödinger equation [12]

$$\left[\frac{d^2}{d\rho^2} + k_c^2 - \frac{L_0(L_0+1)}{\rho^2}\right] R_{cL_0}(\rho) = 0, \qquad (16)$$

where $k_c^2 = 2\sqrt{M_aM_b}Q_c/\hbar^2$ and where the quantity L_0, which is referred to as the channel order, is defined as $L_0 = L + l + 2\lambda + 3/2$. Solutions to Eq. (16) can be expressed in terms of Bessel and Neumann spherical functions, which can be used to construct the solution $\bar{R}_{cL_0}(\rho)$ whose asymptotic behavior for $\rho \to \infty$ is of the diverging-spherical-wave type; that is,

$$\bar{R}_{cL_0}(\rho) \to e^{i(k_c\rho - L_0\pi/2)}\frac{1}{\sqrt{v_c}}, \qquad (17)$$

where $v_c = \hbar k_c/\sqrt{M_aM_b}$. One can then introduce [12] the multiparticle operator j representing the density of the particle flux in the direction of the radius vector $\boldsymbol{\rho}$:

$$j = \frac{i\hbar}{2\sqrt{M_aM_b}}\left[\psi\frac{d}{d\rho}\psi^* - \psi^*\frac{d}{d\rho}\psi\right]. \qquad (18)$$

In this case, the total number of events per unit time that cause a simultaneous actuation of detectors recording the fission fragments A_1 and A_3 or A_2 and A_3 is determined by the integral of the flux density (18) over an element of the surface of the multidimensional sphere ($\rho^5\sin^2\alpha\cos^2\alpha d\alpha$). If we use the function $f^0_{cLl\lambda}$ (12) with $R_{cL_0}(\rho) = \bar{R}_{cL_0}(\rho)$ (17) for the function ψ in formula (18) and consider that the function $Y_c(L,l,\lambda,\alpha)\times(\sin\alpha\cos\alpha)$ is normalized to unity, the total number of events recorded by the detector per unit time is equal to unity.

Let us now investigate the partial widths with respect to the ternary fission of the transition state ψ_t^{JM}. By using the strategies adopted in [10, 5] and formulas (12) and (17), we can represent the asymptotic expression for the function $\left(\psi_t^{JM}\right)_{\rm cl}$ (6) in the form

$$\left(\psi_t^{JM}\right)_{\rm cl} \to \sum_{c\beta Ll\lambda}\sqrt{\frac{\Gamma^J_{tc\beta Ll\lambda}}{\hbar v_c}}U^{JM}_{c\beta Ll} \times \frac{e^{i(k_c\rho - L_0\pi/2)}Y_c(L,l,\lambda,\alpha)}{\rho^{5/2}\sin\alpha\cos\alpha}e^{i\delta_{c\beta lL\lambda}}, \qquad (19)$$

where $\delta_{c\beta lL\lambda}$ is the three-body phase shift for potential scattering. If expression (19) is used for the wave function ψ in formula (18) to calculate the multiparticle fragment-flux density j, we can find that the total probability of detecting ternary-fission fragments in the $c\beta lL\lambda$ channel per unit time is $\Gamma^J_{tc\beta Ll}/\hbar$. This probability is fully consistent with the definition of the partial width with respect to ternary fission. With the aid of a generalization of the results presented in [5] to the case of ternary fission, the amplitude of the partial width with respect to the ternary fission of a transition state can in turn be represented in the form

$$\sqrt{\Gamma^J_{tc\beta Ll\lambda}} = \sqrt{2\pi} \times \left\langle \widehat{A}\left\{U^{JM}_{c\beta Ll}\widetilde{f}_{c\beta Ll\lambda}(\rho,\alpha)\right\}|H_A - E^J_\sigma|\left(\psi_t^{JM}\right)_{\rm sh}\right\rangle, \qquad (20)$$

where the radial function $\tilde{f}_{c\beta Ll\lambda}(\rho,\alpha)$ satisfies Eq. (8), its asymptotic behavior for $\rho\to\infty$ being given by

$$\widetilde{f}_{c\beta Ll\lambda}(\rho,\alpha) \to C_0\frac{1}{\rho^{5/2}}\sin\left(k_c\rho - \frac{L_0\pi}{2} + \delta_{c\beta Ll\lambda}\right)\frac{Y_c(L,l,\lambda,\alpha)}{\sin\alpha\cos\alpha}, \qquad (21)$$

where C_0 is a constant that is determined from the condition that the function $\tilde{f}_{c\beta Ll\lambda}(\rho,\alpha)$ is normalized to the δ function of energy.

If, in formula (20), we use the functions $U^{JM}_{c\beta Ll}$ and $\left(\psi_t^{JM}\right)_{\rm sh}$ possessing correct transformation properties under time inversion, the partial-width amplitude in (20) is real-valued [1].

3. ADIABATIC APPROXIMATION FOR TERNARY FISSION

In this section, the adiabatic approximation used previously [3] in describing binary fission is generalized to the case of ternary fission. In doing this, we make use of experimental data on ternary fission from the review article of Mutterer and Theobald [13].

We assume that, as in the case of binary fission, the nucleus undergoing fission and the ternary-fission fragments A_1 and A_2 have strongly deformed axisymmetric shapes.

We will employ the experimental facts that the atomic weight of the third fission fragment A_3 is noticeably smaller than the atomic weights of the A_1 and A_2 fragments and that its kinetic energy E_3 is noticeably less than the total energy Q_c of the relative motion of the three fission fragments and, hence, than the energies of the relative motion of the A_1 and A_2 fragments in all ternary-fission channels of importance. Therefore the asymptotic momentum $\mathbf{p}_3$ of the third fragment is noticeably less than the asymptotic momenta $\mathbf{p}_1$ and $\mathbf{p}_2$ of the A_1 and A_2 fragments, whence it follows that, to a good approximation, the momenta $\mathbf{p}_1$ and $\mathbf{p}_2$ are oppositely directed, as they are in the case of binary fission. This makes it possible to use, as was done in analyzing binary fission [3], the assumption that the Euler angles ω, ω_1, and ω_2 determining the orientation of the principal symmetry axes of the parent nucleus and of the fission fragments A_1 and A_2 are close to one another.

As in the case of binary fission, we assume that the excitation energies $E_{K_1}^{J_1}$ and $E_{K_2}^{J_2}$ of rotational bands built on the intrinsic states of the A_1 and A_2 fragments with fixed projections K_1 and K_2 of their spins J_1 and J_2 ($J_1 \geq K_1$, $J_2 \geq K_2$) onto the symmetry axes of these fragments are considerably less than the kinetic energy of the relative motion of the A_1 and A_2 fragments over the entire region of their existence. This means that we can disregard the effect of these excitation energies and, hence, of the spins J_1 and J_2 of the A_1 and A_2 fragments on the functions $\tilde{f}_{c\beta Ll\lambda}(r,R)$ and, hence, on the phase shifts $\delta_{c\beta Ll\lambda}$ for potential scattering. We also assume that the spin–orbit and the spin–spin interaction of ternary-fission fragments are weak; therefore, the functions $\tilde{f}_{\sigma_1 K_1 \sigma_2 K_2 J_3 \beta Ll\lambda}$ can be taken, for a first approximation, to be independent of the intermediate spins and, hence, of the index β.

In describing binary fission, it was found [14] that the centrifugal potential $V_{12}^{\mathrm{cf}} = \hbar^2 L(L+1)/(2M_a R^2)$ for the relative motion of the A_1 and A_2 fragments is considerably less than the kinetic energy of the relative motion of these fragments over the entire region of their existence. It follows that the dependence of the radial function $\tilde{f}_{\sigma_1 K_1 \sigma_2 K_2 J_3 Ll\lambda}(\rho,\alpha)$ and of the phase shift $\delta_{\sigma_1 K_1 \sigma_2 K_2 J_3 Ll\lambda}$ on the orbital angular momentum L will manifest itself only through the effect of the orbital angular momentum on the formation of the energy distributions of ternary-fission fragments, which is determined by the function $Y_c(L,l,\lambda,\alpha)$.

Let us take into consideration the experimental fact [13] that, for ternary fission, the angular distribution of the third fission fragment A_3 with respect to the directions along which the A_1 and A_2 fragments move has, with a high probability, an equatorial character and depends only slightly both on the kinetic energy E_3 of the third fragment A_3 and on the total energy Q_c of the relative motion of ternary-fission fragments in all channels that are of importance for the above fission mode. The simplest interpretation of this result makes it possible to consider the radial wave functions $\tilde{f}_{\sigma_1 K_1 \sigma_2 K_2 J_3 Ll\lambda}(\rho,\alpha)$ and the phase shifts $\delta_{\sigma_1 K_1 \sigma_2 K_2 J_3 Ll\lambda}$ as quantities that are approximately independent of those characteristic values of the orbital angular momenta L and l that form the energy and angular distributions of ternary-fission fragments. In this case, we can also assume that the radial functions and the phase shifts are determined by a bounded set of λ values for which they are also approximately constant. Therefore, the radial functions and the phase shifts can be represented, respectively, as $\tilde{f}_{\sigma_1 K_1 \sigma_2 K_2 J_3 Ll\lambda}(\rho,\alpha) \approx \tilde{f}_{\sigma_1 K_1 \sigma_2 K_2 J_3}(\rho,\alpha)$ and as $\delta_{\sigma_1 K_1 \sigma_2 K_2 J_3 Ll\lambda} \approx \delta_{\sigma_1 K_1 \sigma_2 K_2 J_3}$ for all channels that are of importance for ternary fission.

4. PARTIAL WIDTHS WITH RESPECT TO THE TERNARY FISSION OF NUCLEI

In the strong-coupling approximation [1], the orthonormalized wave function $(\psi_{tK_i}^{JM})_{\mathrm{sh}}$ describing a transition state of the parent nucleus in the shell region and possessing correct transformation properties under time inversion can be represented as

$$(\psi_{tK_i}^{JM})_{\mathrm{sh}} = \sqrt{\frac{2J+1}{16\pi^2}}\left[1+\delta_{K_i,0}\left(\frac{1}{\sqrt{2}}-1\right)\right] \times \left\{D_{MK_i}^{J}(\omega)\chi_{tK_i}(q(\omega)) + (-1)^{J+K_i} \times D_{M-K_i}^{J}(\omega)\chi_{\overline{tK_i}}(q(\omega))\right\}, \quad (22)$$

where $D_{MK_i}^{J}(\omega)$ is a generalized Wigner spherical function depending on the Euler angles α,β,γ denoted by ω, $\chi_{tK_i}(q(\omega))$ is the intrinsic wave function describing the transition state and depending on the set of internal coordinates $q(\omega)$ in the intrinsic coordinate frame of the parent nucleus, and $\chi_{\overline{tK_i}}(q(\omega))$ is the time-inverted counterpart of $\chi_{tK_i}(q(\omega))$. The

wave functions $\psi_{\sigma_1}^{J_1M_1}$ and $\psi_{\sigma_2}^{J_2M_2}$ describing the fission fragments A_1 and A_2 and appearing in the definition of the channel functions (2) can also be represented in the form (22) with the substitution of K_1 and K_2 for K_i, M_1 and M_2 for M, J_1 and J_2 for J, π_1 and π_2 for π, σ_1 and σ_2 for t, and $q_1(\omega)$ and $q_2(\omega)$ for $q(\omega)$. By going over to the intrinsic coordinate frame of the parent nucleus and by using the Wigner transformation [1], we can rewrite the spherical harmonics $Y_{LM_L}(\Omega_{\mathbf{R}})$ and $Y_{lm_l}(\Omega_{\mathbf{r}})$ and the wave function $\psi^{J_3M_3}$ for the third spherical fission fragment as

$$Y_{LM_L}(\Omega_{\mathbf{R}}) = \sum_{K_L} D^L_{M_LK_L}(\omega) Y_{LK_L}(\Omega_{\mathbf{R}'}), \quad (23)$$
$$\psi^{J_3M_3} = \sum_{K_3} D^{J_3}_{M_3K_3}(\omega)\psi^{J_3K_3}(q_3),$$

where q_3 is the set of intrinsic variables of the fragment A_3 in the coordinate frame of the parent nucleus. Substituting relations (23) into formula (2) and using the multiplication theorem for generalized spherical harmonics [1], we can recast the channel function $U^{JM}_{c\beta Ll}$ (2) into the form

$$U^{JM}_{c\beta Ll} = \frac{1}{16\pi^2}\sqrt{(2J_1+1)(2J_2+1)} \quad (24)$$
$$\times \sum_{KK_LK_0K_3K_lK_jK_{j_3}} i^l i^L D^J_{MK}(\omega) Y_{LK_L}(\Omega_{\mathbf{R}'})$$
$$\times Y_{lK_l}(\Omega_{\mathbf{r}'})\chi_{\sigma_1K_1}(q_1)\chi_{\sigma_2K_2}(q_2)\psi^{J_3K_3}(q_3)$$
$$\times C^{JK}_{J_0j_3K_0K_{j_3}} C^{J_0K_0}_{J_1jK_1K_j} C^{jK_j}_{J_2LK_2K_L} C^{j_3K_{j_3}}_{J_3lK_3K_l} \ldots,$$

where, for the sake of simplicity, we display one of the four terms of the channel function in the case where $\pi = \pi_1 = \pi_2 = +1$, $K_1 > 0$, and $K_2 > 0$.

Let us now investigate the structure of the partial-width amplitude $\sqrt{\Gamma^J_{tc\beta Ll\lambda}}$ that is obtained for ternary fission upon the substitution of the shell wave function (22) for the transition state of the parent nucleus and the channel function (24) into (20). We have

$$\sqrt{\Gamma^J_{tK_ic\beta Ll\lambda}} = \frac{1}{8\pi^2}\sqrt{(2J_1+1)(2J_2+1)(2J+1)} \quad (25)$$
$$\times \sum_{KK_LK_3K_jK_0K_lK_{j_3}} \left\langle D^J_{MK}(\omega)|D^J_{MK_i}(\omega)\right\rangle i^{-l} i^{-L}$$
$$\times \langle Y_{LK_L}(\Omega_{\mathbf{R}'})Y_{lK_l}(\Omega_{\mathbf{r}'})|A_{tK_i\sigma_1K_1\sigma_2K_2\lambda}\rangle$$
$$\times C^{JK}_{J_0j_3K_0K_{j_3}} C^{J_0K_0}_{J_1jK_1K_j} C^{jK_j}_{J_2L2_2K_L} C^{j_3K_{j_3}}_{J_3lK_3K_l},$$

where

$$A_{tK_i\sigma_1K_1\sigma_2K_2\lambda} = \frac{2\sqrt{2\pi}}{\sqrt{32\pi^2}}\left\langle \tilde{f}_{\sigma_1K_1\sigma_2K_2J_3}(R,r)\right. \quad (26)$$
$$\left.\times\ \chi_{\sigma_1K_1}(q_1)\chi_{\sigma_2K_2}(q_2)\psi^{J_3K_3}(q_3)|V_{123}|\chi_{tK_i}(q)\right\rangle.$$

Formula (25) represents the partial-width amplitude for the case where $\pi = \pi_1 = \pi_2 = +1$ and $K_3 = K_i - K_1 - K_2$. In addition, the cases of $K_3 = K_i + K_1 - K_2$ and $K_3 = K_i - K_1 + K_2$ are also possible.

According to experimental data, the correlations associated with parity violation and left–right asymmetry [15–17] for the A_1 and A_2 fragments originating from the ternary fission of polarized nuclei are close to their counterparts for the binary fission of such nuclei [18, 19]. On this basis, we can conclude that the angular distributions of the ternary-fission fragments A_1 and A_2 are similar to the analogous distributions for the binary fission of nuclei if the ternary-fission fragments A_1 and A_2 travel predominantly along or against the direction of the symmetry axis of the parent nucleus. Using the ideas put forth in [3], we can represent the amplitude in (26) as

$$A_{tK_i\sigma_1K_1\sigma_2K_2J_3} = C^{(A_3)}(\theta_{\mathbf{R}'},\theta_{\mathbf{r}'})B_{tK_i\sigma_1K_1\sigma_2K_2J_3}, \quad (27)$$

where

$$C^{(A_3)}(\theta_{\mathbf{R}'},\theta_{\mathbf{r}'}) = G^{(A_3)}\sum_l a_l^{(A_3)} i^l Y_{l0}(\xi_{\mathbf{r}'}) \quad (28)$$
$$\times \left\{\sum_{L=0}^{L_m} Y_{L0}(\xi_{\mathbf{R}'})Y_{L0}(1)i^L \right.$$
$$\left.\times\ [1+\pi\pi_1\pi_2\pi_3(-1)^l(-1)^L]\right\}.$$

In (28), π is the parity of the parent-nucleus state, $\xi_{\mathbf{R}'} = \cos\theta_{\mathbf{R}'}$, $\xi_{\mathbf{r}'} = \cos\theta_{\mathbf{r}'}$, and $G^{(A_3)}$ is the normalization constant determined from the condition that the integral of the function $\left|C^{(A_3)}\right|$ over the measure $d\Omega_{\mathbf{R}'}d\Omega_{\mathbf{r}'}$ is equal to unity. Only the angular-momentum projections $K_L = 0$ and $K_l = 0$ are used in (28); this reflects the azimuthal symmetry for the directions in which ternary-fission fragments move. The braced expression on the right-hand side of (28) corresponds to the analogous expression for the partial-width amplitude with respect to binary fission [3], takes into account the fact that the directions in which the nascent fragments A_1 and A_2 move in the intrinsic coordinate frame of the parent nucleus are close to the directions along and against its symmetry axis, and depends (this is of particular importance) on the parity of the orbital angular momentum l carried away by the third fission fragment. At fixed indices $\sigma_1K_1\sigma_2K_2J_3$ of the states of ternary-fission fragments, the effect of strongly nonspherical nuclear and Coulomb potentials describing their interactions leads to the emergence of a set of values of the orbital angular momenta L and l in formula (28), L_m being the maximum possible value of L.

Substituting formulas (27) and (28) into (25), we can recast the partial-width amplitude into the form

$$\sqrt{\Gamma^J_{tK_ic\beta Ll\lambda}} = \sqrt{\frac{(2J_1+1)(2J_2+1)}{2J+1}} \times G^{(A_3)} a_l^{(A_3)} Y_{L0}(1)\theta(L_m - L) \times [1 + \pi\pi_1\pi_2\pi_3(-1)^{l+L}] \times C^{JK_i}_{J_0j_3(K_1+K_2)K_3} C^{J_0(K_1+K_2)}_{J_1jK_1K_2} C^{jK_2}_{J_2LK_20} \times C^{j_3K_3}_{J_3lK_30} B_{tK_i\sigma_1K_1\sigma_2K_2J_3}, \quad (29)$$

where $\theta(x)$ is the Heaviside step function. As can be seen from (29), the dependence of the partial width with respect to ternary fission on the channel indices J_1, J_2, J_0, j, j_3, l, and L is of a dynamical character and differs noticeably from the analogous dependences obtained on the basis of various statistical assumptions used, for example, in describing binary fission [7].

5. ANGULAR DISTRIBUTIONS OF TERNARY-FISSION FRAGMENTS

For the wave function $\left(\psi_t^{JM}\right)_{\rm cl}$ describing the transition state of the parent nucleus, we consider the asymptotic expression that is obtained by substituting into (19) the channel function in the form (24) and the partial-fission-width amplitude in the form (29). In (19), there then arises the expression

$$\sum_{KK_0K_jK_3K_{j_3}K_LK_lJ_1J_2J_0jj_3} \frac{(2J_1+1)(2J_2+1)}{16\pi^2\sqrt{2J+1}} \times C^{JK}_{J_0j_3K_0K_{j_3}} C^{J_0K_0}_{J_1jK_1K_j} C^{jK_j}_{J_2LK_2K_L} C^{j_3K_{j_3}}_{J_3lK_3K_l} \times C^{JK_i}_{J_0j_3(K_1+K_2)(K_i-K_1-K_2)} C^{J_0(K_1+K_2)}_{J_1jK_1K_2} C^{jK_2}_{J_2LK_20} \times C^{j_3K_i-K_1-K_2}_{J_3l(K_i-K_1-K_2)0}. \quad (30)$$

Considering that Clebsch–Gordan coefficients satisfy the relation

$$\sum_J C^{JM}_{j_1j_2m_1m_2} C^{JM}_{j_1j_2m_1'm_2'} = \delta_{m_1m_2}\delta_{m_1'm_2'}, \quad (31)$$

we can perform summation over the indices J_1, J_2, J_0, j, and j_3 in (30) and arrive at the form

$$\sqrt{2J+1}\sum_j (2j+1), \quad (32)$$

which reflects the coherent character that the adiabatic approximation has in the case of ternary fission as well. The asymptotic expression (19) for the wave function ψ_t^{JM} describing the transition state then takes the form

$$\left(\psi_t^{JM}\right)_{\rm cl} = \sum_{\sigma_1K_1\sigma_2K_2J_3j} (2j+1)\sqrt{2J+1} \times D^J_{MK_i}(\omega)\chi_{\sigma_1K_1}(q_1)\chi_{\sigma_2K_2}(q_2) \times \psi^{J_3(K_i-K_1-K_2)}(q_3) \times \bar{C}^{(A_3)}(\xi_{\mathbf{R}'}, \xi_{\mathbf{r}'})(-1)^{\bar{\lambda}} \frac{B_{tK_i\sigma_1K_1\sigma_2K_2J_3}}{\sqrt{\hbar v_c}} \times \frac{Y_{\bar{c}}(\bar{L},\bar{l},\bar{\lambda},\alpha)}{\sin\alpha\cos\alpha} e^{i\delta_{\sigma_1K_1\sigma_2K_2J_3}} \frac{e^{ik_c\rho}}{\rho^{5/2}}\ldots, \quad (33)$$

where the function $\bar{C}^{(A_3)}(\xi_{\mathbf{R}'}, \xi_{\mathbf{r}'})$ differs from the quantity $C^{(A_3)}(\xi_{\mathbf{R}'}, \xi_{\mathbf{r}'})$ (28) by the absence of the factor $(i)^{l+L}$ in the sums over l and L and where the function $Y_{\bar{c}}(\bar{L},\bar{l},\bar{\lambda},\alpha)$ is taken at some averaged values $c = \bar{c}$, $L = \bar{L}$, $l = \bar{l}$, and $\lambda = \bar{\lambda}$.

We now calculate the multiparticle flux density j by formula (18), employing the function in (33) instead of the function ψ and integrating it over the surface of a multidimensional sphere, $\rho^5(\sin\alpha)^2(\cos\alpha)^2 d\alpha$, with respect to a complete set of the intrinsic fission-fragment coordinates q_1, q_2, and q_3, and with respect to the Euler angles ω. For the normalized (to unity) differential probability of ternary fission leading to the formation of fission fragments in intrinsic states specified by $\sigma_1K_1\sigma_2K_2J_3$, this yields

$$\frac{dP_{\sigma_1K_1\sigma_2K_2J_3}(E_3,\Omega_{\mathbf{R}},\Omega_{\mathbf{r}})}{dE_3 d\Omega_{\mathbf{R}} d\Omega_{\mathbf{r}}} = \frac{2J+1}{16\pi^2}\int d\omega \left[\left|D^J_{MK_i}(\omega)\right|^2 + \left|D^J_{M-K_i}(\omega)\right|^2\right] \times (\bar{C}^{(A_3)})^2(\xi_{\mathbf{R}'}, \xi_{\mathbf{r}'}) \left|\frac{Y_{\bar{c}}(\bar{L},\bar{l},\bar{\lambda},\arccos x)}{\sqrt{x(1-x)}}\right|^2. \quad (34)$$

The quantity in (34) is independent of the indices σ_1, K_1, σ_2, and K_2 determining those states of the A_1 and A_2 fragments that are significant for ternary fission. For the total differential probability of ternary fission, the formula obtained by performing summation over the σ_1, K_1 and σ_2, K_2 states of the fission fragments A_1 and A_2 is therefore analogous to that in (34).

By integrating the distribution in (34) with respect to the energy E_3 of the third fission fragment, one can obtain the normalized (to unity) angular distributions of ternary-fission fragments:

$$\frac{dP_{J_3}}{d\Omega_{\mathbf{R}} d\Omega_{\mathbf{r}}} = \frac{2J+1}{16\pi^2}\int d\omega \left[\left|D^J_{MK_i}(\omega)\right|^2 + \left|D^J_{M-K_i}(\omega)\right|^2\right] \left|\bar{C}^{(A_3)}(\xi_{\mathbf{R}'}, \xi_{\mathbf{r}'})\right|^2. \quad (35)$$

The angular distributions $dP'_{J_3}/d\Omega_{\mathbf{R}'} d\Omega_{\mathbf{r}'}$ of ternary-fission fragments in the intrinsic coordinate frame are obtained from the distribution in (35) under the condition that the Euler angles ω are considered to

be independent of the angles $\Omega_{\mathbf{R}'}$ and $\Omega_{\mathbf{r}'}$ and upon integration with respect to the angles ω. The result is

$$\frac{dP'_{J_3}}{d\Omega_{\mathbf{R}'}d\Omega_{\mathbf{r}'}} = \left|\bar{C}^{(A_3)}(\xi_{\mathbf{R}'},\xi_{\mathbf{r}'})\right|^2. \qquad (36)$$

In the case of binary fission, this distribution reduces to the angular distribution of the fission fragments A_1 and A_2 in the form [3]

$$\frac{dP'}{d\Omega_{\mathbf{R}'}} = |F_{L_m}(\xi_{\mathbf{R}'})|^2, \qquad (37)$$

where

$$F_{L_m}(\xi_{\mathbf{R}'}) \qquad (38)$$
$$= G_2 \sum_{L=0}^{L_m} Y_{L0}(\xi_{\mathbf{R}'})Y_{L0}(1)[1+\pi\pi_1\pi_2(-1)^L],$$

with G_2 being a normalization constant. Under the transformation $\theta_{\mathbf{R}'} \to \pi - \theta_{\mathbf{R}'}$, which leads to the substitution $\xi_{\mathbf{R}'} \to -\xi_{\mathbf{R}'}$, the quantity $F_{L_m}(\xi_{\mathbf{R}'})$ does not change sign at $\pi\pi_1\pi_2 = +1$ and changes sign at $\pi\pi_1\pi_2 = -1$, so that the quantity $|F_{L_m}(\xi_{\mathbf{R}'})|^2$ and, hence, the angular distribution of fragments in (37) are symmetric with respect to the symmetry axis of the parent nucleus. The function $|F_{L_m}(\xi_{\mathbf{R}'})|^2$ is close in shape to the sum of the smeared delta functions in the directions $\xi_{\mathbf{R}'} = 1$ and $\xi_{\mathbf{R}'} = -1$; this determines the deviation from the A. Bohr formula, which is obtained from (37) and (38) in the limit $L_m \to \infty$. In the case of ternary fission, the angular distribution of the A_1 and A_2 fragments in the intrinsic coordinate frame can differ significantly from the analogous distribution for the binary fission of nuclei. Let us fix the most probable direction at which the the A_3 fragment flies out with respect to the symmetry axes of the parent nucleus, in which case $\theta_{\mathbf{r}'} = \theta^o_{\mathbf{r}'}$. If, in the sum over l on the right-hand side of (28), the contributions of even and odd values of l appear to be commensurate at $\theta_{\mathbf{r}'} = \theta^o_{\mathbf{r}'}$, then the angular distribution of the A_1 and A_2 fragments will be determined by a superposition of even and odd values of L; therefore, the quantity $\bar{C}^{(A_3)}_{L_m}(\theta_{\mathbf{R}'},\theta^o_{\mathbf{r}'})$ will not in general be symmetric under the transformation $\theta_{\mathbf{R}'} \to \pi - \theta_{\mathbf{R}'}$, and the angular distribution of the A_1 and A_2 fragments for ternary fission will differ significantly from the analogous distribution for binary fission. As was mentioned above, data from experiments that studied correlations associated with parity nonconservation and with the right–left asymmetry of the A_1 and A_2 fragments originating from ternary fission lead to the conclusion that the angular distributions of the above fragments for binary fission are close to their counterparts for ternary fission. In order to preserve the approximate symmetry of the emission of the A_1 and A_2 fragments along and against the direction of the symmetry axis of the parent nucleus, it is therefore necessary to assume that, in the sum over l on the right-hand side of (28), the weight of components having a specific parity dominates over the weight of opposite-parity components. In this case, the angular distribution of the A_1 and A_2 fragments originating from ternary fission becomes weakly dependent on the orbital angular momentum l associated with the third fission fragment, with the result that formula (36) reduces to the form

$$\frac{dP'_{J_3}}{d\Omega_{\mathbf{R}'}d\Omega_{\mathbf{r}'}} \approx |F_{L_m}(\xi_{\mathbf{R}'})|^2 \qquad (39)$$
$$\times \left(\sum_l a_l^{(A_3)} Y_{l0}(\xi_{\mathbf{r}'})\right)^2 \frac{(G^{A_3})^2}{G_2^2}.$$

Experiments devoted to ternary fission (see [13]) studied the angular dependence of the direction of alpha-particle emission with respect to the direction at which the A_2 fragment appears. This distribution weakly depends on the alpha-particle energy and can be approximated by the Breit–Wigner formula

$$\frac{dP'(\theta_{\mathbf{r}'})}{d\Omega_{\mathbf{r}'}} = \frac{A}{(\theta_{\mathbf{r}} - \theta^o_{\mathbf{r}'})^2 + \Gamma^2/4}, \qquad (40)$$

where the normalization constant A is determined from the condition

$$\int \frac{dP'(\theta_{\mathbf{r}'})}{d\Omega_{\mathbf{r}'}} d\Omega_{\mathbf{r}'} = 1.$$

The distribution in (40) has a maximum at the angular value of $\theta_{\mathbf{r}'} = \theta^o_{\mathbf{r}'}$, which, in the case of the spontaneous fission of ^{252}Cf, changes as a function of the ratio $R = A_1/A_2$ of the masses of the A_1 and A_2 fragments from 92° at $R = 1$ to 82° at $R = 2$, the $\theta^o_{\mathbf{r}'}$ value averaged over the parameter R being 84.6°. A similar pattern is observed in the case of the thermal-neutron-induced fission of ^{235}U, the $\theta^o_{\mathbf{r}}$ value averaged over R appearing to be 82°. The width Γ of the distribution in (40) is weakly dependent on the parameter R and on the type of fissile nucleus, taking the value of $\Gamma \approx 19°$. By comparing formulas (39) and (40) and taking into account the proximity of the angular distributions of heavy fragments for even and odd values of the orbital angular momenta L, we can obtain the relation

$$f^{(\alpha)}(\theta_{\mathbf{r}'}) = \sum_l a_l^{(\alpha)} Y_{l0}(\theta_{\mathbf{r}'}) = \sqrt{\frac{A}{(\theta_{\mathbf{r}} - \theta^o_{\mathbf{r}'})^2 + \Gamma^2/4}}, \qquad (41)$$

where the coefficients $a_l^{(\alpha)}$ satisfy the normalization condition $\sum_l (a_l^{(\alpha)})^2 = 1$.

Values of the coefficients $a_l^{(\alpha)}$ characterizing the angular distributions of α particles emitted in the thermal-neutron-induced ternary fission of the ^{235}U nucleus

l	0	1	2	3	4	5	6	7	8	9	10	11
$a_l^{(\alpha)}$	0.85	0.12	−0.43	−0.15	0.20	0.13	−0.10	−0.10	0.04	0.08	−0.01	−0.05

By using the completeness and orthonormality of the spherical harmonics $Y_{l0}(\theta_{\mathbf{r}'})$, we can calculate the values of the coefficients

$$a_l^{(\alpha)} = \int f^{(\alpha)}(\theta_{\mathbf{r}'}) Y_{l0}(\theta_{\mathbf{r}'}) d\Omega_{\mathbf{r}'}. \qquad (42)$$

For the distribution in (40) at $\theta^o_{\mathbf{r}'} = 90°$, only the coefficients $a_l^{(\alpha)}$ at even values of l are nonzero. As can be seen from the table, which displays the values of the coefficients $a_l^{(\alpha)}$ at $\theta^o_{\mathbf{r}'} = 82°$, the absolute values of these coefficients decrease fast with increasing orbital angular momentum l, the absolute values of the coefficients for odd values of l being considerably smaller than the absolute values of the coefficients for even values of l: $l = 0, 2, 4$. In (41), the weight of all even orbital angular momenta $l = 0, 2, 4$ is then greater than 90%, while the weight of all odd momenta l is less than 8%. This result makes it possible to understand why the angular distributions of the A_1 and A_2 fragments originating from ternary fission are similar to the angular distributions of the analogous fragments originating from binary fission. At the same time, we can see that, at large deviations of the angle $\theta^o_{\mathbf{r}'}$ from 90°, the contributions of odd values of the orbital angular momentum l in formula (41) increase and, at the angular values of $\theta^o_{\mathbf{r}'} = 0°$ and 180°, become commensurate with the contribution of even values of l. In this situation, we can expect that the symmetry of the angular distributions of the A_1 and A_2 fragments with respect to the symmetry axis of the parent nucleus will be lost and that these distributions will differ significantly from their counterparts for the binary fission of nuclei in the case of the polar direction of the emission of the third fission fragment A_3.

For the distribution in (41), one can calculate the expectation value of the operator $\hat{\mathbf{l}}^2$. The result is

$$\left\langle \hat{\mathbf{l}}^2 \right\rangle = \sum_l l(l+1)(a_l^{(\alpha)})^2 = 4.8.$$

On this basis, the expectation value $\langle l \rangle$ can be estimated at $\langle l \rangle \approx 1.7$. This value of $\langle l \rangle$ is rather small in relation to the expectation value of the orbital angular momentum L associated with the relative motion of the heavy fragments A_1 and A_2 and is consistent with the estimate obtained for the mean orbital angular momentum carried away by the third particle by using experimental results deduced from a comparison of the multipolarities and multiplicities of gamma rays emitted by the excited fragments A_1 and A_2 in the cases of binary and ternary fission [17].

6. CONCLUSION

The results of the present investigation have demonstrated new possibilities that arise if the quantum-mechanical approach and the adiabatic approximation are used to describe dynamics and coherent effects both in the binary and in the ternary fission of nuclei. On the basis of our results, one can perform a more consistent analysis of the possible ternary-fission mechanisms (for example, the one- and the two-step mechanism) and of the origin of various correlation (angular and polarization) effects in the ternary fission of nuclei, including effects associated with T, P, or TP violation.

7. ACKNOWLEDGMENTS

I am grateful to V.E Bunakov, W.I. Furman, A.L. Barabanov, and G.A. Petrov for stimulating discussions.

This work was supported by INTAS (grant no. 99-0229) and by the federal program Universities of Russia (grant no. UR-01.01.011).

REFERENCES

1. A. Bohr and B. Mottelson, *Nuclear Structure* (Benjamin, New York, 1969, 1975; Mir, Moscow, 1971, 1977), Vols. 1, 2.
2. S. G. Kadmensky, Yad. Fiz. **65**, 863 (2002) [Phys. At. Nucl. **65**, 831 (2002)].
3. S. G. Kadmensky, Yad. Fiz. **65**, 1424 (2002) [Phys. At. Nucl. **65**, 1390 (2002)].
4. K. Wildermuth and Y. C. Tang, *A Unified Theory of the Nucleus* (Vieweg, Braunshweig, 1977; Mir, Moscow, 1980).
5. S. G. Kadmensky, Yad. Fiz. **64**, 478 (2001) [Phys. At. Nucl. **64**, 423 (2001)].
6. A. Bohr, in *Proceedings of United Nations International Conference on Peaceful Uses of Atomic Energy* (United Nations, New York, 1956), Vol. 2, p. 191.
7. A. L. Barabanov and D. P. Grechukhin, Yad. Fiz. **47**, 648 (1988) [Sov. J. Nucl. Phys. **47**, 411 (1988)].

8. A. M. Lane and R. G. Thomas, Rev. Mod. Phys. **30**, 257 (1958).
9. N. F. Mott and H. S. W. Massey, *The Theory of Atomic Collisions* (Clarendon, Oxford, 1965; Mir, Moscow, 1969).
10. S. G. Kadmensky and W. I. Furman, *Alpha Decay and Related Nuclear Reactions* (Énergoatomizdat, Moscow, 1985).
11. A. I. Baz', V. S. Skhirtladze, and K. V. Shitikova, Yad. Fiz. **25**, 281 (1977) [Sov. J. Nucl. Phys. **25**, 153 (1977)].
12. L. M. Delves, Nucl. Phys. **9**, 391 (1958/1959); **20**, 275 (1960).
13. M. Mutterer and J. P. Theobald, *Dinuclear Decay Modes* (Institute of Physics Publ., Bristol, 1996), Chap. 12.
14. A. L. Barabanov and W. I. Furman, Z. Phys. A **357**, 411 (1997).
15. A. N. Belozerov, G. A. Danilyan, *et al.*, Pis'ma Zh. Éksp. Teor. Fiz. **54**, 136 (1991) [JETP Lett. **54**, 132 (1991)].
16. F. Goennenwein *et al.*, Nucl. Phys. A **567**, 303 (1994).
17. V. E. Bunakov, F. Goennenwein, *et al.*, Preprint No. 01BU03T, ILL (Grenoble, 2001).
18. A. Koetzle *et al.*, Nucl. Instrum. Methods Phys. Res. A **440**, 750 (2000).
19. A. Z. Alexandrovich, A. M. Gagarski, G. A. Petrov, *et al.*, Nucl. Phys. A **567,** 541 (1994).

Translated by A. Isaakyan

Physics of Atomic Nuclei, Vol. 65, No. 10, 2002, pp. 1795–1797. Translated from Yadernaya Fizika, Vol. 65, No. 10, 2002, pp. 1843–1845.

NUCLEI
Theory

Determination of the Ratio of the Axial-Vector to the Vector Coupling Constant for Weak Interaction in Triton Beta Decay

Yu. A. Akulov* **and B. A. Mamyrin**

Ioffe Institute for Physics and Technology, Russian Academy of Sciences, Politekhnicheskaya ul. 26, St. Petersburg, 194021 Russia

Received October 29, 2001

Abstract—Data on the chemical shifts of the half-lives of atomic and molecular tritium are used to determine the ratio of the axial-vector to the vector coupling constant for weak interaction in triton beta decay. The result is $(G_A/G_V)_t = -1.2646 \pm 0.0035$. © *2002 MAIK "Nauka/Interperiodica".*

The beta-active three-nucleon nucleus of tritium is a convenient object for experimentally testing theoretical ideas of intranuclear interaction and of the role of meson exchange between nucleons in beta decay. Until recently, however, attempts at analyzing theoretical models and at evaluating their parameters on the basis of data on triton beta decay proved to be futile, because values determined experimentally for the relevant half-life and for the endpoint energy of the beta spectrum depended on the type of tritium chemical compound used. Because of this, it was impossible to match the experimental values of the half-life and the endpoint energy of the beta spectrum and to calculate precisely the reduced half-life of a free triton, a quantity that is a fundamental feature of a beta transition and which is used in evaluating relevant coupling constants.

Much attention paid in recent years to the neutrino-mass problem has given impetus to theoretically studying molecular effects in tritium beta decay. These investigations made it possible to assess the effect of the chemical structure of a tritized compound on the values determined experimentally for the endpoint energy of the beta spectrum; however, the effect of the electron cloud of a nucleus on its half-life was considered theoretically only for the simplest atomic structures, such as ^3H, $^3H^+$, and $^3H^-$ [1]. On the other hand, there were studies devoted to a determination of absolute half-life values for some tritium-containing compounds [2]; however, the chemical shifts of the half-life and a precise value of the reduced triton half-life cannot be determined from the available data set because of large errors assigned to many experimental values and because of uncertainties in the chemical structure of tritized compounds used in some experiments.

The development of differential isotope methods for measuring the chemical shifts of the tritium half-life [3] and experiments aimed at measuring the difference of the half-lives for atomic and molecular tritium [4] made it possible to determine the half-life for atomic tritium. The result was $(t_{1/2})_a = 12.264 \pm 0.018$ yr. In doing this, it was of importance that, for a reference on the absolute scale, use was made of the reliably determined value of $(t_{1/2})_m = 12.296 \pm 0.017$ yr, which is the weighted mean of the latest published half-life estimates for molecular tritium. Among these estimates, which are quite consistent with one another, one was obtained by applying the dedicated isotope-helium method [5], while another was deduced by determining the decay exponent through recording beta-electron bremsstrahlung [2].

Having at our disposal the experimental value of the half-life for atomic tritium, we can employ theoretical data on the chemical shifts of the decay constant in order to obtain the absolute value of the half-life for a free triton. Since experimental procedures that make it possible to take into account all channels of the beta-decay reaction were used to determine the half-life of molecular tritium and the difference of the decay constants for atomic and molecular tritium, the resulting value of $(t_{1/2})_a$ corresponds to the total probability of beta decay (that is, it takes into account both processes leading to the formation of electrons belonging to the continuum spectrum and decay into bound states). In going over to the value of the triton half-life $(t_{1/2})_t$, it is then necessary to consider four possible effects determining the final-state interaction of the beta electron in the decay of the nucleus in a free tritium atom. These are decay into bound states (that is, beta-electron formation in one of the shells in the product helium atom), the formation of the continuous-spectrum electron through the substitution process where the beta electron replaces the

*e-mail: akulov.mass@pop.ioffe.rssi.ru

orbital electron, the screening of the nuclear charge by the orbital electron, and the formation of excited electron states in the $^3He^+$ ion through beta decay.

A procedure that can be used to calculate the reduced half-life of the triton $(ft_{1/2})_t$ was considered in detail in [6]. The resulting values of the four corrections to $(t_{1/2})_a$ that take into account the aforementioned atomic effects is $(0.86 \pm 0.08)\%$; for a free triton, this leads to the half-life value of $(t_{1/2})_t = 12.369 \pm 0.020$ yr or $(3.9034 \pm 0.0063) \times 10^8$ s at a mean solar-year duration of 365.25 d. This value corresponds to free-triton decay leading to the direct formation of beta electrons, in which case the shape of the beta spectrum is affected only by the Coulomb field of the nucleus. In determining the reduced half-life of the triton, we must then use the phase-space factor f computed with the standard Fermi function and take, for the upper boundary of the momentum interval accessible to the beta electron, $c^{-1}(E^2 - m_e^2c^4)^{1/2}$, where E is the quantity obtained by subtracting the recoil energy of the helium nucleus from the mass difference (in energy units) between the tritium nucleus and the ^3He nucleus.

The above mass difference determined as the weighted mean of the results of 11 independent experiments [7, 8] is (18529 ± 2) eV $+ m_ec^2$. The recoil energy of the helium nucleus is 3.4 eV; therefore, $E = (18525.6 \pm 2)$ eV $+ m_ec^2$. Using the procedure that makes it possible to calculate the phase-space factor with allowance for the Coulomb interaction of the beta electron with a nucleus of finite dimensions and mass and for processes featuring virtual photons and charged particles (apart from radiative corrections of order α^2), which are products of beta decay [9], we find at the above value of E that $f = (2.894 \pm 0.006) \times 10^{-6}$, whence it follows that $(ft_{1/2})_t = 1129.6 \pm 3$ s. It should be noted that, in evaluating the quantity E, use was made both of mass-spectrometric procedures, where the value determined experimentally for the mass difference between the $^3H^+$ and $^3He^+$ ions is increased by the electron rest energy and is decreased by the binding energy of the s electron in the helium ion, and of procedures based on measuring the endpoint energy E_0 of the tritium beta spectrum and on subsequently increasing it by m_ec^2, as well as by the recoil energy of the daughter ion, and decreasing the result by the chemical shift $\Delta E_0 = E_i - E_f$, where E_i and E_f are, respectively, the initial and final binding energy (the latter being averaged with allowance with for the theoretical values of the final-state weights) of the orbital electrons in the tritium-containing atomic or molecular system used. The weighted mean value determined for the mass difference from mass-spectrometric data differs by not more than 1 eV from the value determined for this quantity on the basis of measurements of the endpoint energy of the beta spectrum for some hydrogen-containing compounds ($C_{20}H_{40}O_2$ [8], valine [10], CH_4 [11]), where one or a few protium atoms in CH groups were replaced by a tritium atom, as well as for molecular tritized hydrogen [7, 12]. This suggests, in particular, that the chemical shifts ΔE_0 of the endpoint energy of the beta spectrum, which are about 20 to 30 eV, are determined theoretically for covalently bonded tritized molecules with an uncertainty not greater than 2 to 3%. Since the logarithmic derivative of the phase-space factor f with respect to E is $(\partial f/\partial E)/f = 1.8 \times 10^{-4}$ 1/eV [1, 13], an uncertainty of about 1 eV in determining E leads to variations of 0.01–0.02% in f, which are insignificant for our present purposes.

For allowed beta transitions, the quantity $ft_{1/2}$ is related to the vector (M_V) and the axial-vector (M_A) matrix element of the beta-decay Hamiltonian by the equation [14]

$$ft_{1/2} = \frac{k/G_V^2}{|M_V|^2 + G_A^2/G_V^2|M_A|^2}, \qquad (1)$$

where G_A and G_V are, respectively, the axial-vector and the vector coupling constant for weak interaction and k is a constant coefficient. Since we have $|M_V| = \sqrt{2}$ and $|M_A| = 0$ for $0^+ \to 0^+$ transitions occurring within $T = 1$ isospin multiplets and leading to final states where the isospin projection is $T_z = 0$ and since $|M_V|_t = 1$ for the triton beta decay, the reduced half-lives with respect to such transitions satisfy the relation

$$(1 + \lambda_t^2|M_A|_t^2)(ft_{1/2})_t = 2(ft_{1/2})_{0^+\to 0^+}, \qquad (2)$$

where $\lambda_t = (G_A/G_V)_t$.

The quantity $(ft_{1/2})_{0^+ \to 0^+}$ determined on the basis of data on eight purely Fermi transitions is $3072.3 \pm 0.9(\text{stat.}) \pm 1.1(\text{syst.})$ s [15]. The value of $|M_A|_t = (0.962 \pm 0.002)\sqrt{3}$ was computed by Saito *et al.* [16], who considered five modifications of the intranuclear potential and who showed that for widely varied shapes of the potential and widely varied structures of the wave functions for the ^3H and ^3He nuclei, the matrix element $|M_A|_t$ shows a relatively weak sensitivity to the existence of delta isobars and meson-exchange currents. Using relation (2), we find for the above values of $(ft_{1/2})_t$, $(ft_{1/2})_{0^+ \to 0^+}$, and $|M_A|_t$ that $\lambda_t = -1.2646 \pm 0.0035$.

For the mixed superallowed $n \to p$ transition, the value of $\lambda_n = (G_A/G_V)_n$ was determined on the basis of data from measurements of the coefficient that characterizes the asymmetry of beta-electron

emission with respect to the spin of the decaying neutron. The results of four such experiments, $\lambda_n = -1.262 \pm 0.005$ [17], $\lambda_n = -1.2594 \pm 0.0038$ [18], $\lambda_n = -1.266 \pm 0.004$ [19], and $\lambda_n = -1.2686 \pm 0.0046 \pm 0.0007$ [20] [the last one is an experiment that was jointly performed by the Russian Research Centre Kurchatov Institute (Moscow) and the Petersburg Nuclear Physics Institute (Gatchina) at the reactor of the Laue–Langevin Institute (Grenoble) in 2000], are consistent within the quoted errors. The weighted mean of these results is $\langle\lambda_n\rangle = -1.2637 \pm 0.0022$, which agrees with the value of λ_t. The latter gives sufficient grounds to treat the ratio G_A/G_V as a universal constant that characterizes beta processes. At the same time, it should be noted that, for the ratio of the axial-vector to the vector coupling constant for weak interaction, Abele *et al.* [21] obtained the value of $\lambda_n = -1.274 \pm 0.003$, which differs considerably from λ_t. Should that result be confirmed, it would be worthwhile to address the question of whether axial-vector interaction is partly suppressed in the presence of pion exchange in the triton.

1. ACKNOWLEDGMENTS

This work was supported by the Russian Foundation for Basic Research (project no. 01-03-32777) and by the State Scientific and Technological Program Fundamental Metrology (project no. 4.06).

REFERENCES

1. M. R. Harston and N. C. Pyper, Phys. Rev. A **48**, 268 (1993).
2. B. Budick, J. Chen, and H. Lin, Phys. Rev. Lett. **67**, 2630 (1991).
3. Yu. A. Akulov, B. A. Mamyrin, and P. M. Shikhaliev, Pis'ma Zh. Tekh. Fiz. **19** (18), 72 (1993) [Tech. Phys. Lett. **19**, 594 (1993)].
4. Yu. A. Akulov and B. A. Mamyrin, Pis'ma Zh. Éksp. Teor. Fiz. **68**, 167 (1998) [JETP Lett. **68**, 175 (1998)].
5. Yu. A. Akulov, B. A. Mamyrin, L. V. Khabarin, *et al.*, Pis'ma Zh. Tekh. Fiz. **14**, 940 (1988) [Sov. Tech. Phys. Lett. **14**, 416 (1988)].
6. Yu. A. Akulov and B. A. Mamyrin, Pis'ma Zh. Tekh. Fiz. **26** (11), 23 (2000) [Tech. Phys. Lett. **26**, 458 (2000)].
7. B. Budick, J. Chen, and H. Lin, Phys. Rev. Lett. **67**, 2626 (1991).
8. H. Kawakami, S. Kato, T. Ohshima, *et al.*, Phys. Lett. B **256**, 105 (1991).
9. D. H. Wilkinson and B. E. F. Macefield, Nucl. Phys. A **232**, 58 (1974).
10. S. Boris, A. Golutvin, L. Lapin, *et al.*, Phys. Rev. Lett. **58**, 2019 (1987).
11. M. Fritschi, E. Holzschuh, W. Kündig, *et al.*, Phys. Lett. B **173**, 485 (1986).
12. S. T. Staggs, R. G. H. Robertson, D. L. Wark, *et al.*, Phys. Rev. C **39**, 1503 (1989).
13. B. Budick, Phys. Rev. Lett. **51**, 1034 (1983).
14. R. J. Blin-Stoyle, *Fundamental Interactions and the Nucleus* (North-Holland, Amsterdam, 1973; Mir, Moscow, 1976).
15. Yu. V. Gaponov and Yu. A. Mostovoĭ, Yad. Fiz. **63**, 1432 (2000) [Phys. At. Nucl. **63**, 1356 (2000)].
16. T.-Y. Saito, Y. Wu, S. Ishikawa, and T. Sasakawa, Phys. Lett. B **242**, 12 (1990).
17. P. Bopp, D. Dubbers, L. Hornig, *et al.*, Phys. Rev. Lett. **56**, 919 (1986).
18. B. G. Erozolimsky, I. A. Kuznetsov, Yu. A. Mostovoĭ, and I. V. Stepanenko, Yad. Fiz. **61**, 572 (1998) [Phys. At. Nucl. **61**, 507 (1998)].
19. P. Liaud *et al.*, Nucl. Phys. A **612**, 53 (1997).
20. *Report on the Activity of the Russian Academy of Sciences in 2000* (Nauka, Moscow, 2001).
21. H. Abele, S. Baebler, D. Dubbers, *et al.*, Phys. Lett. B **407**, 212 (1997).

Translated by A. Isaakyan

Physics of Atomic Nuclei, Vol. 65, No. 10, 2002, pp. 1798–1808. Translated from Yadernaya Fizika, Vol. 65, No. 10, 2002, pp. 1846–1857.

NUCLEI
Theory

Compact and Loosely Bound Structures in Light Nuclei

O. L. Savchenko and A. I. Steshenko

Institute for Theoretical Physics, National Academy of Sciences of Ukraine, Kiev, Ukraine

Received October 12, 2000; in final form, November 19, 2001

Abstract—The role of various components in the wave function of loosely bound light nuclei is considered in terms of the cluster model by taking into account orbital polarization. We show that several structures corresponding to particular modes of nucleon motion can be concurrently important for such structures. Specific examples of simple and fairly flexible trial wave functions are given for the ^{8}Be and ^{6}He nuclei. Explicit expressions are derived for the microscopic wave functions of these nuclei and employed to calculate basic nuclear parameters for commonly used central exchange NN potentials. © *2002 MAIK "Nauka/Interperiodica".*

1. INTRODUCTION

A theoretical study of such many-particle systems as atomic nuclei runs into a number of serious difficulties, one of which involves the construction of a trial wave function. The sought-for function must be characterized by an appropriate set of standard quantum numbers and must satisfy certain symmetry conditions. In this case, it is important to take into account the physically most significant modes of nucleon motion. In the limiting cases, the trial wave function being constructed is commonly assumed to be known. Therefore, the emphasis is on seeking the proper interpolation expression for the wave function in the intermediate region.

A number of more or less successful attempts to simultaneously take into account both compact and loosely bound structures can be found in the literature (see, e.g., Baz' and Zhukov [1, 2]). Formerly, thanks largely to the activity of Yu.A. Simonov, high hopes were pinned on the method of hyposperical functions [3–5] (the method of K harmonics) as a general method for solving the many-body nuclear problem. However, it subsequently emerged that practical application of this method was efficient mainly for compact systems; the results obtained [6, 7] differed only slightly from the results of variational calculations with simple functions of the oscillatory shell model with one variational parameter.

In recent years, highly efficient methods and approaches using the basis functions of various multicluster models have been developed to study bound states of the lightest nuclei ($A < 10$) [8–14]. Stochastic variational methods [8–11] yielded virtually exact numerical solutions to the many-body nuclear problem (see, e.g., the results of Varga and Suzuki [11] obtained for several most commonly used NN potentials). Unfortunately, since the calculations are cumbersome, there are only numerical estimates of some physical quantities for the nuclei under consideration at the output (in general, these are the energy and radius). Therefore, the results of such microscopic calculations cannot be used in full measure to estimate other nuclear parameters; i.e., it is desirable to have an explicit multiparticle wave function to determine the actual efficiency of a given microscopic model. In addition, knowledge of an explicit wave function makes it possible to use it in calculations of the various nuclear processes involving a given system.

In any event, finding a simple and fairly flexible trial wave function of the nucleus that would faithfully describe both compact and loosely bound states in the context of the microscopic model is still an urgent problem. The particularly pressing questions touched upon here are raised in connection with the investigation of unusual nuclei with an anomalous N/Z ratio.

Nuclear-field deformation effects are known to play a significant role in nuclei with $A > 4$. However, specific calculations are generally restricted to spherical symmetry for the functions of individual clusters and to detailing the function that corresponds to the relative cluster motion. Therefore, an attempt was previously made [15] to completely take into account deformation effects in the language of trial functions for the multiparticle oscillatory shell model (without invoking cluster modes). Here, we use a microscopic model that, apart from polarized orbitals, includes cluster modes of nucleon motion and exact projection in angular momentum. Thus, in principle, the model can describe both compact and loosely bound states in light and intermediate-mass nuclei.

Below, we briefly describe the method for constructing a trial wave function (Section 2) and give

1063-7788/02/6510-1798$22.00

the matrix elements of basic physical quantities required for our calculations (Section 3). The results of our variational calculations for the ^{8}Be and ^{6}He nuclei are presented in Section 4.

2. THE MULTIPARTICLE HAMILTONIAN AND TRIAL WAVE FUNCTIONS

Let us represent the A-nucleon system under consideration as two subsystems ($A = A_1 + A_2$) where the interaction between nucleons within each subsystem is known to be stronger than the corresponding interaction between nucleons that belong to different fragments (for simplicity, the calculations are performed for the breakup of the nucleus into two fragments; the generalization to a larger number of fragments can be made by analogy). In this case, the mode of nucleon motion determined by the interaction forces between the subsystems is the softest. After analyzing the corresponding experimental data, we can properly choose the breakup of the A nucleus into fragments and, thereby, make the first step toward constructing the wave function. The most interesting phenomena al low energies are generally related to soft modes, which must be described in terms of the chosen model with the maximum possible accuracy. Thus, if the individual fragments A_1 and A_2 are compact nuclei, then the description of a loosely bound A nucleus will be satisfactory when the $A \to A_1 + A_2$ breakup threshold is correctly reproduced together with basic nuclear parameters.

Each microscopic model uses a particular effective NN potential. The majority of simple effective NN potentials known from the literature were chosen in terms of the models where the function of the shell model with one variational parameter was used as the wave function. Clearly, invoking the NN potentials thus constructed in more sophisticated models can be inefficient. However, if compact systems (e.g., the magic ^{4}He, ^{16}O, or ^{40}Ca nuclei) act as the reference nuclei based on the properties of which a given NN potential is constructed, then using this potential in a more sophisticated model may be justified. Thus, the above potentials may be invoked in the model of polarized orbitals [15], because the results of calculations for the magic ^{4}He and ^{16}O nuclei proved to be similar both in the simple model (with one common variational parameter for all orbitals) and in the modified model (where each orbital contains several independent variational parameters).

Let us now turn to the standard microscopic model of the nucleus [16] with the pair central exchange potential

$$\hat{V}_{ij}(r) = \sum_{S,T=0,1} V_{2S+1,2T+1}(r)\hat{P}_{ST}(ij), \qquad (1)$$

$$r \equiv |\mathbf{r}_i - \mathbf{r}_j|,$$

where the radial dependence of the potential components can be represented without loss of generality as a superposition of Gaussian functions, i.e.,

$$V_{2S+1,2T+1}(r) = \sum_{l=1}^{l_{\rm pot}} V^{(l)}_{2S+1,2T+1} \exp\left(-\frac{r^2}{\mu_l^2}\right); \quad (2)$$

the projection operator $\hat{P}$ in (1) cuts out the state with a certain spin S and isospin T in the interacting nucleon pair (ij).

When describing the nuclear fission $A = A_1 + A_2$, the Hamiltonian $\hat{H}_A$ must asymptotically pass (because of the short-range nature of the nuclear forces) to the sum of internal Hamiltonians for the corresponding subsystems plus the Coulomb interaction between them:

$$\hat{H}_A \to \hat{H}_{A_1} + \hat{H}_{A_2} + \frac{Z_1 Z_2 e^2}{|\mathbf{R}_1 - \mathbf{R}_2|}, \qquad (3)$$

$$\mathbf{R}_l = \frac{1}{A_l}\sum_{i=1}^{A_l} \mathbf{r}_i; \qquad l = 1, 2;$$

i.e., the limiting cases are well known. The question of the intermediate region where the intercluster separation $S = |\mathbf{R}_1 - \mathbf{R}_2|$ is much larger than zero but is not yet large enough to disregard the nuclear interaction between particles from different clusters is still an open question. Therefore, while considering various loosely bound systems, it is necessary to somehow concretize the dependence of the center-of-mass kinetic energy operator $\hat{T}_{\rm c.m.}$ on the fragmentation stage of the A nucleus. Let $\hat{T}_{\rm c.m.}$ in the intermediate region be modeled with the parameter α_S according to the formula

$$\hat{T}_{\rm c.m.}(\alpha_S) = -\frac{\hbar^2}{2Am}\left[1+\alpha_S\left(\frac{A}{A_1}-1\right)\right]\left(\sum_{i=1}^{A_1}\boldsymbol{\nabla}_i\right)^2$$
$$-\frac{\hbar^2}{2Am}\left[1+\alpha_S\left(\frac{A}{A_2}-1\right)\right]\left(\sum_{j=A_1+1}^{A}\boldsymbol{\nabla}_j\right)^2 \quad (4)$$
$$-\frac{\hbar^2}{Am}(1-\alpha_S)\sum_{i=1}^{A_1}\sum_{j=A_1+1}^{A}\boldsymbol{\nabla}_i\boldsymbol{\nabla}_j.$$

In numerical calculations, the parameter α_S ($0 \le \alpha_S \le 1$) in (4) is determined by the extent to which the Pauli exclusion principle applies to the A-nucleon system. Thus, $\alpha_S = 0$ when antisymmetrization applies to the variables of all A nucleons; in the other limiting case where the Pauli exclusion principle applies only to the nuclei that belong to the same cluster, $\alpha_S = 1$.

The total trial wave function Ψ_A can be written as a superposition of a few determinant functions:

$$\Psi_A(1,2,\ldots,A) = \sum_\nu w_\nu \Psi_\nu. \tag{5}$$

Here, the Ψ_ν components (normalized but generally nonorthogonal) are the standard Slater determinants

$$\Psi_\nu = \frac{f_\nu}{\sqrt{A!}} \det\left[\phi_i^{[\nu]}(j)\right],\ f_\nu = \frac{1}{\sqrt{\det\left[\langle\phi_i^{[\nu]}|\phi_j^{[\nu]}\rangle\right]}}, \tag{6}$$

which are filled with single-particle orbitals of the universal form

$$\phi_i(j) = \psi_{\mathbf{n}_i}(\mathbf{r}_j;\mathbf{a}_i,\mathbf{R}_i)\chi_{\sigma\tau}(j) \equiv \psi_{\mathbf{n}_i}(j)\chi_{\sigma\tau}(j),$$
$$\sum_{\sigma\tau}\int |\phi_i|^2 d\mathbf{r} = 1,$$

$$\psi_{\mathbf{n}}(\mathbf{r};\mathbf{a},\mathbf{R}) = \psi_{n^x}(x;a,R^x)\psi_{n^y}(y;b,R^y) \times \psi_{n^z}(z;c,R^z), \tag{7}$$

$$\psi_n(x;a,R) = \frac{1}{\sqrt{a\sqrt{\pi}}N(n;R/a)}\left(\frac{x}{a}\right)^n \times \exp\left\{-\frac{(x-R)^2}{2a^2}\right\},$$

$$N(n;R/a) = \sqrt{\left(\frac{R}{a}\right)^{2n} F\left(-n,-n+\frac{1}{2};0;\frac{a^2}{R^2}\right)}.$$

In (7), $\mathbf{n}_i$ are the quantum numbers ($\{n^x,n^y,n^z\} \equiv \mathbf{n}$) of a three-dimensional harmonic oscillator for the ith orbital, which contains the quantities $\mathbf{a}_i = \{a_i,b_i,c_i\}$ and $\mathbf{R}_i = \{R_i^x,R_i^y,R_i^z\}$ as nonlinear variational parameters; and the functions $\chi_{\sigma\tau}$ and $F(\alpha,\beta;\gamma;z)$ are, respectively the spin–isospin function and the Gauss hypergeometric function [17]. As we see, the single-particle orbitals here slightly differ from the standard orbitals (e.g., from the orbitals of the well-known model by Brink [18]). Each Ψ_ν component in (5) represents a certain characteristic structure or configuration of the system that belongs to a particular type of nucleon motion. It is hoped that the wave function Ψ_A constructed in this way will be flexible enough for a reasonable number of variational parameters $\{\mathbf{a}_i,\mathbf{R}_i\}$.

3. OVERLAP INTEGRALS

To perform variational calculations requires calculating the matrix elements of various physical quantities. Using the standard technique of determinant functions [19], we can express the needed overlap integrals in terms of the partial matrix elements calculated on the basis of functions (7).

We begin our analysis with the overlap integral of the functions Ψ_ν and Ψ_μ, i.e.,

$$\langle\Psi_\nu|\Psi_\mu\rangle = f_\nu f_\mu \det\left[\langle\phi_i^{[\nu]}|\phi_j^{[\mu]}\rangle\right] \equiv f_\nu f_\mu \det\left[(B_{[\nu,\,\mu]})_{ij}\right], \tag{8}$$

where, by the definition of the matrix $B_{[\nu,\,\mu]}$, we have

$$(B_{[\nu,\mu]})_{ij} = \langle\chi_{\sigma_i\tau_i}|\chi_{\sigma_j\tau_j}\rangle \times \int \psi_{\mathbf{n}_i}^{[\nu]}(\mathbf{r};\mathbf{a}_i,\mathbf{R}_i)\psi_{\mathbf{n}_j}^{[\mu]}(\mathbf{r};\mathbf{a}_j,\mathbf{R}_j)d\mathbf{r} = \langle\chi_{\sigma_i\tau_i}|\chi_{\sigma_j\tau_j}\rangle g_{n_i^x n_j^x}(a_iR_i^x;a_jR_j^x) \times g_{n_i^y n_j^y}(b_iR_i^y;b_jR_j^y)g_{n_i^z n_j^z}(c_iR_i^z;c_jR_j^z), \tag{9}$$

$$g_{n_1n_2}(a_1R_1;a_2R_2) \equiv \int_{-\infty}^{\infty} \psi_{n_1}^{[\nu]}(x;a_1,R_1)\psi_{n_2}^{[\mu]}(x;a_2,R_2)dx. \tag{10}$$

The general expression for the matrix elements for single-particle operators [19]

$$\frac{1}{\langle\Psi_\nu|\Psi_\mu\rangle}\left\langle\Psi_\nu\left|\sum_{i=1}^A\hat\Omega_i\right|\Psi_\mu\right\rangle = \sum_{i,j=1}^A \langle\phi_i^{[\nu]}|\hat\Omega_1|\phi_j^{[\mu]}\rangle\left(B^{-1}_{[\nu,\,\mu]}\right)_{ij} \tag{11}$$

yields the following:

(1) the matrix elements for calculating the nuclear mass density distribution $\rho(\mathbf{r})$,

$$\frac{1}{\langle\Psi_\nu|\Psi_\mu\rangle}\left\langle\Psi_\nu\left|\sum_{i=1}^A\delta(\mathbf{r}-\mathbf{r}_i)\right|\Psi_\mu\right\rangle = \sum_{i,j=1}^A \psi_{\mathbf{n}_i}^{[\nu]}(\mathbf{r};\mathbf{a}_i,\mathbf{R}_i)\psi_{\mathbf{n}_j}^{[\mu]}(\mathbf{r};\mathbf{a}_j,\mathbf{R}_j)\left(B^{-1}_{[\nu,\,\mu]}\right)_{ij}; \tag{12}$$

(2) the matrix elements of the kinetic energy operator,

$$\frac{1}{\langle\Psi_\nu|\Psi_\mu\rangle}\left\langle\Psi_\nu\left|-\sum_{i=1}^A\frac{\hbar^2}{2m}\boldsymbol{\nabla}_i^2\right|\Psi_\mu\right\rangle = \sum_{i,j=1}^A \langle\psi_{\mathbf{n}_i}^{[\nu]}|\hat t_x+\hat t_y+\hat t_z|\psi_{\mathbf{n}_j}^{[\mu]}\rangle\left(B^{-1}_{[\nu,\,\mu]}\right)_{ij}, \tag{13}$$

where

$$\langle\psi_{\mathbf{n}_i}^{[\nu]}|\hat t_x|\psi_{\mathbf{n}_j}^{[\mu]}\rangle \equiv \left\langle\psi_{\mathbf{n}_i}^{[\nu]}(\mathbf{r};\mathbf{a}_i,\mathbf{R}_i)\right|-\frac{\hbar^2}{2m}\frac{\partial^2}{\partial x^2}\left|\psi_{\mathbf{n}_j}^{[\mu]}(\mathbf{r};\mathbf{a}_j,\mathbf{R}_j)\right\rangle \tag{14}$$

$$= g_{n_i^y n_j^y}(b_i R_i^y; b_j R_j^y) g_{n_i^z n_j^z}(c_i R_i^z; c_j R_j^z) \times t_{n_i^x n_j^x}(a_i R_i^x; a_j R_j^x),$$

$$t_{n'n}(a', R'; a, R) \equiv \left\langle \psi_{n'}^{[\nu]}(x; a', R') \left| -\frac{\hbar^2}{2m}\frac{\partial^2}{\partial x^2} \right| \psi_n^{[\mu]}(x; a, R) \right\rangle.$$

Quite similar expressions hold for $\langle \psi_{\mathbf{n}_i}^{[\nu]} | \hat{t}_y | \psi_{\mathbf{n}_j}^{[\mu]} \rangle$ (the substitution $x \leftrightarrow y$; $a \leftrightarrow b$) and for $\langle \psi_{\mathbf{n}_i}^{[\nu]} | \hat{t}_z | \psi_{\mathbf{n}_j}^{[\mu]} \rangle$ (the substitution $x \leftrightarrow z$; $a \leftrightarrow c$). Here, in (11)–(13) and below, apart from the matrix $B_{[\nu,\mu]}$, we also use the inverse matrix

$$B^{-1}_{[\nu,\mu]} = \left\| \left(B^{-1}_{[\nu,\mu]} \right)_{ij} \right\|.$$

For the two-particle operators $\sum_{i,j=1}^{A} \hat{\Omega}_{ij}$, there is the general formula [19]

$$\frac{1}{\langle \Psi_\nu | \Psi_\mu \rangle} \left\langle \Psi_\nu \left| \sum_{i,j=1}^{A} \hat{\Omega}_{ij} \right| \Psi_\mu \right\rangle \tag{15}$$

$$= \sum_{k',l',k,l=1}^{A} \langle \phi_{k'}^{[\nu]} \phi_{l'}^{[\nu]} | \hat{\Omega}_{12} | \phi_k^{[\mu]} \phi_l^{[\mu]} \rangle \times \left\{ \left(B^{-1}_{[\nu,\mu]} \right)_{kk'} \left(B^{-1}_{[\nu,\mu]} \right)_{ll'} - \left(B^{-1}_{[\nu,\mu]} \right)_{kl'} \left(B^{-1}_{[\nu,\mu]} \right)_{lk'} \right\}.$$

For the central exchange NN potential (1) and (2), the following expression can be written for even–even nuclei after the summation over the spin–isospin variables:

$$\frac{1}{\langle \Psi_\nu | \Psi_\mu \rangle} \left\langle \Psi_\nu \left| \frac{1}{2} \sum_{i,j=1}^{A} \hat{V}_{ij} \right| \Psi_\mu \right\rangle \tag{16}$$

$$= \sum_{i',i=1}^{Z/2} \sum_{j',j=1}^{Z/2} \sum_{l=1}^{l_{\rm pot}} \left\langle \psi_{\mathbf{n}_{i'}}^{[\nu]}(1) \psi_{\mathbf{n}_{j'}}^{[\nu]}(2) \left| \exp\left\{ -\frac{|\mathbf{r}_1 - \mathbf{r}_2|^2}{\mu_l^2} \right\} \right| \psi_{\mathbf{n}_i}^{[\mu]}(1) \psi_{\mathbf{n}_j}^{[\mu]}(2) \right\rangle \times \left\{ X_d(l) \left(B^{-1}_{[\nu,\mu]} \right)_{ii'} \left(B^{-1}_{[\nu,\mu]} \right)_{jj'} - X_{\rm ex}(l) \left(B^{-1}_{[\nu,\mu]} \right)_{ij'} \left(B^{-1}_{[\nu,\mu]} \right)_{ji'} \right\}$$

$$+ \sum_{i',i=1}^{Z/2} \sum_{j',j=1}^{N/2} \sum_{l=1}^{l_{\rm pot}} \left\langle \psi_{\mathbf{n}_{i'}}^{[\nu]}(1) \psi_{\mathbf{n}_{j'}}^{[\nu]}(2) \left| \exp\left\{ -\frac{|\mathbf{r}_1 - \mathbf{r}_2|^2}{\mu_l^2} \right\} \right| \psi_{\mathbf{n}_i}^{[\mu]}(1) \psi_{\mathbf{n}_j}^{[\mu]}(2) \right\rangle \times \left\{ Y_d(l) \left(B^{-1}_{[\nu,\mu]} \right)_{ii'} \left(B^{-1}_{[\nu,\mu]} \right)_{jj'} - Y_{\rm ex}(l) \left(B^{-1}_{[\nu,\mu]} \right)_{ij'} \left(B^{-1}_{[\nu,\mu]} \right)_{ji'} \right\}$$

$$+ \sum_{i',i=1}^{N/2} \sum_{j',j=1}^{N/2} \sum_{l=1}^{l_{\rm pot}} \left\langle \psi_{\mathbf{n}_{i'}}^{[\nu]}(1) \psi_{\mathbf{n}_{j'}}^{[\nu]}(2) \left| \exp\left\{ -\frac{|\mathbf{r}_1 - \mathbf{r}_2|^2}{\mu_l^2} \right\} \right| \psi_{\mathbf{n}_i}^{[\mu]}(1) \psi_{\mathbf{n}_j}^{[\mu]}(2) \right\rangle \times \left\{ X_d(l) \left(B^{-1}_{[\nu,\mu]} \right)_{ii'} \left(B^{-1}_{[\nu,\mu]} \right)_{jj'} - X_{\rm ex}(l) \left(B^{-1}_{[\nu,\mu]} \right)_{ij'} \left(B^{-1}_{[\nu,\mu]} \right)_{ji'} \right\},$$

where we denoted

$$X_d(l) = \frac{3V_{33}^{(l)} + V_{13}^{(l)}}{2}, \quad X_{\rm ex}(l) = \frac{3V_{33}^{(l)} - V_{13}^{(l)}}{2}, \tag{17}$$

$$Y_d(l) = \frac{3V_{33}^{(l)} + 3V_{31}^{(l)} + V_{13}^{(l)} + V_{11}^{(l)}}{2},$$

$$Y_{\rm ex}(l) = \frac{3V_{33}^{(l)} - 3V_{31}^{(l)} - V_{13}^{(l)} + V_{11}^{(l)}}{2}.$$

Because of the Gaussian radial dependence of the chosen potential, the partial matrix elements on the basis functions (7) are factorized in the form of three cofactors, i.e.,

$$\left\langle \psi_{\mathbf{n}_{i'}}^{[\nu]}(1) \psi_{\mathbf{n}_{j'}}^{[\nu]}(2) \left| \exp\left\{ -\frac{|\mathbf{r}_1 - \mathbf{r}_2|^2}{\mu^2} \right\} \right| \psi_{\mathbf{n}_i}^{[\mu]}(1) \psi_{\mathbf{n}_j}^{[\mu]}(2) \right\rangle$$

$$= j_{n_{i'}^x n_{j'}^x n_i^x n_j^x}(a_{i'} R_{i'}^x, a_{j'} R_{j'}^x; \mu; a_i R_i^x, a_j R_j^x) \times j_{n_{i'}^y n_{j'}^y n_i^y n_j^y}(b_{i'} R_{i'}^y, b_{j'} R_{j'}^y; \mu; b_i R_i^y, b_j R_j^y) \times j_{n_{i'}^z n_{j'}^z n_i^z n_j^z}(c_{i'} R_{i'}^z, c_{j'} R_{j'}^z; \mu; c_i R_i^z, c_j R_j^z), \tag{18}$$

where

$$j_{n'm'nm}(a'_1R'_1, a'_2R'_2; \mu; a_1R_1, a_2R_2) \qquad (19)$$
$$= \int_{-\infty}^{\infty}\int_{-\infty}^{\infty} \psi^{[\nu]}_{n'}(x_1; a'_1R'_1)\psi^{[\nu]}_{m'}(x_2; a'_2R'_2)$$
$$\times \exp\left\{-\frac{(x_1-x_2)^2}{\mu^2}\right\}\psi^{[\mu]}_{n}(x_1; a_1R_1)$$
$$\times \psi^{[\mu]}_{m}(x_2; a_2R_2)dx_1dx_2.$$

As for the Coulomb interaction between protons, it is convenient to use the following integral representation in the context of our algorithm of calculations:

$$\frac{e^2}{r} = \frac{2e^2}{\sqrt{\pi}}\int_0^1 \exp\left(-\frac{r^2}{\mu_o^2}\right)\frac{d\tau}{(1-\tau^2)^{3/2}}, \qquad (20)$$
$$\mu_o \equiv \frac{1}{\tau}\sqrt{1-\tau^2}.$$

In that case,

$$\frac{1}{\langle\Psi_\nu|\Psi_\mu\rangle}\left\langle\Psi_\nu\left|\sum_{i>j=1}^{Z}\frac{e^2}{|\mathbf{r}_i-\mathbf{r}_j|}\right|\Psi_\mu\right\rangle \qquad (21)$$
$$= \frac{2e^2}{\sqrt{\pi}}\sum_{i'>j'=1}^{Z/2}\sum_{i>j=1}^{Z/2}\int_0^1\frac{d\tau}{(1-\tau^2)^{3/2}}$$
$$\times\left\langle\psi^{[\nu]}_{\mathbf{n}_{i'}}(1)\psi^{[\nu]}_{\mathbf{n}_{j'}}(2)\left|\exp\left\{-\frac{|\mathbf{r}_1-\mathbf{r}_2|^2}{\mu_o^2}\right\}\right|\psi^{[\mu]}_{\mathbf{n}_i}(1)\psi^{[\mu]}_{\mathbf{n}_j}(2)\right\rangle$$
$$\times\left\{2\left(B^{-1}_{[\nu,\mu]}\right)_{ii'}\left(B^{-1}_{[\nu,\mu]}\right)_{jj'} - \left(B^{-1}_{[\nu,\mu]}\right)_{ij'}\left(B^{-1}_{[\nu,\mu]}\right)_{ji'}\right\};$$

i.e., in general, the integration over τ remains for the Coulomb energy (21) (for a Gaussian potential, all two-particle integrals can be expressed in terms of elementary functions).

Below, we give another expression for the center-of-mass kinetic energy:

$$\langle\Psi_\nu|\hat{T}_{\mathrm{c.m}}|\Psi_\mu\rangle = -\frac{\hbar^2}{2Am} \qquad (22)$$
$$\times\left(\left\langle\Psi_\nu\left|\sum_{i=1}^{A}\nabla_i^2\right|\Psi_\mu\right\rangle + \left\langle\Psi_\nu\left|\sum_{i\neq j=1}^{A}\nabla_i\nabla_j\right|\Psi_\mu\right\rangle\right),$$

Here, the first term in parentheses is specified by formulas (13) and (14), and the second term is calculated by using the common formula (15) for two-particle operators, i.e.,

$$\frac{1}{\langle\Psi_\nu|\Psi_\mu\rangle}\left\langle\Psi_\nu\left|\sum_{i\neq j=1}^{A}\nabla_i\nabla_j\right|\Psi_\mu\right\rangle \qquad (23)$$
$$= \sum_{i'\neq j'=1}^{A}\sum_{i\neq j=1}^{A}\langle\phi^{[\nu]}_{i'}|\nabla|\phi^{[\mu]}_{i}\rangle\langle\phi^{[\nu]}_{j'}|\nabla|\phi^{[\mu]}_{j}\rangle$$
$$\times\left\{\left(B^{-1}_{[\nu,\mu]}\right)_{ii'}\left(B^{-1}_{[\nu,\mu]}\right)_{jj'} - \left(B^{-1}_{[\nu,\mu]}\right)_{ij'}\left(B^{-1}_{[\nu,\mu]}\right)_{ji'}\right\};$$

explicit expressions for the matrix elements $\langle\phi_1|\nabla|\phi_2\rangle$ as well as for $g_{n_1n_2}$, $t_{n_1n_2}$, and $j_{n'm'nm}$ are given in our preprint [20].

Below, we briefly consider the projection of the determinant functions on states with a certain angular momentum; i.e., we take into account what is called the rotation effect in phenomenological models. Clearly, the determinant functions Ψ_ν introduced above are some packets of states $|JM\rangle$. To obtain states with a certain angular momentum J and its projection M, we must act on the total wave function Ψ_A by the projector $\hat{P}^J_{MK}$, which is convenient to write in terms of the standard Hill–Wheeler integral

$$\hat{P}^J_{MK} = \frac{2J+1}{8\pi^2}\int d\Omega D^{J*}_{MK}(\Omega)\hat{R}(\Omega); \qquad (24)$$

i.e., to determine the eigenvalue of some physical operator $\hat{O}$, we must calculate the overlap integrals

$$\int d\Omega D^{J*}_{MM}(\Omega)\langle\Psi_\nu|\hat{O}|\hat{R}(\Omega)\Psi_\mu\rangle, \qquad (25)$$
$$\int d\Omega D^{J*}_{MM}(\Omega)\langle\Psi_\nu|\hat{R}(\Omega)\Psi_\mu\rangle.$$

When the coordinate system is rotated through Euler angles, the spatial and spin–isospin functions are transformed by using standard formulas [21]. By analogy with (9), we may introduce the matrix $\tilde{B}$:

$$\left(\tilde{B}_{[\nu,\mu]}\right)_{ij} \equiv \int\psi^{[\nu]}_{\mathbf{n}_i}(\mathbf{r}; \mathbf{a}_i, \mathbf{R}_i)\hat{R}(\Omega)\psi^{[\mu]}_{\mathbf{n}_j}(\mathbf{r}; \mathbf{a}_j, \mathbf{R}_j)d\mathbf{r} \qquad (26)$$
$$\sim\int\int\int dxdydz\left(\frac{x}{a_i}\right)^{n^x_i}\left(\frac{y}{b_i}\right)^{n^y_i}\left(\frac{z}{c_i}\right)^{n^z_i}\left(\frac{\tilde{x}}{a_j}\right)^{n^x_j}\left(\frac{\tilde{y}}{b_j}\right)^{n^y_j}\left(\frac{\tilde{z}}{c_j}\right)^{n^z_j}$$
$$\times\exp\left\{-\frac{(x-R^x_i)^2}{2a_i^2} - \frac{(y-R^y_i)^2}{2b_i^2} - \frac{(z-R^z_i)^2}{2c_i^2} - \frac{(\tilde{x}-R^x_j)^2}{2a_j^2} - \frac{(\tilde{y}-R^y_j)^2}{2b_j^2} - \frac{(\tilde{z}-R^z_j)^2}{2c_j^2}\right\};$$

here, the Cartesian coordinates in the rotated frame of reference $\tilde{x} = \tilde{x}_1$, $\tilde{y} = \tilde{x}_2$, $\tilde{z} = \tilde{x}_3$ are expressed in terms of the corresponding coordinates of the original frame of reference using the rotation matrix $||R_{m'm}(\Omega)||$ [21], i.e.,

$$\tilde{x}_m = \sum_{m'=1}^{3} R_{m'm}(\Omega) x_{m'}, \quad m = 1, 2, 3. \tag{27}$$

The integration in (26) can be performed completely if the quadratic form in the exponent is reduced to a diagonal form.

Note that the integration for the two-particle matrix elements, where we have to deal with four different orbitals, is performed by analogy. Thus, for example, upon calculation of the matrix elements

$$\left\langle \psi^{[\nu]}_{\mathbf{n}_i}(\mathbf{r}_1; \mathbf{a}_i, \mathbf{R}_i)\psi^{[\nu]}_{\mathbf{n}_j}(\mathbf{r}_2; \mathbf{a}_j, \mathbf{R}_j) \left| \exp\left\{-\frac{(\mathbf{r}_1 - \mathbf{r}_2)^2}{\mu^2}\right\} \hat{R}(\Omega) \right| \psi^{[\mu]}_{\mathbf{n}_{i'}}(\mathbf{r}_1; \mathbf{a}_{i'}, \mathbf{R}_{i'})\psi^{[\mu]}_{\mathbf{n}_{j'}}(\mathbf{r}_2; \mathbf{a}_{j'}, \mathbf{R}_{j'}) \right\rangle, \tag{28}$$

the quadratic form will be composed of the components of the six-dimensional vector $\mathbf{x} = \mathbf{x}(x_1, x_2, \ldots, x_6)$, where $\mathbf{r}_1 = \mathbf{r}_1(x_1, x_2, x_3)$ and $\mathbf{r}_2 = \mathbf{r}_2(x_4, x_5, x_6)$.

Thus, the integration over particle coordinates can be performed completely. Unfortunately, the final formulas for the projected wave functions are cumbersome. The integration over Euler angles $\Omega(\theta_1, \theta_2, \theta_3)$ is performed numerically; although, judging by the structure of the derived formulas, we cannot rule out the possibility of an exact integration here either.

4. NUMERICAL CALCULATIONS

In nuclear physics, we know several systems that are highly critical to theory. ^{8}Be, a loosely-bound system of eight nucleons whose ground state is realized in the form of a narrow near-threshold resonance, should be attributed to such nuclei. It is hoped that calculations of basic spectroscopic parameters for the ^{8}Be nucleus will become a serious test for the model under consideration.

Taking into account the well-known symmetry of ^{8}Be, we choose the wave function to be

$$\Psi_A(1, 2, \ldots, 8) = w_1 \cdot \Psi_1 + w_2(\Psi_2 + \Psi_3), \tag{29}$$

where the Slater Ψ_ν determinants (6) are constructed by using the following spatial orbitals (7):

(a) for $\nu = 1$,

$$\psi^{[\nu]}_{\mathbf{n}_i}(j) = \begin{cases} \psi_0(x_j; \tilde{a}_1, 0)\psi_0(y_j; \tilde{a}_1, 0)\psi_0(z_j; \tilde{c}_1, 0), & i = 1\text{–}4, \\ \psi_0(x_j; \tilde{a}_2, 0)\psi_0(y_j; \tilde{a}_2, 0)\psi_1(z_j; \tilde{c}_2, 0), & i = 5\text{–}8; \end{cases} \tag{30}$$

(b) for $\nu = 2, 3$,

$$\psi^{[\nu=2]}_{\mathbf{n}_i}(j) = \begin{cases} \psi_0(x_j; a_1, 0)\psi_0(y_j; a_1, 0)\psi_0(z_j; c_1, -sR), & i = 1\text{–}4, \\ \psi_0(x_j; a_2, 0)\psi_0(y_j; a_2, 0)\psi_1(z_j; c_2, R), & i = 5\text{–}8; \end{cases} \tag{31}$$

$$\psi^{[\nu=3]}_{\mathbf{n}_i}(j) = \begin{cases} \psi_0(x_j; a_1, 0)\psi_0(y_j; a_1, 0)\psi_0(z_j; c_1, sR), & i = 1\text{–}4, \\ \psi_0(x_j; a_2, 0)\psi_0(y_j; a_2, 0)\psi_1(z_j; c_2, -R), & i = 5\text{–}8. \end{cases} \tag{32}$$

In these formulas, the quantities $\{\tilde{a}_1, \tilde{c}_1, \tilde{a}_2, \tilde{c}_2; a_1, c_1, a_2, c_2, R, s\}$ are the variational parameters that can be determined by minimizing the functional of the total energy of the nucleus.

To clarify the situation at various distances between the fragments, we will sequentially increase R from $R = 0$ to $R = R_0$. In this case, all the remaining parameters of the functions Ψ_ν listed above are optimized for each specified value of R. Subsequently, starting from the point $R = R_0$, we will continuously modify the orbitals of the determinant functions $\Psi_{\nu=2}$ and $\Psi_{\nu=3}$ in such a way as to obtain the wave functions of two free α particles in the limit $R \to \infty$; to be more precise, we find for $R \geq R_0$

$$\psi^{[\nu=2]}_{\mathbf{n}_i}(j) = \begin{cases} \psi_0(x_j; a_1, 0)\psi_0(y_j; a_1, 0)\psi_0(z_j; c_1, -sR), & i = 1\text{–}4, \\ -\alpha(\xi)\psi_0(x_j; a_1, 0)\psi_0(y_j; a_1, 0)\psi_0(z_j; c_1, sR) + & \\ +\beta(\xi)\psi_0(x_j; a_2, 0)\psi_0(y_j; a_2, 0)\psi_1(z_j; c_2, R), & i = 5\text{–}8, \end{cases} \tag{33}$$

$$\psi_{\mathbf{n}_i}^{[\nu=3]}(j)=\begin{cases}\psi_0(x_j;a_1,0)\psi_0(y_j;a_1,0)\psi_0(z_j;c_1,sR), & i=1\text{–}4,\\ \alpha(\xi)\cdot\psi_0(x_j;a_1,0)\psi_0(y_j;a_1,0)\psi_0(z_j;c_1,-sR)+ & \\ +\beta(\xi)\cdot\psi_0(x_j;a_2,0)\psi_0(y_j;a_2,0)\psi_1(z_j;c_2,-R), & i=5\text{–}8.\end{cases} \quad (34)$$

Here, the functions $\alpha(\xi)$ and $\beta(\xi)$ are equal, by definition, to

$$\alpha(\xi)=\frac{\xi}{\sqrt{1+2\xi\sqrt{1-\xi^2}}}, \quad (35)$$

$$\beta(\xi)=\frac{\sqrt{1-\xi^2}}{\sqrt{1+2\xi\sqrt{1-\xi^2}}},\ \xi\equiv\frac{R-R_0}{\eta_0 R_0},\ 0\le\xi\le 1.$$

The choice of R_0 and η_0 in (35) corresponds to the choice of the deexcitation interval $[R_0,(\eta_0+1)R_0]$ for the second α cluster. As for antisymmetrization in particle permutations, the Pauli exclusion principle applies to all A nucleons of the nucleus up to the point $R\le R_0$. When passing the interval $[R_0,(\eta_0+1)R_0]$, antisymmetrization between the particles of different clusters gradually turns off, with the deexcitation of orbitals (33), (34) and the turnoff of antisymmetrization in formula (4) being modeled by the same functions $\alpha(\xi)$ and $\beta(\xi)$.

The total wave function of the system in the interval $[R_0,(\eta_0+1)R_0]$ under consideration can be represented as

$$\Psi_A(1,2,\ldots,8) \quad (36)$$
$$\sim\beta(\xi)w_1^0\Psi_1+[1+\alpha(\xi)]w_2^0(\Psi_2+\Psi_3),$$

where w_1^0 and w_2^0 are the weights of the corresponding determinant functions at the point $R=R_0$. In addition, it would be natural to set α_S in the Hamiltonian of the microscopic model [see (4)] equal to

$$\alpha_S=\alpha_S(R)=\begin{cases}0, & R<R_0\\ \alpha(\xi), & R_0\le R\le(\eta_0+1)R_0\\ 1, & R>(\eta_0+1)R_0.\end{cases} \quad (37)$$

When calculating the overlap integrals related to particular physical quantities, it is necessary to determine the matrix $B_{[\nu,\mu]}$ and the inverse of it. For ^{8}Be, the matrix $B_{[\nu,\mu]}$ generally has the structure

$$\left(B_{[\nu,\mu]}\right)_{ij}=\begin{cases}\alpha_{\nu\mu}, & i=j=1,2,3,\\ \beta_{\nu\mu}, & i=j=4,5,6,\\ \gamma_{\nu\mu}, & i=j-3,\ j=4,5,6,\\ \delta_{\nu\mu}, & i=j+3,\ j=1,2,3,\\ 0, & \text{others};\end{cases} \quad (38)$$

$$\det\left\|\left(B_{[\nu,\mu]}\right)_{ij}\right\|=\zeta_0^4,\quad \zeta_0\equiv\alpha_{\nu\mu}\beta_{\nu\mu}-\gamma_{\nu\mu}\delta_{\nu\mu}.$$

Given definitions (9) and (30)–(34), it is easy to determine $\alpha_{\nu\mu}$, $\beta_{\nu\mu}$, $\gamma_{\nu\mu}$, and $\delta_{\nu\mu}$.

Based on the above formulas, we performed numerical calculations for several commonly used central exchange NN potentials. The results for the Volkov potential [22] proved to be satisfactory. Some of them are presented in Table 1. This table gives the energy E_{0^+} for the ground 0^+ state of ^{8}Be, the Coulomb energy U_{Coul} of the proton interaction, the rms radii $\langle r^2\rangle^{1/2}$, and optimal values of the variational parameters $\{a_i,\ b_i,\ c_i,\ \tilde{a}_i,\ \tilde{b}_i,\ \tilde{c}_i,\ R,\ s\}$ for the determinant functions Ψ_ν and their nonnormalized weights $\{w_i\}$. The function (29) with ten nonlinear variational parameters that include both orbital polarization and the $(\alpha+\alpha)$-cluster mode of ^{8}Be corresponds to model 1 (the second column in Table 1). The wave function responsible for the calculation of the quantities in the third column (model 2) is a superposition of the two determinant functions

$$\Psi_A(1,2,\ldots,A) \quad (39)$$
$$=w_1\Psi_1(\{\mathbf{r}_i\};\tilde{a}_1=\tilde{b}_1,\tilde{c}_1;\tilde{a}_2=\tilde{b}_2,\tilde{c}_2)$$
$$+w_4\Psi_4(\{\mathbf{r}_i\};\tilde{\tilde{a}}_1=\tilde{\tilde{b}}_1,\tilde{\tilde{c}}_1;\tilde{\tilde{a}}_2=\tilde{\tilde{b}}_2,\tilde{\tilde{c}}_2)$$

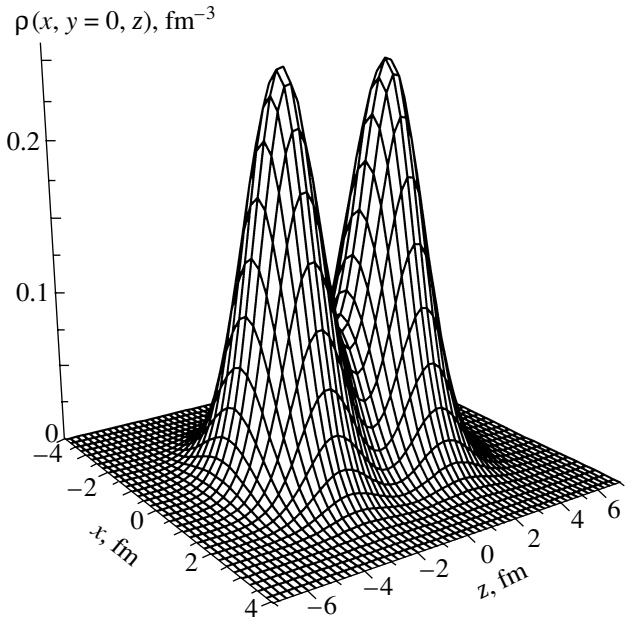

Fig. 1. The mass density distribution $\rho(x,y=0,z)$ for ^{8}Be as a function of the variables x and z in the internal coordinate system rigidly bound to the nucleus.

Table 1. Ground-state parameters for ^{8}Be according to models 1–8 for the Volkov NN potential [22]

Parameter	1	2	3	4	5	6	7	8
E_{0^+} [MeV]	−52.732	−50.017	−36.859	−49.605	−47.910	−36.135	−52.975	−44.836
U_{Coul} [MeV]	3.145	3.339	3.422	3.353	3.366	3.446	3.154	3.279
$\langle r^2\rangle^{1/2}$ [fm]	2.52	2.33	2.19	2.31	2.30	2.15	2.52	2.38
Ψ_1:								
$\tilde{a}_1 = \tilde{b}_1$	1.27	1.22	1.49	1.29	1.32	1.60	1.22	1.27
$\tilde{c}_1$	2.23	2.33	1.49	2.43	2.07	1.60	2.18	1.89
$\tilde{a}_2 = \tilde{b}_2$	1.35	1.29	1.49	1.35	1.32	1.60	1.29	1.34
$\tilde{c}_2$	1.91	1.80	1.49	1.93	2.07	1.60	1.79	1.62
Ψ_2, Ψ_3:								
$a_1 = b_1$	1.49						1.47	1.57
c_1	1.59						1.56	1.56
$a_2 = b_2$	1.28						1.25	1.30
c_2	1.37						1.36	1.36
s	1.28						1.29	1.30
R [fm]	1.76						1.73	1.53
Ψ_4:								
$\tilde{a}_1 = \tilde{b}_1$		1.50	1.86				1.50	1.51
$\tilde{c}_1$		2.70	1.86				2.48	2.10
$\tilde{a}_2 = \tilde{b}_2$		1.53	1.86				1.65	1.72
$\tilde{c}_2$		2.28	1.86				2.37	2.12
w_1	1.74	1.35	1.03	1.00	1.00	1.00	0.97	0.50
$w_2 = w_3$	1.00						0.69	0.21
w_4		0.72	0.69				0.42	0.34

and completely takes into account only orbital polarization. A wave function similar to the preceding one but without deformation, i.e.,

$$\Psi_A(1,2,\ldots,A) = w_1\Psi_1(\{\mathbf{r}_i\};\tilde{a}) + w_4\Psi_4(\{\mathbf{r}_i\};\tilde{\tilde{a}}), \tag{40}$$

corresponds to model 3. Model 4 uses a single-determinant wave function where the s and p orbitals have different polarizations (a total of four variational parameters $\tilde{\tilde{a}}_1 = \tilde{\tilde{b}}_1, \tilde{\tilde{c}}_1, \tilde{\tilde{a}}_2 = \tilde{\tilde{b}}_2, \tilde{\tilde{c}}_2$), while in model 5, the s- and p-orbital polarizations were the same (here, Ψ_A contains only two parameters, $\tilde{a} = \tilde{b}$ and $\tilde{c}$). The simplest approximation is a microscopic version of the $SU(3)$ model with one variational parameter, $\tilde{a} = \tilde{b} = \tilde{c}$ (model 6 in Table 1). Model 7 uses the most complex model wave function among those considered here. The latter differs from the functions of model 1 by an additional determinant filled with orbitals (30) with the independent parameters $\tilde{a}_1 = \tilde{b}_1$, $\tilde{c}_1$, $\tilde{a}_2 = \tilde{b}_2$, $\tilde{c}_2$. Finally, the parameters in the last column of Table 1 were calculated with the preceding wave function (model 7) but without projecting Ψ_A on states with a certain angular momentum.

Let us first consider our calculations with the one-center functions Ψ_A (models 2–6). As we see from Table 1, allowance for oscillatory-field deformation gives the largest increase in binding energy (cf. models 6 and 5). Orbital polarization is also important (cf. model 5 and 4). If the nonlinear variational parameters $\{a_i, b_i, c_i\}$ along the three Cartesian axes are assumed to be identical (i.e., if deformation is ignored), then expanding the basis from one to two determinant functions Ψ_ν changes the energy E of the nucleus only slightly (cf. models 3 and 6). Moreover, as our

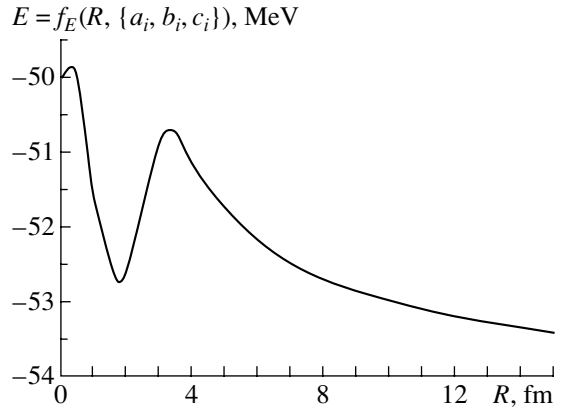

Fig. 2. Total ^{8}Be energy versus variational parameter R.

calculations show, including two, three, or more determinants Ψ_ν with the same $SU(3)$ symmetry in our analysis causes an insignificant change in E even if the possible s- and p-orbital deformations are taken into account (cf. models 2 and 4). Therefore, within the accuracy of our analysis, it will suffice to include one Slater determinant in Ψ_A to allow for deformation effects. The next important step in effectively expanding the variational basis of functions is including the cluster $(\alpha + \alpha)$ mode in our calculations. The inclusion of this cluster model yielded a gain in ^{8}Be energy of about 3 MeV (cf. models 1 and 4, 2).

Figure 1 shows the mass density distribution $\rho(\mathbf{r})$ for ^{8}Be calculated with the wave function (29). The optimal values of the variational parameters that correspond to this function are given in Table 1 (model 1). The calculations were performed in the center-of-mass frame. The surface shown in Fig. 1 corresponds to an axisymmetric distribution $\rho(\mathbf{r})$ in the xz plane at $y = 0$. As we see from this figure, the distance between the density maxima $\rho_{\max}$ (the centers of mass for two α particles) is $D \approx 4.2$ fm, while the density $\rho(\mathbf{r})$ at the point $\mathbf{r} = 0$ is approximately equal to $0.36\rho_{\max}$. If the density $\rho(\mathbf{r})$ is calculated with the parameters of a different model from among those considered here, then Fig. 1 will not change qualitatively, although the distance D and the neck thickness can change appreciably.

The calculated dependence of the ^{8}Be energy $E \equiv f_E(R, \{a_i, b_i, c_i\})$ on R is shown in Fig. 2. This dependence corresponds to the case where, for each fixed R, f_E is optimized in all the remaining variational parameters. Calculations of this kind are occasionally invoked to estimate the nucleus–nucleus interaction potentials. It should be borne in mind that, in the cluster overlap region, the distance D between the density maxima can differ greatly from its asymptotic value, which is $D_{\text{as}} = 2R(1 + s)$ in our case.

Table 2 gives our ground-0^+-state calculations for ^{6}He for three NN potentials: $V1$ [22], $BB1$ [23], and $G5$ [24]. The calculations were performed with two models. The wave function of model 1 was constructed as the Slater determinant for six nucleons filled with orbitals (30). It contained four variational parameters: $\tilde{a}_1 = \tilde{b}_1$, $\tilde{c}_1$ for the first four orbitals and $\tilde{a}_2 = \tilde{b}_2$, $\tilde{c}_2$ for the last two single-particle states. By analogy with the function for ^{8}Be, the wave function of model 2 is a superposition of several Slater determinants: a one-center determinant and two two-center determinants with the centers at the points $\mathbf{R}_1 = (0, 0, \pm R)$ and $\mathbf{R}_2 = (0, 0, \mp sR)$. Model 2 contained ten nonlinear variational parameters; their optimal values for the NN potentials under consideration are given in Table 2.

Recall that the ^{4}He nucleus acts as the core in ^{6}He. Depending on the chosen NN potential, its energy calculated with the simple $SU(3)$-model function is $E_\alpha(V1) = -27.09$ MeV, $E_\alpha(BB1) = -27.37$ MeV, $E_\alpha(G5) = -28.29$ MeV. Comparing these values with the ^{6}He energy in Table 2, we see that two neutrons in ^{6}He will be bound only for model 2 and the NN potentials $V1$ and $G5$. Therefore, we may conclude that the trial wave function of model 2 reproduces the actual situation much better than the single-determinant function of model 1.

We emphasize that we do not claim to describe the nuclear systems considered here with a unique accuracy; these were previously studied more thoroughly (see, e.g., [11, 12]). Our goal was to elucidate the question of how important the compact and loosely bound (cluster) structures are in the investigation of loosely bound nuclei using simple trial functions. Our results are discussed in more detail in [20].

Based on our analysis for loosely bound states, we can propose a general scheme for constructing simple and flexible trial wave functions and the strategy of specific calculations. It involves the following: first, the various deformations that play an important role in forming a given state of the nucleus are estimated in terms of the one-center determinant functions, and, then, the required cluster degrees of freedom are invoked. In this case, the hierarchy of modes of nucleon motion can be established by using the functions Ψ_A nonprojected in angular momentum, which significantly simplifies the calculation. In addition, a simplified calculation with the nonprojected functions Ψ_A also yields the optimal values of almost all variational parameters (cf., e.g., the corresponding parameters of models 7 and 8 from Table 1). Clearly, this point is important in determining the precise position of the global minimum in the total energy of the nucleus, which is calculated with the functions

Table 2. The results of our calculations for ^{6}He for NN potentials [22–24] (the calculations were performed with models 1 and 2; the energies E and $U_{\rm Coul}$ are in MeV; the rms radii, $\{a_i, b_i, c_i\}$, and R are in fm)

Parameter	$V1$ [22]		$BB1$ [23]		$G5$ [24]	
	1	2	1	2	1	2
E	−25.296	−27.396	−24.451	−26.918	−29.636	−30.831
$U_{\rm Coul}$	0.7139	0.7633	0.6820	0.7428	0.7300	0.7591
$r_{\rm rms}^{\rm matter}$	2.51		2.64		2.47	
$r_{\rm rms}^{\rm proton}$	1.86		1.95		1.78	
$r_{\rm rms}^{\rm neutron}$	2.78		2.92		2.76	
$\Psi_{\nu=1}$:						
$\tilde{a}_1 = \tilde{b}_1$	1.31	1.28	1.36	1.34	1.34	1.33
$\tilde{c}_1$	2.19	2.05	2.32	2.16	1.97	1.85
$\tilde{a}_2 = \tilde{b}_2$	1.45	1.36	1.55	1.47	1.60	1.74
$\tilde{c}_2$	2.14	2.05	2.23	2.16	2.00	1.83
$\Psi_{\nu=2,3}$:						
$a_1 = b_1$		1.39		1.41		1.39
c_1		1.37		1.39		1.41
$a_2 = b_2$		1.86		1.85		1.46
c_2		2.54		2.56		2.47
s		1.16		1.13		1.65
R		1.31		1.44		0.91
w_1	1	0.9209	1	0.8509	1	0.8993
w_2	0	0.6223	0	0.7033	0	0.4835

projected in angular momentum and in its projection $\Psi_A^{JM}(1, 2, \ldots, A)$.

REFERENCES

1. A. I. Baz' and M. V. Zhukov, Yad. Fiz. **16**, 60 (1972) [Sov. J. Nucl. Phys. **16**, 31 (1973)].
2. A. I. Baz' and M. V. Zhukov, Yad. Fiz. **16**, 958 (1972) [Sov. J. Nucl. Phys. **16**, 529 (1973)].
3. Yu. A. Simonov, Yad. Fiz. **3**, 630 (1966) [Sov. J. Nucl. Phys. **3**, 461 (1966)].
4. A. M. Badalyan and Yu. A. Simonov, Yad. Fiz. **3**, 1032 (1966) [Sov. J. Nucl. Phys. **3**, 755 (1966)].
5. A. M. Badalyan, F. Calogero, and Yu. A. Simonov, Nuovo Cimento A **68**, 572 (1970).
6. A. I. Baz', Yu. T. Grin, V. F. Demin, and M. V. Zhukov, Fiz. Élem. Chastits At. Yadra **3**, 275 (1972) [Sov. J. Part. Nucl. **3**, 137 (1972)].
7. Yu. F. Smirnov and K. V. Shitikova, Fiz. Élem. Chastits At. Yadra **8**, 847 (1977) [Sov. J. Part. Nucl. **8**, 344 (1977)].
8. V. I. Kukulin, Izv. Akad. Nauk SSSR, Ser. Fiz. **39**, 535 (1975).
9. V. I. Kukulin and V. M. Krasnopol'skiĭ, Yad. Fiz. **22**, 1110 (1975) [Sov. J. Nucl. Phys. **22**, 578 (1975)].

10. V. I. Kukulin and V. M. Krasnopol'sky, J. Phys. G **3**, 795 (1977).
11. K. Varga and Y. Suzuki, Phys. Rev. C **52**, 2885 (1995).
12. J. Wurzer and H. M. Hofmann, Phys. Rev. C **55**, 688 (1997).
13. B. S. Pudliner, V. R. Pandharipande, J. Carlson, *et al.*, Phys. Rev. C **56**, 1720 (1997).
14. R. A. Eramzhan, G. G. Ryzhikh, and Yu. M. Tchuvil'sky, Yad. Fiz. **62**, 42 (1999) [Phys. At. Nucl. **62**, 37 (1999)].
15. A. I. Steshenko, Yad. Fiz. **60**, 599 (1997) [Phys. At. Nucl. **60**, 520 (1997)].
16. P. Ring and P. Schuck, *The Nuclear Many-Body Problem* (Springer-Verlag, Berlin, 1980).
17. *Handbook of Mathematical Functions,* Ed. by M. Abramowitz and I. A. Stegun (National Bureau of Standards, Washington, 1964; Nauka, Moscow, 1979).
18. D. M. Brink, in *Nuclear Physics: Proceedings of the International School of Physics, Enrico Fermi, Course XXXVI, Varenna, 1966,* Ed. by C. Bloch (Academic, New York, 1966).
19. P. O. Löwdin, Phys. Rev. **97**, 1474 (1955).
20. O. L. Savchenko and A. I. Steshenko, nucl-th/0008035.
21. D. A. Varshalovich, A. N. Moskalev, and V. K. Khersonskii, *Quantum Theory of Angular Momentum* (Nauka, Leningrad, 1975; World Scientific, Singapore, 1988).
22. A. B. Volkov, Nucl. Phys. **74**, 33 (1965).
23. D. M. Brink and E. Boecker, Nucl. Phys. A **91**, 1 (1967).
24. I. V. Simenog and A. I. Steshenko, Ukr. Fiz. Zh. **38**, 381 (1993).

Translated by V. Astakhov

Physics of Atomic Nuclei, Vol. 65, No. 10, 2002, pp. 1809–1815. Translated from Yadernaya Fizika, Vol. 65, No. 10, 2002, pp. 1858–1864.

NUCLEI
Theory

Calculation of the Quadrupole Deformation of Nuclei in the Mass Region $A > 16$

B. S. Ishkhanov and V. N. Orlin

Institute of Nuclear Physics, Moscow State University, Vorob'evy gory, Moscow, 119899 Russia

Received December 17, 2001

Abstract—The method for calculating the nuclear-quadrupole-deformation parameter on the basis of a self-consistent anisotropic oscillator potential is modified in such a way that it becomes possible to take phenomenologically into account the resistance of closed nucleon shells against changes in the spherical shape of the nuclear surface. This approach enables one to describe satisfactorily the deformation of beta-stable nuclei in the mass region $A > 16$. The possibility of performing such calculations for nuclei occurring far from the beta-stability valley is also considered. © *2002 MAIK "Nauka/Interperiodica".*

1. INTRODUCTION

As far back as the mid-1950s, attempts were made to calculate the equilibrium deformation of beta-stable nuclei by minimizing the sum of single-particle energies of nucleons moving in a spheroidal mean field (see, for example, [1]). These calculations permitted understanding the relationship between the number of nucleons in the outer (valence) shell of a nucleus and the magnitude of its deformation and explained why the majority of known deformed nuclei have a prolate shape in their ground states. Concurrently, it was revealed that, in order to describe adequately changes in the nuclear shape in response to changes in the nucleonic composition of nuclei, it is necessary to take into account residual two-particle forces; since these forces lead to nucleon pairing, they have a stabilizing effect on closed spherical shells, which play an important role in the entire process of deformation.

Presently, relativistic mean-field calculations and mean-field calculations of the Skyrme–Hartree–Fock type [2–4] are being extensively used to explore the equilibrium shapes of superheavy nuclei and nuclei occurring far from the beta-stability valley (exotic nuclei). However, the results of such calculations depend greatly on the choice of parameters of the nuclear Hamiltonian, to say nothing of the complexity of the underlying mathematical procedure. In view of this, rather simple calculations of nuclear deformations on the basis of the single-particle shell model may still produce valuable results, the more so as the schemes employed in such calculations for single-particle levels have been tested through fits to various data both for spherical and for deformed nuclei and are therefore quite reliable.

After some authors had proposed [5–8] to break down the total sum of single-particle energies, $E_{\text{s.p.}}(Z,N)$, into a smooth (averaged) component $\tilde{E}_{\text{s.p.}}(Z,N)$ and an oscillating term $\delta E_{\text{s.p.}}(Z,N)$, the accuracy of shell-model calculations was significantly improved. The second term can be treated as a microscopic shell-model correction to the macroscopic energy of the nucleus being considered (E_{macro}); by the latter, we mean either the Thomas–Fermi energy calculated with averaged nucleon densities or the equivalent liquid-drop energy of the Weizsäcker model. The smooth term $\tilde{E}_{\text{s.p.}}$ does not have physical significance by itself—it describes the contribution of the single-particle spectrum to the volume, the surface, and other components of the macroscopic energy. Thus, the total energy of a nucleus can be represented in the form

$$E_{\text{tot}} = E_{\text{macro}} + \delta E_{\text{s.p.}}. \qquad (1)$$

It is important to note that, in contrast to the total single-particle energy $E_{\text{s.p.}} = \tilde{E}_{\text{s.p.}} + \delta E_{\text{s.p.}}$, expression (1) contains the macroscopic term E_{macro}, through which the effect of residual two-particle forces is taken into account to a considerable extent.

As was shown by Strutinsky and by other authors (see [5, 6, 9, 10]), changes in the number of intranuclear nucleons lead to oscillations of the energy $\delta E_{\text{s.p.}}$ because of the oscillations of the density of single-particle levels that are grouped into large (magic) shells. The shell-model correction $\delta E_{\text{s.p.}}$ is approximately proportional to the oscillating component of the level density near the Fermi surface [6, 10] and attains a minimum value, which corresponds to the maximum binding energy of the nucleus, at the boundary of the shell—that is, in the region of the

1063-7788/02/6510-1809$22.00

energy gap. As the spherical potential is deformed, oscillations of the energy $\delta E_{\text{s.p.}}$ change form. Concurrently, there appear new magic numbers and new energy gaps that can be associated with stationary or isomeric states of deformed nuclei.

Within this approach, it proved to be possible to explain the observed quadrupole deformations ($\delta \sim 0.2$–0.3) of the ground states of rare-earth elements and actinides [10, 11] and to describe the origin of isomeric states of strongly deformed ($\delta \sim 0.6$) actinide nuclei and those features of their fission that could not be reproduced within the macroscopic liquid-drop model without taking into account microscopic shell effects [12, 13].

However, it is illegitimate to apply this approach to describing the equilibrium shapes of light and medium-mass nuclei ($A < 100$), since the oscillations of the shell correction $\delta E_{\text{s.p.}}$ are not associated with the properties of individual levels—they can be of decisive importance only if there arise sufficiently large inhomogeneities of the single-particle spectrum [6, 10, 12]. Also, it can hardly be used to describe the deformations of exotic nuclei featuring a large excess of neutrons of protons, since available experimental data suggest a significant weakening of shell effects in such nuclei [14]. In all cases, we are dealing here with comparatively shallow minima of the energy $E_{\text{tot}}(\delta)$, so that, in order to reveal them, the form of potential must be matched with the form of the nucleon-density distribution in the stationary or isomeric nuclear state being considered.

The conditions of matching have the simplest form for an anisotropic harmonic-oscillator potential, for which one can obtain an explicit expression for the the quadrupole deformation of a nucleus in the ground state. For deformation values in the region $\delta \gtrsim 0.3$, single-particle states in the realistic Nilsson potential can be approximated by oscillator wave functions. It was shown in [8] that, owing to this, the matching conditions for a harmonic oscillator can be used to estimate the equilibrium deformations of nuclei in the mass regions $A \sim 23$–25, $150 < A < 180$, and $A > 230$.

The above naturally brings about the question of whether the approach described in [8] can be modified in such a way as to adopt it for calculating the quadrupole deformations of ground-state beta-stable nuclei not only in the regions of stable deformations but also in transition regions where a spherical and a spheroidal shape of the nuclear surface compete with each other. Here, we make an attempt at constructing such a modification and show that this is possible if one assumes that, at moderate values of the nuclear deformation ($\delta \lesssim 0.4$), inner filled shells that correspond to spherical magic numbers of nucleons are adiabatically deformed, this occurring no sooner than the quadrupole moment of the outer shell that is being filled reaches a threshold value, which is taken to be a model parameter.

Bearing in mind that the overwhelming majority of deformed nuclei have a prolate shape in the ground state, we restricted our analysis to calculating positive quadrupole deformations in the mass region $A > 16$. The results of these calculations will then be used in describing the shape of giant dipole resonances in light, medium-mass, and heavy nuclei.

In the concluding section of this article, we discuss the possibility of extending the method developed here to the region of exotic nuclei.

2. DESCRIPTION OF THE COMPUTATIONAL PROCEDURE USED

The parameter of the nuclear quadrupole deformation is defined as

$$\delta = \frac{3}{4} Q_0 / Z\langle r^2\rangle \cong \frac{3}{4} \frac{\left\langle \sum\limits_{k=1}^{A} (2x_3^2 - x_1^2 - x_2^2)_k \right\rangle}{\left\langle \sum\limits_{k=1}^{A} (x_1^2 + x_2^2 + x_3^2)_k \right\rangle}, \quad (2)$$

where Q_0 is the intrinsic quadrupole moment of the nucleus being considered; $A = Z + N$ is its mass number; $\langle r^2\rangle$ in the mean square of the radius of the charge distribution in the nucleus; and x_i ($i = 1, 2, 3$) are the nucleon coordinates in the reference frame comoving with the nucleus.

In calculating the deformation in question, it is useful to set, for a first approximation, the mean field of the nucleus to the anisotropic-oscillator potential

$$V = \sum_{i=1}^{3} \frac{1}{2} M\omega_i^2 x_i^2. \quad (3)$$

In this case, we have

$$\left\langle \sum_{k=1}^{A} (x_i^2)_k \right\rangle = \frac{\hbar}{M\omega_i} \Sigma_i, \qquad i = 1, 2, 3, \quad (4)$$

where the quantity

$$\Sigma_i \equiv \sum_{k=1}^{A} \left(n_i + \frac{1}{2} \right)_k = \frac{1}{\hbar\omega_i} \mathcal{E}_i \quad (5)$$

determines the energy of oscillations of the nucleus along the x_i axis [n_i are oscillator quantum numbers characterizing single-particle states in the potential (3)].

For any nucleon configuration specified by a set of the quantum numbers $(n_i)_k$, the deformation of the nucleus can be found from the self-consistency condition requiring that, in the state of equilibrium,

the deformation of the potential be equal to the deformation of the nucleon-density distribution. It was shown in [8] that, for the axisymmetric potential (3) corresponding to $\omega_1 = \omega_2 \neq \omega_3$, this leads to the relation

$$\delta \approx \frac{3(\Sigma_3 - \Sigma_2)}{\Sigma_1 + \Sigma_2 + \Sigma_3}. \qquad (6)$$

Thus, the deformation parameter δ depends on the difference of the numbers of oscillator quanta for oscillations along the symmetry axis 3 (Σ_3) and oscillations orthogonal to it ($\Sigma_2 = \Sigma_1$).

A purely oscillator potential is not appropriate for realistic calculations of the deformation, because such a potential does not ensure an approximate invariability of the potential-well depth within the nucleus and because it does not take into account spin–orbit interaction, which forms main neutron and proton shells. If, however, a spin–orbit term and a term proportional to the square of the orbital angular momentum are added to a purely oscillator potential, there arises the shell-model potential (Nilsson potential [1]), which makes it possible to reproduce many features of the ground states of deformed nuclei.

At large deformations, single-particle states in the Nilsson potential can be characterized by the asymptotic quantum numbers $\mathcal{N} = n_1 + n_2 + n_3$; n_3; Λ, which is the projection of the orbital angular momentum onto the symmetry axis; and Ω, which is projection of the total angular momentum onto the symmetry axis. If we make use of this systematics and calculate the quantities $\Sigma_1 = \Sigma_2 = \sum_{k=1}^{A} \left(\frac{\mathcal{N} - n_3}{2} + \frac{1}{2}\right)_k$ and $\Sigma_3 = \sum_{k=1}^{A} \left(n_3 + \frac{1}{2}\right)_k$, relying on information about the order in which single-particle states are filled in the Nilsson potential, the results obtained for δ will be in qualitative agreement with experimental data in the mass-number regions $A \sim 23$–25, $150 < A < 180$, and $A > 230$. The partition of the right-hand side of relation (6) into two terms as

$$\delta \approx \frac{3(\Sigma_3 - \Sigma_2)_{\text{core}}}{\Sigma_1 + \Sigma_2 + \Sigma_3} + \frac{3(\Sigma_3 - \Sigma_2)_{\text{val}}}{\Sigma_1 + \Sigma_2 + \Sigma_3} \qquad (7)$$

shows that, in the mass regions being considered, nucleons belonging the filled and the unfilled shells (the first and the second term, respectively) make approximately equal contributions to the quadrupole moment of the nucleus.

The above computational procedure (interpretation of Nilsson's orbitals as pure oscillator states) ceases to be valid as soon as the number of protons or neutrons appears to be close to a magic value. This comes as no surprise since spin–orbit interaction and residual pairing forces mix different anisotropic-oscillator states, ensuring a spherical symmetry of closed shells, with the result that the first term in expression (7) vanishes. The mean field in which nucleons belonging to closed shells move is deformed no sooner than the valence-nucleon pressure acting on this field overcomes the stabilizing effect of the spherical shell-model gap and the effect of pairing forces. It follows that, as was indicated in the Introduction, the inclusion of the effect associated with filled neutron and proton shells is of paramount importance in calculating actual nuclear deformations.

The computational procedure used in the present study to take into account the effect of closed shells was the following:

(i) The deformation parameter δ was calculated by formula (7), into which the asymptotic quantum numbers n_3 and $n_\perp = \mathcal{N} - n_3$ were substituted for Nilsson's orbitals.

(ii) It was assumed that single-particle orbitals entering into the composition of a closed shell at $\delta = 0$ remain filled throughout the entire deformation process (in other words, that the closed inner shells of the nuclei being considered are deformed adiabatically).

(iii) A dedicated computational algorithm was applied that simulated the mechanism governing the emergence of deformation of closed shells under the effect of the valence-nucleon pressure.

The initial step of the algorithm consisted in choosing an input deformation value δ_0 (model parameter), whereupon the initial configuration of the ground state of the nucleus being considered is determined for this value by using the diagram of single-particle states. After that, the quantity δ is calculated by formula (7) for the chosen configuration, only the second term of this formula being taken into account almost always, with the exception of the case of a readily deformed core corresponding to the magic numbers of $N, Z = 28$. If the deformation-parameter value obtained in this way exceeds a threshold value δ_{thr} (yet another model parameter), one can conclude that the valence-nucleon pressure on the nuclear surface is sufficient for overcoming the stabilizing effect of closed shells, and formula (7) is used further in a complete form. In this case, the sought configuration of the ground state of the nucleus is gradually shifted toward greater values of δ until the resulting value of the deformation parameter becomes consistent (to within 20%) with that which was preset initially. But if the deformation-parameter value obtained at the first step is less than δ_{thr}, the ground-state configuration of the nucleus is shifted toward smaller values of δ, and the deformation parameter is calculated by formula (7), where the first term is set to zero (because the contribution of filled inner shells to the total quadrupole moment of the nucleus can be disregarded at small deformations).

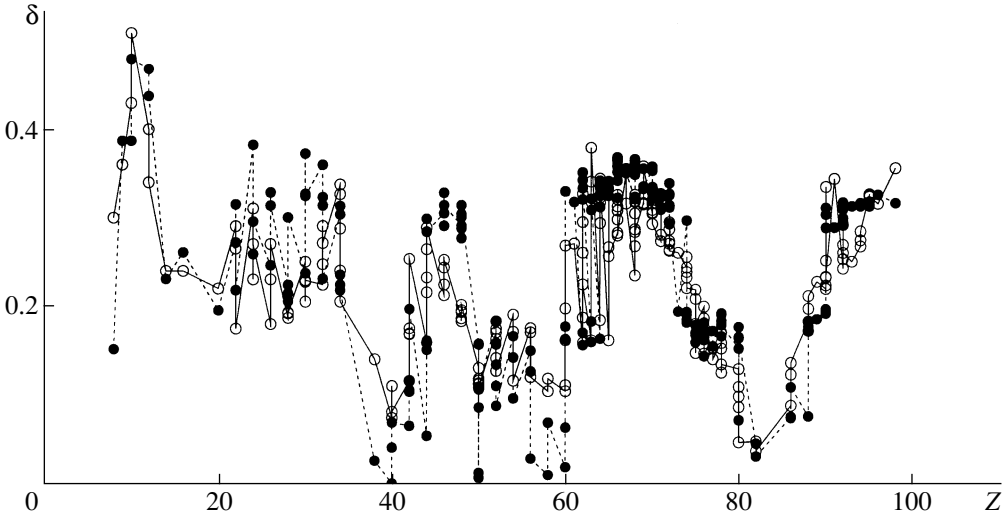

Fig. 1. Quadrupole deformations of the ground states of beta-stable nuclei: (open circles) experimental data from [16] and (closed circles) results of our calculations.

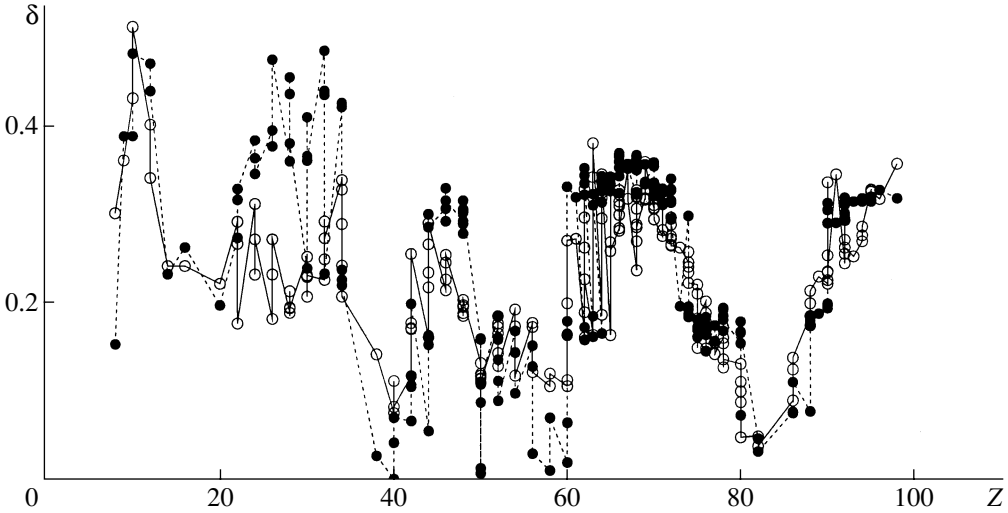

Fig. 2. Theoretical results contrasted against experimental data for the case where the calculation disregarded the effect of closed subshells corresponding to the magic numbers of $Z, N = 28$. The notation for the curves is identical to that in Fig. 1.

3. APPLICATION TO BETA-STABLE NUCLEI

In calculating the deformations of beta-stable nuclei in the mass region $A > 16$, we used the parameter values of $\delta_0 = \delta_{\text{thr}} = 0.2$ and took into account all magic numbers for the main proton and neutron shells in this mass region (8, 20, 28, 50, 82, and 126). For the protons, we additionally took into account the semimagic number of 40 (the oscillator magic number corresponding to $\mathcal{N} = 3$), near which the proton binding energy grows considerably. The diagram of single-particle levels in the Nilsson spheroidal potential was borrowed from [15].

The results of our calculations are shown in Fig. 1 (closed circles), along with experimental data from [16] (open circles). It can be seen from this figure that, by and large, the results of our calculations agree fairly well with experimental data, especially in the regions of stable deformation ($Z \sim 12$, $60 < Z < 80$, $Z > 80$). Even some subtle effects, such as the emergence of deformation in Nd isotopes in response to the growth of neutron excess, could be reproduced. By way of example, we indicate that, in agreement with experimental data, the computed values of the deformation of the ^{142}Nd, ^{145}Nd, and ^{150}Nd nuclei are 0.02, 0.15, and 0.33, respectively.

In comparing our theoretical results with available experimental data, it should be borne in mind that the experimental data reported in [16], which are

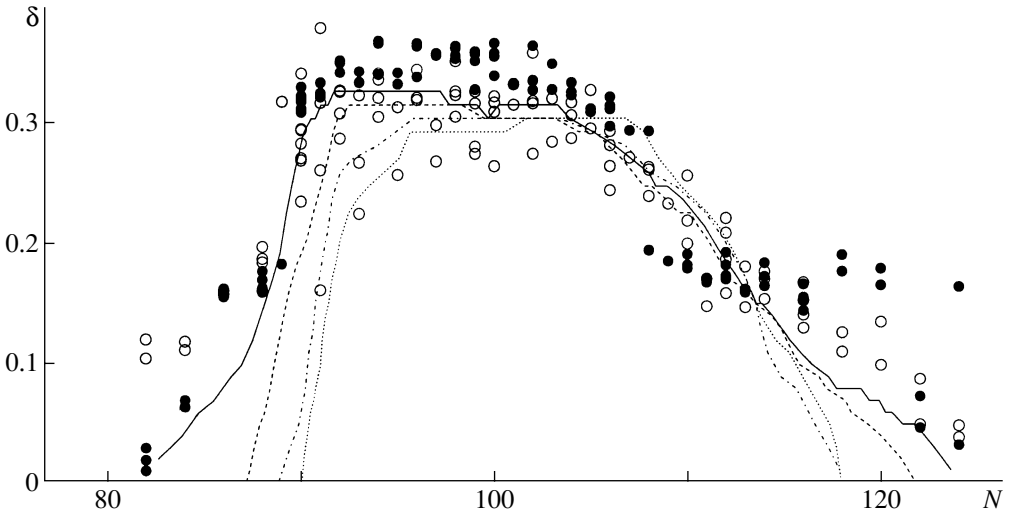

Fig. 3. Deformation of nuclei in the vicinity of rare-earth elements. Open and closed circles represent, respectively, experimental data from [16] and the results of our calculations. The curves were calculated in [10] at the pairing-constant values of $\Delta =$ (solid curve) 0, (dashed curve) 0.8, (dash-dotted curve) 1.2, and (dotted curve) 1.5 MeV.

used here, were obtained from measurements of $E2$-transition probabilities; those results enable one to establish the magnitude of the intrinsic quadrupole moment of the nucleus involved, but not the sign of this quadrupole moment. As is well known from the literature (see, for example, data on the static quadrupole moment in Fig. 2 from [14]), the $Z \sim 40$, 50, and 60 nuclei have a negative deformation of modest magnitude. This explains the discrepancy between theoretical and experimental results that is observed near these values of Z. The discrepancy between the theoretical and experimental results at small deformations can also be attributed to incorrectness of the calculation for $\delta \to 0$ because of classifying orbitals in terms of the asymptotic quantum numbers $\mathcal{N}n_3\Lambda\Omega$.

As was indicated above, closed neutron and proton shells have a profound effect on the nuclear-deformation process. This is illustrated in Fig. 2, which displays the results of the calculations for the case where the magic numbers of $N, Z = 28$ are ignored. It can be seen that, if one disregards the effect of filling of the $1f_{7/2}$ subshell, the calculated values of δ are dramatically exaggerated in the region $20 < Z < 40$.

For beta-stable nuclei in the vicinity of rare-earth elements, Fig. 3 displays data on deformation that were extracted from experimental results (open circles), those that were obtained from the present calculation (closed circles), and those that were computed in [10] for various values of the pairing constant (four curves). The figure demonstrates that the results of the two calculations agree fairly well with each other and with experimental data. We can also conclude that the agreement with experimental data is not improved upon taking into account the effect of pairing on the single-particle spectrum within the model developed by Strutinsky and other authors [5, 6, 9, 10]. This is not surprising, however, because, in the model used here, residual forces have been included, to a considerable extent, in the macroscopic energy E_{macro} [see formula (1)]. As was shown in [9, 12], the correction for the residual forces must be small in relation to the shell-model correction $\delta E_{\text{s.p.}}$.

4. EXOTIC NUCLEI

There is a vast body of experimental data suggesting that shell effects associated with magic numbers manifest themselves not only in the beta-stability valley but also in exotic proton- and neutron-rich nuclei. The latter is corroborated, for example, by the discovery of the doubly magic nucleus ^{48}Ni, which has a record excess of protons, or by the structure of nuclei in the vicinity of the doubly magic nucleus ^{78}Ni, which possesses a large neutron excess [14, 17, 18].

However, many experimental facts indicate that, in exotic nuclei, magic shells are more fragile and that the single-particle energy gaps corresponding to them can readily collapse in the case of a large neutron or a large proton excess. By way of example, we indicate that, from a comparatively low excitation energy of the first 2^+ level in the ^{32}Mg nucleus and from a high probability $B(E2)$ of this excitation, it follows that, in the case of a large neutron excess, the $N = 20$ spherical shell gap disappears, which leads to the deformation of the nucleus in the ground state [19]. A similar effect is observed for the magic number of $N = 28$ in the vicinity of the ^{44}S nucleus [20]. It

Values of the deformation parameter δ for some exotic nuclei

Nucleus	Z	N	$N-Z$	Z_{max}	N_{max}	$(N-Z)_{stab}$	δ_{calcd}
^{28}O	8	20	12	15.9	18.3	1.6	0
^{29}F	9	20	11	16.4	19.0	1.7	0.074
^{32}Mg	12	20	8	17.9	21.0	2.0	0.415
^{44}S	16	28	12	24.0	29.2	3.4	0.338
^{48}Ni	28	20	−8	26.0	31.4	4.0	0.380
^{66}Fe	26	40	14	34.5	44.2	6.7	0.386
^{68}Ni	28	40	12	35.5	45.6	7.0	0.073
^{70}Zn	30	40	10	36.4	47.0	7.4	0.359
^{76}Sr	38	38	0	39.1	51.1	8.4	0.455
^{77}Y	39	38	−1	39.6	51.8	8.6	0.444
^{78}Ni	28	50	22	40.0	52.5	8.8	0.060
^{80}Zr	40	40	0	40.9	53.9	9.2	0.416

is also well known that, in all probability, the doubly magic nucleus ^{68}Ni is spherical, which is suggested by a relatively high position of its first excited level on the energy scale, but that its isotones closest to it in mass ($N = 40$) are probably deformed [21, 22]. This indicates that the semimagic number of $N = 40$ is very fragile in the region of neutron-rich nuclei. The proton semimagic number of $Z = 40$ is more stable, as is suggested by a large number of zirconium isotopes. At a large proton excess, however, the effect of the $Z = 40$ closed subshell also dies out, with the result that the doubly semimagic nucleus ^{80}Zr proves to be deformed [23].

From the aforesaid, it is clear that, in order to extend the approach developed here to the case of exotic nuclei, it is necessary, above all, to consider that closed shells are very fragile in such nuclei. We tried to do this by reducing the value of the parameter δ_{thr} down to 0.1 and by rejecting item 2 of the procedure described in Section 2 (that is, a "spherical" configuration of filled inner shells was employed only at the first step of the computational algorithm). The approach modified in this way was used to calculate the deformations of some light and medium-mass exotic nuclei. In the course of these calculations, we took into account the magic numbers of 8, 20, 28, and 50 and the semimagic number of $Z = 40$, as well as the semimagic number of $N = 40$ if it occurred in a pair with some magic number Z (actually with $Z = 28$). The results of these calculations are presented in the last column of the table. For the maximum possible number of protons (Z_{max}) in a nucleus that have a given mass and which are stable with respect to the nucleon-emission mode of decay, the analogous quantity for the neutron component (N_{max}) of the nucleus, and the value that the neutron–proton difference has at the boundary of beta stability [$(N - Z)_{stab}$]—all of these quantities measure the degree of remoteness of the nuclei being considered from the beta-stability valley—the results computed on the basis of the Weizsäcker semiempirical mass formula are given in the fifth, the sixth, and the seventh column, respectively.

As can be seen from the table, all the nuclei considered here have a highly enriched neutron or a highly enriched proton component. The results of the calculations agree well with experimental data obtained in [17–23] for the energy of the first excited 2^+ state and for quadrupole moments; moreover, these calculations faithfully reproduce the effect of the deformation gap that is formed by Nilsson's orbitals in the vicinity of the point $Z, N = 38$ and which is responsible for the deformation of the ^{76}Sr, ^{77}Y, and ^{80}Zr nuclei [2, 24].

The doubly magic nucleus ^{28}O was not observed in the experiments reported in [25]; at the same time, the odd nucleus ^{29}F, which features nearly the same excess of neutrons, is stable with respect to the nucleon-emission mode of decay. In the literature, this is explained by conjecturing that, under the effect of the odd particle, the ^{29}F nucleus is deformed, going over to an energetically more favorable state, but that the doubly magic nucleus ^{28}O cannot undergo such a transition (see table).

The doubly magic nuclei ^{48}Ni and ^{78}Ni, which occur at the boundary of stability with respect to

the nucleon-emission mode of decay, are also of great interest. Currently available experimental data are insufficient for establishing their shapes. From our estimate—we recall that it is preliminary and rather rough—it follows that the former is severely deformed, but that the latter is nearly spherical.

5. CONCLUSION

By no means is the method proposed here for calculating nuclear deformations intended to take the place of consistent microscopic calculations. Within this method, it is impossible, for example, to describe cases where a nucleus has different shapes in the ground state and in excited states [3] or to predict stability islands for superheavy elements [4] (because the single-particle shell model is underdeveloped for them). Moreover, it is not quite correct in dealing with small deformations. Nonetheless, we hope that, because of the simplicity of the method and because of the reliability of the single-particle level diagrams employed in the calculations based on this method, it will appear to be useful in estimating deformations in the ground states of not only beta-stable nuclei but also many exotic nuclei.

REFERENCES

1. S. G. Nilsson, K. Dan. Vidensk. Selsk. Mat.-Fys. Medd. **29** (16), 1 (1955).
2. R. V. F. Jansens and T. L. Khoo, Annu. Rev. Nucl. Part. Sci. **41**, 321 (1991).
3. A. N. Andreyev *et al.*, Nature **405**, 430 (2000).
4. M. Bender *et al.*, Phys. Rev. C **60**, 034304 (1999).
5. V. M. Strutinsky, Nucl. Phys. A **95**, 420 (1967); **122**, 1 (1968).
6. M. Brack *et al.*, Rev. Mod. Phys. **44**, 320 (1972).
7. V. S. Ramamurthy and S. S. Kapoor, Phys. Lett. B **42B**, 389 (1972).
8. A. Bohr and B. R. Mottelson, *Nuclear Structure,* Vol. 2: *Nuclear Deformations* (Benjamin, New York, 1975; Mir, Moscow, 1977).
9. V. M. Kolomiets *et al.*, Fiz. Élem. Chastits At. Yadra **3**, 392 (1972) [Sov. J. Part. Nucl. **3**, 204 (1972)].
10. V. M. Strutinskiĭ and A. G. Magner, Fiz. Élem. Chastits At. Yadra **7**, 356 (1976) [Sov. J. Part. Nucl. **7**, 138 (1976)].
11. V. Strutinsky, *The Variety of Nuclear Shapes* (World Sci., Singapore, 1988).
12. V. Strutinsky, Nucl. Phys. A **502**, 67c (1989).
13. Yu. Melnikov *et al.*, Nucl. Instrum. Methods Phys. Res. B **33**, 81 (1988).
14. B. Blank and P. H. Regan, Nucl. Phys. News **11**, 15 (2001).
15. C. Gustafson *et al.*, Ark. Fys. **36**, 613 (1967).
16. *Nucleus Ground State Parameters,* http://depni.npi.msu.su/cdfe/service/index.html
17. B. Blank *et al.*, Phys. Rev. Lett. **84**, 1116 (2000).
18. J. M. Daugas *et al.*, Phys. Lett. B **476**, 213 (2000).
19. T. Motobayshi *et al.*, Phys. Lett. B **346**, 9 (1995).
20. T. Glasmacher *et al.*, Phys. Lett. B **395**, 163 (1997).
21. R. Broda *et al.*, Phys. Rev. Lett. **74**, 868 (1995).
22. R. Grzywacz *et al.*, Phys. Rev. Lett. **81**, 766 (1998).
23. C. J. Lister *et al.*, Phys. Rev. Lett. **59**, 1270 (1987).
24. Z. Jana *et al.*, Phys. Rev. Lett. **82**, 292 (1999).
25. O. Tarasov *et al.*, Phys. Lett. B **409**, 64 (1997).

Translated by A. Isaakyan

Physics of Atomic Nuclei, Vol. 65, No. 10, 2002, pp. 1816–1826. Translated from Yadernaya Fizika, Vol. 65, No. 10, 2002, pp. 1865–1876.

NUCLEI
Theory

Partial Radiative Strength Functions for Dipole Transitions in the $^{49,\ 51}$V Nuclei

I. D. Fedorets*

Kazarin Kharkov National University, pl. Svobody 4, Kharkov, 61077 Ukraine

Received April 11, 2001; in final form, December 11, 2001

Abstract—Radiative strength functions for dipole transitions from the compound-nucleus states to excited states of ^{49}V and ^{51}V nuclei are determined from the resonance-averaged intensities of primary γ rays from (p, γ) reactions, measured in the proton-energy range 1.5–3.5 MeV. The obtained data are compared with the predictions of various models. The best description for $E1$ transitions is obtained on the basis of a model taking into account the dependence of the strength function on the energy of photons, temperature, and the nuclear shell structure. © *2002 MAIK "Nauka/Interperiodica".*

1. INTRODUCTION

An analysis of spectroscopic and statistical properties of nuclei like ^{49}V and ^{51}V makes it possible to trace the emergence of collective properties and their manifestations in a system with a small number of valence nucleons. Although lower negative-parity states in these nuclei are successfully described by the shell model, these states exhibit some feature of collectiveness. On lower states of positive parity, which are treated as proton-hole states of the *sd* shell, clearly manifested rotational bands may be constructed. The degrees of collectiveness are different for the two nuclei under investigation since ^{51}V has a filled neutron shell with $N = 28$ and a small deformation parameter $\beta_2 = 0.18$, while ^{49}V is characterized by a much larger deformation ($\beta_2 = 0.27$).

As regards the statistical properties, a statistical description of nuclear states of ^{51}V in terms of the level density [1] can be obtained starting from excitation energies of 2.5 MeV (the spacing between the $1f_{7/2}$ and $2p_{3/2}1f_{5/2}$ shells). Averaged electromagnetic properties of nuclear states can be described by the radiative strength function (RSF) defined as the average reduced partial radiation width normalized to the unit excitation energy. It follows from the results [1] obtained with the help of the reaction of thermal neutron capture that ^{49}V and ^{51}V belong to the class of nuclei for which the E_γ^3 dependence of the strength of primary dipole transitions on the energy of photons, which is typical of *sd*-shell nuclei, is replaced by the E_γ^5 dependence. This means that the one-particle nature of the energy dependence of radiative strength in this nuclear range changes; this dependence is now determined by the effect of a giant dipole resonance (GDR) and is described by the Lorentzian distribution. Since the E_γ^5 energy dependence established in [1] corresponds to the intensities of $E1$ transitions between the excited states of ^{51}V averaged over the final states, this may be regarded as a direct confirmation of the well-known Brink–Axel hypothesis according to which a GDR with the same parameters as for the ground state of a nucleus can be constructed on any of its excited states. However, a verification is required for the following two reasons. First, the averaged intensities of γ transitions obtained in [1] are not absolute. Second, it has been established that the application of the Lorentzian distribution for calculating the RSF of the $E1$ transitions between excited states of spherical or transition nuclei often leads to considerably exaggerated values. In such cases, the application of models in which the strength function of the $E1$ transitions depends not only on the energy of photons but also on the temperature of the final state and on the shell structure of the nucleus was found to be more successful. Zero temperature was used in calculations of the RSF for dipole transitions to the ground state, while the inclusion of the final temperature improved the description of strength functions for transitions to excited states.

The distribution of the strength of the $M1$ transitions below the neutron binding energy in the nuclei under investigation is also of considerable interest. The data concerning the fine structure of the $M1$ strength for nuclei with $N = 28$ and with an even mass number, which were accumulated in experiments on inelastic scattering of electrons, can be satisfactorily described with the help of the shell model using large model spaces [2]. In the inelastic scattering cross section for protons with an energy

*e-mail: ivan.d.fedorets@univer.kharkov.ua

of 200 MeV by ^{51}V, a broad distribution with a peak corresponding to an excitation energy of 10.2 MeV and a width of about 2 MeV was observed in [3]. This distribution was interpreted as a spin $M1$ resonance, which, however, was not observed in experiments on inelastic electron scattering [4] because of considerable fragmentation. It was proposed in [5] that a considerable fraction of the dipole strength in ^{51}V must be manifested at lower values of excitation energy (below 7 MeV). It is also expected that the coupling of a proton hole to the states having a hypothetical quadrupole–octupole structure makes a contribution to the electric dipole excitations in ^{51}V below 7 MeV [6].

The situation with the distribution of the dipole strength below the neutron binding energy could be clarified by using the rare possibility of combined analysis of the entire body of mutually complimenting data on the RSF for dipole transitions to excited states of ^{51}V from the state of thermal neutron capture [1] and from the states of the compound nucleus formed in the (p,γ) reaction. As the result of thermal-neutron capture by a ^{50}V nucleus of spin–parity $J^\pi = 6^+$ in the ground state, a state with J^π equal to $11/2^+$ or $13/2^+$ is formed. The binding energy of a neutron in ^{51}V is $B_n = 11\,051.11(17)$ keV. The direct transitions from this high-lying state observed in [1] populated states having spins $9/2 \le J \le 15/2$ and a negative parity as a rule. The contribution from magnetic dipole transitions must be negligible in this case.

This paper aims at determining the absolute values and analysis of the energy dependence of the RSF of primary dipole γ transitions to the states of the ^{49}V and ^{51}V nuclei, which are excited in the radiative capture of protons with energies from 1.5 to 3.5 MeV by ^{48}Ti and ^{50}Ti nuclei. In contrast to the (n,γ) reaction, the primary γ transitions from the s, p, and d resonances excited in a compound nuclei populate states with $J^\pi \le 7/2^\pm$, and the contribution from the $M1$ strength can be estimated only indirectly.

2. METHOD OF DETERMINING RADIATIVE STRENGTH FUNCTIONS FROM AN ANALYSIS OF EXPERIMENTAL DATA

In order to determine the RSF from experimental data on resonance-averaged intensities of primary dipole transitions to the states of ^{49}V and ^{51}V, which are excited in the (p,γ) reaction, we will use the RSF dependence of the cross section of this reaction, presented in statistical theory. The energy Q released in the (p,γ) reaction on ^{48}Ti and ^{50}Ti nuclei is equal to 6.76 and 8.05 MeV. Such values of Q are high enough for the density of states attainable in compound nuclei to satisfy the requirements of a statistical description. Investigations [7–9] of the resonance (p,p), (p,p'), and (p,γ) reactions on these nuclei in the incident-proton-energy range from 1.0 to 3.86 MeV proved that the spacings between the resonance levels of the same spin and parity in the formed compound nuclei ^{49}V and ^{51}V can be described by the Wigner distribution, while the reduced proton widths are described by the Porter–Thomas distribution. In this case, the energy dependence of the mean spacing between the levels is compatible with the nuclear temperature $T \sim 1.5 \pm 0.2$ MeV, while the reduced proton width Γ_p is considerably larger than the reduced radiative width Γ_γ. The thresholds of the (p,n) reaction on ^{48}Ti and ^{50}Ti considerably exceed 4.8 and 3.0 MeV, respectively, which makes it possible to conduct experiments in a wide range of energies of incident protons before the neutron channel opens and the cross section of the (p,γ) reaction decreases sharply.

Thus, we have all grounds to expect in the present case that the intensity of γ transitions from different initial states of the compound nucleus to the same final state is a random quantity with a broad distribution and that radiative widths do not correlate with other widths of the initial state. We must only take into account the fact that the intensities of a certain type of transitions from different resonances with fixed values of spin and parity to an individual final state experience strong fluctuations obeying the Porter–Thomas distribution. In accordance with the statistical theory, the cross section of capture of a proton with energy E_p followed by the emission of a photon with energy E_γ, corresponding to the primary transition from the state λ of the compound nucleus to the final state f, can be represented in the form

$$\sigma_{p\gamma} = \frac{\pi\lambda\!\!\!^{-2}_p}{2(2I+1)} \sum_J (2J+1) \sum_{l_p j_p} \frac{T_{l_p j_p} T_{\gamma_{\lambda f}}}{T_\lambda}. \quad (1)$$

Here, $\lambda\!\!\!^{-}_p$ is the reduced wavelength of the incident proton; I is the spin of the target nucleus; J is the spin of the compound nucleus; $T_{l_p j_p}$ is the transmission coefficient for protons in the input channel; $T_{\gamma_{\lambda f}}$ is the transmission coefficient for photons with energy $E_\gamma = E_\lambda - E_f$ corresponding to primary transitions from the group of states λ to the final state f; and T_λ is the sum of transmission coefficients corresponding to all open channels of deexcitation of states λ. Summation in expression (1) is carried out over all open reaction channels and states of the compound nucleus with quantum numbers J and π allowed by the corresponding selection rules. The transmission coefficient $T_{\gamma_{\lambda f}}$, which is the probability of the γ transition with multipolarity L, averaged over the resonances of the

compound nucleus, can be expressed in terms of the RSF $S_{\lambda f}(E_\gamma)$:

$$T_{\gamma\lambda f} = 2\pi S_{\lambda f}(E_\gamma)E_\gamma^{2L+1}. \quad (2)$$

Coefficient T_λ in this case has the form

$$T_\lambda = \sum_{l_{p'}j_{p'}} T_{l_{p'}j_{p'}} + \sum_{l_nj_n} T_{l_nj_n} \quad (3)$$

$$+ 2\pi \sum_J \int_0^{E_\lambda} \rho_J(E_\lambda - E_\gamma) S_{\lambda f}(E_\gamma) E_\gamma^{2L+1} dE_\gamma,$$

where $T_{l_{p'}j_{p'}}$ are the transmission coefficients for protons in the output channel; $T_{l_nj_n}$ are the transmission coefficients for the neutron channel; and $\rho_J(E_\lambda - E_\gamma)$ is the density of levels of spin J, parity π, and excitation energy E_f.

Using relations (1)–(3) and experimental data on the partial cross sections of the (p,γ) reaction, we can determine the absolute values of RSF depending on the energy of photons and the properties of states between which the γ transition occurs. Since the dipole mode dominates in the radiative decay of the states of the compound nucleus, we can extract from the experimental data on cross sections the quantity $S_{\lambda f}(E_\gamma) = S_{\lambda f}^{E1}(E_\gamma) + S_{\lambda f}^{M1}(E_\gamma)$, which is the sum of the RSFs for the $E1$ and $M1$ transitions. The reliability of the RSF obtained in this way is determined not only by the error in experimental data, but also, above all, by the validity and accuracy of the transmission coefficients and level densities used in formulas (1)–(3).

Transmission coefficients for protons are often calculated using the optical-potential (OP) parameters from the global systematics [10], which are obtained from an analysis of cross sections of the elastic scattering of protons with an energy higher than 8 MeV. The obvious inadequacy of using these OP parameters at lower proton energies follows from the results obtained in [11], where the authors had to reduce by an order of magnitude the transmission coefficients for protons, calculated by using the OP parameters from [10], to match the results of statistical calculations with the experimental data on the cross sections of the reaction $^{50}\mathrm{Ti}(p,\gamma)^{51}\mathrm{V}$ in the proton energy range from 2.1 to 3.1 MeV. In addition, the situation is complicated by possible rapid changes in the absorption potential for nuclei with shells close to complete filling, which are expected in this case [12].

In the case of target nuclei ^{48}Ti and ^{50}Ti, the values of the parameters of the imaginary part of the OP from the global systematics [10], which are obviously inapplicable at the proton energies used in this work, cannot be replaced by parameters obtained in [12] from an analysis of the cross sections of the (p,n) reaction under the assumption of their equality to the proton absorption cross section. In the case of ^{48}Ti, this cannot be done because of the high threshold of the (p,n) reaction. As regards the second nucleus, the cross section of the (p,n) reaction is strongly suppressed because of the large difference in the values of the spin of ^{50}Ti in the ground state and the spins of the low-lying states of the final nucleus ^{50}V (whose ground-state spin–parity is 6^+), and the role of elastic scattering accompanied by the formation of a compound nucleus increases significantly. In [13], an empirical expression representing the imaginary part of the OP in the form $W = 5.6 - 0.15Z$ (MeV) was proposed for an analysis of the total cross sections of the (p,γ) reaction on even–even nuclei with the magic number of neutrons $N = 28$ from ^{48}Ca to ^{54}Fe. The real part of the OP in this case was the same as in the global systematics [10]. Subsequently, the OP parameters were defined in this way [14, 15] not only for the semimagic nucleus of ^{50}Ti but also for ^{48}Ti. The satisfactory agreement with experimental data achieved in this case can be explained by using the results obtained in the later publication [16]. The analysis of the cross section for low-energy proton absorption by a nearly spherical ($\beta = 0.18$) semimagic nucleus $^{54}_{26}\mathrm{Fe}_{28}$ and a more collective ($\beta = 0.24$) nucleus $^{56}_{26}\mathrm{Fe}_{30}$, which was carried out in [16] on the basis of dispersion theory taking into account channel coupling, predicts a much stronger absorption for ^{56}Fe than for ^{54}Fe. A high degree of correlation was detected between the values of the imaginary part $W_s(E_p)$ of the OP and the density of particle–hole states $2p1h$ over which the absorbed energy of a proton is distributed in the compound nuclei ^{55}Co and ^{57}Co formed in this case. The density of the $2p1h$ states proved to be very sensitive to the energy gap between the proton shells $1f_{7/2}$ and $2p_{3/2}$ in these nuclei, which is determined from experimental data on spectroscopic factors obtained from a one-nucleon transfer reaction. It was noted earlier in [17] that modulations of the density of $2p1h$ states calculated in the exciton model as a function of the mass number A are clearly manifested for incident-proton energies of $E_p \sim 3$ MeV and become noticeably weaker for energies $E_p \geq 6$ MeV. As regards the possible contribution of collective effects to the dependence of W_s on the mass number, it does not exceed 20%. However, in the case of transition from ^{48}Ti to ^{50}Ti, it appears that the expected sharp change in $W_s(A)$ is not observed since (see conclu-

sions drawn in [16]) the gap widths between the shells $1f_{7/2}$ and $2p_{3/2}$ in these nuclei differ only by a factor of $\sim$1.2. The dependence of the imaginary part of the OP on energy E_p used by us here was almost the same as that obtained in [16] for ^{54}Fe. In the energy range from 1.5 to 3.5 MeV for incident protons, this dependence virtually coincides with that obtained earlier in [18] from a simultaneous analysis of polarization data and cross sections of scattering of low-energy protons on the ^{51}V nucleus. At $E_p =$ 2 MeV, the dependence $W_s(E_p)$ and the empirical expression from [13] lead to identical values of the absorption parameter. The geometric parameters and the real part of the OP differ insignificantly from those obtained from the global systematics presented in [10].

Another component of a statistical description, viz., the density of levels, was calculated on the basis of the back-shifted Fermi gas model. Calculations were made with the rigid-body moment of inertia and the following parameters was borrowed from [19]: $a = 5.65$ MeV^{-1} and $\Delta = -0.84$ MeV for ^{49}V and $a = 6.39$ MeV^{-1} and $\Delta = 0.2$ MeV for ^{51}V. These values of the level-density parameter a and of the excitation-energy shift Δ ensured satisfactory agreement between the calculated density and experimental results in a wide range of excitation energies. Information on the discrete part of the level diagram was borrowed from [1, 20] and the NUDAT BNL database [21], obtained from current publications on these nuclei.

In order to determine the absolute values of the RSF for primary dipole transitions in ^{49}V and ^{51}V, we used the partial cross sections of the (p,γ) reaction on ^{48}Ti and ^{50}Ti, which were measured at incident-proton energies in the range from 1.5 to 3.5 MeV [14, 15]. The interval of averaging was chosen so that the spread in the data associated with the Porter–Thomas fluctuations did not exceed 15%. We also used averaged intensities of primary γ transitions to the states of ^{51}V, measured in [11] in the proton energy ranges 2.1–2.5 and 2.6–3.1 MeV. In this case, averaging over the interval of $\sim$900 keV led to a decrease in the spread of data due to fluctuations of width up to 5%, which is much smaller than the error of measurements of the intensity of γ transitions. The quantity $S_{\lambda f}(E_\gamma)$ being determined, which appears in the coefficient $T_{\gamma\lambda f}$ in the numerator of formula (1), was chosen so that the absolute value of the experimentally obtained partial cross section of the (p,γ) reaction could be reproduced. The value of RSF appearing in expression (3) for the total transmission coefficient T_λ was specified in accordance with results obtained within various theoretical approaches. All the remaining parameters determined earlier remained unchanged. The effect of the model dependence on the values of partial RSFs determined in this way was insignificant primarily due to the fact that the average radiation widths in the given case are considerably smaller than the average proton widths (see above).

3. MODELS FOR RADIATIVE STRENGTH FUNCTIONS

In order to calculate the partial cross sections of the (p,γ) reaction in the ^{48,50}Ti nuclei, transmission coefficients for $E1$ primary transitions were used in [11] and then in [14, 15], which were defined by the formula

$$T_\gamma^{E1} = a10^{-14}A^{8/3}E_\gamma^k, \qquad (4)$$

with $k = 5$ introduced by Axel. The empirical dependence of the GDR width on E_γ introduced by Axel is a particular case of the approach to interpreting RSF on the basis of a Lorentzian distribution. This dependence makes it possible to improve the description of the RSF, but only in a narrow region near the neutron binding energy. The substantiation of this approach and the interpretation of the absolute value remain unclear since expression (4) contains the normalization coefficient a. Hence, it is not surprising that, in spite of the successful description of the energy dependence of the partial cross sections of reactions ^{48,50}Ti(p,γ), the total cross sections of these reactions could not be described in [11] and [14, 15]. An analysis of the total cross sections of the (p,γ) reaction, which are determined by the total radiative widths, requires reliable knowledge of the absolute values of RSFs in a wide energy range. This necessitates the development of more substantiated theoretical approaches to the description of RSF for primary dipole transitions from the states of the compound nucleus. The ultimate criterion of the correctness of the choice of model for RSF is the possibility of describing experimental results in the entire range of energies of γ transitions on the basis of this model.

The emission process in primary dipole transitions is determined by the interaction of particle–hole states forming the GDR with more complex configurations, the simplest of which have the $2p$–$2h$ structure. The theoretical approaches to the RSF description that were developed subsequently differ in the method of inclusion of this interaction. The approaches developed in [22–24], where the dependence of the RSF width on the photon energy and on the effective temperature of the nucleus in the state to which the γ transition occurs was introduced on the basis of the theory of finite Fermi systems, have

become most widespread at present. The approach described in [23] is distinguished by the fact that the shell structure of the spectrum of one-particle levels, as well as the effect of the nuclear temperature and the transition energy on the occupation numbers of these levels, was taken into account in calculating the density of the $2p2h$ states. Only those states between which the transition is permitted by the Pauli exclusion principle were taken into account. In the semimicroscopic approach [25], the coupling of particle–hole configurations to many-particle configurations is taken into account in terms of the imaginary part of the OP directly in the low-energy region of the GDR under investigation. In the recent publications [26, 27], a semiclassical model is developed on the basis of the explicit solution of the Vlasov–Landau kinetic equation in which the coupling of simple and complex configurations is described in terms of the photon collision integral. The RSFs presented in [22–24, 26, 27] and depending on the photon energy and the temperature T_f of the final states of the nucleus make it possible to describe electric dipole transitions between excited states and generalize the early model developed by Brink and Axel.

In the present work, we use the following representations of RSFs:

1. The RSF connected with the photoabsorption cross section through the detailed-balance principle is represented in the form of the standard Lorentzian:

$$S_{\lambda f}(E_\gamma) = 8.674\times 10^{-8}\frac{\sigma_r E_\gamma \Gamma_r^2}{(E_\gamma^2 - E_r^2)^2 + (E_\gamma\Gamma_r)^2}; \quad (5)$$

here and below, σ_r, E_r, and Γ_r are the cross section at the maximum, the position, and width of the RSF.

2. The model [22] based on the phenomenological inclusion of the coupling of the particle–hole configurations with more complex states. The energy dependence of the RSF width in this model is modified in accordance with the description of zero sound in an infinite Fermi system. This model can be represented by the equations

$$S_{\lambda f}(E_\gamma, T_f) = 8.674\times 10^{-8}\frac{0.7\sigma_r E_\gamma \Gamma_r \Gamma(E_\gamma, T_f)}{(E_\gamma^2 - E_r^2)^2}, \quad (6)$$

$$\Gamma(E_\gamma, T_f) = \frac{\Gamma_r}{E_r^2}(E_\gamma + 4\pi^2 T_f^2), \quad (7)$$

where T_f is the effective temperature of the nucleus in the state to which the γ transition occurs.

3. The approach used by us earlier (see, for example, [28–30]) in systematic studies of the RSF for dipole transitions in $1f2p$-shell nuclei [23]. In this approach, the strength function of the $E1$ transitions can be written in the form

$$S_{\lambda f}(E_\gamma, T_f) = 8.674 \times 10^{-8}\frac{2\pi}{1+\exp(-E_\gamma/T_f)} \times \frac{\sigma_r E_r^2 \Gamma(E_\gamma, T_f)}{(E_\gamma^2 - E_r^2)^2 + E_r^2\Gamma^2(E_\gamma, T_f)}, \quad (8)$$

where

$$\Gamma(E_\gamma, T_f) = \frac{\Gamma_r \rho_{2p2h}(E_\gamma, T_f)}{\rho_{2p2h}(E_r, T_f = 0)}.$$

In the case of the constant density ρ_{2p2h} of one-particle states, we have

$$\Gamma(E_\gamma, T_f) = \frac{2}{3}\alpha\left[E_\gamma^2 + (2\pi T_f)^2\right]\frac{E_\gamma}{E_0}\coth(E_\gamma/2T_f), \quad (9)$$

where $E_0 = \varepsilon_F A^{-1/3}$ is the distance between the shells, $\alpha \sim \varepsilon_F^{-1}$ is a constant determining the width of one-particle transitions, and ε_F is the Fermi energy. In order to estimate the contribution of $M1$ transitions, we used the following relation derived from the results obtained in [23]:

$$\frac{S_\gamma^{E1}}{S_\gamma^{M1}} = 0.03A\frac{E^2 + (\pi T_f)^2}{B_n^2}, \quad (10)$$

where B_n is the binding energy of a neutron.

4. The model presented in [26, 27] for describing the RSF and taking into account the microcanonical distribution of the initial states of the system and the contributions of various relaxation mechanisms to the GDR decay width. In this model, the RSF for the emission process in the thermodynamic pole approximation has the form

$$S_{\lambda f}(E_\gamma, T_f) = 8.674\,[1-\exp(-E_\gamma/T_f)]^{-1} \times \frac{\sigma_r \Gamma_r E_\gamma \Gamma(E_\gamma, T_f)}{(E_\gamma^2 - E_r^2)^2 + E_\gamma^2\Gamma^2(E_\gamma, T_f)} \quad (11)$$

with the decay width $\Gamma(E_\gamma, T_f)$ equal to the sum of the collision width and the quantity simulating the fragmentation width component in the approximation of independent dissipation sources (collision and one-particle contributions to the width):

$$\Gamma(E_\gamma, T_f) = \frac{\hbar}{\tau_c(E_\gamma, T_f)} + k_s\Gamma_\omega. \quad (12)$$

Here, $\tau_c(E_\gamma, T_f)$ is the collision relaxation time for collective motion, which was determined in the Fermi liquid approximation with the parameters borrowed from [26, 27]; k_s is the normalization factor; and $\Gamma_\omega = 0.75\hbar v_F/R_0$, R_0 being the radius of the nucleus, and v_F being the Fermi velocity.

The normalization factor $k_s(E_\gamma)$ depending on the photon energy was defined as

$$k_s(E_\gamma) = \begin{cases} k_s(E_r) + (k_s(0) - k_s(E_r))|(E_\gamma - E_r)/E_r|^n, & E_\gamma < 2E_r, \\ k_s(0), & E_\gamma \geq 2E_r \end{cases} \quad (13)$$

where the quantities $k_s(0)$ and $k_s(E_r)$ are related to the one-particle contribution to the width $\Gamma(E_\gamma, T_f)$ for $E_\gamma = 0$ and $E_\gamma = E_r$. The quantities $k_s(0)$ and n are regarded as free parameters whose values are extracted from fitting the RSF to experimental data in the low-energy range.

In all model representations for the RSF used here, the temperature T_f of the final state to which the transition of energy E_γ occurs was determined from the formula for the level density and was given by

$$T_f = \frac{1 + \sqrt{1 + 4a(U - E_\gamma - \Delta)}}{2a}, \quad (14)$$

while the temperature of the initial state was defined as

$$T = \frac{1 + \sqrt{1 + 4a(U - \Delta)}}{2a}, \quad (15)$$

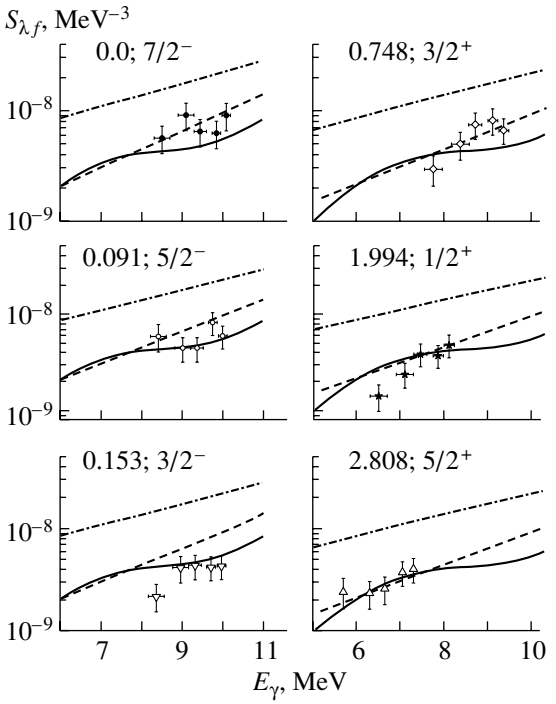

Fig. 1. RSF for γ transitions in ^{49}V for a fixed energy E_f of the final state and varying energy E_λ of the initial states. Theoretical estimates of the RSF: Lorentzian dependence (dash-dotted line), calculations on the basis of formula (8) including temperature T_f alone (dashed curve), the same taking into account the shell effects (solid curve). The experimental values of the RSF (here and in Figs. 2 and 3) were obtained here from the intensities of γ transitions measured in [11, 14, 15].

where U is the energy of the excited nucleus, a is the level-density parameter, and Δ is the energy-shift parameter. It should be noted that the RSF for the electric dipole γ radiation emitted by an excited nucleus is a function of the final-state temperature T_f, while the RSFs associated with photoabsorption depend on the initial-state temperature T.

The values of σ_r, E_r, and Γ_r were chosen so that the experimental data on the cross sections of the (γ, n) reaction on ^{51}V obtained in [31] could be described in the best way by a Lorentzian curve. The obtained parameters (we consider the case with two GDR peaks) were as follows: $\sigma_{r_1} = 58.8$ mb, $\sigma_{r_2} = 28.8$ mb, $E_{r_1} = 17.86$ MeV, $E_{r_2} = 21.22$ MeV, $\Gamma_{r_1} = 4.42$ MeV, and $\Gamma_{r_2} = 5.10$ MeV. In view of the absence of experimental data on the GDR in ^{49}V, we used, in calculations of the RSF for this nucleus, the same parameters as for ^{51}V, but with an energy shift as a whole by 0.4 MeV toward higher values will allowance for the global systematics of data on the GDR [32].

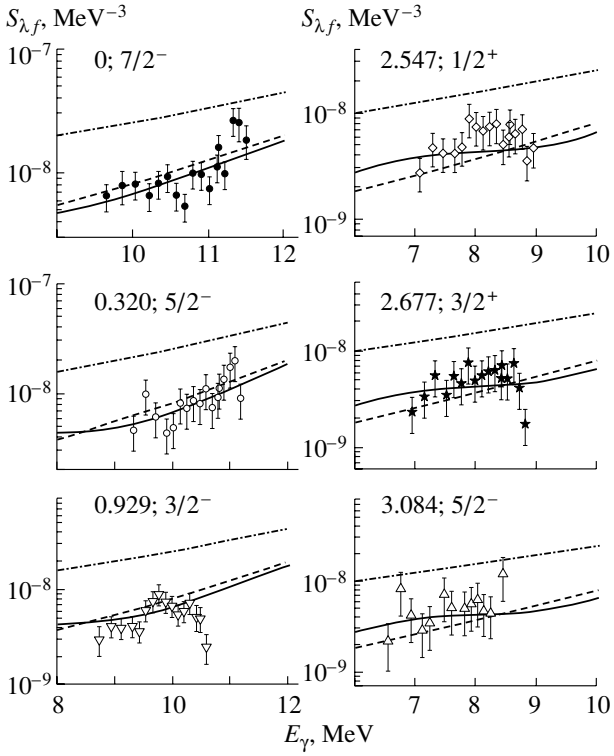

Fig. 2. As in Fig. 1, but for ^{51}V.

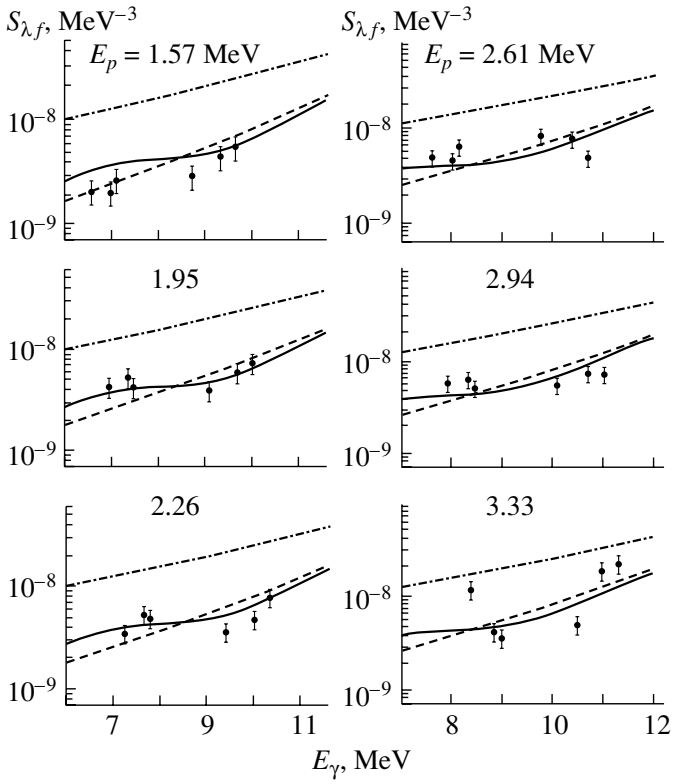

Fig. 3. RSF for γ transitions in ^{51}V for fixed energies E_λ of the initial state and varying energies E_f of final states. The notation for the curves is indentical to that in Fig. 1.

4. RESULTS AND DISCUSSION

The capture of protons with energies from 1.5 to 3.5 MeV by ^{48}Ti and ^{50}Ti nuclei is accompanied by many-particle excitations of the formed compound nuclei ^{49}V and ^{51}V, which is manifested in the observed high density of levels. However, isobar analogs of low-lying neighboring nuclei are among highly excited levels. A simpler nature of these states is manifested in deexcitation by highly intense γ transitions to lower levels of one-particle type. In addition to the analogs clearly identified in the systems ^{49}Ti—^{49}V and ^{50}Ti—^{51}V, these systems may also contain highly fragmented isobar-analog resonances or other states of one-particle nature (of the doorway type), which are difficult to take into consideration. In order to clarify possible structural features in the RSF, which can emerge owing to the presence of such states or irregularities in the level density of the final nucleus, we analyzed here the dependence of the RSF of primary γ transitions on the energy E_λ of the initial states (or the energy E_p of incident protons) for a fixed energy E_f of the final state. It should be noted that the RSF for transitions to the ground state of ^{51}V was determined earlier in [33]. It can be seen from Figs. 1 and 2 that no irregularities are manifested in the dependence of the RSF on the excitation energy of the investigated nuclei. This allows us to reliably average the partial cross sections in the range of excitation energies required for successful suppression of the spread due to the Porter—Thomas fluctuations. The isobar-analog states identified earlier were omitted from the averaging. Figure 3 shows the RSFs for γ transitions in ^{51}V, which were obtained for fixed proton energies (the energy of the initial state) and for varying energy of the final states. The curves in Figs. 1—3 correspond to theoretical estimates of the RSF: the Lorentzian dependence (dash-dotted curve), calculations based on formula (8) including temperature T_f only (dashed curve), and calculations taking into account both temperature and the shell effects (solid curve). At each point, the calculated values of the RSF for transitions between excited states depend only on the temperature T_f since the energy E_γ of the transition to the final state, appearing in expression (14) for T_f, varied in all these cases. Experimental errors also contain the model dependence of the determined value of RSF discussed above. The values of the RSF obtained from the averaged intensities of γ transitions to the final states of ^{49}V and ^{51}V for each individual state have different notation in Figs. 1 and 2 to illustrate the contribution from each of these partial RSFs to the dependence $S_{\lambda f}(E_\gamma)$.

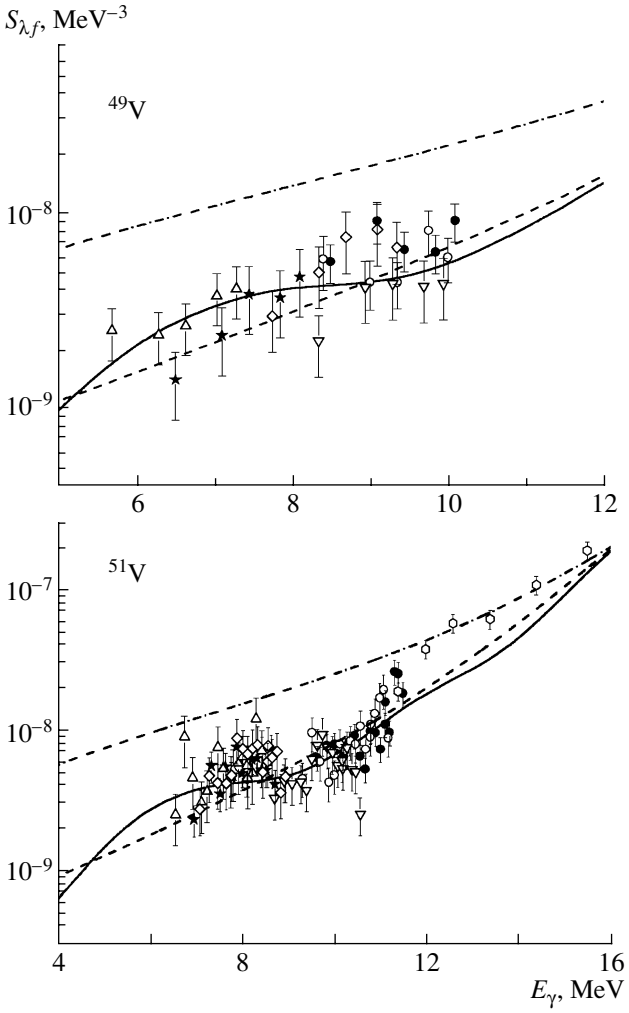

Fig. 4. Complete set of data obtained in this work on RSFs for primary γ transitions in ^{49}V and ^{51}V. The notation is identical to that in Fig. 1. Hexagons correspond to the results on the GDR obtained in [31].

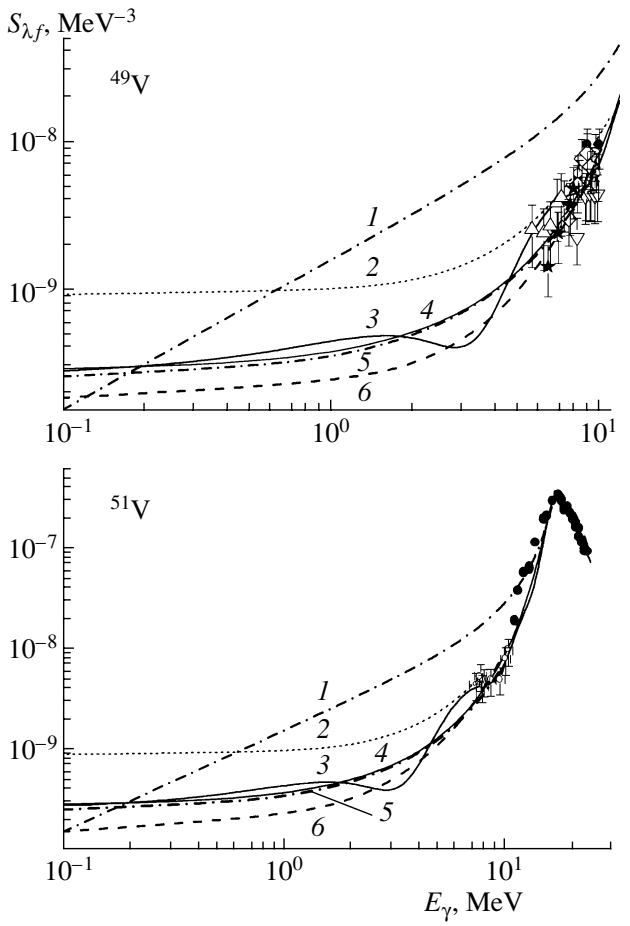

Fig. 5. Comparison of experimental values of RSF for ^{49}V and ^{51}V with those calculated for $E_\gamma \to 0$. Experimental RSFs for ^{49}V are the same as in Fig. 4. Light circles (○) correspond to values of RSFs obtained by us from the intensities of primary γ transitions in ^{51}V measured in [11] for $\overline{E}_p = 2.6$ MeV and in the averaging interval 0.9 MeV; • depict the data on the GDR in ^{51}V from [31]. Curves: *1* describes the Lorentzian dependence; *2* is calculated on the basis of the approach developed in [22]; *3* corresponds to calculations made on the basis of the approach developed in [23] taking into account the temperature and shell structure of the nucleus; *4* is the same as *3*, but taking into account temperature only; *5* corresponds to calculations based on the model [26, 27] with parameters $n = 0, k_s(0) = 0.3$, and $B_c = 0.58$; and *6* is the same as *5*, but with parameters $n = 0.5, k_s(0) = 0.3$, and $B_c = 0.35$.

The final states are presented in Figs. 1 and 2 by the values of their energy, spin, and parity. The data on RSF for primary dipole transitions to the final states of ^{49}V and ^{51}V presented in these figures do not lead to a reliable conclusion concerning the dependence of the RSF on final-state properties other than temperature and transition energy.

In the ^{51}V nucleus with the filled neutron shell, the states at 0.0, 320.08, and 928.66 keV with J^π equal to $7/2^-, 5/2^-$, and $3/2^-$, respectively, correspond to the proton configuration $(1f_{7/2})^3$. In ^{49}V, the states at 0.0, 90.64, and 152.93 keV correspond to the same configuration with the same sequence of values of J^π. The states of ^{51}V at 2547.4 and 2677.4 keV with J^π equal to $1/2^+$ and $3/2^+$, respectively, belong to proton-hole configurations $2s_{1/2}$ and $1d_{3/2}$. In the ^{49}V nucleus, the state at 748.27 keV with $J^\pi = 3/2^+$ belongs to the configuration $1d_{3/2}$, while the state at 1994.70 keV with $J^\pi = 1/2^+$ belongs to the configuration $2s_{1/2}$. Noticeable mixing of configurations starts in ^{51}V with the state at 2410.78 keV with $J^\pi = 3/2^-$. It can be seen from Figs. 1 and 2 that such different natures of the final states affect the energy dependence of the RSFs determined from the resonance-averaged intensities of primary γ transitions in the compound nucleus only slightly.

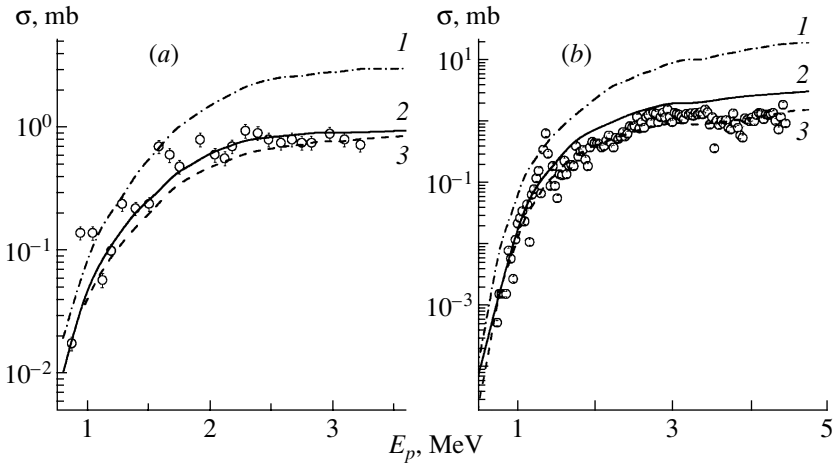

Fig. 6. Total cross sections of the (p, γ) reaction on ^{48}Ti (a) and ^{50}Ti (b).Curves: *1* corresponds to the cross sections calculated with an RSF in the form of a Lorentzian; *2* shows the cross sections calculated with the RSF obtained using the approach developed in [23] taking into account the temperature and the shell structure of the nucleus; and *3* is the same as *2*, but taking into account the temperature alone. The experimental values of cross sections were borrowed from [34, 35].

The complete set of data obtained by us for RSF for dipole transitions in the ^{49}V and ^{51}V is presented in Fig. 4 in the same notation as in Fig. 1. The results of calculations in the thermodynamic pole approximation, which are not presented in the figure, virtually coincide with the dashed curve. Figure 5 illustrates, for the sake of comparison, the behavior of the RSFs calculated by using different theoretical approaches depending on the photon energy asymptotically tending to zero. It can be seen that only the Lorentzian dependence (curve *1*) decreases (linearly) to zero.

All calculations depending on the nuclear temperature for $E_\gamma \to 0$ give nonzero values of the RSF: curve *2* was calculated on the basis of the approach developed in [22]; curve *3* corresponds to calculations based on [23] that take into account the temperature and shell structure of the nucleus; curve *4* is the same as *3*, but taking only the temperature into account; curve *5* was calculated using formulas (11) and (12) with parameters from [26, 27]: $n = 0$, $k_s(0) = 0.3$, and $B_c = 0.58$; and curve *6* is the same as *5*, but with $n = 0.5$, $k_s(0) = 0.3$, and $B_c = 0.35$. The parameter B_c is associated with the determination of the two-particle component of the GDR damping width. Calculations based on [23] and taking into account temperature alone and those made in the thermodynamic pole approximation [26, 27] with the relaxation time from Fermi liquid theory give matching results in the entire photon energy range under investigation. It can be seen from Figs. 4 and 5 that the experimental data on RSF for ^{51}V indicate that a certain structure may exist in the energy dependence of the RSF under investigation. This could indicate the existence of a contribution to the RSF from transitions determined by the particle–hole configuration weakly coupled to the GDR [25].

The results of calculation of the total cross sections of the (p, γ) reaction on the ^{48}Ti and ^{50}Ti nuclei within Hauser–Feshbach theory using the RSF for the $E1$ transitions calculated with the help of expression (8) are shown in Fig. 6 in comparison with the experimental results from [34, 35]. The best agreement with the experimental data was obtained when the contribution from the $M1$ transitions was taken into account with the help of expression (10) for ^{49}V and in the one-particle approximation for ^{51}V.

The contribution of the $M1$ transitions in the energy range under investigation for ^{51}V can now be estimated to a high degree of reliability by comparing our results with the data on primary $E1$ transitions obtained in [1] with the help of the thermal-neutron-capture reaction $^{50}\mathrm{V}(n, \gamma)^{51}\mathrm{V}$. Since the ^{50}V nucleus in the ground state is characterized by $J^\pi = 6^+$, the observed 59 direct γ transitions from the captured state with $J^\pi = 11/2^+$ or $13/2^+$ to lower excited states ^{51}V of negative parity must be pure $E1$ transitions. Unfortunately, the experimental data from [1] on the energy distribution of the strength of the $E1$ transitions are not absolute, which does not allows us to use such a favorable possibility of comparing these two mutually complementing results at the moment.

In a large number of papers that have been published by now, the experimental results on the total cross sections of the (p, γ) reaction on fp-shell nuclei for proton energies below 4 MeV are successfully described within Hauser–Feshbach theory using the OP parameters from the global systematics in [10]

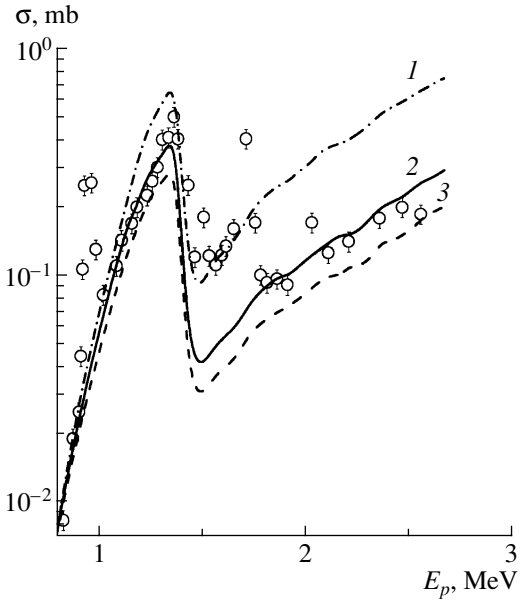

Fig. 7. As in Fig. 6, but for the (p,γ) reaction on ^{49}Ti. Curves: *1* corresponds to the cross sections calculated with RSFs in the form of a Lorentzian and with allowance for the contribution of the $M1$ transitions in the one-particle approximation; *2* corresponds to the cross sections calculated with the RSFs obtained using the approach developed in [23] with allowance for both the temperature and the shell structure of the nucleus, the contribution from the $M1$ transitions being taken into account with the help of formula (10); and *3* is the same as *2*, but taking into account the contribution of the $M1$ transitions in the one-particle approximation. Experimental cross sections were borrowed from [20, 36].

and the RSF in the form of the Lorentzian distribution. For example, the total cross section of the reaction $^{49}\mathrm{Ti}(p,\gamma)^{50}\mathrm{V}$ was successfully described in [36] in this way in the proton-energy range from 0.74 to 3.25 MeV. These experimental results, together with our earlier data [20] on the total cross sections of the (p,γ) reaction on ^{49}Ti, are compared in Fig. 7 with the results of calculations made by us here within statistical theory. Use was made of the RSFs calculated on the basis of formula (8) as well as of the same parameters of the imaginary part $W_s(E_p)$ of the OP for protons as those used in this research. The level density for ^{50}V was calculated with parameters $a = 6.1\ \mathrm{MeV}^{-1}$ and $\Delta = -2.2$ MeV and the moment of inertia reduced to half the value corresponding to the rigid-body case. The results of these calculations taking into account the contribution of the $M1$ transitions through formula (10) are represented in Fig. 7 by the solid curve, which successfully describes the experimental data except in the regions of clearly manifested isobar analogs. This example shows that the experimental data on the total cross section of radiative proton capture can sometimes be correctly described with the help of a combination of incorrect quantities such as OP, RSF, and probably the level density. However, such a description may naturally lead to incorrect conclusions.

5. CONCLUSIONS

New data on partial RSFs have been obtained for dipole transitions from the states of the compound nucleus to excited states of the ^{49}V and ^{51}V nuclei. These data have been compared with the results of calculations of RSFs by using different theoretical approaches. It has been shown that the application of the Lorentzian distribution leads to considerably exaggerated values of RSFs as compared to experimental results. The theoretical approaches [23, 26, 27] taking into account the dependence of the GDR width on the energy of photons and the nuclear temperature in the state to which the γ transition takes place describe the experimental RSFs equally well. The best description is provided by using the approach [23] in which the shell structure of the nucleus is taken into account in addition to temperature. The models [23, 26, 27] based on different theoretical premises and taking into account the coupling the doorway states to more complex configurations, which forms the RSF of primary dipole transitions in different manners, can be regarded as a generalization of the Brink–Axel model in which the $E1$ strength depends only on E_γ.

The energy dependence of the RSFs determined from the intensities of γ transitions averaged over resonances of the compound nucleus depends only slightly on the nature of the final states to which the transitions occurred in the nuclei under investigation. As regards the contribution from the $M1$ transitions, the best agreement between the calculated and experimental RSFs has been reached when this contribution was calculated using the approach developed in [23] for ^{49}V and in the one-particle approximation for ^{51}V. The contribution from the $M1$ transitions could be estimated more precisely by comparing our results with the data [1] on the energy distribution of the strength of the $E1$ transitions in the ^{51}V nucleus excited in the (n,γ) reaction if the intensities of the primary γ transitions presented in [1] were absolute. The application of our results in the calculation of the total cross section of the (p,γ) reaction on ^{49}Ti and a comparison with the results of calculations using the global systematics of the OP and the Lorentzian distribution for the RSF show that a successful description of experimental data on cross sections with the help of model parameters that have not been properly validated does not guarantee correct conclusions.

ACKNOWLEDGMENTS

The author thanks B.A. Nemashkalo for his consistent interest in this work, S.S. Ratkevich for fruitful discussions, and V.A. Plyuiko for kindly providing more detailed information on the theoretical approach developed by him than in his publications on this subject.

REFERENCES

1. S. Michaelsen, K. P. Lieb, and S. J. Robinson, Z. Phys. A **338**, 371 (1991).
2. P. von Neumann-Cosel, A. Poves, J. Retamosa, and A. Richter, Phys. Lett. B **443**, 1 (1998).
3. C. Djalali, N. Marty, M. Morlet, *et al.*, Nucl. Phys. A **388**, 1 (1982).
4. D. Bender, G. Eulenberg, A. Richter, *et al.*, Nucl. Phys. A **398**, 408 (1983).
5. H. Kaiser, P. von Brentano, E. Caurier, *et al.*, Nucl. Phys. A **669**, 368 (2000).
6. J. Enders, P. von Brentano, J. Eberth, *et al.*, Nucl. Phys. A **636**, 139 (1998).
7. N. H. Prochnow, H. W. Newson, E. G. Bilpuch, and G. E. Mitchell, Nucl. Phys. A **194**, 373 (1972).
8. J. Li, E. G. Bilpuch, C. R. Westerfeldt, *et al.*, Phys. Rev. C **44**, 345 (1991).
9. G. U. Din and J. A. Cameron, Phys. Rev. C **45**, 2147 (1992).
10. F. D. Becchetti and G. W. Greenlees, Phys. Rev. **182**, 1190 (1969).
11. B. Erlandsson, K. Nilson, and A. Marcinkowski, Nucl. Phys. A **329**, 1 (1979).
12. M. K. Mehta, S. Kailas, and K. K. Sekharan, Pramana **9**, 419 (1977).
13. S. R. Kennett, L. W. Mitchell, M. R. Anderson, and D. G. Sargood, Nucl. Phys. A **363**, 233 (1981).
14. B. A. Nemashkalo and K. V. Shebeko, Yad. Fiz. **51**, 920 (1990) [Sov. J. Nucl. Phys. **51**, 588 (1990)].
15. K. V. Shebeko, B. A. Nemashkalo, and G. N. Kuptsov, Izv. Akad. Nauk SSSR, Ser. Fiz. **53**, 987 (1989).
16. N. Boukharouba, C. E. Brient, S. M. Grimes, *et al.*, Phys. Rev. C **46**, 2375 (1992).
17. S. M. Grimes, Phys. Rev. C **22**, 436 (1980).
18. E. A. Romanovskiĭ, Yad. Fiz. **41**, 607 (1985) [Sov. J. Nucl. Phys. **41**, 387 (1985)].
19. Yu. V. Sokolov, *Level Density of Atomic Nuclei* (Énergoatomizdat, Moscow, 1990).
20. I. D. Fedorets, I. I. Zalyubovskiĭ, B. A. Nemashkalo, and V. E. Storizhko, Izv. Akad. Nauk SSSR, Ser. Fiz. **50**, 2016 (1986).
21. Z. Chunmei, Nucl. Data Sheets **81**, 183 (1997); NUDAT—The Nuclear Data File Generated at the NNDC by NUDAT, BNL (file as of Jan. 1999).
22. S. G. Kadmenskiĭ, V. P. Markushev, and V. I. Furman, Yad. Fiz. **37**, 277 (1983) [Sov. J. Nucl. Phys. **37**, 165 (1983)].
23. V. K. Sirotkin, Yad. Fiz. **43**, 570 (1986) [Sov. J. Nucl. Phys. **43**, 362 (1986)]; D. F. Zaretskiĭ and V. K. Sirotkin, Izv. Akad. Nauk SSSR, Ser. Fiz. **52**, 984 (1988).
24. J. Kopecky and R. E. Chrien, Nucl. Phys. A **468**, 285 (1987).
25. V. A. Rodin and M. G. Urin, Fiz. Élem. Chastits At. Yadra **31**, 976 (2000).
26. V. A. Plujko, Nucl. Phys. A **649**, 209c (1999).
27. V. A. Plujko, Acta Phys. Pol. B **31**, 435 (2000).
28. S. S. Ratkevich, B. A. Nemashkalo, and I. D. Fedorets, Izv. Akad. Nauk, Ser. Fiz. **61**, 2039 (1997).
29. S. S. Ratkevich, B. A. Nemashkalo, and I. D. Fedorets, Yad. Fiz. **60**, 804 (1997) [Phys. At. Nucl. **60**, 713 (1997)].
30. I. D. Fedorets, Yad. Fiz. **64**, 51 (2001) [Phys. At. Nucl. **64**, 49 (2001)].
31. S. C. Fultz, R. L. Bramblett, J. T. Caldwell, *et al.*, Phys. Rev. **128**, 2345 (1962).
32. Handbook for Calculations of Nuclear Reaction Data. Reference Input Parameter Library (RIPL), IAEA-TECDOC-1034, Aug. 1998, Sci. d. P. Oblozinsky, Chap. 6.
33. B. A. Nemashkalo, V. K. Sirotkin, and K. V. Shebeko, Yad. Fiz. **55**, 123 (1992) [Sov. J. Nucl. Phys. **55**, 69 (1992)].
34. S. R. Kennett, L. W. Mitchell, M. R. Anderson, and D. G. Sargood, Nucl. Phys. A **368**, 337 (1981).
35. S. K. Kennett, M. R. Anderson, L. W. Mitchell, *et al.*, Nucl. Phys. A **346**, 523 (1980).
36. S. R. Kennett, M. R. Anderson, Z. E. Switkowski, and D. G. Sargood, Nucl. Phys. A **344**, 351 (1980).

Translated by N. Wadhwa

Physics of Atomic Nuclei, Vol. 65, No. 10, 2002, pp. 1827–1842. Translated from Yadernaya Fizika, Vol. 65, No. 10, 2002, pp. 1877–1893.

NUCLEI
Theory

On the Information Value of Angular Distributions in Elastic Scattering of Heavy Ions

Yu. A. Pozdnyakov*

Institute for Nuclear Research, National Academy of Sciences of Ukraine, Kiev, Ukraine

Received April 13, 2001; in final form, October 22, 2001

Abstract—A method is developed for computing the total cross section σ_F of complete and incomplete fusion, quasifission, and deep-inelastic collisions, as well as the total cross section σ_D of peripheral reactions, on the basis of analysis of angular distributions for elastic scattering of heavy ions. The method makes it possible, on a unified basis, to explain the mechanism of formation of σ_F and σ_D both for strongly and for weakly bound ions. The method permits the calculation of quantitative characteristics of fusion enhancement (and, accordingly, suppression of peripheral reactions) for strongly bound ions and, conversely, the suppression of fusion (and, accordingly, enhancement of peripheral reactions) for weakly bound ions. The potential of the method is demonstrated for two systems, $^{16}O + {}^{208}Pb$ and $^{9}Be + {}^{28}Si$, the projectile ion being strongly bound in the former system and weakly bound in the latter one.

1. INTRODUCTION

The method of analysis of the angular distributions of elastic scattering (ES) of heavy ions proposed in [1, 2] makes it possible to calculate the total cross section of fusion, incomplete fusion, quasifission, and deep-inelastic collisions σ_F and the total cross section σ_D of peripheral reactions, as well as their distributions over partial waves. It was found [1–4] that the obtained cross sections are in accord with the experimental results in an overwhelming majority of cases.

In the case of strongly bound ions, the method makes it possible to establish the mechanism of formation of σ_F. However, the mechanism of formation of σ_F for weakly bound ions remains unclear [2]. In this paper, the results obtained in [1, 2] are generalized so that the mechanism of formation of σ_F and σ_D for strongly and weakly bound ions is explained on a unified basis.

2. RELATION BETWEEN THE PROBABILITIES OF VARIOUS PROCESSES AND S-MATRIX ELEMENTS OF ES

The proposed method for calculating the total cross sections of fusion, incomplete fusion, quasifission, and deep-inelastic collisions and the total cross section of peripheral reactions is based on the ES incoming-wave-boundary-condition model (IWBCM) [5–11] involving microscopic double-folding potential (DFP) [12] with a phenomenological surface imaginary part. In this model, all reaction channels can be naturally divided into three groups (see Fig. 1). The first (+) group includes only the ES channel. The second (D) group is formed by peripheral (or quasielastic) reactions; the transition to these reactions from the ES channel is taken into account in the IWBCM through the surface imaginary part of the optical potential (OP).

The third (F) group includes all reaction channels to which the transition from the entrance channel is ensured by the boundary conditions. This group is formed by reactions occurring when the colliding-nucleus densities considerably overlap: fusion, incomplete fusion, quasifission, and deep-inelastic collisions. It should be noted that, for not very heavy nuclei, say, for $Z_P Z_T \leq 1000$ (Z_P and Z_T are the charge numbers of the projectile particle and target nucleus, respectively) and for energies up to 10 MeV/nucleon, fusion is the dominating process in the F group of reactions [13–17].

We will henceforth disregard the spins of colliding nuclei. The total partial probabilities (TPP) of transitions between isolated groups of channels will be denoted by $P_{l,\,ab}$, where p and b are the symbols of the initial and final groups, respectively, and l is the orbital angular momentum in the entrance channel. We disregard the probability $P_{l,\,FE}$ of particle return to the entrance channel from the F group of reactions, which is quite justified for heavy ions. If fusion is the main process in the F group, $P_{l,\,FE}$ is the partial probability of ES through a compound nucleus. Figure 1 does not depict the transition from the F

*e-mail: pozdnyak@kinr.kiev.ua

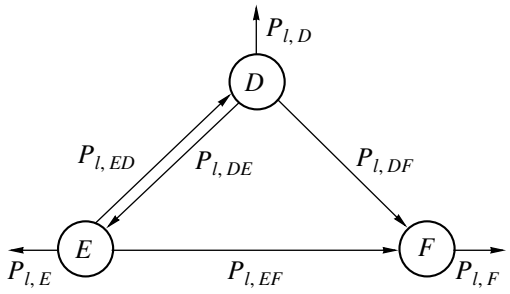

Fig. 1. Schematic diagram of division of reaction channels in the IWBCM.

group to the D group either, since the reactions occurring through the stage of formation of a compound nucleus cannot be attributed to peripheral reactions. The partial probabilities of ES, the TPP of peripheral reactions, and the TPP of reactions in the F group will be denoted by $P_{l,E}$, $P_{l,D}$ and $P_{l,F}$, respectively.

In order to derive the required relations, we consider the unitarity relation for the ES channel, which expresses the law of probability conservation in a given partial wave as

$$\left|S_{ii}^{(l)}\right|^2 \equiv |S_l|^2 \equiv P_{l,\,E} = 1 - \sum_{f\neq i}\left|S_{fi}^{(l)}\right|^2, \quad (1)$$

where $S_{ii}^{(l)}$ are the diagonal and $S_{fi}^{(l)}$ are nondiagonal elements of the S matrix. Summation in relation (1) is carried out over all open reactions channels f differing from the ES channel i. Indices i and f include all the characteristics required for determining the reaction channel. Since the spins of colliding nuclei are disregarded, the total spin of a channel is determined by the angular momentum in the entrance channel, which appears explicitly in the $S_{ii}^{(l)}$ and $S_{fi}^{(l)}$ matrix elements. In accordance with the isolated groups of reaction channels, we divide the sum on the right-hand side of Eq. (1) into the two terms

$$\sum_{f\neq i}\left|S_{fi}^{(l)}\right|^2 = \sum_{f\in F}\left|S_{fi}^{(l)}\right|^2 + \sum_{f\in D}\left|S_{fi}^{(l)}\right|^2. \quad (2)$$

Here, the first term,

$$P_{l,\,F} = \sum_{f\in F}\left|S_{fi}^{(l)}\right|^2, \quad (3)$$

is the TPP of reactions in the F group, while the second term,

$$P_{l,\,D} = \sum_{f\in D}\left|S_{fi}^{(l)}\right|^2, \quad (4)$$

is the TPP of the peripheral reactions.

Taking into account expressions (2)–(4), we write relation (1) in the form

$$|S_l|^2 = 1 - P_{l,\,F} - P_{l,\,D}. \quad (5)$$

It can easily be seen from Fig. 1 that

$$P_{l,F} = P_{l,EF} + P_{l,DF}, \quad (6)$$

where $P_{l,EF}$ are the TPP of the excitation of reactions in the F group through the entrance channel, while $P_{l,DF}$ is the TPP of multistep reactions in the F group, occurring through intermediate states of the system excited in the peripheral region. It should be noted that, if fusion is the dominant process in the F group of reactions, $P_{l,EF}$ and $P_{l,DF}$ are the partial probabilities of the direct and multistep fusion, respectively, while $P_{l,F}$ is the partial probability of fusion.

For $P_{l,EF}$, we can write

$$P_{l,EF} = \left(1 - \left|S_l^{(0)}\right|^2\right)(1 - P_{l,ED}), \quad (7)$$

where $S_l^{(0)}$ are the S-matrix elements of ES, which can be calculated with a nonrenormalized DFP in the absence of peripheral absorption, and $P_{l,ED}$ are the TPP of the escape of particles from the entrance channel in the periphery region, which will also be referred to as the TPP of peripheral processes. It can be seen from formula (7) that the TPP of direct excitation of reactions in the F group is determined by the product of the penetrability of the barrier (formed by the sum of the Coulomb, centrifugal, and nuclear potentials) in the entrance channel and the probability that no reaction occurs in the peripheral region. Obviously, we have

$$P_{l,ED} = P_{l,DE} + P_{l,D} + P_{l,DF}, \quad (8)$$

where $P_{l,DE}$ is the TPP of the return of particles from the D reaction group to the entrance channel, which will be henceforth referred to as the TPP of virtual excitations. Substituting Eq. (8) into Eq. (7) and the obtained result into formula (6), we can write the TPP of reactions in the F group in the form

$$P_{l,F} = \left(1 - \left|S_l^{(0)}\right|^2\right)(1 - P_{l,DE} - P_{l,D}) + \left|S_l^{(0)}\right|^2 P_{l,DF}. \quad (9)$$

Let us use this expression in the unitarity relation (5). This gives

$$|S_l|^2 = \left|S_l^{(0)}\right|^2(1 - P_{l,D} - P_{l,DF}) + \left(1 - \left|S_l^{(0)}\right|^2\right)P_{l,DE}. \quad (10)$$

At the same time, for $|S_l|^2$, we can directly write

$$|S_l|^2 = \left|\tilde{S}_l^{(0)}\right|^2 (1 - P_{l,D}). \quad (11)$$

This formula corresponds to the conventional single-channel ES approximation and has a simple physical meaning: the reflection coefficient in each partial wave is the product of the reflection coefficient for a certain barrier in the absence of peripheral absorption and the probability that none of the observed reactions occurs in the external region. It should be noted that, if there is no barrier in a wave, we have $\left|\tilde{S}_l^{(0)}\right| = 1$. Since $S_l^{(0)}$ are the S-matrix elements of ES, which are calculated in the IWBCM with a nonrenormalized DFP and with zero imaginary part of the OP, $\tilde{S}_l^{(0)}$ should be interpreted as the S-matrix elements of ES, calculated in the same way as $S_l^{(0)}$, but with a renormalized DFP (in general with allowance for the real part of the polarization potential [12]).

Equating the right-hand sides of formulas (10) and (11), we obtain the basic relation of the method, which connects the S-matrix elements $S_l^{(0)}$ and $\tilde{S}_l^{(0)}$:

$$\left|\tilde{S}_l^{(0)}\right|^2 = \left|S_l^{(0)}\right|^2 \frac{1 - P_{l,D} - (P_{l,DF} - P_{l,HF})}{1 - P_{l,D}}, \quad (12)$$

where

$$P_{l,HF} = \frac{1 - \left|S_l^{(0)}\right|^2}{\left|S_l^{(0)}\right|^2} P_{l,DE}. \quad (13)$$

It will be shown below that this probability is the TPP of suppression of reactions in the F group, which, in accordance with (13), is due to virtual excitations in the system.

We will consider two separate cases in which the projectile particle is a strongly bound and a weakly bound ion, respectively.

Strongly Bound Ions

We assume that $P_{l,HF} \ll P_{l,DF}$ in a certain system. In this case, formula (12) can be written in the form

$$\left|\tilde{S}_l^{(0)}\right|^2 = \left|S_l^{(0)}\right|^2 \frac{1 - P_{l,D} - P_{l,DF}}{1 - P_{l,D}}. \quad (14)$$

This relation was derived in [1, 2]. It implies that, if $P_{l,DF} = 0$ for all l, we have $\left|\tilde{S}_l^{(0)}\right| = \left|S_l^{(0)}\right|$. This means that the S-matrix elements $\tilde{S}_l^{(0)}$ are calculated without renormalizing the DFP. A nonzero value of $P_{l,DF}$ leads to the inequality $\left|\tilde{S}_l^{(0)}\right| < \left|S_l^{(0)}\right|$, indicating that the S-matrix elements $\tilde{S}_l^{(0)}$ in the corresponding partial waves can be calculated with a renormalized DFP with the normalization factor $N_F > 1$ (in the general case, with an attractive real part of the polarization potential). It can be seen that the case under investigation is characterized, first, by an enhancement of reactions in the F group (since $P_{l,DF} \neq 0$ by definition), in particular, the enhancement of fusion, and, second, by the enhancement of the real part of the OP, which is required for describing the angular distribution of ES. Such a situation corresponds to strongly bound heavy ions. Thus, formula (14) establishes a close relation between the two well-known phenomena in the physics of heavy ions: enhancement of fusion (see, for example, [18–21]) and a threshold anomaly {enhancement of the real part of the OP for subbarrier and near-barrier energies (see, for example, [20–22])}. According to formula (14), the threshold anomaly occurs because of processes of multistep fusion in the system.

One more consequence of formula (14) is worth noting. It shows that the normalization factor of the DFP must depend on l; the renormalization must be carried out precisely in the waves with nonzero probabilities $P_{l,DF}$.

We can now determine all the probabilities of interest. For example, from formula (11), we have

$$P_{l,D} = 1 - \frac{|S_l|^2}{\left|\tilde{S}_l^{(0)}\right|^2}. \quad (15)$$

The TPP of reactions in the F group can easily be derived from the unitarity relation (5). Using formula (15), we can express $P_{l,F}$ in terms of the S-matrix elements S_l and $\tilde{S}_l^{(0)}$:

$$P_{l,F} = \frac{|S_l|^2}{\left|\tilde{S}_l^{(0)}\right|^2} \left(1 - \left|\tilde{S}_l^{(0)}\right|^2\right). \quad (16)$$

If we omit the factor $|S_l|^2 / \left|\tilde{S}_l^{(0)}\right|^2 < 1$ in this formula, we obtain the well-known expression for the partial fusion probability in the barrier-penetration model [18, 19] in which the probability is calculated without taking into account peripheral reactions.

The TPP of enhancement of reactions in the F group can be determined from expression (14). Taking into account Eq. (15), we have

$$P_{l,DF} = \frac{|S_l|^2}{\left|\tilde{S}_l^{(0)}\right|^2} \left(1 - \frac{\left|\tilde{S}_l^{(0)}\right|^2}{\left|S_l^{(0)}\right|^2}\right). \quad (17)$$

The TPP of reaction excitation in the F group through the entrance channel, $P_{l,EF}$, can be determined from relation (6). Using formulas (16) and (17) for this purpose, we obtain

$$P_{l,EF} = \frac{|S_l|^2}{\left|S_l^{(0)}\right|^2}\left(1 - \left|S_l^{(0)}\right|^2\right). \qquad (18)$$

It is noteworthy to mention an interesting feature of the TPP $P_{l,D}$ of quasielastic reactions. We will first find the TPP of peripheral processes from formula (7). Taking into account relation (18), we obtain

$$P_{l,ED} = 1 - \frac{|S_l|^2}{\left|S_l^{(0)}\right|^2}. \qquad (19)$$

This formula implies that $P_{l,ED} = P_{l,D}$ in the absence of multistep reactions in the F group (when $\left|\tilde{S}_l^{(0)}\right| = \left|S_l^{(0)}\right|$). We subtract the probability $P_{l,DF}$ from both sides of Eq. (19), expand it in the explicit form (17) on the right-hand side of the obtained equality, and use relation (15) for $P_{l,D}$. This gives the relation

$$P_{l,D} = P_{l,ED} - P_{l,DF}, \qquad (20)$$

which can also be obtained from formula (8) in the approximation $P_{l,DE} = 0$. Formula (20) shows that multistep reactions in the F group, apart from the enhancement of reactions in this group (which is observed, for example, for fusion), simultaneously result in the same suppression of peripheral reactions. Consequently, the TPP of enhancement of reactions in the F group can be rightfully referred to as the TPP of suppression of peripheral reactions.

It can easily be verified that the following equalities hold in the case under investigation:

$$P_{l,F} + P_{l,D} = P_{l,EF} + P_{l,ED} = 1 - |S_l|^2. \qquad (21)$$

Weakly Bound Ions

Let us consider the opposite situation. Let us suppose that $P_{l,DF} \ll P_{l,HF}$ for a system. In this case, formula (12) assumes the form

$$\left|\tilde{S}_l^{(0)}\right|^2 = \left|S_l^{(0)}\right|^2 \frac{1 - P_{l,D} + P_{l,HF}}{1 - P_{l,D}}. \qquad (22)$$

It can be seen from this formula that the waves for which $P_{l,HF} \neq 0$ satisfy the inequality $\left|\tilde{S}_l^{(0)}\right| > \left|S_l^{(0)}\right|$. This means that the S-matrix elements $\tilde{S}_l^{(0)}$ for corresponding partial waves are calculated using the DFP with $N_F < 1$ (in the general case, with a repulsive real part of the polarization potential). In this case, the system is characterized, first, by the presence of virtual excitations (since $P_{l,DE} \sim P_{l,HF} \neq 0$ by assumption) and, second, by the attenuation of the real part of the OP, which is required for describing the angular distributions of ES. All this holds for weakly bound compound particles. Thus, formula (22) reflects the close relation between virtual excitations and the DFP attenuation. Namely, virtual excitations in the system are responsible for the attenuation of the DFP. This conclusion is confirmed by calculations made by the coupled-channel method with discretization of the continuous spectrum (see, for example, [23–26]). It will be proved below that suppression of reactions in the F group upon collisions of weakly bound ions with nuclei is a more profound consequence of virtual excitations. In particular, the suppression of fusion during collisions of weakly bound ions with nuclei was considered in [27, 28].

Expressions (15) and (16) for the probabilities $P_{l,D}$ and $P_{l,F}$ for weakly bound ions are the same as for strongly bound ions. The TPP of reaction suppression in the F group can be determined easily from relation (22). Taking into account relation (15), we obtain

$$P_{l,HF} = \frac{|S_l|^2}{\left|S_l^{(0)}\right|^2}\left(1 - \frac{\left|S_l^{(0)}\right|^2}{\left|\tilde{S}_l^{(0)}\right|^2}\right). \qquad (23)$$

As regards the TPP $P_{l,EF}$ of excitation of reactions in the F group through the entrance channel and the TPP $P_{l,ED}$ of peripheral processes, these probabilities must be considered separately in the case of weakly bound ions. We will start from $P_{l,EF}$. Since the TPP $P_{l,DF}$ of reaction enhancement in the F group is neglected for weakly bound ions, we have, in accordance with formula (6),

$$P_{l,F} = P_{l,EF}. \qquad (24)$$

This equality indicates that, in the case of collisions of weakly bound ions with nuclei, reactions in the F group are excited only through the entrance channel. It should be noted, however, that, in accordance with Eqs. (24) and (16), the value of $P_{l,EF}$ for weakly bound ions is calculated with a renormalized DFP, while these probabilities must be calculated with a nonrenormalized DFP by formula (18). It can easily be established that the probabilities $P_{l,EF}$ calculated by formulas (24) and (16) are lower than the probabilities $P_{l,EF}$ calculated by formula (18). This means that the limit (18) cannot be attained for the probabilities $P_{l,EF}$ for weakly bound ions. It is for this reason that reactions in the F group (in particular, fusion) are suppressed.

It follows from the above arguments that expression (18) must be used for determining the probabilities $P_{l,EF}$ for weakly bound ions as well as for strongly bound ions. However, in this case, the following relation holds for the TPP $P_{l,F}$ for excitation of reactions in the F group:

$$P_{l,F} = P_{l,EF} - P_{l,HF}. \tag{25}$$

It is this relation that makes it possible to interpret the probability $P_{l,HF}$ introduced above with the help of formula (13) as the TPP of suppression of group F reactions.

Let us now consider the TPP $P_{l,ED}$ of particle escape from the entrance channel in the peripheral region. It order to find the expression for this probability for weakly bound ions, we substitute the explicit expressions (16) and (7) for $P_{l,F}$ and $P_{l,EF}$, respectively, into formula (24). The expression thus obtained readily leads to

$$P_{l,ED} = 1 - \frac{|S_l|^2}{\left|\tilde{S}_l^{(0)}\right|^2}\frac{1-\left|\tilde{S}_l^{(0)}\right|^2}{1-\left|S_l^{(0)}\right|^2}. \tag{26}$$

This formula can also be derived from relation (8) in the approximation $P_{l,DF} = 0$ by substituting into it the explicit expression for $P_{l,DE}$ using formulas (13), (23), and (15). A comparison of Eqs. (26) and (19) shows that the probabilities $P_{l,ED}$ for weakly and strongly bound ions are different. It can easily be established, however, that formula (26) is transformed into formula (19) after the formal limiting transition $P_{l,DE} \to 0$, for which $\tilde{S}_l^{(0)} \to S_l^{(0)}$.

It can be verified that the probabilities $P_{l,ED}$ calculated in accordance with formula (26) are higher than those calculated by formula (19). This fact explains [see formula (7)] why the probabilities $P_{l,EF}$ for weakly bound ions do not attain their maximum possible value determined by relation (18). The physical reason for higher values of the probabilities $P_{l,ED}$ for weakly bound ions than for strongly bound ions is obviously the breakup of weakly bound projectile ions.

Since, in the case under investigation, we employ relation (25), in which the probability $P_{l,EF}$ is defined by formula (18) for the TPP of reactions in the F group, we must use in the following, in accordance with relation (7), the probability $P_{l,ED}$ defined by formula (19) as the TPP for peripheral processes.

In order to determine the consequences of virtual excitations for the TPP of peripheral reactions, we consider relation (19). Supplementing both sides with probability $P_{l,HF}$, presenting it in the explicit form (23) on the right-hand side of the obtained equality, and using formula (15) for $P_{l,D}$, we obtain

$$P_{l,D} = P_{l,ED} + P_{l,HF}. \tag{27}$$

Consequently, virtual excitations that appear in collisions involving weakly bound particles, apart from the suppression of reactions in the F group, simultaneously result in the same enhancement of peripheral reactions. Consequently, the TPP $P_{l,HF}$ of suppression of reactions in the F group can also be rightfully referred to as the TPP of enhancement of peripheral reactions.

It can easily be verified that equalities (21) remain in force for weakly bound ions.

It is appropriate to mention a peculiar symmetry in the properties of the systems, which is manifested in collisions of strongly and weakly bound ions. Indeed, for strongly bound ions, enhancement of reactions in the F group (in particular, enhancement of fusion) takes place simultaneously with an equivalent suppression of peripheral reactions. Conversely, for weakly bound ions, suppression of reactions in the F group (in particular, suppression of fusion) takes place simultaneously with an equivalent enhancement of peripheral reactions. In order to describe the angular distributions of ES (at least, for subbarrier and near-barrier energies), enhancement of the real part of the OP is required for strongly bound ions and its suppression for weakly bound ions.

Having obtained the expressions for the TPP of various processes, we can easily pass to the corresponding partial and total cross sections. Let $P_{l,X}$ ($X = D$, F, EF, etc.) be any of the above probabilities. Then the partial cross section corresponding to it is defined as

$$\sigma_{l,X} = \frac{\pi}{k^2}(2l+1)P_{l,X}, \tag{28}$$

where k is the wave number in the ES channel. The total cross section can be obtained by simple summation of the partial cross sections:

$$\sigma_X = \sum_{l=0}^{\infty}\sigma_{l,X}. \tag{29}$$

Taking into account relations (21), we can easily verify that the equalities

$$\sigma_{l,F} + \sigma_{l,D} \tag{30}$$
$$= \sigma_{l,EF} + \sigma_{l,ED} = \frac{\pi}{k^2}(2l+1)(1-|S_l|^2)$$

and

$$\sigma_R = \sigma_F + \sigma_D \tag{31}$$
$$= \sigma_{EF} + \sigma_{ED} = \frac{\pi}{k^2}\sum_{l=0}^{\infty}(2l+1)(1-|S_l|^2),$$

where σ_R is the total reactions cross section, are always satisfied in our approach.

Knowing the partial cross sections of reactions in the F group, we can calculate the mean,

$$\langle L_F \rangle = \frac{1}{\sigma_F} \sum_{l=0}^{\infty} l\sigma_{l,F}, \tag{32}$$

and mean square,

$$\langle L_F^2 \rangle = \frac{1}{\sigma_F} \sum_{l=0}^{\infty} l^2\sigma_{l,F}, \tag{33}$$

angular momenta of reactions in this group. If fusion is the dominating process in the F group, formulas (32) and (33) give the mean and mean square angular momenta of fusion, respectively.

Having expressed the quantities in which we are interested in terms of the S-matrix elements for ES, we obtain the desired result. The S-matrix elements S_l can be obtained from an analysis of the corresponding differential cross section of ES according to the IWBCM with a renormalized DFP (if required). Nullifying the imaginary part of the OP (which is of the surface type in the IWBCM) and repeating the calculations, we obtain the S-matrix elements $\tilde{S}_l^{(0)}$. The S-matrix elements $S_l^{(0)}$ differ from $\tilde{S}_l^{(0)}$ only in that they are calculated with the nonrenormalized DFP.

Concluding the section, we note that the proposed method can also be realized on the basis of the optical model. In this case, complete absorption of particles in the interior region (i.e., in the region in which the reactions of the F group proceed intensely) must be ensured by the volume short-range imaginary part of the OP.

3. SENSITIVITY OF THE CALCULATED VALUES TO THE CHOICE OF OP PARAMETERS

In order to calculate the S-matrix elements S_l and $\tilde{S}_l^{(0)}$ required for the realization of the method, we must know the OP parameters. It is well known that, for subbarrier energies, none of these parameters can be fixed as a result of analysis of the experimental ES differential cross section. Consequently, the applicability of this method is confined to near-barrier and above-barrier energies. In this energy range, an analysis of ES angular distributions makes it possible to fix the normalization factor of the DFP and the diffuseness of the imaginary part of the OP (irrespective of its form) [12, 29]. However, its depth and radius cannot be fixed anyway. Consequently, the problem is reduced to an analysis of the sensitivity of the quantities being calculated to the choice of these parameters.

This problem was considered in detail in [2] for OP of the form

$$U(r) = V_{\mathrm{C}}(r) + N_F V_F(r) + iW_S(r). \tag{34}$$

Here, $V_{\mathrm{C}}(r)$ is the Coulomb potential of a uniformly charged sphere; $V_F(r)$ is the microscopic DFP with the normalization factor N_F; $W_S(r)$ is surface-type imaginary part of the OP,

$$W_S(r) = 4a_S \frac{d}{dr} \frac{-W_S^{(0)}}{1 + \exp[(r - R_S)/a_S]} \tag{35}$$
$$(W_S^{(0)} < 0),$$

of depth $W_S^{(0)}$, radius

$$R_S = r_S(A_P^{1/3} + A_T^{1/3}) \tag{36}$$

(A_P and A_T are the mass numbers of the projectile particle and the target nucleus, respectively), and diffuseness a_S. It should be noted that relation (34) does not contain the volume component of the imaginary part of the OP since volume absorption in the IWBCM is taken into account by choosing the solutions of the radial Schrödinger equation in the form of waves converging to the center over the corresponding distances. It was found in [2] that all probabilities and cross sections being calculated weakly depend on the specific choice of parameters $W_S^{(0)}$ and R_S if only the latter belong to the range of values providing an admissible description of the corresponding ES angular distributions.

4. RESULTS OF CALCULATIONS AND DISCUSSION

In this section, we describe and discuss the results of calculations for two systems, $^{16}\mathrm{O} + {}^{208}\mathrm{Pb}$ and $^{9}\mathrm{Be} + {}^{28}\mathrm{Si}$, the projectile ions being strongly bound in one system and weakly bound in the other. In order to verify the method, we selected a sample of data including, apart from the ES angular distributions, the experimental fusion cross sections $\sigma_{F,\mathrm{exp}}$ and/or the total cross sections $\sigma_{D,\mathrm{exp}}$ of quasi-elastic reactions. In some cases, the experimental values of total reaction cross sections $\sigma_{R,\mathrm{exp}}$ are also available. It should be noted that the data on fusion cross sections are concentrated in the energy region of projectile ions that extends up to 10 MeV/nucleon, where fusion dominates in the F group of reactions for the systems under investigation. This circumstance allows us to compare the calculated cross sections σ_F with $\sigma_{F,\mathrm{exp}}$. However, the calculations carried out by us cover a much wider energy range. For this reason, we will stipulate, whenever required, a possible admixture in the calculated cross sections σ_F from reactions differing from fusion.

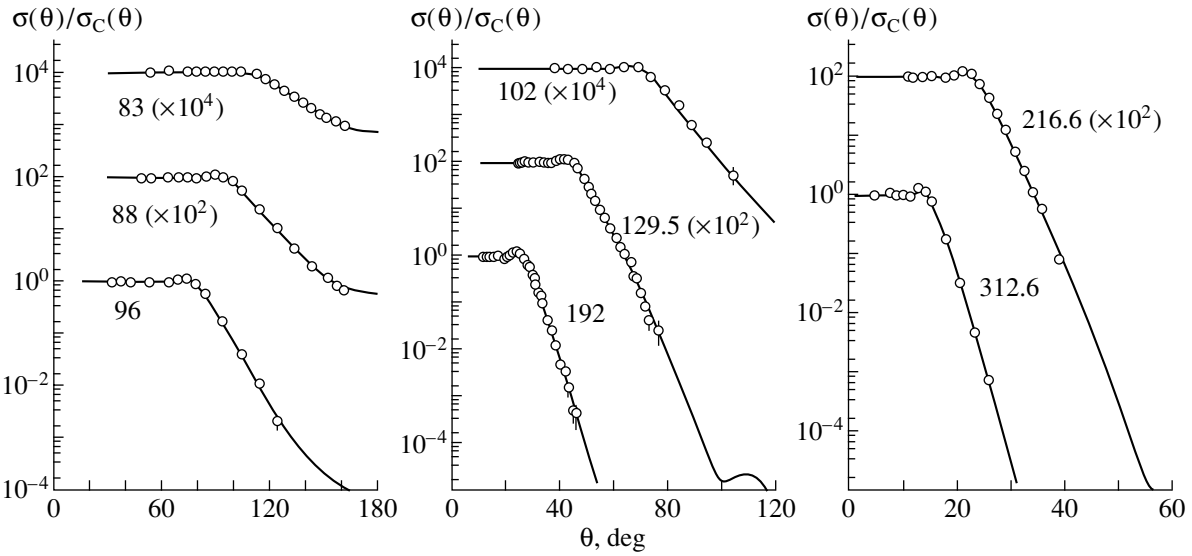

Fig. 2. Angular distributions for the elastic scattering of ^{16}O by ^{208}Pb. Energies of collision (in MeV) are indicated on the curves.

Calculations were made on the basis of the IWBCM model with the OP of the form (34)–(36). Since it is impossible to unambiguously fix the depth $W_S^{(0)}$ and radius R_S of the imaginary part of the OP by fitting the calculated value of the ES cross section to the experimental value, calculations were made for each energy value for several values of $W_S^{(0)}$, covering a wide range and leading to approximately the same correct description of the ES angular distributions. For each value of $W_S^{(0)}$, the cross sections σ_F, σ_D, etc., in which we are interested were calculated. Then we chose the minimal and maximal values for each cross section and determined their arithmetic mean, which was identified with the mean value of the corresponding cross section. The maximum deviation from the mean value in any direction was treated as the error in determining the given cross section.

The densities of colliding nuclei required for calculating the DFP were borrowed from [30] (^{16}O, ^{28}Si, ^{208}Pb) and [31] (^{9}Be).

4.1. $^{16}O + ^{208}Pb$ System

For the ^{16}O + ^{208}Pb system, an almost complete set of data we are interested in is available in the literature. We used the ES differential cross sections, fusion cross sections, and total cross sections of peripheral reactions measured in [32–35], [33, 36–39], and [33, 38, 40], respectively. In those publications where $\sigma_{F,\mathrm{exp}}$ and $\sigma_{D,\mathrm{exp}}$ were measured simultaneously for the same or close values of energy, the experimental values of the total reaction cross section obtained by simple summation of $\sigma_{F,\mathrm{exp}}$ and $\sigma_{D,\mathrm{exp}}$ are also presented. In [37, 41], the mean square angular momenta of fusion, $\langle L_F^2 \rangle_{\mathrm{exp}}$, were determined from an analysis of the angular distributions of fission fragments of ^{224}Th for several values of energy.

The results obtained for the system under investigation are presented in Tables 1 and 2 and in Figs. 2–6.

Table 1 contains energies E_{lab} of projectile ions

Table 1. OP parameters for the ^{16}O + ^{208}Pb system for $W_S^{(0)} = -25$ MeV

E_{lab}, MeV	$E_{\mathrm{c.m.}}/V_B$	N_F	r_S, fm	a_S, fm
82	0.99	1.91	1.311	0.286
83	1.01	1.69	1.287	0.341
88	1.07	1.57	1.263	0.372
90	1.09	1.39	1.235	0.435
94	1.14	1.44	1.247	0.421
96	1.16	1.38	1.230	0.446
102	1.24	1.32	1.226	0.448
129.5	1.57	1.18	1.156	0.643
192	2.33	1.07	1.164	0.616
216.6	2.63	0.84	1.137	0.604
312.6	3.79	0.87	1.075	0.708

Table 2. Comparison of calculated fusion cross sections, total cross sections of peripheral reactions, and total reaction cross sections with the experimental values for the $^{16}O + ^{208}Pb$ system (all cross sections are given in mb)

E_{lab}, MeV	s_{EF}	σ_{DF}	σ_F	$\sigma_{F,exp}$	σ_D	$\sigma_{D,exp}$	σ_R	$\sigma_{R,exp}$
82	4.42 ± 0.46	116.4 ± 22.4	121.1 ± 22.7	109 ± 11	78.8 ± 25.2	115 ± 22	199.9 ± 2.5	224 ± 33
83	9.10 ± 0.61	125.0 ± 24.6	133.8 ± 24.9	108 ± 10	133.1 ± 25.2	129 ± 18	266.1 ± 2.3	237 ± 28
88	147.9 ± 8.2	199.1 ± 10.7	346.4 ± 18.4	350 ± 40	164.0 ± 18.2	222 ± 31	508.7 ± 2.1	572 ± 71
90	232.7 ± 9.2	149.1 ± 15.8	379.7 ± 22.9	377 ± 50	252.5 ± 23.2	201 ± 25	634.5 ± 2.7	578 ± 75
94	378.1 ± 6.2	187.8 ± 3.4	565.9 ± 2.7	509 ± 50	250.6 ± 0.3	–	816.8 ± 2.7	–
96	448.0 ± 14.7	162.2 ± 13.7	604.6 ± 22.9	685 ± 70	297.1 ± 22.7	–	904.2 ± 4.2	–
102	647.9 ± 8.5	157.4 ± 5.5	805.2 ± 3.0	844 ± 90	313.7 ± 1.4	313 ± 28	1118.9 ± 2.8	1157 ± 118
129.5	1167.3 ± 41.0	109.6 ± 25.9	1276.9 ± 66.9	1315 ± 65	829.1 ± 69.0	–	2105.7 ± 3.2	–
192	1908.4 ± 21.7	20.1 ± 14.9	1923.9 ± 32.0	–	1046.2 ± 40.2	–	2970.1 ± 8.3	–
216.6	–	–	2021.5 ± 9.2	1916 ± 172	967.4 ± 6.7	–	2990.3 ± 4.0	–
312.6	–	–	2199.2 ± 33.9	–	1240.2 ± 27.1	1295 ± 194	3435.4 ± 10.8	–

^{16}O in the laboratory system, the ratios of energy E_{cm} in the center-of-mass system to the Coulomb barrier height V_B, and also the OP parameters obtained for $W_S^{(0)} = -25$ MeV. Some of the ES angular distributions are given in Fig. 2 in the form of the ratio of the ES cross section $\sigma(\theta)$ to the Coulomb scattering cross section $\sigma_C(\theta)$, where θ is the scattering angle in the center-of-mass system. It can be seen from Fig. 2 that we obtained a good description of the experimental ES angular distributions, which is a necessary condition for the applicability of the method.

Let us now consider fusion cross sections. It should be noted first of all that, for $E_{c.m.}/V_B \geq 2$, the normalization factor N_F of the DFP fluctuates about unity, which obviously reflects the errors in absolutization of the ES cross sections. In accordance with relations (17), (28), and (29), the cross section of multistep reactions in the F group fluctuates about zero. For this reason, for $E_{c.m.}/V_B \geq 2$, we did not single out the components σ_{EF} and σ_{DF} from σ_F, assuming simply that $\sigma_{DF} \equiv 0$ and $\sigma_F \equiv \sigma_{EF}$ in this energy range. It follows from Table 2 and Fig. 3*a* that the calculated cross sections σ_F coincide with the experimental fusion cross sections $\sigma_{F,exp}$ to within the errors. Figure 4*a* shows the ratios σ_{DF}/σ_F illustrating the role of multistep fusion processes in the formation of the total fusion cross section. It can be seen from the figure that, for barrier energies $E_{lab} = 82$ and 83 MeV, the contribution of multistep fusion to the fusion cross section exceeds 95%. However, the ratio σ_{DF}/σ_F sharply decreases with increasing energy. For example, for energy $E_{lab} = 90$ MeV, which is slightly higher than the Coulomb barrier, the contribution of multistep fusion processes to σ_F decreases to approximately 40%, while the corresponding contribution for a higher energy $E_{lab} = 129.5$ MeV amounts to approximately 10%.

These results are in accord with the modern concepts of the fusion mechanism for not very heavy nuclei, which were mainly obtained from calculations by the coupled-channel method (see, for example, [42–44]). It should be noted, however, that the calculations of the fusion cross section for the $^{16}O + ^{208}Pb$ system on the basis of the coupled-channel method are confined to the energy of $E_{lab} = 102$ MeV, while the method proposed here makes it possible to carry out calculations for much higher energies, for which the coupled-channel method is virtually inapplicable.

Figure 5 gives the mean $\langle L_F \rangle$ and the mean square $\langle L_F^2 \rangle$ angular momenta of reactions in the F group obtained by us and as the result of calculations based

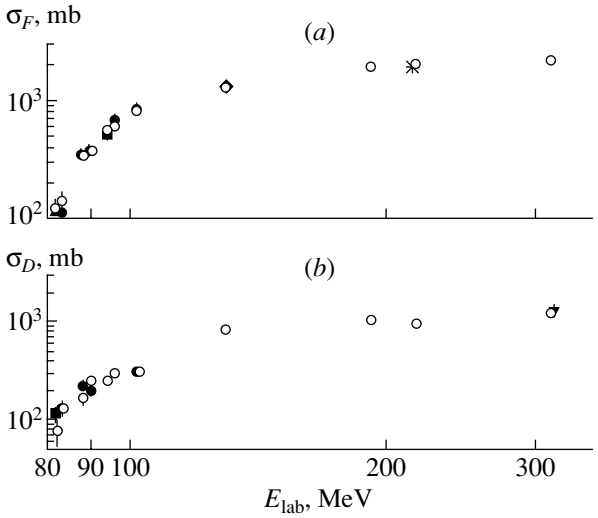

Fig. 3. Comparison of experimental results (dark symbols) with calculated values (○) of fusion cross sections (*a*) and total cross sections of peripheral reactions (*b*) for the $^{16}O + ^{208}Pb$ system. Experimental results were borrowed from [33] (●), [36] (*), [37] (♦), [38] (■), and [39] (▲).

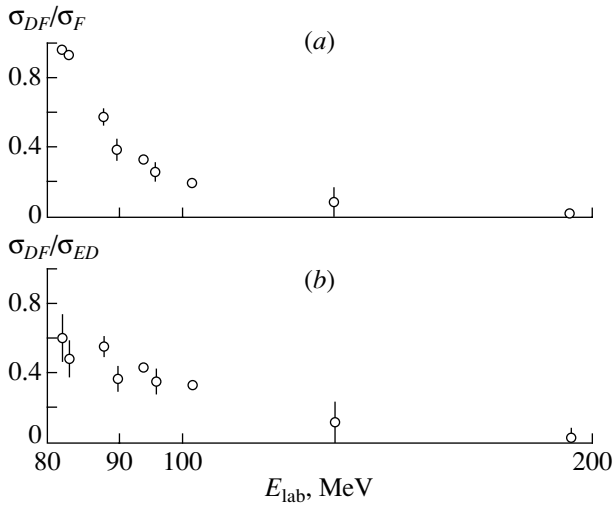

Fig. 4. Ratios σ_{DF}/σ_F (*a*) and σ_{DF}/s_{ED} (*b*) for the $^{16}O + ^{208}Pb$ system.

on the coupled-channel method [44], as well as experimental mean square angular momenta $\langle L_F^2 \rangle_{exp}$ of fusion borrowed from [37, 41]. Our values of $\langle L_F \rangle$ and $\langle L_F^2 \rangle$ are smaller by 10% and 15–20%, respectively, than the values calculated by the coupled-channel method. At the same time, a comparison of the values of $\langle L_F^2 \rangle$ calculated by us with the experimental values shows that the maximum discrepancy (reaching approximately 25%) is observed for the barrier energy of $E_{lab} = 83$ MeV and decreases with increasing energy. Indeed, the discrepancy does not exceed 15% for $E_{lab} = 90$ MeV and amounts to 8% for $E_{lab} \approx 215$ MeV. Moreover, it follows from Fig. 5*b* that, for energies $E_{lab} \geq 90$ MeV, the energy dependence of $\langle L_F^2 \rangle$ obtained by us is in good agreement with the experimental dependence. In principle, this situation is typical of all models in which it is assumed that fusion is determined by passage through the barrier formed by the sum of the Coulomb, centrifugal, and nuclear potentials (see, for example, [21, 43, 45, 46]). It should be noted that good agreement between the theoretical and experimental values of $\langle L_F^2 \rangle$ for $E_{lab} \approx 215$ MeV indicates that incomplete fusion and deep-inelastic collisions for the $^{16}O + ^{208}Pb$ system do not play any important role in reactions of the group *F* even in the case of such a high energy. However, their role may naturally increase at higher energies.

Discussing the possible reasons for the discrepancy between the theoretical and experimental values of the mean square angular momenta of fusion for near-barrier energies, we must mention the following two circumstances. First, we must consider the remark made in [47], according to which the discrepancy between the calculated (on the basis of other models) and experimental values of $\langle L_F^2 \rangle$ may be (at least, partly) due to distortions of angular distributions of fission fragments, from which the experimental values of $\langle L_F^2 \rangle$ are determined, as a result of evaporation of preequilibrium neutrons, as well as preequilibrium and sequential fission. Second, in ac-

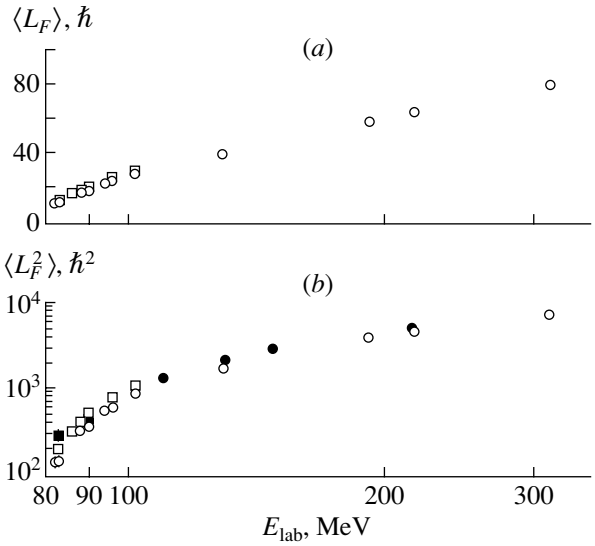

Fig. 5. Mean (*a*) and mean square (*b*) angular momenta of fusion for the $^{16}O + ^{208}Pb$ system: light symbols correspond to calculations made in [44] (□) and to our calculations (○); dark symbols correspond to the experimental results obtained in [37] (●) and in [41] (■).

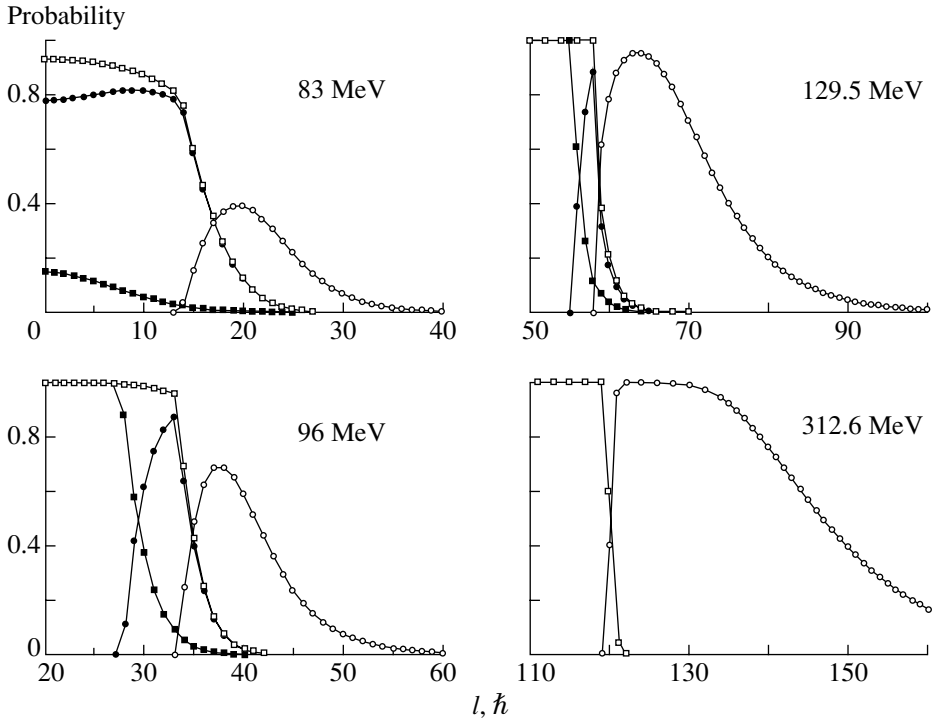

Fig. 6. Total partial probabilities $P_{l,EF}$ (■), $P_{l,DF}$ (●), $P_{l,F}$ (□) and $P_{l,D}$ (○) for the $^{16}O + ^{208}Pb$ system.

cordance with formula (14), the normalization factor N_F of the DFP must depend on l. However, our results were obtained with N_F independent of the angular momentum. Thus, the introduction of an l-dependent N_F may improve the agreement between the calculated and experimental values of $\langle L_F^2 \rangle$. Yet, a different viewpoint on the formation of spin distributions of fusion also exists [21, 48]. According to this viewpoint, the increase in $\langle L_F^2 \rangle$ is associated with the long-range component of the imaginary part of the OP, which is responsible for fusion.

Let us now consider the total cross sections of peripheral reactions. Table 2 and Fig. 3*b* show that the values of σ_D and $\sigma_{D,\mathrm{exp}}$ virtually coincide to within their errors in all cases. Figure 4*b* shows the ratios σ_{DF}/σ_{ED} demonstrating suppression of peripheral reactions due to the fact that part of the transitions in the peripheral region culminate at the second stage by the excitation of reactions in the F group. It follows from the figure that the suppression of peripheral reactions for near-barrier energies attains 50–60%. As the energy increases, the ratio σ_{DF}/σ_{ED} decreases, but not as sharply as σ_{DF}/σ_F.

It should also be noted that the total reaction cross sections σ_R obtained from an analysis of ES coincide with the experimental values $\sigma_{R,\mathrm{exp}}$ and with the sum of cross sections σ_F and σ_D to within the errors of measurements. It should be recalled, however, that the relation $\sigma_F + \sigma_D = \sigma_R$ holds exactly for fixed $W_S^{(0)}$.

Let us now consider the probabilities $P_{l,EF}$, $P_{l,DF}$, $P_{l,F}$, and $P_{l,D}$ presented in Fig. 6 for several values of energy that cover the entire energy range considered here. It can be seen from the figure that an increase in energy leads to an increase in the maximal value of $P_{l,F}$, which gradually attains a value of $P_{l,F} \approx 1$. The range of angular momenta contributing to the fusion cross section (and, probably, to other reaction channels in the F group at the highest energies) increases simultaneously. In addition, the higher the energy, the steeper the right slope of $P_{l,F}$, so that the shape of the distribution $P_{l,F}$ in partial waves tends to a rectangular step upon an increase in energy.

The spin distributions of $P_{l,D}$ have the form of an asymmetric peak whose height and width increase with energy up to the value of $E_{\mathrm{lab}} = 192$ MeV (not shown in the figure). For $E_{\mathrm{lab}} = 192$ MeV, the peak value of $P_{l,D}$ attains the value of $P_{l,D} \approx 1$. A further increase in energy expands the range of angular momenta for which $P_{l,D} \approx 1$. Figure 6 also shows that the left slope of $P_{l,D}$ becomes steeper and steeper, while its right slope becomes more gently inclined, upon an increase in energy.

An interesting feature of the distributions of $P_{l,F}$ and $P_{l,D}$ is that their overlap region becomes narrower with increasing energy. This means that, as

energy of collision of two nuclei increases, fusion and peripheral reactions occur more and more independently.

Figure 6 also gives furnishes information about the energy dependence of the distribution of the probabilities $P_{l,DF}$ and $P_{l,EF}$ in partial waves and about the role of these distributions in the formation of $P_{l,F}$ and $P_{l,D}$. It can be seen from the figure that the shape of each of the distributions $P_{l,DF}$ and $P_{l,EF}$ for the energy of $E_{\text{lab}} = 83$ MeV resembles a Fermi step, but the distribution of $P_{l,F}$ is mainly formed at the expense of $P_{l,DF}$. However, $P_{l,DF}$ acquires a nearly symmetric pick-like shape upon an increase in energy, the height of this distribution first increasing and then decreasing abruptly. For the energy of $E_{\text{lab}} =$ 192 MeV, the contribution of $P_{l,DF}$ to $P_{l,F}$ can already be disregarded.

At the same time, it can easily be seen that the distribution $P_{l,EF}$ becomes broader upon an increase in energy, and the value of $P_{l,EF} \approx 1$ is attained for larger and larger number of waves. Thus, with increasing energy, $P_{l,F}$ is formed at the expense of $P_{l,EF}$ to a greater and greater extent.

The results presented in Fig. 6 show that the distribution of $P_{l,DF}$ forms the high-spin part of $P_{l,F}$ in the energy range in which multistep fusion plays a significant role. However, since $P_{l,DF}$ for strongly bound ions is part of the TPP of particle escape from the entrance channel in the peripheral region [see formula (20)], $P_{l,DF}$ is the low-spin component of $P_{l,ED}$ in accordance with the figure. Consequently, the suppression of peripheral reactions accompanying the enhancement of fusion in the case of strongly bound ions is associated with the transition of particles from reactions of group D to reactions of group F in the partial waves corresponding to the low-spin component of $P_{l,ED}$.

It is interesting to note that, although the results presented in Fig. 6 were obtained with the normalization factor N_F of the DFP, independent of the angular momentum, these results necessitate the application of an l-dependent N_F; it can be seen that renormalization of the DFP is required for a bounded interval of angular momenta.

4.2. ^{9}Be + ^{28}Si System

For the ^{9}Be + ^{28}Si system, rich information on the ES differential cross sections is available [49–51]. Measurements were also made for fusion and total cross sections of direct reactions [51, 52] for the same energies as for ES (or, at least, for close energies). The experimental values of the total reaction cross section $\sigma_{R,\text{exp}}$ can be determined by summing $\sigma_{F,\text{exp}}$ and $\sigma_{D,\text{exp}}$.

Table 3. OP parameters for the ^{9}Be + ^{28}Si system at $W_S^{(0)} = -30$ MeV

E_{lab}, MeV	$E_{\text{c.m.}}/V_B$	N_F	r_S, fm	a_S, fm
12	1.10	0.76	1.195	0.560
14	1.28	0.54	1.041	0.684
17	1.55	0.56	1.025	0.679
20	1.83	0.42	0.905	0.765
23	2.10	0.46	0.944	0.718
26	2.37	0.52	0.953	0.750
30	2.74	0.43	0.897	0.756
45	4.11	0.55	0.925	0.760
60	5.47	0.40	0.960	0.723
121.0	11.0	0.45	0.862	0.882
201.6	18.4	0.48	0.815	0.919

The results obtained for the ^{9}Be + ^{28}Si system are presented in Tables 3 and 4 and in Figs. 7–11.

In Table 3, the values of the OP parameters determined for $W_S^{(0)} = -30$ MeV are indicated for each energy value. The theoretical curves depicted in Fig. 7 show that these curves are in accord with the experimental angular distributions for the elastic scattering of ^{9}Be on ^{28}Si.

The results concerning the fusion cross sections are given in Table 4 and in Fig. 8*a*. A comparison of the calculated fusion cross sections σ_F with the experimental cross sections shows that their values agree to within the measurement errors in most cases. For the energies of $E_{\text{lab}} = 45$ and 60 MeV, the discrepancy between σ_F and $\sigma_{F,\text{exp}}$ amounts approximately to 7–10%. It follows from Fig. 8*a*, however, that the fusion cross sections calculated for the two energy values considered agree with the experimental ones for other energies quite close to the energies of interest. In addition, the fusion cross section obtained for the energy of $E_{\text{lab}} = 30$ MeV in [52] is approximately equal to half the value of cross section obtained in [51] and calculated by us. All this indicates an error, which was not taken into account in [52].

Table 4. Comparison of the calculated fusion cross sections, total cross sections of peripheral reactions, and total reaction cross sections with experimental values for the $^{9}Be + {}^{28}Si$ system (all cross sections are given in mb)

E_{lab}, MeV	s_{EF}	σ_{HF}	σ_F	$\sigma_{F,exp}$	σ_D	$\sigma_{D,exp}$	σ_R	$\sigma_{R,exp}$
12	214.2 ± 1.5	82.0 ± 32.6	132.4 ± 31.3	150 ± 50	158.1 ± 31.7	–	290.2 ± 0.7	–
14	482.3 ± 2.9	198.4 ± 39.5	288.8 ± 38.1	310 ± 60	305.8 ± 42.9	330 ± 50	586.8 ± 6.6	640 ± 70
17	780.0 ± 3.3	238.4 ± 57.6	541.6 ± 54.3	560 ± 80	365.1 ± 55.4	–	906.2 ± 1.7	–
20	961.7 ± 2.4	309.6 ± 9.6	652.2 ± 7.2	680 ± 70	449.0 ± 4.6	390 ± 40	1101.2 ± 2.6	1070 ± 60
23	1091.2 ± 1.0	311.9 ± 33.3	779.3 ± 32.3	900 ± 90	463.9 ± 36.9	–	1243.0 ± 4.8	–
26	1196.5 ± 0.7	335.1 ± 40.4	861.4 ± 39.9	940 ± 90	590.9 ± 46.2	455 ± 40	1453.1 ± 7.1	1395 ± 80
30	1270.3 ± 0.3	408.3 ± 41.0	862.2 ± 40.9	950 ± 90	605.2 ± 51.9	575 ± 60	1467.3 ± 11.1	1525 ± 90
45	1382.8 ± 0.5	568.8 ± 0.5	818.1 ± 0.1	600 ± 155	961.2 ± 19.6	–	1779.3 ± 19.6	–
60	1385.5 ± 2.4	614.4 ± 2.3	771.7 ± 3.9	1100 ± 250	1049.9 ± 12.9	–	1821.2 ± 9.4	–
121.0	1077.7 ± 0.1	654.8 ± 1.4	422.9 ± 1.4	–	1616.7 ± 17.3	–	2039.3 ± 18.4	–
201.6	635.7 ± 11.2	381.2 ± 13.0	265.7 ± 13.0	–	1731.0 ± 17.0	–	1983.7 ± 17.1	–

Since incomplete fusion and deep-inelastic collisions may occur with an appreciable probability in the system under investigation for energies $\geq$10 MeV/nucleon of projectile ions in the F-group reactions, it cannot be ruled out that the cross sections σ_F calculated for the two highest energies of $E_{lab} = 121.0$ and 201.6 MeV include the above-mentioned reactions also.

Figure 9*a* shows the ratios σ_{HF}/σ_{EF} reflecting the role of virtual excitations in the suppression of fusion in collisions of weakly bound ions with nuclei. It can be seen from the figure that virtual excitations reduce the fusion cross section by 30–40% on average up to the energy of $E_{lab} = 60$ MeV, while the decrease for the highest energies may reach 60%. Thus, the energy dependence of σ_{HF}/σ_{EF} is rather weak. A completely different situation is observed in the opposite case of enhancement of fusion for strongly bound ions, where the energy dependence of the ratio σ_{DF}/σ_F, reflecting the role of multistep fusion processes in the formation of the fusion cross section, is very strong (see Fig. 4*a* for the $^{16}O + {}^{208}Pb$ system).

Let us consider the mean and mean square angular momenta of fusion. Experimental data on these quantities are not available for the given system. For this reason, Fig. 10 shows only the results of calculations. We can only state in the present case that the calculated values of $\langle L_F \rangle$ and $\langle L_F^2 \rangle$ vary smoothly with energy and attain saturation starting from approximately 80 MeV. It can also be noted that the values of $\langle L_F \rangle$ and $\langle L_F^2 \rangle$ calculated for $E_{lab} = 121.0$ and 201.6 MeV may prove to be exaggerated in relation to the mean and mean square angular momenta of fusion if incomplete fusion and deep-inelastic collisions make a noticeable contribution to the cross section of F-group reactions for these energies.

The results on total cross sections of peripheral reactions are given in Table 4 and in Fig. 8*b*. A comparison of the calculated values of the cross section σ_D with the experimental cross sections $\sigma_{D,exp}$ shows that these values agree in three cases out of four to within the error of measurements. The discrepancy between σ_D and $\sigma_{D,exp}$ attains approximately 10% only in one case, for $E_{lab} = 26$ MeV.

For energies $E_{lab} > 30$ MeV, no data are available for comparison with the calculated values of σ_D. Nevertheless, we may assume that these calculated

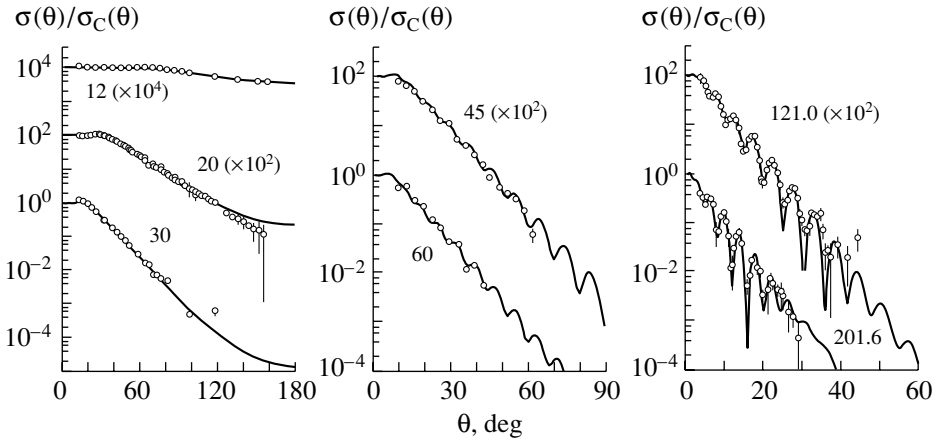

Fig. 7. Angular distributions for the elastic scattering of ^{9}Be on ^{28}Si. Collision energies (in MeV) are indicated on the curves.

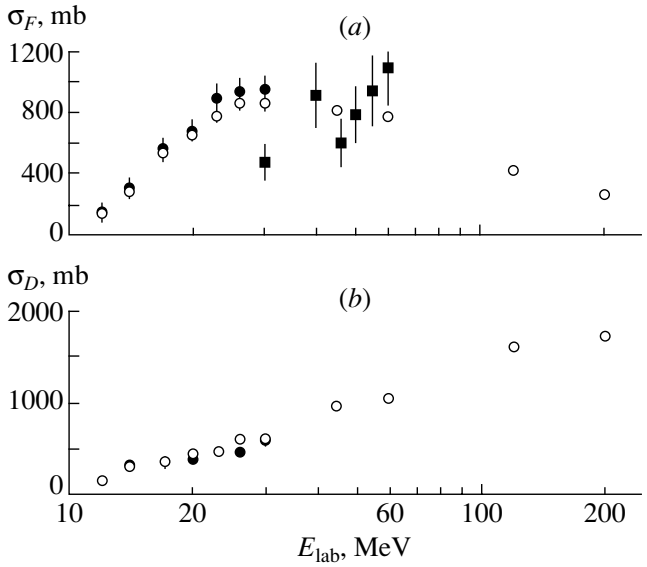

Fig. 8. Comparison of experimental (dark symbols) and calculated (○) fusion cross sections (*a*) and total cross sections of peripheral reactions (*b*) for the ^{9}Be + ^{28}Si system. The displayed experimental results were borrowed from [51] (●) and [52] (■).

values are reliable since their energy dependence is reasonable. Indeed, the cross section σ_D increases rather smoothly with energy, its growth being moderated between $E_{\rm lab} = 121.0$ and 201.6 MeV, which indicates the possible saturation at an energy of $E_{\rm lab} \approx 200$ MeV.

Since the suppression of fusion for weakly bound ions is accompanied by a simultaneous enhancement of peripheral reactions (see Section 2), the ratios σ_{HF}/σ_D shown in Fig. 9*b* may serve as a quantitative characteristic of this enhancement. It can be seen from the figure that the increase in the cross section of peripheral reactions in a wide energy range (up to the energy of $E_{\rm lab} = 60$ MeV) amounts on average to 60%. For the energies of $E_{\rm lab} = 121.0$ and 201.6 MeV, the ratio σ_{HF}/σ_D decreases to 40 and 20%, respectively. This is due to the fact that the cross section σ_{EF} incorporating σ_{HF} decreases upon an increase in energy, while the value of σ_D continues to increase or at least attains saturation.

It should be noted that, in all cases, the sum of σ_F and σ_D agrees, to within the errors, with the reactions cross sections σ_R obtained from an analysis of ES and with the experimental reaction cross sections $\sigma_{R,\rm exp}$.

Proceeding to discuss the TPP of various processes, we note that it is convenient to consider the probabilities $P_{l,F}$, $P_{l,HF}$, $P_{l,ED}$, and $P_{l,D}$ in the case of weakly bound ions. Figure 11 shows these probabilities for several energy values considered here, from the lowermost to an essentially above-barrier value. It should be noted from the outset that the properties of the distributions of $P_{l,F}$ and $P_{l,D}$ obtained for

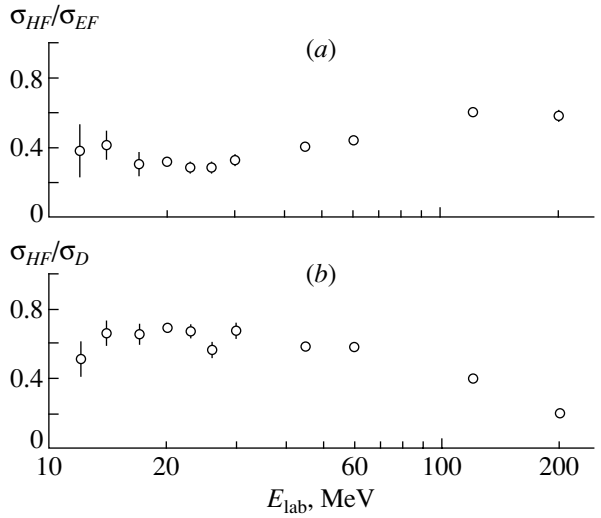

Fig. 9. Ratios σ_{HF}/s_{EF} (a) and σ_{HF}/σ_D (b) for the ^{9}Be + ^{28}Si system.

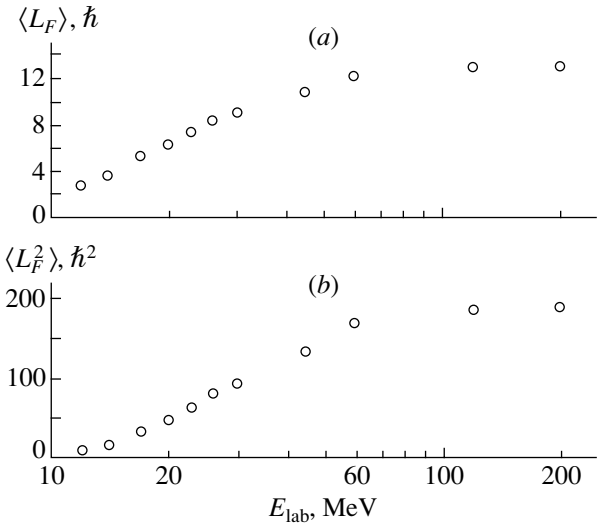

Fig. 10. Mean (a) and mean square (b) angular momenta of fusion for the ^{9}Be + ^{28}Si system.

the ^{9}Be + ^{28}Si system are similar to the properties of these distributions obtained for the ^{16}O + ^{208}Pb system. The only difference is that the upper boundary of angular momenta contributing to fusion in the case under investigation increases with energy up to 60 MeV, after which the growth is terminated. This is not observed for the ^{16}O + ^{208}Pb system (see Fig. 6). However, this difference is only due to the fact that the interval of values of $E_{\text{c.m.}}/V_B$ for the ^{9}Be + ^{28}Si system is much wider than for the ^{16}O + ^{208}Pb system.

Let us now consider the spin distributions of $P_{l,HF}$ and $P_{l,ED}$ and analyze their role in the formation of $P_{l,F}$ and $P_{l,D}$ in the case of weakly bound particles. It follows from Fig. 11 that the distribution of $P_{l,HF}$ has the shape of an almost symmetric peak whose height increases with energy, its width remaining approximately constant up to $E_{\text{lab}} = 60$ MeV. Starting from 60 MeV, a value of $P_{l,HF} \approx 1$ is attained for larger and larger number of orbital angular momenta, while the width of the distribution increases, its shape approaching a rectangular one more and more closely. In this case, the distribution of $P_{l,ED}$ for all energies has the form of an asymmetric peak whose height, width, and asymmetry increase with energy. Starting from $E_{\text{lab}} = 121.0$ MeV, a value of $P_{l,ED} \approx 1$ is attained for larger and larger number l. Thus, the properties of distributions of the probabilities $P_{l,ED}$ and $P_{l,D}$ in partial waves are completely analogous. The contributions of the probabilities $P_{l,HF}$ and $P_{l,ED}$ to the formation of the spin distribution of $P_{l,D}$ are comparable up to the energy of $E_{\text{lab}} = 121.0$ MeV, but, starting from $E_{\text{lab}} = 121.0$ MeV, the contribution of $P_{l,ED}$ becomes predominant.

The results presented in Fig. 11 show that the low-spin part of $P_{l,D}$ is formed at the expense of $P_{l,HF}$. However, since $P_{l,HF}$ is part of $P_{l,EF}$ in the case of weakly bound particles [see formula (25)], $P_{l,HF}$ is the high-spin component of this distribution in accordance with Fig. 11. Consequently, the suppression of fusion (in the general case of group-F reactions) accompanied by enhancement of peripheral reactions in the case of weakly bound ions is associated with the escape of particles from the channel of direct excitation of F-group reactions in the high-spin component of $P_{l,EF}$.

Since the renormalization of the DFP in the case of ES of weakly bound ions is determined by the range of angular momenta in which $P_{l,HF} \neq 0$, it follows from Fig. 11 that the normalization factor N_F of the DFP must depend on l; the renormalization is required for a bounded interval of angular momenta.

5. CONCLUSIONS

We have proposed a new approach to the analysis of the angular distribution of elastic scattering of heavy ions, which provides much more information as compared to the traditional optical model. In particular, the method makes it possible to calculate the total cross section σ_F of fusion, incomplete fusion, quasifission, and deep-inelastic collisions, as well as the total cross section σ_D of peripheral reactions. It also provides, on a unified basis, the explanation for the mechanism of formation of σ_F and σ_D both for strongly bound and for weakly bound heavy ions. Incomplete fusion, quasifission, and deep-inelastic collisions can be neglected for nuclei with $Z_P Z_T \leq 1000$ for collision energies up to 10 MeV/nucleon.

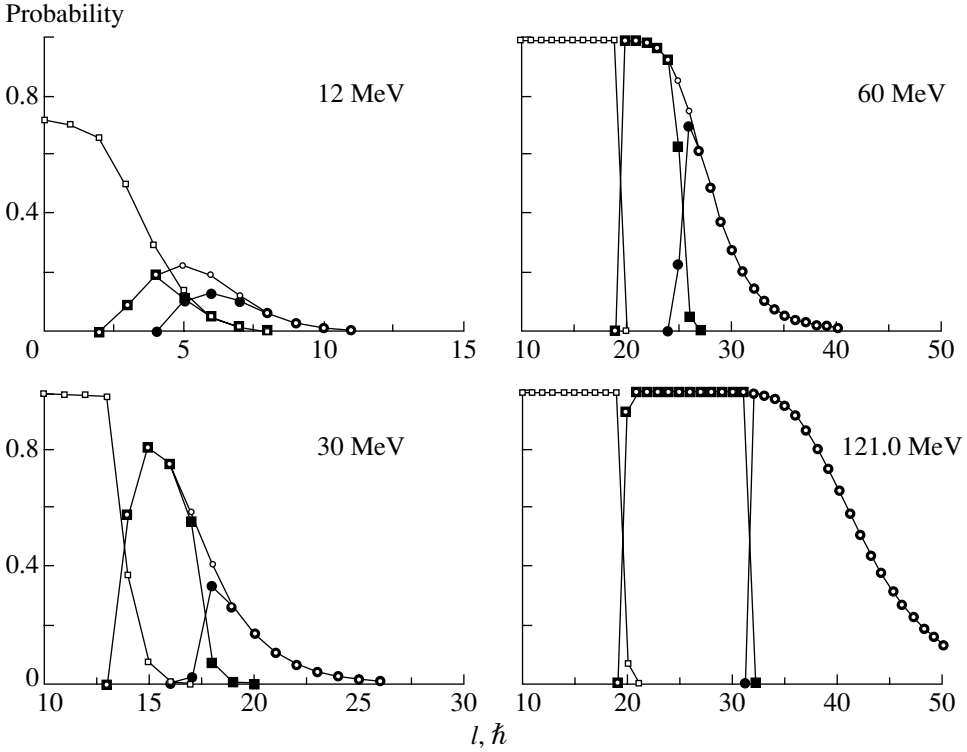

Fig. 11. Total partial probabilities $P_{l,F}$ (□), $P_{l,HF}$ (■), $P_{l,ED}$ (●), and $P_{l,D}$ (○) for the ^{9}Be + ^{28}Si system.

Consequently, cross sections σ_F calculated in this case are fusion cross sections.

We have established a close relation between multistep fusion processes and the threshold anomaly (enhancement of the real part of the OP for subbarrier and near-barrier energies) for strongly bound ions, on one hand, and virtual excitations (virtual breakup) and attenuation of the real part of the OP for weakly bound ions, on the other hand.

It has been shown that the enhancement of fusion is accompanied by the suppression of peripheral reactions and, vice versa, the suppression of fusion is accompanied by the enhancement of peripheral reactions. The method developed by us makes it possible to calculate the quantitative characteristics for the enhancement of fusion (and, accordingly, the suppression of peripheral reactions) for strongly bound ions and, conversely, the suppression of fusion (and, accordingly, the enhancement of peripheral rections) for weakly bound ions. This is so both for total cross sections and for partial probabilities.

The calculations made for two systems, ^{16}O + ^{208}Pb and ^{9}Be + ^{28}Si, the projectile ion being strongly bound in one of these systems and weakly bound in the other, proved that the calculated fusion cross sections and the total cross sections of peripheral reactions are in good agreement with the available experimental cross sections. The discrepancy between the theory and experiment is observed only for the mean square fusion angular momenta for near-barrier energies. This apparently necessitates the introduction of an l-dependent normalization factor in the DFP.

For the above systems, we have studied the role of multistep fusion and virtual excitations in the formation of fusion cross sections (in the general case, the total cross section of fusion, incomplete fusion, quasifission, and deep-inelastic collisions) and the total cross section of peripheral reactions as well as the energy dependence of spin distributions of probabilities of various processes occurring in the collisions of ^{16}O with ^{208}Pb and ^{9}Be with ^{28}Si.

It should be emphasized that the method developed by us is an alternative to a more complex and laborious coupled-channel method, requiring a large body of input data. The latter method can hardly be employed for heavy ions and for energies noticeably exceeding the Coulomb barrier height. At the same time, the application of our method does not involve considerable difficulties (other conditions being equal).

If the required ES angular distributions are available, the method can be used to calculate σ_F and σ_D for reactions involving unstable nuclei, for which a direct measurement of these cross sections is impeded by a low intensity of secondary beams.

ACKNOWLEDGMENTS

The author wishes to express his sincere gratitude to R.S. Poznyak for his help in preparing this paper.

REFERENCES

1. Yu. A. Pozdnyakov and K. O. Terenetsky, in *Proceedings of First Kiev International School on Nuclear Physics, 1990* (Naukova Dumka, Kiev, 1991), p. 461.
2. Yu. A. Pozdnyakov and K. O. Terenetskiĭ, Yad. Fiz. **53**, 400 (1991) [Sov. J. Nucl. Phys. **53**, 249 (1991)].
3. Yu. A. Pozdnyakov, K. O. Terenetsky, and I. V. Borodavko, Yad. Fiz. **59**, 257 (1996) [Phys. At. Nucl. **59**, 238 (1996)].
4. Yu. A. Pozdnyakov and K. O. Terenetsky, in *Proceedings of the Fourth International Conference on Radioactive Nuclear Beams, Omiya, Japan, 1996* (RNB4 Organizing Committee, Omiya, 1996), p. 131.
5. V. M. Strutinsky, Nucl. Phys. **68**, 221 (1965).
6. G. H. Rawitscher, Nucl. Phys. **85**, 337 (1966).
7. Y. Eisen and Z. Vager, Nucl. Phys. A **187**, 219 (1972).
8. G. N. Afanas'ev and V. M. Shilov, Yad. Fiz. **26**, 92 (1977) [Sov. J. Nucl. Phys. **26**, 48 (1977)].
9. V. I. Belyak, Izv. Akad. Nauk SSSR, Ser. Fiz. **43**, 2429 (1979).
10. Yu. A. Pozdnyakov and K. O. Terenetskiĭ, Izv. Akad. Nauk SSSR, Ser. Fiz. **47**, 2187 (1983).
11. V. P. Verbitskiĭ, A. P. Il'in, Yu. A. Pozdnyakov, and K. O. Terenetskiĭ, Izv. Akad. Nauk SSSR, Ser. Fiz. **49**, 945 (1985).
12. G. R. Satchler and W. G. Love, Phys. Rep. **55**, 183 (1979).
13. U. Mosel, in *Treatise on Heavy-Ion Science* (Plenum, New York, 1984), Vol. 2, p. 3.
14. W. U. Schröder and J. R. Huizenga, in *Treatise on Heavy-Ion Science* (Plenum, New York, 1984), Vol. 2, p. 115.
15. C. K. Gelbke and D. H. Boal, Prog. Part. Nucl. Phys. **19**, 33 (1987).
16. C. E. Aguiar, V. C. Barbosa, C. H. Dasso, and R. Donangelo, Phys. Rev. C **46**, R45 (1992).
17. H. Fuchs and K. Möhring, Rep. Prog. Phys. **57**, 231 (1994).
18. L. C. Vaz, J. M. Alexander, and G. R. Satchler, Phys. Rep. C **69**, 373 (1981).
19. M. Beckerman, Phys. Rep. **129**, 145 (1985).
20. C. Mahaux, H. Ngô, and G. R. Satchler, Nucl. Phys. A **449**, 354 (1986).
21. G. R. Satchler, Phys. Rep. **199**, 147 (1991).
22. N. Keeley, J. A. Christley, N. M. Clarke, *et al.*, Nucl. Phys. A **582**, 314 (1995).
23. M. Yahiro, M. Nakano, Y. Iseri, and M. Kamimura, Prog. Theor. Phys. **67**, 1467 (1982).
24. Y. Sakuragi, M. Yahiro, and M. Kamimura, Prog. Theor. Phys. **70**, 1047 (1983).
25. Y. Sakuragi, Phys. Rev. C **35**, 2161 (1987).
26. K. Katori, T. Shimoda, T. Fukuda, *et al.*, Nucl. Phys. A **480**, 323 (1988).
27. M. C. S. Figueira, E. M. Szanto, A. S. de Toledo, *et al.*, Phys. Rev. C **46**, 1139 (1992).
28. M. C. S. Figueira, E. M. Szanto, R. M. Anjos, *et al.*, Nucl. Phys. A **561**, 453 (1993).
29. Yu. A. Pozdnyakov and K. O. Terenetskiĭ, Ukr. Fiz. Zh. **35**, 1158 (1990).
30. A. K. Chaudhuri, Nucl. Phys. A **459**, 417 (1986).
31. G. D. Alkhazov, S. L. Belostotskiĭ, A. A. Vorob'ev, *et al.*, Pis'ma Zh. Éksp. Teor. Fiz. **29**, 88 (1979) [JETP Lett. **29**, 80 (1979)].
32. J. B. Ball, C. B. Fulmer, E. E. Gross, *et al.*, Nucl. Phys. A **252**, 208 (1975).
33. F. Videbaek, R. B. Goldstein, L. Grodzins, *et al.*, Phys. Rev. C **15**, 954 (1977).
34. S. C. Pieper, M. H. Macfarlane, D. H. Gloeckner, *et al.*, Phys. Rev. C **18**, 180 (1978).
35. C. Olmer, M. Mermaz, M. Buenerd, *et al.*, Phys. Rev. C **18**, 205 (1978).
36. L. C. Vaz, D. Logan, E. Duek, *et al.*, Z. Phys. A **315**, 169 (1984).
37. B. B. Back, R. B. Betts, J. E. Gindler, *et al.*, Phys. Rev. C **32**, 195 (1985).
38. E. Vulgaris, L. Grodzins, S. G. Steadman, and R. Ledoux, Phys. Rev. C **33**, 2017 (1986).
39. C. R. Morton, D. J. Hinde, J. R. Leigh, *et al.*, Phys. Rev. C **52**, 243 (1995).
40. M. Buenerd, C. K. Gelbke, B. G. Harvey, *et al.*, Phys. Rev. Lett. **37**, 1191 (1976).
41. R. Vandenbosch, *ANL-PHYS-86-1* (Argonne National Laboratory, 1986), p. 155.
42. S. G. Steadman and M. J. Rhoades-Brown, Annu. Rev. Nucl. Part. Sci. **36**, 649 (1986).
43. G. R. Satchler, M. A. Nagarajan, J. S. Lilley, and I. J. Thompson, Ann. Phys. (N.Y.) **178**, 110 (1987).
44. I. J. Thompson, M. A. Nagarajan, J. S. Lilley, and M. J. Smithson, Nucl. Phys. A **505**, 84 (1989).
45. N. Vinh Mau, J. C. Pacheco, J. L. Ferrero, and R. Bilwes, Nucl. Phys. A **560**, 879 (1993).
46. S. V. S. Sastry, S. K. Kataria, A. K. Mohanty, and I. J. Thompson, Phys. Rev. C **54**, 3286 (1996).
47. C. V. K. Baba, Nucl. Phys. A **553**, 719c (1993).
48. G. R. Satchler, M. A. Nagarajan, J. S. Lilley, and I. J. Thompson, Phys. Rev. C **41**, 1869 (1990).
49. J. S. Eck, T. R. Ophel, P. D. Clark, and D. C.Weisser, Nucl. Phys. A **334**, 519 (1980).
50. M. S. Zisman, J. G. Cramer, D. A. Goldberg, *et al.*, Phys. Rev. C **21**, 2398 (1980).
51. M. Hugi, J. Lang, R. Müller, *et al.*, Nucl. Phys. A **368**, 173 (1981).
52. J. S. Eck, J. R. Leigh, T. R. Ophel, and P. D. Clark, Phys. Rev. C **21**, 2352 (1980).

Translated by N. Wadhwa

Physics of Atomic Nuclei, Vol. 65, No. 10, 2002, pp. 1843–1846. Translated from Yadernaya Fizika, Vol. 65, No. 10, 2002, pp. 1894–1897.

ELEMENTARY PARTICLES AND FIELDS
Experiment

Longitudinal Development of Giant Air Showers and Problem of Estimating the Energy of Primary-Cosmic-Ray Particles

E. E. Antonov[1)], L. G. Dedenko[1)*], A. A. Kirillov, T. M. Roganova, G. F. Fedorova, and E. Yu. Fedunin[1)]

Institute of Nuclear Physics, Moscow State University, Vorob'evy gory, Moscow, 119899 Russia

Received July 25, 2001; in final form, February 6, 2002

Abstract—The attenuation length for the charged-particle density at a distance of 600 m from the shower axis may differ from that adopted in experimental investigations by 40–50%. This casts some doubt on experimental estimates previously obtained for the energy of primary-cosmic-ray particles in the region of ultrahigh energies. © *2002 MAIK "Nauka/Interperiodica"*.

INTRODUCTION

In order to estimate the energies of giant air showers, use is made of the charged-particle density at the distance of $r = 600$ m from the shower axis, $\rho(600)$. The value of this classification parameter, which was first proposed by Hillas [1], is determined in a specific shower for a zenith angle θ and is then rescaled for the vertical direction ($\theta = 0^\circ$); this rescaled value enters into the formula that is employed to estimate the energy in question and which is substantiated either experimentally (the calorimetry method, which is applied at the Yakutsk EAS array [2]) or computationally (at the AGASA array [3]). Since each giant air shower is an individual event and since the parameter $\rho(600)$ is rescaled for some average set of showers on the basis of the attenuation length λ as determined by the method of the section of the spectra by equal-intensity lines [4], there naturally arises the problem of estimating the error in such rescaling. Since this problem is very complicated, one can compare, at the first step, the values of the attenuation length that are obtained in the calculations for the charged-particle density at the distance of 600 m in an individual and an average shower with each other, on one hand, and with those that are given by the method proposed in [4] and those that are actually employed in [2, 3], on the other hand. This is one of the objectives of the present study. There is yet another problem, that of whether the model of quark–gluon strings (also known as the QGS model or QGSM) [5], which is used in the calculations, conforms to direct experimental data. A giant air shower of energy $E = 3.2 \times 10^{20}$ eV was recorded at the Fly's Eye array [6]. The method of recording fluorescent light from the shower makes it possible to reconstruct the cascade curve for this individual event. A determination of the degree to which the computed profiles of showers (an average shower and individual ones) can reproduce the above individual curve is another objective of our study. It is also of interest to approximate individual cascade curves calculated for the total number of particles and for charged-particle density on the basis of the QGS model with allowance for the Landau–Pomeranchuk–Migdal effect [7]. In addition, we would like to note the following: it was shown in [8] that, if one compares the results that perturbative QCD and the standard QGS model yield for the multiplicity of secondaries from an event of hadron interaction at high energies, it turns out that the rate at which this multiplicity grows with energy is not higher in perturbative QCD than in the QGS model. As a limiting case, we will consider, however, an additional version of the hadron-interaction model, that which was considered in [9, 10]. This version relies on the QGS model up to the threshold energy of $E_{\rm thr} = 10^{16}$ eV and employs the following law for the multiplicity n of secondaries at higher values of the energy E_0 of primary particles:

$$n = \sqrt{2E_0 m}/E_{\rm c.m.}. \qquad (1)$$

Here, m is the proton mass and $E_{\rm c.m.} = 0.5$ GeV is the characteristic energy of secondaries in the c.m. frame. The mean energy T of secondaries in the laboratory frame was taken to be

$$T = KE_0/n, \qquad (2)$$

where K is the inelasticity factor. For the sake of simplicity, the spectrum of secondaries in the laboratory frame was specified in the form

$$W(E_0, E)dE = ne^{-E/T}dE/T, \qquad (3)$$

[1)]Moscow State University, Vorob'evy gory, Moscow, 119899 Russia.
[*]E-mail:ddn@dec1.npi.msu.su

1063-7788/02/6510-1843$22.00

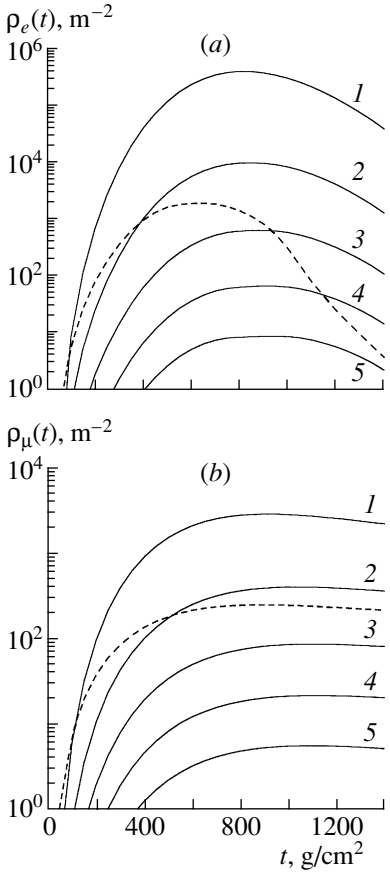

Fig. 1. (*1*, *2*, *3*, *4*, *5*) Cascade curves for (*a*) electrons and (*b*) muons at the distances of $r = 100$, 300, 600, 1000, and 1500 m, respectively. The dashed curve in either panel corresponds to the version proposed in [9, 10] and to $r = 600$ m [$\rho_e(t)$ is the electron density, while $\rho_\mu(t)$ is muon density].

where E is the energy of a secondary particle.

1. CASCADE CURVES FOR THE ELECTRON AND MUON DENSITIES

The calculated individual and average cascade curves for the electron and muon densities at various distances from the shower axis make it possible to estimate the attenuation of these components of extensive air showers. For distances of 100, 300, 600, 1000, and 1500 m from the axis of an inclined shower ($\theta = 44°$) generated by a proton of energy 3.2×10^{20} eV, the solid curves in Fig. 1 represent the results of the QGSM calculations both (Fig. 1*a*) for electrons and (Fig. 1*b*) for muons. First of all, it should be noted that there is a significant difference between the attenuation of electrons and the attenuation of muons: in the atmosphere-depth interval 1300–1500 g/cm^2, the attenuation lengths for electrons and muons at the distance of 600 m from the shower axis are $\lambda_e = 205$ g/cm^2 and $\lambda_\mu = 3000$ g/cm^2, respectively. Since vertical showers and inclined showers that are characterized by a large zenith angle are dominated by electrons and muons, respectively, it follows from the above that the use of the same value for the attenuation length at all zenith angles seems illegitimate. This is not the whole story, however: even for electrons, the attenuation length λ_e depends on the distance from the shower axis: at $r = 100$, 300, 600, 1000, and 1500 m, the attenuation-length values are 160, 185, 205, 225, and 245 g/cm^2, respectively. This increase in the attenuation length is consistent with the change in the depth of the maximum of the corresponding average cascade curve for the electron densities at the above distances. For example, the depth of the maximum increases from $\sim$850 g/cm^2 for the density calculated at the distance of $r = 100$ m from the shower axis through $\sim$1000 g/cm^2 for the density at $r = 600$ m to 1050–1100 g/cm^2 for the density at $r = 1000$–1500 m. For muons, a much slower (than in the preceding case of electrons) growth of the attenuation length λ_μ at small distances from the shower axis gives way to a decline at large distances ($r \geq 1500$ m). As to the case of all charged particles (the sum of electrons and muons), their attenuation length λ for the density calculated at the distance of $r = 600$ m from the shower axis is 354 g/cm^2. The calculated standard deviation of this attenuation length is $\sigma_\lambda = 12$ g/cm^2. Thus, we see that, both for individual showers and for an average one, the calculated value of the attenuation length for the charged-particle density at the distance of 600 m from the shower axis differs significantly from that which was adopted in the case of the Yakutsk array (about 540 g/cm^2) and from that which was adopted in the case of the AGASA array (about 500 g/cm^2). Since the experimental values of the attenuation length were determined by means of the procedure proposed in [4], it necessary to perform, in addition, a simulation of this procedure and to compare the results of this simulation with experimental data. However, the comparison considered here is also of great interest. The cascade curves for the densities according to the calculations at the distance of $r = 600$ m from the shower axis that were performed within the version of the model from [9, 10] are represented by the dashed curves in Figs. 1*a* and 1*b*. It can be seen that, in this case, the muon density increases by a factor greater than 3 and that the density of electrons decreases; therefore, the fraction of muons in inclined showers whose zenith angles are larger than 30° would be nearly equal to unity, in contradiction with direct data from [2, 3].

2. CASCADE CURVES FOR THE TOTAL NUMBER OF PARTICLES

For the total number of particles, Fig. 2 shows average cascade curves calculated on the basis of the QGS model [11], its modification involving the violation of Lorentz invariance [12], and the model version from [9, 10]; also shown in this figure are experimental data from [6]. We note that, for the computed curves, the depths of the shower maximum are 875, 836, and 575 g/cm^2, respectively, to be compared with the experimental value of $815 \pm (40) + 45 - 35$ g/cm^2 (the systematic error is given parenthetically, while the statistical error is represented by the last two numbers). From the theoretical curves displayed in Fig. 2 and from the data given there, one can see that the model assuming a sharp increase in the multiplicity of secondaries (recall that this assumption was put forth in [9, 10]) yields results that cannot be reconciled with experimental data at energies above 10^{19} eV. Moreover, the fraction of muons that was computed according to [9, 10] at a distance of 600 m from the shower axis exceeds considerably the experimental value from [2, 3] (see above).

We note that the depths $t_{\max}$ of the shower maxima for individual cascade curves can vary over rather broad intervals—namely, the greatest distinction between the depths of the maxima for individual showers is $\Delta t_{\max} = 170$ g/cm^2. The depth of the maximum for the average cascade curve is $t_{\max} = 875$ g/cm^2. If we take into account the experimental error ($\sigma = 60$ g/cm^2), the individual curve presented in [6] is by and large compatible with the results of the calculations based on the QGS model.

3. APPROXIMATION OF INDIVIDUAL AND AVERAGE CASCADE CURVES

On the basis of our calculations, we propose estimating the individual and mean cascade curves for the total number $N(t)$ of particles in a shower at a depth t in the atmosphere according to the formula

$$N(t) = N_{\max} \exp((t - t_{\max})^2/2S_i^2), \qquad (4)$$

where $t_{\max}$ is the depth of the maximum, $N_{\max}$ is the number of particles at the maximum, and $S_i = |t_i - t_{\max}|$. Here, t_i are the depth values ($i = 1$ and $i = 2$ label these depth values before and after the maximum, respectively) at which

$$N_i = N(t_i) = N_{\max} \exp(-0.5). \qquad (5)$$

The quantities S_1 and S_2 are used in (4) before and after the maximum, respectively. The cascade depth t is measured from the first-interaction vertex t_0, which is reckoned from the upper boundary of the atmosphere

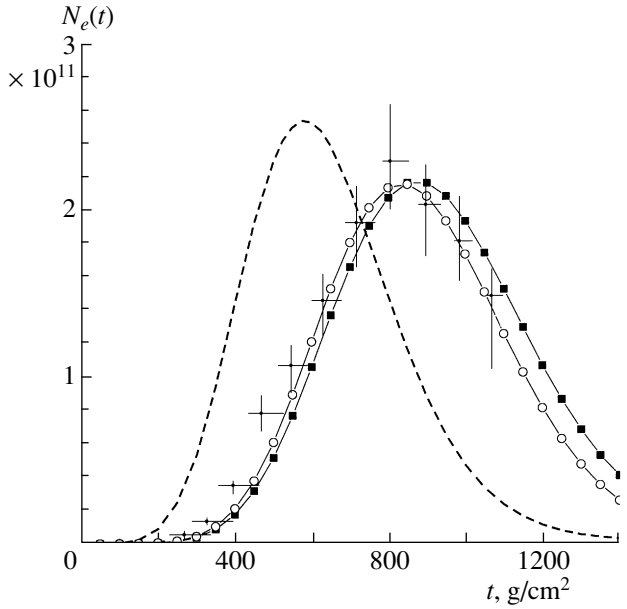

Fig. 2. Mean cascade curves for the total number of particles according to calculations based on (curve connecting boxes) the QGS model [11], (curve connecting circles) its modification from [12], and (dashed curve) the model version from [9, 10]. Points with error bars represent experimental data from [6].

and which is distributed, because of fluctuations, according to the law

$$f(t_0)dt_0 = \exp(-t_0/\lambda(E_0))dt_0/\lambda(E_0), \qquad (6)$$

where $\lambda(E_0)$ is the range of the primary particle of energy E_0 before undergoing interaction with the nuclei of air atoms. The energy dependence of the mean values of $N_{\max}$ and $t_{\max}$ in the region $E_0 > 10^{11}$ GeV is determined by the formulas

$$\bar{N}_{\max} = (0.712 + 3.00 \log(E_0/10^{11}\ \text{GeV})) \times 10^{11}, \qquad (7)$$

$$\bar{t}_{\max} = 806 + 60 \log(E_0/10^{11}\ \text{GeV})\ [\text{g/cm}^2]. \qquad (8)$$

For the sake of simplicity, we can assume that the quantities $N_{\max}$ and $t_{\max}$ are distributed according to the Gaussian law with standard deviations $0.01\bar{N}_{\max}$ and 11 g/cm^2, respectively. The quantities S_1 and S_2 can be taken to be

$$S_1 = 223 + 14 \log(E_0/10^{11}\ \text{GeV})\ [\text{g/cm}^2], \qquad (9)$$

$$S_2 = 256 + 20 \log(E_0/10^{11}\ \text{GeV})\ [\text{g/cm}^2]. \qquad (10)$$

The fluctuations of S_1 and S_2 can be disregarded because their standard deviations are approximately equal to 2–9 g/cm^2.

4. CONCLUSION

Our calculations on the basis of the QGS model [5] have revealed that the attenuation lengths for the charged-particle density at the distance of 600 m from the shower axis differ significantly (by 40–50%) from those that are adopted at the largest arrays studying extensive air showers. In all probability, the dissipation of the primary-particle energy within the QGS model is somewhat slower than that which is suggested by experimental data. A new, convenient approximation has been proposed for cascade curves associated with the total number of particles. If the model used in [5] is modified in accordance with the assumption that Lorentz invariance is violated [12], the agreement between model results and experimental data is improved. The assumption that the multiplicity of secondaries in hadron interaction increases sharply at energies in excess of 10^{16} eV contradicts experimental data in the energy region $\geq 10^{19}$ eV, which have been considered here [9, 10].

5. ACKNOWLEDGMENTS

We are grateful to G.T. Zatsepin for stimulating discussions.

This work was supported by the Russian Foundation for Basic Research, project no. 00-15-96632 (G.T. Zatsepin scientific school).

REFERENCES

1. A. M. Hillas *et al.*, in *Proceedings of the 12th International Cosmic Ray Conference, Hobart, 1971,* Vol. 3, p. 1007.
2. A. V. Glushkov *et al.*, in *Proceedings of the 20th International Cosmic Ray Conference, Moscow, 1987,* Vol. 5, p. 494.
3. M. Nagano *et al.,* J. Phys. G **18**, 423 (1992).
4. G. Clark *et al.,* in *Proceedings of the 8th International Cosmic Ray Conference, Jaipar, 1963,* Vol. 4, p. 65.
5. A. B. Kaĭdalov, K. A. Ter-Martirosyan, and Yu. M. Shabel'skiĭ, Yad. Fiz. **43**, 1282 (1986) [Sov. J. Nucl. Phys. **43**, 822 (1986)].
6. D. J. Bird *et al.*, Astrophys. J. **441**, 144 (1995).
7. A. B. Migdal, Zh. Éksp. Teor. Fiz. **32**, 633 (1957) [Sov. Phys. JETP **5**, 527 (1957)].
8. I. M. Dremin, V. A. Nechitailo, M. Biyajima, *et al.*, Phys. Lett. B **403**, 149 (1997).
9. O. E. Krasnova, S. I. Nikolsky, and V. A. Romakhin, Izv. Akad. Nauk, Ser. Fiz. **65**, 1191 (2001).
10. S. I. Nikolsky, in *Proceedings of the 27th International Cosmic Ray Conference, Hamburg, 2001,* Vol. 4, p. 1389.
11. E. E. Antonov, L. G. Dedenko, A. A. Kirillov, *et al.*, Pis'ma Zh. Éksp. Teor. Fiz. **73**, 506 (2001) [JETP Lett. **73**, 446 (2001)].
12. S. Coleman and S. L. Glashow, Phys. Rev. D **59**, 116008 (1999).

Translated by A. Isaakyan

Physics of Atomic Nuclei, Vol. 65, No. 10, 2002, pp. 1847–1861. Translated from Yadernaya Fizika, Vol. 65, No. 10, 2002, pp. 1898–1912.

ELEMENTARY PARTICLES AND FIELDS
Experiment

Description of Gamma–Hadron Families on the Basis of the Quasiscaling Model for a Normal Nuclear Composition of Primary Cosmic Rays

M. Kalmakhelidze, N. Roinishvili, and M. Svanidze

Institute of Physics, Georgian Academy of Sciences, ul. Tamarishvili 6, GE-380077 Tbilisi, Georgia

Received January 24, 2002

Abstract—The nuclear composition of primary cosmic rays is investigated in the energy range 10^{15}–10^{16} eV. These investigations are performed by comparing the properties of the gamma-hadron families observed by the Pamir and the Pamir–Chacaltaya collaborations with the properties of families generated on the basis of the MC0 quasiscaling model for various nuclear compositions. It is shown that all properties of experimental families are in good agreement with the predictions of the MC0 model for a normal nuclear composition, but that these experimental results are at odds with the results of the calculations that assume a nuclear composition enriched in heavy nuclei. © *2002 MAIK "Nauka/Interperiodica".*

1. INTRODUCTION

In order to obtain deeper insights into the origin of primary cosmic rays and into the properties of the sources of this radiation and of interstellar (intergalactic) space, where the radiation propagates from a source to the Earth, it is of paramount importance to study the nuclear composition of primary cosmic rays. The nuclear composition of primary cosmic rays has received adequate study up to energies on the order of 10^{12} eV. In [1–3], this nuclear composition was explored by direct methods up to about 10^{15} eV. However, the results obtained there do not possess sufficient statistical significance and are therefore not quite reliable. At higher energies, information about the nuclear composition is extracted from data either on extensive air showers (EAS) or on the families of gamma rays and hadrons recorded by x-ray emulsion chambers. Despite many years of investigations, the results are very contradictory: the nuclear composition can vary from a so-called normal composition [4, 5] (even that dominated by protons [6]) to a heavy and a superheavy one (see [6, 7] and [8], respectively). Relevant data are given in Table 1, along with the references to the sources from which they were borrowed.

It should be emphasized that knowledge of the nuclear composition in the energy range 10^{15}–10^{16} eV is of crucial importance, because the observed spectra of cosmic rays have a knee in precisely this region. The reason for this may be either a cusp in the spectrum of primary cosmic rays—in particular, because of the disappearance of some component of cosmic rays from their composition—or a change in the properties of the inelastic interaction of cosmic-ray particles with the nuclei of atoms belonging to Earth's atmosphere [1, 9].

The present study is devoted to exploring the nuclear composition of primary cosmic rays in the region immediately after the knee in the energy spectrum of cosmic rays. Here, we employ the properties of gamma–hadron families recorded and processed by the Pamir and the Pamir–Chacaltaya collaboration.

Going ahead, we note that the generation efficiency for families stemming from different primary nuclei, ϵ_A, depends greatly on their atomic number A. Therefore, the fraction f_A of various components in the nuclear composition of families,

$$f_A = \epsilon_A C_A / \Sigma(\epsilon_A C_A), \qquad (1)$$

where C_A is the fraction of A nuclei in primary cosmic rays, differs significantly from that dictated by the nuclear composition of primary cosmic rays (compare Tables 1 and 2).

Table 2 illustrates the main difficulty in determining the composition of primary cosmic rays on the basis of data on the families. Even if the properties of families generated by heavy nuclei differ drastically from the properties of proton-generated families, the effect of the former on the mean features of the families is modest since the nuclear composition of the families is enriched in protons. Only 16.4% of families are generated by iron nuclei even in the case of primary cosmic rays having a heavier composition where iron constitutes about 60%.

The method used to obtain the data in Table 2 and the procedure proposed for deducing the nuclear composition of primary cosmic rays will be discussed below.

1063-7788/02/6510-1847$22.00

Table 1. Nuclear compositions of primary cosmic rays at $E_0 = 10^{15}$ eV, C_A, %

Nuclear composition	p	He	CNO	SiMg	Fe	$\langle \ln A \rangle$
Normal [4, 5]	40	20	10	10	20	1.7
Heavy [6, 7]	15	10	17	0	58	3.0
Superheavy [8]	7	5	12	6	70	3.4

Table 2. Nuclear compositions of the families, f_A, %

Nuclear composition	p	He	CNO	SiMg	Fe
Normal [4, 5]	75.0	16.6	3.2	2.4	2.8
Heavy [6, 7]	56.0	16.6	11.0	0	16.4
Superheavy [8]	40.0	12.6	12.0	4.4	31.0

Gamma–hadron families are produced by nuclear–electromagnetic cascades developing in the atmosphere after the interaction of primary-cosmic-ray particles with nuclei of air in the upper atmosphere. This is a very complicated process, a multistep and ramified one; it follows that, in order to deduce the required nuclear composition, it is necessary to compare data on experimental families with data on families that are simulated by the Monte Carlo method on the basis of a model that takes into account both nuclear and electromagnetic cascades.

Not less than a dozen of such models are known at present [5, 10–17]. The later versions presented in [5, 12, 15] differ only slightly from one another. All of these are of a quasiscaling character. The scaling property is violated in the pionization region, but this has but a small effect on the properties of the families, since they are determined predominantly by particles originating from fragmentation processes; it is slightly violated in the fragmentation region as well, because the primary cosmic-ray particle interacts with a nucleus from air rather with a nucleon. All the aforementioned models ensure good agreement with experimental data at accelerator energies and present an extrapolation of the properties of nuclear interactions at low energies to ultrahigh energies. These models differ insignificantly by the details of interaction, by the number of secondary-particle flavors, and by the way in which diffractive processes and processes involving the production of jets with high transverse momenta are taken into account.

In the majority of the scaling models, the intensity of the families generated in the case of a normal nuclear composition is two to four times as great as that which was observed experimentally [18–21]. In view of this, one occurs on the horns of a dilemma as to whether to admit a violation of the scaling property in the fragmentation region or to employ a much heavier nuclear composition of primary cosmic rays [7, 8]. This was the motivation for investigating compositions dominated by heavy elements (see Table 1). The study of Dunaevsky *et al.* [21], who analyzed possible solutions to this dilemma, is of interest as an example.

In the present study, x-ray-emulsion data are analyzed on the basis of the MC0 model [5], which relies on the theory of quark–gluon strings. It takes into account diffractive processes, the generation of jets having high transverse momenta, and the production of strange and charmed particles. A detailed description of the model is given in [5].

We note that the CORSIKA code, which includes various versions of the strong-interaction model, is the most popular at present. In [22–24], the predictions of the MC0 model were compared with the results of simulations according to the CORSIKA code implemented in the DPM and the VENUS version. It was shown there that the MC0 model leads to a faster attenuation of the hadron component than each of the CORSIKA versions. As will be seen from the following, the fast attenuation of the hadron component in the MC0 model ensures agreement between the results that this model yields and the observed intensity of gamma families. The MC0 and the CORSIKA model yield different results for mean features of the families as well, those within MC0 being closer to experimental values than those within CORSIKA. In view of all the above, we have chosen MC0 as the basic model in our further analysis.

On the basis of the MC0 model, we have simulated the nuclear-electromagnetic cascades in the atmosphere that are generated by various nuclei having a power-law energy spectrum. The exponent γ of the integrated energy spectrum of primary cosmic rays was taken to be 1.7. For protons, we also simulated a series of families featuring a knee in the energy spectrum. In that case, we took, as input quantities, $\gamma = -1.7$ for energies before the knee (3×10^{15} eV) and $\gamma = -2.2$ for energies after the knee.

The present article consists of five sections. In addition to the Introduction and the Conclusion, it includes three main sections devoted to studying the problems in question on the basis of experiments and on the basis of a simulation. In Section 2, we consider the problem of the intensities of the families at the Pamir altitude (4370 m above sea level) and discuss the computed and observed intensities. In Section 3, we describe the properties of experimental and simulated families. In Section 4, we assess the degree to which the model is able to reproduce experimental data, taking into account the possible systematic errors of the relevant experiments. In the Conclusion, we present the main results of our investigation.

2. INTENSITY OF GAMMA–HADRON FAMILIES

In Subsections 2.1 and 2.2, we study the intensity of gamma–hadron families from the experimental and from the computational point of view. At the end of Subsection 2.2, we compare experimental and simulated results and discuss the dilemma of a heavy nuclear composition versus a violation of the scaling property in the fragmentation region. Owing to a rather large inelasticity factor in the MC0 model, good agreement between the observed and the predicted intensity of the families is achieved within the quasiscaling approach.

2.1. Experiment

By a gamma–hadron family, one usually means a set of electron–photon showers of gamma rays, electrons, positrons (for the sake of brevity, all electron–photon showers from γ, e^+, and e^- are referred to here as gammas), and hadrons ($\pi^+, \pi^-, n, p\ldots$) arising in the interaction of primary-cosmic-ray particles with the nuclei of air atoms. The families that are analyzed in the present study satisfy the conditions

$$100 \le \Sigma E_\gamma < 1000 \text{ TeV}, \qquad (2)$$
$$n_\gamma \ge 10, \quad E_\gamma, E_h^\gamma \ge 4 \text{ TeV}, \quad R_\gamma \ge 1 \text{ cm},$$

where n_γ is the number of electron–photon showers in a gamma family, E_h^γ (E_γ) is the hadron (gamma) energy, and R_γ is the mean radius of a family as reckoned from its energy-weighted center. Only those particles that are within the distance of 15 cm from this center are included in the families.

In processing the families, we use here the so-called aggregation procedure consisting in that gammas ($\gamma_i\gamma_j$) occurring at a distance R_{ij} less than 0.15 mm are treated as one gamma particle of energy $E_\gamma = E_{\gamma i} + E_{\gamma j}$. For the majority of such gammas, the darkening spots overlap, so that the measuring device used perceives them as a single spot. The other gammas are combined by means of the aggregation procedure both in actual and in simulated families. In this way, all gammas within the region $R_{ij} <$ 0.15 mm are combined.

Let us pay special attention to the condition $R_\gamma \ge$ 1 cm. For the first time, this condition is used here to select families. This is explained by two circumstances. On one hand, the features of the families characterized by $R_\gamma < 1$ cm are strongly distorted by the process of darkening-spot formation on the film of the x-ray emulsion chamber used. A large part of the corresponding darkening spots overlap, some of them being united almost completely. It is especially difficult to reproduce this in simulated families. In view of this, we prefer to remove them from the analysis. Similar considerations apply to $\Sigma E_\gamma > 1000$ TeV families. In their central part, there is a narrow lump of gammas that can hardly be disentangled. On the other hand, it was noticed in [25] that the relative fraction of narrow families is greater in the experiment than in the simulation (see Fig. 1*a*) and that their properties differ from the properties of other families. By way of example, we indicate that, in the experiment, families occurring within the region $R_\gamma < 1$ cm feature virtually no hadrons and that their spectrum of E_γ is similar to the spectrum of E_γ in purely electromagnetic cascades. This is yet another argument in favor of removing the set of $R_\gamma < 1$ cm families from the analysis. Figure 1*b* demonstrates how the distributions of R_γ in the model and in the experiment become closer to each other as soon as $R_\gamma < 1$ cm families are eliminated from the latter.

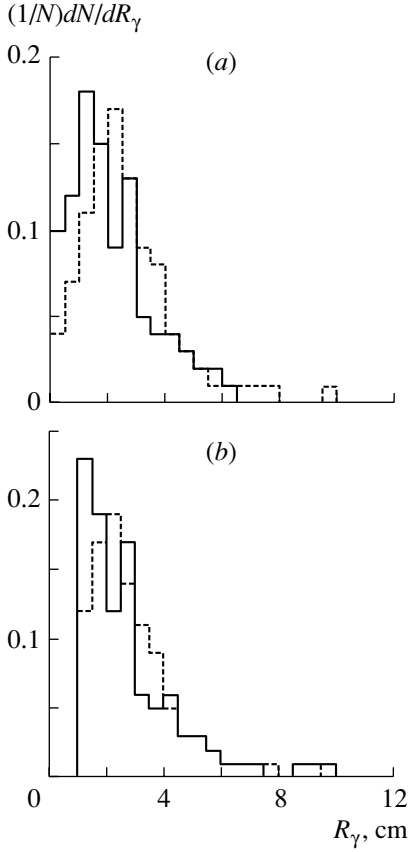

Fig. 1. Normalized differential distributions of the families with respect to R_γ for (*a*) all families and (*b*) families with $R_\gamma \ge 1$ cm: (solid-line histogram) experimental data and (dashed-line histogram) results of the calculation for a normal nuclear composition.

If the selection criteria

$$\Sigma E_\gamma \ge 100 \text{ TeV}, \quad E_h^\gamma, E_\gamma \ge 4 \text{ TeV} \qquad (3)$$

are applied, the intensity of gamma–hadron families at the Pamir altitude (4370 m above see level, 596 g/cm^2) proves to be equal to [10]

$$0.69 \pm 0.15 \text{ m}^{-2} \text{ yr}^{-1} \text{ sr}^{-1}. \quad (4)$$

The interval of ± 0.15 m^{-2} yr^{-1} sr^{-1} includes both statistical and possible systematic errors.

The total number of families studied here, which includes narrow ones ($R_\gamma < 1$ cm) is equal to 226. If the selection criterion $R_\gamma \geq 1$ cm is applied to them, their total number will be 174.

Thus, the experimental intensity of the families that satisfy the criteria in (2) is

$$I_{\text{expt}} = (0.69 \pm 0.15) \times 174/226 \quad (5)$$
$$= 0.53 \pm 0.12 \text{ m}^{-2} \text{ yr}^{-1} \text{ cm}^{-1}.$$

2.2. Calculation

The vertical intensity of gamma–hadron families can be represented in the form

$$I^v_{\text{fam}} = \Sigma[I_A(E \geq E_0)\epsilon_A(E \geq E_0)] \times \Omega_0/\Omega^{\text{fam}}_A, \quad (6)$$

where $I_A(E \geq E_0)$ is the intensity of a nucleus of atomic number A and energy in the range $E \geq E_0$; $\epsilon_A(E \geq E_0)$ is the family-generation efficiency under the conditions specified above; and Ω_0 and Ω_{fam} are the solid angles for primary particles and their families, respectively. For the last two quantities, we have

$$\Omega_0 = 2\pi, \quad \Omega_{\text{fam}} = 2\pi/(1 + T/\lambda_{\text{att}}), \quad (7)$$

where T is the pressure at the altitude where the array used is deployed (for the Pamir array, this is 596 g/cm^2), while λ_{att} is the mean attenuation length for the families.

In turn, we have

$$\epsilon_A = N^A_{\text{fam}}/N_A(E \geq E_0), \quad (8)$$

where $N_A(E \geq E_0)$ is the number of simulated cascades that were generated by a primary particle of atomic number A and N^A_{fam} is the number of families that satisfy the selection criteria applied.

It is convenient to define I_A in fractions of I—that is, to normalize it to the total intensity of primary cosmic rays. Specifically, we then have

$$C_A = I_A/I. \quad (9)$$

It can be seen from Eqs. (5)–(8) that, in determining the calculated intensity, the model specifies only ϵ_A (generation efficiency); as to C_A and the energy spectra of nuclei, they are dictated by the presumed nuclear composition. The calculations have shown that, within the errors, λ_{att} is independent of A and is equal to 75 ± 6 g/cm^2, which is in good agreement with the experimental value of $\lambda^{\text{expt}}_{\text{att}} = 78 \pm 4$ g/cm^2 [10].

We note that, up to a very high energy, the vertical intensity of all primary-cosmic-ray particles,

$$I^v(E > E_0) = \Sigma I^v_A(E > E_0), \quad (10)$$

was determined experimentally to a fairly high precision. It is common practice to describe this intensity by the empirical expression proposed in [4]. We also used this expression, but we replaced the exponent $\gamma = -1.6$ of the integrated energy spectrum by the value of $\gamma = -1.7$, which is more popular at present. As a result, we obtained $I^v(E > 10^{15} \text{ eV}) = 50 \pm 20$ m^{-2} yr^{-1} sr^{-1}. From the data given in the later study of Watson [1], who quoted the differential vertical intensity, one can obtain the value of $I^v(E > 10^{15} \text{ eV}) = 47 \pm 12$ m^{-2} yr^{-1} sr^{-1}. Taking these two results into account, we adopt, for our further analysis, the estimate

$$I^v(E > 10^{15}\text{eV}) = 50 \pm 15 \text{ m}^{-2} \text{ yr}^{-1} \text{ sr}^{-1}. \quad (11)$$

For the family-generation efficiency, the results of the calculations based on the MC0 model are presented in Table 3. In the first line of this table, we display the values of $N^{\text{sim}}_A(E \geq E_0)$, the actual number of primary particles simulated isotropically in the zenith-angle interval between 0° and 43°. For the group of C, N, and O nuclei and the group of Si and Mg nuclei, as well as for Fe, the minimal primary energy in the calculations was

$$E^A_0 = A^{0.5} \times 10^{15} \text{ eV}. \quad (12)$$

For the remaining nuclei (p, He), $E_0 = 10^{15}$ eV. This choice of $\Theta_{\max}$ and E_0 is dictated by the fact that nuclei of energy below the above values of E_0 for $\Theta > \Theta_{\max}$ produce not more than 2% of the total number of families.

Given in the second line of Table 3 is the number of primary particles that is reduced to the full solid angle and to the energy of $E_0 = 10^{15}$ eV; that is,

$$N_A(E \geq 10^{15} \text{ eV}) \quad (13)$$
$$= N^{\text{sim}}_A/(1 - \cos 43°)/(E^A_0/10^{15} \text{ eV})^{1.7}.$$

Further, the notation for the as-yet-unspecified quantities in Table 3 is the following: N^{fam}_A is the total number of families generated by a given nucleus; ϵ_A is the efficiency of their production—it is equal to $N^{\text{fam}}_A/N_A(E \geq 10^{15} \text{ eV})$; and E_A is the mean energy of nuclei responsible for family generation.

All the data in the table, with the exception of those in the last column, were computed under the assumption that the exponent of the energy spectrum of nuclei is $\gamma = -1.7$. The data in the last column

Table 3. Efficiency ϵ_A of family generation by various nuclei and mean energy E_A responsible for these families

	p	He	CNO	SiMg	Fe	$p(-2.2)$
$N_A^{\rm sim} \times 10^3$	63.6	87	30	20	30	62
$N_A \times 10^3$	237	324	912	1113	3450	231
$N_A^{\rm fam}$	682	416	461	434	756	409
$\epsilon_A \times 100$	0.29 ± 0.01	0.13 ± 0.01	0.051 ± 0.003	0.038 ± 0.003	0.022 ± 0.001	0.18 ± 0.01
E_A, PeV	15.0	29.0	53.0	66.0	80.0	9.0

Table 4. Some computed parameters (see main body of the text)

Nuclear composition	$\epsilon \times 100$	$I_{\rm fam}$, $\rm m^{-2}\ yr^{-1}\ sr^{-1}$	$E_{\rm fam}$, PeV
Normal [4]	0.16	0.71 ± 0.22	22.0
Heavy [6, 7]	0.076	0.35 ± 0.11	32.0
Superheavy [8]	0.051	0.23 ± 0.07	45.0
Normal $\gamma = -2.2$	0.11	0.49 ± 0.15	17.0

Table 5. Mean values of the parameters P, their statistical errors σ_P in experimental families, and the sensitivity S of the parameters to the atomic number of the primary-cosmic-ray nucleus

	n_h	R_γ, cm	R_γ^E, cm	$E_\gamma R_\gamma$, TeV cm	d	q_n	q_E
P	3.1	2.8	2.4	27.0	0.63	0.11	0.14
σ_P	0.3	0.1	0.1	2.0	0.01	0.01	0.01
S	1.38	1.33	1.26	1.04	0.96	0.65	0.60

correspond to the case where the proton spectrum has a knee at the point $\rm E_{knee} = 3 \times 10^{15}$ eV, with the exponent being $\gamma = -1.7$ before the knee and $\gamma = -2.2$ after it.

The data in Tables 1 and 3 make it possible to determine the family-generation efficiency ϵ at a given nuclear composition C_A and a given exponent γ and to predict the intensity $I_{\rm fam}$ of the families, the mean energy $E_{\rm fam}$ of primary nuclei responsible for family generation, and the mean mass number of these nuclei that is expressed in terms of $\langle \ln A \rangle$. All this is done according to the formulas

$$\epsilon = \Sigma(C_A \epsilon_A)/\Sigma C_A, \tag{14}$$

$$I_{\rm fam}^v = I_0^v \Sigma[C_A \epsilon_A (1 + T/\lambda_{\rm att}^A)], \tag{15}$$

$$E_{\rm fam} = \Sigma(C_A \epsilon_A E_A)/\Sigma(C_A \epsilon_A), \tag{16}$$

$$\langle \ln A \rangle = \Sigma(C_A \ln A)/\Sigma C_A. \tag{17}$$

For the nuclear compositions investigated here, the values of C_A and $\langle \ln A \rangle$ are given in Table 1, while the values of ϵ_A and E_A are displayed in Table 3. The efficiency of family generation due to specific nuclei and due to their mixtures (various nuclear compositions) is shown in Fig. 2*a* as a function of $\ln A$ and as a function of $\langle \ln A \rangle$, respectively. The predicted intensities of the families at various nuclear compositions are presented in Fig. 2*b*.

As can be seen from Table 4 and from Fig. 2*b*, only the normal composition with $\gamma = -1.7$ and the normal composition allowing for a knee in the primary proton spectrum ensure agreement with the experimental value of the intensity of the gamma–hadron families. In the latter case, all components of primary cosmic rays but protons have $\gamma = -1.7$; as to protons, this value of the exponent γ is replaced for them by -2.2 at the point 3×10^{15} eV. For the intensity of the families, the two heavier compositions from [6–8] lead to results that fall significantly short of the experimental value.

It should be emphasized that the possible systematic errors in measurements of gamma energies (see Subsection 4.2 below) only strengthen the reliability of our conclusions because the intensity predicted with allowance for the systematic errors is equal to $0.58 \pm 0.18\ \rm m^{-2}\,yr^{-1}\,sr^{-1}$ for the normal composition and to $0.28 \pm 0.08\ \rm m^{-2}\,yr^{-1}\,sr^{-1}$ for the heavy one.

Thus, we can draw the following conclusions:

(i) The MC0 model solves the dilemma of a heavy nuclear composition versus a violation of scaling in the fragmentation region. Within this quasiscaling model, it is possible to attain agreement between the computed and the experimental intensity of the families for a normal nuclear composition. This result is achieved owing to a relatively large inelasticity factor in the MC0 model for hadron interactions with the nuclei of atmosphere atoms.

(ii) Within the MC0 model, heavier nuclear compositions lead to an underestimation of the intensity of the families.

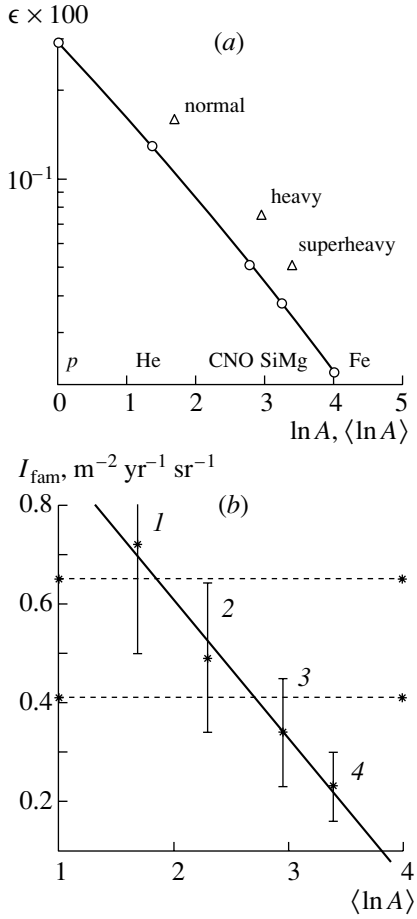

Fig. 2. (*a*) Family-generation efficiency (circles) for specific nuclei as a function of $\ln A$ and (triangles) for various nuclear compositions as a function of $\langle \ln A \rangle$. (*b*) Intensity of gamma families for (*1*) a normal nuclear composition, (*2*) a normal nuclear composition with allowance for a knee in the proton spectrum, (*3*) a heavy nuclear composition, and *(4)* a superheavy nuclear composition; in this panel, the horizontal dashed lines bound the region of experimental data.

3. FEATURES OF GAMMA–HADRON FAMILIES

Gamma–hadron families are characterized by a number of measurable parameters that are defined and described in the next two subsections. As before, problems associated with measurement of these parameters are considered in the first of these subsections [Subsection (3.1)]. In Subsection 3.2, we analyze the results of our calculations and specific problems that arise in simulating the families in question. On the basis of simulated families, we find parameters that are sensitive to the atomic number of the parent nucleus. A brief conclusion on the agreement of parameter values that are computed for a normal nuclear composition with experimental data is given in Subsection 3.2.

3.1. Experiment

By convention the class of measured parameters can be broken down into four subclasses:

(i) Energy features of gammas. These are n_γ, the number of gamma particles; E_γ, their mean energy; and ΣE_γ, the total energy of gamma particles in a family.

(ii) Spatial features of gammas. These include R_γ, the radius of a family (it is defined as the mean distance between the center of a family and a gamma particle in it); $E_\gamma R_\gamma$, the mean product that is analogous to the transverse momentum in hadron–hadron interactions; $R_\gamma^E = \Sigma E_\gamma R_\gamma / \Sigma E_\gamma$, the energy-weighted radius of a family; and d, the ratio of the number $n_{\rm in}$ of initial gammas to the number $n_{\rm obs} = n_\gamma$ of observed ones ($d = n_{\rm in}/n_{\rm obs}$). In order to determine the number of initial gammas that are responsible for narrow groups of spots on the film employed, the so-called decascading procedure was applied that involved combining the observed gammas occurring within a distance R_{ij} into a single gamma particle if $R_{ij}/(1/E_i + 1/E_j) < 10$ TeV mm.

(iii) The energy features of hadrons. These are n_h, the number of hadrons; E_h^γ, the mean energy transfer from a hadron to the soft component (apparent hadron energy); ΣE_h^γ, the total apparent energy of hadrons; $q_E = \Sigma E_h^\gamma / (\Sigma E_\gamma + \Sigma E_h^\gamma)$, the energy fraction in the hadron component of a family; and $q_n = n_\gamma/(n_\gamma + n_h)$, the fraction of hadrons in the total multiplicity of a family.

(iv) The spatial features of hadrons, including R_h and $E_h^\gamma R_h$. We emphasize that these are not considered in the present study, since the number of hadrons is small as a rule; therefore, their spatial characteristics exhibit very wide fluctuations.

The parameters that belong to a given subclass suffer from the same types of systematic errors.

In the first class, they are determined by the errors in the gamma energy. For the measured energies between 4 and 50 TeV, the relative error is approximately equal to 20%. At high energies, there arise effects associated with the saturation of darkening spots from individual gammas. If possible, these effects are taken into account during the primary treatment of the families in determining the energies of individual gammas. Moreover, it was indicated in Subsection 2.1 that, in the analysis of events, only families characterized by $\Sigma E_\gamma < 1000$ TeV were included in statistics and that gammas occurring at distances satisfying the condition $R_{ij} < 0.15$ mm were combined into a single gamma particle. In our opinion, this selection removes the bulk of systematic errors

in the parameters belonging to the first subclass. In Subsection 4.2, we discuss this issue in greater detail.

The complications that may be involved in determining the spatial features of gammas (second subclass) have already been mentioned in Subsection 2.1. It should be recalled that the procedure applied in that case includes not only the aggregation of gammas occurring at distances $R_{ij} < 0.15$ mm but also the elimination of families for which $R_\gamma < 1$ cm.

In the third subclass, there arise problems in determining the apparent hadron energy E_h^γ from the darkening of the corresponding spot. However, the situation is simpler here than that around gammas: the spot is saturated later (the density distribution is flatter), and there is no overlap since the mean distance between hadrons is much longer than that between gammas. However, the relationship between the apparent energy and the density of darkening has received less adequate study for hadrons than for gammas [26]. These problems will be discussed in Subsection 3.2 in connection with a determination of the apparent energy in simulated families.

As was indicated at the beginning of this subsection, the parameters of the fourth subclass are not used in the present study.

The mean values of the parameters of gamma–hadron families are given in Table 5, along with the statistical errors in them.

Specifically, the first, the second, and the third line of this table present, respectively, the mean parameter values, their statistical errors, and the sensitivity S of the parameters to the atomic number of a primary-cosmic-ray nucleus. This sensitivity is determined with the aid of simulated families for primary protons and iron nuclei as

$$S = (\langle P_{\mathrm{Fe}}\rangle - \langle P_p v\rangle/D_p, \qquad (18)$$

where $\langle P_{\mathrm{Fe}}\rangle$ is the mean value of a given parameter for families induced by iron nuclei, $\langle P_p\rangle$ is the analogous quantity for protons, and D_p is the variance of this parameter for a primary proton.

We note that all the parameters are defined in such a way that $\langle P_p\rangle$ is less than $\langle P_{\mathrm{Fe}}\rangle$. In order to achieve this, we had to modify the initial definition of a parameter in two cases. For example, the parameter d was introduced in [27] as the ratio $n_{\mathrm{obs}}/n_{\mathrm{in}}$. We redefined it via the substitution $d \to 1/d$. The parameter q_E proposed in [28] as $\Sigma E_\gamma/\Sigma(E_\gamma + E_h^\gamma)$ was transformed as $q_E \to 1 - q_E$.

By way of example, the distributions of two parameters—R_γ, which is sensitive to the atomic number of the primary nucleus, and n_γ, which is insensitive to it—are displayed in Figs. 3*a* and 3*b*, respectively.

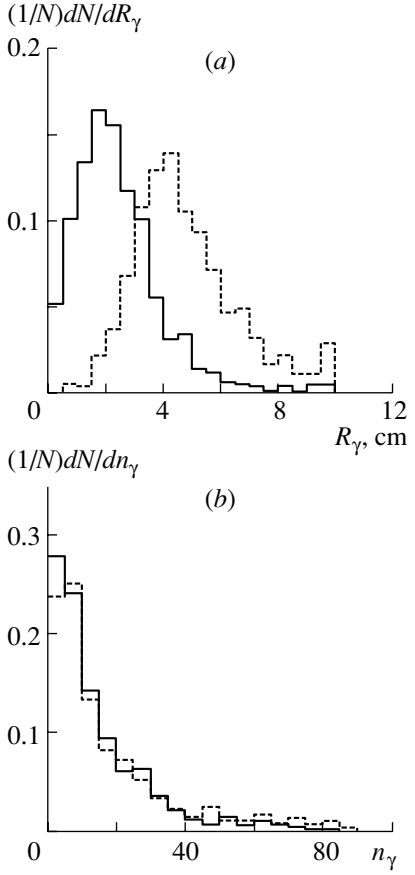

Fig. 3. Normalized differential distributions of gamma–hadron families with respect to (*a*) R_γ and (*b*) n_γ for families generated by (solid-line histograms) protons and (dashed-line histograms) Fe nuclei.

It can easily be seen that, in Table 5, the parameters are given in the order of reduction of their sensitivity. The features of the families for which $S < 0.5$ were not included in Table 5. In attempts at investigating the nuclear composition, they may have only an adverse effect—having a very low sensitivity, these parameters are useless, whereas systematic errors in them may distort eventual results.

3.2. Calculation

The mean value of a given parameter P for families corresponding to a specific nuclear composition C_A can be represented as

$$P = \Sigma(C_A\epsilon_A P_A)/\Sigma(C_A\epsilon_A), \qquad (19)$$

where P_A is the mean value of this parameter in the families generated by a nucleus of atomic number A and ϵ_A is the efficiency of family generation by a nucleus whose atomic number is precisely this A and whose energy is in excess of 10^{15} eV.

Table 6. Mean values of the parameters P_A and their variances D_P in simulated families (p^* is the proton spectrum with allowance for a knee)

	n_h	R_γ, cm	R_γ^E, cm	$E_\gamma R_\gamma$, TeV cm	d	q_n	q_E
p	2.7	2.8	2.4	24.0	0.59	0.10	0.10
D_p	2.4	1.5	1.6	15.0	0.16	0.07	0.11
p^*	2.5	2.7	2.3	24.0	0.60	0.10	0.10
D_{p^*}	2.4	1.4	1.5	14.0	0.16	0.08	0.10
He	3.3	3.2	2.9	30.0	0.63	0.12	0.20
D_{He}	2.8	1.6	1.7	17.0	0.16	0.08	0.11
CNO	4.3	4.0	3.6	34.0	0.69	0.14	0.15
D_{CNO}	3.2	1.7	1.9	17.0	0.13	0.08	0.10
SiMg	5.0	4.5	4.1	38.0	0.72	0.16	0.16
D_{SiMg}	4.0	1.8	2.0	19.0	0.13	0.08	0.11
Fe	6.3	4.8	4.4	40.0	0.74	0.18	0.19
D_{Fe}	4.7	1.9	2.1	18.0	0.13	0.09	0.11

As before, the model specifies the values of P_A and ϵ_A, C_A and the slopes of the energy spectra of A nuclei being dictated by the nuclear composition.

It has already been indicated that, in selecting and processing simulated families, we employed all those procedures that were applied to experimental data. The simulation of events involved that of the detection of a hadron in the x-ray emulsion chamber and a determination of the energy transfer from this hadron to the soft component, $E_h^\gamma = K_\gamma E_h$. For a hadron to be recorded, it is necessary that this hadron undergo interaction within the chamber and that the energy transfer E_h^γ be greater than the threshold energy value of 4 TeV. The probability of hadron interaction and the coefficient K_γ are determined by the structure of the x-ray emulsion chamber. Dedicated investigations show that, for the carbon chambers of the Pamir experiment, the probability of hadron interaction is approximately equal to 0.7 and that the distribution $f(K_\gamma)$ of K_γ for that experiment has a form close to that of an incomplete gamma function [29]:

$$f(K_\gamma) = AK_\gamma^\alpha \times \exp(-K_\gamma/\beta), \qquad (20)$$
$$\langle K_\gamma \rangle = (\alpha+1)\beta.$$

At $\alpha = 1.5$ and $\beta = 0.075$, we have $\langle K_\gamma \rangle = 0.188$. However, the condition $E_h^\gamma > 4$ TeV renders $\langle K_\gamma \rangle$ dependent on E_h (see Fig. 4*a*). Therefore, a parameter that plays a crucial role is not $\langle K_\gamma \rangle$ but K_{eff}, which is given by

$$K_{\mathrm{eff}} = \int\int K_\gamma f(K_\gamma) F(E_h) dE_h dK_\gamma, \qquad (21)$$

where $F(E_h)dE_h$ is the differential energy spectrum of hadrons. According to our calculations, $K_{\mathrm{eff}} = 0.23$ for simulated families.

Table 7. Expected values of the parameters of the families for various nuclear compositions

Nuclear composition	n_h	R_γ	R_γ^E, cm	$E_\gamma R_\gamma$, TeV cm	d	q_n	q_E
Normal	3.2	3.0	2.6	26.0	0.62	0.11	0.11
Heavy	3.6	3.3	2.9	29.0	0.64	0.12	0.12
Superheavy	4.2	3.7	3.3	32.0	0.66	0.13	0.14

These values are quite compatible with those proposed in the calculations of Malinowski *et al.* [29] (see Fig. 4*b*). The K_γ distribution obtained in [29] under the conditions corresponding to the Pamir chambers are shown in Fig. 4*b*, along with the approximation that we use. These two distributions are in reasonably good agreement.

Knowing the interaction probability for a given hadron, its energy, and the distribution function $f(K_\gamma)$ and using the Monte Carlo method, one can obtain, for each hadron, answers to the following questions: Has it undergone interaction? What is the value of the energy transfer from it, $E_h^\gamma = K_\gamma E_h$? Has it been recorded (that is, is E_h^γ greater than $E_{\mathrm{thr}} = 4$ TeV)? This algorithm was applied to simulated families in order to obtain the values of n_h, q_n, and q_E.

For various primary nuclei, Table 6 presents the values of the chosen sensitive ($S > 0.5$) parameters P_A of the families and the variances D_P of these parameters. The dependences of n_h and R_γ on A are shown in Fig. 5*a*, while the corresponding dependence of d is given in Fig. 5*b*.

For all nuclei, the properties of the families were computed under the assumption that the slope of the integrated energy spectrum is $\gamma = -1.7$. In the third and the fourth line of Table 6, we quote data for families generated by protons whose energy spectrum has a knee at the point $E_0 = 3 \times 10^{15}$ eV, with the slope parameter being $\gamma = -1.7$ before the knee and -2.2 after it. As can be seen, these data differ only slightly from those that were obtained for a spectrum whose slope parameter is equal to the constant value of $\gamma = -1.7$ (lines 1 and 2).

By using relation (19) and data presented in Tables 1, 3, and 6 (various compositions C_A, generation efficiency ϵ_A, and mean values of the parameters P_A),

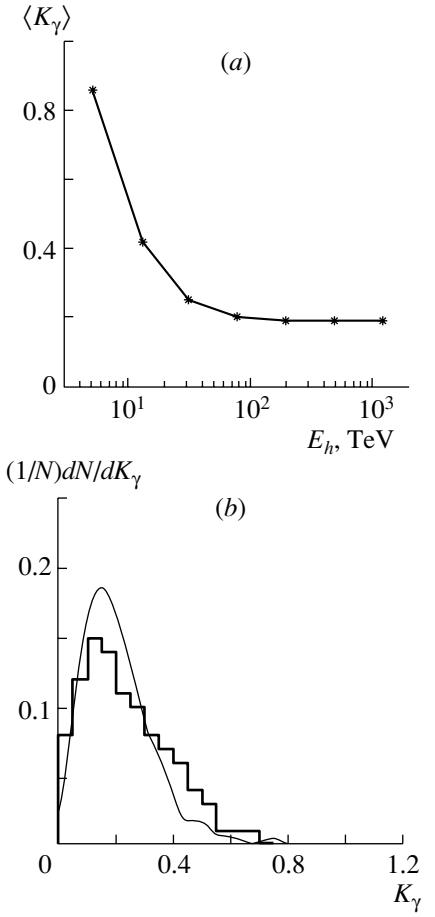

Fig. 4. (*a*) $\langle K_\gamma \rangle$ as a function of E_h. (*b*) Normalized differential distribution of electron–photon showers induced by hadrons with respect to K_γ: (histogram) data from [29] and (curve) approximation of the present study.

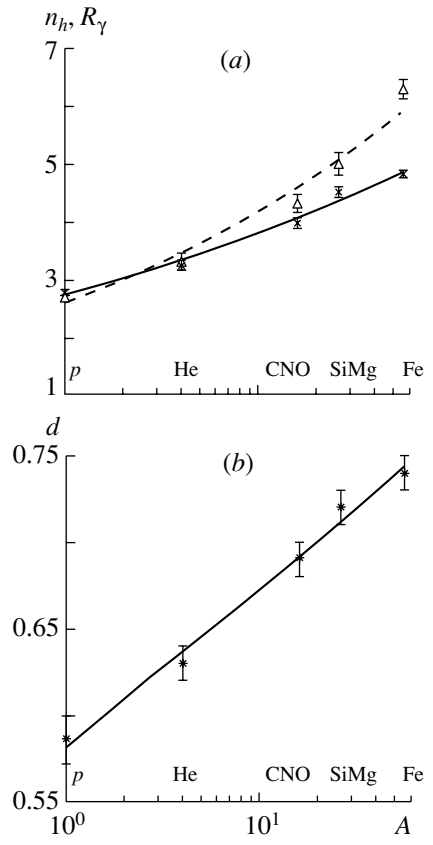

Fig. 5. (*a*) Graphs representing (triangles) n_h and (asterisks) R_γ versus A; (*b*) d as a function of A.

we can deduce the parameter values expected for given nuclear compositions (see Table 7).

From a comparison of the data in Tables 5 and 7, it can be deduced that, for the normal nuclear composition, the predicted features of the families are in good agreement with their experimental counterparts, but the predictions based on the assumption of the heavy (and the more so of the superheavy) composition deviate significantly from experimental results.

4. COMPARISON OF EXPERIMENTAL DATA WITH THE RESULTS PRODUCED BY THE MC0 MODEL

In Subsections 4.1 and 4.2, we perform a detailed comparison of experimental data with the results obtained on the basis of the MC0 model. In Subsection 4.1, we reveal parameters that are sensitive to the nuclear composition and, among them, select those that do not correlate with one another. These parameters are then subjected to a χ^2 test. All of these, are in better agreement with the predictions in the case of the normal composition than in the case of a heavier one. In Subsection 4.2, we extend our analysis to weakly sensitive parameters in order to explore the possible systematic errors. Here, good agreement with the results of the calculations is achieved for the normal nuclear composition as well.

4.1. Compatibility of the MC0 Model with Experimental Data

In order to draw conclusions on the nuclear composition of primary cosmic rays from a comparison of experimental data (see Table 5) with the predictions of the MC0 model (Table 7), it is necessary to find

Table 8. Values of χ^2_P for various parameters and values of χ^2_3

Nuclear composition	$\chi^2_{n_h}$	$\chi^2_{R_\gamma}$	χ^2_d	χ^2_3
Normal	0.11	3.4	0.95	1.5
Heavy	2.7	20.0	0.24	7.7
Superheavy	13.0	54.0	7.20	25.0

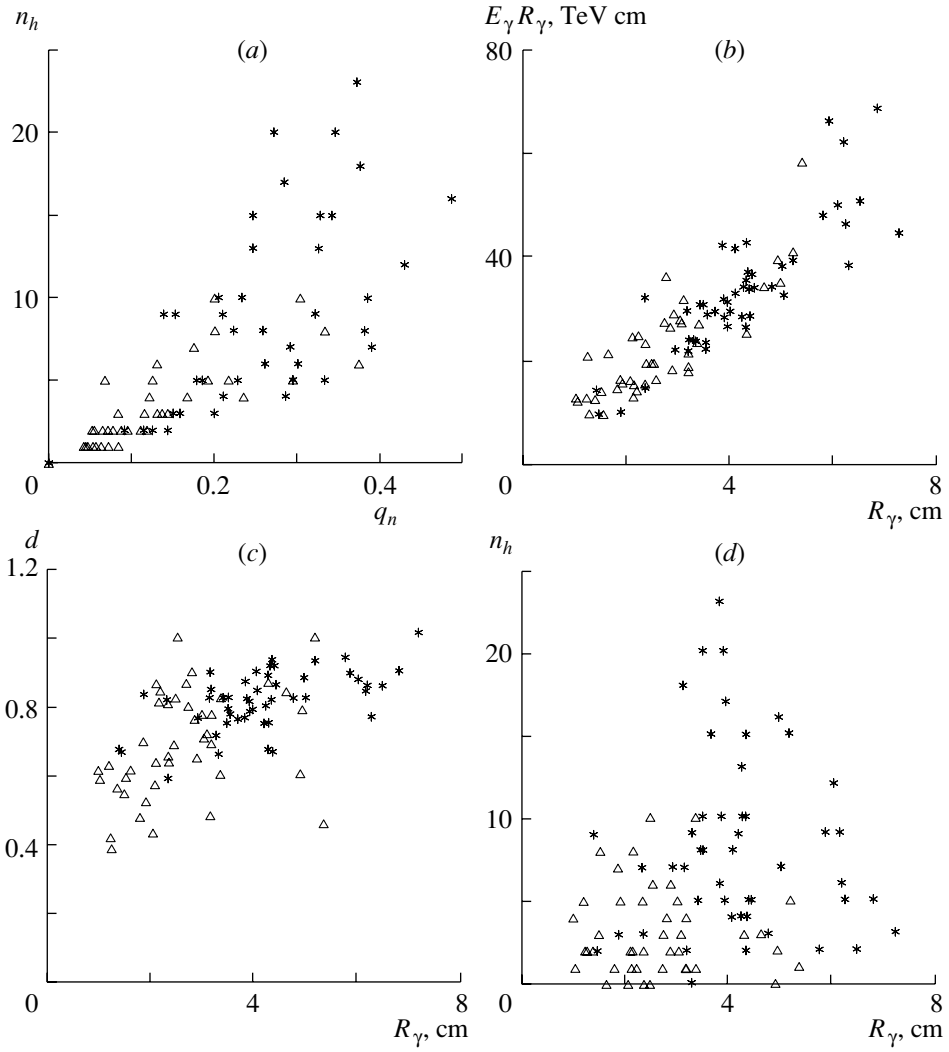

Fig. 6. Correlations between (*a*) n_h and q_n, $k = 0.60 \pm 0.02$ (by k, we henceforth denote the corresponding correlation coefficient); (*b*) R_γ and $E_\gamma R_\gamma$, $k = 0.88 \pm 0.01$; (*c*) d and R_γ, $k = 0.34 \pm 0.03$; and (*d*) n_h and R_γ, $k = 0.00 \pm 0.04$, for (triangles) a primary proton and (asterisks) a primary iron nucleus.

out which of the features subjected to analysis are uncorrelated. Otherwise, traditional (for instance, the χ^2 criterion) and relatively new (neuron networks) approaches may yield erroneous results in assessing the degree of agreement (disagreement) of experimental and calculated results.

Among the seven parameters chosen in our study that are sensitive to the nuclear composition (Table 6), there are two groups of features strongly correlated within a group. These are the energy features of the hadrons involved—n_h, q_n, and q_E (for example, see Fig. 6*a*)—and the spatial features of gammas—R_γ, R_γ^E, and $E_\gamma R_\gamma$ (see Fig. 6*b*). The parameter d, which weakly correlates with the parameters from either group (see Fig. 6*c*), stands apart. The parameters belonging to the different groups do not correlate (see Fig. 6*d*).

Relying on the aforesaid, we have chosen n_h, R_γ, and d as sensitive and uncorrelated parameters for a comparison of measured and computed data. For these, we have computed the χ_P^2 functional individually as

$$\chi_P^2 = [(P_{\rm expt} - P_{\rm mod})/\sigma P_{\rm expt}]^2 \qquad (22)$$

and the total functional for the three uncorrelated parameters as

$$\chi_3^2 = [(n_{h\rm expt} - n_{h\rm mod})/\sigma n_{h\rm expt}]^2 + [(R_{\gamma\rm expt} - R_{\gamma\rm mod})/\sigma R_{\gamma\rm expt}]^2 + [(d_{\rm expt} - d_{\rm mod})/\sigma d_{\rm expt}]^2/3. \qquad (23)$$

In expressions (22) and (23), $P_{\rm expt}$ and $P_{\rm mod}$ are the mean values of the corresponding parameters, while $\sigma P_{\rm expt}$ is the root-mean-square deviation of

Table 9. Values of the parameters P and corresponding χ^2_P, along with experimental data

Experiment and nuclear composition		n_h	R_γ, cm	d	q_n	$E_\gamma R_\gamma$, TeV cm	n_γ	E_γ, TeV
Experiment	P	3.1	2.8	0.63	0.11	27.0	21.0	12.1
	σ_P	0.3	0.01	0.01	0.01	2.0	2.0	0.5
Normal	P	3.2	3.0	0.62	0.11	26.0	24.0	11.1
	χ^2_P	0.11	3.4	0.95	0.06	1.3	13.0	3.1
Heavy	P	3.6	3.3	0.64	0.12	29.0	25.0	10.8
	χ^2_P	2.71	20.0	0.24	1.5	0.86	20.0	7.0
Superheavy	P	4.2	3.7	0.66	0.13	32.0	26.0	10.5
	χ^2_P	13.0	54.0	7.2	9.5	5.2	25.0	12.4

the parameter P_{expt}. Instead of the total variance of the parameters $(\sigma^2_{\text{expt}} + \sigma^2_{\text{mod}})$, we use here only the corresponding experimental value σ^2_{expt}, since the computed error is much less than the experimental one (the number of the families is three to five times greater in the calculations than in the experiments being discussed). The results are compiled in Table 8.

Since the number of degrees of freedom is equal to unity for an individual parameter and since χ^2_3 is the average of χ^2 over these three parameters, each χ^2 must be close to unity in the case of good agreement between theoretical and experimental results. This expectation comes true only for the normal composition, but it is not realized for the heavy and the ultraheavy composition. It should be emphasized that relatively large values of $\chi^2_{R_\gamma}$, χ^2_d, and χ^2_3 for the normal composition may suggest the presence of some systematic effects that have not yet been removed completely (this problem will be analyzed in Subsection 4.2). Figure 7 shows χ^2_3 as a function of $\langle \ln A \rangle$. The dashed straight line corresponds to $\chi^2_3 = 4$. If nuclear compositions for which $\chi^2_3 \geq 4$ are rejected, the probability of making an error—that is, of discarding a correct hypothesis—is less than 1%. On this basis, we can state that all nuclear compositions for which $\langle \ln A \rangle$ is greater than 2.5 are ruled out by the mean values of the features of experimental gamma families because χ^2_3 is greater than four for them (see Fig. 7).

4.2. Systematic Errors

In Subsection 4.1, it was shown that the MC0 model featuring a normal nuclear composition of primary cosmic rays yields results that are in reasonably good agreement with experimental data. Nevertheless, two circumstances cast some doubt on the overall description.

First, the experimental mean radius of the families, $R_\gamma = 2.8 \pm 0.1$ cm, is much less than the computed radii, $R_\gamma = 3.0$–3.3 cm, for all nuclear compositions considered here (see Tables 5, 7). This explains the high value of $\chi^2_{R_\gamma} = 3.4$—and, accordingly, $\chi^2_3 = 1.5$—for the normal nuclear composition (see Table 8). For the heavier compositions, the corresponding values are still greater.

Second, the experimental mean value of $n_\gamma = 21 \pm 2$ is less than the computed value of $n_\gamma = 24$–26 for any nuclear composition. It should be noted that n_γ is virtually independent of the atomic number of the incident nucleus; therefore, we did not use this parameter.

This arouses a suspicion that R_γ and n_γ suffer from systematic experimental errors. It is desirable to find their common source.

In this section, we are going to embark on a more comprehensive analysis of the consistency between

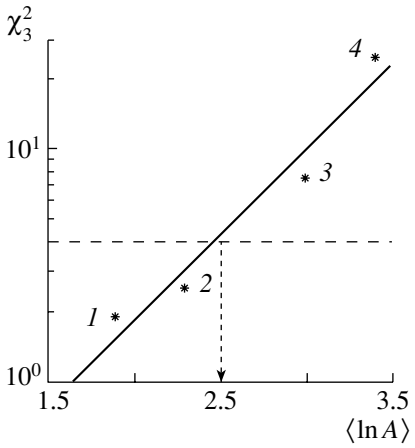

Fig. 7. χ^2_3 as a function of $\langle \ln A \rangle$. The notation for the nuclear compositions is identical to that in Fig. 2*b*.

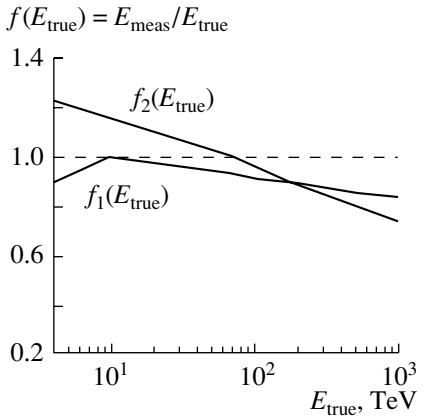

Fig. 8. Two types of the distortion function: $f_1(E)$ and $f_2(E)$.

the MC0 results and experimental data, taking into account the possible systematic errors in experimentally determined parameter values.

With this aim in view, the values of almost all parameters of the gamma families, both those that were measured experimentally and those that were predicted by the MC0 model, are given in Table 9, along with χ^2_P values for each parameter and each composition.

As was indicated above, the most glaring discrepancy between the model results and the experimental data is observed in the parameters R_γ and n_γ. For a heavier composition, this discrepancy is still more pronounced. Inaccuracy in determining the energy E_γ of the electron–photon shower according to the darkening D corresponding to it may be the common cause of all large deviations. The algorithm for going over from D to E_γ is rather complicated. In addition to the theoretical relationship between the energy of a gamma particle and the number n_e of electrons in the cascade generated by this gamma particle, this algorithm includes the properties of the film used (rescaling from D to n_e and saturation of this dependence at large n_e) and the conditions under which the film is exposed (its background and the gap between the film and the lead). All these effects are calculable and can be tested experimentally. However, we cannot rule out the possibility that some uncertainty may still remain. These effects, primarily concerning isolated quanta, do not exhaust the problem—there are still cooperative phenomena in the families, such as a partial overlap of electron–photon showers and even their aggregation (this aggregation was taken into account here in processing simulated families).

With the aim of assessing the effect of the errors in measuring energy on the parameter values, we supplemented the simulation of the families by introducing a hypothetical distortion function $f(E_{\rm true})$ through the replacement of the true value $E_{\rm true}$ by the measured value $E_{\rm meas}$:

$$E_{\rm meas} = f(E_{\rm true})E_{\rm true}. \quad (24)$$

For the distortion function, we used two versions. The first is

$$f_1(E_{\rm true}) = 10\ {\rm TeV}/E_{\rm true}(E_{\rm true}/10\ {\rm TeV})^\alpha, \quad (25)$$

where the exponent α satisfies the condition $\alpha > 1$ (or $\alpha < 1$) below 10 TeV and the condition $\alpha < 1$ (or $\alpha > 1$) above 10 TeV, ensuring the underestimation (or overestimation) of the true energy. The second version has the form

$$f_2(E_{\rm true}) = 70\ {\rm TeV}/E_{\rm true}(E_{\rm true}/70\ {\rm TeV})^\beta, \quad (26)$$

where $\beta < 1$ over the entire range of $E_{\rm true}$. The parameters α and β were varied.

Figure 8 displays typical examples of the distortion function. For a given choice of α, the function $f_1(E)$ reflects an underestimation of the energy both below and above $E_{\rm true} = 10$ TeV. On the contrary, $f_2(E)$ overestimates the true energy up to 70 TeV and underestimates it above this point. The form $f_2(E)$ of the distortion function was borrowed from the article of Dunaevsky *et al.* [30], who simulated the propagation of gammas belonging to the families through the lead of the chamber and their subsequent detection by a film, taking into account all of the aforementioned features.

In our calculations, we preassigned different values of α in such a way as to ensure the underestimation (overestimation) of the energy by 10, 20, 50, −20, and −40% near the measured threshold of 4 TeV and the underestimation of the energy by −5, −10, and −20% at the true energy of 100 TeV.

For the normal nuclear composition, Figs. 9*a* and 9*b* display χ^2_P as a function of, respectively, the overestimation and the underestimation of energy. From these figures, it can be seen that, even at a 10% underestimation of energy near the threshold ($E_{\rm true} = 4.4$ TeV for $E_{\rm meas} = 4$ TeV) or at zero underestimation of energy at 100 TeV ($E_{\rm meas} = E_{\rm true}$ for $E_{\rm true} > 100$ TeV), all χ^2_P values are acceptable. Concurrently, it turned out that, in a reasonable interval of distortions of high energies, the values of χ^2_P depend only slightly on the degree of underestimation of energy at $E_{\rm true}$ greater than 100 TeV (see Fig. 9*b*.) Since a 10% error is quite possible, we arrive once again at the conclusion that, under the assumption of the normal nuclear composition, the results obtained on the basis of the MC0 model are in very good agreement with experimental data.

The emerging pattern is totally different for the heavy nuclear composition and the more so for the superheavy one. In Subsection 4.1, we have shown that

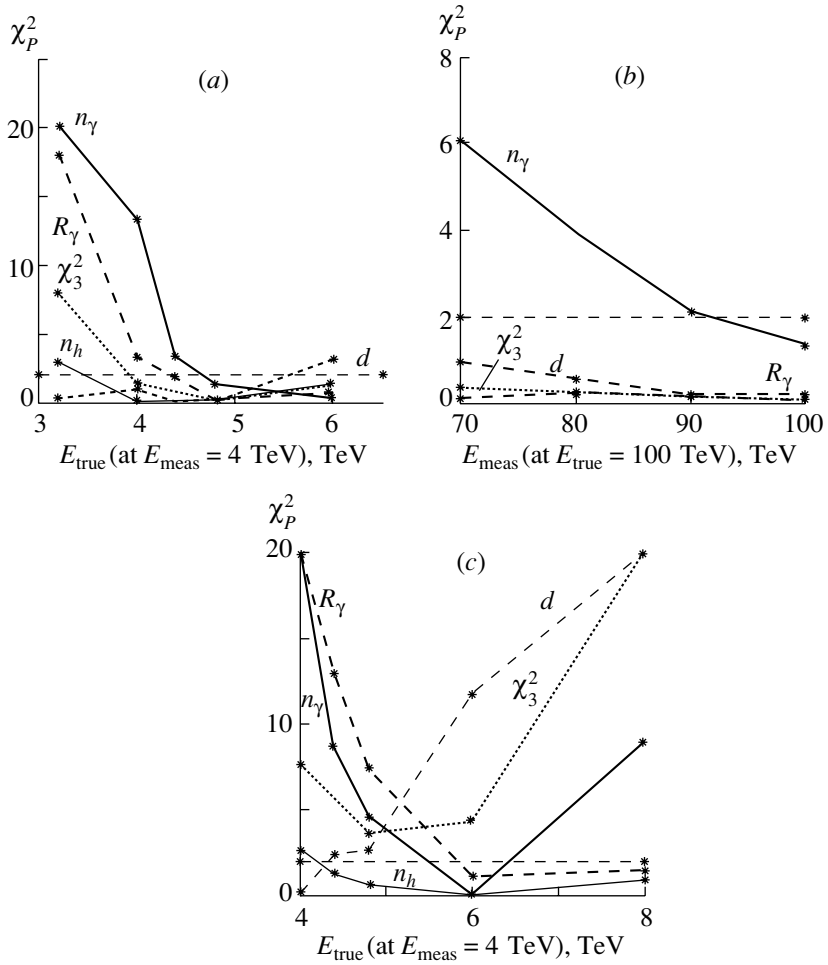

Fig. 9. Dependences of χ_P^2 and χ_3^2 (each of the parameters that are generically denoted by P—R_γ, n_γ, n_h, d, and χ_3^2—is indicated on the corresponding curve) on (*a*) the degree of overestimation of energy near the measured threshold (4 TeV) for the normal nuclear composition ($E_{\text{meas}} = E_{\text{true}}$ at $E_{\text{true}} > 100$ TeV), (*b*) the degree of underestimation of energy near the true energy of 100 TeV at the normal nuclear composition (the threshold value is $E_{\text{true}} = 4.8$ TeV), and (*c*) the degree of overestimation of energy near the measured threshold (4 TeV) for the heavy nuclear composition.

the results of the calculations assuming the heavy nuclear composition are at odds with experimental data. Figure 9*c*, which, for the heavy nuclear composition, presents data that are analogous to those in Fig. 9*a*, demonstrates that no distortion function is able to improve the agreement between the MC0 model and experimental data under the assumption of the heavy nuclear composition. For the case of the normal nuclear composition and for the case of the heavy one, Table 10 gives χ_P^2 values obtained upon introducing the distortion function at, respectively, a 10% and a 20% overestimation of energy near the threshold. We note that, in the case of the superheavy nuclear composition, the values of χ_P^2 are so great that this possibility is not discussed in the following.

To conclude the above discussion, we present information about the intensity of the families that is predicted if the above distortion functions are used. Since the number of events passing the criteria for selecting the families decreases as soon as the distortion function is introduced, the predicted intensity of the families also decreases. For the normal nuclear composition, the intensity in question proves to be $I_{\text{fam}} = 0.58 \pm 0.18$ m^{-2} yr^{-1} sr^{-1} at $E_{\text{true}} =$ 4.4 TeV. For the heavy nuclear composition, it is $I_{\text{fam}} = 0.25 \pm 0.08$ m^{-2} yr^{-1} sr^{-1} at $E_{\text{true}} = 4.8$ TeV. We recall that the experimental value of the intensity is $I_{\text{fam}} = 0.53 \pm 0.12$ m^{-2} yr^{-1} sr^{-1}. From the above values, it can be seen that, upon the removal of the possible systematic errors, the conclusions on the nuclear composition that were drawn in Section 2 only become more firmly validated.

In the present study, we have used a few procedures to simulate the process of detection of electron–photon showers initiated by gammas and hadrons. These are the aggregation procedure (unification of

Table 10. Values of χ^2_P for the normal and the heavy nuclear composition upon introducing the distortion function

Nuclear composition	E_{true}, TeV	n_h	R_γ, cm	d	q_n	$E_\gamma R_\gamma$, TeV cm	n_γ	E_γ, TeV	χ^2_3
Normal	4.4	0.09	1.85	0.11	0.02	0.11	3.4	1.37	0.70
Heavy	4.8	0.63	7.39	2.65	1.84	1.88	4.63	2.15	3.60

closely spaced electron–photon showers), the procedure that assigns each hadron a coefficient K_γ characterizing energy transfer from this hadron to the soft component, and the possible overestimation of of the energy threshold E_{thr} for gamma and hadron detection. All this may seem incorrect and unnatural. But in fact, an x-ray emulsion chamber distorts to some extent, as any complicated array does, nuclear–electromagnetic cascades incident on it. As a result, one has to deal with the measured values P_{meas} rather than with true parameters P_{true}. For a comparison of the parameters measured experimentally with the results of model calculations to be meaningful, it is necessary to simulate processes occurring in x-ray emulsion chambers. Codes that are developed by the Pamir collaboration to solve this problem are referred to as the passage-through-the-chamber codes [30]. These are rather complicated codes analogous to the JEANT code [31], which is used in accelerator problems to simulate distortions introduced by facilities like ATLAS and CMS [32, 33].

In the present study, the passage-through-the-chamber code was broken down into a few steps (aggregation, K_γ, E_{thr}, $E_{\text{true}} \to E_{\text{meas}}$) in order to trace separately the effect of each process involved. The results of this approach made it possible to draw conclusions on the role of each type of distortion in a determination of the measurable parameters of the families.

5. CONCLUSION

It has been proven that, under the assumption of a normal nuclear composition (which is close to the nuclear composition at 10^{14} eV), the MC0 model predicts the intensity of the families that is in perfect agreement with experimental observations. This resolves the long-standing problem of heavy nuclear composition versus a strong violation of the scaling property in the fragmentation region.

Further, it has been shown that, in the case of a normal nuclear composition, the MC0 model is able to describe not only the intensity of the families but also all of their basic features (there are nearly 15 of them).

In order to analyze the nuclear composition of primary cosmic rays on the basis of simulated events that are generated by primary protons and iron nuclei, we have found those features of the families that are sensitive to the atomic number A of the incident nucleus. Among them, we selected three parameters that do not correlate with one another. These are the number of hadrons, n_h; the radius of a gamma family, R_γ; and the parameter d characterizing the electromagnetic structure of an event.

It turned out that the mean experimental values of the chosen parameters are close to their counterparts obtained in the computations assuming the normal nuclear composition of primary cosmic rays and are at odds with them for the heavy nuclear composition (15% p, 58% Fe) and the more so for the superheavy one (7% p, 70% Fe). In our analysis, we have used the quantity $\Sigma\chi^2_P/3$ averaged over the above three parameters. It proved to be 1.5 for the normal nuclear composition and 7.7 and 25 for the heavy and the superheavy one, respectively.

Despite fairly good overall agreement between the theoretical and experimental results in the case of the normal nuclear composition, two of the basic features of the families, n_γ and R_γ, exhibit considerable deviations from the expected values: $\chi^2_{n_\gamma} = 13.0$ and $\chi^2_{R_\gamma} = 3.4$. Our investigations have revealed that, if we admit a 10% underestimation of energy near the threshold for gamma detection (4 TeV) and introduce an appropriate distortion function in the computed properties of the families, the relevant χ^2 values become $\chi^2_{n_\gamma} = 3.4$ and $\chi^2_{R_\gamma} = 1.8$. In the case of a 20% underestimation of energy, the two χ^2 values in question are both close to unity. On the other hand, no distortion function can ensure agreement between the experimental and computed values of mean features of the families for the heavy and the superheavy nuclear composition.

The basic conclusions of the present analysis can be formulated as follows:

(i) Under the assumption of the normal nuclear composition, the results obtained on the basis of the MC0 model are in perfect agreement with experimental data on gamma–hadron families.

(ii) In the energy region around 10^{16} eV, which is above the knee in the energy spectrum of primary cosmic rays, their nuclear composition is close the nuclear composition at energies of about 10^{14} eV.

(iii) Models of the nuclear–electromagnetic cascade that assume a nuclear composition enriched in heavy elements (iron) contradict experimental data on the families. They predict an overly low intensity of the families and incorrect values of the mean features.

(iv) All quasiscaling models [6, 12, 14, 15, 22–24], with the exception of MC0, predict an intensity of the families that is two to three times as great as that which is observed experimentally. This means that, in all of them (with the exception of MC0), the attenuation length for the hadron component is overly great. The best agreement between the measured mean features of the families with the results produced by the MC0 model [22–24] is also a corollary of a stronger attenuation of hadrons. Therefore, a rather large inelasticity factor in the interactions of cosmic-ray particles with the nuclei of atoms of the atmosphere is a feature peculiar to inelastic interactions at high energies.

ACKNOWLEDGMENTS

We are grateful to all participants of the Pamir collaboration for a long-term, fruitful cooperation; to R. Mukhamedshin for providing access to the code that he developed for simulating nuclear–electromagnetic cascades, and to M. Tamada for placing at our disposal the database of the Pamir–Chacaltaya collaboration. Stimulating discussions with all of them are gratefully acknowledged.

REFERENCES

1. A. A. Watson, in *Proceedings of the 25th International Cosmic Ray Conference, 1997,* Vol. 8, p. 257.
2. JACEE Collab., in *Proceedings of the 25th International Cosmic Ray Conference, 1997,* Vol. 4, p. 1.
3. RUNJOB Exper., in *Proceedings of the 25th International Cosmic Ray Conference, 1997,* Vol. 4, pp. 133, 141.
4. S. I. Nicolsky, in *Proceedings of 3rd International Symposium on Cosmic Ray and Particle Physics, 1984,* p. 507.
5. G. F. Fedorova and R. A. Mukhamedshin, Bull. Soc. Sci. Lett. Lodz **16**, 137 (1994).
6. M. Tamada, J. Phys. G **23**, 497 (1997).
7. J. R. Ren *et al.*, Phys. Rev. D **38**, 1404 (1988).
8. M. Shibata, Phys. Rev. D **24**, 1847 (1981).
9. T. Shibata, in *Proceedings of the 24th International Cosmic Ray Conference, 1995,* Vol. 8, p. 10; T. Stanev, P. L. Bierman, and T. K. Gaisser, astro-ph/9303006.
10. Pamir Collab., in *Proceedings of the 20th International Cosmic Ray Conference, 1997,* Vol. 7, p. 385.
11. J. A. Wrotniak, Zesz. Nauk. Uniw. Lodz. **7**, 148 (1977).
12. A. M. Dunaevsky *et al.*, in *Proceedings of the 16th International Cosmic Ray Conference, 1977,* Vol. 7, p. 337; A. M. Dunaevsky and S. A. Karpova, Bull. Soc. Sci. Lett. Lodz **16**, 23 (1994).
13. Yu. A. Fomin and G. B. Khricstiansen, in *Proceedings of the 14th International Cosmic Ray Conference, 1975,* Vol. 7, p. 2574.
14. S. A. Azimov, E. J. Mullajanovand, and T. S. Yuldashbaev, in *Proceedings of the 18th International Cosmic Ray Conference, 1983,* Vol. 5, p. 462.
15. J. Knapp and D. Heck, KfK, 5196B (1993).
16. A. Krys, A. Tomaszevski, and J. A. Wrotniak, in *Proceedings of the 16th International Cosmic Ray Conference, 1979,* Vol. 7, p. 188.
17. A. Krys, A. Tomaszevski, and J. A. Wrotniak, Zesz. Nauk. Uniw. Lodz. **32**, 5 (1980).
18. N. N. Roinishvili, J. Phys. G **20**, 215 (1995).
19. Pamir Collab., Mt. Fuji Collab., and the Chacaltaya Collab., Nucl. Phys. B **191**, 1 (1981).
20. A. Krys, J. A. Wrotniak, *et al.*, in *Proceedings of the 17th International Cosmic Ray Conference, 1981,* Vol. 5, p. 315.
21. A. M. Dunaevsky *et al.*, in *Proceedings of 5th Symposium on Very High Energy Cosmic Ray Interaction, 1988,* p. 143.
22. H. Biolobrzeska *et al.*, in *Proceedings of the 25th International Cosmic Ray Conference, 1997,* Vol. 6, p. 265.
23. H. Bielawska *et al.*, in *Proceedings of the 25th International Cosmic Ray Conference, 1997,* Vol. 6, p. 269.
24. H. Biolobrzeska *et al.*, in *Proceedings of the 25th International Cosmic Ray Conference, 1997,* Vol. 6, p. 273.
25. Pamir Collab., in *Proceedings of the 21st International Cosmic Ray Conference, 1990,* HE-2, 4-22.
26. W. Michalak, Zesz. Nauk. Uniw. Lodz. **60**, 137 (1980).
27. S. A. Asimov *et al.*, in *Proceedings of the 20th International Cosmic Ray Conference, 1987,* Vol. 5, p. 304.
28. H. Bielawska and A. Tomaszevski, *UL Pamir Collaboration Workshop, 1980,* p. 38.
29. A. Malinowski *et al.*, *UL Pamir Collaboration Workshop, 1980,* p. 49.
30. A. M. Dunaevsky *et al.*, in *Proceedings of 5th Symposium on Very High Energy Cosmic Ray Interaction, 1988,* p. 93.
31. CERN Program Library Long Writeup W5013 (1997).
32. ATLAS Letter of Intent CERN/LHCC/92-4 LHCC/I2 (1992).
33. CMS Letter of Intent CERN/LHCC 92-3 LHCC/I1 (1992).

Translated by A. Isaakyan

Physics of Atomic Nuclei, Vol. 65, No. 10, 2002, pp. 1862–1867. Translated from Yadernaya Fizika, Vol. 65, No. 10, 2002, pp. 1913–1917.

ELEMENTARY PARTICLES AND FIELDS
Theory

Contribution of Higher Meson Resonances to the Electromagnetic Pion-Mass Difference

V. A. Andrianov and S. S. Afonin

Institute of Physics, St. Petersburg State University, Universitetskaya nab. 7/9, St. Petersburg, 199164 Russia

Received May 10, 2001; in final form, March 13, 2002

Abstract—Some modifications of the formula for calculating the electromagnetic pion-mass difference are proposed on the basis of the chiral-symmetry-restoration phenomenon at high energies and the operator-product expansion of quark densities for vector (ρ) and axial-vector (a_1) meson fields. All calculations are performed through taking into account higher meson resonances in the vector and axial-vector channels. It is shown that the inclusion of only the first ρ^0 and a_1 radial excitations improves the results of the calculation for the electromagnetic pion-mass difference in relation to the known ones. The electromagnetic ρ- and a_1-meson decay constants and the constant L_{10} of the effective chiral Lagrangian are estimated with the aid of the generalized Weinberg sum rules. © *2002 MAIK "Nauka/Interperiodica"*.

1. INTRODUCTION

It is well known that the correlation functions for vector (V) and axial-vector (A) meson fields are related to some experimentally observed characteristics of pseudoscalar mesons—in particular, with the electromagnetic pion-mass difference $\Delta m_\pi|_{\rm em}$ [1]. Recent experimental data of ALEPH [2] and OPAL [3] collaborations on hadronic τ decays ($\tau \to (VA)\nu_\tau$, $\tau \to \pi\nu_\tau$) indicate that, in order to check both perturbative and nonperturbative QCD parameters, it is necessary to take into account more degrees of freedom in pseudoscalar channels for the $VV-AA$ correlation functions. In particular, the authors of [4] performed an analysis of experimental data [2] obtained by the ALEPH collaboration for the correlation function difference $\Pi^V - \Pi^A$ by studying the decay $\tau \to (V, A)\nu_\tau$. It turned out that this difference virtually vanishes even at intermediate energies of $\lesssim$3 GeV. A small contribution of the first radial excitations of vector mesons to $\Pi^V - \Pi^A$ can be seen experimentally, but the contribution of the next ones is nearly negligible.

As follows from [1, 5], the bulk of the pion-mass-difference effect generally has an electromagnetic origin. There are various approaches to calculating the electromagnetic contribution to $\Delta m_\pi|_{\rm em}$ [5–15]. One simple way to calculate this quantity in the chiral limit and to the lowest order in the electromagnetic interactions was proposed in [1], where it was calculated within the current algebra by using the Weinberg sum rules [16], these sum rules being saturated by one vector [$\rho(770)$] and one axial-vector [$a_1(1260)$] meson. From the Particle Data Group [17] (see also [18]), it is known, however, that there is a series of heavier meson states whose quantum numbers are those of the $\rho(770)$ meson [$\rho(1450)$, $\rho(2150)$] and which represent radial excitations of the $\rho(770)$ meson in terms of potential quark models. In the axial-vector channel, there can exist radial excitations of the $a_1(1260)$ resonance as well. However, their mass spectrum has not yet been accurately identified [19–21]. Thus, there arises the problem of assessing the contribution of these higher meson resonances to the electromagnetic pion-mass difference $\Delta m_\pi|_{\rm em}$.

In this study, we analyze the contribution of the first radial (V, A) excitations to the electromagnetic pion-mass difference $\Delta m_\pi|_{\rm em}$. Our analysis is based on modifications of the relation derived in [1] (DGMLY relation). Two ways are proposed. The first one explores an additional Weinberg sum rule following from the requirement of chiral-symmetry restoration at high energies [22] and the operator-product expansion (OPE) [23]. The second one does not use this sum rule. It should be emphasized that our goal is not to calculate $\Delta m_\pi|_{\rm em}$ strictly (this quantity is known from experimental data), but we are going to employ this difference to calculate some physical parameters of hadron resonances and to investigate the contribution of higher meson resonances to saturation of physical observables.

The article is organized as follows. In Section 2, we recall the idea underlying the derivation of the DGMLY relation for the electromagnetic pion-mass difference and present a scheme for obtaining the Weinberg sum rules from the requirement of chiral symmetry restoration at high energies and OPE.

1063-7788/02/6510-1862$22.00

Section 3 is devoted to extending the classical formula from [1] by taking into account higher meson (V, A) resonances. There, we also calculate some electromagnetic decay constants for the ρ^0 and a_1 mesons and the constant L_{10} of the effective chiral Lagrangian [24], which can be determined, in particular, from the decay $\pi \to e\nu\gamma$. The results are discussed in Section 4.

2. THE ELECTROMAGNETIC PION-MASS DIFFERENCE AND THE WEINBERG SUM RULES

In the chiral limit, the electromagnetic pion-mass difference $\Delta m_\pi|_{\rm em}$ is given by the known relation [1, 8, 11, 25, 26]

$$(m^2_{\pi^+} - m^2_{\pi^0})|_{\rm em} = \frac{2e^2C}{f_\pi^2}, \qquad (1)$$

where f_π represents the weak pion decay constant and the constant C is

$$C = -\frac{1}{8\pi^2}\frac{3}{4}\int\limits_0^\infty dp^2 p^2 [\Pi^V(p^2) - \Pi^A(p^2)]; \qquad (2)$$

here,

$$\Pi^C(p^2) = \int d^4x \exp(ipx)\langle(\bar q(x)\Gamma q(x)\bar q(0)\Gamma q(0))\rangle, \qquad (3)$$

$$C \equiv V, A; \quad \Gamma \equiv \gamma_\mu, \gamma_\mu\gamma_5$$

represents the two-point correlation functions for vector and axial-vector quark densities in Euclidean space. In the large-N_c limit (planar limit), the correlation functions for color-singlet quark densities are saturated completely by narrow meson resonances [27, 28]; that is,

$$\Pi^C(p^2)|_{\rm planar} = \sum_n \frac{Z_n^C}{p^2 + m^2_{C,n}}, \qquad (4)$$

where $m_{C,n}$ and Z_n^C denote, respectively, the masses and the residues of corresponding resonances.

On the other hand, it follows from the asymptotic freedom of QCD that the high-energy asymptotic behavior of these correlation functions is described by perturbation theory and OPE [23]. To the lowest order, this behavior is given by

$$\Pi^C(p^2)|_{p^2\to\infty} \sim p^2 \ln\frac{p^2}{\mu^2}, \qquad (5)$$

where μ is a normalization point for fermion currents.

From a comparison of (4) and (5), one can infer that an infinite set of resonances with equal quantum numbers must exist in order to reproduce the perturbative asymptotic form (5). In the chiral limit and in the large-N_c approach, it can be shown that, in V, A channels, we have [22, 29]

$$\left(\Pi^V(p^2) - \Pi^A(p^2)\right)_{p^2\to\infty} \equiv \frac{\Delta_{VA}}{p^6} + \mathcal{O}\left(\frac{1}{p^8}\right), \qquad (6)$$

$$\Delta_{VA} \simeq -16\pi\alpha_s\langle\bar q q\rangle^2,$$

where, by definition,

$$\Pi^{V,A}_{\mu\nu}(p^2) \equiv (-\delta_{\mu\nu}p^2 + p_\mu p_\nu)\Pi^{V,A}(p^2). \qquad (7)$$

It follows from relation (6) that, because of a fast convergence of the difference $\Pi^A - \Pi^V$ with increasing p^2, one may expect chiral symmetry restoration at high energies, with the difference $\Pi^A - \Pi^V$ being approximated by an order parameter of chiral-symmetry breaking (CSB) in QCD (that is, the quark condensate $\langle\bar q q\rangle$). The asymptotic form (6) represents the so-called condition of chiral-symmetry restoration in V,A channels. It leads to a set of sum rules (see, for example, [22]) for spectral characteristics of V, A mesons—namely, the expansion of (6) in powers of p^2 leads to

$$\sum_n Z_n^V - \sum_n Z_n^A = 4f_\pi^2, \qquad (8)$$

$$\sum_n Z_n^V m^2_{V,n} - \sum_n Z_n^A m^2_{A,n} = 0, \qquad (9)$$

$$\sum_n Z_n^V m^4_{V,n} - \sum_n Z_n^A m^4_{A,n} = \Delta_{VA}. \qquad (10)$$

Relations (8) and (9) are the Weinberg sum rules [16]. Equation (10) represents an additional sum rule following from OPE. The vector and axial-vector residues are related to the electromagnetic meson widths by the equation [30]

$$Z_n^{(V,A)} = 4f^2_{(V,A),n}m^2_{(V,A),n}, \qquad (11)$$

where $f_{(V,A),n}$ are (dimensionless) electromagnetic decay constants.

The Weinberg sum rules ensure convergence of the integral in Eq. (2) in the ultraviolet limit. As a result, one obtains

$$(m^2_{\pi^+} - m^2_{\pi^0})|_{\rm em} = \frac{3}{4}\frac{\alpha_{\rm em}}{\pi f_\pi^2} \qquad (12)$$

$$\times \sum_{k=1}^\infty \left\{f^2_{A,k}m^4_{A,k}\ln m^2_{A,k} - f^2_{V,k}m^4_{V,k}\ln m^2_{V,k}\right\}.$$

Substituting the two-resonance ansatz ($k = 1$) for V, A correlation functions into (12), one arrives at the equation [1]

$$\Delta m_\pi|^{(2)}_{\rm em} \equiv (m_{\pi^+} - m_{\pi^0})|^{(2)}_{\rm em} \qquad (13)$$

$$= \frac{3\alpha_{\rm em}}{4\pi(m_{\pi^+}+m_{\pi^0})}\frac{m_{a_1}^2 m_\rho^2}{m_{a_1}^2-m_\rho^2}\ln\frac{m_{a_1}^2}{m_\rho^2}.$$

Using the Weinberg relation $m_{a_1}=\sqrt{2}\ m_\rho$, one finds $\Delta m_\pi|_{\rm em}^{(2)}=5.21$ MeV. The experimental value is $(m_{\pi^+}-m_{\pi^0})|_{\rm expt}=4.59$ MeV [17]. In fact, the Weinberg relation is not exact. The substitution of the physical a_1-meson mass $m_{a_1}=1230$ MeV into (13) yields the estimate $\Delta m_\pi|_{\rm em}^{(2)}=5.79$ MeV (the relative deviation from the experimental value is 26%). We note that there are other contributions to the difference $m_{\pi^+}-m_{\pi^0}$—specifically, those that are caused by the isospin-symmetry breaking (that is, the inequality of the u- and d-quark masses [31–33] in the QCD). The total magnitude of these contributions is $\Delta m_\pi|_{\rm QCD}=0.17\pm0.03$ MeV [24]. The correction of order $1/N_c$ does not exceed 7%, as follows from [15, 26]. The effect of weak interactions is less than 1% [34]. Thus, the contribution of electromagnetic interactions alone proves to be

$$\Delta m_\pi|_{\rm em}=4.42\pm0.03\ {\rm MeV}, \qquad (14)$$

and we will make a comparison just with (14) (as this was done, for example, in [9, 11]). Thus, the relative discrepancy of the result in (13) with (14) is 31% for the two-resonance ansatz. In the next section, we will try to estimate this difference, taking into consideration higher meson resonances in the vector and axial-vector channels.

3. CALCULATION OF ELECTROMAGNETIC PION-MASS DIFFERENCE WITH ALLOWANCE FOR HIGHER V-, A-MESON RESONANCES

Now, we proceed to calculate the electromagnetic pion-mass difference $\Delta m_\pi|_{\rm em}$ in the case where there are two vector and two axial-vector resonances—that is, within the so-called four-resonance ansatz. The utilization of the Weinberg sum rules (8) and (9) made it possible to eliminate the parameters f_ρ and f_{a_1} from (13). In the four-resonance case, one has three sum rules of chiral-symmetry restoration (CSR) that involve four unknown parameters $f_\rho, f_{a_1}, f_{\rho'}$, and $f_{a_1'}$. The problem can be solved in a self-consistent way by applying an approximate inequality $m_{a_1'}\gtrsim m_{\rho'}$, which follows from the properties of the mass spectrum obtained, in particular, in [29, 35]. Let us introduce a presumably small parameter $\delta_m\equiv\dfrac{m_{a_1'}^2-m_{\rho'}^2}{m_{\rho'}^2}\ll1$. Saturating the correlation functions in (2) by four resonances and retaining only the first power of δ_m, one obtains the following result for the $\Delta m_\pi|_{\rm em}^{(4)}$:

$$(m_{\pi^+}^2-m_{\pi^0}^2)|_{\rm em}^{(4)}\simeq\frac{3}{4}\frac{\alpha_{\rm em}}{\pi f_\pi^2}\left\{f_{a_1}^2m_{a_1}^4\ln m_{a_1}^2\right. \qquad (15)$$
$$\left.-\ f_\rho^2m_\rho^4\ln m_\rho^2-\delta_f m_{\rho'}^4\ln m_{\rho'}^2+\epsilon m_\rho^2(1+2\ln m_\rho^2)\right\}.$$

Here, the unknown parameters $f_\rho^2, f_{a_1}^2$, and $\delta_f\equiv f_{\rho'}^2-f_{a_1'}^2$ should be computed from the CSR sum rules within a four-resonances consideration, namely,

$$\begin{aligned} m_\rho^2f_\rho^2-m_{a_1}^2f_{a_1}^2+m_{\rho'}^2\delta_f&=f_\pi^2+\epsilon,\\ m_\rho^4f_\rho^2-m_{a_1}^4f_{a_1}^2+m_{\rho'}^4\delta_f&=2m_{\rho'}^2\epsilon, \qquad (16)\\ m_\rho^6f_\rho^2-m_{a_1}^6f_{a_1}^2+m_{\rho'}^6\delta_f&=-4\langle\bar qq\rangle^2+3m_{\rho'}^4\epsilon, \end{aligned}$$

where $\epsilon\equiv f_{a_1'}^2m_{\rho'}^2\delta_m$.

Using experimental values of $m_\rho=770$ MeV, $m_{a_1}=1230\pm40$ MeV, $m_{\rho'}=1465\pm25$ MeV, and $f_\pi=93$ MeV and bearing in mind an averaged value for the quark condensate $[\langle\bar qq\rangle=-235\pm15\ ({\rm MeV})^3]$ and a model estimate for the small parameter ϵ (for example, from [35] and the condition $f_{a_1'}\lesssim f_{\rho'}$), one can find from (15) and (16) that

$$f_\rho\approx0.18,\quad f_{a_1}\approx0.11,\quad f_{\rho'}^2-f_{a_1'}^2\approx0.0034, \qquad (17)$$

and, for the electromagnetic pion-mass difference $\Delta m_\pi|_{\rm em}$, that

$$\Delta m_\pi|_{\rm em}^{(4)}\approx3.85\pm0.16\ {\rm MeV}. \qquad (18)$$

The inclusion of the correction for a nonzero value of the quark condensate improves the result for $\Delta m_\pi|_{\rm em}^{(4)}$ by 5%. The relative deviation from (14) amounts to 13% for the ansatz being considered. We note that $\Delta m_\pi|_{\rm em}^{(4)}$ grows in response to an increase in the quark-condensate value [for example, $\Delta m_\pi|_{\rm em}^{(4)}=4.42$ MeV for $\langle\bar qq\rangle=-300\ ({\rm MeV})^3$] and that, if, for f_π, one uses the value that it would have in the chiral limit, $f_\pi=87$ MeV [24], the result changes by less than 1%.

As follows from data presented [8], $f_\rho=0.20\pm0.01$ (from the decay $\rho^0\to e^+e^-$) and $f_{a_1}=0.10\pm0.02$ (from the decay $a_1\to\pi\gamma$). The constant $f_{\rho'}$ has not yet been determined experimentally because the electromagnetic decay of the ρ' meson is strongly suppressed by hadronic decay channels. Nevertheless, Eq. (17) provides a lower bound on this constant, $f_{\rho'}\gtrsim0.06$. Our numerical estimates for f_ρ and f_{a_1} agree with those given in [37].

We also are able to compute the constant L_{10} that appears in the effective chiral Lagrangian [24] and

which depends on the mean-square electromagnetic pion radius $\langle r_\pi^2\rangle$ and on the axial-vector pion form factor F_A for the decay $\pi \to e\nu\gamma$ (see, for example, [36]). Using the relation

$$L_{10} = -\frac{1}{16}\frac{d}{dp^2}\left(p^2\left(\Pi^V(p^2) - \Pi^A(p^2)\right)\right)_{p^2=0} \quad (19)$$

and Eqs. (4) and (11), one easily obtains the following result for L_{10} [29]:

$$L_{10} = \frac{1}{4}\left(\sum_n f_{A,n}^2 - \sum_n f_{V,n}^2\right). \quad (20)$$

For the case of $n = 1, 2$, this leads to the estimate $L_{10} \approx -6.0 \times 10^{-3}$, which is consistent with that of [4] from hadronic τ decays: $L_{10} = -(6.36 \pm 0.09|_{\text{expt}} \pm 0.16|_{\text{theor}}) \times 10^{-3}$.

Let us now find out how the above scheme for calculating $\Delta m_\pi|_{\text{em}}$ works in the case where one takes into account new resonances in the CSR sum rules. By virtue of CSR at high energies, one may expect that fulfillment of the inequality $m_{a_1'}^2 - m_{\rho'}^2 \ll m_{\rho'}^2$ entails fulfillment of the inequality $m_{a_1''}^2 - m_{\rho''}^2 \ll m_{\rho''}^2$. Since the mass $m_{\rho''}$ is known, only one new variable $f_{\rho''}^2 - f_{a_1''}^2$ appears in the set of Eqs. (16). As an additional condition, one can set the constant f_{a_1} to its experimental value of $f_{a_1} \approx 0.10$. A numerical solution then yields $\Delta m_\pi|_{\text{em}}^{(6)} \approx 3.94$ MeV [relative deviation from (14) amounts to 11%], $f_\rho \approx 0.18$, $f_{\rho'}^2 - f_{a_1'}^2 \approx 0.0023$ (and, consequently, $f_{\rho'} \gtrsim 0.05$), $f_{\rho''}^2 - f_{a_1''}^2 \approx 0.0003$, and $L_{10} \approx -6.2 \times 10^{-3}$. One can see that the addition of higher resonances in calculating the electromagnetic pion-mass difference improves the results, making them more consistent with the experimental value.

One can estimate the contribution of higher resonances to (12) in a different way. Namely, taking into account in (12) the inequality

$$\frac{m_{A,k}^2 - m_{V,k}^2}{m_{V,k}^2} \ll 1, \quad k > 1, \quad (21)$$

which is a consequence of CSR at high energies, we arrive at

$$\sum_{k=2}^{n}\left(m_{A,k}^4 f_{A,k}^2 \ln m_{A,k}^2 - m_{V,k}^4 f_{V,k}^2 \ln m_{V,k}^2\right) \quad (22)$$
$$\simeq (m_\rho^4 f_\rho^2 - m_{a_1}^4 f_{a_1}^2)\ln \bar{m}_{V,n}^2 + \sum_{k=2}^{n}\left(\frac{m_{A,k}^2}{m_{V,k}^2} - 1\right) m_{A,k}^4 f_{A,k}^2,$$

where we have introduced the averaged mass $\bar{m}_{V,n}$ as

$$\sum_{k=2}^{n}\left(m_{V,k}^4 f_{V,k}^2 - m_{A,k}^4 f_{A,k}^2\right)\ln m_{V,k}^2 \quad (23)$$
$$\equiv \ln \bar{m}_{V,n}^2 \sum_{k=2}^{n}\left(m_{V,k}^4 f_{V,k}^2 - m_{A,k}^4 f_{A,k}^2\right).$$

Under the assumptions made and at the values admitted here for the V-, A-meson spectral characteristics, the second term in (22) is two to three orders of magnitude less than the first one (at least if n is not large). Therefore, we may henceforth neglect it. Expression (12) can be recast into the form

$$\Delta m_\pi|_{\text{em}}^{(n)} = \frac{3}{4}\frac{\alpha_{\text{em}}}{\pi f_\pi^2 (m_{\pi^+} + m_{\pi^0})} \quad (24)$$
$$\times\left\{(m_{a_1}^4 f_{a_1}^2 \ln m_{a_1}^2 - m_\rho^4 f_\rho^2 \ln m_\rho^2) - (m_{a_1}^4 f_{a_1}^2 - m_\rho^4 f_\rho^2)\ln \bar{m}_{V,n}^2\right\}.$$

The second term in (24) (which has the factor $\ln \bar{m}_{V,n}^2$) is a correction to (13) [Eq. (13) is written in a form where the constants f_ρ and f_{a_1} are eliminated by means of the one-channel Weinberg sum rules]. Were the second one-channel sum rule (9) exactly valid, this term would vanish.

If we assume quite a good convergence of the CSR sum rules (such that the inclusion of $k > 2$ resonances therein would not lead to a significant change in the spectral characteristics of $k \le 2$ mesons), then the quantity $\bar{m}_{V,n}$ differs, in practice, from $m_{\rho'}$ slightly within our approximation. Thus, we can set $\ln \bar{m}_{V,n} \simeq \ln m_{\rho'}$, and the generalization for Eq. (13) then has the form

$$\overline{\Delta m_\pi}|_{\text{em}} \simeq \frac{3}{4}\frac{\alpha_{\text{em}}}{\pi f_\pi^2 (m_{\pi^+} + m_{\pi^0})} \quad (25)$$
$$\times\left\{m_\rho^4 f_\rho^2 \ln\frac{m_{\rho'}^2}{m_\rho^2} - m_{a_1}^4 f_{a_1}^2 \ln\frac{m_{\rho'}^2}{m_{a_1}^2}\right\},$$

where the overbar means that the averaged mass approximation is used for higher meson resonances. In contrast to what we had in the preceding method, expression (25) does not contain the quark condensate, whose value varies considerably in the literature.

As follows from the derivation of formula (25), we should substitute there those values of f_ρ and f_{a_1} that they have in the ansatz that is being considered, which includes a given number of resonances (since the Weinberg sum rules must be satisfied). By way of example, we indicate that, in the four-resonance case, these are $f_\rho \approx 0.18$ and $f_{a_1} \approx 0.11$, relation (25) then yielding the result $\overline{\Delta m_\pi}|_{\text{em}}^{(4)} = 3.64$ MeV, which is almost coincident with that in (18) without allowance for the quark condensate. Compared with

the one-channel consideration, the last value is better. In addition, the advantage of formula (25) over (13) is obvious in the case where one substitutes directly, for f_ρ and f_{a_1}, their experimental values and varies them within their experimental bounds: $f_\rho = 0.20 \pm 0.01$, $f_{a_1} = 0.10 \pm 0.02$, and $m_{a_1} = 1230 \pm 40$ MeV. Relation (13) [more strictly, Eq. (12) with $k = 1$] then leads to the absurd estimate $\Delta m_\pi|_{\rm em} = 102^{+160}_{-120}$ MeV, which is associated with poor fulfillment of the one-channel Weinberg sum rules. At the same time, the result given by Eq. (25) appears to be quite acceptable: $\overline{\Delta m_\pi}|_{\rm em} = 7.4 \pm 3.3$ MeV. Thus, the second term in (24) is on the same order of magnitude as the first one. Consequently, the inclusion of higher meson resonances is of importance. One may expect from Eq. (24) that, upon going over from the four-resonance ansatz to the six-resonance one, etc., the resulting correction will grow slowly in the right direction, since the inclusion of higher meson resonances with $k > 2$ effectively leads to a slight increase in the averaged mass $\bar{m}_{V,n}$ and since the corresponding contribution enters into (24) with a negative sign. As a result, the transition from the two-resonance ansatz to the four-resonance one changes the electromagnetic pion-mass difference in the right direction and the inclusion of higher meson resonances ($k > 2$) produces a similar result, but the latter only leads to an insignificant correction.

4. CONCLUSION

We have presented two methods for taking into account both vector ($\rho', \rho'', \ldots$) and axial-vector ($a_1', \ldots$) higher meson resonances in calculating the electromagnetic pion-mass difference $\Delta m_\pi|_{\rm em}$. These methods are based on the idea of chiral-symmetry restoration at high energies and on the operator-product expansion of the correlation functions for vector and axial-vector quark densities. All calculations have been performed in the chiral limit in the large-N_c approximation, and use has been made here of the asymptotic freedom of QCD.

First, $\Delta m_\pi|_{\rm em}$ has been calculated in the four-resonance approximation, where, in addition to the ρ and a_1 mesons, their first excitations (namely, the ρ' and a_1' mesons) have been taken into consideration. The conventional Weinberg sum rules have been supplemented with the third sum rule (10), which follows from the operator-product expansion. In the calculation, it has also been assumed that $m_{a_1'} \gtrsim m_{\rho'}$, which is expected by virtue of asymptotic chiral-symmetry restoration. As a result, the electromagnetic pion-mass difference has been estimated at $\Delta m_\pi|^{(4)}_{\rm em} \approx 3.85 \pm 0.16$ MeV, which improves the agreement between theoretical predictions and the experimental value of $\Delta m_\pi|_{\rm expt} = 4.42 \pm 0.03$ MeV (where the correction due to this isospin-symmetry breaking was taken into account) by 18%. For the ρ^0- and a_1-meson electromagnetic decay constants, we have obtained the estimates $f_\rho \approx 0.18$ and $f_{a_1} \approx 0.11$, which are in good agreement with the results deduced in [8, 37] by using different model approaches. The calculation of the constant L_{10} of effective chiral Lagrangian [24] has yielded here the value of $L_{10} \approx -6.0 \times 10^{-3}$, which is in good agreement with experimental data following from hadronic τ-decays [4]: $L_{10} = -(6.36 \pm 0.09|_{\rm expt} \pm 0.16|_{\rm theor}) \times 10^{-3}$. Moreover, it has been shown that the inclusion of the next resonances improves the result insignificantly, by about a few percent.

The second approach represents an extension of Eq. (13) for $\Delta m_\pi|^{(2)}_{\rm em}$ toward including higher resonances. First of all, it turns out that, when we use experimental values for the masses of the ρ and a_1 mesons and for their decay constants, the generalized Eq. (25) works better than (12) in the one-channel ($k = 1$) case. Second, one can see from the generalized Eq. (24) that the inclusion of the ρ' and a_1' meson reduces the discrepancy and that the inclusion of higher resonances ($k > 2$) also leads to an improvement.

Finally, we note that an attempt was made in [38] to estimate, on the basis of phenomenology, a number of quantities, including $\Delta m_\pi|_{\rm em}$, with the aid of two-point correlation functions saturated by an infinite number of resonances of relevant mesons. In that study, the mass spectrum of higher excitations was parametrized by a trajectory of the Regge–Veneziano type, in contrast to [35], where the mass spectrum of vector meson resonances was calculated within quasilocal quark models [39] without introducing any preliminary assumptions on the form and structure of the spectrum of higher meson resonances. The value obtained for the electromagnetic pion-mass difference was $\Delta m_\pi|^{(\infty)}_{\rm em} = 3.2$ MeV; that is, the discrepancy with (14) makes up 28%, which indicates an unsatisfactory approximation of the spectral characteristics of vector meson excitations in [38]. A somewhat different approach to including meson excitations and to calculating their spectral characteristics that is based on the Nambu–Jona-Lasinio model with separable four–quark interactions can be found in [40].

ACKNOWLEDGMENTS

We are grateful to A.A. Andrianov for stimulating discussions and enlightening comments.

This work was supported by the Russian Foundation for Basic Research (project no. 01-02-17152), by

the INTAS Call 2000 Grant (project no. 587), by the Ministry of Higher Education of the Russian Federation (grant no. E00-33-208), by the Program Universities of Russia: Basic Research (grant no. 992612), and a grant for young scientists from St. Petersburg (no. M01-2.4K-194).

REFERENCES

1. T. Das, G. S. Guralnik, V. S. Mathur, *et al.*, Phys. Rev. Lett. **18**, 759 (1967).
2. ALEPH Collab. (R. Barate *et al.*), Eur. Phys. J. C **4**, 409 (1998).
3. OPAL Collab. (K. Ackerstaff *et al.*), Eur. Phys. J. C **7**, 571 (1999); hep-ex/9808019.
4. M. Davier, A. Hocker, L. Girlanda, and J. Stern, Phys. Rev. D **58**, 096014 (1998).
5. R. Socolow, Phys. Rev. B **137**, 1221 (1965).
6. T. Minamikawa *et al.*, Prog. Theor. Phys. Suppl. **37–38**, 56 (1966); Prog. Theor. Phys. **61**, 548 (1979), and references therein.
7. R. D. Peccei and J. Sola, Nucl. Phys. B **281**, 1 (1987).
8. G. Ecker, J. Gasser, A. Pich, and E. de Rafael, Nucl. Phys. B **321**, 311 (1989).
9. W. A. Bardeen, J. Bijnens, and J.-M. Gerard, Phys. Rev. Lett. **62**, 1343 (1989).
10. D. Espriu, E. de Rafael, and J. Taron, Nucl. Phys. B **345**, 22 (1990); Erratum: **355**, 278 (1991).
11. J. Bijnens and E. de Rafael, Phys. Lett. B **273**, 483 (1991).
12. J. Donoghue, B. Holstein, and D. Wyler, Phys. Rev. D **47**, 2089 (1993).
13. J. Bijnens, Phys. Lett. B **306**, 343 (1993).
14. J. Bijnens, E. de Rafael, and H. Zheng, Z. Phys. C **62**, 437 (1994).
15. B. Moussallam, hep-ph/9804271.
16. S. Weinberg, Phys. Rev. Lett. **18**, 507 (1967).
17. D. E. Groom *et al.*, Eur. Phys. J. C **15**, 1 (2000).
18. V. V. Anisovich, hep-ph/0110326.
19. C. A. Baker *et al.*, Phys. Lett. B **449**, 114 (1999).
20. VES Collab. (V. Dorofeev), hep-ex/9905002.
21. O. A. Zaĭmidoroga, Fiz. Élem. Chastits At. Yadra **30**, 5 (1999) [Phys. Part. Nucl. **30**, 1 (1999)].
22. A. A. Andrianov and V. A. Andrianov, Zap. Nauchn. Semin. LOMI **245**, 5 (1996); hep-ph/9705364; A. A. Andrianov, D. Espriu, and R. Tarrach, Nucl. Phys. B **533**, 429 (1998); A. A. Andrianov and V. A. Andrianov, in *Proceedings of the International Workshop on Hadron Physics, Coimbra, 1999,* Ed. by A. H. Blin *et al.* (American Inst. of Physics, New York, 2000), p. 382; hep-ph/9911383; A. A. Andrianov, V. A. Andrianov, and R. Rodenberg, JHEP **06**, 3 (1999).
23. M. A. Shifman, A. I. Vainstein, and V. I. Zakharov, Nucl. Phys. B **147**, 385 (1979); **147**, 448 (1979).
24. J. Gasser and H. Leutwyler, Nucl. Phys. B **250**, 465 (1985).
25. M. Knecht and R. Urech, Nucl. Phys. B **519**, 329 (1998).
26. M. Knecht and R. Urech, Preprint CPT-97, p. 3524; hep-ph/9709348.
27. G. 't Hooft, Nucl. Phys. B **72**, 461 (1974).
28. E. Witten, Nucl. Phys. B **160**, 57 (1979).
29. M. Knecht and E. de Rafael, Phys. Lett. B **424**, 335 (1998); hep-ph/9712457.
30. L. J. Reinders, H. Rubinstein, and S. Yazaki, Phys. Rep. **127**, 1 (1985).
31. D. Gross, S. B. Treiman, and F. Wilczek, Phys. Rev. D **19**, 2188 (1979).
32. J. Gasser, Ann. Phys. (N.Y.) **136**, 62 (1981).
33. J. Gasser and H. Leutwyler, Ann. Phys. (N.Y.) **158**, 142 (1984).
34. M. Knecht, S. Peris, and E. de Rafael, Phys. Lett. B **443**, 255 (1998); hep-ph/9809594.
35. A. A. Andrianov, V. A. Andrianov, and S. S. Afonin, in *Proceedings of the 15th Workshop on High Energy Physics and Quantum Field Theory, Tver, 2000,* Ed. by M. N. Dubinin and V. I. Savrin, p. 233; hep-ph/0101245.
36. S. Narison, hep-ph/0012019.
37. A. A. Andrianov and D. Espriu, JHEP **10**, 022 (1999); A. A. Andrianov, D. Espriu, and R. Tarrach, Nucl. Phys. B (Proc. Suppl.) **86**, 275 (2000).
38. M. Golterman and S. Peris, hep-ph/0101098.
39. A. A. Andrianov and V. A. Andrianov, Int. J. Mod. Phys. A **8**, 1981 (1993); Teor. Mat. Fiz. **94**, 3 (1993); in *Proceedings of the School-Seminar "Hadrons and Nuclei from QCD," Tsuruga, Vladivostok, Sapporo, 1993* (World Sci., Singapore, 1994), p. 341; hep-ph/9309297; Nucl. Phys. B (Proc. Suppl.) **39**, 257 (1995); A. A. Andrianov, V. A. Andrianov, and V. L. Yudichev, Teor. Mat. Fiz. **108**, 1069 (1996); A. A. Andrianov, V. A. Andrianov, D. Espriu, and R. Tarrach, hep-ph/0009199.
40. M. K. Volkov, Yad. Fiz. **60**, 2094 (1997) [Phys. At. Nucl. **60**, 1920 (1997)]; M. K. Volkov and V. L. Yudichev, Phys. Part. Nucl. **31**, 282 (2000).

Translated by V. Andrianov

Physics of Atomic Nuclei, Vol. 65, No. 10, 2002, pp. 1868–1876. Translated from Yadernaya Fizika, Vol. 65, No. 10, 2002, pp. 1920–1928.

ELEMENTARY PARTICLES AND FIELDS
Theory

T-odd Correlation in the $K_{l3\gamma}$ Decay

V. V. Braguta*, A. A. Likhoded, and A. E. Chalov

Institute for High-Energy Physics, Protvino, Moscow oblast, 142284 Russia

Received June 14, 2001; in final form, September 28, 2001

Abstract—The dependence of the $K^+ \to \pi^0 l^+ \nu_l \gamma$ decay rate on the T-odd kinematical variable $\xi = \mathbf{q} \cdot [\mathbf{p}_l \times \mathbf{p}_\pi]/m_K^3$ is investigated in the tree and one-loop approximations of the Standard Model (SM). It is shown that the partial width of the decay on the tree level is an even function of the variable ξ, whereas the odd component is generated by the electromagnetic final-state interaction and determined by the imaginary parts of one-loop diagrams. The ξ-odd components of the partial widths of the $K^+ \to \pi^0 e^+ \nu_e \gamma$ and $K^+ \to \pi^0 \mu^+ \nu_\mu \gamma$ decays calculated in the one-loop approximation are smaller by four orders of magnitude than the even components evaluated from the tree-level SM diagrams. © *2002 MAIK "Nauka/Interperiodica".*

1. INTRODUCTION

Investigations of the rare radiative decays of K mesons offer an interesting possibility in the search for new physics beyond the Standard Model (SM). In particular, signals of the new CP-violating interactions are of special interest. In contrast to the SM, where violation of the CP symmetry is due to the complex phase in the Cabibbo–Kobayashi–Maskawa (CKM) matrix, the CP violation in the SM extensions appears naturally. For example, it may be due to the complex coupling constants characterizing the interaction of the new charged Higgs bosons with fermions [1], hypothetical tensor interactions [2], etc. The CP violation effects can be revealed in the experimental studies of the values sensitive to the T-odd contributions. Examples of such values are offered by the T-odd correlation ($\xi = \mathbf{q} \cdot [\mathbf{p}_l \times \mathbf{p}_\pi]/m_K^3$) in the $K^\pm \to \pi^0 \mu^\pm \nu\gamma$ decay [3] or the transverse muon polarization in the $K^\pm \to \mu^\pm \nu\gamma$ decay [4]. Current experiments cannot obtain the level of accuracy needed for an analysis of the differential distributions in the $K^\pm \to \pi^0 \mu^\pm (e^\pm) \nu_{\mu(e)} \gamma$ decays. However, up to $\sim 7.0 \times 10^5$ events of the $K^+ \to \pi^0 \mu^+ \nu_\mu \gamma$ decay are expected in the planned OKA experiment [5]. This would make possible a detailed study of the differential distributions for this process and either reveal the manifestations of new interactions or set more stringent limits on the parameters of extended models.

In the search for possible T-odd effects in the $K^+ \to \pi^0 \mu^+ \nu_\mu \gamma$ decay, it is especially important to estimate the SM contribution to the distribution with respect to ξ, which arises from the final-state electromagnetic interactions and provides a natural background for the new interactions.

Of special interest in the studies of possible T-odd effects is the Weinberg model with three Higgs doublets [1, 6]. This model allows for the complex Yukawa constants, which gives rise to interesting phenomena. It was shown [3] that the study of the T-odd correlation in the $K^+ \to \pi^0 \mu^+ \nu_\mu \gamma$ decay makes it possible either to discover the terms linear in the CP-violating coupling constants or to set more stringent limits on the three-doublet Weinberg model parameters.

In this study, we consider the dependence of the partial width of the $K^+ \to \pi^0 l^+ \nu_l \gamma$ decay on the kinematic variable $\xi = \mathbf{q} \cdot [\mathbf{p}_l \times \mathbf{p}_\pi]/m_K^3$ in the SM. In the general case, a differential distribution of the partial width $\rho(\xi) = d\Gamma/d\xi$ can be represented as a sum of the even ($f_{\rm even}$) and odd ($f_{\rm odd}$) functions of the variable ξ. In the tree approximation of the SM, the $f_{\rm odd}$ component vanishes. In what follows, we demonstrate that this effect is a direct consequence of the fact that the imaginary parts of the form factors of the decay evaluated in the chiral perturbation theory are equal to zero. However, the radiative corrections due to the final-state interactions [7] give rise to the imaginary parts of the form factors that appear in the expression for the amplitude of the $K^+ \to \pi^0 l^+ \nu_l \gamma$ decay. This, in turn, determines the nonvanishing odd contribution to the ξ distribution, which is calculated below in the one-loop approximation. The matrix element of the $K^+ \to \pi^0 l^+ \nu_l \gamma$ decay is evaluated in the leading approximation of the chiral perturbation theory, that is, to within $O(p^4)$ terms [8].

*e-mail: braguta@mail.ru

1063-7788/02/6510-1868$22.00

In order to describe the T-odd effects, we introduce, in addition to $f_{\rm odd}$, a quantity defined by the formula $A_\xi = (N_+ - N_-)/(N_+ + N_-)$, where N_+ and N_- are the numbers of events with $\xi > 0$ and $\xi < 0$, respectively. In this ratio, the numerator depends only on $f_{\rm odd}(\xi)$, whereas the denominator is proportional to $f_{\rm even}(\xi)$. As a consequence, this value is sensitive to the effects described by odd functions of ξ.

In what follows, we show that the one-loop SM contribution to $f_{\rm odd}$ is much smaller than $f_{\rm even}$ ($f_{\rm odd}/f_{\rm even} \sim 10^{-4}$). Hence, the proposed observables A_ξ and $f_{\rm odd}$ are sensitive to T-odd contributions and so are of particular interest in the search for the effects beyond the SM.

Another variable that is sensitive to violations of the CP symmetry, is the transverse polarization P_T of the muon produced in the $K^+ \to \pi^0\mu^+\nu$ and $K^+ \to \mu^+\nu\gamma$ decays [4, 7, 9]. In the framework of the SM, a nonzero transverse polarization, as well as the ξ dependence of the amplitude of the $K^+ \to \pi^0 l^+\nu_l\gamma$ decay, results from the final-state interactions. In these reactions, the value of P_T is sensitive to the T-odd effects; however, the experimental measurement of P_T presents a challenge [10]. The measurement of the A_ξ and $f_{\rm odd}$ values presents no technical problems to offer a major advantage over the case of the transverse polarization of the muon. A relatively small rate of processes appropriate for the measurements of A_ξ and $f_{\rm odd}$ could run into experimental difficulties; however, the expected number of the $K^+ \to \pi^0\mu^+\nu_\mu\gamma$ events in the OKA experiment makes it possible either to discover the CP-violating effects or to obtain more stringent limits on the parameters of the SM extensions.

In the second section, we study the dependence of the partial width of the $K^+ \to \pi^0 l^+\nu_l\gamma$ decay on the T-odd correlation in the tree approximation of the SM. The third section is devoted to an analysis of the one-loop SM contributions to the T-odd correlation. The last section summarizes the main results and conclusions.

2. T-ODD CORRELATION ON THE TREE LEVEL

The Feynman diagrams describing the $K^+(p) \to \pi^0(p')l^+(p_l)\nu_l(p_\nu)\gamma(q)$ decay on the tree level of the SM are shown in Fig. 1. In this approximation, the decay amplitude can be presented in the following form [8]:

$$T = \frac{G_{\rm F}}{\sqrt{2}} e V_{us}^* \epsilon^\mu(q)^* \times \left((V_{\mu\nu} - A_{\mu\nu})\bar{u}(p_\nu)\gamma^\nu(1-\gamma_5)v(p_l) + \frac{F_\nu}{2p_l q}\bar{u}(p_\nu)\gamma^\nu(1-\gamma_5)(m_l - \hat{p}_l - \hat{q})\gamma_\mu v(p_l) \right), \quad (1)$$

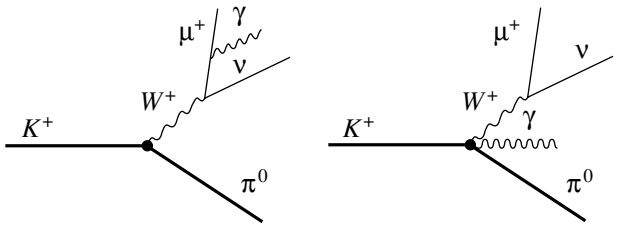

Fig. 1. Feynman diagrams describing the $K^+ \to \pi^0 l^+\nu_l\gamma$ decay in the tree approximation of the SM for the muon channel.

where

$$V_{\mu\nu} = i\int d^4x e^{iqx}\langle\pi^0(p')|TV_\mu^{\rm em}(x)V_\nu^{4-i5}(0)|K^+(p)\rangle, \quad (2)$$

$$A_{\mu\nu} = i\int d^4x e^{iqx}\langle\pi^0(p')|TV_\mu^{\rm em}(x)A_\nu^{4-i5}(0)|K^+(p)\rangle, \quad (3)$$

and F_ν is the matrix element of the K_{l3}^+ decay:

$$F_\nu = \langle\pi^0(p')|V_\nu^{4-i5}(0)|K^+(p)\rangle. \quad (4)$$

Here p', p_l, q, p_ν, and p are the 4-momenta of the pion, lepton, photon, neutrino, and kaon, respectively. In the leading order of the chiral perturbation theory, $A_{\mu\nu} = 0$ and the expressions for F_μ and $V_{\mu\nu}$ can be written as

$$F_\mu = \frac{1}{\sqrt{2}}(p+p')_\mu,$$

$$V_{\mu\nu} = V_1\left(g_{\mu\nu} - \frac{W_\mu q_\nu}{qW}\right) + V_2\left(p'_\mu q_\nu - \frac{p'q}{qW}W_\mu q_\nu\right) + \frac{p_\mu}{(pq)}F_\nu,$$

$$W_\mu = (p_l + p_\nu)_\mu,$$

$$V_1 = \frac{1}{\sqrt{2}}, \quad V_2 = -\frac{1}{\sqrt{2}pq}.$$

Then the matrix element of the decay takes the form

$$T = \frac{G_{\rm F}}{2} e V_{us}^* \epsilon^\mu(q)^* \bar{u}(p_\nu)(1+\gamma_5) \times \left((\hat{p}+\hat{p}')\left(\frac{p_\mu}{(pq)} - \frac{(p_l)_\mu}{(p_l q)}\right) - (\hat{p}+\hat{p}')\frac{\hat{q}\gamma_\mu}{2(p_l q)} + \left(\gamma_\mu - \frac{\hat{q}p_\mu}{(pq)}\right)\right)u(p_l), \quad (5)$$

and the expression for the partial width of the $K^+ \to \pi^0 l^+\nu_l\gamma$ decay can be obtained by integration over the phase space.

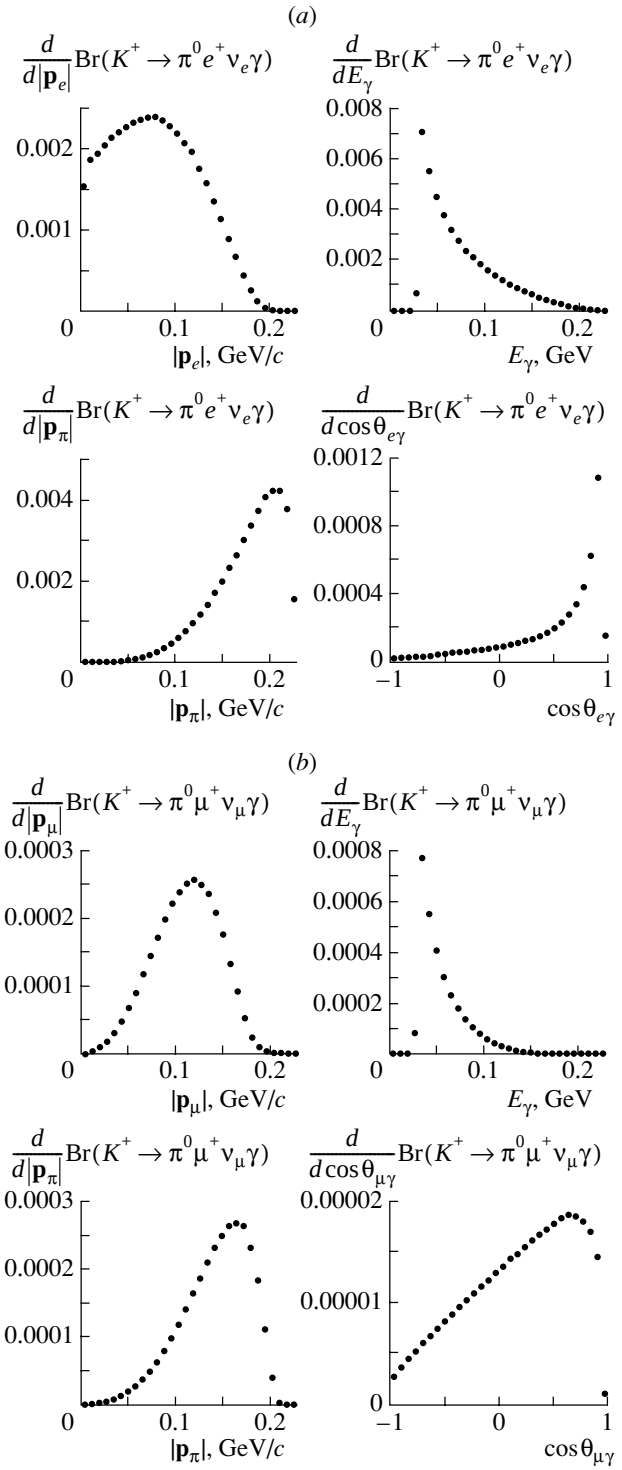

Fig. 2. Differential distributions of the relative partial width of the process with respect to the lepton, photon, and pion momenta and the angle between the lepton and photon momenta in cases of the (*a*) electron and (*b*) muon decay channels.

Figure 2 shows differential distributions of the partial decay width with respect to the final momenta of the particles and the angle between the lepton and photon momenta calculated in the tree approximation of the SM. For the electron decay channel (Fig. 2*a*), the partial decay width exhibits a maximum at small values of the lepton and photon momenta, maximum values of the pion momentum, and small values of the angle between the lepton and photon momenta.

In the case of the muon decay channel (Fig. 2*b*),

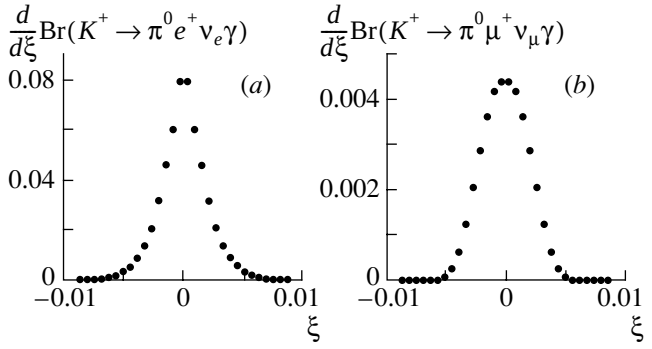

Fig. 3. The relative partial width of the $K^+ \to \pi^0 l^+ \nu\gamma$ decay in the tree approximation of the SM for the (a) electron and (b) muon decay channels.

the maximum partial decay width is observed at medium values of the lepton momentum, small values of the photon momentum, maximum values of the pion momentum, and small values of the angle between the lepton and photon momenta.

Taking into account the kinematical cutoff at the photon energy $E_\gamma > 30$ MeV and the lepton–photon opening angle $\theta_{l\gamma} > 20^\circ$ in the kaon rest frame, which are typical of both current and future experiments, the branching fractions of the electron and muon decay modes are equal to

$$\mathrm{Br}(K^+ \to \pi^0 e^+ \nu_e \gamma) = 3.18 \times 10^{-4},$$
$$\mathrm{Br}(K^+ \to \pi^0 \mu^+ \nu_\mu \gamma) = 2.15 \times 10^{-5}.$$

These values are in good agreement with the earlier computations (see, for example, [8]) and the existing experimental limitations [11].

In the search for possible CP-odd contributions, our attention is focused on the distribution of the partial decay width with respect to the variable $\xi = \mathbf{q} \cdot [\mathbf{p}_l \times \mathbf{p}_\pi]/m_K^3$, which changes its sign at the CP or T conjugation. This distribution,

$$\rho(\xi) = d\Gamma/d\xi, \tag{6}$$

offers a good indicator of the time-reversal invariance violation. It is evident that the function $\rho(\xi)$ can be written as the sum

$$\rho = f_{\mathrm{even}}(\xi) + f_{\mathrm{odd}}(\xi),$$

where $f_{\mathrm{even}}(\xi)$ and $f_{\mathrm{odd}}(\xi)$ are the even and odd functions of the variable ξ, respectively. The function $f_{\mathrm{odd}}(\xi)$ can be represented in the form:

$$f_{\mathrm{odd}} = g(\xi^2)\xi. \tag{7}$$

Upon integration of $\rho(\xi)$ over the whole range of ξ values, only the function $f_{\mathrm{even}}(\xi)$ gives a nonvanishing contribution to the total decay width. The function $\rho(\xi)/\Gamma_{\mathrm{tot}}$ for the $K^+ \to \pi^0 \mu^+ \nu_\mu \gamma$ and $K^+ \to \pi^0 e^+ \nu_e \gamma$ decays is plotted in Fig. 3. As is seen, the distributions obtained in the tree approximation of the SM (that is, without T-odd contributions) are symmetric with respect to the line $\xi = 0$; that is, the number of events in the $K^+ \to \pi^0 l^+ \nu_l \gamma$ decay with $\xi > 0$ is the same as that with $\xi < 0$. The explanation is as follows: the square of the matrix element for this decay in the tree approximation of the SM is expressed in terms of the scalar products of the momenta of the outgoing particles; hence, the terms linear in ξ are absent. For this reason, the distribution $\rho(\xi)$ is an even function of the variable ξ.

Let us introduce, in addition to the differential distribution $\rho(\xi)$, the integral asymmetry parameter

$$A_\xi = \frac{N_+ - N_-}{N_+ + N_-}, \tag{8}$$

where N_+ and N_- are the numbers of events with $\xi > 0$ and $\xi < 0$, respectively. This value is convenient in the analysis of data on the $K^+ \to \pi^0 l^+ \nu_l \gamma$ decay, because the numerator of A_ξ depends only on $f_{\mathrm{odd}}(\xi)$, making the ratio very sensitive to the T-odd effects beyond the SM.

3. T-ODD CORRELATION DUE TO FINAL-STATE INTERACTIONS

In the SM, the final-state electromagnetic interactions may generate nonzero values of the asymmetry A_ξ and the odd component of $\rho(\xi)$ on the one-loop diagram level. The most general expression for the amplitude of the $K^+ \to \pi^0 l^+ \nu_l \gamma$ decay (with regard for the one-loop electromagnetic corrections and gauge invariance) has the form

$$T_{\text{one-loop}} = \frac{G_{\mathrm{F}}}{\sqrt{2}} e V_{us}^* \epsilon_\nu^* \bar{u}(p_\nu)(1+\gamma_5) \tag{9}$$
$$\times \left(C_1 \left(p^\nu - \frac{(pq)}{(p_l q)} p_l^\nu \right) + C_3 \left((p')^\nu - \frac{(p'q)}{(p_l q)} p_l^\nu \right) \right.$$

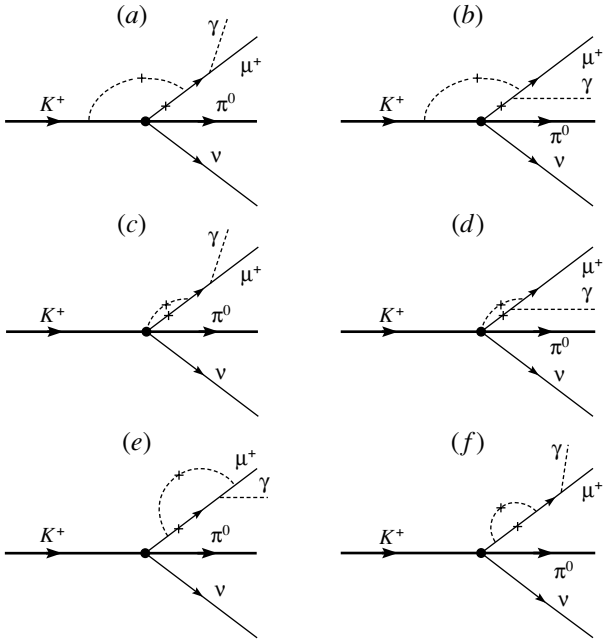

Fig. 4. Feynman diagrams contributing to the imaginary part of the form factors (9) in the one-loop approximation of the SM.

$$+C_5\left(p^\nu-\frac{(pq)}{(p_lq)}p_l^\nu\right)\hat{p'}+C_7\left((p')^\nu-\frac{(p'q)}{(p_lq)}p_l^\nu\right)\hat{p'}$$
$$+C_9(\hat{q}p^\nu-(pq)\gamma^\nu)+C_{10}(\hat{q}p_l^\nu-(p_lq)\gamma^\nu)$$
$$+C_{11}(\hat{q}(p')^\nu-(p'q)\gamma^\nu)+C_{12}\hat{q}\gamma^\nu$$
$$+C_{13}\hat{p'}(\hat{q}p^\nu-(pq)\gamma^\nu)+C_{14}\hat{p'}(\hat{q}p_l^\nu-(p_lq)\gamma^\nu)$$
$$+C_{15}\hat{p'}(\hat{q}(p')^\nu-(p'q)\gamma^\nu)+C_{16}\hat{p'}\hat{q}\gamma^\nu\Big)v(p_l),$$

where the coefficients C_i are the kinematical factors arising from the one-loop contributions. The square of the matrix element involving the one-loop contributions can be represented as the sum

$$|T_{\text{one-loop}}|^2=|T_{\text{even}}|^2+|T_{\text{odd}}|^2\,, \qquad (10)$$

where

$$|T_{\text{odd}}|^2=-2G_{\text{F}}^2e^2|V_{us}|^2m_K^4\xi \qquad (11)$$
$$\times\left(\text{Im}(C_1)m_l\left(2\frac{1}{(p_lq)}-4\frac{(pq)}{(p_lq)^2}\right)\right.$$
$$-\text{Im}(C_3)m_l\left(2\frac{1}{(p_lq)}+4\frac{(p'q)}{(p_lq)^2}\right)$$
$$+\text{Im}(C_5)\left(4+2m_l^2\frac{(pq)}{(p_lq)^2}+\frac{1}{p_lq}(2m_K^2-2m_\pi^2\right.$$
$$\left.+4(pp')-4(pp_l)-4(pq)-4(p'p_l)-4(p'q))\right)$$
$$+\text{Im}(C_7)\left(2m_l^2\frac{(p'q)}{(p_lq)^2}+4\frac{m_\pi^2}{(p_lq)}\right)$$
$$+\text{Im}(C_9)\left(8\frac{(pp_l)}{(p_lq)}-8\frac{m_K^2}{(pq)}\right)$$
$$+\text{Im}(C_{10})\left(8\frac{m_l^2}{(p_lq)}+8\frac{(p_lq)}{(pq)}-8\frac{(pp_l)}{(pq)}-8\right)$$
$$+\text{Im}(C_{11})\left(8\frac{(p'q)}{(pq)}+8\frac{(p'p_l)}{(p_lq)}-8\frac{(pp')}{(pq)}\right)$$
$$+\text{Im}(C_{12})\left(4\frac{m_l}{(pq)}-8\frac{m_l}{(p_lq)}\right)$$
$$+\text{Im}(C_{13})m_l\left(4\frac{m_K^2}{(pq)}-4\frac{(pp_l)}{(p_lq)}\right)$$
$$+\text{Im}(C_{14})m_l\left(4+4\frac{(pp_l)}{(pq)}-4\frac{m_l^2}{(p_lq)}-4\frac{(p_lq)}{(pq)}\right)$$
$$+\text{Im}(C_{15})m_l\left(4\frac{(pp')}{(pq)}-4\frac{(p'q)}{(pq)}-4\frac{(p'p_l)}{(p_lq)}\right)$$
$$+\text{Im}(C_{16})\Big(-8+4\frac{m_K^2}{(pq)}-4\frac{m_\pi^2}{(pq)}+8\frac{(pp')}{(pq)}$$
$$\left.-8\frac{(pp_l)}{(pq)}-8\frac{(p'p_l)}{(pq)}-8\frac{(p'q)}{(pq)}+4\frac{m_l^2}{(p_lq)}+8\frac{(p_lq)}{(pq)}\right)\Big).$$

It follows from the expressions (10) and (11) that the nonvanishing contribution to $f_{\text{odd}}(\xi)$ and A_ξ (linear in ξ) is determined by the one-loop electromagnetic corrections giving rise to the imaginary parts of the form factors C_i. These imaginary parts can be determined from the condition of unitarity of the S matrix [7]:

$$S^+S=1.$$

Since $S=1+iM$, we arrive at

$$M_{fi}-M_{if}^*=i\sum_n M_{nf}^*M_{ni}, \qquad (12)$$

where the indices i, f, and n correspond to the initial, final, and intermediate states of the system of particles. Making use of the T invariance of the matrix element, we obtain

$$\text{Im}M_{fi}=\frac{1}{2}\sum_n M_{nf}^*M_{ni},$$
$$M_{fi}=(2\pi)^4\delta(P_f-P_i)T_{fi}.$$

Figure 4 shows the one-loop diagrams describing the electromagnetic radiative corrections for the $K^+\to\pi l^+\nu_l\gamma$ decay. These corrections give rise to the imaginary parts of the form factors that appear in formula (9) and so give a contribution to $f_{\text{odd}}(\xi)$. The expressions for the imaginary parts of these diagrams giving a nonvanishing contribution to $f_{\text{odd}}(\xi)$ can be found using formula (1). All these one-loop diagrams can be divided into two groups. The first group includes the diagrams in Figs. 4*a*, 4*c*, and 4*e*.

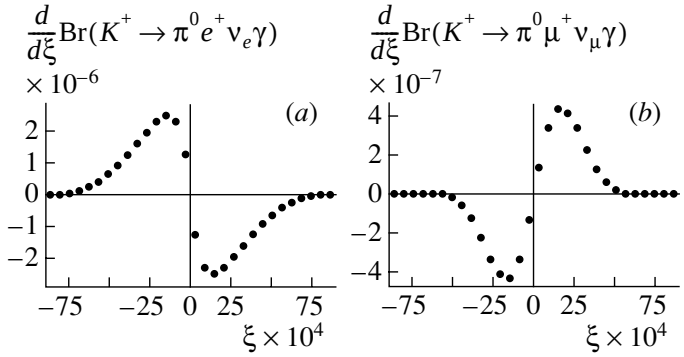

Fig. 5. Contributions of the ξ-odd distribution component f_{odd} to the relative partial width for the (a) electron and (b) muon decay channels.

The imaginary part of these diagrams can be written as follows:

$$\mathrm{Im}T_1 = \frac{\alpha}{2\pi}\frac{G_\mathrm{F}}{\sqrt{2}} eV_{us}^* \bar{u}(p_\nu)(1+\gamma_5) \quad (13)$$
$$\times \int \frac{d^3k_\gamma}{2\omega_\gamma}\frac{d^3k_l}{2\omega_l}\delta(k_\gamma + k_l - q - p_l)$$
$$\times \hat{R}_\mu(\hat{k}_l - m_l)\gamma^\mu \frac{\hat{q} + \hat{p}_l - m_l}{(q+p_l)^2 - m_l^2}\gamma^\delta \varepsilon_\delta^* v(p_l).$$

The second group includes the diagrams in Figs. 4b, 4d, and 4f. The corresponding imaginary part has the form

$$\mathrm{Im}T_2 = \frac{\alpha}{2\pi}\frac{G_\mathrm{F}}{\sqrt{2}} eV_{us}^* \bar{u}(p_\nu)(1+\gamma_5) \quad (14)$$
$$\times \int \frac{d^3k_\gamma}{2\omega_\gamma}\frac{d^3k_l}{2\omega_l}\delta(k_\gamma + k_l - q - p_l)$$
$$\times \hat{R}_\mu(\hat{k}_l - m_l)\gamma^\delta \varepsilon_\delta^* \frac{\hat{k}_\mu - \hat{q} - m_l}{(k_\mu - q)^2 - m_l^2}\gamma^\mu v(p_l),$$

where

$$\hat{R}_\mu = (V_{\mu\nu} - A_{\mu\nu})\gamma^\nu - \frac{F_\nu}{2(p_l q)}\gamma^\nu(\hat{p}_l + \hat{q} - m_l)\gamma_\mu. \quad (15)$$

Calculation of the integrals (13) and (14) and their dependence on the kinematical variables are given in Appendix 1. The expressions for the imaginary parts of the form factors C_i are presented in Appendix 2.

4. DISCUSSION OF THE RESULTS

Prior to discussing the numerical results, it should be noted that we neglect the contribution of the one-loop diagrams to the even component of the distribution with respect to ξ because these contributions are much smaller than those of the SM tree diagrams to f_{even}. The contribution of the SM tree diagrams to f_{odd} equals zero; hence, the contribution of the one-loop diagrams to f_{odd} is significant. Proceeding to analyze the dependence of the differential probability of the $K^+ \to \pi^0 l^+ \nu_l \gamma$ decay on the kinematical variable ξ, we will separately treat the two decay modes, $K^+ \to \pi^0 e^+ \nu_e \gamma$ and $K^+ \to \pi^0 \mu^+ \nu_\mu \gamma$, because their partial widths as the functions of ξ differ substantially.

$\boldsymbol{K^+ \to \pi^0 e^+ \nu_e \gamma}$. Figure 5$a$ shows the odd contribution to the partial decay width arising from the imaginary parts of the one-loop diagrams presented in Fig. 4. In the kinematical domain of the parameter ξ, this function varies in the interval from -2.0×10^{-6} to 2.0×10^{-6}, the sign of the function f_{odd} being opposite to the sign of ξ. Since the total distribution is the sum of the even and odd components, the number of the experimentally observed events with negative values of ξ should exceed the number of observed events with positive values of ξ.

The asymmetry for this decay mode is equal to

$$A_\xi(K^+ \to \pi e^+ \nu_e \gamma) = -0.59 \times 10^{-4}.$$

$\boldsymbol{K^+ \to \pi^0 \mu^+ \nu_\mu \gamma}$. Figure 5$b$ shows the odd component of the distribution of the relative partial decay width for the muon channel. This function varies from -4.0×10^{-7} to 4.0×10^{-7}, and the sign of f_{odd} coincides with the sign of ξ. The difference in behavior of f_{odd} in the cases of muon and electron decay modes can be explained as follows: the contributions of the imaginary parts of the form factors C_1, C_{12}, C_{13}, and C_{14} proportional to the lepton mass are significant in the former case and negligibly small in the latter case. In the case of the muon decay mode, the number of experimentally observed events with positive values of ξ should exceed the number of events with negative values of ξ.

The difference in the behavior of f_{odd} for the electron and muon decay modes can help to separate the contribution of the radiative SM corrections from the contributions of new physics. In the extensions

of the SM, CP-violation can occur on the tree level and the sign of the distribution with respect to ξ is independent of the lepton flavor, as is the case in the Weinberg model [1].

The value of the asymmetry for this decay mode is equal to

$$A_\xi(K^+ \to \pi\mu^+\nu_\mu\gamma) = 1.14 \times 10^{-4}.$$

It should be noted that the value of $f_{\rm odd}$ for both decay channels is smaller than the tree-level SM contribution by a factor of 10^4, indicating a strong suppression of the ξ-odd effects in the SM. The SM background contribution to the odd component of the distribution over ξ leaves a window for detecting the CP-violating effects in these decay channels on a level of up to 10^{-4}.

From the analysis of the integral asymmetry A_ξ, it follows that the number of events necessary to reliably observe the ξ-odd effects is on the order of 10^8. In this context, it is especially important to study the differential distribution of the partial decay width.

ACKNOWLEDGMENTS

The authors are grateful to L.B. Okun' for his interest in this study and critical comments and to V.A. Rubakov, V.F. Obraztsov, and A.K. Likhoded for stimulating discussions.

This study was supported in part by the Russian Foundation for Basic Research (project nos. 99-02-16558 and 00-15-96645) and by the Ministry of Education of the Russian Federation (project no. E00-3.3-62).

APPENDIX 1

To perform integration in formulas (13) and (14), we introduce the notation

$$P = p_l + q,$$

$$d\rho = \frac{d^3k_\gamma}{2\omega_\gamma}\frac{d^3k_l}{2\omega_l}\delta(k_\gamma + k_l - P).$$

In what follows, we either present explicit expressions for the integrals in terms of these parameters or write the systems of equations in these parameters such that the integrals can be taken using the solutions of these equations.

Thus, we obtain

$$J_{11} = \int d\rho = \frac{\pi}{2}\frac{P^2 - m_l^2}{P^2},$$

$$J_{12} = \int d\rho\frac{1}{(pk_\gamma)} = \frac{\pi}{2I}\ln\left(\frac{(Pp)+I}{(Pp)-I}\right),$$

where

$$I^2 = (Pp)^2 - m_K^2P^2;$$

$$\int d\rho\frac{k_\gamma^\alpha}{(pk_\gamma)} = a_{11}p^\alpha + b_{11}P^\alpha,$$

where the parameters a_{11} and b_{11} are determined by the expressions

$$a_{11} = -\frac{1}{(Pp)^2 - m_K^2P^2}\left(P^2J_{11} - \frac{J_{12}}{2}(Pp)(P^2 - m_l^2)\right),$$

$$b_{11} = \frac{1}{(Pp)^2 - m_K^2P^2}\left((Pp)J_{11} - \frac{J_{12}}{2}m_K^2(P^2 - m_l^2)\right);$$

$$\int d\rho k_\gamma^\alpha = a_{12}P^\alpha,$$

where

$$a_{12} = \frac{(P^2 - m_l^2)}{2P^2}J_{11};$$

$$J_1 = \int d\rho\frac{1}{(pk_\gamma)((p_l - k_\gamma)^2 - m_l^2)}$$
$$= -\frac{\pi}{2I_1(P^2 - m_l^2)}\ln\left(\frac{(pp_l)+I_1}{(pp_l)-I_1}\right),$$

$$J_2 = \int d\rho\frac{1}{(p_l - k_\gamma)^2 - m_l^2}$$
$$= -\frac{\pi}{4I_2}\ln\left(\frac{(Pp_l)+I_2}{(Pp_l)-I_2}\right),$$

where

$$I_1^2 = (pp_l)^2 - m_l^2m_K^2, \quad I_2^2 = (Pp_l)^2 - m_l^2P^2;$$

and

$$\int d\rho\frac{k_\gamma^\alpha}{(p_l - k_\gamma)^2 - m_l^2} = a_1P^\alpha + b_1p_l^\alpha,$$

where

$$a_1 = -\frac{m_l^2(P^2 - m_l^2)J_2 + (Pp_l)J_{11}}{2((Pp_l)^2 - m_l^2P^2)},$$

$$b_1 = \frac{(Pp_l)(P^2 - m_l^2)J_2 + P^2J_{11}}{2((Pp_l)^2 - m_l^2P^2)}.$$

The following integrals are expressed through parameters, the values of which can be determined from the solutions of the corresponding systems of equations. These integrals are as follows:

$$\int d\rho\frac{k_\gamma^\alpha}{(pk_\gamma)((p_l - k_\gamma)^2 - m_l^2)} = a_2P^\alpha + b_2p^\alpha + c_2p_l^\alpha,$$

where

$$\begin{cases} a_2(Pp) + b_2 m_K^2 + c_2(pp_l) = J_2 \\ a_2(Pp_l) + b_2(pp_l) + c_2 m_l^2 = -\frac{1}{2} J_{12} \\ a_2 P^2 + b_2(Pp) + c_2(Pp_l) = (p_l q) J_1; \end{cases}$$

$$\int d\rho \frac{k_\gamma^\alpha k_\gamma^\beta}{(pk_\gamma)((p_l - k_\gamma)^2 - m_l^2)}$$
$$= a_3 g^{\alpha\beta} + b_3(P^\alpha p^\beta + P^\beta p^\alpha) + c_3(P^\alpha p_l^\beta + P^\beta p_l^\alpha)$$
$$+ d_3(p^\alpha p_l^\beta + p^\beta p_l^\alpha) + e_3 p_l^\alpha p_l^\beta + f_3 P^\alpha P^\beta + g_3 p^\alpha p^\beta,$$

where

$$\begin{cases} 4a_3 + 2b_3(Pp) + 2c_3(Pp_l) + 2d_3(pp_l) \\ \qquad + g_3 m_K^2 + e_3 m_l^2 + f_3 P^2 = 0 \\ c_3(pp_l) + b_3 m_K^2 + f_3(Pp) - a_1 = 0 \\ c_3(Pp) + d_3 m_K^2 + e_3(pp_l) - b_1 = 0 \\ a_3 + b_3(Pp) + d_3(pp_l) + g_3 m_K^2 = 0 \\ b_3(pp_l) + c_3 m_l^2 + f_3(Pp_l) = -\frac{1}{2} b_{11} \\ b_3(Pp_l) + d_3 m_l^2 + g_3(pp_l) = -\frac{1}{2} a_{11} \\ a_3 P^2 + 2b_3 P^2(Pp) + 2c_3 P^2(Pp_l) \\ \qquad + 2d_3(Pp_l)(Pp) + e_3(Pp_l)^2 + f_3(P^2)^2 \\ \qquad + g_3(Pp)^2 = (p_l q)^2 J_1; \end{cases}$$

and

$$\int d\rho \frac{k_\gamma^\alpha k_\gamma^\beta}{(p_l - k_\gamma)^2 - m_l^2} = a_4 g_{\alpha\beta} + b_4(P^\alpha p_l^\beta + P^\beta p_l^\alpha)$$
$$+ c_4 P^\alpha P^\beta + d_4 p_l^\alpha p_l^\beta,$$

where

$$\begin{cases} a_4 + d_4 m_l^2 + b_4(Pp_l) = 0 \\ b_4 m_l^2 + c_4(Pp_l) = -\frac{1}{2} a_{12} \\ 4a_4 + 2b_4(Pp_l) + c_4 P^2 + d_4 m_l^2 = 0 \\ a_4 P^2 + 2b_4 P^2(Pp_l) + c_4(P^2)^2 + d_4(Pp_l)^2 \\ \qquad = \frac{(P^2 - m_l^2)^2}{4} J_2. \end{cases}$$

APPENDIX 2

In this Appendix, we present expressions for the imaginary parts of the form factors C_i in terms of the parameters computed in the Appendix 1:

$$C_1 = \frac{\alpha}{\sqrt{2}\pi} m_l (4a_3 + b_3 m_K^2 + d_3 m_K^2$$
$$- 2a_2 m_l^2 + 2b_3 m_l^2 - 2c_2 m_l^2 + 6c_3 m_l^2$$
$$+ 2d_3 m_l^2 + 3e_3 m_l^2 + 3f_3 m_l^2 - b_3 m_\pi^2 - d_3 m_\pi^2$$
$$- 2b_3(p'p_l) - 2d_3(p'p_l) - 2b_3(p'q) - 2d_3(p'q)$$
$$- 4a_2(p_l q) + 4b_3(p_l q) - 2c_2(p_l q) + 8c_3(p_l q)$$
$$+ 2d_3(p_l q) + 2e_3(p_l q) + 6f_3(p_l q)$$
$$+ 2b_3(pp') + 2d_3(pp'));$$

$$C_5 = -\frac{\alpha}{\sqrt{2}\pi}(4a_3 - 4a_2 m_l^2 + 3b_3 m_l^2$$
$$- 4c_2 m_l^2 + 4c_3 m_l^2 + 3d_3 m_l^2$$
$$+ 2e_3 m_l^2 + 2f_3 m_l^2 - 4a_2(p_l q)$$
$$+ 4b_3(p_l q) + 4c_3(p_l q) + 4f_3(p_l q));$$

$$C_9 = -\frac{\alpha}{\sqrt{2}\pi}(2a_3 + b_3 m_K^2 - a_2 m_l^2 + b_3 m_l^2$$
$$- c_2 m_l^2 + 2c_3 m_l^2 + d_3 m_l^2 + 2f_3 m_l^2 - b_3 m_\pi^2$$
$$- 2b_3(p'p_l) - 2b_3(p'q) - 2a_2(p_l q)$$
$$+ 2b_3(p_l q) + 2c_3(p_l q) + 4f_3(p_l q) + 2b_3(pp'));$$

$$C_{10} = \frac{\alpha}{\sqrt{2}\pi}\frac{1}{(p_l q)}(-a_1 m_l^2 - b_1 m_l^2 + 2b_4 m_l^2$$
$$+ c_4 m_l^2 + d_4 m_l^2 + 2a_3(p_l q) + a_2 m_K^2(p_l q)$$
$$- c_3 m_K^2(p_l q) - f_3 m_K^2(p_l q) - e_3 m_l^2(p_l q)$$
$$+ f_3 m_l^2(p_l q) - a_2 m_\pi^2(p_l q)$$
$$+ c_3 m_\pi^2(p_l q) + f_3 m_\pi^2(p_l q)$$
$$- 2a_2(p'p_l)(p_l q) + 2c_3(p'p_l)(p_l q) + 2f_3(p'p_l)(p_l q)$$
$$- 2a_2(p'q)(p_l q) + 2c_3(p'q)(p_l q)$$
$$+ 2f_3(p'q)(p_l q) + 2f_3(p_l q)^2 + 2a_2(p_l q)(pp')$$
$$- 2c_3(p_l q)(pp') - 2f_3(p_l q)(pp') - 2a_2(p_l q)(pp_l)$$
$$+ 2b_3(p_l q)(pp_l)$$
$$+ 2c_3(p_l q)(pp_l) + 2f_3(p_l q)(pp_l) - 2a_2(p_l q)(pq)$$
$$+ 2b_3(p_l q)(pq) + 2c_3(p_l q)(pq) + 2f_3(p_l q)(pq));$$

$$C_{12} = -\frac{\alpha}{4\sqrt{2}\pi}\frac{m_l}{(p_l q)^2}(-2a_{12} m_l^2 - 2J_{11} m_l^2$$
$$- 2a_{12}(p_l q) - 4a_4(p_l q) + 2J_{11}(p_l q) - a_{11} m_K^2(p_l q)$$
$$+ b_{11} m_K^2(p_l q) + 8a_1 m_l^2(p_l q) + 8b_1 m_l^2(p_l q)$$
$$- 4b_4 m_l^2(p_l q) - 2c_4 m_l^2(p_l q) - 2d_4 m_l^2(p_l q)$$
$$- 4J_2 m_l^2(p_l q) - b_{11} m_\pi^2(p_l q) - 2b_{11}(p'p_l)(p_l q)$$
$$- 2b_{11}(p'q)(p_l q) + 8a_1(p_l q)^2 + 4a_3(p_l q)^2$$
$$+ 4b_1(p_l q)^2 - 4b_4(p_l q)^2 - 4c_4(p_l q)^2$$
$$- 4J_2(p_l q)^2 + 2a_2 m_K^2(p_l q)^2 - 2b_2 m_K^2(p_l q)^2$$
$$+ 2c_2 m_K^2(p_l q)^2 + 2g_3 m_K^2(p_l q)^2 + 8c_3 m_l^2(p_l q)^2$$
$$+ 6e_3 m_l^2(p_l q)^2 + 2f_3 m_l^2(p_l q)^2 - 2a_2 m_\pi^2(p_l q)^2$$
$$- 2c_2 m_\pi^2(p_l q)^2 - 4a_2(p'p_l)(p_l q)^2 - 4c_2(p'p_l)(p_l q)^2$$
$$- 4a_2(p'q)(p_l q)^2 - 4c_2(p'q)(p_l q)^2 + 12c_3(p_l q)^3$$

$$+ 4e_3(p_lq)^3 + 4f_3(p_lq)^3 + 2b_{11}(p_lq)(pp')$$
$$+ 4a_2(p_lq)^2(pp') + 4c_2(p_lq)^2(pp') - 2a_{11}(p_lq)(pp_l)$$
$$- 4b_{11}(p_lq)(pp_l) + 2J_{12}(p_lq)(pp_l) - 8a_2(p_lq)^2(pp_l)$$
$$- 4b_2(p_lq)^2(pp_l) + 4b_3(p_lq)^2(pp_l) - 8c_2(p_lq)^2(pp_l)$$
$$+ 8d_3(p_lq)^2(pp_l) + 4J_1(p_lq)^2(pp_l) - 2a_{11}(p_lq)(pq)$$
$$- 4b_{11}(p_lq)(pq) + 2J_{12}(p_lq)(pq) - 4a_2(p_lq)^2(pq)$$
$$+ 4b_3(p_lq)^2(pq) - 4c_2(p_lq)^2(pq)$$
$$+ 4d_3(p_lq)^2(pq));$$

$$C_{13} = -\frac{\alpha}{\sqrt{2}\pi} m_l(2a_2 - b_3 + 2c_2 - 2d_3);$$

$$C_{14} = \frac{\alpha}{\sqrt{2}\pi}\frac{m_l}{(p_lq)}(2a_1 + 2b_1 - 4b_4$$
$$- 2c_4 - 2d_4 + a_2(p_lq) + 3c_3(p_lq)$$
$$+ 2e_3(p_lq) + f_3(p_lq));$$

$$C_{16} = \frac{\alpha}{4\sqrt{2}\pi}\frac{1}{(p_lq)^2}(-4a_{12}m_l^2 - 4J_{11}m_l^2$$
$$- 4a_{12}(p_lq) - 8a_4(p_lq) + 4J_{11}(p_lq)$$
$$- 2a_{11}m_K^2(p_lq) + 16a_1m_l^2(p_lq)$$
$$+ 16b_1m_l^2(p_lq) + b_{11}m_l^2(p_lq) - 8b_4m_l^2(p_lq)$$
$$- 4c_4m_l^2(p_lq) - 4d_4m_l^2(p_lq) - 8J_2m_l^2(p_lq)$$
$$+ 16a_1(p_lq)^2 + 4a_3(p_lq)^2 + 8b_1(p_lq)^2$$
$$- 8b_4(p_lq)^2 - 8c_4(p_lq)^2 - 2J_{12}(p_lq)^2$$
$$- 8J_2(p_lq)^2 - 4b_2m_K^2(p_lq)^2 + 4g_3m_K^2(p_lq)^2$$
$$- 2a_2m_l^2(p_lq)^2 - 2c_2m_l^2(p_lq)^2 + 4c_3m_l^2(p_lq)^2$$
$$+ 4e_3m_l^2(p_lq)^2 - 4a_2(p_lq)^3 + 4c_3(p_lq)^3$$
$$- 2a_{11}(p_lq)(pp_l) - 4b_{11}(p_lq)(pp_l)$$
$$+ 4J_{12}(p_lq)(pp_l) - 8a_2(p_lq)^2(pp_l)$$
$$- 8b_2(p_lq)^2(pp_l) + 4b_3(p_lq)^2(pp_l)$$
$$- 8c_2(p_lq)^2(pp_l) + 8d_3(p_lq)^2(pp_l)$$
$$+ 8J_1(p_lq)^2(pp_l) - 2a_{11}(p_lq)(pq)$$
$$- 4b_{11}(p_lq)(pq)$$
$$+ 4J_{12}(p_lq)(pq) + 4b_3(p_lq)^2(pq));$$

$$C_3 = C_7 = C_{11} = C_{15} = 0.$$

REFERENCES

1. S. Weinberg, Phys. Rev. Lett. **37**, 657 (1976).
2. R. J. Tesarek, hep-ex/9903069.
3. A. Likhoded, V. Braguta, and A. Chalov, hep-ex/0011033 (in press).
4. A. Likhoded, V. Braguta, and A. Chalov, hep-ph/0105111.
5. V. F. Obraztsov, Nucl. Phys. B (Proc. Suppl.) **99**, 257 (2001).
6. J. F. Donoghue and B. Holstein, Phys. Lett. B **113B**, 382 (1982); L. Wolfenstein, Phys. Rev. D **29**, 2130 (1984); G. Barenboim *et al.*, Phys. Rev. D **55**, 4213 (1997); M. Kobayashi, T.-T. Lin, and Y. Okada, Prog. Theor. Phys. **95**, 361 (1996); S. S. Gershtein *et al.*, Z. Phys. C **24**, 305 (1984); R. Garisto and G. Kane, Phys. Rev. D **44**, 2038 (1991); G. Belanger and C. Q. Geng, Phys. Rev. D **44**, 2789 (1991).
7. L. B. Okun' and I. B. Khriplovich, Yad. Fiz. **6**, 821 (1967) [Sov. J. Nucl. Phys. **6**, 598 (1967)].
8. J. Bijnens, G. Ecker, and J. Gasser, Nucl. Phys. B **396**, 81 (1993).
9. A. R. Zhitnitskiĭ, Yad. Fiz. **31**, 1024 (1980) [Sov. J. Nucl. Phys. **31**, 529 (1980)]; C. Q. Geng and J. N. Ng, Phys. Rev. D **42**, 1509 (1990); C. H. Chen, C. Q. Geng, and C. C. Lih, hep-ph/9709447; G. Hiller and G. Isidori, Phys. Lett. B **459**, 295 (1999).
10. Yu. G. Kudenko, hep-ex/0103007.
11. Particle Data Group (D. E. Groom *et al.*), Eur. Phys. J. C **15**, 501 (2000).

Translated by R. Rogalyov

Physics of Atomic Nuclei, Vol. 65, No. 10, 2002, pp. 1877–1886. From Yadernaya Fizika, Vol. 65, No. 10, 2002, pp. 1929–1938.

ELEMENTARY PARTICLES AND FIELDS
Theory

Subthreshold K^--Meson Production in Proton–Nucleus Reactions Revisited*

E. Ya. Paryev

Institute for Nuclear Research, Russian Academy of Sciences, pr. Shestidesyatiletiya Oktyabrya 7a, Moscow, 117312 Russia

Received July 16, 2001; in final form, December 20, 2001

Abstract—The inclusive K^--meson production in proton–nucleus collisions in the subthreshold energy regime is studied in the framework of an appropriate spectral function approach for incoherent primary proton–nucleon and secondary pion–nucleon production processes, which takes properly into account the nuclear mean-field potential effects on these processes as well as the final state interaction (FSI) among the outgoing nucleons participating in the one-step antikaon creation process. A detailed comparison of the model calculations of the K^- differential cross sections is given for the reactions $p + {}^{9}\mathrm{Be}$, $p + {}^{63}\mathrm{Cu}$, and $p + {}^{197}\mathrm{Au}$ at subthreshold energies with the currently available experimental data obtained recently at the ITEP proton synchrotron and at SIS/GSI. It is found that the calculations with inclusion of the influence of both the nuclear density-dependent mean-field potentials and the elementary NN-FSI effects on the K^- production from direct mechanism are able to reproduce, contrary to previous estimates based on the use only of the density-dependent mean fields in calculating the K^- yield from this mechanism, the energy dependences of the invariant differential cross sections for "hard" antikaon creation in $p^{9}\mathrm{Be}$ and $p^{63}\mathrm{Cu}$ collisions. It is further shown that the NN-FSI effects play a minor role in describing the data on the spectrum of relatively soft K^- mesons from $p^{197}\mathrm{Au}$ interactions at incident energy of 2.5 GeV. It is also shown that the relative strength of the proton- and pion-induced reaction channels in the subthreshold energy regime is governed by the kinematics of the experiment under consideration. The influence of the nucleon, kaon, and antikaon mean-field potentials on the K^- yield is explored. It is demonstrated that, in line with previous findings, the K^- optical potential has a strong effect on this yield at low antikaon momenta, which is greater than those from nucleon and kaon effective potentials. At high antikaon momenta, the K^- yield is found to be mainly determined, along with the elementary NN-FSI effects, by the nucleon mean field and the scenario with zero K^+ potential is favorable.

1. INTRODUCTION

In a recent publication [1], the possibility of describing the first experimental data [2] on subthreshold antikaon production in $p^{9}\mathrm{Be}$ and $p^{63}\mathrm{Cu}$ collisions within the spectral function approach based both on the direct mechanism of K^- production ($pN \to NNKK^-$) and on the two-step mechanism associated with the creation of antikaons by intermediate pions ($pN_1 \to \pi NN$, $\pi N_2 \to NKK^-$) was investigated. It has been shown that, within such an approach, the measured yields of rather "hard" K^- mesons with momentum of 1.28 GeV/c at lab. angle of 10.5° from $p+{}^{9}\mathrm{Be}$ and $p+{}^{63}\mathrm{Cu}$ reactions are reproduced quite well at beam energies $\epsilon_0 > 2.4$ GeV by calculations for primary production process $pN \to NNKK^-$ (which is dominant) affected by the attractive nucleon and antikaon density-dependent effective potentials, whereas at lower bombarding energies they are underestimated by these calculations. Application of the corresponding density-independent fields with depths taken at the nuclear saturation density ρ_0 improves significantly the agreement of the results of calculations with the experimental data in the far subthreshold energy region (at energies of $\epsilon_0 \leq 2.4$ GeV), but overestimates the data by a factor of 2 at higher incident energies. Evidently, the use of the density-independent mean-field potentials in calculations [1] for the one-step reaction channel $pN \to NNKK^-$ allows one to get an upper estimate of the respective cross sections, since in this case the enhancement of the K^- production via the above channel was the most due to the maximum density-independent shift of the elementary production threshold to lower energy. In fact a certain averaging of the antikaon production over all densities $\rho_N \leq \rho_0$ takes place.

*This article was submitted by the author in English.

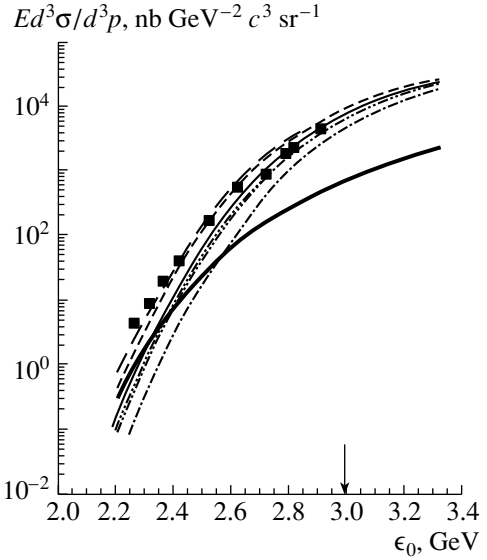

Fig. 1. Lorentz-invariant cross sections for the production of K^- mesons with momentum of 1.28 GeV/c at lab. angle of 10.5° in $p + {}^9$Be reactions as functions of the laboratory kinetic energy ϵ_0 of the proton. The experimental data are from the experiment [2]. The curves are our calculation. The dashed curves with one, two, and three dots and the thin solid curve are calculations [1] for primary production process (1) with the density-dependent potentials without including the FSI effects among the outgoing nucleons at $V_0 = 40$ MeV and $U_N(\rho_N) = 0$, $U_{K^+}(\rho_N) = 0$, $U_{K^-}(\rho_N) = 0$; $U_N(\rho_N) = -34(\rho_N/\rho_0)$ MeV, $U_{K^+}(\rho_N) = 22(\rho_N/\rho_0)$ MeV, $U_{K^-}(\rho_N) = -126(\rho_N/\rho_0)$ MeV; $U_N(\rho_N) = -34(\rho_N/\rho_0)$ MeV, $U_{K^+}(\rho_N) = 0$, $U_{K^-}(\rho_N) = 0$; and $U_N(\rho_N) = -34(\rho_N/\rho_0)$ MeV, $U_{K^+}(\rho_N) = 0$, $U_{K^-}(\rho_N) = -126(\rho_N/\rho_0)$ MeV, respectively. The short-dashed curve denotes the same as the thin solid curve, but it is supposed in addition that the FSI effects between the outgoing nucleons are included. The thick solid curve is calculation [1] for the secondary production process (22) at $U_N^0 = -34$ MeV, $U_{K^+}^0 = 0$, $U_{K^-}^0 = -126$ MeV. The long-dashed curve is the sum of the short-dashed and thick solid curves. The arrow indicates the threshold for the reaction $pN \to NNKK^-$ occurring on a free nucleon at the kinematics under consideration.

Therefore, the existing disagreement between the calculations [1] with the nuclear density-dependent potentials and the data [2] at energies far below the free K^--production threshold indicates that higher order processes might play an important role here. Taking into consideration that, in the far subthreshold energy region, the relative momenta of the outgoing particles (two nucleons and kaon) participating in the primary proton-induced reaction channel $pN \to NNKK^-$ are small, the latter discrepancy might be entirely due to a final-state interaction (FSI) between them (mainly among the final nucleons, since KN interaction, as is well known, is rather weak with respect to the strong NN interaction). Such FSI may greatly modify the angular-momentum distribution of antikaons produced in this channel. It has been neglected in [1] in calculating the "in-medium" differential cross section for K^- production in pN collisions for kinematics of the experiment [2]. It is the purpose of the present study to address these issues by computing the above cross section using the Watson–Migdal FSI theory [3–5] as well as by reanalyzing the data [2] employing the novel cross section in calculations for the direct antikaon production mechanism. Furthermore, new experimental data on subthreshold K^- production in p^{197}Au interactions have been obtained recently by the KaoS Collaboration at SIS/GSI [6]. Namely, the double differential cross section for the K^- production at a lab. angle of 40° in p^{197}Au collisions at 2.5-GeV beam energy has been measured in [6]. The aim of this paper is also to present an analysis of these data using the spectral function approach [1] that has been modified in line with the above-mentioned to account for the NN-FSI effects in the primary creation process. It is clear that such analysis will permit improving our understanding of the phenomenon of the subthreshold antikaon production in composite hadronic systems. In the paper, we also present our predictions for the differential cross section for K^- production on ^{9}Be target nuclei at 2.25-GeV incident energy, which might be measured at, for example, the ITEP proton synchrotron or at the Cooler Synchrotron COSY–Jülich. The spectral function approach employed is explained in detail in [1]; in what follows, we briefly recall its main assumptions and describe the respective modifications.

2. THE MODEL

Apart from participation in elastic scattering, an incident proton can produce a K^- directly in the first inelastic pN collision due to nucleon Fermi motion. Since we are interested in a few-GeV region (up to 3 GeV), we have taken into account the following elementary process which requires the least amount of energy and, hence, has the lowest free production threshold:

$$p + N \to N + N + K + K^-, \qquad (1)$$

where $\{NNK\}$ stands for $\{ppK^+\}$, $\{ppK^0\}$, or $\{pnK^+\}$ for the specific isospin channel. As before in [1], in the following calculations, we will include the medium modification of the final hadrons (nucleons, kaon, and antikaon) participating in the production process (1) by using their in-medium masses m_h^* determined below. The kaon and antikaon masses in

the medium $m^*_{K^\pm}$ can be obtained from the mean-field approximation to the effective chiral Lagrangian [7–9]; i.e.,

$$m^*_{K^\pm}(\rho_N) = m_K + U_{K^\pm}(\rho_N), \quad (2)$$

where m_K is the rest mass of a kaon in free space; the $K^\pm$ optical potentials $U_{K^\pm}(\rho_N)$ are proportional to the nuclear density ρ_N,

$$U_{K^\pm}(\rho_N) = U^0_{K^\pm}\frac{\rho_N}{\rho_0}; \quad (3)$$

and [1]

$$U^0_{K^+} = 22\ \text{MeV}, \quad U^0_{K^-} = -126\ \text{MeV}. \quad (4)$$

To study the sensitivity [1] of the low-momentum antikaon production in proton–nucleus reactions to the choice of the K^-–nucleus optical potential, we will also employ in the following calculations instead of antikaon potential (3), (4) both the shallow potential of the type (3) with central depth

$$U^0_{K^-} = -55\ \text{MeV}, \quad (5)$$

predicted very recently by the self-consistent chirally motivated coupled-channel approach [10], and the deep K^- potential extracted [11–13] from the analysis of kaonic atom data, viz.,

$$U_{K^-}(\rho_N) = -129\left[-0.15 + 1.7\left(\frac{\rho_N}{\rho_0}\right)^{0.25}\right]\frac{\rho_N}{\rho_0}\ \text{MeV}. \quad (6)$$

It is easily seen that, in the nuclear interior, the potential (6) amounts to

$$U_{K^-}(\rho_0) = -200\ \text{MeV}. \quad (7)$$

It should be noted that this depth is similar to that found in [14, 15] in the framework of the relativistic mean-field model. The effective mass m^*_N of secondary nucleons produced in reaction (1) can be expressed via the scalar mean-field potential $U_N(\rho_N)$ as follows [1]:

$$m^*_N(\rho_N) = m_N + U_N(\rho_N), \quad (8)$$

where m_N is the bare nucleon mass. The potential $U_N(\rho_N)$ was assumed to be proportional to the nuclear density:

$$U_N(\rho_N) = U^0_N\frac{\rho_N}{\rho_0} \quad (9)$$

with [1]

$$U^0_N = -34\ \text{MeV}. \quad (10)$$

We have also taken into account in the calculation of the K^--production cross section from the one-step process (1) the influence of the nuclear optical potential $V_0 \approx 40$ MeV on the incoming (with kinetic energy ϵ_0) proton [1]. The total energy of the struck target nucleon N just before the collision (1) can be easily expressed [1] through the respective recoil and excitation energies of the residual $(A-1)$ system. In our method, the K^--production cross section for pA collisions from primary reaction channel (1) can be expressed [1] as the corresponding density-averaged integral of the product of the in-medium inclusive elementary antikaon production cross section (which was assumed to be the same for pp and pn interactions) and nucleon spectral function $P(\mathbf{p}_t, E)$ over the struck target nucleon momentum $\mathbf{p}_t$ and removal energy E (formulas (21)–(23) from [1]). The in-medium invariant inclusive cross section for K^- production in the elementary process (1) has been described in [1] by the four-body phase-space calculations without including any FSI effects between the reaction products. Because in the far subthreshold energy region of interest the relative momenta of the outgoing particles (two nucleons and kaon) are small, such FSI among them (mainly between the final nucleons, since KN interaction is rather weak with respect to the strong NN interaction) may strongly influence the energy dependence of the antikaon production cross section measured in [2]. Following the Watson–Migdal theory of FSI [3–5] for two-body processes, we may assume that the total reaction amplitude $M_{pN\to NNKK^-}$ for the production process (1) factorizes approximately as[1)]

$$M_{pN\to NNKK^-} = M^{(0)}_{pN\to NNKK^-}M_{\text{FSI}}, \quad (11)$$

where $M^{(0)}_{pN\to NNKK^-}$ represents the short-range production amplitude, which is a smooth and slowly varying function of invariant energy $\sqrt{s}$ at beam energies of interest, while M_{FSI} describes the on-mass-shell elastic scattering among protons in the exit channel in line with the assumption [1] that any difference between the K^--meson production cross sections in pp and pn interactions is disregarded. Among the different ways [3–5, 16–44] to account for the FSI between two particles at low relative energies, we employ here the Jost approximation [4, 36–44] and express M_{FSI} as an inverse S-wave Jost function:

$$M_{\text{FSI}}(q) = \frac{1}{J_0(q)} = \frac{q+i\alpha}{q-i\beta}, \quad (12)$$

where q is the relative momentum of the final protons, while the parameters α and β in the absence

[1)] It should be pointed out that the validity of such a procedure in the meson production processes close to threshold is a matter of current debate [16–19].

of Coulomb force[2] are related to the S-wave pp-scattering length a_0 and effective range r_0 as follows [4, 27, 37, 42]:

$$\alpha = (1/r_0)[1 + (1 - 2r_0/a_0)^{1/2}], \quad (13)$$
$$\beta = (1/r_0)[1 - (1 - 2r_0/a_0)^{1/2}].$$

Using the standard values for $a_0 = -7.81$ fm and $r_0 = 2.77$ fm [45], one can readily find that

$$\alpha = 164.35\ \text{MeV}/c, \quad \beta = -21.90\ \text{MeV}/c. \quad (14)$$

This parameter set will be employed in our subsequent calculations. It may be noted that, for large q, the amplitude $M_{\rm FSI}$ goes to unity, which means that, for high relative energies, the FSI is expected to be of relatively little importance [3–5]. Finally, using Eqs. (11), (12), expressions (25)–(28) from [1] describing the in-medium invariant inclusive cross section for K^- production in the elementary process (1), as is easy to show, can be represented in the following FSI-modified form:

$$E'_{K^-}\frac{d\sigma_{pN\to NNKK^-}[\sqrt{s}, \mathbf{p}'_{K^-}, \rho(\mathbf{r})]}{d\mathbf{p}'_{K^-}} \quad (15)$$
$$= \sigma_{pN\to NNKK^-}(\sqrt{s}, \sqrt{s^*_{\rm th}}) f_4^{\rm FSI}(s, \mathbf{p}'_{K^-}),$$

$$f_4^{\rm FSI}(s, \mathbf{p}'_{K^-}) = I_3(s_{NNK}, m^*_{K^+}, m^*_N, m^*_N, F_{\rm FSI}) / \left[2I_4(s, m^*_{K^+}, m^*_{K^-}, m^*_N, m^*_N, F_{\rm FSI})\right], \quad (16)$$

$$I_3(s, m^*_{K^+}, m^*_N, m^*_N, F_{\rm FSI}) = \left(\frac{\pi}{2}\right)^2 \quad (17)$$
$$\times \int\limits_{4m^{*2}_N}^{(\sqrt{s}-m^*_{K^+})^2} \frac{\lambda(s_{NN}, m^{*2}_N, m^{*2}_N)}{s_{NN}} \frac{\lambda(s, s_{NN}, m^{*2}_{K^+})}{s}$$
$$\times F_{\rm FSI}(s_{NN}) ds_{NN},$$

$$I_4(s, m^*_{K^+}, m^*_{K^-}, m^*_N, m^*_N, F_{\rm FSI}) = \frac{\pi}{2} \quad (18)$$
$$\times \int\limits_{4m^{*2}_N}^{(\sqrt{s}-m^*_{K^+}-m^*_{K^-})^2} \frac{\lambda(s_{NN}, m^{*2}_N, m^{*2}_N)}{s_{NN}} F_{\rm FSI}(s_{NN})$$
$$\times I_3(s, m^*_{K^-}, \sqrt{s_{NN}}, m^*_{K^+}, F_{\rm FSI} = 1) ds_{NN},$$

where the so-called FSI enhancement factor $F_{\rm FSI}$ is given by

$$F_{\rm FSI}(s_{NN}) = |M_{\rm FSI}(q)|^2 = \frac{q^2 + \alpha^2}{q^2 + \beta^2} \quad (19)$$

and

$$q = \frac{1}{2\sqrt{s_{NN}}}\lambda(s_{NN}, m^{*2}_N, m^{*2}_N). \quad (20)$$

Using (14), one can easily find that, for instance, the enhancement factor $F_{\rm FSI}$ is equal to 56.3, 3.6, and 1.7 at relative momenta of 0, 100, and 200 MeV/c, respectively. It is thus expected that the production of antikaons in one-step process (1) will be enhanced when the nucleons emerge with a low relative momentum in the final state. The squared invariant energy s available in the first-chance pN collision (1), function $\lambda(x, y, z)$, and the squared invariant energy s_{NNK} of the final nucleons and kaon, appearing in (15)–(18), are defined before in [1] by Eqs. (18), (29), and (30), respectively. The in-medium antikaon momentum $\mathbf{p}'_{K^-}$ is related to the vacuum one $\mathbf{p}_{K^-}$ by Eq. (24) from [1]. The quantity $\sigma_{pN\to NNKK^-}(\sqrt{s}, \sqrt{s^*_{\rm th}})$ in (15) represents the "in-medium" total cross section for K^- production in reaction (1). This cross section is equivalent [1] to the vacuum cross section $\sigma_{pN\to NNKK^-}(\sqrt{s}, \sqrt{s_{\rm th}})$ in which the free threshold $\sqrt{s_{\rm th}}$ is replaced by the effective threshold $\sqrt{s^*_{\rm th}}$. The latter is related to the vacuum threshold $\sqrt{s_{\rm th}} = 2(m_N + m_K)$ and to the mean-field potentials $U_{K^\pm}(\rho_N)$, $U_N(\rho_N)$ introduced above by Eq. (20) from [1]. As before in [1], we will employ in our calculations of the antikaon production from primary process (1) for the free total cross section $\sigma_{pN\to NNKK^-}(\sqrt{s}, \sqrt{s_{\rm th}})$ the fit (31) from [1] of the available experimental data close to the threshold for the $pp \to ppK^+K^-$ reaction. Therefore, the relevant pp-FSI effects in $\sigma_{pN\to NNKK^-}(\sqrt{s}, \sqrt{s_{\rm th}})$ are automatically included. It should be noted that a special question regards the validity of incorporation of the elementary NN-FSI effects into the analysis of $p + A$ reactions. The possible screening of these effects in the nuclear medium is an open subject, which has not yet been investigated theoretically. Since in the subthreshold energy region the outgoing nucleons are mainly emitted in forward directions close to each other with small relative momenta and "laboratory" (relative to the target system) momenta substantially greater

[2] It should be noted that the use of the Coulomb-corrected [40] effective-range approximation parameters a_0^c, r_0^c in Eq. (13) instead of those a_0, r_0, as shown in our calculations, reduces the "low-energy" ($\epsilon_0 \le 2.5$ GeV) and "high-energy" ($\epsilon_0 > 2.5$ GeV) parts of the antikaon excitation function analyzed below only by about 13 and 7%, respectively.

than the Fermi momentum, one may hope that the bare NN-FSI is not drastically suppressed in nuclei, but only partially loses its strength here. The latter has been taken into account in our approach by using in (20) the effective nucleon mass m_N^* instead of the free one m_N. The energy dependence of the inclusive invariant cross section (15) for a given kinematics (for fixed three-momentum of the produced antikaon) close to threshold $\sqrt{s_{NNK,\mathrm{th}}} = 2m_N^* + m_{K^+}^*$ is almost entirely governed by the medium-FSI-modified three-body phase-space integral (17). As is easy to see from Eqs. (16), (17), (20), the relevant relative NN momentum q for fixed excess energy $\epsilon_{NNK} = \sqrt{s_{NNK}} - 2m_N^* - m_{K^+}^*$ varies from zero up to $q_{\max} \approx \sqrt{m_N^* \epsilon_{NNK}}$. For example, the momentum $q_{\max}$ is approximately equal to 100, 150, and 220 MeV/c at excess energies of 10, 25, and 50 MeV, respectively. Therefore, at beam energies far below the free threshold energy[3] of our main interest, where the corresponding excess energies ϵ_{NNK} are sufficiently small,[4] the K^- production on nuclei from primary reaction channel (1) will be enhanced (see below) due to the elementary pp-FSI compared to the case [1] without including this FSI. In what follows, we employ expressions (15)–(20) in our calculations of the antikaon-production cross sections on ^{9}Be, ^{63}Cu, and ^{197}Au target nuclei from the one-step reaction channel (1) in the framework of the model [1] developed earlier. For K^--production calculations in the case of the ^{197}Au target nucleus reported here, we have used for the nuclear density $\rho(\mathbf{r})$ normalized to unity the Woods–Saxon distribution (35) from [1] with $R = 6.825$ fm and $a = 0.55$ fm [46]. The nucleon spectral function $P(\mathbf{p}_t, E)$ (which represents the probability of finding the nucleon with momentum $\mathbf{p}_t$ and removal energy E in the nucleus) for this target nucleus is assumed to be the same as that for ^{208}Pb [47]. The latter was taken from [48].

Let us consider now briefly the adopted [1] two-step K^--production mechanism. Kinematical considerations show that, in the bombarding-energy range of our interest (≤ 3.0 GeV), the following two-step production process may contribute to the K^- production in pA interactions at subthreshold energies. An incident proton can produce in the first inelastic collision with an intranuclear nucleon also a pion through the elementary reaction

$$p + N_1 \to N + N + \pi. \tag{21}$$

Then, the intermediate pion, which is assumed to be on-shell, produces the antikaon on another nucleon of the target nucleus via the elementary subprocess with the lowest free production threshold (1.98 GeV for kinematics of the experiment [2]),

$$\pi + N_2 \to N + K + K^-, \tag{22}$$

provided that this subprocess is allowed energetically. As before [1], we will use in the subsequent calculations of the K^--production cross section from secondary reaction channel (22) the same in-medium modifications of the masses of final hadrons (kaon, antikaon, and nucleon) as those (2), (8) for hadrons from primary pN collisions due to the corresponding mean-field potentials $U_{K^\pm}(\rho_N)$ and $U_N(\rho_N)$. In the present work, these potentials are also assumed to be density-independent with depths (4), (5), (7), and (10) taken at the nuclear saturation density. In line with the above-mentioned, the FSI between the outgoing kaon and nucleon participating in the K^--production process (22) is assumed to be negligible due to the weakness of the KN interaction. As a result, we will calculate hereafter the K^- yield in pA collisions from the secondary channel (22) following strictly the approach [1]. It should also be pointed out that, in our calculations of the antikaon production from pion-induced reaction channel (22) in the case of the ^{197}Au target nucleus presented below, the ratio of the differential cross section for pion creation on this nucleus from the primary process (21) to the effective number of nucleons participating in it is supposed to be the same as that for ^{63}Cu adjusted for the kinematics relating to ^{197}Au.

Now, let us proceed to discuss the results of our calculations for antikaon production in pBe, pCu, and pAu interactions within the model outlined above.

3. RESULTS

At first, we will concentrate on the reanalysis of the experimental data [2] on the K^- excitation functions for $p + {}^9$Be and $p + {}^{63}$Cu reactions.

Figures 1 and 2 show a comparison of the calculated invariant differential cross sections for the production of K^- mesons with momentum of 1.28 GeV/c at the lab. angle of 10.5° from primary $pN \to NNKK^-$ and secondary $\pi N \to NKK^-$ channels with the data from the experiment [2], respectively, for $p + {}^9$Be and $p + {}^{63}$Cu reactions at the various bombarding energies. It is seen again that, indeed, our old calculations [1] for primary

[3] It is determined from the condition that $\sqrt{s_{NNK}} = 2m_N + m_K$ and, for instance, equals 2.99 GeV for kinematics of the experiment [2] in which the K^- mesons with momentum of 1.28 GeV/c have been detected at the lab angle of 10.5°.

[4] Thus, for example, our estimates show that the main contribution to the K^- production in primary process (1) at incident energy of 2.25 GeV for kinematics of the experiment [2] comes from the excess energies ϵ_{NNK} falling in the range between zero and approximately 50 MeV.

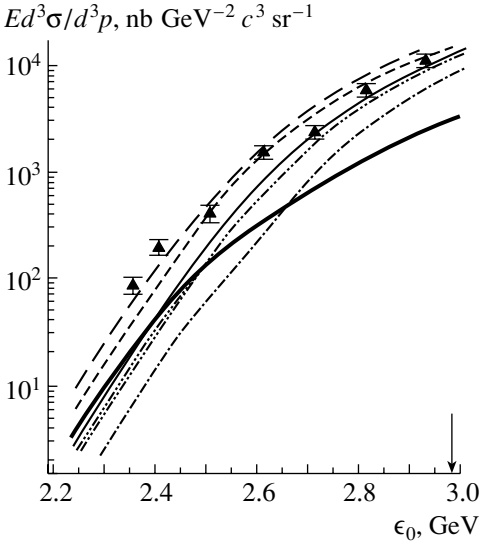

Fig. 2. As in Fig. 1, but for $p + {}^{63}$Cu reactions.

antikaon-production process (1) with the nuclear density-dependent mean-field potentials without including the FSI effects among the outgoing nucleons underestimate substantially the far subthreshold data points and the scenario with the medium modifications only of the final antikaon and nucleons (thin solid curves in Figs. 1, 2) is favorable. Furthermore, the medium modifications of the nucleons in the exit channel are of major importance compared to those for the final kaon and antikaon. The calculations [1] for secondary K^--production channel (22), when in-medium modifications of the masses of the outgoing antikaon and nucleon are included (thick solid curves in Figs. 1, 2), miss essentially the data at all beam energies of interest. Additional inclusion of the FSI effects between the final nucleons participating in the primary production process (1) enhances the K^- yield from this process by about factors of 2.5 and 1.2, respectively, at low ($\epsilon_0 = 2.2$ GeV) and high ($\epsilon_0 = 3.0$ GeV) incident energies (compare short-dashed and thin solid curves in Figs. 1, 2) as well as brings the theoretical predictions in much better agreement (especially at energies ≤ 2.6 GeV) with the experimental data.[5)] Moreover, adding to the antikaon yield in the latter case also the contribution from the pion-induced channel (22) results in a very good description (long-dashed curves) of the data [2]. The good agreement with these data achieved within our present calculations indicates that the use of the elementary NN-FSI effects in $p + A$ reactions seems not unreasonable. On the other hand, it leaves minor room for K^- production via higher order processes such as collisions of initial proton with nucleon clusters. Inspection of Figs. 1 and 2 also tells us that the two-step (thick solid curve) to one-step (short-dashed curve) K^--production cross-section ratio increases with decreasing incident energy down to 2.2 GeV. In the present model calculations of the antikaon yield from the one-step production mechanism, this ratio is about 1/1.8 and 1/1.6 at low kinetic energies ($\epsilon_0 \approx 2.2$–2.3 GeV), about 1/4.5 and 1/2.5 at intermediate incident energies ($\epsilon_0 \approx 2.4$–2.5 GeV), and about 1/12 and 1/5 at high beam energies ($\epsilon_0 \approx 2.7$–2.9 GeV), respectively, for ^{9}Be and ^{63}Cu target nuclei. This demonstrates that the proton-induced reaction channel clearly dominates the K^- production only at bombarding energies ≥ 2.4 GeV, whereas at lower incident energies its dominance, contrary to [1], is less pronounced.

Let us focus now on the analysis of the experimental data [6] on the K^- spectrum from p^{197}Au interactions.

The results of our calculations for the double differential cross sections for the production of K^- mesons from primary $pN \to NNKK^-$ and secondary $\pi N \to NKK^-$ channels at lab angle of 40° in the interaction of protons of energy 2.5 GeV with ^{197}Au nuclei and the preliminary experimental data [6] are considered in Fig. 3. It is clearly seen that the calculations for proton- and pion-induced reaction channels (dash-dotted and dotted curves) significantly underpredict the data in line with our previous findings of Figs. 1, 2 when no self-energy effects have been employed. Our full calculations (the sum of results obtained both for primary and secondary antikaon-production processes, long-dashed curve at the right in Fig. 3) with adopting the same in-medium nucleon and antikaon optical potentials as well as the elementary NN-FSI effects as those which allowed us to describe above the data on antikaon excitation functions [2] reproduce reasonably well the preliminary data [6]. The use in the calculation of the K^- optical potential (6), extracted from the kaonic atom data, instead of potential (3), (4) (the curve with alternating short and long dashes at the right) leads to a better description of the experimental data at antikaon momenta ≤ 0.5 GeV/c, and this counts in favor of the conclusion that the K^- nuclear potential can be as attractive as that derived from the kaonic atom studies [11–13]. The calculations also demonstrate that the K^- spectra from the one-step (1) and two-step (21), (22) reaction channels (and, consequently, the total antikaon spectrum) are fully dictated by the K^- mean-field potential at the laboratory antikaon momenta $p_{\rm lab} \leq 0.4$ GeV/c. The existing

[5)] It should be emphasized that the inclusion only of the NN-FSI effects alone in calculating the K^- yield from primary process (1), as is easy to see from Figs. 1 and 2, does not allow one to describe these data.

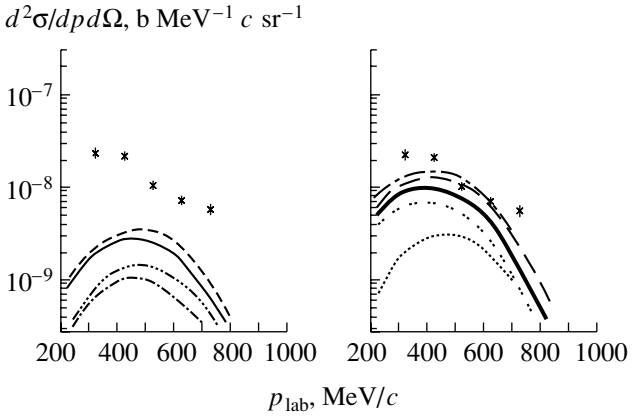

Fig. 3. Double differential cross sections for the production of K^- mesons at a lab. angle of 40° in the interaction of protons of energy 2.5 GeV with ^{197}Au nuclei as functions of antikaon momentum. The experimental data (crosses) are from the experiment [6]. The curves are our calculation for primary and secondary K^--production processes. Left part: the dashed curves with one and three dots and the thin solid curve are calculations for primary production process (1) with the density-dependent potentials without including the FSI effects among the outgoing nucleons at $V_0 = 40$ MeV and $U_N(\rho_N) = 0$, $U_{K^+}(\rho_N) = 0$, $U_{K^-}(\rho_N) = 0$; $U_N(\rho_N) = -34(\rho_N/\rho_0)$ MeV, $U_{K^+}(\rho_N) = 0$, $U_{K^-}(\rho_N) = 0$; and $U_N(\rho_N) = -34(\rho_N/\rho_0)$ MeV, $U_{K^+}(\rho_N) = 0$, $U_{K^-}(\rho_N) = -126(\rho_N/\rho_0)$ MeV, respectively. The short-dashed curve denotes the same as the thin solid curve, but it is supposed in addition that the FSI effects between the outgoing nucleons are included. Right part: the dotted, two-dot, and thick solid curves are calculations for the secondary production process (22) at $U_N^0 = 0$, $U_{K^+}^0 = 0$, $U_{K^-}^0 = 0$; $U_N^0 = 0$, $U_{K^+}^0 = 0$, $U_{K^-}^0 = -126$ MeV; and $U_N^0 = -34$ MeV, $U_{K^+}^0 = 0$, $U_{K^-}^0 = -126$ MeV, respectively. The long-dashed curve is the sum of the short-dashed (depicted at the left) and thick solid curves. The curve with alternating short and long dashes denotes the same as the long-dashed curve, but it is supposed in addition that in the calculation the K^- optical potential (6), extracted from the kaonic atom data, is used instead of potential (3), (4).

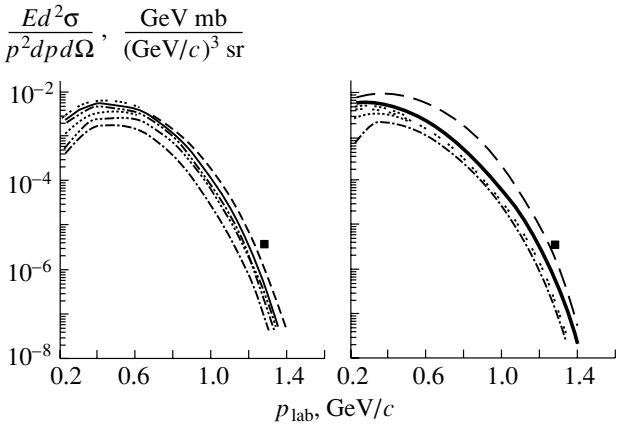

Fig. 4. Lorentz-invariant inclusive cross sections for the production of K^- mesons at the lab. angle of 10.5° in the interaction of 2.25-GeV protons with the ^{9}Be nuclei as functions of antikaon momentum. The experimental data point at 1.28 GeV/c (full square) is from the experiment [2]. The curves are our calculation for primary and secondary K^--production processes. Left part: the dashed curves with one, two, and three dots and the thin solid curve denote the same as in Fig. 1. The dotted and three-dot curves denote the same as the thin solid curve, but it is supposed in addition that, in the calculation, respectively, the shallow (3), (5) and deep (6) antikaon potentials are used instead of potential (3), (4). The short-dashed curve denotes the same as the thin solid curve, but it is supposed in addition that the FSI effects between the outgoing nucleons are included. Right part: the dash-dotted, dotted, two-dot, three-dot, and thick solid curves are calculations for the secondary production process (22) at $U_N^0 = 0$, $U_{K^+}^0 = 0$, $U_{K^-}^0 = 0$; $U_N^0 = 0$, $U_{K^+}^0 = 0$, $U_{K^-}^0 = -55$ MeV; $U_N^0 = 0$, $U_{K^+}^0 = 0$, $U_{K^-}^0 = -126$ MeV; $U_N^0 = 0$, $U_{K^+}^0 = 0$, $U_{K^-}^0 = -200$ MeV; and $U_N^0 = -34$ MeV, $U_{K^+}^0 = 0$, $U_{K^-}^0 = -126$ MeV, respectively. The long-dashed curve is the sum of the short-dashed (depicted at the left) and thick solid curves.

disagreement (within about a factor of 1.5) between the calculations with the antikaon potential (6) and the experimental data [6] in this momentum range, as well as the complete lack of other data in the literature for K^--meson creation here, indicates the strong need nowadays for further measurements of the differential cross sections for K^- production in pA collisions at low antikaon momenta to reach more reliable conclusions on the actual magnitude of the K^- optical potential in nuclear matter. Inconsistent with our previous findings of Figs. 1 and 2, the inclusion only of the $pN \to NNKK^-$ channel, as is clear from Fig. 3, substantially underpredicts the data, and in the considered heavy target nucleus, the majority of antikaons stem from pion-induced process $\pi N \to NKK^-$. Since the latter channel is dominant at the kinematics under consideration, it becomes evident that, while the FSI among the final nucleons participating in the one-step process (1) increases (by a factor of about 1.4) the K^--production cross section from this process (compare short-dashed and thin solid curves at the left), it nevertheless, contrary to the preceding cases, where process (1) is found to be of importance, only slightly contributes to the total antikaon yield.

Finally, in Fig. 4, we show the predictions of the above model for the Lorentz-invariant inclusive cross sections for the production of K^- mesons at the lab. angle of 10.5° from proton- and pion-induced reaction channels for the $p + {}^9\text{Be} \to K^- + X$ re-

action at 2.25-GeV beam energy. The data point[6] at 1.28 GeV/c was taken from [2]. It can be seen that the simultaneous inclusion of the attractive antikaon (3), (4) and nucleon (9), (10) effective potentials in calculating the K^--production cross sections from primary $pN \to NNKK^-$ and secondary $\pi N \to NKK^-$ channels (respectively, thin and thick solid curves in Fig. 4) leads to an enhancement of the K^- yields from these channels by about a factor of 4.5 at high and low antikaon momenta compared to the case without adopting these potentials (dash-dotted curves at the left and right). Additional inclusion of the FSI effects among the outgoing nucleons participating in the one-step process (1) (short-dashed curve at the left) enhances the high-momentum part ($p_{\rm lab} \geq 0.8$ GeV/c) of the antikaon spectrum from this process yet by a factor of about 1.2–2.5 and has practically no effect on its low-momentum part ($p_{\rm lab} \leq 0.6$ GeV/c). As a result, our overall calculations (the sum of contributions both from the one-step (1) and from the two-step (21), (22) reaction channels, long-dashed curve at the right in Fig. 4) reproduce quite well the measured [2] K^- double differential cross section at 1.28 GeV/c (cf. Fig. 1). It is also clearly seen that the high-momentum part ($p_{\rm lab} \geq 1.0$ GeV/c) of the K^- spectrum from the one-step antikaon-production mechanism is mainly governed by the nucleon (density-dependent) mean-field potential and elementary NN-FSI effects under consideration. The kaon and antikaon optical potentials are of secondary importance here. This is consistent with our previous findings of Figs. 1 and 2. The same part of the antikaon spectrum from the two-step K^--production mechanism is almost entirely determined by the nucleon effective potential alone. The low-momentum parts ($p_{\rm lab} \leq 0.4$ GeV/c) of these spectra, as in the preceding case, are almost completely controlled by the antikaon potential. Moreover, they react sensitively on this potential at antikaon momenta $p_{\rm lab} \approx 0.2$–0.3 GeV/c; i.e., the K^- yields here are about a factor of 2–3 larger when a deep potential (6) is applied compared to a shallow one (3), (5) (compare three-dot and dotted curves at the left and right in Fig. 4). This gives an opportunity, as was also noted before [1, 49, 50], to determine the K^- potential in nuclear matter experimentally (to distinguish at least between shallow and deep K^- optical potentials) by the measurements of the differential cross sections for subthreshold "soft" (low-momentum) antikaon production on different target nuclei. Examination of Fig. 4 shows that the two-step (thick solid curve) to one-step (short-dashed curve) K^--creation cross section ratio is about 2.5/1 and 1/3, respectively, at low ($p_{\rm lab} \approx 0.2$–0.4 GeV/c) and high ($p_{\rm lab} \approx 0.8$–1.0 GeV/c) antikaon momenta. This indicates the dominance of the one-step and two-step K^--production mechanisms, respectively, in the hard and soft subthreshold antikaon production in p^9Be collisions. It should, however, be stressed that the latter is in line with the findings inferred above (see Figs. 1–3) about the role played by the direct K^--production mechanism in the subthreshold hard and soft antikaon creation, respectively, in p^9Be and p^{63}Cu interactions [2] and in p^{197}Au collisions [6].

Taking into account what was considered above, one may conclude that the FSI effects between the nucleons originating from the primary K^--production channel (1) are quite important in order to describe the experimental data [2] on hard antikaon creation in p^9Be and p^{63}Cu interactions within the approach [1] when the influence of the nuclear density-dependent nucleon and antikaon mean-field potentials on this channel is included. The good agreement with these data achieved within the present model favors the possibility of employing the elementary NN-FSI effects in $p + A$ reactions. On the other hand, these effects are found to be negligible in reproducing the data [6] on K^- production in p ^{197}Au collisions due to the dominance here, contrary to the measurements [2], of the secondary pion-induced reaction channel (22). Consistent with previous findings of [1], our present results also show the strong sensitivity of the soft K^- production in pA interactions at subthreshold incident energies to the in-medium antikaon optical potential. According to these results, the measurements of the differential cross sections for K^- creation on different target nuclei are most promising at antikaon momenta $p_{\rm lab} \leq$ 400 MeV/c to distinguish between shallow and deep antikaon potentials. The experimental data [6] available presently in the indicated momentum range favor a deep K^- optical potential. However, these data are too poor to draw more definite conclusions on the actual magnitude of the K^- potential in a nuclear medium. Therefore, further measurements of the low-momentum antikaon production in pA collisions at subthreshold beam energies are needed nowadays to get a better understanding of the K^- properties in nuclear matter.

4. CONCLUSIONS

In this paper, we have presented the reanalysis of the experimental data [2] on the antikaon excitation functions for p + ^{9}Be and p + ^{63}Cu reactions as well as the analysis of the data [6] on the K^- spectrum

[6] It corresponds to the lowest data point in Fig. 1.

from $p\,^{197}$Au interactions in the subthreshold energy regime using the spectral function approach [1] that has been modified to account for the FSI between the outgoing nucleons participating in primary proton–nucleon production process. The NN-FSI correction of the invariant inclusive cross section for antikaon production in this process was made in line exactly with the Watson–Migdal theory of FSI adopting the inverse Jost function method. It was shown that this correction is important for reproducing the energy dependences [2] of the Lorentz-invariant cross sections for hard K^- production in p^9Be and p^{63}Cu collisions within the present approach when the influence of the nuclear density-dependent nucleon and antikaon effective potentials on the proton-induced reaction channel is included. On the other hand, it was found to play a negligible role in describing the data [6] on spectrum of relatively soft antikaons from p^{197}Au interactions at an incident energy of 2.5 GeV. In this case, contrary to those mentioned above, the pion-induced reaction channel was found to be dominant and, therefore, only attractive nucleon and antikaon mean fields were essential. The good agreement with the experimental data achieved within the present approach favors the possibility of employing the elementary NN-FSI effects in $p + A$ reactions as well as leaves minor room for subthreshold K^- production via other mechanisms in these reactions.

The influence of the nucleon, kaon, and antikaon mean-field potentials on the K^- yield has also been explored. It was demonstrated that, in line with our previous findings of [1], the K^- optical potential has a strong effect on this yield at low antikaon momenta, which is greater than those from nucleon and kaon effective potentials. At high antikaon momenta, the K^- yield is mainly governed, along with the considered elementary NN-FSI effects, by the nucleon mean field and the scenario with zero K^+ potential is favorable. Our results indicate that the measurements of the differential cross sections for subthreshold K^- production on different target nuclei are most promising at laboratory antikaon momenta $p_{\mathrm{lab}} \leq 400$ MeV/c to distinguish between shallow and deep K^- optical potentials. The experimental data [6] available here currently favor a deep antikaon potential. However, these data are too scarce to draw more reliable conclusions on the actual magnitude of the K^- optical potential in a nuclear medium. Therefore, further measurements of the subthreshold soft antikaon production in pA interactions are needed nowadays to achieve a better understanding of the K^- properties in nuclear matter.

ACKNOWLEDGMENTS

The author is grateful to Yu.T. Kiselev and V.A. Sheinkman for their interest in this work.

REFERENCES

1. E. Ya. Paryev, Eur. Phys. J. A **9**, 521 (2000).
2. A. V. Akindinov, M. M. Chumakov, Yu. T. Kiselev, *et al.*, Preprint No. ITEP 41-99, ITEP (Moscow, 1999).
3. K. M. Watson, Phys. Rev. **88**, 1163 (1952).
4. M. L. Goldberger and K. M. Watson, *Collision Theory* (Wiley, New York, 1964).
5. A. B. Migdal, Zh. Éksp. Teor. Fiz. **28**, 3 (1955) [Sov. Phys. JETP **1**, 2 (1955)].
6. KaoS Collab. (W. Scheinast), Acta Phys. Pol. B **31**, 2305 (2000).
7. X. S. Fang, C. M. Ko, G. Q. Li, and Y. M. Zheng, Phys. Rev. C **49**, R608 (1994).
8. G. Q. Li and C. M. Ko, Nucl. Phys. A **594**, 460 (1995).
9. G. Q. Li and C. M. Ko, Phys. Rev. C **54**, 1897 (1996).
10. A. Cieply, E. Friedman, A. Gal, and J. Mares, nucl-th/0104087.
11. E. Friedman, A. Gal, and C. J. Batty, Phys. Lett. B **308**, 6 (1993).
12. E. Friedman, A. Gal, and C. J. Batty, Nucl. Phys. A **579**, 518 (1994).
13. E. Friedman, Nucl. Phys. A **639**, 511c (1998).
14. E. Friedman, A. Gal, J. Mares, and A. Cieply, Phys. Rev. C **60**, 024314 (1999).
15. A. Gal, nucl-th/0101010.
16. C. Hanhart and K. Nakayama, Phys. Lett. B **454**, 176 (1999).
17. J. A. Niskanen, Phys. Lett. B **456**, 107 (1999).
18. V. V. Baru, A. M. Gasparian, J. Haidenbauer, *et al.*, nucl-th/0006075; Yad. Fiz. **64**, 633 (2001) [Phys. At. Nucl. **64**, 579 (2001)].
19. F. Kleefeld, Acta Phys. Pol. B **31**, 2225 (2000).
20. B. J. Morton, E. E. Gross, E. V. Hungerford, *et al.*, Phys. Rev. **169**, 825 (1968).
21. H. P. Noyes and H. M. Lipinski, Phys. Rev. C **4**, 995 (1971).
22. J. P. Naisse, Nucl. Phys. A **278**, 506 (1977).
23. A. Moalem, L. Razdolskaja, and E. Gedalin, hep-ph/9505264.
24. G. Fäldt and C. Wilkin, Phys. Lett. B **382**, 209 (1996).
25. G. Fäldt and C. Wilkin, Phys. Rev. C **56**, 2067 (1997).
26. G. Fäldt and C. Wilkin, Z. Phys. A **357**, 241 (1997).
27. C. Wilkin, *Final-State Interaction Theory, Presentation at the ANKE Collaboration Meeting, 2001*.
28. A. Sibirtsev and W. Cassing, nucl-th/9802025.
29. J. T. Balewski, A. Budzanowski, H. Dombrowski, *et al.*, Phys. Lett. B **388**, 859 (1996).
30. J. T. Balewski, A. Budzanowski, C. Goodman, *et al.*, Eur. Phys. J. A **2**, 99 (1998).
31. V. Bernard, N. Kaiser, and Ulf-G. Meissner, Eur. Phys. J. A **4**, 259 (1999).
32. N. Kaiser, nucl-th/9907114.
33. N. Kaiser, Eur. Phys. J. A **5**, 105 (1999).
34. P. Moskal, H. H. Adam, J. T. Balewski, *et al.*, Phys. Lett. B **482**, 356 (2000).
35. A. V. Akindinov, M. M. Chumakov, Yu. T. Kiselev, *et al.*, Preprint No. ITEP 37-99, ITEP (Moscow, 1999).

36. B. L. Druzhinin, A. E. Kudryavtsev, and V. E. Tarasov, Z. Phys. A **359**, 205 (1997).
37. R. Shyam and U. Mosel, Phys. Lett. B **426**, 1 (1998).
38. A. Sibirtsev and W. Cassing, Eur. Phys. J. A **2**, 333 (1998).
39. A. Sibirtsev and W. Cassing, nucl-th/9904046.
40. R. Shyam, Phys. Rev. C **60**, 055213 (1999).
41. A. Sibirtsev, K. Tsushima, W. Cassing, and A. W. Thomas, nucl-th/0004022.
42. A. I. Titov, B. Kämpfer, and B. L. Reznik, Eur. Phys. J. A **7**, 543 (2000).
43. P. Moskal, H. H. Adam, A. Budzanowski, *et al.*, nucl-ex/0007018.
44. V. Abaev, V. Koptev, and H. Ströher, Preprint No. 2403, PNPI (Gatchina, 2001).
45. O. Dumbrajs, R. Koch, H. Pilkuhn, *et al.*, Nucl. Phys. B **216**, 277 (1983).
46. A. Sibirtsev and W. Cassing, nucl-th/9909053.
47. C. Ciofi degli Atti and S. Simula, Phys. Rev. C **53**, 1689 (1996).
48. E. Ya. Paryev, Eur. Phys. J. A **7**, 127 (2000).
49. A. Sibirtsev and W. Cassing, Nucl. Phys. A **641**, 476 (1998).
50. FHS Collab. (Yu. T. Kiselev), J. Phys. G **25**, 381 (1999).

Physics of Atomic Nuclei, Vol. 65, No. 10, 2002, pp. 1887–1893. From Yadernaya Fizika, Vol. 65, No. 10, 2002, pp. 1939–1945.

ELEMENTARY PARTICLES AND FIELDS
Theory

The $\phi \to \gamma(a_0(980) + f_0(980)) \to \gamma K\bar{K}$ Decays*

N. N. Achasov and **V. V. Gubin**

Sobolev Institute for Mathematics, Siberian Division, Russian Academy of Sciences, Universitetskiĭ pr. 4, Novosibirsk, 630090 Russia

Received July 24, 2001

Abstract—We study the decay $\phi \to \gamma K^+K^-$ taking into account the scalar meson production $\phi \to \gamma(a_0 + f_0) \to \gamma K^+K^-$ and the final-state radiation. We note that the relative sign between the final-state radiation amplitude and the scalar-meson production amplitude is fixed in the K^+K^- loop model which describes data on the $\phi \to \gamma f_0 \to \gamma\pi\pi$ and $\phi \to \gamma a_0 \to \gamma\pi\eta$ decays. As consequence, this model predicts the definite interference between the final-state radiation and the scalar resonance production amplitudes. We calculate the mass spectra of the $\phi \to \gamma K^+K^-$ decay and the differential cross sections for $e^+e^- \to \phi \to \gamma K^+K^-$ and for $e^+e^- \to \phi \to \gamma K^0\bar{K}^0$ reactions. © *2002 MAIK "Nauka/Interperiodica".*

1. INTRODUCTION

As was shown in a number of papers (see [1–6] and references therein), the study of the radiative decays $\phi \to \gamma a_0 \to \gamma\pi\eta$ and $\phi \to \gamma f_0 \to \gamma\pi\pi$ can shed light on the problem of the scalar $a_0(980)$ and $f_0(980)$ mesons. These decays have been studied not only theoretically but also experimentally. The present time data have already been obtained from Novosibirsk with the detectors SND [7–10] and CMD-2 [11], which give the following branching ratios: $\mathrm{BR}(\phi \to \gamma\pi\eta) = (0.88 \pm 0.14 \pm 0.09) \times 10^{-4}$ [9], $\mathrm{BR}(\phi \to \gamma\pi^0\pi^0) = (1.221 \pm 0.098 \pm 0.061) \times 10^{-4}$ [10] and $\mathrm{BR}(\phi \to \gamma\pi\eta) = (0.9 \pm 0.24 \pm 0.1) \times 10^{-4}$, $\mathrm{BR}(\phi \to \gamma\pi^0\pi^0) = (0.92 \pm 0.08 \pm 0.06) \times 10^{-4}$ [11].

These data give evidence in favor of the four-quark ($q^2\bar{q}^2$) [1, 3, 12–17] nature of the scalar $a_0(980)$ and $f_0(980)$ mesons and in favor of the one-loop mechanism $\phi \to K^+K^- \to \gamma a_0$ and $\phi \to K^+K^- \to \gamma f_0$ (see Fig. 1) suggested in [1].

It is clear that the relative sign between the final-state radiation amplitude and the $\phi \to \gamma(a_0 + f_0) \to \gamma K^+K^-$ amplitude in the K^+K^- loop model (see Figs. 1 and 2) is fixed. As a consequence, this model predicts the definite interference between the final state radiation amplitude and the scalar resonance production. That is why the study of the $\phi \to \gamma K^+K^-$ decay is very important. Such an investigation requires high statistics. It can be carried out in the $\gamma N \to \phi N(\Delta) \to \gamma K^+K^-N(\Delta)$ reactions at Jefferson Laboratory and in the $e^+e^- \to \phi \to \gamma K^+K^-$ reaction at DAΦNE. Note that, if the f_0 and σ mesons mixing is taken into account in the $\phi \to \gamma(a_0 + f_0(\sigma)) \to \gamma K^+K^-$ reaction, then the interference sign is not fixed. But the influence of the σ meson on the signal is small and is considered as a correction to the interference term.

We calculate the $\phi \to \gamma K^+K^-$ spectra and the differential cross sections for $e^+e^- \to \phi \to \gamma K^+K^-$ using parameters of $a_0(980)$ and $f_0(980)$ mesons from [17, 9, 10] which describe the $\phi \to \gamma a_0 \to \gamma\pi\eta$ and $\phi \to \gamma f_0 \to \gamma\pi\pi$ decays and show that the contribution of the interference between the scalar resonance production and the final-state radiation is an order of magnitude higher than the contribution of the scalar resonance production. That is the reason that today's facilities give good capabilities to investigate our issue.

We also calculate the differential cross section for $e^+e^- \to \phi \to \gamma K^0\bar{K}^0$, which is very important for the determination of the background affecting the precision measurements of CP violation.

The paper is organized as follows.

All needed formulas are considered in Section 2. In Section 3, the calculations are carried out and the results obtained are discussed. A brief summary is given in the Conclusion. Note that [18] was dedicated to the $e^+e^- \to \phi \to \gamma K\bar{K}$ reactions in the ϕ meson region. Unfortunately, the authors of [18] considered mistakenly that the relative sign between the final-state radiation amplitude and the $e^+e^- \to \gamma(a_0 + f_0) \to \gamma K^+K^-$ amplitude is not fixed in the K^+K^- loop model. In addition, they took parameters of $a_0(980)$ and $f_0(980)$ mesons a priori to some extent.

*This article was submitted by the authors in English.

**e-mail: achasov@math.nsc.ru

***e-mail: gubin@math.nsc.ru

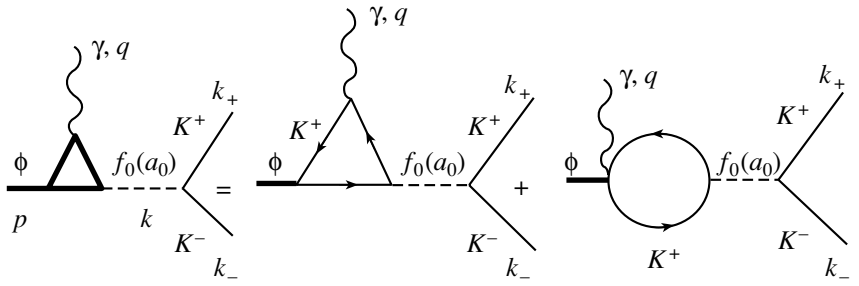

Fig. 1. Diagrams of the K^+K^- loop model.

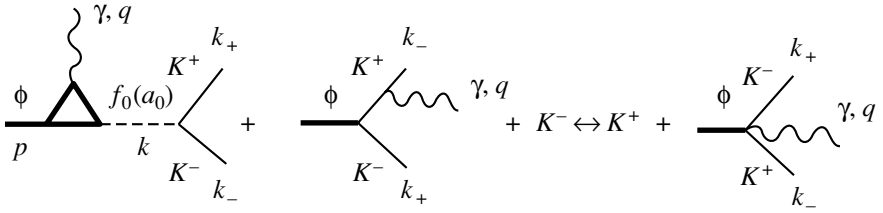

Fig. 2. Diagrams of the signal $\phi \to \gamma K^+K^-$ and background processes.

2. MODEL

Let us consider the production of the scalar $R = a_0, f_0$ meson through the loop of the charged K mesons, $\phi \to K^+K^- \to \gamma R$ (see [1, 19]). The diagrams are presented in Fig. 1. The production amplitude $\phi \to \gamma R$ in the rest frame of the ϕ meson is

$$M = g_{RK^+K^-} g(m^2) \vec{e}(\phi)\vec{e}(\gamma), \tag{1}$$

where $\vec{e}(\phi)$ and $\vec{e}(\gamma)$ are the polarization vectors of the ϕ meson and the photon, respectively, and $t = m^2 = k^2$. The expressions for $g(m^2)$ were obtained in the pointlike particle model, which is adequate for compact hadrons, the four-quark ($q^2\bar{q}^2$) or $q\bar{q}$ states [1], and in the extended scalar $K\bar{K}$ molecule model [4]. The amplitude of the decay $\phi \to (\gamma f_0 + \gamma a_0) \to \gamma K^+K^-$, the signal amplitude, is

$$M_s = M_s^\mu e^\mu(\phi) = \left(\frac{g^2_{f_0K^+K^-}}{D_{f_0}(m)} + \frac{g^2_{a_0K^+K^-}}{D_{a_0}(m)}\right) g(m^2) \times \left(q^\mu \frac{e(\gamma)p}{pq} - e^\mu(\gamma)\right) e^\mu(\phi), \tag{2}$$

where $s = p^2$. The mass spectrum is given by

$$\frac{d\Gamma_s}{dm} = \frac{m}{(2\pi)^3 36 s\sqrt{s}} \times \left| g(m^2)\left(\frac{g^2_{f_0K^+K^-}}{D_{f_0}(t)} + \frac{g^2_{a_0K^+K^-}}{D_{a_0}(t)}\right)\right|^2 \times (s-t)b\sqrt{1 - \frac{4m^2_{K^+}}{m^2}}. \tag{3}$$

We introduce symmetrical angle cut $-b \le \cos\theta_{K\gamma} \le b$, where $\theta_{K\gamma}$ is the angle between the photon and the K^+-meson momenta in the dikaon rest frame. We also consider the f_0- and σ-meson mixing. In this case, the amplitude is

$$M_s = \left(\sum_{RR'} g_{R_0K_s^+K^-} G^{-1}_{RR'}(m) g_{R'K^+K^-} + \frac{g^2_{a_0K^+K^-}}{D_{a_0}(m)}\right) g(m^2) \left(q^\mu \frac{e(\gamma)p}{pq} - e(\gamma)^\mu\right) e^\mu(\phi), \tag{4}$$

where we take into account the mixing of the f_0 and σ mesons, $R, R' = f_0, \sigma$ by means of the matrix of the inverse propagators $G(m)$. All necessary expressions can be found in [3]. The mass spectrum in this case is

$$\frac{d\Gamma_s}{dm} = \frac{m}{(2\pi)^3 36 s\sqrt{s}} \left| g(m^2) \times \left(\sum_{RR'} g_{RK^+K^-} G^{-1}_{RR'}(m) g_{R'K^+K^-} + \frac{g^2_{a_0K^+K^-}}{D_{a_0}(m)}\right)\right|^2 \times (s-t)b\sqrt{1 - \frac{4m^2_{K^+}}{m^2}}. \tag{5}$$

Let us consider the background related to the final-state radiation (see Fig. 2). The amplitude of the process is

$$M_{\text{fin}} = 2e g_{\phi K^+K^-} T^\mu e^\mu(\phi), \tag{6}$$

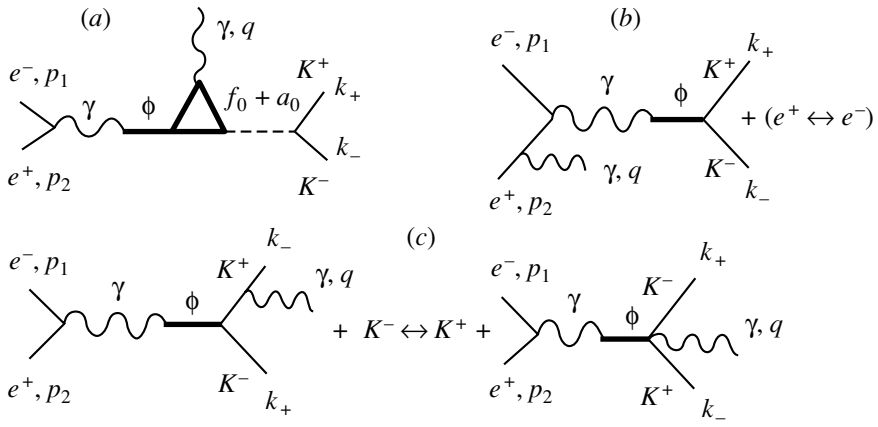

Fig. 3. Diagrams of the signal $e^+e^- \to \phi \to \gamma K^+K^-$ and background processes.

$$T^\mu = \frac{e(\gamma)k_-}{qk_-}\left(k_+ - \frac{p}{2}\right)^\mu + \frac{e(\gamma)k_+}{qk_+}\left(k_- - \frac{p}{2}\right)^\mu + e(\gamma)^\mu.$$

The mass spectrum is

$$\frac{d\Gamma_{\rm fin}}{dm} = \frac{\alpha m g^2_{\phi K^+K^-}}{12\pi^2\sqrt{s}}\left(\frac{v(x)}{x}(x^2 - (1-\xi)(1-x)) + (1-\xi)\left(1 - x - \frac{\xi}{2}\right)\frac{1}{x}\ln\frac{1+v(x)}{1-v(x)}\right), \quad (7)$$

where $v(x) = b\sqrt{1 - \xi/(1-x)}$. We identify $\xi = 4m^2_{K^+}/s$ and $x = 2\omega/\sqrt{s}$, $t = s(1-x) = m^2$ for convenience.

The interference between the amplitudes (2) and (6) gives the expression

$$\frac{d\Gamma_{\rm int}}{dm} = \frac{\alpha m g_{\phi K^+K^-}}{\sqrt{4\pi\alpha s}} \times {\rm Re}\left[g(m^2)\left(\frac{g^2_{f_0K^+K^-}}{D_{f_0}(m)} + \frac{g^2_{a_0K^+K^-}}{D_{a_0}(m)}\right)\right] \times \left\{v(x) + \frac{\xi}{2}\ln\frac{1-v(x)}{1+v(x)}\right\}. \quad (8)$$

For the decay $\phi \to \gamma(f_0 + a_0) \to \gamma K^0\bar{K}^0$, due to the destructive interference between the a_0 and f_0 mesons (recall that $g_f K^+K^- = g_{f_0}K^0\bar{K}^0$ and $g_{a_0}K^+K^- = g_{a_0}K^0\bar{K}^0$), we have

$$\frac{d\Gamma_s}{dm} = \frac{m}{(2\pi)^3 36 s\sqrt{s}}\left|g(m^2)\left(\frac{g^2_{f_0K^0\bar{K}^0}}{D_{f_0}(t)} - \frac{g^2_{a_0K^0\bar{K}^0}}{D_{a_0}(t)}\right)\right|^2 \times (s-t)b\sqrt{1 - \frac{4m^2_{K^0}}{m^2}} \quad (9)$$

$$\frac{d\Gamma_s}{dm} = \frac{m}{(2\pi)^3 36 s\sqrt{s}}\left|g(m^2)\right. \times \left.\left(\sum_{RR'} g_{RK^0\bar{K}^0}G^{-1}_{RR'}(m)g_{R'K^0\bar{K}^0} - \frac{g^2_{a_0K^0\bar{K}^0}}{D_{a_0}(m)}\right)\right|^2 \times (s-t)b\sqrt{1 - \frac{4m^2_{K^0}}{m^2}}. \quad (10)$$

Let us consider the reaction $e^+e^- \to \phi \to (\gamma f_0 + \gamma a_0) \to \gamma K^+K^-$ (see Fig. 3). The amplitude of the reaction is

$$M_{ee} = e\bar{u}\gamma^\mu u\frac{em^2_\phi}{f_\phi s D_\phi(s)}M^\mu_s. \quad (11)$$

The differential cross section is

$$\frac{d\sigma_\phi}{dm} = \frac{\alpha^2}{24\pi s^3}\left(\frac{m^2_\phi}{f_\phi}\right)^2 \times \frac{m}{|D_\phi(s)|^2}\left|g(m^2)\left(\frac{g^2_{f_0K^+K^-}}{D_{f_0}(m)} + \frac{g^2_{a_0K^+K^-}}{D_{a_0}(m)}\right)\right|^2 \times (s-t)\sqrt{1 - \frac{4m^2_{K^+}}{m^2}} \quad (a + \frac{a^3}{3})b. \quad (12)$$

The coupling constants $g_{f_0K^+K^-}$ and f_ϕ are related to the widths in the following way:

$$\Gamma(f_0 \to K^+K^-, m) = \frac{g^2_{f_0K^+K^-}\sqrt{m^2 - 4m^2_{K^+}}}{16\pi m^2}, \quad (13)$$

$$\Gamma(V \to e^+e^-, s) = \frac{4\pi\alpha^2}{3}\left(\frac{m^2_V}{f_V}\right)^2\frac{1}{s\sqrt{s}}.$$

We introduce two symmetrical angle cuts: $-a \le \cos\theta_\gamma \le a$, where θ_γ is the angle between the photon momentum and the electron beam in the center-of-mass frame of the reaction under consideration, and $-b \le \cos\theta_{K\gamma} \le b$, where $\theta_{K\gamma}$ is the angle between the photon and the K^+-meson momenta in

the dikaon rest frame. Notice that the kaons are slow in our case, $\sqrt{1-4m_K^2/m^2} \le 0.25$, which is why the $\theta_{K\gamma}$ angle cut hardly changes the results (at $150^\circ > \theta_{K\gamma} > 30^\circ$, changes are within 13%) in contrast to the pion production [6, 20].

The basic background to the process under study has come from the initial electron radiation (see Fig. 3*b*) and the radiation from the final kaons (Fig. 3*c*). The initial-state radiation does not interfere with the final-state radiation or with the signal in the differential cross section integrated over all angles since the charged kaons are in the $C = -1$ state. This is true also when the angle cuts are symmetrical.

Introducing the symmetrical angle cuts considerably decreases the background from the initial-state radiation because the photons in this case are mainly emitted along the beams.

Let us consider the background related to the final-state radiation. The amplitude of the process is

$$M_{\rm fin} = e^2 \bar{u}\gamma^\mu u \frac{em_\phi^2}{f_\phi}\frac{1}{sD_\phi(s)} 2g_{\phi K^+K^-}T^\mu. \qquad (14)$$

It is convenient to present the differential cross section in the form [6, 20]

$$\frac{d\sigma_f}{dm} = 2\sigma_0(s)\frac{m}{s}F(x,a,b), \qquad (15)$$

$$F(x,a,b) = \frac{2\alpha}{\pi(1-\xi)^{3/2}} \times \left\{\frac{3}{2}\left(a - \frac{a^3}{3}\right)F_1 + \frac{3}{4}a(1-a^2)F_2\right\},$$

$$F_1 = \frac{1}{x}\left(x^2 - \frac{\xi(1-\xi)(1-x)}{(1-b^2)(1-x)+b^2\xi}\right)f(x) + (1-\xi)\left(1-x-\frac{\xi}{2}\right)\frac{1}{x}\ln\frac{1+v(x)}{1-v(x)}. \qquad (16)$$

$$F_2 = \frac{1}{x}\left(\frac{\xi^2(x-1)}{(1-b^2)(1-x)+b^2\xi} + 2x - 2 - x^2\right)v(x) + \xi\left(2-x-\frac{\xi}{2}\right)\frac{1}{x}\ln\frac{1+v(x)}{1-v(x)}.$$

The nonradiative cross section $e^+e^- \to K^+K^-$ is

$$\sigma_0(s) = \frac{\pi\alpha^2}{3s}(1-\xi)^{3/2}|F_\phi(s)|^2, \qquad (17)$$

where $|F_\phi(s)|^2 = (g_{\phi K^+K^-}/f_\phi)^2 m_\phi^4/|D_\phi(s)|^2$.

The interference between the amplitudes from Eqs. (11) and (14) is equal to [6, 20]

$$\frac{d\sigma_{\rm int}}{dm} = \frac{\alpha^3}{s^2}\left(\frac{g_{\phi K^+K^-}}{f_\phi}\right)\left(\frac{mm_\phi^4}{f_\phi\sqrt{4\pi\alpha}|D_\phi|^2}\right) \times {\rm Re}\left[\frac{g^2_{f_0K^+K^-}g(m^2)}{D_{f_0}(m)} + \frac{g^2_{a_0K^+K^-}g(m^2)}{D_{a_0}(m)}\right] \times \left\{v(x) + \frac{\xi}{2}\ln\frac{1-v(x)}{1+v(x)}\right\}\left(a + \frac{a^3}{3}\right). \qquad (18)$$

In a similar way, let us give the expression for the differential cross section of the initial-state radiation [6, 20]:

$$\frac{d\sigma_i}{dm} = 2\sigma_0(t)\frac{m}{s}H(x,a,b), \qquad (19)$$

$$H(x,a,b) = \frac{\alpha}{\pi}\left[\left(\frac{2(1-x)+x^2}{x}\ln\frac{1+a}{1-a} - ax\right) \times \left(\frac{3b}{2} - \frac{b^3}{2}\right) + \frac{3a(1-x)(b^3-b)}{x}\right].$$

Evaluating $H(x,a,b)$, we ignored the electron mass.

The total cross section of the one-photon annihilation with soft-photon radiation and with virtual corrections of order α is given by

$$\sigma(s) = \tilde{\sigma}(s)\left\{1 + \frac{2\alpha}{\pi}\left[(L-1)\ln\frac{2\omega_{\rm min}}{\sqrt{s}} + \frac{3}{4}L + \frac{\pi^2}{6} - 1\right]\right\}, \qquad (20)$$

$$\tilde{\sigma}(s) = (\sigma_\phi(s) + \sigma_{\rm int}(s) + \sigma_i + \sigma_f)\frac{1}{|1-\Pi(s)|^2},$$

where $\omega_{\rm min}$ is the minimal photon energy registered and $L = \ln(s/m_e^2)$ is the "main" logarithm. The electron vacuum polarization of order α is

$$\Pi(s) = \frac{\alpha}{3\pi}\left(L - \frac{5}{3}\right), \qquad (21)$$

where the contribution of muons and light hadrons is ignored.

For the propagator of the ϕ meson, we use the expression

$$D_\phi(s) = m_\phi^2 - s - is\frac{g^2_{\phi K^+K^-}}{48\pi}\left[\left(1 - \frac{4m^2_{K^+}}{s}\right)^{3/2} + \frac{1}{Z(s)}\left(1 - \frac{4m^2_{K^0}}{s}\right)^{3/2} + 0.1p^3_{\pi\rho}\right], \qquad (22)$$

where $g_{\phi K^+K^-} = 4.68$, $p_{\pi\rho} = \sqrt{(s-(m_\pi - m_\rho)^2)(s-(m_\pi+m_\rho)^2)}/(2\sqrt{s})$, and

the factor $Z(s) = 1 + \alpha\pi(1+v^2)/(2v)$, $v = (1 - 4m^2_{K^+}/s)^2$, takes into account the radiative correction $g_{\phi K^+K^-}/Z(s) = g_{\phi K^0\bar{K}^0}$ (see details in [21]).

For the scalar meson propagators, we use the expressions

$$D_R(m^2) = m_R^2 - m^2 + \sum_{ab} g_{Rab}[\mathrm{Re}P_R^{ab}(m_R^2) - P_R^{ab}(m^2)], \quad (23)$$

where $\sum_{ab} g_{Rab}[\mathrm{Re}P_R^{ab}(m_R^2) - P_R^{ab}(m^2)] = \Pi_R(m^2) = \Pi_{RR}(m^2)$ takes into account the finite width corrections of the resonance that are the one-loop contribution to the self-energy of the R resonance from the two-particle intermediate ab states. In the $q^2\bar{q}^2$ model of the scalar particle and in the model of the $K\bar{K}$ molecule, the f_0 and a_0 mesons are strongly coupled to the $K\bar{K}$ channel under the threshold of which they are. The ordinary resonance expression of the propagator, in view of that, is changed considerably, and taking into account $\sum_{ab} g_{Rab}[\mathrm{Re}P_R^{ab}(m_R^2) - P_R^{ab}(m^2)]$ corrections is necessary.

For the pseudoscalar ab mesons and $m_a \geq m_b$, $s > m_+^2$, one has [13, 19, 20]

$$P_R^{ab}(m^2) = \frac{g_{Rab}}{16\pi}\left[\frac{m_+m_-}{\pi m^2}\ln\frac{m_b}{m_a}\rho_{ab}^m \times \left(i + \frac{1}{\pi}\ln\frac{\sqrt{m^2-m_-^2}-\sqrt{m^2-m_+^2}}{\sqrt{m^2-m_-^2}+\sqrt{m^2-m_+^2}}\right)\right]. \quad (24)$$

For $m_- < m < m_+$,

$$P_R^{ab}(m^2) = \frac{g_{Rab}}{16\pi}\left[\frac{m_+m_-}{\pi m^2}\ln\frac{m_b}{m_a} - |\rho_{ab}(m)| + \frac{2}{\pi}|\rho_{ab}(m)|\arctan\frac{\sqrt{m_+^2-m^2}}{\sqrt{m^2-m_-^2}}\right]. \quad (25)$$

For $m < m_-$,

$$P_R^{ab}(m^2) = \frac{g_{Rab}}{16\pi}\left[\frac{m_+m_-}{\pi m^2}\ln\frac{m_b}{m_a} - \frac{1}{\pi}\rho_{ab}(m) \times \ln\frac{\sqrt{m_+^2-m^2}-\sqrt{m_-^2-m^2}}{\sqrt{m_+^2-m^2}+\sqrt{m_-^2-m^2}}\right] \quad (26)$$

and

$$\rho_{ab}(m) = \sqrt{\left(1-\frac{m_+^2}{m^2}\right)\left(1-\frac{m_-^2}{m^2}\right)}, \quad (27)$$
$$m_\pm = m_a \pm m_b.$$

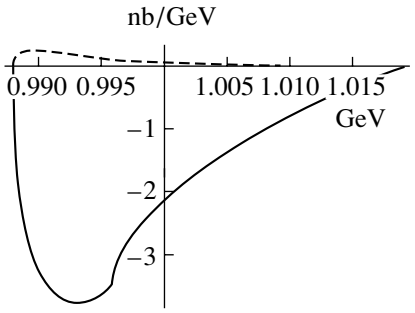

Fig. 4. The $e^+e^- \to \gamma K^+K^-$ differential cross section $d\sigma_\phi/dm + d\sigma_{\mathrm{int}}/dm$ (solid curve), see text, and the differential cross section of the signal $d\sigma_\phi/dm$ (dashed curve), see Eq. (12). The angle cuts are $a = 0.7$, $b = 0.955$.

The constants g_{Rab} are related to the width

$$\Gamma(R \to ab, m) = \frac{g_{Rab}^2}{16\pi m}\rho_{ab}(m). \quad (28)$$

The function $g(m^2)$ has the following expression [1]. For $m < 2m_{K^+}$,

$$g(m^2) = \frac{e}{2(2\pi)^2}g_{\phi K^+K^-}\left\{1 + \frac{1-\rho^2(m^2)}{\rho^2(m_\phi^2)-\rho^2(m^2)} \times \left[2|\rho(m^2)|\arctan\frac{1}{|\rho(m^2)|} - \rho(m_\phi^2)\lambda(m_\phi^2) + i\pi\rho(m_\phi^2) - (1-\rho^2(m_\phi^2)) \times \left(\frac{1}{4}(\pi + i\lambda(m_\phi^2))^2 - \left(\arctan\frac{1}{|\rho(m^2)|}\right)^2\right)\right]\right\}, \quad (29)$$

where

$$\rho(m^2) = \sqrt{1 - \frac{4m_{K^+}^2}{m^2}}, \quad (30)$$
$$\lambda(m^2) = \ln\frac{1+\rho(m^2)}{1-\rho(m^2)}.$$

For $m > 2m_{K^+}$,

$$g(m^2) = \frac{e}{2(2\pi)^2}g_{\phi K^+K^-}\left\{1 + \frac{1-\rho^2(m^2)}{\rho^2(m_\phi^2)-\rho^2(m^2)} \times \left[\rho(m^2)(\lambda(m^2) - i\pi) - \rho(m_\phi^2)(\lambda(m_\phi^2) - i\pi) - \frac{1}{4}(1-\rho^2(m_\phi^2))((\pi + i\lambda(m_\phi^2))^2 - (\pi + i\lambda(m^2))^2)\right]\right\}. \quad (31)$$

We use the constant $g_{\phi K^+K^-} = 4.68$ related to the width in the following way:

$$\Gamma(\phi \to K^+K^-) = \frac{1}{3}\frac{g_{\phi K^+K^-}^2}{16\pi}m_\phi\rho^3(m_\phi^2). \quad (32)$$

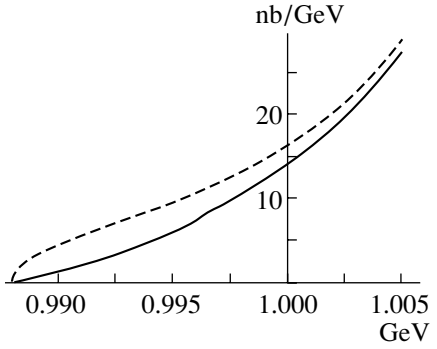

Fig. 5. The $e^+e^- \to \gamma K^+K^-$ differential cross section $d\sigma_\phi/dm + d\sigma_{\rm int}/dm + d\sigma_f/dm + d\sigma_i/dm$ (solid curve) and the differential cross section of the background $d\sigma_f/dm + d\sigma_i/dm$ (dashed curve); see text. The angle cuts are $a = 0.7$, $b = 0.955$.

3. RESULTS

To demonstrate, we present the spectra for the $e^+e^- \to \gamma K^+K^-$ reaction $d\sigma_\phi/dm + d\sigma_{\rm int}/dm$ and $d\sigma_\phi/dm + d\sigma_{\rm int}/dm + d\sigma_f/dm + d\sigma_i/dm$ in Figs. 4 and 5 using the constants obtained from our fitting of the SND data [17]:

$$g_{f_0K^+K^-} = 4.021 \pm 0.011 \text{ GeV}, \qquad (33)$$
$$g_{f_0\pi^0\pi^0} = 1.494 \pm 0.021 \text{ GeV},$$
$$m_{f_0} = 0.996 \pm 0.0013 \text{ GeV},$$
$$g^2_{f_0K^+K^-}/4\pi = 1.29 \pm 0.017 \text{ GeV}^2,$$
$$g_{\sigma K^+K^-} = 0,$$
$$g_{\sigma\pi^0\pi^0} = 2.58 \pm 0.02 \text{ GeV},$$
$$m_\sigma = 1.505 \pm 0.012 \text{ GeV},$$
$$C = 0.622 \pm 0.04 \text{ GeV}^2$$

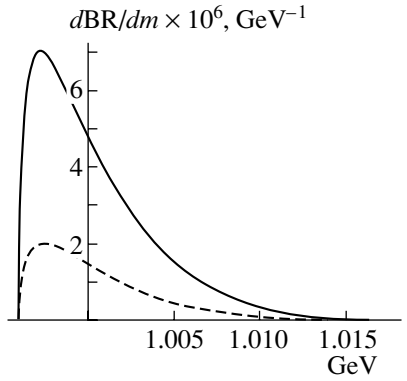

Fig. 6. The differential branching ratio of the $\phi \to \gamma(a_0 + f_0) \to \gamma K^0\bar{K}^0$ decay. The solid curve is the differential branching ratio for the set of parameters (33) and (34); the dashed line is the differential branching ratio for the set of parameters (35) and (36).

and

$$m_{a_0} = 985.51 \pm 0.8 \text{ MeV}, \qquad (34)$$
$$g_{a_0K^+K^-} = 2.747 \pm 0.428 \text{ GeV},$$
$$g^2_{a_0K^+K^-}/(4\pi) = 0.6 \pm 0.015 \text{ GeV}^2.$$

The branching ratio of the final-state radiation decay $\phi \to \gamma K^+K^-$ is $\mathrm{BR}(\phi \to \gamma K^+K^-, b = 0.955, 2m_K < m < 1.01 \text{ GeV}) = 9.41 \times 10^{-5}$. For the pure signal, we have $\mathrm{BR}(\phi \to \gamma(a_0 + f_0) \to \gamma K^+K^-, b = 0.955,\ 2m_K < m < 1.01 \text{ GeV}) = 2.15 \times 10^{-6}$ (note that it is 99.6% of $\mathrm{BR}(\phi \to \gamma(a_0 + f_0) \to \gamma K^+K^-, b = 0.955,\ 2m_K < m < m_\phi)$), and for the signal-plus-interference term, we have $\mathrm{BR}(\phi \to \gamma(a_0 + f_0) \to \gamma K^+K^-, \quad b = 0.955, \quad 2m_K < m < 1.01 \text{ GeV}) = -1.54 \times 10^{-5}$. For comparison, the branching ratio for the $\phi \to \gamma(a_0 + f_0) \to \gamma K^0\bar{K}^0$ for this set of parameters is equal to $\mathrm{BR}(\phi \to \gamma(a_0 + f_0) \to \gamma K^0\bar{K}^0, b = 1.0, 2m_{K_0} < m < m_\phi) = 4.36 \times 10^{-8}$ (see Fig. 6).

In Figs. 7 and 8, we present the variant of the SND data fitting [9, 10] without f_0 and σ mixing:

$$m_{f_0} = 0.9698 \pm 0.0045 \text{ GeV}, \qquad (35)$$
$$g^2_{f_0K^+K^-}/(4\pi) = 2.47 \pm^{0.73}_{0.51} \text{ GeV}^2,$$
$$g^2_{f_0\pi^+\pi^-}/(4\pi) = 0.54 \pm^{0.09}_{0.08} \text{ GeV}^2$$

and

$$m_{a_0} = 994 \pm^{33}_{8} \text{ MeV}, \qquad (36)$$
$$g^2_{a_0K^+K^-}/(4\pi) = 1.05 \pm^{0.36}_{0.25} \text{ GeV}^2.$$

Analogously, for the pure signal we have $\mathrm{BR}(\phi \to \gamma(a_0 + f_0) \to \gamma K^+K^-, \quad b = 0.955, \quad 2m_K < m < 1.01) = 8.12 \times 10^{-7}$, and for the signal-plus-interference term, we have $\mathrm{BR}(\phi \to \gamma(a_0 + f_0) \to \gamma K^+K^-, b = 0.955, \quad 2m_K < m < 1.01 \text{ GeV}) = -9.58 \times 10^{-6}$. The branching ratio for the $\phi \to$

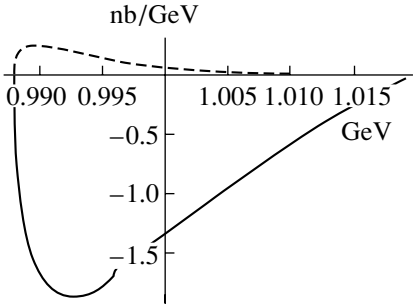

Fig. 7. The $e^+e^- \to \gamma K^+K^-$ differential cross section $d\sigma_\phi/dm + d\sigma_{\rm int}/dm$ (solid curve), see text and differential cross section of the signal $d\sigma_\phi/dm$ (dashed curve), see Eq. (12). The angle cuts are $a = 0.7$, $b = 0.955$.

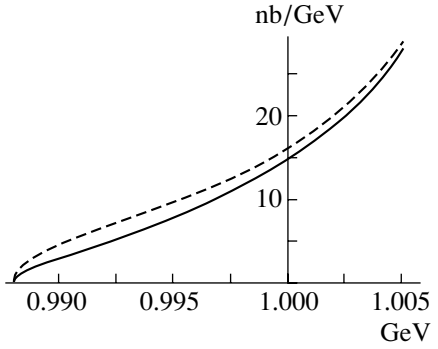

Fig. 8. The $e^+e^- \to \gamma K^+K^-$ differential cross section $d\sigma_\phi/dm + d\sigma_{\rm int}/dm + d\sigma_f/dm + d\sigma_i/dm$ (solid curve) and the differential cross section of the background $d\sigma_f/dm + d\sigma_i/dm$ (dashed curve); see text. The angle cuts are $a = 0.7$, $b = 0.955$.

$\gamma(a_0 + f_0) \to \gamma K^0\bar{K}^0$ for this set of parameters is equal to $\mathrm{BR}(\phi \to \gamma(a_0 + f_0) \to \gamma K^0\bar{K}^0,\ \ b = 1.0,\ 2m_{K^0} < m < m_\phi) = 1.29 \times 10^{-8}$.

It is seen from our analysis that the pictures are the same qualitatively for both sets of parameters, but the branching ratio for the signal plus interference is predicted within 1.5 and the branching ratio for the pure signal is predicted within 2.5.

4. CONCLUSION

Thus, the analysis tells us that the research of the decays $\phi \to \gamma K^+K^-$ in the processes $e^+e^- \to \phi \to \gamma K^+K^-$ and $\gamma N \to \phi N(\Delta) \to \gamma K^+K^- N(\Delta)$ is the real problem that could be investigated in Novosibirsk at VEPP-2000, in Frascati at DAΦNE, and in Newport News at Jefferson Laboratory. This research could give much information about the inner structure of the a_0 and f_0 mesons and allow us to check the hypothesis of the considerable $s\bar{s}$ part in the a_0 and f_0 mesons.

ACKNOWLEDGMENTS

We are grateful to V.V. Kulikov for a stimulating discussion.

This work was supported in part by INTAS–Russian Foundation for Basic Research (grant no. IR-97-232) and by the Russian Foundation for Basic Research (project no. 02-02-16061).

REFERENCES

1. N. N. Achasov and V. N. Ivanchenko, Nucl. Phys. B **315**, 465 (1989).
2. F. E. Close, N. Isgur, and S. Kumano, Nucl. Phys. B **389**, 513 (1993).
3. N. N. Achasov and V. V. Gubin, Yad. Fiz. **61**, 274 (1998) [Phys. At. Nucl. **61**, 224 (1998)]; Phys. Rev. D **56**, 4084 (1997).
4. N. N. Achasov, V. V. Gubin, and V. I. Shevchenko, Yad. Fiz. **60**, 89 (1997) [Phys. At. Nucl. **60**, 81 (1997)]; Phys. Rev. D **56**, 203 (1997).
5. J. L. Lucio and M. Napsuciale, *Contribution to 3rd Workshop on Physics and Detectors for DAPHNE (DAPHNE 99), Frascati, Italy, 1999;* hep-ph/0001136.
6. N. N. Achasov and V. V. Gubin, Yad. Fiz. **61**, 1473 (1998) [Phys. At. Nucl. **61**, 1367 (1998)]; Phys. Rev. D **57**, 1987 (1998).
7. M. N. Achasov *et al.*, Phys. Lett. B **438**, 441 (1998).
8. M. N. Achasov *et al.*, Phys. Lett. B **440**, 442 (1998); hep-ex/9807016.
9. M. N. Achasov *et al.*, Phys. Lett. B **479**, 53 (2000); hep-ex/0003031.
10. M. N. Achasov *et al.*, Phys. Lett. B **485**, 349 (2000); hep-ex/0005017.
11. R. R. Akhmetshin *et al.*, Phys. Lett. B **462**, 380 (1999).
12. R. L. Jaffe, Phys. Rev. D **15**, 267, 281 (1977).
13. N. N. Achasov, S. A. Devyanin, and G. N. Shestakov, Usp. Fiz. Nauk **142**, 361 (1984) [Sov. Phys. Usp. **27**, 161 (1984)]; Z. Phys. C **22**, 53 (1984); Yad. Fiz. **32**, 1098 (1980) [Sov. J. Nucl. Phys. **32**, 566 (1980)].
14. N. N. Achasov and G. N. Shestakov, Usp. Fiz. Nauk **161** (6), 53 (1991) [Sov. Phys. Usp. **34**, 471 (1991)]; Z. Phys. C **41**, 309 (1988).
15. N. N. Achasov, Usp. Fiz. Nauk **168**, 1257 (1998) [Phys. Usp. **41**, 1149 (1998)]; hep-ph/9904223; Nucl. Phys. A **675**, 279c (2000).
16. O. Black, A. Fariborz, F. Sannino, and J. Schechter, Phys. Rev. D **59**, 074026 (1999).
17. N. N. Achasov and V. V. Gubin, Phys. Rev. D **63**, 094007 (2001).
18. J. L. Lucio and M. Napsuciale, Nucl. Phys. B **440**, 237 (1995).
19. N. N. Achasov, *The Second DAΦNE Physics Handbook,* Ed. by L. Maiani, G. Pancheri, and N. Paver (Laboratory Nazionali di Frascati, Frascati, 1995), p. 671.
20. N. N. Achasov, V. V. Gubin, and E. P. Solodov, Yad. Fiz. **60**, 1279 (1997) [Phys. At. Nucl. **60**, 1152 (1997)]; Phys. Rev. D **55**, 2672 (1997).
21. M. N. Achasov *et al.*, Phys. Rev. D **63**, 072002 (2001).

Physics of Atomic Nuclei, Vol. 65, No. 10, 2002, pp. 1894–1899. Translated from Yadernaya Fizika, Vol. 65, No. 10, 2002, pp. 1946–1952.

ELEMENTARY PARTICLES AND FIELDS
Theory

Some Problems of the Jet Calculus in the Perturbative QCD

I. M. Dremin

Lebedev Institute of Physics, Leninskiĭ pr. 53, Moscow, 117924 Russia

Received January 24, 2002; in final form, April 8, 2002

Abstract—Some problems of the jet calculus in perturbative QCD are discussed. The first one is related to specifying the order of perturbation. Because of the cancellation of the leading-order (LO) and next-to-leading-order (NLO) terms in the ratio r of the mean multiplicities in gluon and quark jets, the results presently obtained for this ratio should be associated with the 4NLO approximation. The second problem reveals itself in calculations where corrections to some quantities (in particular, to r') are greater at present energies than lower order terms. Some features that characterize jets and which do not suffer from this deficiency are proposed. Yet another problem lies in interpreting negative cumulant-moment values, which are considered as an indication of a changeover from attraction to repulsion in sets of specific particle content. Finally, the problem of generalizing QCD equations for generating functions is briefly discussed.

Numerous achievements of perturbative QCD (pQCD) in predicting and describing the properties of quark and gluon jets are well known and were described in many review articles (see, for example, [1–5]). Here, I would like to discuss some problems related to relevant calculations and often left behind the scene.

First, let me recall some simplest definitions [1, 6] concerning jet multiplicities in QCD. The generating function G is defined by the formula

$$G(y,u)=\sum_{n=0}^{\infty}P_n(y)u^n, \tag{1}$$

where $P_n(y)$ is the multiplicity distribution at the scale $y=\ln(p\theta/Q_0)=\ln(2Q/Q_0)$. Here, p is the initial momentum; θ is the jet-divergence angle (jet opening angle), which is assumed here to be fixed; Q is the jet virtuality; and $Q_0=$ const. In (1), u is an auxiliary variable, which is often omitted to avoid encumbering the notation. The analytic properties of generating functions in u are of special interest (see [1, 3]) in view of some analogies with statistical physics, but we will not consider them here.

The moments of the distribution are defined as

$$F_q=\frac{\sum\limits_n P_n n(n-1)\dots(n-q+1)}{\left(\sum\limits_n P_n n\right)^q} \tag{2}$$
$$=\frac{1}{\langle n\rangle^q}\frac{d^qG(y,u)}{du^q}\bigg|_{u=1},$$

$$K_q=\frac{1}{\langle n\rangle^q}\frac{d^q\ln G(y,u)}{du^q}\bigg|_{u=1}, \tag{3}$$

where F_q and K_q are factorial and cumulant moments, which are responsible for, respectively, total and genuine (not reducible to lower ranks) correlations. These moments are not independent. They are related by specific equations that can easily be derived from the definitions of the moments in terms of the generating function:

$$F_q=\sum_{m=0}^{q-1}C_{q-1}^m K_{q-m}F_m. \tag{4}$$

The QCD equations for the generating functions are[1)]

$$G'_G=\int_0^1 dx K_G^G(x)\gamma_0^2 \tag{5}$$
$$\times[G_G(y+\ln x)G_G(y+\ln(1-x))-G_G(y)]$$
$$+n_f\int_0^1 dx K_G^F(x)\gamma_0^2$$
$$\times[G_F(y+\ln x)G_F(y+\ln(1-x))-G_G(y)],$$

$$G'_F=\int_0^1 dx K_F^G(x)\gamma_0^2 \tag{6}$$

[1)] To eliminate the nonperturbative region from the ensuing consideration, the limits of integration in these equations are often chosen as $\exp(-y)$ and $1-\exp(-y)$, which tend to 0 and 1 at high energy y (see Fig. 2 below).

1063-7788/02/6510-1894$22.00

$$\times [G_G(y+\ln x)G_F(y+\ln(1-x)) - G_F(y)],$$

where $G'(y) = dG/dy$, n_f is the number of active flavors, and

$$\gamma_0^2 = \frac{2N_c\alpha_S}{\pi}. \quad (7)$$

The running coupling constant in the two-loop approximation is

$$\alpha_s(y) = \frac{2\pi}{\beta_0 y}\left(1 - \frac{\beta_1}{\beta_0^2}\frac{\ln 2y}{y}\right) + O(y^{-3}), \quad (8)$$

where

$$\beta_0 = \frac{11N_c - 2n_f}{3}, \quad \beta_1 = \frac{17N_c^2 - n_f(5N_c + 3C_F)}{3}. \quad (9)$$

The labels G and F correspond to gluons and quarks, and the kernels of the equations are

$$K_G^G(x) = \frac{1}{x} - (1-x)[2 - x(1-x)], \quad (10)$$

$$K_G^F(x) = \frac{1}{4N_c}[x^2 + (1-x)^2], \quad (11)$$

$$K_F^G(x) = \frac{C_F}{N_c}\left[\frac{1}{x} - 1 + \frac{x}{2}\right], \quad (12)$$

where $N_c = 3$ is the number of colors and $C_F = (N_c^2 - 1)/2N_c = 4/3$ in QCD.

From the above, one can obtain equations for any moment of the multiplicity distribution both in quark and in gluon jets. For this, it is only necessary to equate terms involving identical powers of u on the two sides of the equations. In particular, the equations for average multiplicities read

$$\langle n_G(y)\rangle' = \int dx\gamma_0^2[K_G^G(x)(\langle n_G(y+\ln x)\rangle + \langle n_G(y+\ln(1-x)\rangle - \langle n_G(y)\rangle) + n_f K_G^F(x)(\langle n_F(y+\ln x)\rangle + \langle n_F(y+\ln(1-x)\rangle - \langle n_G(y)\rangle)], \quad (13)$$

$$\langle n_F(y)\rangle' = \int dx\gamma_0^2 K_F^G(x)(\langle n_G(y+\ln x)\rangle + \langle n_F(y+\ln(1-x)\rangle - \langle n_F(y)\rangle). \quad (14)$$

Their solutions can be sought in the form

$$\langle n_{G,F}\rangle \propto \exp\left(\int^y \gamma_{G,F}(y')dy'\right), \quad (15)$$

where the lower limit of integration has not been fixed because its variation results in the substitution of a new normalization constant that is not shown in the above relation, but which is considered in practice as a fitted parameter depending on the nonperturbative component of the underlying dynamics of a process.

Using the perturbative expansion

$$\gamma_G \equiv \gamma = \gamma_0(1 - a_1\gamma_0 - a_2\gamma_0^2 - a_3\gamma_0^3) + O(\gamma_0^5), \quad (16)$$

one obtains the solution in the form [6–8]

$$\langle n_{G,F}\rangle = A_{G,F}y^{-a_1c^2}\exp(2c\sqrt{y} + \delta_{G,F}(y)), \quad (17)$$

where $c = (4N_c/\beta_0)^{1/2}$ and

$$\delta_G(y) = \frac{c}{\sqrt{y}}[2a_2c^2 + \frac{\beta_1}{\beta_0^2}(\ln 2y + 2)] + \frac{c^2}{y}[a_3c^2 - \frac{a_1\beta_1}{\beta_0^2}(\ln 2y + 1)]) + O(y^{-3/2}). \quad (18)$$

The corresponding expression for $\delta_F(y)$ can easily be derived from the formulas for γ_F that are presented below.

Usually, the ratio of average multiplicities in gluon and quark jets,

$$r = \frac{\langle n_G\rangle}{\langle n_F\rangle} = \frac{A_G}{A_F}\exp(\delta_G(y) - \delta_F(y)), \quad (19)$$

is introduced instead of γ_F, and its perturbative expansion

$$r = r_0(1 - r_1\gamma_0 - r_2\gamma_0^2 - r_3\gamma_0^3) + O(\gamma_0^4) \quad (20)$$

is used. The analytic expressions for the parameters a_i and r_i and their numerical values for all $i \le 3$ were calculated from the perturbative solutions of the above equations (the review is given in [3]). Within these approximations, experimental data on the mean multiplicity in e^+e^- annihilation are well described, as can only be seen from Fig. 1. However, data on the ratio r can be described to a much poorer precision of about 15% on the basis of this analytic approach (see Fig. 2), even though each subsequent perturbative approximation improves the agreement.

However, it should be mentioned here that a computer solution to the equations in question provides an accurate quantitative fit to experimental data [9, 10]. This brings about the question of the accuracy of perturbative approximations for this particular characteristic and indicates that higher order corrections are still comparatively large for this ratio up to the highest presently available energies. Let us also note that exact solutions to these equations for fixed coupling constant were given in [11, 12].

The relation between the anomalous dimensions γ of gluon and quark jets is

$$\gamma_F = \gamma - \frac{r'}{r}, \quad (21)$$

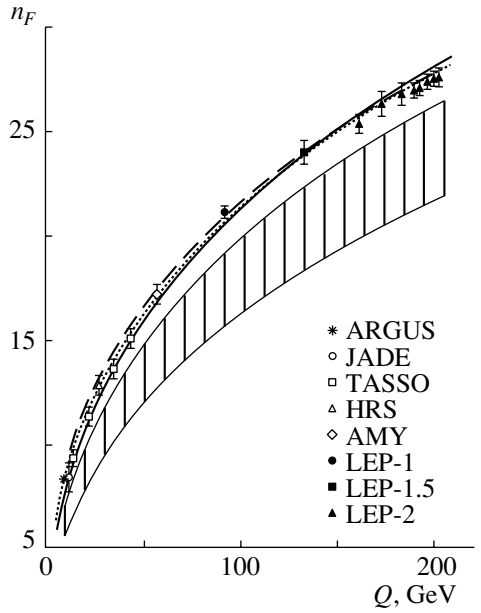

Fig. 1. Average multiplicity of charged particles in e^+e^- annihilation as a function of energy. The results of various fits according to formulas of perturbative QCD and of Monte Carlo models are shown [the solid and the dotted line represent the fits of (18) with one and two adjusted parameters, respectively, while the dashed line is predicted by the HERWIG Monte Carlo model; the vertically shaded area indicates gluon-jet data multiplied by the theoretical value of the ratio r (20)]. The energy Q is given in GeV in all figures.

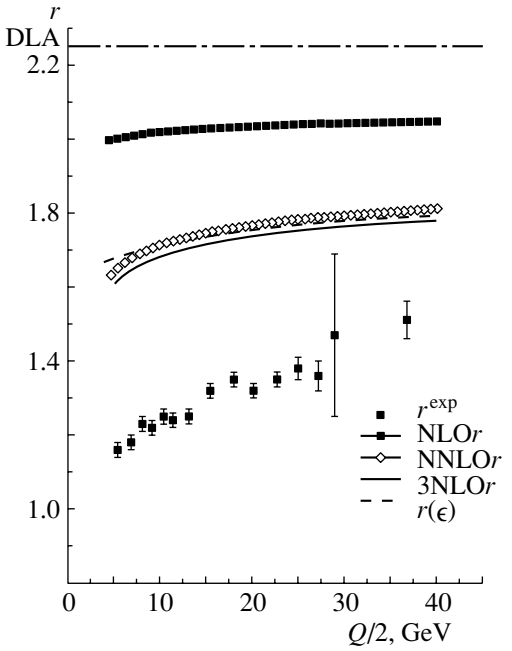

Fig. 2. Experimentally measured ratio r of the multiplicities in gluon and quark jets as a function of energy along with the predictions of analytic QCD and of the HERWIG Monte Carlo model. Various QCD approximations described in this article and the 4NLO(ϵ) approximation with the integration limits e^{-y} and $1-e^{-y}$ instead of usual 0 and 1 in Eqs. (5) and (6) are indicated in the figure.

where

$$r' \equiv dr/dy = Br_0r_1\gamma_0^3 \times [1 + \frac{2r_2}{r_1}\gamma_0 + (\frac{3r_3}{r_1} + B_1)\gamma_0^2 + O(\gamma_0^3)] \quad (22)$$

with $r_0 = \dfrac{N_c}{C_F} = 9/4$, $B = \beta_0/8N_c$, and $B_1 = \beta_1/4N_c\beta_0$.

Thus, we have

$$\gamma_F = \gamma_0[1 - a_1\gamma_0 - (a_2 + Br_1)\gamma_0^2 - (a_3 + 2Br_2 + Br_1^2)\gamma_0^3 - (a_4 + B(3r_3 + 3r_2r_1 + B_1r_1 + r_1^3))\gamma_0^4]. \quad (23)$$

These expressions present two problems, a terminological and a computational one.

Terminology. The two leading terms in the energy behavior of quark- and gluon-jet multiplicities are absolutely identical, as can be seen from Eq. (17), and cancel in their ratio r (19). Therefore, this ratio is $r_0 = 9/4$ both in the leading-order (LO) and in the next-to-leading-order (NLO) approximation. The commonly used notation DLA (double-logarithmic approximation), which is shown on the ordinate in Fig. 2 near the value of $r = 9/4$, should actually be treated as the LO + NLO prediction of QCD for the ratio r. Thus, the term $r_1\gamma_0$ in (20) describes 2NLO corrections. In the literature, it is often referred to, however, as a term of the multiloop logarithmic approximation (MLLA or NLO term), which is incorrect. It is this notation that is commonly used in plots. In our Fig. 2, the notation featuring the letter r is employed, which implies, for example, that 3NLOr indicates the inclusion of the term γ_0^3 in the perturbative expansion of r but that this term contributes to the 4NLO-order terms in the expansion of the anomalous dimensions.

The shift and misuse of the terminology for the anomalous dimensions γ and for the ratio r is clearly displayed in the explicit expression (23) for γ_F. Its last 4NLO term contains a_4, which has not yet been calculated. Together with it, the contribution from r is present with all terms calculated already that contain r_i only for $i \le 3$. In this sense, one should say that the r_3 term in r corresponds to the 4NLO contribution, even though it is proportional to γ_0^3. It is precisely this terminology that is used in Fig. 2.

Calculations. The cancellation of two leading terms in the ratio r also reveals itself in the proportionality of the scale (energy) derivative r' to γ_0^3.

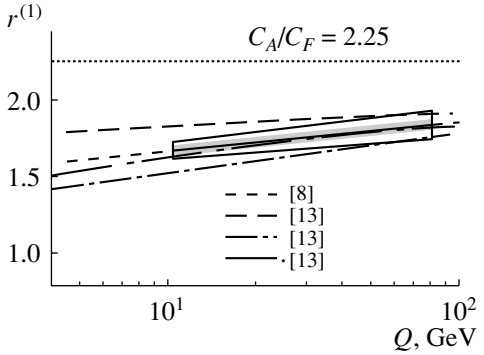

Fig. 3. Ratio of the slopes of the energy dependences of the mean multiplicities in gluon and quark jets according to experimental data and some theoretical calculations. The Casimir operator is $C_A = 3$ in QCD. The mean experimental values are shown within the frame corresponding to the experimental error bars.

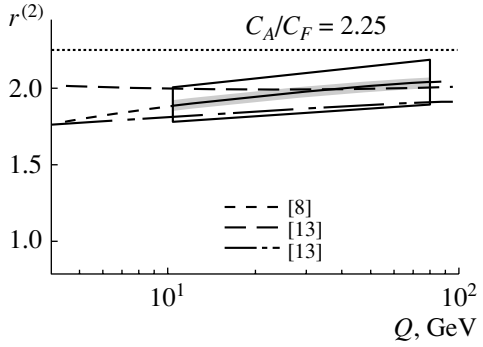

Fig. 4. Ratio of the curvatures of the energy dependences of the mean multiplicities in gluon and quark jets according to experimental data and some theoretical calculations. As in Fig. 3, the mean experimental values are shown within the frame corresponding to the experimental error bars.

Therefore, it can be calculated to $O(\gamma_0^5)$ terms. The leading term is very small (about 0.02 at the Z^0 resonance). Asymptotically, all corrections vanish. However, they are still quite important at present energies of Z^0. The second term in the bracketed expression on the right-hand side of (22) is greater than unity since $2r_2/r_1 \approx 4.9$ and $\gamma \approx 0.45$–0.5. Even the third term is approximately about 0.4. The problem of convergence of the series at Z^0 energies and below becomes crucial. The derivative of the ratio r (its energy slope) is very sensitive to higher order perturbative corrections.

Therefore, it is desirable to use, at present energies, characteristics that are less sensitive to these corrections. In particular, these corrections partially cancel in the ratio of derivatives (slopes):

$$r^{(1)} = \frac{\langle n_G \rangle'}{\langle n_F \rangle'}. \tag{24}$$

The same is true for the ratio of curvatures (or second derivatives):

$$r^{(2)} = \frac{\langle n_G \rangle''}{\langle n_F \rangle''}. \tag{25}$$

The QCD predictions for them,

$$r < r^{(1)} < r^{(2)} < 2.25, \tag{26}$$

were recently confirmed by experiments (see Figs. 3, 4 from [13]).

Interpretation. The next question I would like to raise concerns an as-yet-unclear physical interpretation of oscillations of cumulant moments in QCD. Usually exploited phenomenological distributions of probability theory do not involve oscillations. For example, all cumulant moments of the Poisson distribution are identically zero. One interprets this as the absence of genuine correlations not reducible to lower rank correlations. For the negative binomial distribution, one easily obtains

$$H_q = \frac{K_q}{F_q} = \frac{2}{q(q+1)} > 0. \tag{27}$$

Since F_q are always positive by definition, this inequality implies positive values of K_q.

In the LO approximation, the gluodynamics equation for the generating function,

$$[\ln G(y)]'' = \gamma_0^2 (G(y) - 1), \tag{28}$$

leads to the relation

$$q^2 K_q = F_q \text{ or } H_q = \frac{1}{q^2}. \tag{29}$$

However, H_q moments become negative, with a minimum at the rank of $q_{\min} \approx \dfrac{24}{11\gamma_0} + 0.5 \approx 5$, even in the NLO approximation [14]. This minimum is rather stable. It slowly moves to higher ranks with increasing energy and disappears in the asymptotic region, as is required according to formula (29). In higher orders of the perturbative expansion, the oscillations of higher rank cumulant moments show up [15]. They are confirmed by experiments [16, 17] (see Fig. 5).

It should be emphasized here that the plots of $D_q = q^2 H_q$ would be even more instructive than that of H_q for revealing the oscillations. In this case, they can easily be compared with the LO prediction, according to which $D_q^{\mathrm{LO}} = 1$. Also, a comparison with the results of the negative binomial distribution would become simplified. The plot of the results for the negative binomial distribution (NBD) shows a monotonic increase in D_q^{NBD} from 1 at $q = 1$ to 2 for $q \to \infty$, and this differs significantly from QCD oscillations.

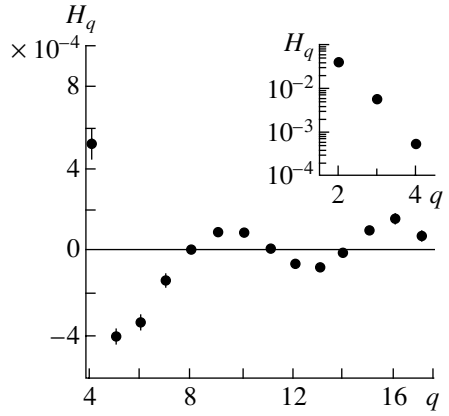

Fig. 5. Oscillations of the measured ratio H_q of the cumulant and factorial moments as a function of the rank q according to experimental data on the multiplicity distributions of charged particles in e^+e^- annihilation at the Z^0 energy (the inset in the right upper corner shows data for the moments of rank 2, 3, and 4).

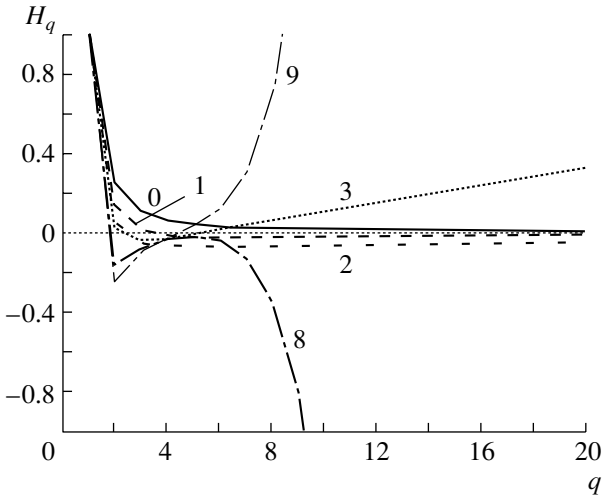

Fig. 6. Moments H_q in the modified dipole approach [21, 22]. They strongly diverge in higher orders of modified perturbation theory for large ranks q and change sign in subsequent orders. The calculations were performed at the Z^0 energy. The order of the perturbative approximation for the corresponding calculation is shown in the right upper corner and on each line.

Apart from the changing character of genuine correlations, the laws of energy–momentum conservation can also contribute to the emergence of these oscillations. If the former factor is more important, this would imply that attraction (clustering) gives way to repulsion (and vice versa) in particle systems at specific values of the number of particles. It would be interesting to find other examples of such behavior in hadronic systems.

Generalization. Finally, there exists the problem of whether it is possible to generalize the equations for the generating functions. On one hand, we understand that, even if treated as kinetic equations, these equations are of limited applicability because of the disregard of nonperturbative effects, a simplified treatment of conservation laws, etc. Some phenomenological attempts at removing these limitations were made from the very beginning [18–20]. In [18], it was proposed to treat the hadronization of partons at the final stage of jet evolution by analogy with ionization in electromagnetic cascades, where it leads to their saturation and to a finite length of the shower. Three different stages of the cascade were considered in the modified kinetic equations proposed in [19, 20]. However, no quantitative results were obtained.

The most successful modification of above equations was proposed in [21] by using the dipole approach to QCD with more accurate kinematical bounds. It was shown that the ratio r can be obtained in good agreement with experimental data. Nevertheless, a further study of higher rank moments of the multiplicity distribution predicted by the modified equations revealed their extremely high sensitivity to higher orders of the perturbative expansion [22]. This is illustrated in Fig. 6, where the moments diverge in high orders and where the change in the signs of high-rank moments in subsequent orders of the perturbative expansion is the only trace of oscillations to be noticed. Such results give no way to draw definitive conclusions. Thus, no successful generalization is at work nowadays. In view of this, the general theoretical trend at present is to calculate directly nonperturbative effects in some jet characteristics (see, for example, [23, 24]).

On the other hand, the success of numerical solutions to the existing equations [9, 10] raises the questions of whether a generalization will give any other noticeable contribution and whether our failure to describe more precisely the ratio r is due to some defects of a purely perturbative expansion at available energies. A more rigorous treatment of the numerical solutions to the equations in question is therefore required. Moreover, it was stated in [25] that the renormalization-group improvement of perturbative results provides a good description of experimental data.

In conclusion, I would like to emphasize once again that, although some fundamental questions concerning the calculation of the properties of quark–gluon jets and the validity of the QCD equations for the generating functions in higher orders have not yet been resolved, the accuracy of pQCD calculations is sufficiently high in practice, especially if one considers that the expansion parameter is rather large.

ACKNOWLEDGMENTS

This work was supported by the Russian Foundation for Basic Research (project nos. 00-02-16101, 02-02-16779).

REFERENCES

1. I. M. Dremin, Usp. Fiz. Nauk **164**, 785 (1994) [Phys. Usp. **37**, 715 (1994)].
2. V. A. Khoze and W. Ochs, Int. J. Mod. Phys. A **12**, 2949 (1997).
3. I. M. Dremin and J. W. Gary, Phys. Rep. **349**, 301 (2001).
4. V. A. Khoze, W. Ochs, and J. Wosiek, *At the Frontier of Particle Physics,* Ed. by M. Shifman (World Sci., Singapore, 2001), Vol. 2, p. 1101.
5. I. M. Dremin, Usp. Fiz. Nauk **172**, 551 (2002).
6. Yu. L. Dokshitzer, V. A. Khoze, A. H. Mueller, and S. I. Troyan, *Basics of Perturbative QCD,* Ed. by J. Tran Thanh Van (Frontières, Gif-sur-Yvette, 1991).
7. I. M. Dremin and J. W. Gary, Phys. Lett. B **459**, 341 (1999).
8. A. Capella, I. M. Dremin, J. W. Gary, *et al.*, Phys. Rev. D **61**, 074009 (2000).
9. S. Lupia, Phys. Lett. B **439**, 150 (1998); in *Proceedings of the XXXIII Moriond Conference on QCD and Strong Interactions, 1998,* Ed. by J. Tran Thanh Van (Frontières, Gif-sur-Yvette, 1998), p. 363.
10. S. Lupia and W. Ochs, Phys. Lett. B **418**, 214 (1998); Nucl. Phys. B (Proc. Suppl.) **64**, 74 (1998).
11. I. M. Dremin and R. C. Hwa, Phys. Rev. D **49**, 5805 (1994).
12. I. M. Dremin and R. C. Hwa, Phys. Lett. B **324**, 477 (1994).
13. J. W. Gary, in *Proceedings of the 31st International Symposium on Multiparticle Dynamics, Datong, China, 2001,* Ed. by L. Liu and Y. Wu (World Sci., Singapore, 2002) (in press); OPAL Collab., Physics Note PN488 (2001).
14. I. M. Dremin, Phys. Lett. B **313**, 209 (1993).
15. I. M. Dremin and V. A. Nechitailo, Mod. Phys. Lett. A **9**, 1471 (1994); Pis'ma Zh. Éksp. Teor. Fiz. **58**, 945 (1993) [JETP Lett. **58**, 881 (1993)].
16. I. M. Dremin, V. Arena, G. Boca, *et al.*, Phys. Lett. B **336**, 119 (1994).
17. SLD Collab. (K. Abe *et al.*), Phys. Lett. B **371**, 149 (1996).
18. I. M. Dremin, Pis'ma Zh. Éksp. Teor. Fiz. **31**, 215 (1980) [JETP Lett. **31**, 185 (1980)].
19. J. Ellis and K. Geiger, Phys. Rev. D **52**, 1500 (1995).
20. J. Ellis and K. Geiger, Nucl. Phys. A **590**, 609c (1995).
21. P. Eden, in *Proceedings of the XXXIV Moriond Conference on QCD and Strong Interactions, 1999,* Ed. by J. Tran Thanh Van (Editions Frontières, Gif-sur-Yvette, 1999).
22. I. M. Dremin and P. Eden, in *Proceedings of the 31st International Symposium on Multiparticle Dynamics, Datong, China, 2001,* Ed. by L. Liu and Y. Wu (World Sci., Singapore, 2002) (in press).
23. Yu. L. Dokshitzer, *Talk at the IPPP Workshop on Multiparticle Production in QCD Jets, Durham, 2001.*
24. A. Banfi, Yu. L. Dokshitzer, G. Marchesini, and G. Zanderighi, JHEP **0007**, 002 (2000); **0103**, 007 (2001); Phys. Lett. B **508**, 269 (2001).
25. K. Hamacher, *Talk at the IPPP Workshop on Multiparticle Production in QCD Jets, Durham, 2001.*

Translated by I. Dremin

Physics of Atomic Nuclei, Vol. 65, No. 10, 2002, pp. 1900–1907. Translated from Yadernaya Fizika, Vol. 65, No. 10, 2002, pp. 1953–1960.

ELEMENTARY PARTICLES AND FIELDS
Theory

Quark Masses and Specific Scaling in Deep-Inelastic Processes

A. V. Kisselev, V. A. Petrov, and R. A. Ryutin

Institute for High Energy Physics, Protvino, Moscow oblast, 142284 Russia

Received September 5, 2001

Abstract—Within an operator-product expansion, the problem of the quark-mass dependence of the heavy-flavor contribution to the structure function F_2 in the current-fragmentation region is considered at high values of the momentum transfer squared Q^2. A linear combination of the structure functions F_2^c and F_2 is found that possesses a specific scaling property for $Q^2 \to \infty$ at small fixed values of the Bjorken variable x. A lower bound on the ratio F_2^c/F_2 is calculated and is compared with data obtained at the HERA collider. © *2002 MAIK "Nauka/Interperiodica".*

1. INTERACTION

Data from the HERA collider on open-charm production in deep-inelastic processes indicate [1, 2] that the charm contribution to the structure function F_2^c amounts to 40% at the measured values of x and Q^2 and that, with decreasing x, it grows faster than the structure function F_2. Recent measurements of processes involving open-beauty production revealed that the contribution of b quarks to the total structure function F_2^b is 2 to 3% [3].

It is often assumed that, as the energy of colliding particles, W, and the square of the momentum transfer, Q^2, increase, mass effects become negligible. However, arguments were adduced in [4, 5] that the difference of the structure functions for deep-inelastic processes involving open heavy-quark production in the current-fragmentation region and the structure functions for processes where heavy quarks do not appear explicitly under similar conditions is a scale-invariant quantity at high values of Q^2; that is, it depends only on the Bjorken variable x and on the heavy-quark mass m_Q. This result makes it possible to obtain, for F_2^c, a model-independent lower bound (more specifically, that which is independent of the choice of gluon distribution in a nucleon) that is in good agreement with experimental data on F_2^c [4, 5].

In this study, we explore the problem of the mass-scale effect on the behavior of observables within an operator-product expansion [6].

For a further analysis, it is convenient to consider, instead of the observables F_2^Q ($Q = c, b$), the quantities

$$F_2^{Q\bar{Q}} = F_2^Q/e_Q^2. \tag{1}$$

For the light quarks $q = u, d, s$, which are taken to be massless in the following, we define

$$F_2^{q\bar{q}} = F_2^q/e_q^2, \tag{2}$$

where $e_{Q(q)}$ are the electric charges of the quarks.

Let us write the operator-product expansion for $F_2^{Q\bar{Q}}$ as

$$\begin{aligned}\frac{1}{x}F_2^{Q\bar{Q}}(x, Q^2, m_Q^2) &= C_g\left(\frac{Q^2}{\mu^2}, \frac{m_Q^2}{\mu^2}, \alpha_s(\mu^2)\right) \otimes f_g(\mu^2)[x] \\ &+ C_Q\left(\frac{Q^2}{\mu^2}, \frac{m_Q^2}{\mu^2}, \alpha_s(\mu^2)\right) \otimes f_Q(\mu^2)[x] \\ &+ C_q\left(\frac{Q^2}{\mu^2}, \frac{m_Q^2}{\mu^2}, \alpha_s(\mu^2)\right) \otimes f_q(\mu^2)[x],\end{aligned} \tag{3}$$

where C_i are coefficient functions, while f_i are quantities that are defined as single-nucleon matrix elements of the corresponding composite operators and which can be identified with the distributions of quarks and gluons in a nucleon. Finally, μ is the renormalization point for the composite operators. The symbol $\otimes$ denotes convolution with respect to the variable x; that is,

$$a \otimes b[x] = \int_x^1 \frac{dz}{z} a(z) b\left(\frac{x}{z}\right). \tag{4}$$

In (3), we have omitted the contributions of higher twists. In order to avoid encumbering the presentation, we will not henceforth indicate explicitly α_s in the arguments of the coefficient functions.

It is well known that C_i and f_i depend individually on the renormalization scheme used. In calculating

coefficient functions, preference is usually given to the modified minimal-subtruction ($\overline{\mathrm{MS}}$) renormalization scheme since calculations within other schemes (for example, within the MOM scheme) are more involved.

However, the MOM scheme has some advantages, including the universality of the algorithm for calculating coefficient functions for all orders in the coupling constant α_s. Advantages of using a subtraction scheme to remove divergences in diagrams involving heavy quarks were indicated by Collins [7], who proposed a mixed renormalization scheme commonly known as the Collins–Wiczek–Zee (CWZ) scheme.

The objective of this study is to show that effects associated with the heavy-quark mass m_Q survive in the limit of high values of Q^2. A linear combination of the structure functions F_2 and F_2^c that possesses scale-invariant properties will be found, and it will be shown that this scaling occurs in various renormalization schemes. In addition, a lower bound on the ratio F_2^c/F_2 will be calculated as a function of x at fixed values of Q^2. The results will be compared with experimental data.

2. ASYMPTOTIC RELATIONS BETWEEN STRUCTURE FUNCTIONS

We will be interested in the behavior of F_2^c at high values of Q^2 and low values of x. We assume that, in this region, heavy quarks are predominantly produced on gluons, but that they are not involved in the evolution of light quarks and gluons.

We can then write

$$\frac{1}{x}F_2^{Q\bar{Q}}(x,Q^2,m_Q^2) = C_g\left(\frac{Q^2}{\mu^2},\frac{m_Q^2}{\mu^2}\right)\otimes f_g(\mu^2)[x] + C_Q\left(\frac{Q^2}{\mu^2},\frac{m_Q^2}{\mu^2}\right)\otimes f_Q(\mu^2)[x]. \quad (5)$$

Setting $\mu^2=\mu_0^2$, where $\Lambda_{\mathrm{QCD}}^2 \ll \mu_0^2 \ll Q^2$, and neglecting intrinsic charm (beauty) in a nucleon (that is, assuming that there exists a scale μ_0^2 at which the heavy-quark distribution function is small in relation to the gluon distribution function), we can find from (5) that the following relation holds:

$$\frac{1}{x}F_2^{Q\bar{Q}}(x,Q^2,m_Q^2) = C_g\left(\frac{Q^2}{\mu_0^2},\frac{m_Q^2}{\mu_0^2}\right)\otimes f_g(\mu_0^2)[x]. \quad (6)$$

Let us define the quantity

$$\Delta F_2 = F_2^{q\bar{q}}(x,Q^2) - F_2^{Q\bar{Q}}(x,Q^2,m_Q^2). \quad (7)$$

Assuming that, at low values of x, the main contribution to the structure function for deep-inelastic processes not involving heavy-flavor production is determined in terms of the gluon distribution [that is, by a formula that is similar to (6)], we obtain

$$\frac{1}{x}\Delta F_2 = \Delta C_g \otimes f_g(\mu_0^2)[x], \quad (8)$$

where

$$\Delta C_g = C_g\left(y,\frac{Q^2}{\mu_0^2},0\right) - C_g\left(y,\frac{Q^2}{\mu_0^2},\frac{m_Q^2}{\mu_0^2}\right) \quad (9)$$

with $y \simeq Q^2/2kq$ (see Appendix A).

In Appendix A, we will calculate the gluon coefficient function in the first order in α_s within the MOM scheme. Using the expression obtained there and Eq. (9), we arrive at

$$\Delta C_g \simeq \Delta C_g^{(1)}\left(y,\frac{m_Q^2}{\mu_0^2}\right) \quad (10)$$
$$= \frac{\alpha_s}{8\pi}\left\{(y^2+(1-y)^2)\ln\left[1+\frac{m_Q^2}{\mu_0^2 y(1-y)}\right] - \frac{m_Q^2(1+2y(1-y))}{m_Q^2+\mu_0^2 y(1-y)}\right\}.$$

Thus, we can see that, at high values of Q^2, ΔF_2 tends to the finite limit $\Delta F_2(x,m_Q^2)$, which depends only on x and on the heavy-quark mass. It is shown in Appendix A that this result is not an artifact of the MOM scheme, although the expression for the quantity ΔC_g of course depends on the renormalization scheme used.

On the basis of the explicit expression (10) for ΔC_g, one can straightforwardly demonstrate that, for $y \le 0.1$ (it is precisely the region of low values of y that is of importance in investigating the behavior of the structure function for $x \ll 1$), we have

$$\Delta C_g > 0. \quad (11)$$

In Appendix B, an exact expression for the coefficient function $C_g(y,Q^2/\mu^2)$ in the massless case is derived within the MOM scheme in the first order in α_s at arbitrary values of Q^2 and μ^2. From the expressions obtained there, it follows, in particular, that

$$C_g\left(y,\frac{Q^2}{\mu_0^2}\right)\Big|_{Q^2=m_Q^2} > \Delta C_g\left(y,\frac{m_Q^2}{\mu_0^2}\right). \quad (12)$$

On the basis of expressions (8), (11), and (12), we then arrive at the following conclusion:

$$F_2^{q\bar{q}}(x,Q^2)\big|_{Q^2=m_Q^2} > \Delta F_2(x,m_Q^2) > 0. \quad (13)$$

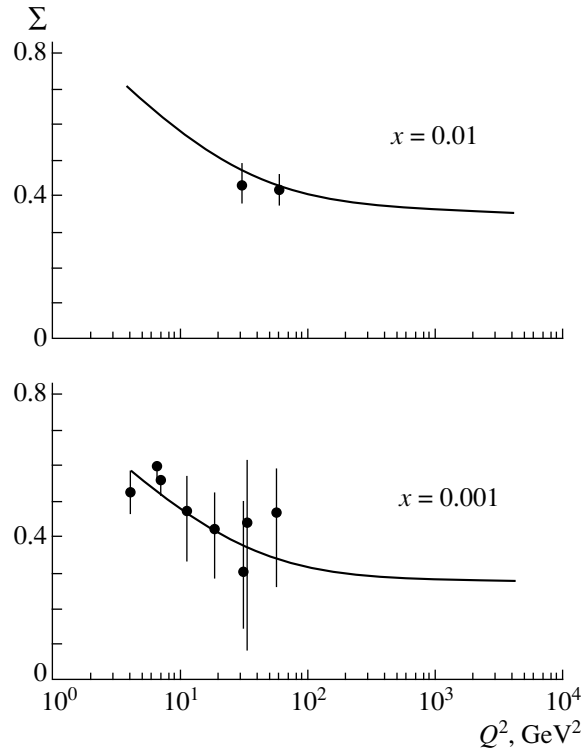

Fig. 1. Difference $\Sigma = F_2 - 2.75F_2^c$ as a function of Q^2 for two fixed values of x. The solid curves represent a fit to data on F_2^c from [2, 8]. The displayed experimental points are characterized by x values that are the closest to the values of 0.01 and 0.001.

In the following, we will use inequalities (13) to obtain a lower bound on F_2^c/F_2, which is the ratio of two observables.

3. ESTIMATING THE CHARM CONTRIBUTION TO THE STRUCTURE FUNCTION

In the preceding section, it was shown that [see Eqs. (8) and (10)] the difference of the light- and heavy-flavor contributions to the structure functions for deep-inelastic processes possesses the scale-invariant property in the limit $Q^2 \to \infty$.

By using this result, we can easily show that the quantity

$$\Sigma_\alpha(x,Q^2) \equiv F_2(x,Q^2) + \alpha F_2^c(x,Q^2,m_c^2) - (4\alpha+11)F_2^b(x,Q^2,m_b^2) \quad (14)$$

(here, α is an arbitrary constant), which is a linear combination of observables [5], has a scaling behavior.

In order to eliminate the b-quark contribution from (14), we set $\alpha = -2.75$. We then obtain the prediction that, in the limit $Q^2 \to \infty$, the linear combination

$$\Sigma = F_2 - 2.75F_2^c \quad (15)$$

must tend to some function that depends only on the Bjorken variable x and on the heavy-quark mass.

For ΔC_g, we now use the explicit expression that we have obtained in the first order in α_s. In this way, we find that, in the region $m_Q^2 \ll Q^2$, the above difference tends to its scaling limit as

$$\frac{1}{x}\Sigma = \frac{1}{9}\left[7\Delta C_g^{(1)}\left(\frac{m_c^2}{\mu_0^2}\right) - \Delta C_g^{(1)}\left(\frac{m_b^2}{\mu_0^2}\right)\right] \otimes f_g(\mu_0^2)[x] + \frac{m_b^2 - 7m_c^2}{Q^2}\ln\left(\frac{Q^2}{\mu_0^2}\right) h \otimes f_g(\mu_0^2)[x], \quad (16)$$

where

$$h(y) = \frac{1}{9}y(1-y)[(2-3y)^2 + 3y^2]. \quad (17)$$

Since $m_b^2 - 7m_c^2 > 0$, we conclude that the correction in expression (16) for $\Sigma(x,Q^2)$ must tend to an upper bound that is independent on Q^2.

In order perform a comparison with available experimental data, we have chosen, for F_2^c, the parametrization that is consistent with expression (16) for $\Sigma(x,Q^2,m_Q^2)$ and have constructed a fit to HERA data from [2]. (The details are given in Appendix C.)

Figure 1 shows the Q^2 dependence of the quantity Σ at $x = 0.01$ and 0.001. These two values were chosen for the variable x because there exists a set of experimental points for various values of Q^2 and values of x that are close to the chosen ones. As can be seen, the experimental data are in good agreement with our conclusion that the above linear combination of the structure functions tends to the scaling limit.

As was shown in [5], the inequalities in (13) make it possible to obtain the following constraint on the ratio of the measured structure functions:

$$\frac{F_2^c(x,Q^2)}{F_2(x,Q^2)} > 0.4\left(1 - \frac{F_2(x,m_c^2)}{F_2(x,Q^2)}\right). \quad (18)$$

It is important to emphasize that, in order to obtain this constraint, we have not used any parametrization for F_2^c and that it is independent of the behavior of the gluon distribution in a nucleon.

In Fig. 2, we present the results of the calculations by formula (18) for two values of the c-quark mass (curves) along with data of the ZEUS collaboration from [2]. Although our curves represent lower bounds on the ratio F_2^c/F_2, they are close to the experimental points, approaching them from below.

Our estimates demonstrate that the displayed theoretical curves are also in good agreement with new preliminary data of the ZEUS collaboration [8], this being so for the maximal value of $Q^2 = 565$ GeV^2 measured by this collaboration inclusive.

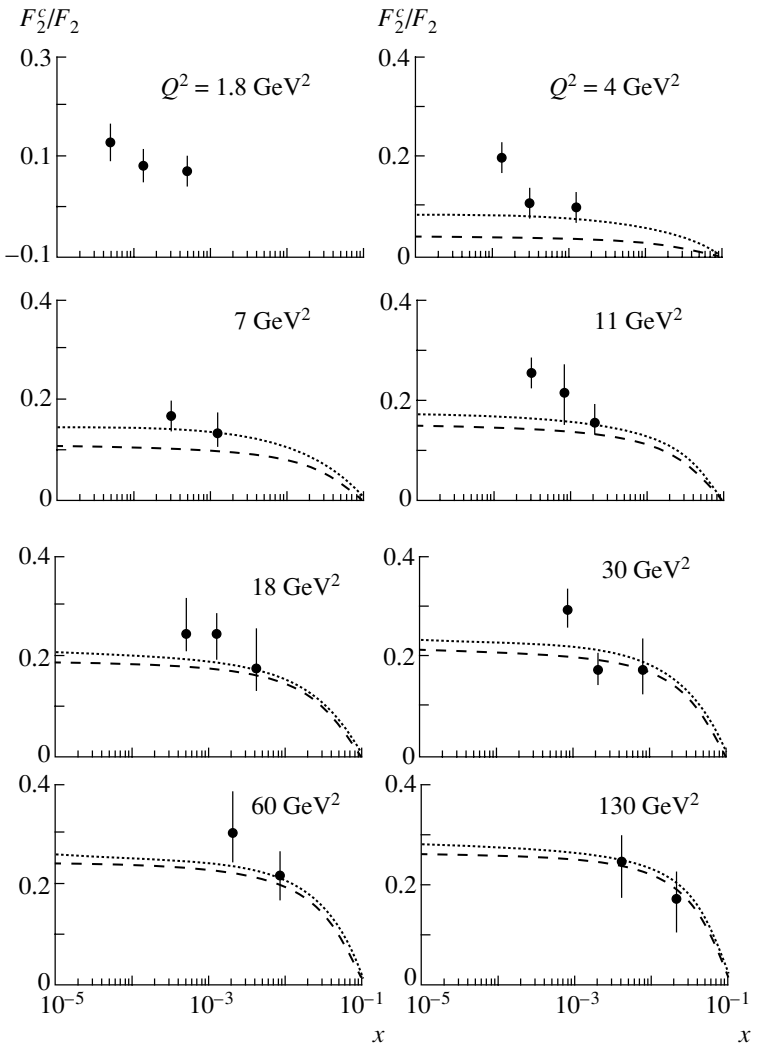

Fig. 2. Ratio F_2^c/F_2 as a function of x at fixed values of Q^2. The dashed (dotted) curves represent the results obtained by calculating the lower bound on the ratio F_2^c/F_2 at the c-quark mass of $m_c = 1.7$ (1.3) GeV. The displayed experimental points were borrowed from [2].

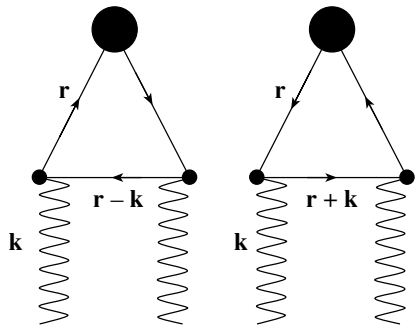

Fig. 3. First-order diagrams in α_s that contribute to the matrix element of the composite operator $A_{Qg}^{(1)}$.

4. CONCLUSION

The operator-product-expansion method has been used here to analyze quark-mass effects in deep-inelastic processes. By means of calculations performed in the first order in the coupling constant within various renormalization schemes, a new scaling property has been found in deep-inelastic processes. Namely, a particular linear combination of the structure function for a deep-inelastic process and the structure function for a deep-inelastic process involving open-charm production is a scale-invariant quantity in the limit of high values of the momentum transfer squared Q^2.

It has been shown that this specific scaling property is in accord with experimental data obtained at the HERA collider for F_2^c and F_2. Obviously, the inclusion of higher orders could change the theoretical conclusion on the above scaling property. With an eye to a further investigation of this question, we treat here our result of the calculations in the lowest

order as an indication of an interesting physical phenomenon.

For the ratio F_2^c/F_2 as a function of the variable x at fixed values of Q^2, we have also calculated a lower bound that is independent of the form of gluon distribution in a nucleon. It has been compared with data of the ZEUS collaboration.

ACKNOWLEDGMENTS

We are grateful to L.K. Gladilin for placing at our disposal complete experimental results of the ZEUS collaboration that were obtained for the ratio F_2^c/F_2.

APPENDIX A

In this appendix, we calculate the gluon coefficient function C_g under the condition $m_Q^2/Q^2 \ll 1$ in the first order in α_s.

For this purpose, we take a gluon of fixed virtuality k^2 (assuming that $-k^2 < 0$ and $-k^2/Q^2 \ll 1$) as a target for a deep-inelastic process. We denote by $F_{2,g}^{Q\bar{Q}}$ the heavy-flavor contribution to the structure function for this process. By analogy with (5), we write the operator-product expansion for $F_{2,g}^{Q\bar{Q}}$ in the order under consideration as

$$\frac{1}{x}F_{2,g}^{Q\bar{Q}} = C_g^{(1)} \otimes A_{gg}^{(0)} + C_Q^{(0)} \otimes A_{Qg}^{(1)}, \qquad (A.1)$$

where A_{gg} (A_{Qg}) is the matrix element of the corresponding composite operator between one-gluon states.

Let us first consider the MOM scheme. Within this scheme, the matrix elements of the composite operators are normalized as follows:

$$A_{Qg}|_{k^2=-\mu^2} = 0, \quad A_{gg}(z)|_{k^2=-\mu^2} = -2\delta(1-z). \qquad (A.2)$$

In order to determine $F_{2,g}^{Q\bar{Q}}$, we make use of the results presented in [4], where an exact expression for $F_{2,g}^{Q\bar{Q}}$ was obtained in the first order in α_s. We have

$$\frac{1}{y}F_{2,g}^{Q\bar{Q}} = -g_{\alpha\beta}F_{\alpha\beta}, \qquad (A.3)$$

where

$$F_{\alpha\beta} = \frac{\alpha_s}{8\pi}\left(\left[F_1^{(a)} + F_1^{(b)}\right]A_{\alpha\beta} + \left[F_2^{(a)} + F_2^{(b)}\right]B_{\alpha\beta}\right), \qquad (A.4)$$

$$A_{\alpha\beta} = g_{\alpha\beta} - \frac{k_\alpha k_\beta}{k^2}, \qquad (A.5)$$

$$B_{\alpha\beta} = \left(q_\alpha - k_\alpha\frac{qk}{k^2}\right)\left(q_\beta - k_\beta\frac{qk}{k^2}\right)\frac{k^2}{(qk)^2}, \qquad (A.6)$$

From Eq. (A.3), it follows that

$$\frac{1}{y}F_{2,g}^{Q\bar{Q}} = -\frac{\alpha_s}{8\pi}(3F_1 - F_2), \qquad (A.7)$$

where

$$F_{1(2)} = F_{1(2)}^{(a)} + F_{1(2)}^{(b)}.$$

The expressions for $F_{1(2)}$ are given by [4]

$$F_1 = F_1^{(a)} + F_1^{(b)} = (y^2 + (1-y)^2) \qquad (A.8)$$
$$\times \ln\left[\frac{Q^2(1-y)}{y(m_Q^2 - k^2y(1-y))}\right] + \frac{m_Q^2}{m_Q^2 - k^2y(1-y)} - 2 + 6y(1-y),$$

$$F_2 = F_2^{(a)} + F_2^{(b)} = (y^2 + (1-y)^2) \qquad (A.9)$$
$$\times \ln\left[\frac{Q^2(1-y)}{y(m_Q^2 - k^2y(1-y))}\right] + \frac{m_Q^2(1-2y)^2}{m_Q^2 - k^2y(1-y)} - 2 + 6y(1-y),$$

where k and q are, respectively, the gluon and the virtual-photon momentum; $q^2 = -Q^2$; $y \simeq Q^2/2kq \simeq Q^2/(W+Q^2)$; and $W = (q+k)^2$. With the aid of expressions (A.7)–(A.9), we obtain

$$\frac{1}{y}F_{2,g}^{Q\bar{Q}} = -\frac{\alpha_s}{4\pi}\left\{(y^2 + (1-y)^2) \times \ln\left[\frac{Q^2(1-y)}{y(m_Q^2 - k^2y(1-y))}\right] - 2 + \frac{m_Q^2(1+2y(1-y))}{m_Q^2 - k^2y(1-y)} + 6y(1-y)\right\}. \qquad (A.10)$$

In order to determine $C_g^{(1)}$ from relation (A.1), it is also necessary to calculate the matrix element of the quark composite operator $A_{Qg}^{(1)}$ in the same order. The corresponding diagrams are depicted in Fig. 3.

Choosing the axial gauge

$$d_{\mu\nu}(k,n) = -g_{\mu\nu} + \frac{k_\mu n_\nu + k_\nu n_\mu}{kn}, \qquad (A.11)$$

where $n^2 = 0$, we obtain

$$A_{Qg}^{(1),J} = -i2\pi\alpha_s\int\frac{d^4r}{(2\pi)^4}d_{\mu\nu}(k,n)\left(\frac{rn}{kn}\right)^{J-1} \qquad (A.12)$$
$$\times \frac{1}{4kn}\mathrm{tr}\left[\gamma_\mu(\hat{r}+m_Q)\hat{n}(\hat{r}+m_Q)\gamma_\nu(\hat{r}-\hat{k}+m_Q)\right] \times \frac{\delta_+((r-k)^2 - m_Q^2)}{(r^2 - m_Q^2)^2}.$$

Taking into account the equalities

$$\int d^4r f(r^2)\delta_+((r-k)^2-m_Q^2)r_\mu = \int d^4r f(l^2)y' k_\mu, \tag{A.13}$$

$$\int d^4r f(r^2)\delta_+((r-k)^2-m_Q^2)r_\mu r_\nu \tag{A.14}$$
$$= \int d^4r f(l^2)\left\{\frac{1}{2}g_{\mu\nu}(m_Q^2-(1-y')l^2 - y'(1-y')k^2) + y'^2 k_\mu k_\nu\right\},$$

we arrive at

$$\frac{1}{4kn}\mathrm{tr}\left[\gamma_\mu(\hat{r}+m_Q)\hat{n}(\hat{r}+m_Q)\gamma_\nu(\hat{r}-\hat{k}+m_Q)\right] \tag{A.15}$$
$$= g_{\mu\nu}(l^2+y'k^2) + 4y' r_\mu r_\nu - 2y'(k_\mu r_\nu + k_\nu r_\mu)$$
$$= g_{\mu\nu}(2y'm_Q^2 + (l^2+y'k^2)((1-y')^2+y'^2)) - 4y'^2(1-y')k_\mu k_\nu,$$

where $y' = rn/kn$ and $l^2 = m_Q^2 - r^2$. As a result, the equality in (A.12) takes the form

$$A_{Qg}^{(1),J} = -i2\pi\alpha_s \tag{A.16}$$
$$\times \int \frac{d^4r}{(2\pi)^4} y'^{J-1}\cdot\frac{\delta_+(k^2-l^2-2kr)}{l^4}$$
$$\times (l^2((1-y')^2+y'^2)+y'(k^2+2m_Q^2))$$
$$= -\frac{\alpha_s}{8\pi}\int\limits_0^1 y'^{J-1}dy' \int\limits_{-k^2y'+m_Q^2/(1-y')}^{\mu^2y'+m_Q^2/(1-y')} \frac{dl^2}{l^4}$$
$$\times\left(l^2((1-y')^2+y'^2)+y'\left(\frac{m_Q^2}{y'(1-y')}+2m_Q^2\right)\right).$$

Going over to y space, we arrive at

$$A_{Qg}^{(1)}(y,m_Q^2,k^2,\mu^2) = -\frac{\alpha_s}{8\pi}\left\{((1-y)^2+y^2)\right. \tag{A.17}$$
$$\times\ln\left[\frac{m_Q^2+\mu^2y(1-y)}{m_Q^2-k^2y(1-y)}\right] + m_Q^2(1+2y(1-y))$$
$$\left.\times\left(\frac{1}{m_Q^2-k^2y(1-y)}-\frac{1}{m_Q^2+\mu^2y(1-y)}\right)\right\}.$$

By using Eqs. (A.1), (A.10), and (A.17) and the fact that $-A_{gg}^{(0)}(z) = C_Q^{(0)}(z) = 2\delta(1-z)$, we finally obtain the sought expression for $C_g^{(1)}$ within the MOM scheme; that is,

$$C_g^{(1),\mathrm{MOM}}(y,Q^2,m_Q^2,\mu^2) \tag{A.18}$$
$$= \frac{\alpha_s}{8\pi}\left\{(y^2+(1-y)^2)\ln\left[\frac{Q^2(1-y)}{y(m_Q^2+\mu^2y(1-y))}\right]\right.$$
$$\left. -2+6y(1-y)+\frac{m_Q^2(1+2y(1-y))}{m_Q^2+\mu^2y(1-y)}\right\}.$$

In the limit $m_Q \to 0$, we find from (A.18) that

$$C_g^{(1),\mathrm{MOM}}(y,Q^2,0,\mu^2) \tag{A.19}$$
$$= \frac{\alpha_s}{8\pi}\left\{(y^2+(1-y)^2)\ln\left[\frac{Q^2}{\mu^2y^2}\right]-2+6y(1-y)\right\}.$$

Expression (10) in the main body of the text for $\Delta C_g^{(1)}$ now follows from (A.18) and (A.19). The quantity $\Delta C_g^{(1),\mathrm{MOM}}$ possesses the following property:

$$\Delta C_g^{(1),\mathrm{MOM}}(y,Q^2,m_Q^2=0,\mu^2) = 0. \tag{A.20}$$

We note that, in the MOM scheme, the coefficient function $C_g^{(1)}$ can be found without calculating the composite operator $A_{Qg}^{(1)}$ if an analytic expression for $F_{2,g}^{Q\bar{Q}}$ is known (as in our case). From formulas (A.1) and (A.2), it follows that, in all orders in α_s, we have the relation

$$C_g^{\mathrm{MOM}}(y,m^2,Q^2,\mu^2) \tag{A.21}$$
$$= -\frac{1}{2y}F_{2,g}^{Q\bar{Q}}(y,m_Q^2,Q^2,k^2)\Big|_{k^2=-\mu^2},$$

where μ is the renormalization point for the composite operators. Indeed, we can again obtain formula (A.18) by using the explicit expression for $F_{2,g}^{Q\bar{Q}}$ from [4].

For the case of heavy flavors, Collins [7] proposed the mixed CWZ renormalization scheme based on the idea put forth in [9]. It coincides with the $\overline{\mathrm{MS}}$ scheme in the case where all partons are considered to be massless and ensures the suppression of the heavy-quark contributions in the case where the heavy-quark masses exceed considerably the external-momentum scale. In order to perform a regularization within this scheme, use is made of the subtraction scheme at zero momenta for diagrams involving heavy quarks and of the $\overline{\mathrm{MS}}$ scheme for the remaining diagrams. In the case being considered, we have

$$C_g^{(1),\mathrm{CWZ}}(y,Q^2,m_Q^2) = \frac{\alpha_s}{8\pi} \tag{A.22}$$
$$\times\left\{(y^2+(1-y)^2)\ln\left[\frac{Q^2(1-y)}{m_Q^2y}\right]-1+8y(1-y)\right\}.$$

For the massless case, the result coincides with the known expression within the $\overline{\mathrm{MS}}$ scheme (see, for example, [10]); that is,

$$C_g^{(1),\mathrm{CWZ}}(y,Q^2) = \frac{\alpha_s}{8\pi} \tag{A.23}$$

Table 1. Values of the parameters in expression (A.31) for F_2

a	b	c	d	e	f	g	h, GeV^2
3.1	0.76	0.124	−0.188	−2.91	−0.043	3.69	1.4

$$\times\left\{(y^2+(1-y)^2)\ln\left[\frac{Q^2(1-y)}{\mu^2 y}\right]-1+8y(1-y)\right\}.$$

From (A.22), it can be seen that $C_g^{(1),\mathrm{CWZ}}(y,Q^2,m_Q^2)$ does not have a finite limit for $m_Q\to 0$. This is because the heavy-quark mass regularizes the divergences here. However, we can sidestep this problem by performing subtractions within the CWZ scheme at the point $-\mu^2$ rather than at zero momentum values. By calculating the gluon coefficient function within the CWZ scheme modified in this way, we arrive at expression (A.18), which was obtained above within the MOM scheme, and at the expression for $\Delta C_g^{(1),\mathrm{CWZ}}(y,Q^2,m_Q^2,\mu^2)$ in the form

$$\Delta C_g^{(1),CWZ}(y,Q^2,m_Q^2,\mu^2) \tag{A.24}$$
$$=\frac{\alpha_s}{8\pi}\left\{(y^2+(1-y)^2)\ln\left[y(1-y)+\frac{m_Q^2}{\mu^2}\right]+\frac{\mu^2 y(1-y)(1+2y(1-y))}{m_Q^2+\mu^2 y(1-y)}\right\}.$$

We note that, in contrast to $\Delta C_g^{(1),\mathrm{MOM}}(y,Q^2,m_Q^2,\mu^2)$ given by (A.20), the quantity $\Delta C_g^{(1),\mathrm{CWZ}}(y,Q^2,m_Q^2,\mu^2)$ does not vanish at $m_Q=0$. This is associated with the use of the different renormalization procedures for massless and for massive quarks. For this reason, we give preference to the MOM scheme.

APPENDIX B

Below, we present the results of the calculations for the gluon coefficient function C_g in the first nontrivial order in α_s at $m_Q=0$. These calculations are based on formula (A.21) and on the expression for $F_{2,g}^{Q\bar{Q}}(y,m_Q^2,Q^2,k^2)$ from [4]. The result is

$$C_g^{(1)}(y,Q^2,0,\mu^2) \tag{A.25}$$
$$=\frac{\alpha_s}{16\pi}\left[3(F_1^{(a)}+F_1^{(b)})-(F_2^{(a)}+F_2^{(b)})\right]\Big|_{k^2=-\mu^2},$$

where the expressions for $F_{1(2)}^{(a)}$ and $F_{1(2)}^{(b)}$ are the following:

$$F_1^{(a)}=L\left[1+\frac{1}{4}((1-t_2)^2-1)\left(1+\frac{1}{U^2}\right)\right]-\frac{((1-t_2)^2-1)}{2U^2}-2, \tag{A.26}$$

$$F_2^{(a)}=L\left[1+\frac{1}{4}((1-t_2)^2-1)\left(-1+\frac{3}{U^2}\right)\right]-\frac{3((1-t_2)^2-1)}{2U^2}-2, \tag{A.27}$$

$$F_1^{(b)}=-\frac{3}{2}\left\{L\frac{1}{4}\left(1-\frac{1}{U^2}\right)\left[((1-t_2)^2-1)+\frac{1}{U^2}(3((1-t_2)^2-1)+2(2+t_1)(2-t_2))\right]+\frac{(1-U^2)\left((4-t_2)^2-4\right)+2\left((1-t_2)^2-1\right)}{2U^4}\right\}, \tag{A.28}$$

$$F_2^{(b)}=-\frac{3}{2}\left\{L\frac{1}{4}\left(1-\frac{1}{U^2}\right)\left[-((1-t_2)^2-1)+\frac{3}{U^2}(3((1-t_2)^2-1)+2(2+t_1)(2-t_2))\right]+\frac{3(1-U^2)((4-t_2)^2-4)+2(3-2U^2)((1-t_2)^2-1)}{2U^4}\right\}. \tag{A.29}$$

In formulas (A.26)–(A.29), we have introduced the notation

$$t_1=\frac{-k^2Q^2}{(kq)^2}=4y^2(1-y)^2\frac{-k^2}{Q^2}, \tag{A.30}$$

$$t_2=\frac{Q^2}{kq}+\frac{-k^2}{kq}=2y(1-y)\left(1+\frac{-k^2}{Q^2}\right),$$

$$U=\sqrt{1-t_1},$$

Table 2. Values of the parameters in expression (A.32) for F_2^c

$\bar{a}$	$\bar{b}$	$\bar{c}$	$\bar{g}$	$\bar{h}$, GeV^2
0.28	0.15	−0.08	5.00	1.86

$$L = \frac{1}{U}\ln\left[\frac{1+U}{1-U}\right].$$

It should be emphasized that, in the calculations, we did not assume that $\mu^2/Q^2 \ll 1$ or that $-k^2/Q^2 \ll 1$. In other words, the expressions obtained here for the massless quark are exact in the first order in the coupling constant.

APPENDIX C

Here, we present the parametrizations that we choose for F_2 and F_2^c. For F_2, we use the parametrization of the H1 collaboration [1]; that is,

$$F_2(x,Q^2) = \left[ax^b + cx^d(1+e\sqrt{x}) \times \left(\ln Q^2 + f\ln^2 Q^2 + \frac{h}{Q^2}\right)\right](1-x)^g, \quad \text{(A.31)}$$

with the parameter values being given in Table 1.

For F_2^c, we use an expression that is qualitatively consistent with the asymptotic behavior of the quantity $\Sigma = F_2 - 2.75F_2^c$ with respect to the variable Q^2 [see (16)]; that is,

$$F_2^c(x,Q^2) = \frac{1}{2.75}F_2(x,Q^2) - \bar{a}x^{\bar{b}}(1-x)^{\bar{g}}\left[1 + x^{\bar{c}}\frac{\bar{h}}{Q^2}\ln Q^2\right], \quad \text{(A.32)}$$

where F_2 is given by (A.31). A fit to HERA data from [2] that correspond to values in the range $6.5 \le Q^2 \le 130$ GeV^2 yields the parameter values presented in Table 2 at $\chi^2/\mathrm{NDF} = 34.6/36 = 0.96$.

REFERENCES

1. H1 Collab. (S. Aid *et al.*), Nucl. Phys. B **470**, 3 (1996).
2. ZEUS Collab. (J. Breitweg *et al.*), Eur. Phys. J. C **12**, 35 (2000).
3. H1 Collab. (C. Adloff *et al.*), Phys. Lett. B **467**, 156 (1999).
4. A. V. Kisselev and V. A. Petrov, Z. Phys. C **75**, 277 (1997).
5. A. V. Kisselev and V. A. Petrov, Yad. Fiz. **60**, 1680 (1997) [Phys. At. Nucl. **60**, 1533 (1997)].
6. J. C. Collins, *Renormalization* (Cambridge Univ. Press, Cambridge, 1984; Mir, Moscow, 1988).
7. J. C. Collins, Phys. Rev. D **58**, 094002 (1998).
8. ZEUS Collab., Paper submitted to the 30th International Conference on High−Energy Physics (ICHEP2000), Osaka, Japan, 2000, Abstract 853.
9. J. C. Collins, F. Wilczek, and A. Zee, Phys. Rev. D **18**, 242 (1978).
10. E. Laenen, S. Riemersma, J. Smith, and W. L. van Neerven, Phys. Rev. D **49**, 5753 (1994).

Translated by A. Isaakyan

Physics of Atomic Nuclei, Vol. 65, No. 10, 2002, pp. 1908–1917. From Yadernaya Fizika, Vol. 65, No. 10, 2002, pp. 1961–1791.

ELEMENTARY PARTICLES AND FIELDS
Theory

Two-Photon Correlations as the Signal of a Sharp Transition in Quark–Gluon Plasma*

I. V. Andreev

Lebedev Institute of Physics, Russian Academy of Sciences, Leninskiĭ pr. 53, Moscow, 117924 Russia

Received May 18, 2001; in final form, November 29, 2001

Abstract—The photon production arising due to time variation of a medium has been considered. The Hamilton formalism for photons in a time-variable medium (plasma) has been developed with application to inclusive photon production. The results have been used for calculation of the photon production in the course of the transition from a quark–gluon phase to a hadronic phase in relativistic heavy-ion collisions. The relative strength of the effect and the specific two-photon correlations have been evaluated. It is demonstrated that the opposite-side two-photon correlations are indicative of a sharp transition from the quark–gluon phase to hadrons. © *2002 MAIK "Nauka/Interperiodica".*

1. INTRODUCTION

The formation of a quark–gluon plasma (QGP) in relativistic heavy-ion collisions with subsequent transition to hadrons has been under discussion for many years. Numerous measurable signals from the QGP phase (such as J/ψ suppression) have been suggested. At the same time, the observation of enhanced antibaryon production [1] together with lattice calculations [2], which predict low temperature of the transition, is indicative of a fast QGP–hadron transition [3] without formation of a mixed phase. In this paper, we consider a new specific mechanism of photon production which is effective in the case of the sharp transition from QGP to hadrons (see [4]).

The phenomenon under consideration is the photon production in the course of evolution of strongly interacting matter. Let us consider photons in a medium at the initial moment t_0 having momentum $\mathbf{k}$ and energy ω_{in}. Let the properties of the medium (dielectric permittivity) change within a time interval $\delta\tau$ so that the final photon energy is ω_{fin}. As a result of the energy change, the production of extra photons with momenta $\pm\mathbf{k}$ takes place, these photons exhibiting specific two-photon correlations. Moreover, the photons with opposite momenta and opposite helicities are produced even in the absence of the initial photons. Such kind of processes was first considered a few years ago [5, 6], elaborated for pions [7, 8], and applied to the pion production in high-energy heavy-ion collisions [9]. The conditions for a strong effect are the following: first, the ratio of the energies $\omega_{\text{in}}/\omega_{\text{fin}}$ must not be too close to unity, and second, the transition should be fast enough.

The calculation of the effect requires consideration of the Hamilton equations of motion. In Section 2, we present in short the corresponding formalism which is extended in Section 3 to the case of a time-dependent medium. A simple method of calculation of the photon correlations is presented in Section 4 with subsequent estimation in Section 5 of the polarization operator and the evolution parameter determining the strength of the transition effect. In Section 6, we calculate the transition effects in heavy-ion collisions and present the results of the work.

2. BASIC FORMULATIONS

We are interested in time evolution of the photon creation and annihilation operators $a_i^\dagger(\mathbf{k},t)$ and $a_i(\mathbf{k},t)$ in a medium. In this section, the medium is considered in its rest frame. The properties of the medium (plasma) will be described by the transverse polarization operator $\Pi(\omega,\mathbf{k},T,\mu,m)$ which depends on energy ω, momentum $\mathbf{k}$, temperature $T=1/\beta$, chemical potential μ, and the mass m of the charged particles of the plasma. To determine the evolution law of $a_i^\dagger(\mathbf{k},t)$ and $a_i(\mathbf{k},t)$, we will use the Hamilton formalism.

The Lagrangian of the electromagnetic field in the medium is taken in the form

$$L=\frac{1}{2}\int d^3x\left(\mathbf{E}(\mathbf{x},t)\hat{\epsilon}\mathbf{E}(\mathbf{x},t)-\mathbf{H}^2(\mathbf{x},t)\right), \quad (1)$$

where the dielectric permittivity $\hat{\epsilon}$ acts as the factor $\epsilon(\omega,\mathbf{k})$ in the momentum space (otherwise it acts as an operator). The object of quantization is the real-valued vector potential $\mathbf{A}(\mathbf{x},t)$. In the case under consideration, we can use the gauge conditions

$$A_0(\mathbf{x},t)=0, \quad \text{div}\mathbf{A}(\mathbf{x},t)=0, \quad (2)$$

*This article was submitted by the author in English.

1063-7788/02/6510-1908$22.00

so that

$$\mathbf{E}(\mathbf{x},t) = -\dot{\mathbf{A}}(\mathbf{x},t), \quad \mathbf{H}(\mathbf{x},t) = \mathrm{curl}\mathbf{A}(\mathbf{x},t). \quad (3)$$

The second equation (2) means that the vector potential is transverse ($\mathbf{k}\cdot\mathbf{A}=0$), having two components A_i (usual linear polarizations). The transverse dielectric permittivity $\hat{\epsilon}$ is connected with the photon transverse polarization operator $\hat{\Pi}$ through equation

$$\epsilon(\omega,k) = 1 - \Pi(\omega,k)/\omega^2, \quad (4)$$

where $\Pi(\omega,k)$ will be considered as a real-valued and even function of ω and k (see Section 5). Turning to the momentum representation

$$\mathbf{A}(\mathbf{x},t) = \int \frac{d^4k}{(2\pi)^2} e^{-ik_0t+i\mathbf{k}\cdot\mathbf{x}}\mathbf{A}(\mathbf{k},k_0) \quad (5)$$

and using Eqs. (1)–(5), the action of the system can be written in the form

$$S = \frac{1}{2}\int d^4k A_i(-\mathbf{k},-k_0) \quad (6)$$
$$\times \left[k_0^2 - \mathbf{k}^2 - \Pi(\mathbf{k},k_0)\right] A_i(\mathbf{k},k_0).$$

Variation of the action provides the equation

$$\left[k_0^2 - \mathbf{k}^2 - \Pi(\mathbf{k},k_0)\right] A_i(\mathbf{k},k_0) = 0, \quad i=1,2, \quad (7)$$

and the energy ω of the photon in the medium is given by the usual dispersion equation

$$\omega^2 - \mathbf{k}^2 - \Pi(\omega,\mathbf{k}) = 0. \quad (8)$$

Let us note in advance that $\Pi(\omega,k)$ will be a positive and slowly varying function of k playing essentially the role of the effective photon mass squared.

Introducing the time- and momentum-dependent field coordinates $\mathbf{q}(\mathbf{k},t)$,

$$\mathbf{A}(\mathbf{x},t) = \int \frac{d^3k}{(2\pi)^{3/2}} e^{i\mathbf{k}\cdot\mathbf{x}}\mathbf{q}(\mathbf{k},t), \quad (9)$$
$$\mathbf{q}(-\mathbf{k},t) = \mathbf{q}^\dagger(\mathbf{k},t),$$

and coming one step back in (6), we get the Lagrangian in the form

$$L = \frac{1}{2}\int d^3k \left[\dot{q}_i(-\mathbf{k},t)\dot{q}_i(\mathbf{k},t)\right. \quad (10)$$
$$\left. - \mathbf{k}^2 q_i(-\mathbf{k},t)q_i(\mathbf{k},t) - q_i(-\mathbf{k},t)\hat{\Pi}(\mathbf{k})q_i(\mathbf{k},t)\right],$$

where the polarization operator $\hat{\Pi}(\mathbf{k})$ in $(\mathbf{k},t)$ representation acts either to the left or to the right, giving equivalent results. In this form, the polarization term is related to the potential energy (unlike $\dot{q}$ terms) ensuring the physically sensible form of the Hamiltonian in the case under consideration. The Lagrange equations, given by variation of (10), evidently have the oscillator form

$$\ddot{q}_i(\mathbf{k}) + \omega^2 q_i(\mathbf{k}) = 0, \quad (11)$$

with ω being determined by Eq. (8). Note that

$$\hat{\Pi}(\mathbf{k})q_i(\mathbf{k}) = \Pi(\omega,\mathbf{k})q_i(\mathbf{k}) \quad (12)$$

for plane-wave solutions of the equations of motion.

Turning to the Hamilton formalism for quantum fields, we introduce the canonically conjugated momentum

$$p_i(\mathbf{k},t) = \frac{\delta L}{\delta\dot{q}_i(\mathbf{k},t)} = \dot{q}_i(-\mathbf{k},t), \quad i=1,2 \quad (13)$$

and postulate the canonical equal-time commutation relations

$$[q_i(\mathbf{k}_1,t), p_j(\mathbf{k}_2,t)] = i\delta_{ij}\delta(\mathbf{k}_1-\mathbf{k}_2), \quad (14)$$

with all other commutators being zero. Let us note that the presence of the opposite sign of $\mathbf{k}$ on the right-hand side of (13) is necessary for compatibility of (14) with commutation relations in coordinate space

$$\left[A_i(\mathbf{x}_1,t), \dot{A}_j(\mathbf{x}_2,t)\right] = i\delta_{ij}\delta(\mathbf{x}_1-\mathbf{x}_2). \quad (15)$$

Below, this opposite sign of the momentum $\mathbf{k}$ will result in important physical consequences describing production of photon pairs with opposite directions of momenta of the photons.

The Hamiltonian is introduced in the usual way:

$$H = \int d^3k p_i(\mathbf{k})\dot{q}_i(\mathbf{k}) - L \quad (16)$$
$$= \frac{1}{2}\int d^3k (p_i(-\mathbf{k})p_i(\mathbf{k}) + \mathbf{k}^2 q_i(-\mathbf{k})q_i(\mathbf{k})$$
$$+ q_i(-\mathbf{k})\hat{\Pi}(\mathbf{k})q_i(\mathbf{k})),$$

and the Hamilton equations for Heisenberg operators

$$\dot{q}_i(\mathbf{k}) = i\,[H, q_i(\mathbf{k})] = p_i(-\mathbf{k}), \quad (17)$$
$$\dot{p}_i(-\mathbf{k}) = i\,[H, p_i(-\mathbf{k})] = -\omega^2 q_i(\mathbf{k})$$

connect $q_i(\mathbf{k})$ with $p_i(-\mathbf{k})$, being consistent with Eqs. (11) and (12).

Let us at last introduce the photon creation and annihilation operators $a^\dagger(\mathbf{k})$ and $a(\mathbf{k})$ through decomposition

$$A_i(\mathbf{x},t) = \int \frac{d^3k}{(2\pi)^{3/2}}\frac{1}{(2\omega)^{1/2}} \quad (18)$$
$$\times \left(a_i(\mathbf{k},t)e^{i\mathbf{k}\cdot\mathbf{x}} + a_i^\dagger(\mathbf{k},t)e^{-i\mathbf{k}\cdot\mathbf{x}}\right).$$

These operators are defined here for a stationary medium in the initial and final states with constant ω and are connected with the canonical coordinates and momenta by equations

$$q_i(\mathbf{k}) = \frac{1}{\sqrt{2\omega}}\left(a_i(\mathbf{k}) + a_i^\dagger(-\mathbf{k})\right), \quad (19)$$

$$p_i(-\mathbf{k}) = i\sqrt{\frac{\omega}{2}}\left(a_i^\dagger(-\mathbf{k}) - a_i(\mathbf{k})\right),$$

as can be seen from the comparison of representations (9) and (18) and the corresponding time derivatives. The creation and annihilation operators exhibit a simple time dependence

$$a(t) \sim e^{-i\omega t}, \quad a^\dagger(t) \sim e^{i\omega t} \tag{20}$$

corresponding to running waves (photons) and satisfy the commutation relations

$$\left[a_i(\mathbf{k}_1), a_j^\dagger(\mathbf{k}_2)\right] = \delta_{ij}\delta(\mathbf{k}_1 - \mathbf{k}_2), \tag{21}$$

which follow from canonical commutation relations (14).

3. PHOTON EVOLUTION IN TIME-DEPENDENT MEDIUM

Let the polarization operator be a time-dependent function of parameters. In this case, the Hamilton equations (17) (as well as the Lagrange equation (11) which is their consequence) remain valid with time-dependent energy $\omega(t)$. This is confirmed by the fact that their solution represents the time-dependent canonical transformation conserving commutator (14). Indeed, the solution to (17) can be written in the form (cf. [10])

$$\begin{aligned} q_i(\mathbf{k},t) &= s_1(t)q_i(\mathbf{k},0) + s_2(t)p_i(-\mathbf{k},0), \\ \dot{q}_i(\mathbf{k},t) &= p_i(-\mathbf{k},t) = \dot{s}_1(t)q_i(\mathbf{k},0) \\ &\quad + \dot{s}_2(t)p_i(-\mathbf{k},0), \end{aligned} \tag{22}$$

where $s_1(t)$ and $s_2(t)$ are two linearly independent real-valued solutions of the classical equation (11) with time-dependent energy ω and the initial conditions

$$\begin{aligned} s_1(0) = 1, \quad \dot{s}_1(0) = 0, \\ s_2(0) = 0, \quad \dot{s}_2(0) = 1. \end{aligned} \tag{23}$$

One can see from (22) that the canonical commutator transforms in the following way:

$$\begin{aligned} &[q_i(\mathbf{k},t), p_i(\mathbf{k},t)] \\ &= W(s_1,s_2)\,[q_i(\mathbf{k},0), p_i(\mathbf{k},0)]\,, \end{aligned} \tag{24}$$

where

$$W(s_1,s_2) = s_1(t)\dot{s}_2(t) - s_2(t)\dot{s}_1(t) \tag{25}$$

is the Wronskian determinant of (11), which does not depend on time for this equation (due to absence of a term with a first-order derivative in the equation), this constant determinant being equal to 1 due to initial conditions (23).

Let us consider evolution of the photons from the initial state with energy ω_1 to the asymptotic final state with energy ω_2. The final-state annihilation and creation operators are given by

$$\begin{aligned} a_i(\mathbf{k},t) &= \frac{1}{\sqrt{2\omega_2}}\left(\omega_2 q_i(\mathbf{k},t) + ip_i(-\mathbf{k},t)\right), \\ a_i^\dagger(\mathbf{k},t) &= \frac{1}{\sqrt{2\omega_2}}\left(\omega_2 q_i(-\mathbf{k},t) - ip_i(\mathbf{k},t)\right), \end{aligned} \tag{26}$$

as follows from (19). We substitute solutions (22) for $q_i(\mathbf{k},t), p_i(\mathbf{k},t)$ and introduce two linearly independent complex-valued classical solutions $\xi(t)$, $\xi^*(t)$ instead of $s_1(t), s_2(t)$:

$$\begin{aligned} \xi(t) &= s_1(t) + i\omega_1 s_2(t), \\ \xi^*(t) &= s_1(t) - i\omega_1 s_2(t) \end{aligned} \tag{27}$$

with the initial conditions

$$\xi(0) = \xi^*(0) = 1, \quad \dot{\xi}(0) = i\omega_1, \quad \dot{\xi}^*(0) = -i\omega_1. \tag{28}$$

Then, using (19) for the initial state, we obtain the Bogolyubov transformation [11] connecting the creation and annihilation operators in the initial and final states (let us recall that these operators were defined only for asymptotic states having constant energy ω):

$$\begin{aligned} a_i(\mathbf{k},t) &= u(\mathbf{k},t)a_i(\mathbf{k},0) + v(\mathbf{k},t)a_i^\dagger(-\mathbf{k},0), \\ a_i^\dagger(\mathbf{k},t) &= v^*(\mathbf{k},t)a_i(-\mathbf{k},0) + u^*(\mathbf{k},t)a_i^\dagger(\mathbf{k},0) \end{aligned} \tag{29}$$

with

$$\begin{aligned} u(\mathbf{k},t) &= \frac{1}{2}\sqrt{\frac{\omega_2}{\omega_1}}\left[\xi^*(t) + \frac{i}{\omega_2}\dot{\xi}^*(t)\right], \\ v(\mathbf{k},t) &= \frac{1}{2}\sqrt{\frac{\omega_2}{\omega_1}}\left[\xi(t) + \frac{i}{\omega_2}\dot{\xi}(t)\right]. \end{aligned} \tag{30}$$

It follows from (30) that

$$u^*(t)u(t) - v^*(t)v(t) = \frac{i}{2\omega_1}W(\xi,\xi^*), \tag{31}$$

where

$$W(\xi,\xi^*) = \xi(t)\dot{\xi}^*(t) - \dot{\xi}(t)\xi^*(t) \tag{32}$$

is again the time-independent Wronskian determinant. Thus,

$$u^*u - v^*v = 1 \tag{33}$$

due to initial conditions (28). In turn, as follows from (29), condition (33) ensures conservation of the commutator

$$\left[a_i(\mathbf{k},t), a_i^\dagger(\mathbf{k},t)\right] = \left[a_i(\mathbf{k},0), a_i^\dagger(\mathbf{k},0)\right] \tag{34}$$

(the latter commutator is equal to $V/(2\pi)^3$ for a system having the volume V). In view of condition (33), the Bogolyubov coefficients u and v can be presented in the form

$$u = \cosh r(\mathbf{k})e^{i\alpha_1}, \quad v = \sinh r(\mathbf{k})e^{i\alpha_2}, \tag{35}$$

where $r(\mathbf{k})$ is the main parameter which determines the photon production, while the phases α_1 and α_2 do not play an important role and will not be considered below.

To find the coefficients u and v (for fixed momentum $\mathbf{k}$), one must turn to the classical equations for an oscillator of variable frequency (energy). Let us seek a solution to the equation

$$\ddot{\xi} + \omega^2(t)\xi = 0. \tag{36}$$

In the initial state, where the energy ω_1 is constant, we take a single wave

$$\xi(t) = e^{i\omega_1 t}, \quad t < t_{\rm in} = 0. \tag{37}$$

At large enough time, $t > t_{\rm fin}$, when the energy ω_2 becomes constant again, the general solution has the form

$$\xi(t) = C_1 e^{i\omega_2 t} + C_2 e^{-i\omega_2 t}, \quad t > t_{\rm fin}. \tag{38}$$

Substituting (37) and (38) into (30), we determine the corresponding Bogolyubov coefficients

$$u = \sqrt{\frac{\omega_2}{\omega_1}} C_1^* e^{-i\omega_2 t}, \tag{39}$$

$$v = \sqrt{\frac{\omega_2}{\omega_1}} C_2 e^{-i\omega_2 t}, \quad t > t_{\rm fin},$$

where constants C_1 and C_2 satisfy the relationship

$$|\, C_1 \,|^2 - |\, C_2 \,|^2 = \frac{\omega_1}{\omega_2} \tag{40}$$

due to condition (33).

To find the final expressions for coefficients u and v, one must know the full solution of (36) connecting the asymptotic expressions (37) and (38). Here, one can use an analogy between the above problem and the problem of a wave propagating through (above) one-dimensional potential barrier. In the latter case, Eq. (38) (after substitution of x for t) represents the incoming and reflected waves and Eq. (37) represents the outgoing wave. The reflection coefficient

$$|\, C_2/C_1 \,|^2 = |\, v/u \,|^2 = \tanh^2 r \tag{41}$$

gives the desired ratio of the Bogolyubov coefficients (to within phases). Therefore, one can use the well-known quantum-mechanical results. Shifting the initial time $t_{\rm in}$ to a large negative value, we use a reference model of the energy variation:

$$\omega^2(t) = \frac{\omega_2^2 + \omega_1^2}{2} + \frac{\omega_2^2 - \omega_1^2}{2} \tanh\left(\frac{2t}{\delta\tau}\right). \tag{42}$$

The problem with such form of the potential barrier can be found in textbooks [12]. It contains the important parameter $\delta\tau$ giving the characteristic time of the energy variation. The evolution parameter r is given now by

$$r = \tanh^{-1}|v/u| = \frac{1}{2}\ln\left(\frac{\tanh(\pi\omega_2\delta\tau/4)}{\tanh(\pi\omega_1\delta\tau/4)}\right). \tag{43}$$

For a sharp transition ($\omega_i\delta\tau \ll 1$), formula (43) yields

$$r = \frac{1}{2}\ln\left(\frac{\omega_2}{\omega_1}\right), \tag{44}$$

$$\left|\frac{v}{u}\right|^2 = \left(\frac{\omega_2 - \omega_1}{\omega_2 + \omega_1}\right)^2, \quad \omega_i\delta\tau \ll 1.$$

This is the case of the most intensive pair production. For a large transition time $\delta\tau$, the process becomes adiabatic and the evolution parameter falls exponentially:

$$r = \left|e^{-\pi\omega_2\delta\tau/2} - e^{-\pi\omega_1\delta\tau/2}\right|, \quad \omega_i\delta\tau \gg 1. \tag{45}$$

Note that the above results (44) for a sharp transition can be obtained immediately from Hamilton equations (17). Suggesting that the canonical coordinate q and momentum p are finite, we see from these equations that $\dot{q}$ and $\dot{p}$ are finite as well, so that q and p are continuous functions of time at the transition point,

$$q(-\delta t) = q(\delta t), \tag{46}$$

$$p(-\delta t) = p(\delta t), \quad \delta t \to 0,$$

coinciding on both sides of the sharp boundary between the media with different photon energies ω_1 and ω_2. Being expressed according to (19) through the creation and annihilation operators $a^\dagger, a$ on both sides of the boundary, equations (46) lead to the Bogolyubov transformation (29) between pairs of operators $a^\dagger, a$ on the opposite sides of the boundary with the coefficients

$$|u| = \frac{\omega_2 + \omega_1}{2\sqrt{\omega_1\omega_2}}, \quad |v| = \left|\frac{\omega_2 - \omega_1}{2\sqrt{\omega_1\omega_2}}\right|. \tag{47}$$

The latter equations correspond to (44).

4. INCLUSIVE PHOTON PRODUCTION IN A SIMPLE MODEL

Below, we will be interested in inclusive photon production in heavy-ion collisions. We restrict the consideration to a symmetric case when the photons with opposite momenta $\pm\mathbf{k}$ are produced in an equivalent way (central collisions of identical nuclei). For simplicity, the Bogolyubov coefficients $u(\mathbf{k}), v(\mathbf{k})$ [and therefore the evolution parameter $r(\mathbf{k})$—see (35)] are assumed to be real-valued and to depend on $k = |\mathbf{k}|$. In order to reveal the main features of the photon production and photon correlations (and for further references and comparison), we formulate

in this section a simple model: fast simultaneous transition of a large homogeneous system at rest (the movement of the system will be considered in Section 6).

For physical interpretation of the evolution effect, it is helpful to introduce the complex-valued vectors of the photon circular polarization

$$\mathbf{e}_\pm = (\mathbf{e}_1 \pm i\mathbf{e}_2)/\sqrt{2}, \quad \mathbf{k}\cdot\mathbf{e}_\pm = 0 \tag{48}$$

and the corresponding components of operators $\mathbf{a}(\mathbf{k})$ and $\mathbf{a}^\dagger(\mathbf{k})$

$$a_\pm = (a_1 \pm ia_2)/\sqrt{2}, \quad a_\pm^\dagger = (a_1^\dagger \mp ia_2^\dagger)/\sqrt{2}, \tag{49}$$

so that

$$\mathbf{a}(\mathbf{k}) = \mathbf{e}_+ a_-(\mathbf{k}) + \mathbf{e}_- a_+(\mathbf{k}), \quad a_\pm = \mathbf{e}_\pm \cdot \mathbf{a}. \tag{50}$$

The components $a_\pm, a_\pm^\dagger$ satisfy the standard commutation relations in the form (21) with $i = \pm$ and represent the creation and annihilation operators of the photons with definite spin projection ± 1 on the direction of the photon momentum (the helicity).

In what follows, we will denote the creation and annihilation operators in the final state as $b^\dagger, b$, leaving the notation $a^\dagger$, and a for the operators in the initial state. In terms of the components $b_\pm$, the helicity operator is

$$S_{b3} = i(b_1^\dagger b_2 - b_2^\dagger b_1) \tag{51}$$
$$= b_+^\dagger b_+ - b_-^\dagger b_- = N_{b+} - N_{b-}$$

for any momentum $\mathbf{k}$, the photon number operator is

$$N_b = b_+^\dagger b_+ + b_-^\dagger b_- = N_{b+} + N_{b-}, \tag{52}$$

and the Bogolyubov transformation takes the form

$$b_\pm(\mathbf{k}) = ua_\pm(\mathbf{k}) + va_\pm^\dagger(-\mathbf{k}), \tag{53}$$
$$b_\pm^\dagger(\mathbf{k}) = u^* a_\pm^\dagger(\mathbf{k}) + v^* a_\pm(-\mathbf{k}),$$

where subscripts $\pm$ indicate helicities related to the corresponding momenta $\mathbf{k}$ or $-\mathbf{k}$.

The resulting average number of photons and their correlations depends on the initial state. We suggest that the initial state is a statistical (Gaussian) mixture of the coherent states [5, 13] of the photons of each polarization. Then, using Eqs. (33) and (53), we obtain the photon momentum distribution (relative single-photon inclusive cross section including averaging over the initial state):

$$\left(\frac{dN}{d^3k}\right)_\pm \equiv \left(\frac{1}{\sigma}\frac{d\sigma}{d^3k}\right)_\pm = \langle N_{b\pm}(\mathbf{k})\rangle \tag{54}$$
$$= \langle b_\pm^\dagger(\mathbf{k}) b_\pm(\mathbf{k})\rangle = \left(1+|v|^2\right)\langle N_{a\pm}(\mathbf{k})\rangle$$
$$+ |v|^2\langle N_{a\pm}(-\mathbf{k})\rangle + |v|^2\frac{V}{(2\pi)^3}.$$

As one can see from (54), the photons are created in pairs having opposite directions of their momenta and opposite spin directions (the same helicities). If both kinds of polarizations are equally represented in the initial state for every momentum $\mathbf{k}$, then the same property is valid for the final state,

$$\langle S_{b3}(\mathbf{k})\rangle = 0, \tag{55}$$

and the photons produced with opposite momenta possess equal helicities. The intensity of the transition production is given by the Bogolyubov coefficient $|v|^2$ and the last term on the right-hand side of (54) represents the result of the ground state rearrangement (the initial ground state is not the ground state for operators b which operate in a different medium in the final state). We suggest that $\mathbf{k} \to -\mathbf{k}$ symmetry takes place. Then, the resulting photon momentum distribution can be written in the form

$$\frac{dN}{d^3k} = \langle b_\lambda^\dagger(\mathbf{k}) b_\lambda(\mathbf{k})\rangle \tag{56}$$
$$= \frac{2V}{(2\pi)^3}\left[n(\mathbf{k}) + (2n(\mathbf{k})+1)\sinh^2 r\right]$$

(the sum taken over helicities λ), where $n(\mathbf{k})$ is the average level occupation number of the single mode in the initial state and we used the parametrization (35). The photon production in the course of the transition, given by the second term on the right-hand side of (56), is weak for a small evolution parameter $r(k)$, being of the order of r^2.

The evolution effect is better seen in photon correlations. The two-photon inclusive cross section is given by

$$\frac{1}{\sigma}\frac{d^2\sigma}{d^3k_1 d^3k_2} = \langle b_\lambda^\dagger(\mathbf{k}_1) b_\mu^\dagger(\mathbf{k}_2) b_\lambda(\mathbf{k}_1) b_\mu(\mathbf{k}_2)\rangle \tag{57}$$
$$= \langle b_\lambda^\dagger(\mathbf{k}_1) b_\lambda(\mathbf{k}_1)\rangle\langle b_\mu^\dagger(\mathbf{k}_2) b_\mu(\mathbf{k}_2)\rangle$$
$$+ \langle b_\lambda^\dagger(\mathbf{k}_1) b_\mu(\mathbf{k}_2)\rangle\langle b_\mu^\dagger(\mathbf{k}_2) b_\lambda(\mathbf{k}_1)\rangle$$
$$+ \langle b_\lambda^\dagger(\mathbf{k}_1) b_\mu^\dagger(\mathbf{k}_2)\rangle\langle b_\lambda(\mathbf{k}_1) b_\mu(\mathbf{k}_2)\rangle.$$

The first term on the right-hand side of (57) is the product of single-photon distributions, the second term gives the Hanbury–Brown–Twiss effect (HBT, called also the Bose–Einstein correlations), and the third term is essential if the time evolution effect takes place giving opposite side photon correlations.

The production of photons with opposite directions of their momenta was already pointed out after (54). However, it was implicitly suggested there that the volume of the system is arbitrarily large, $V \to \infty$. In a real situation, we deal with large but finite size of the colliding nuclei. The finite size of the photon source will smooth out the effect. The same is valid for the HBT effect responsible for the same side correlations. The special technique was elaborated in a

number of papers to describe the source size effect for the HBT correlations, including use of the Wigner phase space density [14] and the method of equivalent classical currents [15] which can be used here. Instead, we directly modify the creation and annihilation operators [5] in such a way that they are nonzero only inside some region in the coordinate space which is described by the function $f(\mathbf{x})$:

$$\tilde{b}_\lambda(\mathbf{x}) = b_\lambda(\mathbf{x})f(\mathbf{x}), \quad \tilde{b}^\dagger_\lambda(\mathbf{x}) = b^\dagger_\lambda(\mathbf{x})f(\mathbf{x}). \quad (58)$$

Then, the modified (smoothed out) operators in the momentum space are

$$\tilde{b}^\dagger_\lambda(\mathbf{k}_1) = \int d^3k f(\mathbf{k}_1 - \mathbf{k}) b^\dagger_\lambda(\mathbf{k}), \quad (59)$$

$$\tilde{b}_\lambda(\mathbf{k}_2) = \int d^3k f(\mathbf{k} - \mathbf{k}_2) b_\lambda(\mathbf{k}),$$

where the Fourier transform $f(\mathbf{k}_i - \mathbf{k})$ is sharply peaked around the point $\mathbf{k} = \mathbf{k}_i$ (smoothed δ function).

The introduced operators satisfy modified commutation relations

$$\left[\tilde{b}_\lambda(\mathbf{k}_1), \tilde{b}^\dagger_\nu(\mathbf{k}_2)\right]_- \quad (60)$$

$$= \delta_{\lambda\nu} \int d^3k f(\mathbf{k}_1 - \mathbf{k}) f(\mathbf{k} - \mathbf{k}_2)$$

$$= \delta_{\lambda\nu} \int \frac{d^3x}{(2\pi)^3} f^2(\mathbf{x}) e^{i(\mathbf{k}_1 - \mathbf{k}_2)\cdot\mathbf{x}} = \delta_{\lambda\nu} F(\mathbf{k}_1 - \mathbf{k}_2).$$

Here, $F(\mathbf{k}_1 - \mathbf{k}_2)$ is the form factor of the photon source (Fourier transform of the source density) and it also represents the smoothed δ function which has a width of the order of the inverse size of the source. In particular,

$$F(0) = V/(2\pi)^3, \quad (61)$$

where V is the effective volume of the source at the stage of the transition in the medium. Let us note that above we in fact already used (61) substituted for $\delta^3(0)$ in the contribution of the ground state rearrangement to the evolution effect in (54). This factor also appears when one makes use of the level occupation function $n(\mathbf{k})$ [see (56)], having its origin in the correspondence of discrete and continuous Fourier decompositions. Using operators modified in the three-dimensional coordinate space, we suggest that the volume V changes insignificantly in the course of the time transition.

Now one can apply the Bogolyubov transformation (53) to estimate the correlators of the modified operators:

$$\langle \tilde{b}^\dagger_\pm(\mathbf{k}_1)\tilde{b}_\pm(\mathbf{k}_2)\rangle = \int d^3k \left[u^2(k)n(\mathbf{k}) \quad (62)\right.$$

$$\left. + v^2(k)(n(\mathbf{k}) + 1)\right] f(\mathbf{k}_1 - \mathbf{k}) f(\mathbf{k} - \mathbf{k}_2)$$

$$= \frac{V}{(2\pi)^3}\left[n(\mathbf{k}) + (2n(\mathbf{k}) + 1)\sinh^2 r\right] G(\mathbf{k}_1 - \mathbf{k}_2)$$

and, in a similar way,

$$\langle \tilde{b}_\pm(\mathbf{k}_1)\tilde{b}_\pm(\mathbf{k}_2)\rangle = \langle \tilde{b}^\dagger_\pm(\mathbf{k}_1)\tilde{b}^\dagger_\pm(\mathbf{k}_2)\rangle \quad (63)$$

$$= \frac{V}{(2\pi)^3}(2n(\mathbf{k}) + 1)\sinh r(k)\cosh r(k) G(\mathbf{k}_1 + \mathbf{k}_2),$$

with other correlators vanishing in the course of statistical averaging in the case of a sharply peaked form factor. In the above equations, $G(\mathbf{k}_1 \pm \mathbf{k}_2)$ is the normalized form factor ($G(0) = 1$) and we took into account that the functions $f(\mathbf{k}_1 - \mathbf{k})$ and $f(\mathbf{k} - \mathbf{k}_2)$, as well as the form factor $G(\mathbf{k}_1 \pm \mathbf{k}_2)$, are sharply peaked functions of their arguments (at zero momentum) having a characteristic scale of the order of the inverse size of the source, this scale being much smaller than the characteristic scales of the distribution $n(\mathbf{k})$ and the evolution parameter $r(k)$. Thus, the last two functions can be evaluated for any of momenta $\mathbf{k}_1, \mathbf{k}_2 \approx \pm\mathbf{k}$ (we suggest that the process is $\mathbf{k} \to -\mathbf{k}$ symmetric). Equations (62) and (63), together with (57), show that the correlations arising due to the identity of photons (the HBT effect) are the same-side momentum correlations of photons having the same helicities, whereas photons arising due to the transition effect have the opposite-side momentum correlations and approximately opposite spin directions (the same helicities again).

Returning to the two-photon correlations given by (57) (sum over helicities), we obtain the relative correlation function which is measured in experiment:

$$C(\mathbf{k}_1, \mathbf{k}_2) = 1 + \frac{1}{2}G^2(\mathbf{k}_1 - \mathbf{k}_2) \quad (64)$$

$$+ \frac{1}{2}R_0^2(\mathbf{k})G^2(\mathbf{k}_1 + \mathbf{k}_2)$$

with

$$R_0(\mathbf{k}) = \frac{(2n(\mathbf{k}) + 1)\sinh r(k)\cosh r(k)}{n(\mathbf{k}) + (2n(\mathbf{k}) + 1)\sinh^2 r(k)}, \quad (65)$$

according to Eqs. (62) and (63). As can be seen from expressions (64) and (65), the transition effect depends strongly on the evolution parameter $r(k)$, see Eqs. (43)–(45). Below, after necessary modifications, we apply the above considerations to photon transition radiation in heavy-ion collisions.

5. THE EVOLUTION PARAMETER FOR PHOTONS IN PLASMA

To find the evolution parameter $r(k)$, one must know the photon energy in plasma. The spectrum of photons in plasma is given by dispersion equation

$$\omega_k^2 = k^2 + \Pi(\omega_k, k, T, \mu, m) \quad (66)$$

with $k = |\mathbf{k}|$. Here, Π is the polarization operator for transverse photons, which depends on the temperature $T = \beta^{-1}$, the chemical potential μ, and the mass m of charged particles. Below, we use an approximate form of Π extracted from original expression [16]:

$$\Pi(\omega, k) = \omega_a^2 \left[1 - \frac{\omega^2 - k^2}{k^2}\left(\ln\left(\frac{\omega + vk}{\omega - vk}\right) - 1\right)\right] \quad (67)$$

with

$$\omega_a^2 = \frac{4g\alpha}{\pi\beta^2}\int\limits_{m\beta}^{\infty} dx\left(x^2 - m^2\beta^2\right)^{1/2} n_{\mathrm{F}}(x, \mu\beta), \quad (68)$$

where $\alpha = 1/137$, v^2 is the average squared velocity of charged particles in the plasma, the factor g takes into account the number of types of particles and their electric charges ($g = 5/3$ for u, d quarks), and n_{fin} is the occupation number of the charged particles:

$$n_{\mathrm{F}}(\beta\omega) = \left(e^{\beta\omega - \beta\mu} + 1\right)^{-1} + \left(e^{\beta\omega + \beta\mu} + 1\right)^{-1} \quad (69)$$

(the Fermi distribution). The polarization operator for scalar charged particles is approximately half that for fermions, with the Bose distribution substituted for the Fermi distribution. In the case under consideration, the imaginary part of the polarization is small (no Landau damping) and it was neglected in the calculations.

For small masses of charged particles, $\beta m \ll 1$, the asymptotic expression for the polarization operator takes the known simple form

$$\omega_a^2 = \frac{2\pi g\alpha}{3}\left(T^2 + \frac{3}{\pi^2}\mu^2\right). \quad (70)$$

This form can be used for a quark–gluon phase. For large masses of fermions (constituent quarks and nucleons) such as $\beta m > 1 (m > \mu)$, it is convenient to use the expansion

$$\omega_{a(\mathrm{F})}^2 = \frac{8g\alpha m}{\pi\beta}\sum_{n=1}^{\infty}\frac{(-1)^{n-1}}{n}\cosh(n\beta\mu)K_1(n\beta m), \quad (71)$$

where $K_1(x)$ is the exponentially decreasing modified Bessel function and the main contribution comes from the first few terms of the series. An analogous expansion was also used for bosons (pions) having no chemical potential:

$$\omega_{a(B)}^2 = \frac{4\alpha m}{\pi\beta}\sum_{n=1}^{\infty}\frac{1}{n}K_1(n\beta m). \quad (72)$$

We considered the polarization operator and photon spectrum for three possible kinds of plasma: QGP with u, d light quarks; constituent quark ($m = 350$ MeV)—pion plasma; and hadronic (pions and nucleons) plasma. The chemical potential (baryonic one) was taken to be equal to 100 MeV per quark corresponding to a typical value for CERN-SPS energies (say, 160 GeV per nucleon in Pb–Pb collisions). The temperature T_c of the transition was taken equal to a rather small value of 140 MeV characteristic of the final hadrons [17] ($T_c = 200$ MeV was also tested, giving close results). Under the above conditions, the asymptotic values ω_a in (70)–(72) are equal to 24, 11.7, 11.2, and 2.5 MeV for light quarks, constituent quarks, pions, and nucleons, respectively.

Let us note that the approximation (67), where we use the average squared velocity $v^2 = \langle v^2\rangle$, suggests that higher moments of the velocity distribution do not differ significantly from corresponding powers of v^2. So we calculated the ratio $\langle v^4\rangle/\langle v^2\rangle^2$ and verified that it differs from unity inessentially, being 1 for QGP, 1.11 for constituent quarks (valons), 1.06 for pions, and reaching 1.25 for nucleons, whose contribution is small by itself. The corresponding values of v^2 used in our estimations are 1, 0.545, 0.731, and 0.300.

Evidently, the polarization operator in (66) plays the role of (momentum-dependent) photon mass squared (m_γ^2). The thermal mass squared at zero photon momentum k is equal to

$$\omega_0^2 = \omega_a^2\left(1 - \frac{v^2}{3}\right), \quad (73)$$

and it approaches ω_a^2 for large momenta. The slope of the dispersion curve at the origin is

$$\left.\frac{d\omega_k^2}{dk^2}\right|_{k=0} = \left(1 - \frac{1}{5}v^2\right)\Big/\left(1 - \frac{1}{3}v^2\right) = 1 + c, \quad (74)$$

varying from 1 at $v = 0$ to 1.2 at $v = 1$. In a rough approximation, the polarization operator taken at the dispersion curve can be represented by the simple expression

$$\Pi(\omega_k, k) = m_\gamma^2(k) = \omega_0^2 + \frac{c\omega_0^2 k^2}{\omega_0^2 + dk^2}, \quad (75)$$

$$d = 1 - \frac{2}{5}v^2,$$

reproducing the position of the point ω_0, asymptotic value ω_a, and the slope (74). In the presence of charged particles of two different types (say pions and nucleons), expression (75) should be modified in an appropriate way to take into account the presence of two contributions and to ensure the new correct slope $d\omega^2/dk^2$. The simple approximation (75) appears to be rather close to polarization operator (67) taken at the dispersion curve (66) (the two expressions also

have a common point at some finite k), and it will be used below for estimation of the evolution parameter $r(k)$. The zero-momentum photon masses $m_\gamma(0)$ were found to be 19.5, 14.4, and 10.0 MeV for QGP, valon–pion, and nucleon–pion plasma, respectively.

The evolution parameter $r(k)$, which gives the strength of the transition radiation, was determined in (43)–(45) for the reference model (42). This quantity depends strongly on the transition time $\delta\tau$. We suggest that this time interval is not large, being of the order of 1 fm/c. Then, for small momenta k ($\omega(k)\delta\tau \ll 1$), the parameter $r(k)$ is universal and it can be well approximated by the expression which follows from (44):

$$r(k) = \frac{m_{\gamma 1}^2(k) - m_{\gamma 2}^2(k)}{4(\langle m_\gamma^2(k)\rangle + k^2)} = \frac{\delta m_\gamma^2(k)}{4\langle\omega^2(k)\rangle}, \qquad \omega(k)\delta\tau \ll 1, \tag{76}$$

where $m_{\gamma i}^2$ are the photon thermal masses squared on both sides of the transition and $\langle m_\gamma^2\rangle$ is their average. The zero-momentum evolution parameter $r(0)$ is equal to 0.324, 0.154, and 0.178 for QGP–hadron, QGP–valon, and valon–hadron transitions, respectively. Higher momentum behavior of $r(k)$ is model-dependent. Below, this value will be taken in the form

$$r(k) = \frac{\delta m_\gamma^2}{4k^2}\exp\left(-\frac{\pi}{2}k\delta\tau\right). \tag{77}$$

Equation (77) is a simple version of the asymptotic form of (45), and it can be well sewed together with (76) giving a monotonically decreasing function of the momentum. Let us note that, on general grounds, one expects that $r(k)$ falls exponentially at large $k\delta\tau$ if the time dependence of the energy $\omega(k,t)$ in the course of the transition has no singularities (nonanalyticity) at the real time axis. Below, Eqs. (76) and (77) will be used for estimation of the transition effect in heavy-ion collisions. Only the QGP–hadron transition will be considered. In view of the fact that the evolution parameter $r(k)$ appears to be small for all momenta k, all expressions will be estimated in the lowest order in $r(k)$.

6. TRANSITION EFFECT IN HEAVY-ION COLLISIONS

Let us apply the above considerations to the photon production in heavy-ion collisions. We suggest that the QGP is formed at the initial stage of the ion collision. Then, the plasma expands and cools. The expansion is taken to be longitudinal and boost-invariant [18]. The lattice calculations [2] show a rather low critical temperature of the deconfinement and chiral phase transition, $T_c \approx 150$ MeV. These calculations also predict a sharp drop of the pressure to a very small value when the temperature approaches T_c, thus provoking instability in the presence of overcooling. So we do not expect a long-living mixed phase and consider a fast transition from quark to hadron matter with the characteristic transition proper time duration $\delta\tau$ of the order of 1 fm/c.

To calculate the transition effect, one must shift to the rest frame of each moving element of the system and integrate over proper times τ and spacetime rapidities η of the elements of the system. Then, the invariant single-photon distribution over transverse momentum k_T and rapidity y in the central rapidity region $y = 0$ reads

$$\left.\frac{dN}{d^2k_T dy}\right|_{y=0} = I_{\rm QGP} + I_{\rm tr}^{(1)} = \int \tau d\tau \int d\eta \int d^2x_T \left(p\frac{dR_\gamma}{d^3p}\right) + \int d\eta \int d^2x_T \frac{2p\tau_c}{(2\pi)^3} r^2(p) \tag{78}$$

with $p = k_T\cosh\eta$.

The first term on the right-hand side of (78) describes the photon production from hot QGP. Here, R_γ is the QGP production rate per unit four-volume in the rest frame of the matter [19]:

$$p\frac{dR_\gamma}{d^3p} = \frac{5\alpha\alpha_s}{18\pi^2}T^2\exp(-p/T)\ln(1+\frac{\kappa p}{T}), \tag{79}$$

with $\alpha = 1/137$, $\alpha_s = 0.4$, and $\kappa = 0.58$. This expression can also be used for a hadron gas as its uncertainty is larger than the difference between the first-order QGP and hadron-gas production rates [20]. Contributions from hadronic resonances are not considered here. The second term on the right-hand side of (78) describes photon production due to the transition from QGP to hadrons in the vicinity of proper time τ_c [cf. (56)]. The time of the transition is taken to be small in this term in comparison with total duration of the photon production process. The evolution parameter $r(p)$ is given here by formulas (76) and (77).

As the last step, one must specify the temperature evolution in (78). We suggest that the temperature depends on proper time of the volume element with a powerlike dependence:

$$(T/T_0) = (\tau/\tau_0)^{-1/b}, \tag{80}$$

where τ_0 and T_0 are the initial proper time and initial temperature, respectively. For final estimation, we use $b = 3$, typical of the hydrodynamic picture, and choose a low transition temperature $T_c = \beta_c^{-1} =$ 140 MeV. After the transition, photons live for some

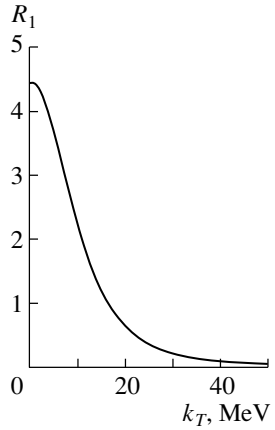

Fig. 1. The relative strength of the transition radiation for the transition from QGP to hadrons.

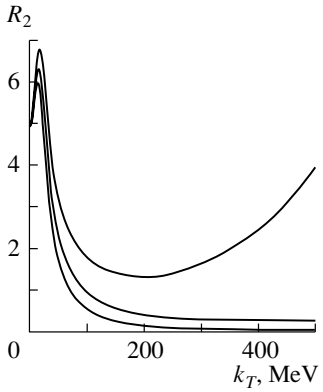

Fig. 2. The relative strength of the opposite side two-photon correlations for the transition times $\delta\tau = 0, 0.5$, and 1 fm/c (top to bottom)—see Eqs. (87) and (88).

time in the hadronic medium, and we suggest a thermal momentum distribution of the hadrons (modified by the expansion of the system). We neglect thermal photon production below T_c and do not introduce a special freeze-out temperature. An alternative way is to introduce the final temperature $T_{\rm fin} < T_c$. Not pretending to achieve high accuracy, we shall not distinguish between T_c and $T_{\rm fin}$ below.

Using expressions (79) and (80), the photon production rate in the QGP phase in (78) can be integrated over spacetime rapidities η:

$$I_{\rm QGP} = \frac{5\alpha\alpha_s}{9\pi^2}(2\pi)^{1/2} b \frac{(k_T\tau_c)^2}{(k_T\beta_c)^{2b-2}} \int d^2x_T J_{\rm QGP} \tag{81}$$

with

$$J_{\rm QGP} \cong \int_{k_T\beta_0}^{k_T\beta_c} dx \frac{x^{2b-3}e^{-x}}{(4x+1)^{1/2}} \times \ln\left(1 + \kappa x + \frac{\kappa x}{4x+1}\right). \tag{82}$$

The remaining integral (82) over the temperature can be easily evaluated in various subregions of the photon momentum k_T. Below, we will be interested in rather low photon momenta k_T (up to 500 MeV) where the transition effect is expected to be more pronounced. In this momentum region, the integral (82) depends mainly on the final temperature T_c (at asymptotically large momenta k_T, it depends on the initial temperature T_0). The final proper time τ_c in (81) depends on the initial conditions in general. However, for two main variants of the initial conditions used in the literature [21], $\tau_0 T_0 = 1, T_0/T_c = 3/2$ ($\tau_0 = 1$ fm/c) and $\tau_0 T_0 = 1/3, T_0/T_c = 5/2$ ($\tau_0 = 0.2$ fm/c), the proper time τ_c changes insignificantly, being 3.125 and 3.375 fm/c, respectively (for $b = 3$). Below, we will use for τ_c an average value $\tau_c = 3.25$ fm/c.

Let us note that the photon production rate in (78) can be expressed through the photon occupation number $n(k)$:

$$p\frac{dR_\gamma}{d^3p} = \frac{2k_T}{(2\pi)^3}\frac{dn(k_T\cosh\eta)}{d\tau} \tag{83}$$

(with two polarizations included). In particular, taking (83) into account, one can see that, if the velocities of the volume elements, as well as proper time interval, in the first term on the right-hand side of Eq. (78) are small, then (78) is reduced to (56), as it should be. The estimation of (79) shows that the photon occupation number $n(k)$ in Eq. (83) is numerically small:

$$n(k) \ll 1.$$

This means, in particular, that the transition radiation is dominated by the ground state rearrangement rather than by the photon amplification.

The transition contribution $I^{(1)}_{\rm tr}$ in (78) appears essential only at small momenta k_T. So, dealing with single-photon distributions, one can use formula (76) for the evolution parameter $r(k)$. The resulting relative strength of the transition radiation

$$R_1(k_T) = I^{(1)}_{\rm tr}/I_{\rm QGP} \tag{84}$$

is large only in the momentum region $k_T \le 20$–30 MeV independently of the transition duration (see Fig. 1).

The transition effect is more pronounced in photon correlations [cf. Eqs. (64) and (65)] where it is a first-order effect with respect to $r(k)$. Let us note that the HBT effect for photons now has a more complicated form than that in (64) because of finite duration [15] of the process of photon emission from QGP and it will not be exposed here. We consider only the transition effect [the third term in Eqs. (57) and (64), which gives opposite side correlations], estimating its contribution to the two-photon correlation function in the

central rapidity region. Suggesting fast transition, we can evaluate the contribution in the vicinity of a fixed proper time τ_c. For this purpose, one only has to shift to the rest frame of each element of the expanding volume and perform integration with respect to η. Then, the extension of the invariant correlator in (63) to the case of expanding volume takes the form

$$2k\langle\tilde{b}_\pm(\mathbf{k}_1)\tilde{b}_\pm(\mathbf{k}_2)\rangle = G(\mathbf{k}_{1T}+\mathbf{k}_{2T})I_{\rm tr}^{(2)} \qquad (85)$$

with

$$I_{tr}^{(2)} = \int d^2x_T \int d\eta \frac{2\tau_c k_T \cosh\eta}{(2\pi)^3} r(k_T\cosh\eta), \qquad (86)$$

where we neglected $n(k)$ in comparison with unity (see above). Therefore, the normalized two-photon correlation function is given by [cf. Eqs. (64) and (65)]

$$C(\mathbf{k}_{1T},\mathbf{k}_{2T})\Big|_{y_1=y_2=0} = 1 + C_{\rm HBT} \qquad (87)$$
$$+ \frac{1}{2}R_2^2(k_T)G^2(\mathbf{k}_{1T}+\mathbf{k}_{2T})$$

with

$$R_2(k_T) = \frac{I_{\approx\diagdown}^{(2)}}{I_{\rm QGP}+I_{\rm tr}^{(1)}}, \qquad (88)$$

where $C_{\rm HBT}$ is the contribution due to the HBT effect.

We calculated the ratio $R_2(k_T)$ for various transition times $\delta\tau = 0$, 0.5, and 1 fm/c up to $k_T =$ 500 MeV. The results are shown in Fig. 2. In the region of $k_T < 100$ MeV, the ratio $R_2(k_T)$ is large for all these $\delta\tau$, being equal to 4.94 at $k_T = 0$, reaching the maximum value $R_2 \sim 6$ at $k_T \sim 20$ MeV, and falling to $R_2 = 1.78$ for $\delta\tau = 0$, $R_2 = 0.95$ for $\delta\tau = 0.5$ fm/c, and $R_2 = 0.55$ for $\delta\tau = 1$ fm/c at $k_T = 100$ MeV. At larger transverse momenta, behavior of the ratio R_2 depends strongly on the transition time $\delta\tau$: in the k_T interval from 200 to 500 MeV, the ratio $R_2(k_T)$ increases for $\delta\tau = 0$, remains approximately constant for $\delta\tau = 0.5$ fm/c, and decreases for $\delta\tau = 1$ fm/c. The asymptotic behavior of the ratio $R_2(k_T)$ at large photon momenta k_T depends on the relationship between the temperature-dependent single-particle production rate (decreasing as $\exp(-\beta k)$) and the $\delta\tau$-dependent evolution parameter (decreasing as $\exp(-\pi k\delta\tau/2)$ in our reference model). In any case, one can hope to see the effect of the transition in the region $k_T \le 100$ MeV, where the peak of the ratio $R_2(k_T)$ is always present.

7. CONCLUSION

Estimation of photon emission accompanying the transition between quark–gluon and hadron states of matter in heavy-ion collisions shows that opposite-side photon correlations can serve as a sign of the transition if transition time is not large.

ACKNOWLEDGMENTS

The work was supported by the Russian Foundation for Basic Research (project no. 00-02-101).

REFERENCES

1. NA35 Collab. (J. Bartke *et al.*), Nucl. Phys. A **566**, 503c (1994); WA85 Collab. (S. Abatzis *et al.*), Nucl. Phys. A **566**, 225c (1994).
2. T. Blum *et al.*, Phys. Rev. D **51**, 5153 (1995).
3. L. P. Csernai, I. N. Mishustin, and A. Mocsy, in *Proceedings of the 4th Rio de Janeiro International Workshop on Relativistic Aspects of Nuclear Physics* (World Scientific, Singapore, 1995), p. 137.
4. I. V. Andreev, hep-ph/0012148; in *Proceedings of E.S. Fradkin Memorial Conference* (Scientific World, Moscow, 2001), Vol. II, p. 507.
5. I. V. Andreev and R. M. Weiner, Phys. Lett. B **373**, 159 (1996).
6. M. Asakawa and T. Csorgo, Heavy Ion Phys. **4**, 233 (1966).
7. I. V. Andreev, Mod. Phys. Lett. A **14**, 459 (1999).
8. M. Asakawa, T. Csorgo, and M. Gyulassy, Phys. Rev. Lett. **83**, 4013 (1999).
9. I. V. Andreev, Yad. Fiz. **63**, 2080 (2000) [Phys. At. Nucl. **63**, 1988 (2000)].
10. A. I. Baz, Ya. B. Zeldovich, and A. M. Perelomov, *Scattering, Reactions, and Decays in Nonrelativistic Quantum Mechanics* (Nauka, Moscow, 1971), p. 277.
11. N. N. Bogoliubov, Bull. Acad. Sci. USSR, Ser. Phys. **11**, 77 (1947).
12. L. D. Landau and E. M. Lifshitz, *Course of Theoretical Physics,* Vol. 3: *Quantum Mechanics: Non-Relativistic Theory* (Nauka, Moscow, 1974; Pergamon, New York, 1977).
13. R. J. Glauber, Phys. Rev. **131**, 2766 (1963); E. C. G. Sudarshan, Phys. Rev. Lett. **10**, 277 (1963).
14. S. Pratt, Phys. Rev. Lett. **53**, 1219 (1984).
15. I. V. Andreev, M. Plumer, and R. M. Weiner, Int. J. Mod. Phys. A **8**, 4577 (1993).
16. E. S. Fradkin, Tr. Fiz. Inst. Akad. Nauk SSSR **29**, 7 (1965).
17. H. G. Ritter, in *Proceedings of the 5th Rio de Janeiro International Workshop on Relativistic Aspects of Nuclear Physics* (World Scientific, Singapore, 1997), p. 325.
18. J. D. Bjorken, Phys. Rev. D **27**, 140 (1983).
19. J. Kapusta, R. Lichard, and D. Seibert, Phys. Rev. D **44**, 2774 (1991).
20. H. Nadeau, J. Kapusta, and P. Lichard, Phys. Rev. C **45**, 3034 (1992).
21. J. J. Neumann, G. Fai, and D. Seibert, in *Proceedings of the 4th Rio de Janeiro International Workshop on Relativistic Aspects of Nuclear Physics* (World Scientific, Singapore, 1995), p. 325.

Physics of Atomic Nuclei, Vol. 65, No. 10, 2002, pp. 1918–1920. From Yadernaya Fizika, Vol. 65, No. 10, 2002, pp. 1972–1974.

LETTERS TO THE EDITOR

BCS–Bose Crossover in Color Superconductivity*

B. O. Kerbikov

Institute of Theoretical and Experimental Physics,
Bol'shaya Cheremushkinskaya ul. 25, Moscow, 117259 Russia

Received April 23, 2002

During the last two to three years, color superconductivity has become one of the QCD focal points—see review papers [1–3]. To a large extent (but not completely), the basic ideas of the subject are traced back to the BCS theory of superconductivity and its later development. It is known that the discovery of high-temperature superconductors (HTSCs) gave rise to new ideas and approaches and revealed interest in the problem of the transition from the BCS regime to the Bose–Einstein (BE) condensation. The BCS–BE crossover is important for the physics of HTSCs since the underlying distinction of HTSCs from ordinary superconductors is that they are characterized by a much smaller value of the dimensionless parameter $\xi n^{1/3}$, where ξ is the coherence length and n is the carrier density. In the BCS, or weak coupling regime, $\xi^3 n \sim (10^8 - 10^{10})$, while in the opposite strong coupling case, $\xi^3 n \lesssim 1$ and we deal with compact pairs of composite bosons, which may undergo BE condensation. It has been suggested (see, e.g., [4]) that the description of HTSCs might require an intermediate approach between the BCS and BE limits. The evolution from weak to strong coupling was theoretically investigated [5] before the discovery of HTSCs. It was shown that the transition proceeds via a smooth crossover though the two limits are physically quite different (see also [6]).

Having reminded these well-known facts, we may formulate the question which forms the core of the present article. As model calculations show [7], the onset of the color superconducting phase in a two-flavor QCD (the so-called 2SC phase) occurs at rather low quark densities n, namely, at n only three times larger than the quark density in normal nuclear matter, or even at lower ones [8].

Thus, it is natural to ask in which region regarding the BCS–BE crossover does it happen?

According to [7], in a QCD with two massless flavors, transition to the superconducting 2SC phase occurs at $n^{1/3} \simeq 0.2$ GeV (the dimension of n is $1/\mathrm{fm}^3$ or GeV^3). As for the corresponding value of ξ, we may only rely on some estimates since accurate calculations are lacking. One should also keep in mind a possible distinction between the correlation length and the pair size. The two quantities coincide in the BCS regime [9], while in the BE region the pair size is smaller than the coherence length [6, 10]. With these reservations being made, we quote the value $\xi \simeq 0.8$ fm from [11]. A rather close result, namely, $\xi \simeq 0.6$ fm, follows from the BCS estimate $\xi \simeq 1/\pi\Delta$ [12], where $\Delta \simeq 0.1$ GeV [1, 7]. Thus, the diquark pair in the "newly born" color superconducting phase is rather compact. This is easy to understand from simple physical considerations. In the color antitriplet $\overline{3}$ state, the one-gluon exchange leads to a quark–quark potential which is only by a factor of two weaker than the quark–antiquark one. Instanton or Nambu–Jona-Lasinio (NJL) models also result in a rather strong q–q attraction. Consider the NJL "weak coupling" solution [1, 3] $\Delta = 2\omega_{\mathrm{D}} \exp(-1/\rho_{\mathrm{NJL}})$, where ω_{D} is the Debye frequency, $\rho_{NJL} = 8g^2\mu^2/\pi^2$, $g^2 \simeq 2\ \mathrm{GeV}^2$ is the NJL coupling constant, and $\mu \simeq 0.4$ GeV is the chemical potential corresponding to the onset of the 2SC phase. We immediately see that $\rho_{\mathrm{NJL}} \simeq 0.3 > \rho_{\mathrm{BCS}}$; i.e., the quark–quark interaction is stronger than phonon-mediated electron–electron interaction and in this sense the newly born color superconducting phase does not correspond to the standard BCS weak-coupling limit.

We conclude that the onset of the color superconducting phase corresponds to $\xi n^{1/3} \sim (1\ \mathrm{fm})(0.2\ \mathrm{GeV}) \sim 1$, $\xi\mu \sim (\mathrm{fm})(0.4\ \mathrm{GeV}) \sim 2$.

These values are at least two orders of magnitude smaller than those corresponding to the BCS regime. In order to understand to which region of the BCS–BE "phase diagram" they correspond, one has to resort to model calculations performed for the system of electrons. Most results have been obtained for the system in two dimensions [6]. Crossover in three dimensions has been studied in [13]. Transition between the two regimes occurs in a narrow range of the parameter $\xi n^{1/3}$, and for electron systems with simple model potentials (finite range, separable, Gaussian),

*This article was submitted by the author in English.

1063-7788/02/6510-1918$22.00

the value $\xi n^{1/3} \simeq 1$ corresponds to the lower limit of a BCS-like region. Needless to say, the extrapolation of this result to the system of massless quarks may be considered only as an educated guess and the problem deserves a dedicated study.

The importance of the BCS–BE crossover for the color superconductivity problem was first outlined in [3] and [14, 15]. In [14] the low-density regime was investigated by extrapolating the single-gluon-exchange model, which is an adequate tool at asymptotically high densities. A smooth transition from $\xi n^{1/3} \gg 1$ to $\xi n^{1/3} = 10$ at $\mu = 0.8$ GeV was observed.

Let us indicate how the crossover problem in color superconductivity theory should be approached. The starting point is the thermodynamic potential $\Omega(\Delta, \mu, T)$, where the diquark condensate Δ is of the form $\Delta \propto \langle q\hat{0}q\rangle$, $\hat{0} = \varepsilon_{\alpha\beta 3}\varepsilon_{ij}C\gamma_5$; α, β are the color indices; i, j, flavor indices; and C, the charge-conjugation operator [1]. The dependence of Ω on the chiral condensate $\varphi \propto \langle \bar{q}\hat{R}q\rangle$, $R = \varepsilon_{\alpha\beta}\varepsilon_{ij}$ in the region where the two condensates Δ and φ possibly coexist [7] may be dropped due to the color superconductivity version of the Anderson theorem [16]. For a wide class of models with four-quark interaction, the thermodynamic potential Ω was first analytically calculated in [7]. With Ω at hand, one can write a self-constituent set of mean-field equations to determine the gap Δ and the chemical potential μ:

$$\frac{\partial\Omega}{\partial\Delta} = 0, \quad -\frac{\partial\Omega}{\partial\mu} = n. \tag{1}$$

Up to now, only the first of equations (1) has been used in color superconductivity theory, while the chemical potential has been considered as an independent variable. To display the crossover from the BCS to the low-density BE regime, one also needs the second equation [6]. It enables one to consider the region of $\mu < 0$ values characteristic for a dilute gas of tightly bound diquarks ($\mu = -\varepsilon_{B/2}$ in the limit of dilute composite bosons with binding energy ε_B).

In order to find the quantities Δ and μ vs. the dimensionless physical parameter $\xi n^{1/3}$, Eqs. (1) should be complemented by the equation which determines the parameter ξ:

$$\xi^2 = \frac{\int d\mathbf{r}\phi(r)r^2}{\int d\mathbf{r}\phi(r)}, \tag{2}$$

where $\phi(r) = \langle q(r)\hat{0}q(0)\rangle$. Analytic expressions for Δ and μ as functions of $\xi n^{1/3}$ have been obtained for electron systems with simple model interaction [13]. The necessity of implementing a similar program for color superconductivity directly follows from our conclusion that the suggested onset of this phase occurs within the BCS–BE crossover region.

Another question is what are the physical consequences of the fact that the formation of the color superconducting gap is at least partly due to the existence of preformed Bose pairs of quarks. At present we can again rely only on the corresponding studies of the electron systems [5, 17]. The key point here is that the physical origin of the critical temperature T_c is absolutely different in the limits of weak and strong coupling [5]. In the BCS region, T_c corresponds to the breaking of Cooper pairs, while in the BE limit, T_c corresponds to the center-of-mass motion of the pairs and to the population of zero-momenta state. Transition from weak to strong coupling regimes results in a decrease in T_c compared to the mean-field value. Formally, this should also follow from Eqs. (1) and (2).

Finally, we note that calculations of the parameters μ and T at which the transition into the color superconducting phase occurs have been performed neglecting the gluon condensate. General arguments presented in [18] show that the color-magnetic field "frozen" into the quark system in the form of the gluon condensate shifts the transition toward higher densities (see also [19]). Therefore, Eqs. (1) for the BCS–BE crossover should be embedded into the background gluon field.

ACKNOWLEDGMENTS

The author is grateful to V.I. Shevchenko and Dirk van der Marel for useful discussion and remarks and to Kazunori Itakura and Egor Babaev for indication on [14] and [15].

This work was financially supported by the Russian Foundation for Basic Research (project no. 00-02-17836), INTAS (grant no. 110), and NWO (grant no. 01-250).

REFERENCES

1. K. Rajagopal and F. Wilczek, hep-ph/0011333.
2. M. Alford, hep-ph/0102047.
3. B. Kerbikov, hep-ph/0110197.
4. Y. I. Uemura *et al.*, Phys. Rev. Lett. **66**, 2665 (1991).
5. P. Noziers and S. Schmitt-Rink, J. Low Temp. Phys. **59**, 195 (1985).
6. V. M. Loktev, R. M. Quick, and S. G. Sharapov, Phys. Rep. **349**, 1 (2001).
7. J. Berges and K. Rajagopal, Nucl. Phys. B **538**, 215 (1999).
8. M. Buballa, J. Hosek, and M. Oertel, hep-ph/0105079.
9. A. V. Svidzinsky, *Nonuniform Problems of the Superconductivity Theory* (Nauka, Moscow, 1982).

10. F. Pistolesi and G. C. Strinati, Phys. Rev. B **53**, 15168 (1996).
11. T. Schafer, Nucl. Phys. A **642**, 45c (1998).
12. P. G. de Gennes, *Superconductivity in Metals and Alloys* (Perseus Books, Massachusetts, 1989).
13. M. Marini, F. Pistolesi, and G. C. Strinati, Eur. Phys. J. B **1**, 151 (1998).
14. H. Abuki, T. Hasuda, and K. Itakura, Phys. Rev. D **65**, 074014 (2002).
15. E. Babaev, Int. J. Mod. Phys. A **16**, 1175 (2002).
16. B. Kerbikov, hep-ph/0106324.
17. V. B. Geshkenbein, L. B. Ioffe, and A. I. Larkin, Phys. Rev. B **55**, 3173 (1997).
18. N. Agasyan, B. Kerbikov, and V. Shevchenko, Phys. Rep. **320**, 131 (1999).
19. D. Ebert *et al.*, hep-ph/0106110.

Physics of Atomic Nuclei, Vol. 65, No. 10, 2002, pp. 1921–1930. Translated from Yadernaya Fizika, Vol. 65, No. 10, 2002, pp. 1975–1984.

FUTURE PUBLICATION

Probabilistic Scission of a Fissile Nucleus into Fragments

G. D. Adeev and P. N. Nadtochy

A probabilistic criterion is proposed for the scission of a fissile nucleus into fragments. The probability that a nucleus undergoes disintegration into fragments is estimated by considering the scission of the neck between two would-be fragments as a fluctuation. The energy of the prescission configuration and the energy of the separated-fragment configuration are computed on the basis of a macroscopic model that takes into account a finite range of nuclear interaction and the diffuseness of the nuclear surface. The effect of probabilistic scission on fission-process observables, such as the first and second moments of the mass and the energy distribution of fragments, the mean multiplicities of prescission neutrons, and mean fission times, is demonstrated within Langevin dynamics. It is shown that the Strutinsky criterion, according to which nuclear scission occurs at a finite neck thickness of $0.3R_0$, is a good approximation to the probabilistic scission criterion in dynamical calculations employing the one-body nuclear-viscosity mechanism modified in such a way that the wall-formula contribution is reduced, the reduction factor satisfying the condition $k_s < 0.5$.

Fluctuations of Charged-Particle Multiplicities in Narrow Intervals of Rapidity in π^-A$^-$ Interactions at a Primary Momentum of 40 GeV/c

K.G. Akhobadze, T. S. Grigalashvili, E. Sh. Ioramashvili, E. S. Mailyan, M. I. Nikoladze, and L. V. Shalamberidze

Maximum fluctuations of charged-particle multiplicities in narrow intervals of rapidity in $\pi^- A$ (A = H, D, C, Cu, Pb) interactions at a primary momentum of 40 GeV/c are investigated for $P_\perp$ processes. The observed fluctuations are studied by the method of factorial moments. The results reveal that the dependence of the factorial moments on rapidity gaps obeys a power law. This suggests that fluctuations of a dynamical character exist in the aforementioned processes. Experimental results are compared with the predictions of the model of quark–gluon strings in the form of the FRITIOF-7.02 code.

Production of the $f_0(980)$ Resonance in the Reaction $\pi^- p \to \pi^0\pi^0 n$

N. N. Achasov and G. N. Shestakov

The predictions of the model that relies on the mechanism of one-pion exchange and which describes well GAMS data on the rearrangement of the S-wave mass spectrum of the $\pi^0\pi^0$ system in the region of the $f_0(980)$ resonance with increasing $-t$ in the reaction $\pi^- p \to \pi^0\pi^0 n$ are compared with detailed data recently obtained at the Brookhaven National Laboratory (BNL) for the m and t distributions of $\pi^- p \to \pi^0\pi^0 n$ events. Our analysis revealed that these predictions are not consistent with those BNL data. On this basis, it is expected that some other mechanism—most probably, this is the mechanism of a_1 exchange—is responsible for the phenomenon discovered in the BNL experiments under discussion.

Energy Dependence of an Effective Nucleon–Nucleon Interaction and Position of the Nucleon-Drip Line

M. Baldo, U. Lombardo, E. E. Saperstein, and M. V. Zverev

A semimicroscopic version of the self-consistent theory of finite Fermi systems is proposed. In this approach, the standard theory of finite Fermi systems is supplemented with relations that the microscopic theory makes it possible to obtain for the outer values of the invariant components of the Landau–Migdal amplitude. The Landau–Migdal amplitude at the nuclear surface is expressed in terms of the off-shell T matrix for free nucleon–nucleon scattering at the energy E equal to the doubled chemical potential of the nucleus being considered. A strong energy dependence of the free T matrix at small E changes the properties of nuclei near the nucleon-drip line. It is shown that, upon taking into account the energy dependence of the effective interaction, the position of the neutron-drip line is shifted considerably toward greater values of the neutron excess. This effect is illustrated for the example of the tin-isotope chain.

1063-7788/02/6510-1921$22.00

Anomalous Magnetic Moment of the Muon in the Left–Right Models

G. G. Boyarkina, O. M. Boyarkin, and V. V. Makhnach

The effect of Higgs bosons on the anomalous magnetic moment of the muon is considered within the model that is based on the $SU(2)_L \times SU(2)_R \times U(1)_{B-L}$ gauge group and which involves a bidoublet and two triplets of Higgs fields (left–right model). For the Yukawa coupling constants and the masses of Higgs bosons, the regions are found where the model leads to agreement with experimental results obtained at the Brookhaven National Laboratory (BNL) for the anomalous magnetic moment of the muon. In order to explore corollaries from the constraints obtained for the parameters of the Higgs sector, the processes $e^+e^- \to \mu^+\mu^-$, $\tau^+\tau^-$ and $\mu^+\mu^- \to \mu^+\mu^-$, $\tau^+\tau^-$ are considered both within the left–right model and within the model involving two Higgs doublets (two-Higgs-doublet model, or 2HDM). It is shown that, if the mass of the lightest neutral Higgs boson does indeed lie in the range 3.1–10 GeV, as is inferred from the condition requiring the consistency of the 2HDM with the data of the BNL experiment, this Higgs boson may be observed as a resonance peak at currently operating e^+e^- colliders (VEPP-4M, CESR, KEKB, PEP-II, SLC). In order to implement this program, however, it is necessary to reduce considerably the scatter of energy in the e^+ and e^- beams used, since the decay width of the lightest neutral Higgs boson is extremely small at such mass values. It is demonstrated that, in the case of the left–right model, for which the mass of the lightest neutral Higgs boson is not less than 115 GeV, the resonance peak associated with it may be detected at a muon collider.

Refraction Effects in the Reaction $^{13}C(^3He, t)^{13}N$ at an Energy of 60 MeV

N. Burtebaev, A. Duisebaev, and S. B. Sakuta

In the angular range 10°–120°, the angular distributions of tritons from the reaction $^{13}C(^3He, t)^{13}N$ induced by incident ^3He nuclei of energy 60 MeV are measured for transitions to the ground ($J^\pi = 1/2^-$) state of the ^{13}N nucleus and to its excited states at $E_x = 2.365$ MeV ($1/2^+$) and $E_x = 3.51$ MeV ($3/2^-$) + 3.55 MeV ($5/2^+$). A theoretical analysis is performed within the distorted-wave method under the assumption of the one-step charge-exchange mechanism, a microscopic form factor that includes central and tensor components of the nucleon–nucleon interaction being used in this analysis. It is shown that an acceptable description of the experimental data in question is achieved with potentials whose volume integrals do not exceed 300 MeV fm^3.

Total Cross Section for γN Interaction in the Energy Range $\sqrt{s} = 40$–250 GeV

G. M. Vereshkov, O. D. Lalakulich, Yu. F. Novosel'tsev, and R. V. Novosel'tseva

The results are presented that were obtained by directly measuring the total cross section for γN interaction by recording photoproduction processes at the Baksan underground scintillation telescope of the Institute for Nuclear Research (Russian Academy of Sciences, Moscow). It is confirmed that, in the energy range $\sqrt{s} = 40$–130 GeV, the photon–hadron cross sections grow faster than hadron–hadron cross sections. It is shown that the growth of the number of additive quarks in photon-hadronization products may be one of the reasons behind this effect. Experimental data on the cross sections for γN and $\gamma\gamma$ interactions are compared, and the status of the results obtained from direct and indirect cross-section measurements in the high-energy region is discussed.

Background of External Gamma Radiation in the Proportional Chambers of the SAGE Experiment

V. N. Gavrin and V. V. Gorbachev

The effect of external gamma radiation on the counting of ^{71}Ge decays in the proportional counters of the SAGE experiment, which is aimed at measuring the neutrino flux from the Sun, is considered. The systematic error of the SAGE result due to radon decay in the air surrounding the counters and the background counting rate in the counters due to the gamma radiation of the surrounding shielding are determined.

Contribution of the Hadron Component of a Virtual Photon to the Structure Function for Charm Leptoproduction at High x and Q^2

D. Yu. Golubkov and Yu. A. Golubkov

The contribution of the hadron component of a virtual photon to the structure function for charm leptoproduction is calculated. This contribution is due to the scattering of c quarks from the virtual photon on the quarks and gluons of the proton. A comparison of the results of our calculations with the charmed structure function measured by the European muon collaboration (EMC) in $\mu^+ p$ scattering reveals that such processes may explain the observed excess of the charmed structure function over the predictions of the model of photon–gluon fusion at high momentum transfers. In order to describe the EMC results, it is therefore unnecessary to invoke the hypothesis that the proton wave function involves a nonperturbative admixture of charmed quarks (intrinsic-charm hypothesis).

On the Diffractive Disintegration of Deuterons and of Exotic Nuclei ^{6}He and ^{19}C

M. V. Evlanov, A. M. Sokolov and V. K. Tartakovsky

A theory of the diffractive disintegration of loosely bound two-cluster nuclei in the nuclear and Coulomb fields of nuclei having a diffuse boundary is developed. The energy spectra of charged products originating from the disintegration of ^{2}H, ^{6}He, and ^{19}C nuclei are calculated within the proposed approach; the results are found to be rather sensitive to the nuclear structure. For some angles of neutron and proton emission from the reaction $^{12}\mathrm{C}(d, np)^{12}\mathrm{C}$, the resulting cross sections are in satisfactory agreement with data of recent kinematically complete experiments that studied the disintegration of intermediate-energy deuterons.

Survivability of Excited Superheavy Nuclei

A. S. Zubov, G. G. Adamian, N. V. Antonenko, S. P. Ivanova, and W. Scheid

The survivability of even–even and odd superheavy nuclei is analyzed on the basis of a statistical model and with the aid of nuclear properties predicted by various theoretical models. In this analysis, use is made of various methods for computing level densities. For $Z < 114$ nuclei, calculations on the basis of all models predicting nuclear properties lead to close values for the ratio of the width with respect to the neutron channel to the width with respect to the fission channel. For $Z \geq 114$ nuclei, different values are obtained for this ratio. The dependence of the results on model parameters is discussed. The collective-enhancement factor is taken into account in the calculation.

Scattering of $\pi^\pm$ Mesons on a ^{9}Be Nucleus in the Region of the Δ_{33} Resonance

E. T. Ibraeva

Within the Glauber diffraction theory of multiple scattering, the differential cross sections for the elastic and inelastic scattering of $\pi^\pm$ mesons are calculated for energies ranging between 130 and 260 MeV. This is a region around the broad resonance Δ_{33} in the $\pi^\pm N$ system, its maximum occurring approximately at 165 MeV. The wave function for the ^{9}Be nucleus was constructed on the basis of the $2\alpha N$ multicluster model. The sensitivity of the differential cross sections in question to the wave functions of the target nucleus that are computed with different intercluster interaction potentials, to the contribution of wave-function components, and to the contribution of different scattering multiplicities in the Glauber operator Ω is investigated. A comparison with experimental data and with the results of calculations performed by other authors is performed, and conclusions on the quality of wave functions and on the advantages of the computational method used are drawn from this comparison.

Effect of Nuclear-Surface Diffuseness on the Energy and Width of a Giant Dipole Resonance

B. S. Ishkhanov and V. N. Orlin

The effect of nuclear-surface diffuseness on the position of a giant dipole resonance on the energy scale and on the width of this resonance is investigated. Approximating formulas that make it possible to describe experimental systematics in the mass range $16 < A < 240$ are obtained for these quantities.

Deuteron photodisintegration in the Bethe–Salpeter Formalism: Effects of Negative-Energy Components

K. Yu. Kazakov and D. V. Shul'ga

Relativistic covariance requires that analysis of the reaction $\gamma d \to pn$ within a field-theoretical model of the nucleon–nucleon interaction include negative-energy states. Relativistic effects and contributions of negative-energy states in the Bethe–Salpeter amplitude to the differential cross section, to the asymmetry of linearly polarized photons, and to the tensor asymmetries of the target deuteron are estimated within the Bethe–Salpeter formalism for describing the interaction of an electromagnetic field with a two-nucleon system. It is found that the contribution of these states becomes significant with increasing photon energy, but it does not change the qualitative behavior of observables as functions of scattering angles.

Measurement of the Total and Differential Cross Sections for the Reaction $\pi^- p \to \eta n$ with the Aid of the CRYSTAL BALL Detector

N. G. Kozlenko, V. V. Abaev, V. S. Bekrenev, S. P. Kruglov, A. A. Koulbardis, I. V. Lopatin, A. B. Starostin, B. Draper, S. Hayden, D. Huddleston, D. Isenhower, C. Robinson, M. Sadler, K. Algower, R. Cadman, H. Spinka, J. Comfort, K. Craig, A. Ramirez, T. Kycia, M. Clajus, A. Marusic, S. McDonald, B. M. K. Nefkens, N. Phaisangittisacul, S. Prakhov, J. Price, W. B. Tippens, D. Peterson, W. J. Briscoe, A. Shafi, I. I. Strakovsky, G. Staudenmaier, D. M. Manley, D. Olmstead, D. Peaslee, N. Knecht, G. Lolos, Z. Papandreou, I. Supek, I. Slaus, A. Gibson, D. Grosnic, D. Koetke, R. Manweiler, and Sh. Stanislaus

The first results of the Crystal Ball collaboration that were obtained in 1998 by measuring the total and differential cross sections for the reaction $\pi^- p \to \eta n$ are presented. These new experimental results on the total cross sections are compared with the predictions of the K-matrix model of pion–nucleon scattering. The angular distribution near the reaction threshold (685 MeV/c) is determined by the contribution of the S wave, but, from the momentum of 720 MeV/c, the angular distributions exhibit the contribution of the P wave.

Process $\gamma\gamma \to \nu\overline{\nu}$ in a Strong Magnetic Field

A. V. Kuznetsov, N. V. Mikheev, and D. A. Rumyantsev

A general analysis of the three-vertex loop amplitude in a strong magnetic field is performed, the asymptotic form of the electron propagator in a field being used in this analysis. Vertex combinations of the scalar–vector–vector (SVV), the pseudoscalar–vector–vector (PVV), the vector–vector–vector (VVV), and the axial–vector–vector (AVV) form are considered with the aim of exploring the photon–neutrino process $\gamma\gamma \to \nu\overline{\nu}$. It is shown that only the SVV amplitude grows linearly with increasing strength of the magnetic field, the remaining amplitudes, those of the PVV, the VVV, or the AVV type, featuring no contributions that exhibit a linear growth. The process $\gamma\gamma \to \nu\overline{\nu}$ is investigated within the model that is obtained by extending the Standard Model for electroweak interactions via the inclusion of left–right symmetry and which admits the existence of an effective scalar $\nu\nu ee$ coupling. The possible astrophysical manifestations of the process being considered are discussed.

dt, d^3He, and $p\alpha$ Scattering in the Regions of the ^{5}He* and ^{5}Li* Resonances

A. V. Kulik and V. D. Mur

It is shown that the simplest strong-interaction models employing the Breit boundary condition or a delta-function potential and involving only three free parameters describe adequately the properties of the dt and d^3He systems in the regions of the ^{5}He$^*(3/2^+)$ and ^{5}Li$^*(3/2^+)$ resonances—that is, for energies of $E \lesssim 3E_C$ and $E \lesssim 2E_C$, where E_C is the corresponding Coulomb energy. For these systems, the complex scattering length, the effective range, and the shape parameters are extracted from experimental data on the reaction cross sections and on proton polarization in $p\alpha$ scattering (in the case of the d^3He system). The astrophysical function is extrapolated to the low-energy region $0 \le E < 0.1E_C$, which is of importance for thermonuclear investigations, but which is hardly accessible to direct measurements.

Temperature Generalization of the Quasiparticle Random-Phase Approximation with Allowance for a Continuum

E. V. Litvinova, S. P. Kamerdzhiev, and V. I. Tselyaev

The method developed previously by the present authors on the basis of the quasiparticle random-phase approximation with allowance for a single-particle continuum is generalized to the case of finite temperatures and is implemented numerically for the isovector $E1$ resonance in the odd nuclei of tin isotopes—specifically, in the stable nucleus ^{120}Sn and in the unstable nucleus ^{104}Sn. The temperature dependence of the integrated features of the resonance and the temperature dependence of its envelope are discussed.

On the Microscopic Mechanism of Collisions between Extremely Light Nuclei

J. V. Mebonia, P. J. Saralidze, K. I. Sulakadze, and G. E. Skhirtladze

The method previously proposed by the present authors for studying three-body problems is generalized with the aim of exploring more complicated nuclear processes. The idea underlying the method consists in preserving the unitarity property for the scattering amplitude determined approximately. A specific analysis is performed for elastic collisions of ^{3}He nuclei and for quasielastic deuteron–triton collisions. Theoretical results obtained by our method are compared with experimental data, and the agreement is found to be quite satisfactory.

Familon Energy–Momentum Losses by a Magnetized Plasma

N. V. Mikheev and E. N. Narynskaya

Familon emission from a dense magnetized plasma via the processes $e^- \to e^-\phi$ and $e^- \to \mu^-\phi$ is investigated. The contribution of these processes to the energy losses by a supernova remnant is calculated. It is shown that, at a late stage of the cooling of such a remnant, the energy losses of a plasma through familon emission may be commensurate with the energy losses by neutrino emission. It is found that the asymmetry of familon emission in the process $e^- \to \mu^-\phi$ induces a force acting on the plasma.

What New Information about the Microscopic Quark Structure of Meson–Baryon Degrees of Freedom in Nucleons Can Be Deduced from Data on Quasielastic Pion Knockout

I. T. Obukhovsky, V. G. Neudatchin, L. L. Sviridova, and N. P. Yudin

The emergence of $B + \pi$ virtual subsystems, which manifest themselves in quasielastic-knockout processes of the $N(e, e'\pi)B$ type, where B is the final-state baryon in various excited states, is considered within the microscopic quark model of a $^3P_0$ localized scalar fluctuation of the QCD vacuum. The relevant technique for taking into account the rearrangement of quark degrees of freedom is demonstrated. The model provides a good description of known momentum distributions for $B = N$ channels. The momentum distributions are predicted for $N \to \pi + B$ channels, where $B = \Delta$, $N^*(1535)$, or $N^{**}(1440)$. It would be of interest to study these channels in exclusive coincidence experiments at accelerators producing electron beams of energy ranging between 5 and 10 GeV.

Photoproduction as a Limiting Case of Inelastic Scattering

A. A. Petrukhin and D. A. Timashkov

Formulas that make it possible to describe, within a unified conceptual framework, both the photoproduction cross section and nucleon structure functions determining the cross section for inelastic lepton interaction at low Q^2 are obtained on the basis of the generalized vector-dominance model and Regge theory.

Exact Solutions to the Three-Body Problem for the Case of S-Wave Interactions of the Centrifugal Type

V. V. Pupyshev

The simplest exact solutions to the three-body Schrödinger and Faddeev equations for S-wave pair interactions inversely proportional to the distances squared are constructed and investigated for the case of zero total angular momentum of three particles.

Measurement of the Energy of Medium-Mass and Heavy Cosmic-Ray Nuclei on the Basis of the Specific Energy Deposition at the Maximum of Hadron Cascades in a Dense Medium

I. D. Rapoport, A. N. Turundaevsky, and V. Ya. Shestoperov

The possibility of measuring the energy of cosmic-ray nuclei in the region above 1 TeV by recording the greatest specific energy deposition in hadron cascades initiated in a dense medium is investigated. The method being discussed makes it possible to improve the accuracy of measurements that use a thin ionization calorimeter in studying high-energy cosmic rays at high altitudes. Attainable accuracies of energy measurements are considered for the cases of light and heavy nuclei. The results obtained by simulating such measurements are compared with the results of the Kosmos-1713 satellite-borne experiment.

On the Binding of Atoms with Antiatoms

T. K. Rebane and N. D. Markovsky

The dissociation stability of $X^+Y^+X^-Y^-$ Coulomb molecules consisting of X^+Y^- atoms and X^-Y^+ antiatoms is investigated. On the basis of multiparameter variational calculations, it is found that such molecules are stable to dissociation into X^+Y^- and Y^+Y^- atoms if the mass ratio for the X and Y particles lies in the range $0.4710 < m_X/m_Y < 2.1231$. This condition is satisfied for the $e^+e^+e^-e^-$, $\pi^+\mu^+\pi^-\mu^-$, $t^+d^+t^-d^-$, $p^+K^+p^-K^-$, and $d^+p^+d^-p^-$ molecules.

Comment on the Use of Chiral Anomaly in Measuring the Number of Colors

R. N. Rogalyov

The dependence of vertices of the $PPP\gamma$ type, where P is a pseudoscalar meson, on the number N_c of colors is analyzed with allowance for the N_c dependence of the quark charges. It is shown that processes that are best suited for measuring N_c include, in addition to the decay $\eta \to \pi^+\pi^-\gamma$, the reactions $K\gamma \to K\pi$ and $\pi^\pm\gamma \to \pi^\pm\eta$. The results of the measurement of the cross section $\sigma(\pi^-\gamma \to \pi^-\eta)$ at the VES facility (Institute for High Energy Physics, Protvino) are consistent with the value of $N_c = 3$.

Hadronization as Valon Confinement in the Course of the Cooling of Nuclear Matter

I. I. Roizen and O. D. Chernavskaya

A modified three-phase model of the evolution of nuclear matter in the course of its cooling—from quark–gluon plasma through an intermediate phase that is saturated with massive constituent quarks Q (valons), pions, and kaons ($Q\pi K$) to hadronic matter (H)—is used to calculate the relative multiplicities of various sorts of hadrons produced in the central pseudorapidity region in collisions of ultrarelativistic heavy ions. The intermediate $Q\pi K$ phase is considered in detail; it is proven that the perfect-gas approximation is indeed applicable here. This phase must exist until the mean spacing between valons reaches the confinement radius (at a temperature of $T_H \simeq 110 \pm 5$ MeV), in which case valons are quickly bound, forming final hadrons. For the yields of various hadrons, the results are presented that were computed by means of a thermodynamic description of the $Q\pi K$ phase and a simple combinatorial mechanism of the hadronization process, and it is shown that these results are in good agreement with experimental data obtained at the AGS, SPS, and RHIC accelerators. The approach under consideration represents an alternative view on the nature of the observed yields of hadrons. To a considerable extent, this approach is free from obvious problems plaguing commonly known models that assume the possibility of an early (high-temperature) freezing of the chemical composition of hadronic matter (there, a medium whose density is higher than the density of hadronic matter is unjustifiably considered in the approximation of a perfect hadron gas). Many predictions for the expected yields of hadrons are made both for the aforementioned facilities and for the LHC accelerator, which is being now constructed at CERN.

Photoproduction of J/ψ Mesons at High Energies in the Parton Model and in the k_T-Factorization Approximation

V. A. Saleev

Within the parton model and in the k_T-factorization approximation, the photoproduction of J/ψ mesons on protons at high energies is considered in the leading order in α_s. It is shown that, for a specific choice of

the charmed-quark mass and of the value for the J/ψ-meson wave function at the origin, the predictions given by the two approaches for the total cross sections describing the production of J/ψ mesons and for their z spectra are nearly coincident and are consistent with experimental data obtained at the HERA ep collider. At the same time, the parton model and the theory of semihard processes predict sharply different shapes of the transverse-momentum spectrum for J/ψ mesons and sharply different transverse-momentum dependences of the ratio of the cross sections for the production of longitudinally and transversely polarized J/ψ mesons. An experimental verification of this phenomenon may clearly demonstrate nontrivial effects of small-x physics.

Physics of Charmed Hadrons: An Experimental Survey

S. V. Semenov

Basic experimental results in charmed-particle physics that have been obtained over the past few years are surveyed. Prospects for studying the properties of charmed particles within the near future are discussed.

Results of a Numerical Integration of an Integral Equation for a Two-Fermion System

N. B. Skachkov and T. M. Solov'eva

A two-particle system is described by integral equations whose kernels are dependent on the total energy of the system. Such equations can be reduced to an eigenvalue problem featuring an eigenvalue-dependent operator. This nonlinear eigenvalue problem is solved by means of an iterative procedure developed by the present authors. The energy spectra of a two-fermion system formed by particles of identical masses are obtained for two cases, that where the total spin of the system is equal to zero and that where the total spin of the system is equal to unity. The splitting of the ground-state levels of positronium and dimuonium, the frequency of the transition from the ground state of orthopositronium to its first excited state, and the probabilities of parapositronium and paradimuonium decays are computed. The results obtained in this way are found to be in good agreement with experimental data.

Investigation of the Nucleon Spin in Neutrino Processes

S. I. Timoshin

The possibilities for deducing new information about the spin properties of nucleons from observables of the neutral-weak-current-induced deep-inelastic scattering of neutrinos and antineutrinos on polarized nucleons are discussed.

Relativistic Treatment of the Hard-Bremsstrahlung Process $pp \to pp\gamma$ and Possibility of Discriminating between Different Types of Nucleon–Nucleon Interaction

N. A. Khokhlov, V. G. Neudatchin and V. A. Knyr

Previous results of the present authors, who showed that observables of the hard-bremsstrahlung process $pp \to pp\gamma$ at beam energies ranging between 350 and 500 MeV are highly sensitive to the type of nucleon–nucleon potential (meson-exchange potentials versus the Moscow potential), are generalized by means of a relativistic analysis, which includes, above all, a modified current operator. As a result, the relevant cross sections decrease, while their angular dependence changes. However, the above high sensitivity to the type of potential survives and is observed even at the lowest beam energy of 280 MeV considered here, for which there are experimental data. They seem to favor one of the versions of the Moscow potential.

A Dependence of Fast-Particle Spectra in π^+, K^+, and p Interactions with Al and Au Targets at 250 GeV/c

N. M. Agababyan, M. R. Atayan, E. A. De Wolf, K. Dziunikowska, A. M. F. Endler, Z. Sh. Garutchava, G. R. Gulkanyan, R. Sh. Hakobyan, D. Kisielewska, W. Kittel, S. S. Mehrabyan, Z. V. Metreveli, K. Olkiewicz, F. K. Rizatdinova, N. A. Sotnikova, L. N. Smirnova, L. G. Sveshnikova, M. D. Tabidze, L. A. Tikhonova, A. V. Tkabladze, A. G. Tomaradze, F. Verbeure, Sh. M. Yandarbiev, and S. A. Zotkin

EHS/NA22 Collaboration

The A dependence of charged-particle spectra in π^+, K^+, and p interactions with Al and Au targets at 250 GeV/c is presented and compared with the predictions of the model of quark–gluon strings (QGS). It is

shown that the A dependence of the invariant inclusive charged-particle spectra with respect to the Feynman variable x is very weak between Al and Au targets. The QGS model leads a larger difference between fast-particle spectra for different beam particles both for Al and for Au targets. The prediction of the QGS model for the leading-particle spectrum over an energy range between 250 GeV and 10 TeV in pAu(Pb) reactions is in reasonable agreement with NA22 data and with the results of a cosmic-ray experiment.

Study of Single Muons with the Large-Volume Detector at the Gran Sasso Laboratory

M. Aglietta, E. D. Alyea, P. Antonioli, G. Badino, G. Bari, M. Basile, V. S. Berezinsky, F. Bersani, M. Bertaina, R. Bertoni, G. Bruni, G. Cara Romeo, C. Castagnoli, A. Castellina, A. Chiavassa, J. A. Chinellato, L. Cifarelli, F. Cindolo, A. Contin, V. L. Dadykin, L. G. Dos Santos, R. I. Enikeev, W. Fulgione, P. Galeotti, P. Ghia, P. Giusti, F. Gomez, R. Granella, F. Grianti, V. I. Gurentsov, G. Iacobucci, N. Inoue, E. Kemp, F. F. Khalchukov, E. V. Korolkova, P. V. Korchaguin, V. B. Korchaguin, V. A. Kudryavtsev, M. Luvisetto, A. S. Malguin, T. Massam, N. Mengotti Silva, C. Morello, R. Nania, G. Navarra, L. Periale, A. Pesci, P. Picchi, I. A. Pless, O. G. Ryazhskaya, O. Saavedra, K. Saitoh, G. Sartorelli, M. Selvi, N. Taborgna, V. P. Talochkin, G. C. Trinchero, S. Tsuji, A. Turtelli, P. Vallania, S. Vernetto, C. Vigorito, L. Votano, T. Wada, R. Weinstein, M. Widgoff, V. F. Yakushev, I. Yamamoto, G. T. Zatsepin, and A. Zichichi

The LVD Collaboration

The present study is based on a sample of 2.9×10^6 single muons observed by the large-volume detector (LVD) at the underground Gran Sasso Laboratory throughout 36 500 live hours from June 1992 to February 1998. We measured the muon intensity at slant depths from 3 to 20 km w.e. The majority of the events were induced by high-energy downward muons produced by meson decays in the atmosphere. The analysis of these muons revealed that the power-law index γ of the π and K spectrum is $\gamma = 2.76 \pm 0.05$. The remainder are horizontal muons produced by neutrino interactions in the rock surrounding the LVD. The value of this flux near 90° is $(6.1 \pm 2.7) \times 10^{-13}$ cm^{-2} s^{-1} sr^{-1}. The results are compared with Monte Carlo simulations and with world-averaged data.

Three-Body Dispersion-Relation N/D Equations for the Coupled Decay Channels $\bar{p}p\ (J^{PC} = 0^{-+}) \to \pi^0\pi^0\pi^0, \eta\pi^0\pi^0, \eta\eta\pi^0, \bar{K}K\pi^0$

A.V. Anisovich

For a few years, the data of the Crystal Barrel collaboration on various $\bar{p}p(J^{PC} = 0^{-+}) \to$ *three mesons* channels have been successfully analyzed by extracting the leading amplitude singularities (pole singularities) with the aim of obtaining information about two-meson resonances. But these analyses did not take into account three-body final-state interactions in an explicitly correct way. This problem is considered in the present study. Here, it is demonstrated how the coupled three-body equations may be written for the $\pi^0\pi^0\pi^0$, $\eta\pi^0\pi^0$, $\eta\eta\pi^0$, and $\bar{K}K\pi^0$ channels in $\bar{p}p$ annihilation at rest by using the three-body dispersion-relation N/D method.

Analytic Estimates of the Product Yields for Nuclear Reactions at Ultralow Energies

V. M. Bystritsky and F. M. Pen'kov

Simple analytic expressions for estimating product yields from reactions between light nuclei at ultralow collision energies are given. It is shown that, even in the case of total-absorption targets and of a large spread of incident-beam energies, these expressions can be factorized and naturally define the effective target thickness and the range of particle collision energies in the entrance channel that defines the yield of reaction products.

Neutron Scattering in Argon and *ne* Interaction

T. L. Enik, V. A. Ermakov, R. V. Kharjuzov, L. V. Mitsyna, V. G. Nikolenko, S. S. Parzhitski, A. B. Popov, G. S. Samosvat, and V. A. Vtjurin

As a preparation for a new experiment to measure the ne scattering length a_{ne}, the total neutron cross section for gaseous argon was determined by the time-of-flight method at the Dubna booster IBR-30 in the energy range from about 5 eV to about 30 keV. A combined one-level analysis of the newly obtained and other

known data on the cross sections for Ar and ^{36}Ar made it possible to refine some neutron parameters and to calculate the scattering cross section σ_s and the scattering length a separately for ^{36}Ar and ^{40}Ar at any energy.

nd Scattering at Low Energies in a Two-Body Potential Model

Yu. V. Orlov and Yu. P. Orevkov

The S-wave phase shift $\delta(E)$ for the spin-doublet nd scattering at a low energy E is calculated within a two-body approach. The effective-range-theory formula $k\cot\delta = (1+k^2/\kappa_0^2)^{-1}(-1/a + C_2k^2 + C_4k^4)$ is used to obtain approximate analytic results with various potentials. The corresponding coefficients C_2 and C_4 are obtained from our previous calculations of the asymptotic normalization parameter function $C_T^2(a\kappa)$, where κ is the triton wave number and a is the doublet nd scattering length. The model describes $\delta(E)$ reasonably well, the results being quite sensitive to the choice of effective nd potential.

Spacetime Symplectic Extension

Yu. F. Pirogov

It is conjectured that, at the origin of spacetime, there lies a symplectic rather than metric structure. The complex symplectic symmetry $Sp(2l, C)$, $l \geq 1$, instead of the pseudoorthogonal one $SO(1, d-1)$, $d \geq 4$, is proposed as the spacetime group of local structure. A discrete sequence of metric spacetimes of fixed dimensionalities $d = (2l)^2$ and signatures, with $l(2l-1)$ timelike and $l(2l+1)$ spacelike directions, defined over a set of Hermitian rank-2 spin-tensors, is considered as an alternative to pseudo-Euclidean extra-dimensional spacetimes. The basic concepts of the symplectic framework are developed in general, and the ordinary and next-to-ordinary spacetime cases with $l = 1$ and 2, respectively, are elaborated in more detail. In particular, the scheme provides the rationale for the four dimensions and $1+3$ signature of ordinary spacetime.

Leading-Particle Effects in the Spectra of Λ_c and $\overline{\Lambda}_c$ Baryons Produced in $\Sigma^- p$, pp, and $\pi^- p$ Interactions

O. I. Piskounova

The spectra of leading and nonleading charmed baryons (Λ_c and $\overline{\Lambda}_c$) and the asymmetries between these spectra measured in $\Sigma^- A$, $\pi^- A$, and pA collisions at $p_L = 600$ GeV/c in the E781 experiment are simultaneously described within the model of quark–gluon strings (QGS model or QGSM). It is shown that the charmed-baryon spectra can be fitted by QGSM curves calculated with the diquark-fragmentation parameter of $a_f^{\Lambda_c} = 0.006$. It was found in that experiment that the asymmetry between the spectra of Λ_c and $\overline{\Lambda}_c$ in $\pi^- A$ collisions is of nonzero value. It may be described in our model only under the assumption that the string junction is transferred from a target proton to the kinematical region of projectile-pion fragmentation.

Nonperturbative Quark Dynamics in a Baryon

Yu. A. Simonov

The method of field correlation functions is used to calculate the nonperturbative dynamics of quarks in a baryon. A general expression for the $3q$ Green's function is obtained by using the Fock–Feynman–Schwinger (world-line) path-integral formalism, where dynamics is entirely contained in the $3q$ Wilson loop with spin-field insertions. Using the lowest cumulant contribution for the Wilson loop, one obtains a Y-shaped string with a deep hole at the string-junction position. Using the einbein formalism for the quark kinetic terms, one automatically obtains constituent quark masses calculable in terms of the string tension.The resulting effective action for $3q$ plus Y-shaped strings is quantized in the path-integral formalism to produce two versions of Hamiltonian, one in the c.m. and the other in the light-cone system. The hyperspherical formalism is used to calculate masses and wave functions. Simple estimates in the lowest approximation yield baryon masses in good agreement with experimental data without fitting parameters.

Generation of the Angular Momentum of Fission Fragments in the Cluster Model

T. M. Shneidman, G. G. Adamian, N. V. Antonenko, S. P. Ivanova, R. V. Jolos, and W. Scheid

The role of bending vibrations in generating the angular momentum of primary fission fragments is investigated on the basis of the dinuclear-system concept. For the spontaneous fission of ^{252}Cf, the angular momenta of fragments are calculated versus the neutron multiplicity and are compared with available experimental data. Various cluster compositions of the ^{252}Cf fission modes at the scission point are considered.

Search for Solar *pp* Neutrinos on the Basis of an Upgrade of the CTF Detector

O. Yu. Smirnov, O. A. Zaimidoroga, and A. V. Derbin

The possibility of using an ultrapure liquid organic scintillator as a low-energy solar-neutrino detector is discussed. The detector having an active volume of 10 tons and a 4π coverage will count 1.8 *pp* neutrinos and 5.4 ^{7}Be neutrinos per day with an energy threshold of 170 keV for recoil electrons. The evaluation of the detector sensitivity and backgrounds is based on the results obtained by the Borexino collaboration with the counting test facility (CTF). A detector can be built at the LNGS underground laboratory as an upgrade of the CTF detector by using already developed technologies. The investigation was performed at the Laboratory of Particle Physics at the Joint Institute for Nuclear Research (JINR, Dubna) and the Petersburg Nuclear Physics Institute (PNPI, Gatchina).